



**US Army Corps
of Engineers**
Waterways Experiment
Station

AD-A270 195



Technical Report CERC-93-16
September 1993

②

Hydrodynamic and Water Quality Modeling of Lower Green Bay, Wisconsin

Volume I Main Text and Appendixes A-E

*by David J. Mark, Norman W. Scheffner,
H. Lee Butler
Coastal Engineering Research Center*

*Barry W. Bunch, Mark S. Dortch
Environmental Laboratory*

DTIC
S **ELECTE** **D**
A **UCT 06 1993**

Approved For Public Release; Distribution Is Unlimited

93 10 5 149

Prepared for U.S. Army Engineer District, Detroit

93-23369



37576

The contents of this report are not to be used for advertising, publication, or promotional purposes. Citation of trade names does not constitute an official endorsement or approval of the use of such commercial products.



PRINTED ON RECYCLED PAPER

Hydrodynamic and Water Quality Modeling of Lower Green Bay, Wisconsin

Volume I

Main Text and Appendixes A-E

by David J. Mark, Norman W. Scheffner,
H. Lee Butler
Coastal Engineering Research Center
Barry W. Bunch, Mark S. Dortch
Environmental Laboratory
U.S. Army Corps of Engineers
Waterways Experiment Station
3909 Halls Ferry Road
Vicksburg, MS 39180-6199

Accession For		
NTIS	CRA&I	<input checked="" type="checkbox"/>
DTIC	AS	<input type="checkbox"/>
Unannounced		<input type="checkbox"/>
Justification		
By		
Distribution/		
Availability Codes		
Dist	Avail and/or Special	
A-1		

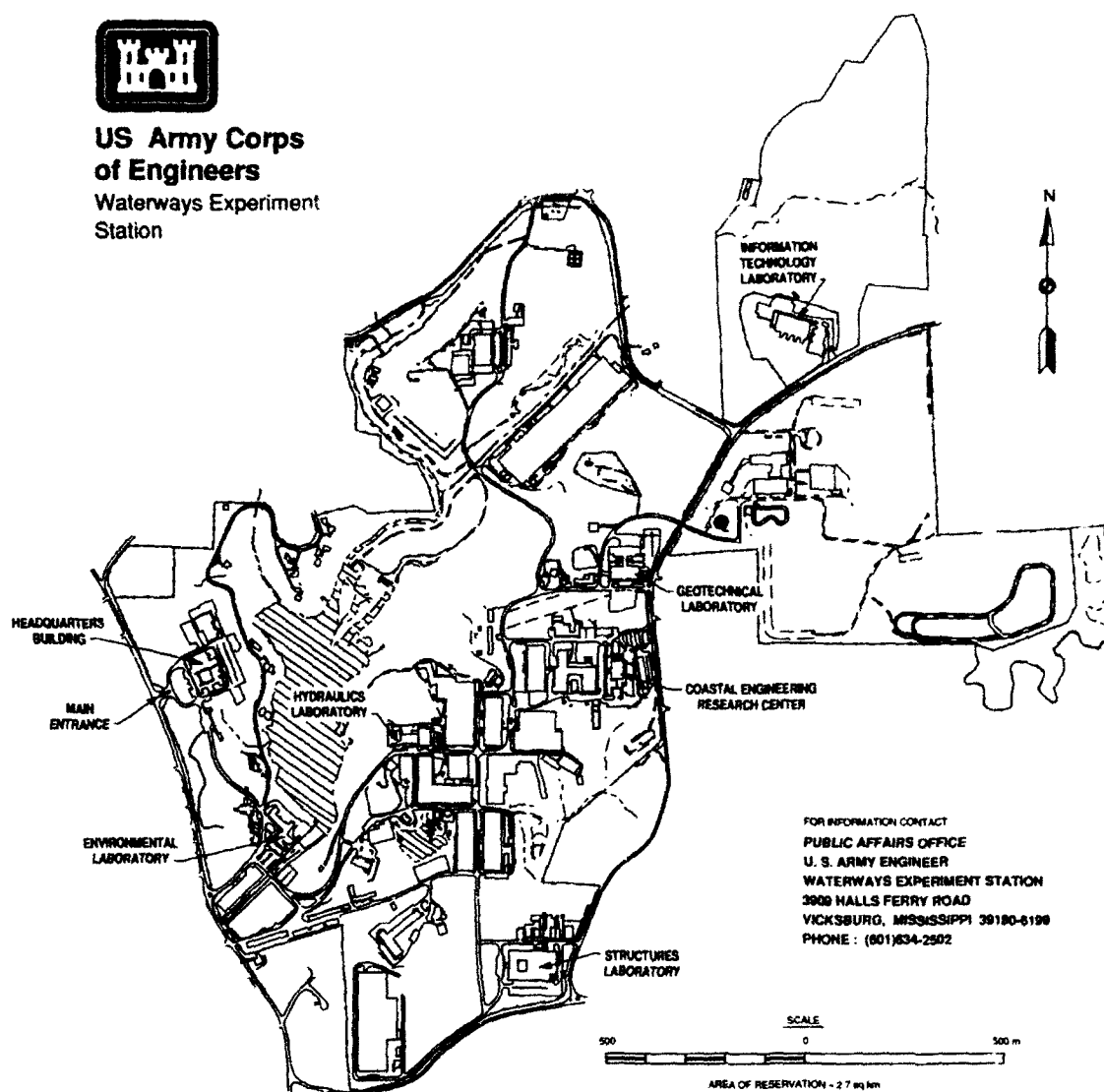
Final report

Approved for public release; distribution is unlimited

Prepared for U.S. Army Engineer District, Detroit
Detroit, MI 48231-1027



**US Army Corps
of Engineers**
Waterways Experiment
Station



Waterways Experiment Station Cataloging-in-Publication Data

Mark, David J.

Hydrodynamic and water quality modeling of lower Green Bay, Wisconsin. Volume I, Main text and appendixes A-E / by David J. Mark ... [et al.], Coastal Engineering Research Center ; prepared for U.S. Army Engineer District, Detroit.

377 p. : ill. ; 28 cm. — (Technical report ; CERC-93-16 vol. 1)

Includes bibliographical references.

1. Water quality — Green Bay (Wis. and Mich.) — Mathematical models. 2. Hydrodynamics — Mathematical models. 3. Green Bay (Wis. and Mich.) I. Mark, David J. II. United States. Army. Corps of Engineers. Detroit District. III. Coastal Engineering Research Center (U.S.) IV. U.S. Army Engineer Waterways Experiment Station. V. Series: Technical report (U.S. Army Engineer Waterways Experiment Station) ; CERC-93-16 vol. 1.

TA7 W34 no.CERC-93-16 v.1

Contents

Preface	v
Conversion Factors, Non-SI to SI Units of Measurement	vii
1—Introduction	1
Description of Kidney Island	2
Overview of Previous Studies	3
Scope of Work	7
Organization of Report	9
2—Field Data Acquisition	10
Overview of Hydrodynamic and Meteorological Processes	10
Review of Physical Data	14
Review of Water Quality Data	17
3—Description of the Hydrodynamic Model	23
Governing Equations	23
Transformation of Governing Equations	27
Non-Dimensionalization of Governing Equations	30
Finite Difference Approximations of Governing Equations	32
4—Implementation of the Hydrodynamic Model	35
Numerical Grid Development	35
Calibration of the Hydrodynamic Model	44
Validation of the Hydrodynamic Model	54
Diagnostic Analyses of Calibration and Validation Results	57
Wind Drag Formulation	69
5—Description of the Water Quality Model	74
General Structure	74
Solution Schemes	76
Linkage to Hydrodynamic Model	76
Kinetic Formulations	78
6—Calibration of the Water Quality Model	81
Transport Verification	81
Water Quality Calibration	83
Calibration Input Data	83
Calibration Evaluation Methods	85

7—Scenario Descriptions and Results	139
Scenario Conditions	140
Meteorological Conditions	141
Selection of Seiche/Wind Events	142
Selection of River Flow Rates	144
Selection of Long-Term Lake Levels	152
Analysis of Hydrodynamic Impacts Resulting from CDF Expansion ..	152
Input Description for Water Quality Scenario Analyses	160
Methods of Scenario Analysis	162
Water Quality Scenario Results	165
8—Investigation of Sediment Resuspension Potential	181
Description of Modeling Algorithm	181
Application of Modeling Approach	183
9—Summary and Conclusions	190
References	195
Appendix A: Charter of the Technical Review Panel	A1
Appendix B: Water Quality Model Kinetic Formulations	B1
Appendix C: Water Quality Model Kinetic Notation and Units	C1
Appendix D: Water Quality Model Scenario Figures	D1
Appendix E: DO Measurements During August 1992	E1
SF 298	

Preface

This report describes the results of a combined hydrodynamic, sediment transport, and water quality modeling effort undertaken to investigate the water quality impact of enlarging an existing confined disposal facility (CDF) in lower Green Bay, Wisconsin. The CDF is used for the disposal of dredged material from the Green Bay/Fox River navigation channel. The report describes the various components of the study and presents details of the prototype data used in the hydrodynamic and water quality computations. Comparisons of hydrodynamic and water quality results are shown to demonstrate the impact of the proposed CDF modification on the lower Green Bay area. This study was performed as a joint endeavor between the U.S. Army Engineer Waterways Experiment Station's (WES) Coastal Engineering Research Center (CERC) and Environmental Laboratory (EL) for the U.S. Army Engineer District, Detroit (CENCE). The CERC's responsibilities included developing, testing, and implementing a long wave, two-dimensional hydrodynamic model for simulating currents within the lower bay. The EL's duties included simulating transport and fate of water quality constituents (e.g., dissolved oxygen) with a two-dimensional water quality model.

A Technical Review Panel (TRP) was established to provide oversight on model development and application. The guidance provided by the TRP during the course of this study was extremely helpful, and appreciation is extended to the following TRP members: Dr. Keith W. Bedford, professor, Ohio State University; Dr. David Lam, Environment Canada National Water Research Institute (Burlington, Canada); Dr. Kwang Lee, professor, University of Wisconsin at Milwaukee; Mr. Dale Patterson, Wisconsin Department of Natural Resources; and Dr. Steve McCutcheon, U.S. Environmental Protection Agency. Appreciation is also extended to Messrs. W. Scott Parker, Deputy District Engineer, Programs and Project Management Division (PPM); Robert L. Gregory, PPM; and David Barilovich, Engineering Division of the CENCE. The final report was prepared by Mr. David J. Mark, CERC, and Drs. Barry W. Bunch, EL, Norman W. Scheffner, CERC, and Mark S. Dortch, EL. Description of the hydrodynamic model was written by Ms. Mary A. Cialone, CERC, and Dr. Billy Johnson, HL. Report preparation was aided by Messrs. Fulton C. Carson, CERC, and C. Jace Pugh, EL, together with Ms. C. Jaudon McKay, CERC.

The hydrodynamic component of this study was performed under the general supervision of Dr. James R. Houston and Mr. Charles C. Calloun, Jr.,

Director and Assistant Director, respectively, CERC. Direct supervision of the hydrodynamic portion of this project was provided by Mr. H. Lee Butler, Chief, Research Division, and Mr. Bruce A. Ebersole, Chief, Coastal Processes Branch, Research Division, CERC. Near the completion of this study, supervision was provided by Dr. Martin Miller, Chief, Oceanography Branch, Research Division, CERC.

General supervision for the water quality component of this study was performed by Drs. John Harrison and John W. Keeley, Director and Assistant Director, respectively, Environmental Laboratory (EL). Direct supervision was provided by Dr. Donald L. Robey, Chief, Ecosystem Research and Simulation Division, and Dr. Mark S. Dortch, Group Chief, Ecosystem Research and Simulation Division, Water Quality Modeling Group, EL. Mr. Butler served as project manager.

During the early phases of this study, COL Larry B. Fulton, EN, was Commander and Director of WES and Dr. Robert W. Whalin was Technical Director. In January 1992, COL Leonard G. Hassell, EN, became Commander of WES and Dr. Robert W. Whalin became Director. At the time of publication of this report, COL Bruce K. Howard was Commander of WES and Dr. Robert W. Whalin was Director.

Conversion Factors, Non-SI to SI Units of Measurement

Non-SI units of measurement used in this report can be converted to SI units as follows:

Multiply	By	To Obtain
acres	4,046.873	square meters
cubic feet	0.02831685	cubic meters
dyne	0.00001	newtons
feet	0.3048	meters
knots (international)	0.5144444	meters per second
miles (U.S. statute)	1.609347	kilometers

1 Introduction

As one component of its mission, the U.S. Army Engineer District, Detroit (CENCE) is responsible for maintaining the navigation channel servicing the Port of Green Bay, WI. During maintenance operations, the CENCE deposits dredged material in a confined disposal facility (CDF) named Kidney Island, located in close proximity to Green Bay's southern shore (Figure 1). Originally constructed in 1979, Kidney Island will reach its capacity in 1993, necessitating the need for developing a new CDF. One possible solution involves expanding Kidney Island. However, because the CDF is in close proximity to the Fox River mouth, where high waste loads exit the river, concern exists that the expansion may adversely affect water quality conditions in the lower bay. By modifying current patterns, greater quantities of pollutants may be transported into regions of the lower bay which serve as spawning waters.

Waste loads entering lower Green Bay via the Fox River can be attributed, in part, to seven major point source dischargers releasing treated industrial and municipal wastes below DePere Dam. Additional loadings can be attributed to effluent discharged upstream of the dam. Five papermills/packaging plants and two public wastewater treatment plants discharge into the 7.3-mile¹ reach of the Fox River between its mouth and DePere Dam. Both the lower Fox River and lower bay exhibit eutrophic conditions during much of the summer; these systems can be characterized by elevated nutrient and algal concentrations as well as low Secchi depths. Furthermore, dissolved oxygen data measured in regions of the lower bay contain measurements where concentrations were lower than the State of Wisconsin water quality standard for dissolved oxygen (i.e., 5 mg/L) during brief periods in the summer.

This report describes the hydrodynamic and water-quality modeling approach used for determining whether the proposed expansion of Kidney Island will adversely impact water quality conditions in lower Green Bay. The hydrodynamic model is used for estimating current patterns in the lower bay. This information is subsequently used as input to the water quality model for predicting the transport of water quality constituents, such as dissolved oxygen. The assessment as to whether the CDF will impact water quality conditions is

¹ A table of factors for converting non-SI units of measurement to SI units is presented on page vii.

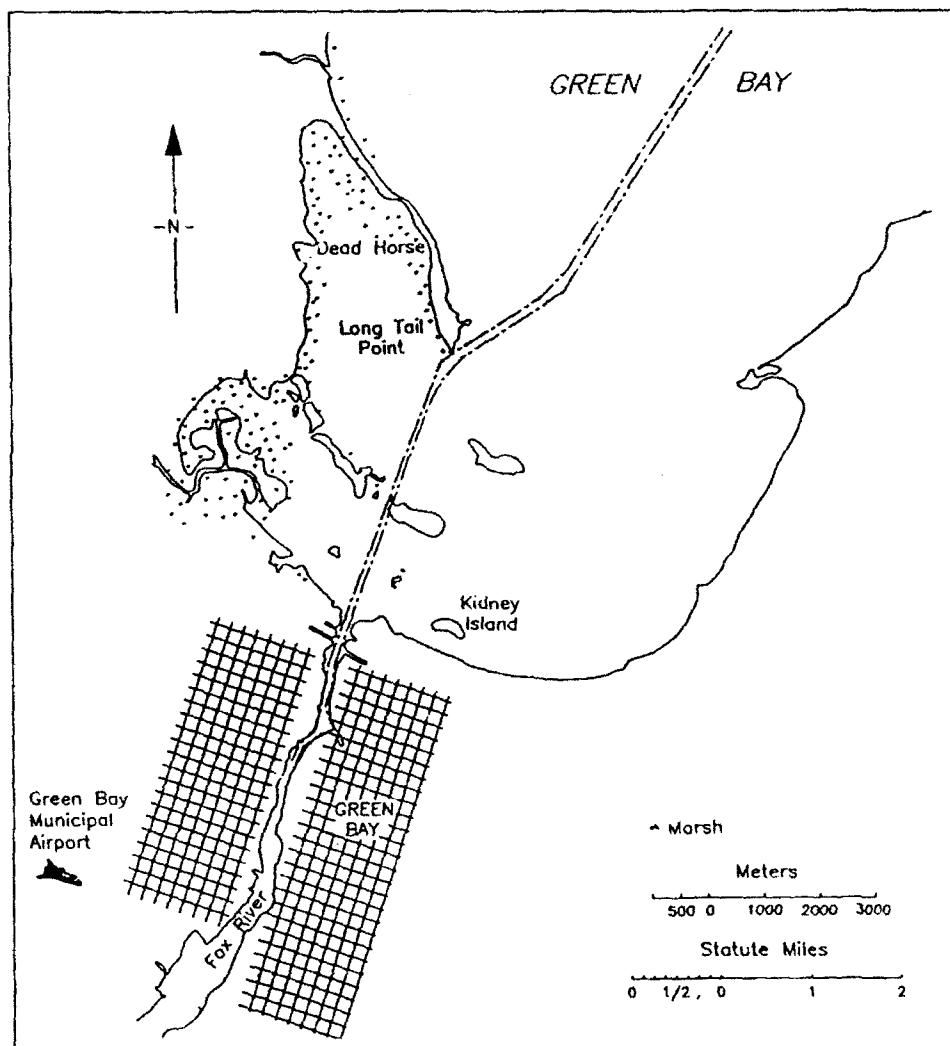


Figure 1. Lower Green Bay location map

made by comparing simulated spatial and temporal variations in dissolved oxygen concentrations between pre- and post-expansion CDF configurations.

Description of Kidney Island

Kidney Island is located approximately 3,600 ft east of the Green Bay Harbor entrance channel and about 800 ft north of the shoreline. Presently, this island has a planform area of 55 acres, and is enclosed with a rock dike having a crest elevation 10 ft above the low-water datum of 576.8 ft International Great Lakes Datum (IGLD) of 1955. A single layer of interlocking sheetpiling serves as a cutoff wall and runs along the center of the dike to prevent leakage of dredged material into the surrounding waters. Primary treatment of water draining from the CDF is accomplished via a series of weirs and sand filters to remove suspended solids from the effluent.

As shown in Figure 2, the proposed expansion will be constructed immediately north of the existing CDF, and will have essentially the same shape as the original facility. The western edge of the proposed expansion will be located approximately 2,750 ft from the navigation channel. The expansion will have a planform area of 126 acres, and the enclosing dike will have a crest elevation of 14 ft, or 4 ft above the original structure. As with the original CDF, only dredged material will be deposited in this facility, and a cutoff wall will prevent contamination of surrounding waters.

Overview of Previous Studies

The expansion of Kidney Island was initially proposed in the early 1980s. In 1983, the CENCE contracted a study to Dr. Kwang W. Lee, professor in the Department of Civil Engineering at the University of Wisconsin at Milwaukee, to estimate the impacts of the proposed expansion. In his study, Dr. Lee concluded that the expansion had the potential to adversely impact water quality conditions and, through changing sediment resuspension and deposition patterns, create navigational hazards in certain areas of the lower bay. After a preliminary review of the report, the CENCE requested that the U.S. Army Engineer Waterways Experiment Station (WES) review Dr. Lee's study.

Several issues were raised by WES concerning the conclusions drawn by Dr. Lee. First, the model was calibrated and validated with time-series studies of measured water surface levels collected at two gauges. These gauges were located at the confluence of the East and Fox Rivers and at the Pulliam Power Plant, which is situated at the Fox River mouth. A model calibrated solely with water surface levels only assures that the model conserves mass and can accurately reproduce wave propagation. It does not, however, ensure that the model reproduces current patterns because the model can significantly over- and underestimate water velocities while satisfactorily reproducing water surface elevations. Since the model was tested solely with measured water surface levels, and was tested against data collected at only one site within the bay proper, there is no assurance that the current patterns generated with the model are accurate. Calibrating and validating the model with measured velocities would ensure the accuracy of model-generated current patterns.

Second, model results presented by Dr. Lee were not sufficient to support the conclusions discussed in his report. For example, Dr. Lee noted that expanding the present CDF will result in increased flows entering Peats Lake and thereby concludes that water quality and the nutrient budget in this region will be affected. However, no assessment is presented to quantify the change in water volume being transported into Peats Lake. Furthermore, no qualitative or quantitative assessment was made to estimate the change in nutrient or contaminant loadings entering, or the change in water quality conditions within this region. Concerning sediment resuspension and deposition, no analysis was presented to qualify or quantify changes in these processes other than noting an increase in water velocities in some areas of the lower bay. Thus, the conclusions presented in Lee (1984) were based on conjecture as opposed to an analysis of the modeling results.

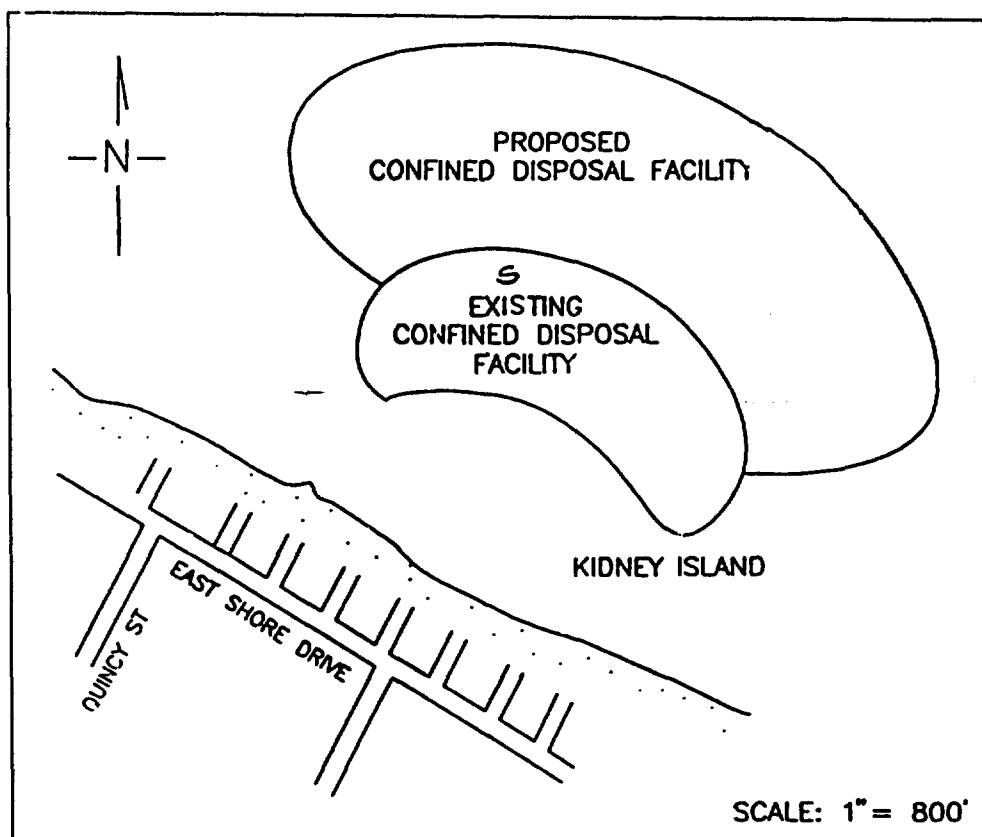


Figure 2. Green Bay existing and proposed CDF configuration

After reviewing the limitations of the original study, the CENCE rejected the findings presented in Lee (1984) and requested that WES conduct a study to estimate potential impacts on water quality conditions. The WES study is documented in Swain and Bird (1987). Techniques used, along with data required for model calibration and validation, were discussed with and obtained from the Wisconsin Department of Natural Resources (WDNR).

During the initial certification process, the WDNR requested that the Corps address their concern that the expansion would reduce mixing of the river and bay waters at the river mouth, thereby decreasing the assimilative capacity of waters, adversely impacting water quality conditions in this zone. While the state initially requested that the Corps perform a water quality study focusing on impacts of the proposed project on dissolved oxygen (DO) levels at the mouth of the river, a compromise was reached whereby a combined hydrodynamic and mass transport model to calculate circulation and mass transport in the lower bay for both existing and proposed CDF configurations would suffice. Instead of modeling DO, a conservative tracer was used to depict the transport of pollutants through the river/bay system.

A series of dynamic steady-state scenarios (i.e., steady river flows and seiches) were used to estimate the impact on water quality conditions. One series of tests examined the distribution of Fox River discharge as it enters the bay to quantify the percentage of discharge flowing into the eastern, central,

and western regions of the lower bay. This test was designed to address the conclusion presented in Lee (1984) that the CDF expansion would result in greater river flows entering Peats Lake. Test results show an insignificant change in river water transported into this region as a result of expanding Kidney Island, thus refuting the claim made in Lee (1984).

A second series of tests examined the transport of a conservative substance through the Fox River/lower Green Bay system. This series is composed of three tests, each having a different flow rate specified at the DePere Dam boundary. Average lake level, wind velocity, and seiche period and amplitude were specified in each simulation. These tests were conducted where the lower bay is represented by both the existing and proposed CDF configurations. Flow field parameters were stored for subsequent input to the mass transport model.

For each of the scenarios described above, the conservative substance (or tracer) was added to the system either as an instantaneous or as a continuous release. It was found that, for the instantaneous release tests, the CDF expansion does not significantly affect the transport of material within the lower bay. For the continuous release cases, very little difference in concentrations is noted in the Fox River and in the navigation channel. An insignificant change in concentration is found at locations west of the channel.

Upon the completion of this study, the CENCE submitted the model and its results to the WDNR for their review. The WDNR performed a limited study in estimating impacts on dissolved oxygen resulting from the CDF expansion. Based on steady-state tracer concentrations supplied by WES, the WDNR averaged the tracer concentrations within the east, north, west, and south regions of the critical zone encompassing the Fox River mouth. Making several assumptions in forming a relationship between the conservative tracer and a biochemical-oxygen-demanding (BOD) substance, the WDNR estimated the change in dissolved oxygen concentrations would be less than 0.04 mg/L. Noting no appreciable change in dissolved oxygen, the WDNR concluded that the expansion of Kidney Island would not result in a violation of the state's dissolved oxygen standards.

In April 1987, the WDNR issued a Notice of Preliminary Determination of Water Quality Certification to the CENCE. Following state statutes, the state advertised their intention to issue a construction permit to the Corps of Engineers for expanding Kidney Island.

The Wisconsin Department of Justice Public Intervenor's Office (PIO) took exception to this action and acquired the assistance of Dr. Lee as their primary technical expert to challenge the WES report. In a report sponsored by the PIO, Dr. Lee provided a review and critique of the hydrodynamic and transport modeling effort performed by WES. Criticisms expressed by Dr. Lee include:

- a. The rectilinear grid, despite its high resolution, is incapable of resolving irregular landforms or features.

- b. The grid boundaries for the transport model are too close to the critical zone, degrading modeling results.
- c. Tracer concentrations specified at the boundaries, chosen because they were representative of point source BOD distributions, provide a distorted solution because the BOD distribution in the lower bay does not resemble the single source conservative tracer distribution.
- d. The transport model was not calibrated or validated, therefore, model results are questionable.
- e. Only a limited number of conditions were simulated, neglecting reasonable ranges in conditions (e.g., variability in long-term lake levels).

Additional criticisms were made by Dr. Lee concerning the analysis procedures used by the WDNR to assess DO impacts. First, averaging the tracer concentrations within the critical zone limits the maximum DO impact. Second, the analysis ignored ambient water quality conditions, or loadings presently in the water. Third, the logic of relating a non-conservative substance, such as BOD, to a conservative substance is inaccurate. Dr. Lee concludes that the model results are inadequate to conclude that the expansion will not adversely impact waste-load allocation and other water quality concerns.

A hearing was held in January 1988 in which the state was the primary respondent. Pre-hearing testimony was taken from Dr. Lee and two state officials, including Mr. Dale Patterson of the WDNR. At the subsequent hearing, Dr. Lee and the two state officials presented the major testimony, essentially repeating their pre-hearing information.

In August 1988, the hearing examiner, Mr. Patrick T. Currie, issued a Findings of Facts which reversed the initial determination by the WDNR to grant a water quality certification for the CDF expansion. This decision was reviewed by the Secretary of the WDNR, Mr. Carroll D. Besadny. In February 1989, the hearing examiner's decision was substantially amended. The key findings contained in the Decision on the Petition for Review include:

Fact 26. "The analysis by the department, based on information supplied to it by the Corps, inadequately evaluated the impacts on dissolved oxygen caused by the redistribution of biochemical oxygen-demanding contaminants. In the evaluation, results in the critical zone, which encompassed 16 RMA nodes and 81 Corps nodes, were averaged to estimate the impact of the CDF expansion. This averaging underestimates the maximum impact to DO. In order to determine if the activity will cause a violation of the DO standard, it is necessary to estimate the impact on the individual nodes rather than the average impact within the critical zone."

Fact 27. "There is not a reasonable assurance the activity will be conducted in a manner which will not result in a violation of the 5 mg/L DO standard in Green Bay, including the area known as Peats Lake. Consequently there is not a reasonable assurance that the activity will be conducted in a manner which

will not result in a violation of the water quality standard adopted under section 144.025 (2)(b), Wis. Stats., as required by section MR 299.05(1)(b)3., Wis. Adm. Code."

Although the hearing examiner's decision was amended, the Secretary of the WDNR, Mr. Besadny, upheld the decision to deny issuing the water quality certification for constructing the CDF expansion.

Scope of Work

In 1990, the CENCE requested that WES aid them in developing a study approach that would successfully address the concerns and satisfy the requirements specified in the Besadny decision. A scope-of-work for a third study, to be conducted by WES, was developed with input and cooperation provided by the WDNR, PIO, and its chief expert witness, Dr. Lee.

The agreed scope of work consisted of three major tasks. The first task involves developing a depth-integrated hydrodynamic model of lower Green Bay. It was recognized by the participants in scoping this study that: 1) the lower bay is very shallow and is well mixed most of the time and the primary hydrodynamic processes can be adequately described by a two-dimensional model approach, and 2) no existing model could accurately depict every hydrodynamic and water quality process in this extremely complicated system. All previous studies of the lower bay realized these facts and adopted a two-dimensional model approach, including the study conducted by the State of Wisconsin for developing waste-load allocation (Patterson 1984).

The hydrodynamic model selected by WES employs a boundary-fitted computational grid for smoothly depicting irregular coastal landforms. This feature addresses a concern of the previous WES study (i.e., Swain and Bird 1987) that a rectilinear grid is incapable of representing Kidney Island and bathymetry gradients in shallower regions.

The second task is the development of a water quality model for directly measuring potential impacts on DO concentrations. Water quality constituents affecting DO concentrations are simulated via their kinetic processes. In addition to DO, modeled constituents include algae, labile and refractory carbonaceous BOD, temperature, nitrate-nitrogen, ammonium-nitrogen, total organic nitrogen, total organic phosphorus, and orthophosphate-phosphorous. Furthermore, sediment oxygen demand is specified as a benthic boundary condition, and reaeration is simulated using a wind-driven, gas transfer formulation. There are also provisions for a conservative tracer.

The assessment of whether the proposed CDF expansion will adversely impact water quality conditions will be made by comparing changes in DO concentration patterns resulting from the expansion. Furthermore, water quality will be tested over a range of plausible hydrodynamic and hydrologic conditions. For example, tests will be conducted using several river flows, seiche conditions and lake levels, reflecting the historical range in levels for the lower

bay. Also, the study will address water quality in the mid- to late-summer time span, or when the water temperature is highest and the demand for DO is at its greatest.

The third task involves estimating changes in sediment resuspension potential in the lower bay as a result of the proposed expansion. Nutrients and toxins have an affinity for cohesive sediment, such as clays and silts, and can be adsorbed by sediment particles. Furthermore, elevated polychlorobiphenyls and heavy metal concentrations have been found in sediment cores collected in the lower bay (Kennedy 1991). A potential increase in concentrations of these materials in the water column could be induced by higher current velocities and the associated resuspension of cohesive sediment which had adsorbed these materials prior to deposition. A qualitative assessment is made by determining those areas in the lower bay where the potential for sediment resuspension will increase due to expanding Kidney Island. This qualitative assessment focuses on delineating those areas that can be expected to experience an increase in bottom shear stress, the process controlling resuspension of sediment.

A Technical Review Panel (TRP) was established as an advisory body to provide expert review and guidance on model development and application as well as to provide technical oversight for this study effort. The panel's charter is presented in Appendix A. Prospective TRP members were nominated by the CENCE, PIO, and WES. Qualifications for serving as a TRP member include technical expertise in hydrodynamic and/or water quality modeling, experience in performing modeling studies conducted in the Great Lakes and familiarity with water quality problems associated with the Great Lakes. Members serving on the TRP were: Dr. Keith W. Bedford, Ohio State University; Dr. David Lam, Environment Canada; Dr. Kwang W. Lee, University of Wisconsin-Milwaukee; Dr. Steven McCutcheon, U.S. Environmental Protection Agency; and Mr. Dale Patterson, WDNR.

Serving in a technical advisory capacity, the TRP is to provide technical oversight and guidance for this study effort. As such, the TRP operated and made recommendations by consensus. However, recommendations made by the TRP were not required to be unanimous.

The objective of this study is to assess potential impacts on water quality conditions in lower Green Bay resulting from modified current patterns induced by the CDF expansion. It is not the intent of the Corps that the model documented in this report be perceived to support, supersede, or undermine the waste-load allocation (WLA) model presently in use by the WDNR. The "Corps" model was developed to simulate phenomena at different spatial and temporal scales than those represented in the WLA model. Application of the Corps model to investigate phenomena other than those for which it was developed may not be appropriate and is, therefore, not recommended.

Organization of Report

This report is divided into nine chapters, with the first chapter being the introduction. Chapter 2 provides an overview of the dominant hydrodynamic and water quality processes of the lower bay, together with an analysis of prototype data collected within the study area. The governing equations and solution algorithm contained in the hydrodynamic model, and its implementation to lower Green Bay are discussed in Chapters 3 and 4, respectively.

The water quality model is described in Chapter 5, and its implementation to the lower bay is described in Chapter 6. Chapter 7 contains a description and analysis of the series of scenarios that were performed to assess the impact of the expansion on the water quality in lower Green Bay. A qualitative investigation of potential increases in sediment resuspension is presented in Chapter 8. A summary of project tasks, together with the conclusions drawn by WES from the modeling results, are presented in Chapter 9. Conclusions presented in this chapter do not necessarily reflect those drawn by the TRP.

2 Field Data Acquisition

The basic purpose of the lower Green Bay study is to investigate potential impacts on water quality resulting from the expansion of the Kidney Island CDF. Current patterns within the lower bay may be modified by expanding the CDF, resulting in greater quantities of pollutants being transported into areas that are relatively unaffected by the pollutants. Hydrodynamic, meteorologic, and water quality data are required for calibrating and validating the numerical models used for simulating the hydrodynamic and water quality processes occurring in lower Green Bay. The following description contains a summary of measured field data provided for use in this study.

This discussion is organized in the following format. First, an overview of the hydrodynamic and meteorological processes that affect current patterns in the lower bay is presented. Second, *measured hydrodynamic and meteorological data sets* are discussed from the standpoint of the time periods for which these data are available and synopticity of the data. Third, water-quality data are discussed.

Overview of Hydrodynamic and Meteorological Processes

From a hydrodynamic standpoint, processes influencing the current patterns and transport of pollutants within the lower bay, should the CDF be expanded, include: long-term lake water level fluctuations; river discharges; seiche action; and wind speeds and directions. A brief summary is presented for each of the above factors. Figure 3 illustrates the study area and shows the locations of various water surface level gauges and current meters where data are available for calibrating and verifying the hydrodynamic model.

Lake water level

Green Bay water levels are dependent on annual and seasonal variations in precipitation within the Lake Michigan/Lake Huron drainage basin and also on the regulated discharge exiting Lake Superior. Concerning seasonal variations,

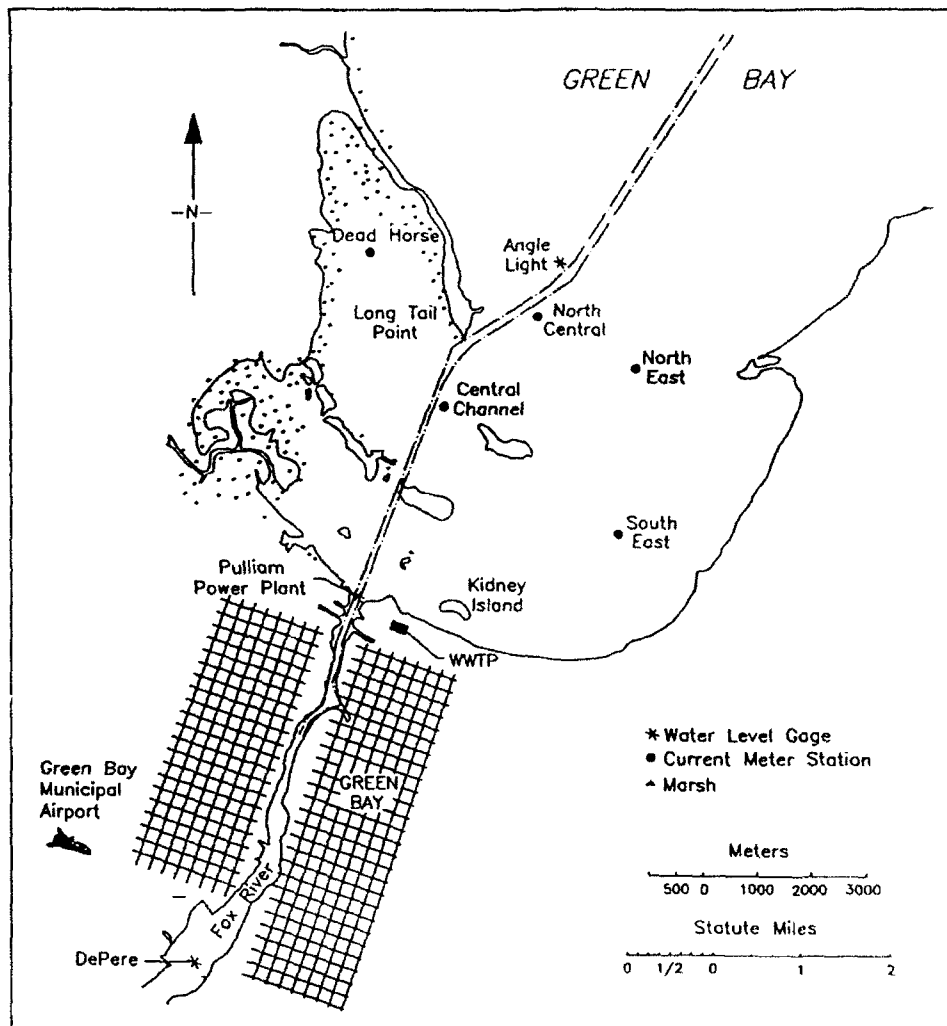


Figure 3. Locations of water surface gauges and current meters

water levels are generally lowest in mid-winter and continually rise during the first half of a year, reaching peak water levels in early to midsummer. Thereafter, these levels decrease until minimum levels are again experienced during the winter, completing the seasonal cycle. Monthly average water levels collected at Green Bay for May through August of years 1953 through 1980 are presented in Table 1. The monthly average water levels for these months ranged from 578.6 ft IGLD to 578.9 ft IGLD. The highest monthly average water level for this period occurred in June 1974 at a level of 581.1 ft IGLD, whereas the minimum average water level was experienced in May 1964 at a level of 575.9 ft IGLD. Thus, over this 28-year period, average summertime water levels varied over a range of 5 ft. Furthermore, Patterson (1984) noted that this 5-ft range in water levels is equivalent to 25 percent of the lower bay's total water volume.

For the years 1982 through 1984, monthly average water levels are presented in Table 2. For 1983 and 1984, water levels experienced during the summer months were approximately 1 ft greater than the average water levels

Table 1
Monthly Average Water Elevations for the Period 1953-1980

Month	Monthly Average Water Elevation		
	Mean (ft IGLD)	Highest (ft IGLD)	Lowest (ft IGLD)
May	578.63	580.67	575.86
June	578.79	581.12	575.92
July	578.94	581.08	576.00
August	578.88	580.96	575.95

Table 2
Monthly Average Water Elevations for the Years 1982-1984

Month	Monthly Average Water Elevation		
	Year 1982 (ft IGLD)	Year 1983 (ft IGLD)	Year 1984 (ft IGLD)
May	578.96	579.90	579.77
June	579.00	580.17	580.11
July	579.03	580.08	580.18
August	578.99	580.02	580.20

recorded from 1953 through 1980. However, the gauging station was relocated in 1980, which may affect the measured water levels.

River Inflow

The Fox River is the largest river draining into the lower bay. The East River, the second largest river in the area, joins the Fox River in the City of Green Bay, WI. East River flow rates are approximately 5 percent of the flow measured in the Fox River (Patterson 1984).

Because the U.S. Geological Survey (USGS) does not maintain gaging stations within the modeling area, it was necessary to substitute flow rates measured at other USGS gauging stations. For the Fox River, flow rates measured at Rapid Croche Dam are substituted for those imposed at the DePere Dam boundary. No adjustments were made to the discharge data to account for increased flows from the additional drainage area. Because Rapid Croche Dam is located approximately 9 miles upstream of DePere Dam, it was felt that additional flow volume would be negligible to the total flow volume discharging from Rapid Croche Dam.

Flows collected on the Kewaunee River were substituted for those on the East River. Kewaunee River is located to the east of the lower bay and discharges into Lake Michigan. Because both rivers are within the vicinity of lower Green Bay, the drainage basin response to storms for these rivers should be temporally similar. However, flow rates assigned to East River were adjusted to account for the spatial differences in drainage areas between the Kewaunee and East River basins. (The East River basin is approximately one-fourth the size of the Kewaunee River basin.)

Seiche activity

Seiche oscillation periods and nodal positions for Lake Michigan and Green Bay are discussed in Mortimer and Fee (1976) and Rao, Mortimer, and Schwab (1976). Dominant lake modes affecting the hydrodynamics in lower Green Bay have periods of 9.0, 3.7, and 2.2 hr, which represent modes 1, 3, and 5, respectively.

Green Bay is also affected by inter-lake oscillations occurring between Lakes Michigan and Huron. This oscillation mode has a period of approximately 12 hr. Because semidiurnal tidal effects have approximately the same period, tidal effects can increase seiche amplitudes if the seiche is in phase with the tidal oscillations. Green Bay experiences a maximum tidal range of 10 cm.

Seiche amplitudes were not discussed by Mortimer. However, Patterson (1984) estimated a mean seiche range of 0.60 ft for May and June, and a mean of 0.46 for July and August. For September and October, the mean seiche range is 0.64 ft.

Wind speeds and directions

Strong wind events associated with the passage of cold fronts through the Great Lakes region occur approximately every 5 to 7 days during the fall and spring, and 7 to 10 days during the summer. Durations for other localized events, such as thunderstorms, usually range from 3-6 hr, depending on the intensity of a particular weather front.

Weather data were obtained from the U.S. Air Force Environmental Technical Applications Center, Scott Air Force Base, Illinois, which maintains a database of meteorological data. Specifically, data obtained include synoptic wind speeds and directions measured at the Green Bay Municipal Airport. These data were recorded at hourly intervals.

Based on an analysis of 1982 weather data, Patterson (1984) found that the mean wind speed for July through August was estimated at 6.4 knots, whereas a mean speed of 7.6 knots was estimated for September through October. For the years 1982 through 1984, average wind speeds and directions were analyzed for the combined months of June, July, and August. Average wind

speeds for eight compass directions are presented in Table 3. Wind directions presented in this table denote the direction from which the winds are coming.

Table 3 Average Wind Speeds and Dominant Wind Directions for Years 1982 through 1984			
Compass Direction	Average Wind Velocity (m/sec)	Maximum Wind Velocity (m/sec)	Frequency (percent)
North	3.4	9.3	8.1
Northeast	4.0	11.8	10.8
East	3.4	8.7	8.2
Southeast	3.6	15.9	7.6
South	4.1	11.3	17.5
Southwest	4.3	12.9	17.3
West	4.1	11.8	14.9
Northwest	3.8	12.3	8.7

Light or variable winds, though not noted in the table, represent conditions having a frequency of 6.9 percent.

Wind directions experienced at the Green Bay Airport are primarily from the south, southwest, and west directions; winds from these directions have a combined frequency of 50 percent. Note that winds used in this analysis were recorded at Green Bay Airport. Because the distance from the airport to the bay is 6 miles, wind speeds and directions recorded at the airport may vary from those experienced on the bay.

Review of Physical Data

Wind speeds and directions

Meteorological data for Austin Straubel Field (Green Bay Airport) were obtained for the years 1949 through 1987. Austin Straubel Field is located at the edge of metropolitan Green Bay, approximately 6 miles south-southwest of the Kidney Island CDF. From the hourly data for this station, daily averages for cloud cover, dry air temperature, dew-point temperature, barometric pressure, wind speed, and wet bulb temperature have been calculated and stored in data files for further use. Hourly wind direction data for this station have also been received.

Additional meteorological data for the years 1986 through 1988 have been obtained from the Green Bay Metropolitan Sewer District. A meteorological station is located on the grounds of the wastewater treatment plant. These data

include wind speed and direction, dry and wet bulb temperatures, and rainfall.

River discharge

As previously stated, the USGS does not maintain a gauge within the East River basin, and on the Fox River the gauge nearest to the study area is located at Rapid Croche Dam, approximately 9 miles upstream of DePere Dam. Patterson substituted Kewaunee River flows for East River flows in his study. Kewaunee River flows were adjusted to account for differences in basin areas. The USGS maintains a database containing daily-average discharges for all gauges in the United States. This database was obtained, and contains Kewaunee River flow rates for the years 1980 through 1990.

Current velocity

Synoptic current speed and direction data were obtained for five current stations located in lower Green Bay. These data were obtained from the WDNR. These data were recorded at 10-min intervals over the period from 15 June 1984 through 31 August 1984. Figure 4 illustrates the time span over which these data are available.

Of the five meters deployed during June 1984, only three were in continuous operation throughout this month: the north central, northeast, and southeast meters. The Dead Horse Bay meter was in operation from 15 June through 27 June. No additional data were collected during the rest of the deployment period. The central channel meter began operation on 29 June and remained in operation for the rest of the month.

For July, the Dead Horse Bay current meter was not recording over the entire month and three other meters were malfunctioning during parts of this period. All water speeds and directions contained in the Dead Horse Bay current meter data set were equal to zero. Current meters which malfunctioned during July are the northeast, central channel, and southeast meters. In all cases, water directions remained constant, but speeds did fluctuate. The northeast meter appears to have been fixed and functioning properly on 26 July. The southeast meter was malfunctioning for the entire month, whereas the central channel meter did not collect data on 26 July or the period from 29 July through 31 July.

Three meters were operating in August 1984. Of these three, only the northeast meter was functioning for the entire month. The north central meter ceased operating 9 August, whereas the southeast meter began operating on 9 August and remained operational for the rest of the month.

Current data were recorded with Endeco 174 shallow-water meters. When new, these meters have a manufacturer-defined speed threshold of 2.57 cm/s. This type of meter employs an impeller that rotates due to current flows. Velocity measurements are computed by counting the number of impeller

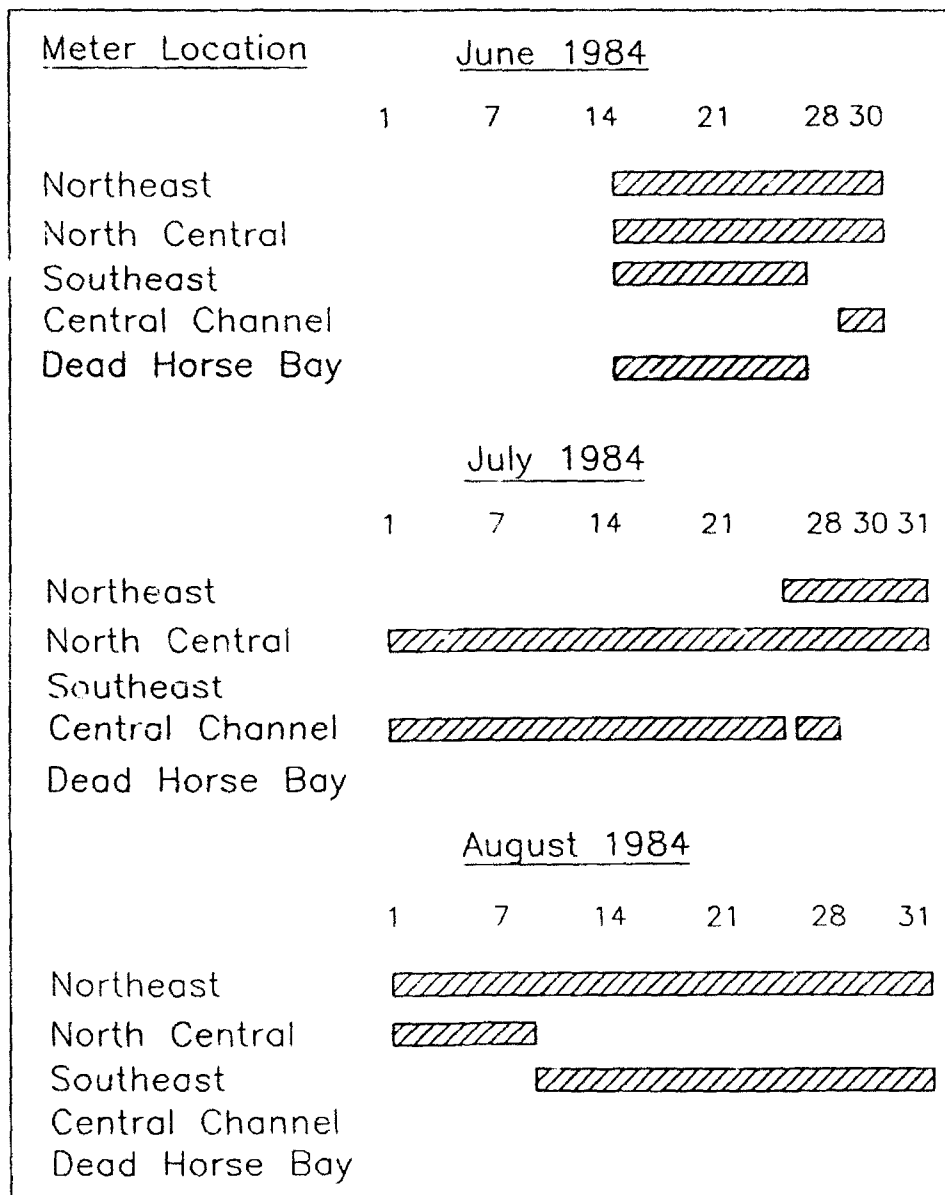


Figure 4. Time period of current meter measurements

revolutions completed over a user-defined time period. The period at which these meters recorded this information was 10 min. Furthermore, these meters were deployed at approximately mid-depth, which was 1 m below the water surface for those stations situated in shallower water.¹

¹ Personal Communication, August 1991, Dr. Kwang Lee, Professor, Department of Civil Engineering, University of Wisconsin, Milwaukee, WI.

Water surface level

Time series of water surface levels have been obtained from five gauging stations operating in lower Green Bay during the 1980s. Of those five gauges, only the National Oceanic and Atmospheric Administration's (NOAA's) Pulliam Power Plant gauging station, located at the mouth of the Fox River, is a permanent gauge. Three temporary gauges, maintained by the USGS, were placed at the Angle Light station, Chicago and Northwestern (C&NW) Railroad bridge (located at the southern limit of the City of Green Bay), and at DePere Dam. The fifth gauge was operated by the Green Bay Metropolitan Sewerage District (GBMSD) and was located in the vicinity of the Amoco storage facility.

The temporary C&NW bridge and DePere gauges located on the Fox River were in operation during the summers of 1982 and 1983. The Angle Light gauging station was operated during the summers of 1982 through 1984. The time periods over which these gauges were in operation are summarized in Table 4. As part of the Green Bay Mass Balance Study, the GBMSD collected water levels at Angle Light during 1986 and at the Amoco facility, located midway between the Fox River mouth and the confluence of the East and Fox Rivers, from 1987 through 1990.

Table 4 Operation Periods of Temporary USGS Water Surface Elevation Gauges for Years 1982 through 1986			
Gauge Station	Year	Beginning Month	Ending Month
Angle Light	1982	June	September
	1983	June	November
	1984	June	October
	1986	May	October
C&NW Bridge	1982	May	October
	1983	June	October
DePere Dam	1982	May	November
	1983	June	October

Review of Water Quality Data

Water quality data were obtained from Mr. Dale Patterson, WDNR. These data were used by the WDNR in developing a waste-load allocation model of the lower Green Bay/Fox River system (Patterson 1985). Additional data were obtained from other investigators for various projects during the same time frame. The data collected by WDNR were also retrieved as part of a STORET database.

Two types of water quality data were collected by the WDNR and other investigators during this period. Grab samples were collected at various locations in the lower Fox River and lower Green Bay. The dates and type of data collected during midsummer 1983 are indicated in Tables 5 and 6. The second type of data consisted of continuous monitoring of dissolved oxygen

Table 5
Sampling Dates and Parameters for WDNR Synoptic Surveys, July-August 1983 (WDNR 1985)¹

Date	Parameter Sampled											
	DO	Temp	TKN	NH ₃	NO ₂ ⁻ NO ₃ ⁻	TP	DP	Chl-a	Seiche	VSS	Cr ¹	pH
7-21-83	x	x	x	x	x	x	x	x	x	x	x	x
7-28-83	x	x	x	x	x	x	x	x		x	x	x
8-1-83	x	x	x	x	x	x	x	x		x	x	x
8-16-83	x	x	x	x	x	x	x	x		x	y	x
8-23-83	x	x	x	x	x	x	x	x	x	x	x	x
8-31-83	x	x	x	x	x	x	x	x	x	x	x	x

¹ On 7-21-83, these samples were collected at stations located on the bay only.

Table 6
Sampling Dates and Parameters for Green Bay Metropolitan Sewerage District and University of Wisconsin, Green Bay, July - August 1983 (WDNR 1985)

Date	Parameter Sampled											
	DO	Temp	TKN	NH ₃	NO ₂ ⁻ NO ₃ ⁻	TP	DP	Chl-a	Seiche	VSS	Cl	pH
7-1-83	x	x		x			x		x			x
7-6-83	x	x		x			x		x			x
7-8-83	x	x							x			
7-12-83	x	x		x	x		x		x			x
7-14-83	x	x		x			x		x			x
7-19-83	x	x							x			
7-20-83	x	x		x			x					x
8-9-83	x	x							x			
8-15-83	x	x							x			
8-17-83	x	x							x			
8-23-83	x	x							x			
8-25-83	x	x							x			

and temperature probes operated by GBMSD. These were located along the Fox River and on Kidney Island, Grassy Island, and Angle Light.

Grab sample data during 1983 were collected by the WDNR and GBMSD - University of Wisconsin, Green Bay (UWGB). These data are reported in Appendix 2 of the WDNR waste-load allocation report (Patterson 1985). Many of the data contained in Appendix 2 of the WDNR report were also retrieved during a STORET database search. The locations of these stations in relation to the water quality model grid were established using the maps contained in that report and the results of the STORET data search (Figures 5 and 6).

Of the continuous monitoring stations operated by GBMSD, eight were "operational" during the summer of 1983. This does not imply that they were actively recording data but that they were in place. The locations of these stations are shown in Figure 7. One station located at the Proctor and Gamble intake pipe was not used for comparisons due to temperature differences between the water in the pipe and the river. Patterson (1985) attributed this to heating occurring in the buried pipe. Only the station at Depere Dam had a continuous record of data over the calibration period. The records for the Main Street Bridge monitoring station and the Schmidt Dock station are nearly complete during the calibration period. These stations are missing data during only a few short periods. The stations at the C&NW bridge and Angle Light are missing data over large portions of the calibration period.

No data were collected at the Grassy Island station during the calibration period. Several data gaps occurred at the Kidney Island monitoring station during the calibration period. Patterson rated each of the monitoring stations based upon the perceived quality of the data as indicated by calibration logs and monitor reliability. A summary of his ratings of the continuous monitoring stations is provided in Table 7.

Hourly temperature and DO data from automated monitoring stations located in the Fox River and lower Green Bay were obtained for a portion of the year 1983. Nine stations were located in this region, four of which sampled both the surface and bottom waters. The station with the most complete record is the WDNR sampling station downstream of DePere Dam, with hourly values reported from May 1 through October 31, 1983. Only a few days within this period at this station did not have any observations. Records for the other stations during this time are not as complete.

Meteorological data for Austin Straubel Field (Green Bay Airport) for the period of record, 1949 through 1987, were obtained from the U.S. Air Force Environmental Technical Applications Center, Scott Air Force Base, Illinois. Austin Straubel Field is located slightly over 6 miles southwest of the Fox River mouth and Kidney Island CDF. Hourly data from the airport were used to compute daily average values of cloud cover, dry and wet bulb temperatures, dew-point temperatures, and barometric pressure. This information was used to generate average daily solar radiation for the calibration period and the scenario runs.

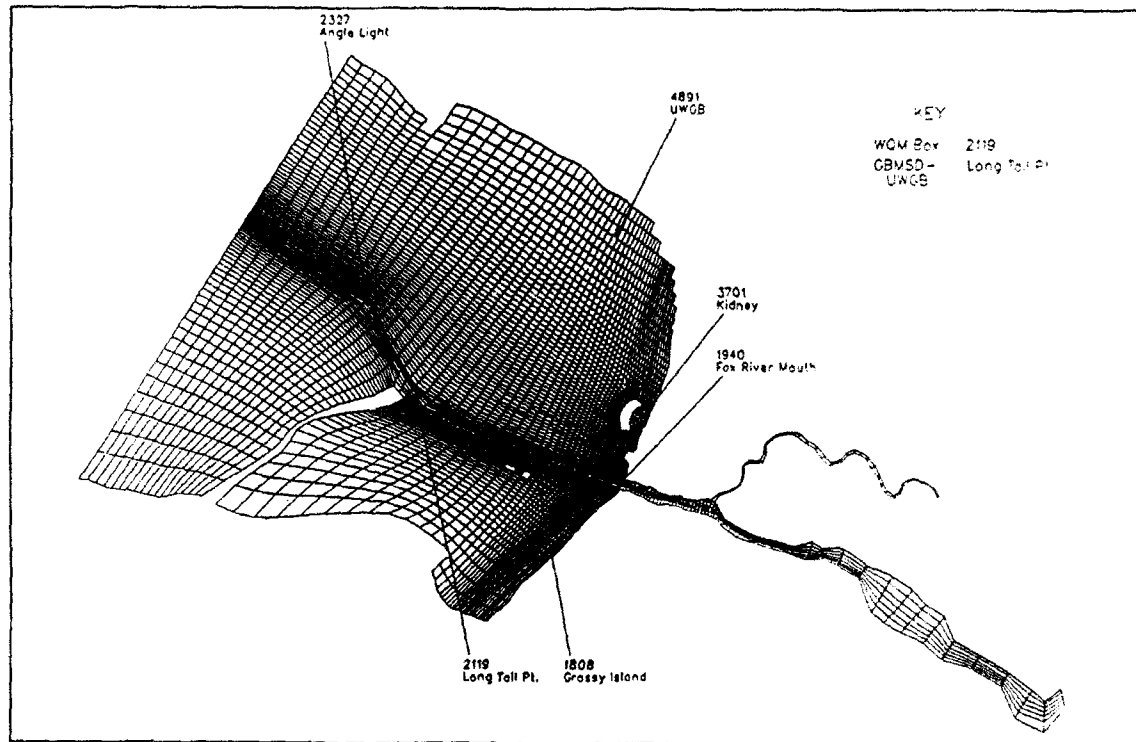


Figure 5. GBMSD and UWGB water quality grab sample stations

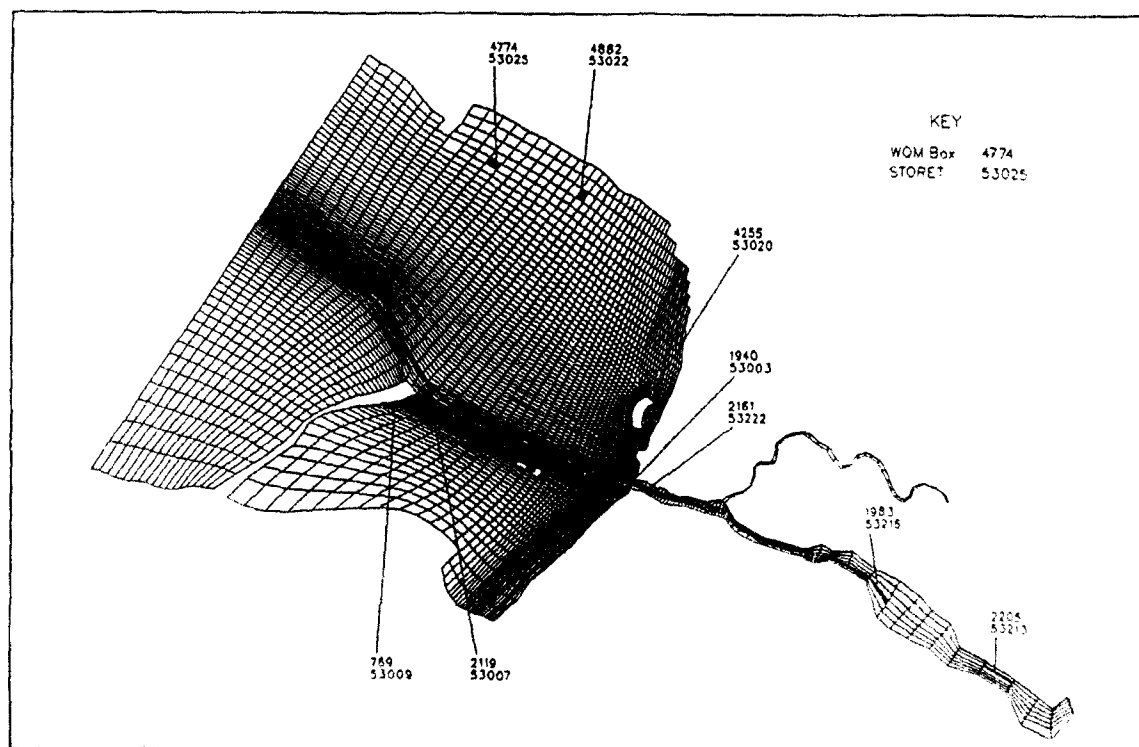


Figure 6. Wisconsin Department of Natural Resources grab sample data stations

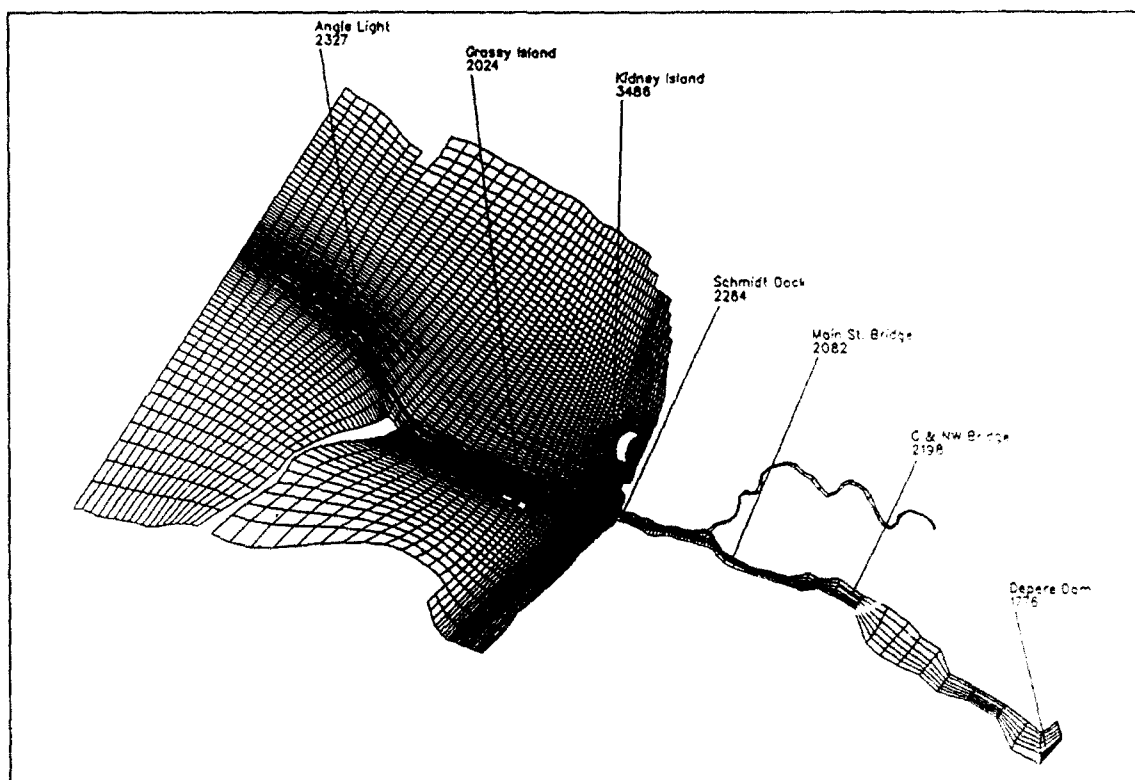


Figure 7. Continuous DO monitoring stations in place during calibration period

Table 7 Perceived Quality of Continuous DO Monitoring Stations Operating During July - August 1983 (WDNR 1985)	
Station	General Data Quality
Depere Dam	Very reliable and accurate
Chicago and Northwestern Railroad Bridge	Fair
Main Street Bridge	Good
Schmidt Dock	very good
Grassy Island	Very poor
Angle Light	Good
Kidney Island	Fair to poor

Data on point source loads for the eight dischargers along the lower Fox River for the calibration period were provided by WDNR. These data were in the form of input decks to the model used by them for their wasteload allocation study. For the calibration period the loadings were generated by WDNR from information contained in Discharger Monitoring Reports (WDNR 1986). The location of the point source dischargers was determined from maps in the WDNR waste-load allocation report and data obtained from the STORET retrieval.

Permit loads were used for the point source loads during the scenario runs. These loads were generated using information contained in the WDNR report. Permit loadings are a function of the Fox River flow at Rapid Croche Dam. These flows were obtained from a USGS database contained on a compact disk.

3 Description of the Hydrodynamic Model

The numerical hydrodynamic model CH3D (Curvilinear Hydrodynamics in Three Dimensions) was selected for providing detailed hydrodynamic flow field information for input to the water quality model. The basic model was developed by Sheng (1986) but was extensively modified in its application to the Chesapeake Bay Study (Johnson et al. 1991). These modifications include implementing different basic numerical formulations of the governing equations as well as substantial recoding of the model to provide more efficient computing. Physical processes impacting circulation which are modeled include seiche, wind and river inflow, and the effect of the earth's rotation (i.e., Coriolis effect).

This model possesses the ability to define a basin in a boundary-fitted coordinate system, allowing grid coordinate lines to conform with irregular coastal features, such as a shoreline or navigation channel. The solution algorithm employs an external-internal mode-splitting technique. In the external mode, finite difference approximations of the vertically integrated Navier-Stokes equations are solved, yielding water surface elevations and depth-averaged x- and y-direction unit flow rates. This information is then processed in the internal mode to determine the x-, y-, and z-direction velocity distributions through the water column. Because the lower Green Bay model is applied in a two-dimensional, depth-averaged (i.e., external) mode, the internal mode is not discussed in this chapter.

Governing Equations

The hydrodynamic equations used in CH3D are derived from the classical Navier-Stokes equations formulated in a Cartesian coordinate system (Figure 8a). Assuming that the vertical water accelerations are small in comparison with the gravitational acceleration (i.e., hydrostatic pressure conditions exist), and that the fluid is homogeneous and incompressible, the depth-averaged approximation yields the following in-plan, two-dimensional form of the governing equations:

$$\begin{aligned} \frac{\partial U}{\partial t} + \frac{\partial}{\partial x} \left(\frac{UU}{H} \right) + \frac{\partial}{\partial y} \left(\frac{UV}{H} \right) + gH \frac{\partial S}{\partial x} \\ - fV - \frac{\tau_{sx}}{\rho} + \frac{\tau_{Bx}}{\rho} + A_H \left(\frac{\partial^2 U}{\partial x^2} + \frac{\partial^2 U}{\partial y^2} \right) = 0 \end{aligned} \quad (1)$$

$$\begin{aligned} \frac{\partial V}{\partial t} + \frac{\partial}{\partial x} \left(\frac{UV}{H} \right) + \frac{\partial}{\partial y} \left(\frac{VV}{H} \right) + gH \frac{\partial S}{\partial y} \\ + fU - \frac{\tau_{sy}}{\rho} + \frac{\tau_{By}}{\rho} + A_H \left(\frac{\partial^2 V}{\partial x^2} + \frac{\partial^2 V}{\partial y^2} \right) = 0 \end{aligned} \quad (2)$$

$$\frac{\partial S}{\partial t} + \frac{\partial U}{\partial x} + \frac{\partial V}{\partial y} = 0 \quad (3)$$

where

x, y, t = independent space and time variables

S = water surface displacement measured relative to an arbitrary datum

h = static water depth measured from the same datum

H = total water depth ($h+S$)

U, V = unit flow rate components in the x - and y -directions, respectively

τ_{Bx}, τ_{By} = bottom shear stress in the x - and y -directions, respectively

f = Coriolis parameter

A_H = generalized dispersion coefficient

g = gravitational acceleration

τ_{sx}, τ_{sy} = surface shear stress in the x - and y -directions, respectively

ρ = water density (assumed to be constant)

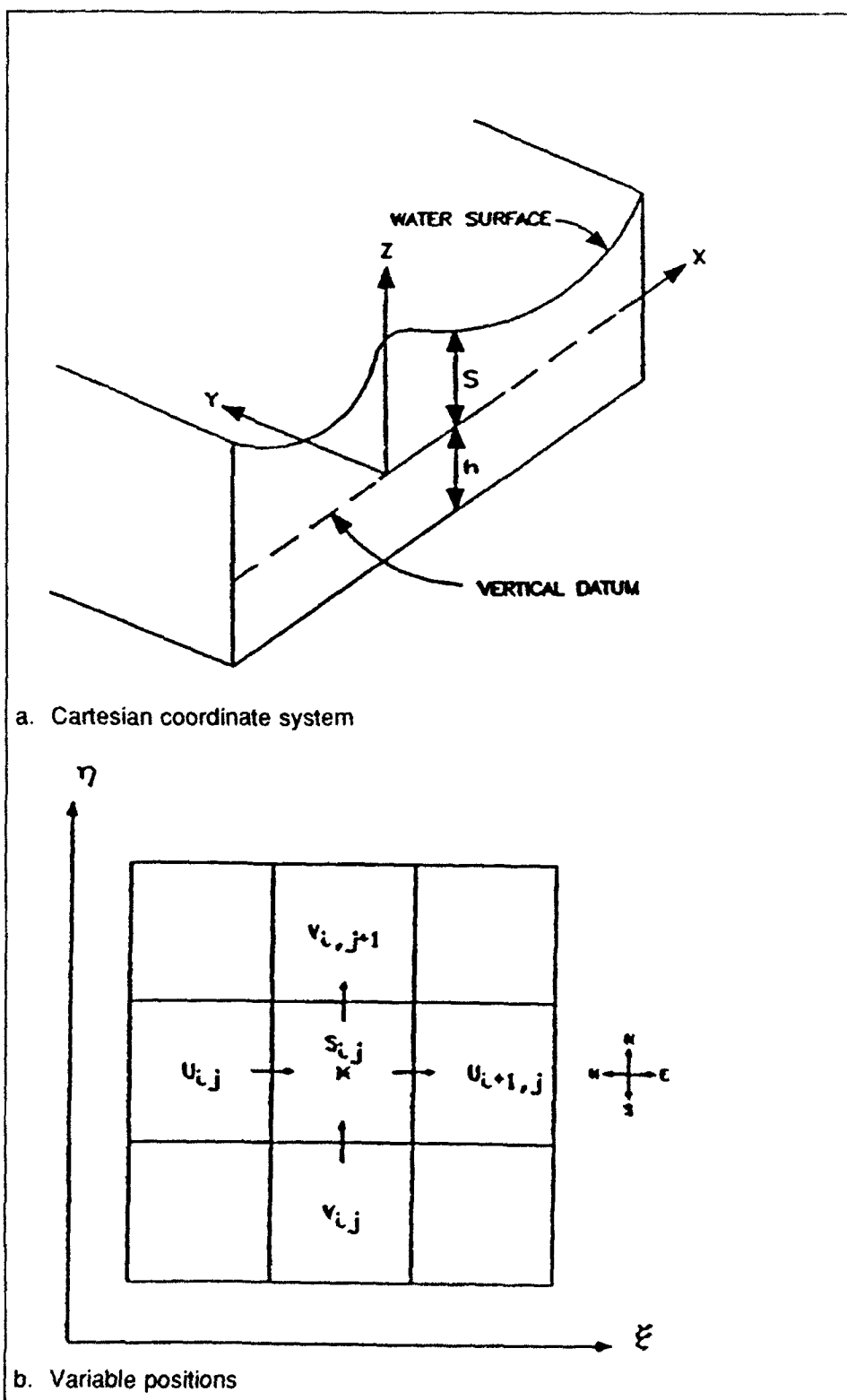


Figure 8. Definition sketches

Bottom shear stress formulation

The CH3D model uses the following quadratic expression to represent the bottom shear stress in the x-momentum equation:

$$\tau_{Bx} = \frac{g}{C_z^2 H^2} \sqrt{U^2 + V^2} U$$

where

g = gravitational acceleration

C_z = Chezy's resistance factor

H = water depth

U, V = unit flow rate components in the x- and y-directions, respectively

A similar expression is used for τ_{By} in the y-momentum equation.

Rather than specifying the Chezy resistance factor, Manning's n , which is independent of depth, is input to the model. These coefficients are related through the following equation:

$$C_z = \frac{H^{1/6}}{n}$$

Furthermore, CH3D has an option for defining Manning's n as a function of depth and can be used to specify changes in bottom roughness at different water depths.

Surface shear stress formulation

The surface shear stress τ_s is formulated as:

$$\tau_s = \rho_a C_D |W|W$$

where ρ_a is the air density, W is the wind velocity, and C_D is a dimensionless wind drag coefficient. CH3D uses the wind drag formulation presented in Garratt (1977):

$$C_D = \frac{(0.75 + 0.067\omega)}{1000}$$

where ω is the resultant wind speed. This formulation requires wind speeds specified in units of meters per second. Furthermore, an upper limit of 3.0×10^{-3} is specified for this coefficient. Thus, for wind speeds greater than 65 knots, a constant drag coefficient is applied.

Coriolis effect

Although it is not a true force, the Coriolis effect accounts for the apparent deflection in a fluid's trajectory that is induced by the rotation of the earth. The Coriolis parameter f is expressed as:

$$f = 2v \sin \lambda$$

where v is the angular speed of the earth's rotation (7.292×10^{-5} rad/sec) and λ is the latitude of the study area.

Transformation of Governing Equations

The governing equations contained in CH3D were developed in a non-orthogonal curvilinear coordinate system. This system, however, necessitates the transformation of the governing equations into a non-orthogonal curvilinear or boundary-fitted coordinate system (ξ, η). Both independent (e.g., x, y) and dependent variables (e.g., U, V) in the governing equations are transformed into the (ξ, η) curvilinear system. Furthermore, CH3D employs contravariant components, as opposed to covariant components, in the transformation of the governing equations. Thus, velocities are defined perpendicular to a cell face, as opposed to parallel to a cell face.

The flow rate components in physical space (i.e., $U(i)$ and $V(j)$) are related to the contravariant components (i.e., U^i, V^i, U^j, V^j) by the following equations:

$$U(i) = \frac{g_{11}}{|g|} U^i + \frac{g_{12}}{|g|} V^i$$

$$V(j) = \frac{g_{21}}{|g|} U^j + \frac{g_{22}}{|g|} V^j$$

where:

$$g_{ij} = \begin{bmatrix} x_{\xi}^2 + y_{\xi}^2 & x_{\xi}x_{\eta} + y_{\xi}y_{\eta} \\ x_{\eta}x_{\xi} + y_{\eta}y_{\xi} & x_{\eta}^2 + y_{\eta}^2 \end{bmatrix}$$

or

$$g_{ij} = \begin{bmatrix} g_{11} & g_{12} \\ g_{21} & g_{22} \end{bmatrix}$$

and $|g|$ is the determinant of the metric tensor g_{ij} :

$$|g| = g_{11}g_{22} - g_{12}g_{21}$$

Whereas scalar quantities in the physical plane are identical to themselves in the transformed plane, all spatial derivatives containing these terms must be transformed. The surface slope terms are transformed as follows:

$$\frac{\partial S}{\partial x} = g^{11} \frac{\partial S}{\partial \xi} + g^{12} \frac{\partial S}{\partial \eta}$$

$$\frac{\partial S}{\partial y} = g^{21} \frac{\partial S}{\partial \xi} + g^{22} \frac{\partial S}{\partial \eta}$$

where g^{ij} are inverse metric tensor components:

$$g^{ij} = \frac{1}{|g|} \begin{bmatrix} x_{\eta}^2 + y_{\eta}^2 & -(x_{\eta}x_{\xi} + y_{\eta}y_{\xi}) \\ -(x_{\xi}x_{\eta} + y_{\xi}y_{\eta}) & x_{\xi}^2 + y_{\xi}^2 \end{bmatrix} = \frac{1}{|g|} \begin{bmatrix} g_{22} & -g_{21} \\ -g_{12} & g_{11} \end{bmatrix}$$

or

$$g^{ij} = \begin{bmatrix} g^{11} & g^{12} \\ g^{21} & g^{22} \end{bmatrix}$$

The transformed governing equations developed by Sheng (1986) are as follows:

ξ -Momentum

$$\begin{aligned} \frac{\partial U}{\partial t} + Inertia^* + gH \left(g^{11} \frac{\partial S}{\partial \xi} + g^{12} \frac{\partial S}{\partial \eta} \right) \\ - \frac{g_{12}}{|g_u|} fU - \frac{g_{22}}{|g_u|} f\bar{V} - \frac{\tau_{s\xi}}{\rho} \end{aligned} \quad (4)$$

η -Momentum

$$+ \frac{g(g_{11}U^2 + 2g_{12}U\bar{V} + g_{22}\bar{V}^2)^{1/2}}{C_z^2 H^2} U + Diffusion^* = 0$$

$$\begin{aligned} \frac{\partial V}{\partial t} + Inertia^* + gH \left(g^{21} \frac{\partial S}{\partial \xi} + g^{22} \frac{\partial S}{\partial \eta} \right) \\ + \frac{g_{11}}{|g_v|} f\bar{U} + \frac{g_{12}}{|g_v|} fV - \frac{\tau_{s\eta}}{\rho} \end{aligned} \quad (5)$$

$$+ g \frac{(g_{11}\bar{U}^2 + 2g_{12}\bar{U}V + g_{22}V^2)^{1/2}}{C_z^2 H^2} V + Diffusion^* = 0$$

Continuity

$$\frac{\partial S}{\partial t} + \frac{1}{|g_s|} \frac{\partial}{\partial \xi} (|g_u|U) + \frac{1}{|g_s|} \frac{\partial}{\partial \eta} (|g_v|V) = 0 \quad (6)$$

where

- U, V = contravariant unit flow rate components in the transformed plane (superscripts have been dropped for convenience)
 g^{ij} = inverse metric tensor components
 g_{ij} = metric tensor components
 $|g_s|$ = determinant of the metric tensor, $|g|$, at an S -point
 $|g_u|$ = determinant of the metric tensor, $|g|$, at a U -face
 $|g_v|$ = determinant of the metric tensor, $|g|$, at a V -face
 \bar{U} = average x -direction unit flow rate at a V -face
 \bar{V} = average y -direction unit flow rate at a U -face

The inertial and diffusion terms in contravariant coordinates are quite lengthy and thus are omitted in this report. However, these terms are presented in Johnson et al. (1991).

Non-Dimensionalization of Governing Equations

The dimensionless forms of the governing equations are used to facilitate relative magnitude comparisons of the various terms in the governing equations and to minimize the effects of round-off errors during computations. The following dimensionless variables are used:

$$(u^*, v^*, w^*) = (u, v, wX_r/Z_r)/U_r$$

$$(x^*, y^*, z^*) = (x, y, zX_r/Z_r)/X_r$$

$$(\tau_x^*, \tau_y^*) = (\tau_x^w, \tau_y^w)/\rho_o f Z_r U_r$$

$$t^* = tf$$

$$S^* = gS/fU_r X_r = S/S_r$$

$$A_{II}^* = A_{II}/A_{IIr}$$

$$K_{II}^* = K_{II}/K_{IIr}$$

These definitions yield the following dimensionless parameters in the governing equations:

$$\text{Vertical Prandtl (Schmidt) Number: } Pr_v = A_v/K_v$$

$$\text{Froude Number: } F_r = U_r/(gZ_r)^{1/2}$$

$$\text{Rossby Number: } R_o = U_r/fX_r$$

$$\text{Densimetric Froude Number: } Fr_D = F_r / \sqrt{\epsilon}$$

$$\epsilon = (\rho_r - \rho_o)/\rho_o$$

where

U_r , ρ_r , X_r , Z_r , A_{vr} , and K_{vr} are arbitrary reference values of the velocity, density, length, depth, dispersion, and diffusion.

Using the dimensionless variables (asterisks have been dropped) and the parameters previously defined, the vertically integrated equations constituting the external mode are:

$$\frac{\partial S}{\partial t} + \beta \left(\frac{\partial U}{\partial \xi} + \frac{\partial V}{\partial \eta} \right) = 0 \quad (7)$$

$$\frac{\partial U}{\partial t} = -H \frac{\partial S}{\partial \xi} + \tau_{xx} - \tau_{bx} + V \quad (8)$$

$$\begin{aligned} & - R_o \left[\frac{\partial}{\partial x} \left(\frac{UU}{H} \right) + \frac{\partial}{\partial y} \left(\frac{UV}{H} \right) \right] \\ & + E_H \left[\frac{\partial}{\partial x} \left(A_H \frac{\partial U}{\partial x} \right) + \frac{\partial}{\partial y} \left(A_H \frac{\partial U}{\partial y} \right) \right] \end{aligned}$$

where

$$\beta = gZ_r/f^2X_r^2 \equiv (R_o/F_r)^2 - \frac{R_o}{Fr_D^2} \frac{H^2}{2} \frac{\partial \rho}{\partial x}$$

$$\begin{aligned}
\frac{\partial V}{\partial t} = & -H \frac{\partial \zeta}{\partial y} + \tau_{xy} - \tau_{by} - U \\
& - R_o \left[\frac{\partial}{\partial x} \left(\frac{UV}{H} \right) + \frac{\partial}{\partial y} \left(\frac{VV}{H} \right) \right] \\
& + E_H \left[\frac{\partial}{\partial x} \left(A_H \frac{\partial V}{\partial x} \right) + \frac{\partial}{\partial y} \left(A_H \frac{\partial V}{\partial y} \right) \right] \\
& - \frac{R_o}{Fr_D^2} \frac{H^2}{2} \frac{\partial p}{\partial y}
\end{aligned} \tag{9}$$

Finite Difference Approximations of Governing Equations

The finite difference approximations to the governing equations are based on a Eulerian system where the velocities and water surface fluctuations are computed at discrete locations within the flow field. A network of grid cells is used to define the parameter locations. A representative grid cell in computational space (ξ, η) is shown in Figure 8b. In this staggered grid, the water surface fluctuation is defined at the cell center (i, j) , ξ -direction unit flow rates (U) are defined at the "west" (i, j) and "east" $(i+1, j)$ cell faces, and the η -direction unit flow rates (V) are computed at the "south" (i, j) and "north" $(i, j+1)$ cell faces. The finite difference approximations of the governing equations follow. Note that the continuity equation is split into two parts. The sum of these equations is the original continuity equation.

ξ -Momentum

$$\begin{aligned}
\frac{U_{i,j}^* - U_{i,j}^n}{\Delta t} + U_{i,j}^n + \theta H g^{11} \left(\frac{S_{i,j}^* - S_{i-1,j}^*}{\Delta \xi} \right) + \\
(1-\theta) H g^{11} \left(\frac{S_{i,j}^n - S_{i-1,j}^n}{\Delta \xi} \right) + H g^{12} \left(\frac{S_{i-1/2,j+1/2}^n - S_{i-1/2,j-1/2}^n}{\Delta \eta} \right) =
\end{aligned} \tag{10}$$

$$\frac{g_{12}}{|g_u|} U_{ij}^n - \frac{g_{22}}{|g_u|} \bar{V} - \frac{\tau_{\xi}}{\rho} + \theta(FRIC) U_{ij}^* + (1-\theta)(FRIC) U_{ij}^n + D_{ij}^n = 0$$

where

- n = previous time level
- $*$ = intermediate time level
- $n+1$ = solve for this time level
- θ = weighting factor between successive time levels
- I = inertia
- D = dispersion

and

η -Momentum

$$\begin{aligned} & \frac{V_{ij}^{n+1} - V_{ij}^n}{\Delta t} + I_{ij}^n + \theta H g^{21} \left(\frac{S_{i+1/2,j-1/2}^n - S_{i-1/2,j-1/2}^n}{\Delta \xi} \right) + \\ & \theta H g^{22} \left(\frac{S_{ij}^{n+1} - S_{ij-1}^{n+1}}{\Delta \eta} \right) + (1-\theta) H g^{22} \left(\frac{S_{ij}^n - S_{ij-1}^n}{\Delta \eta} \right) + \frac{g_{11}}{|g_v|} \bar{U} + \end{aligned} \quad (11)$$

$$\frac{g_{12}}{|g_v|} V_{ij}^n - \frac{\tau_{\eta}}{\rho} + \theta(FRIC) V_{ij}^{n+1} + (1-\theta)(FRIC) V_{ij}^n + D_{ij}^n = 0$$

ξ -Continuity

$$\begin{aligned} & \frac{S_{ij}^* - S_{ij}^n}{\Delta t} + \theta \beta \frac{|g_u|}{|g_s|} \left(\frac{U_{i+1,j}^* - U_{ij}^*}{\Delta \xi} \right) + (1-\theta) \beta \frac{|g_u|}{|g_s|} \left(\frac{U_{i+1,j}^n - U_{ij}^n}{\Delta \xi} \right) + \\ & \beta \frac{|g_v|}{|g_s|} \left(\frac{V_{ij}^{n+1} - V_{ij}^n}{\Delta \eta} \right) = 0 \end{aligned} \quad (12)$$

η -Continuity

$$\frac{S_{ij}^{n+1} - S_{ij}^*}{\Delta t} + \beta \theta \frac{|g_v|}{|g_s|} \left(\frac{V_{ij+1}^{n+1} - V_{ij}^{n+1}}{\Delta \eta} \right) + (1-\theta) \beta \frac{|g_v|}{|g_s|} \left(\frac{V_{ij+1}^n - V_{ij}^n}{\Delta \eta} \right) -$$

$$\beta \frac{|g_v|}{|g_s|} \left(\frac{V_{ij+1}^n - V_{ij}^n}{\Delta \eta} \right) = 0$$

The computational procedure used in CH3D is based on an Alternating Direction Implicit scheme (Roache 1976). Using this method, the ξ - and η -momentum equations are solved separately, and each calculation in time is made in two stages. In the first stage, the ξ -continuity and ξ -momentum equations are solved along each row of the grid to progress from time level n to an intermediate time level $*$. The ξ -direction unit flow rate components and water surface fluctuations are solved implicitly, and the η -direction unit flow rate components are supplied from time level n . The ξ -direction unit flow rates from this step represent those at time level $n+1$, whereas the water surface fluctuations are only an approximation to those at time level $n+1$. The η -direction unit flow rate components remain at time level n . In the second stage, the η -continuity and η -momentum equations are solved along each column for the η -direction unit flow rates and the water surface fluctuations at time level $n+1$. ξ -direction unit flow rate components are supplied from the first-stage calculations.

As shown in the finite difference approximations to the governing equations, a weighting factor θ is used to place the water surface slope and bottom friction terms between time levels n and $n+1$. When the weighting factor equals 0.0, these terms are evaluated at the previous time level n (explicit treatment), whereas when the weighting factor equals 1.0, they are evaluated at the new time level $n+1$ (implicit treatment). Usually a value between 0.0 and 1.0 is used.

4 Implementation of the Hydrodynamic Model

Implementation of the hydrodynamic model is described in several sections. First, a discussion of the numerical grid is given, which describes its development and the bathymetry used in depicting the lower bay. Second, model calibration is discussed. This section includes an overview of the boundary-forcing conditions, a qualitative description of the events occurring during this period, a discussion of the calibration procedure, followed by an analysis of the model results. Third, the validation procedure is presented and is given in a format similar to the calibration procedure; a qualitative description of the events is discussed, and is followed by the presentation of the validation results. Fourth, an assessment of overall model performance is presented together with a diagnostic analysis of model calibration and validation results. Fifth, a discussion of wind drag coefficients is presented.

Numerical Grid Development

The lower Green Bay grid was constructed using a non-orthogonal grid system, permitting coordinate lines to smoothly follow the irregular landforms in the study area, including the shoreline, Kidney Island, and Long Tail Point, as well as the navigation channel. Presented in Figure 9, overall grid dimensions were 93 by 79 cells. Within the bay proper, the grid measured 41 by 79 cells. The grid's finest resolution was placed at the confluence of the Fox River and the bay. Cells in this area measured approximately 75 ft by 125 ft in the east-west and north-south directions, respectively. The coarsest grid resolution was placed at the northwest corner of the grid where cells measured approximately 1,550 ft by 2,700 ft.

As per the recommendations made by the TRP, a second grid was constructed for investigating the sensitivity of model results to the grid aspect ratio of cells in the northern section of the original (coarse) grid. Compared with the original grid, the second was constructed by doubling the number of cells in the north-south direction from the grid's northern edge to approximately Grassy Island (Figure 10). Cell resolution was also doubled in the east-west direction from the grid's eastern edge to Kidney Island. As a consequence of doubling the resolution in both the north-south and east-west directions, the northeast section of the grid has four times the resolution of the original grid.

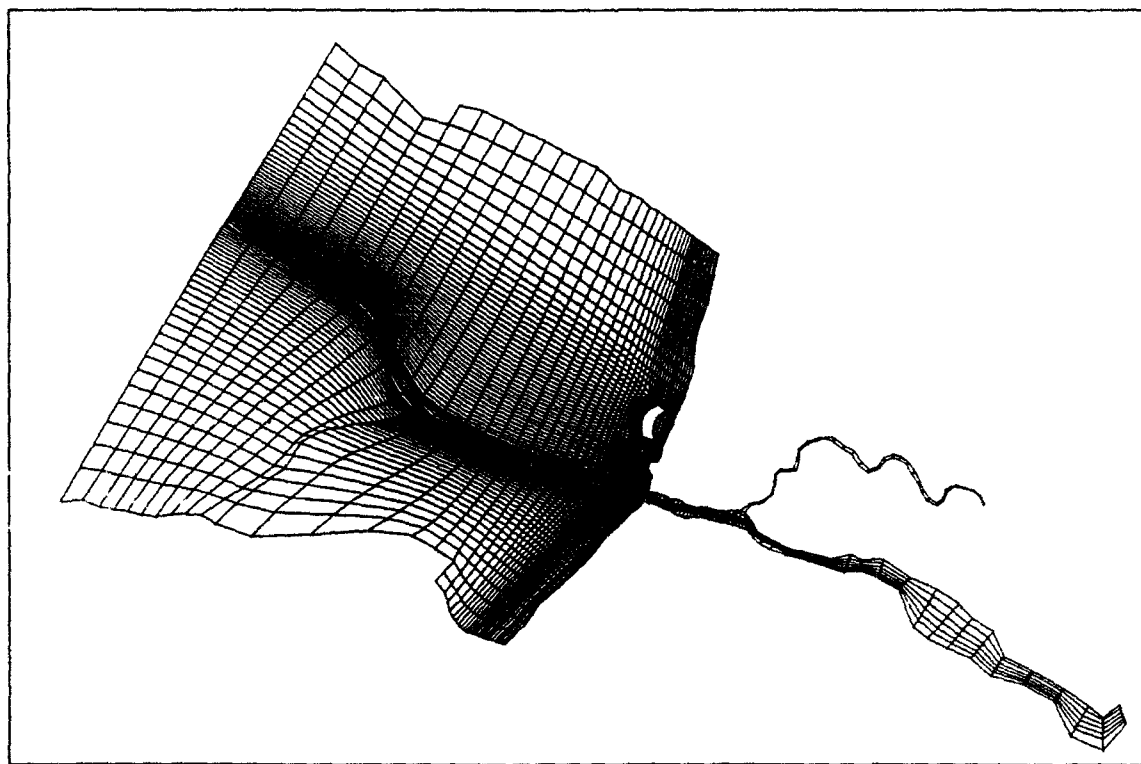


Figure 9. Coarse-resolution numerical grid

For areas south of Grassy Island and west of Kidney Island, grid resolution was unchanged.

The second, or fine resolution, grid was constructed with an overall dimension of 109 by 87 cells. Within the lower bay, omitting the Fox and East Rivers, the second grid measured 57 by 87 cells. At the northern grid boundary, cell widths in the north-south directions were approximately 1,100 ft, whereas in the east-west direction, cell widths ranged from 100 ft in the vicinity of the channel to 2,600 ft at the grid's western edge. The grid's finest resolution was placed at the Fox River mouth. Cell resolution in this area remained unchanged.

Lower Green Bay contains several areas that can become exposed during periods of lower lake levels or during extreme seiche action. These areas, delineated by Patterson¹ and presented in Figure 11, include: Frying Pan Shoals, Grassy and Cat Islands, Peats Lake, and Dead Horse Bay. Areas denoted by solid black in this figure represent islands that are always exposed, regardless of changing lake levels. Areas designated with a double cross-hatch, such as portions of Grassy Island, become exposed when lake levels are

¹ Personal correspondence, 12 April 1991. D. Patterson, Wisconsin Department of Natural Resources, Madison, WI.

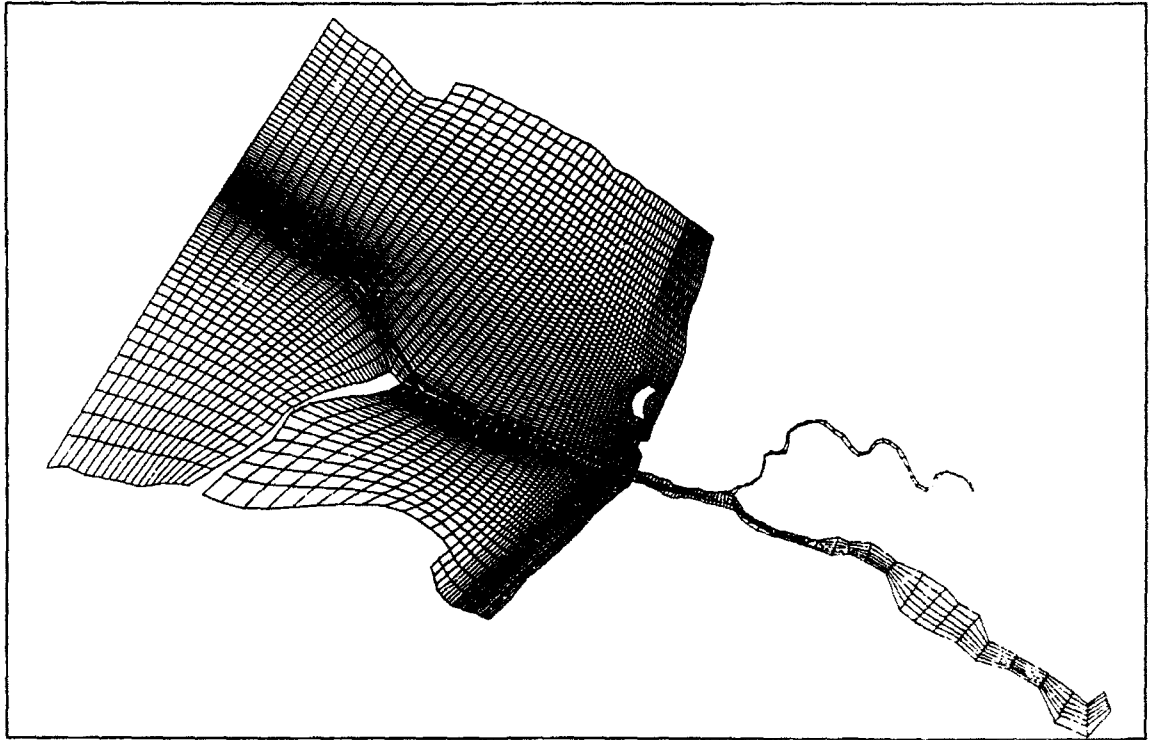


Figure 10. Fine-resolution numerical grid

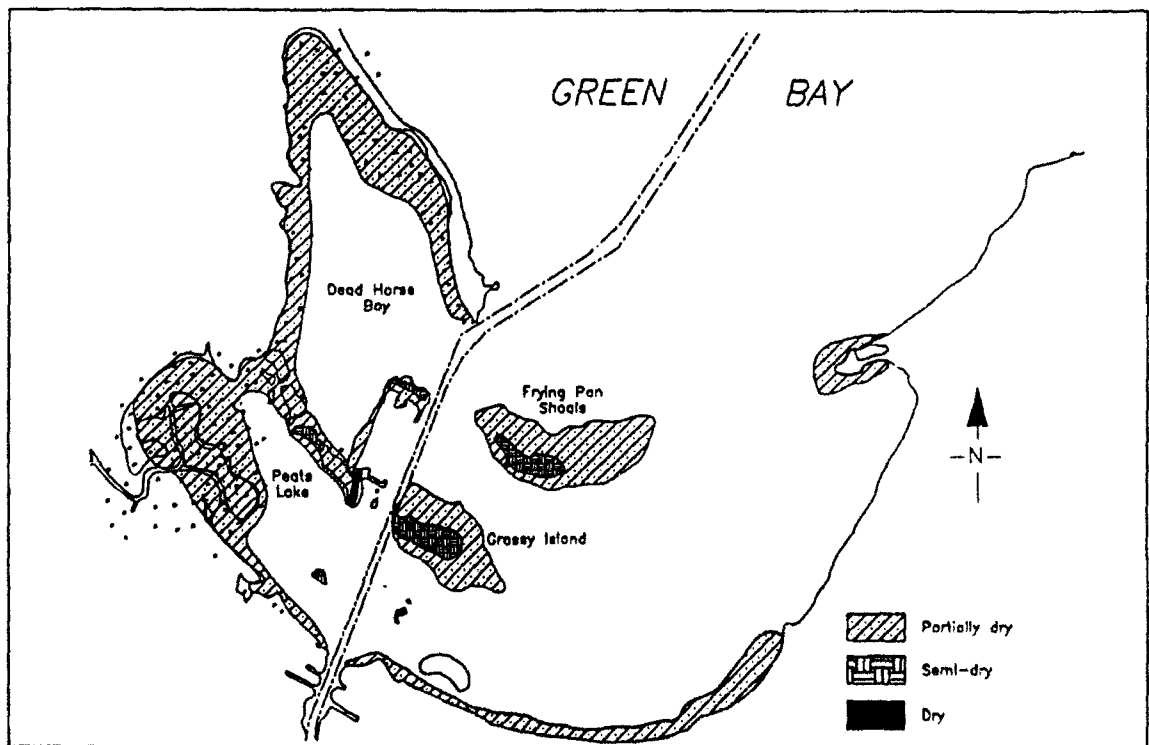


Figure 11. Location of shallow-water areas in lower Green Bay

below 578.5 ft IGLD. Sites denoted with a single crosshatch represent locations having elevations that are approximately 1 ft below the low water datum of 576.8 ft IGLD.

Grid sensitivity tests

Two sets of tests were performed for investigating the model's sensitivity to specification of bathymetry. These tests were performed using the coarse numerical grid, together with the original depth data set (denoted as "old depths" in the comparisons) and with the modified depth data set containing the information provided by Patterson (denoted as "new depths" in the comparisons). It is important to note that these tests were conducted with an uncalibrated model.

The first set of comparisons, referred to as Case A, represent flow field conditions in the lower bay during a calm wind event. These tests began at 2200 on 27 July 1982 and concluded 24 hr later at 2200 on 28 July. A 60-sec time-step was used in this simulation. A flow rate of 3,000 cfs is specified for the Fox River at the DePere Dam boundary, whereas a zero flow condition is specified at the upstream boundary of the East River. The open water boundary was driven with a time series of water surface fluctuations recorded at the Angle Light gauging station. This information was obtained from Lee (1984) and was supplied to the model in 1-hr increments. Wind speeds and directions were supplied from vector plots contained in Lee and represent hourly averaged data; however, these data were supplied to the model every 2 hr.

The second set of comparisons, referred to as Case B, represent conditions in the lower Green Bay during an extreme wind/seiche event where the predominant wind direction is from the north-northeast, or along the Bay's longitudinal axis. This comparison replicates the period from 26 June 1983 at 2300 through 27 June at 2300. Total simulation time was 24 hr and a 60-sec time-step was used in each simulation. Similar procedures were used in Case B tests as those described for Case A. The open-water boundary was driven with water surface fluctuations recorded at Angle Light gauging station. These data were obtained from the Lee report. Wind speeds and directions were specified hourly. A zero flow condition was specified at the upstream boundary of the East River, whereas a flow rate of 3,000 cfs was specified at the Fox River boundary.

For Cases A and B, comparisons are made at 15 numerical gauges. Locations for gauges 1 through 12 are presented in Figure 12. The remaining three gauges are located at the outer open water boundary, Fox River mouth and DePere Dam. Plots displaying time-series of water surface fluctuations together with water velocity magnitudes and directions are contained in Volume 2 of this report. Water velocity directions are defined with the standard oceanographic convention: an angle equal to zero defines water flowing from south to north, and angles increase in the clockwise direction. For both Cases A and B, modifications to the bathymetry had a negligible effect on the predicted water surface levels, except at the DePere Dam gauge. The

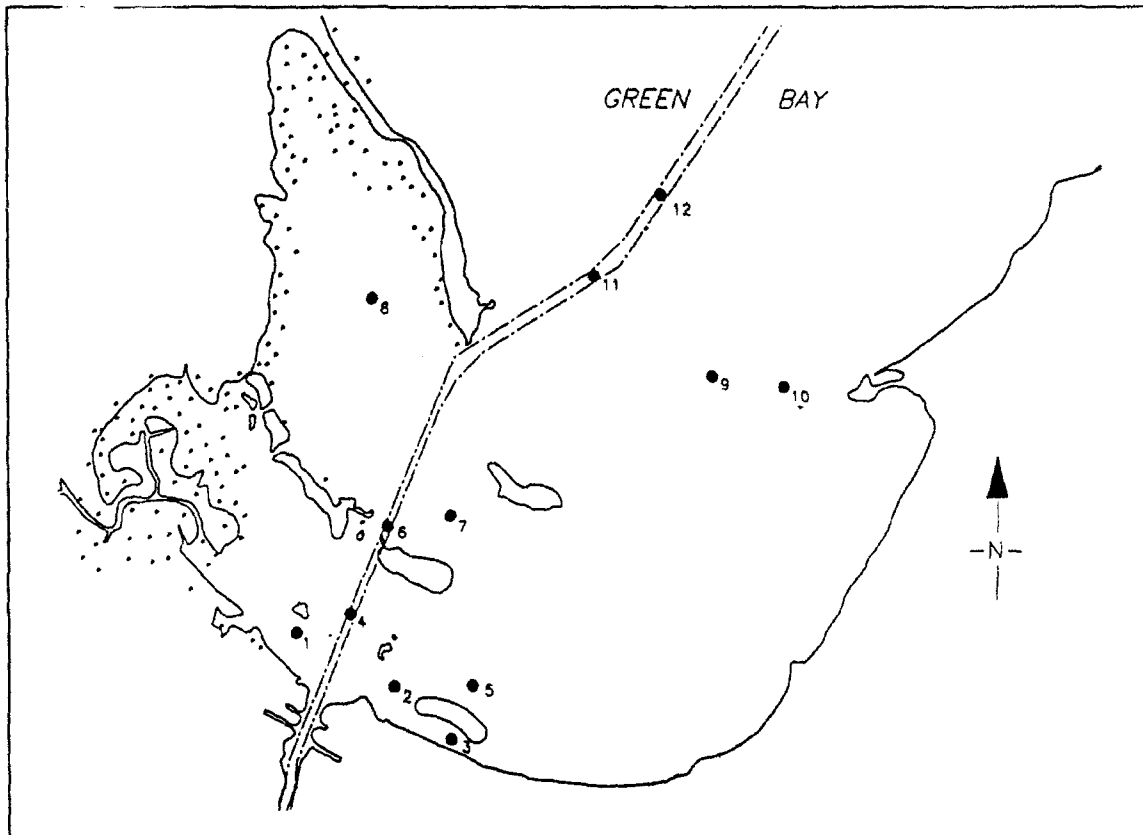


Figure 12. Location of gauges in sensitivity tests

differences in water levels computed at the dam are attributed to modifications of depths in the lower bay and also to modifying the depths of cells adjacent to the channel in the upper reach of the lower Fox River.

Modification of water depths had a greater impact on water velocities than on the water surface levels. The greatest change in velocities occurred in the vicinity of Kidney Island, numerical gauges 2 and 3, and at the mouth of the Fox River. Velocities computed at these gauges are presented in Figures 13 and 14. It is in these areas that depths were changed the most. Behind Kidney Island, for example, water velocities were approximately 40 percent greater with the modified depths as opposed to the original depths. The original data set contained water depths of approximately 7 ft, whereas in the modified data set, these depths averaged 4 ft. Thus, the cross-sectional area of the channel running behind Kidney Island had been reduced by approximately 40 percent, which is consistent with the increase in velocities computed with the modified depths.

Modified depths also had a pronounced effect on water velocities computed at the Fox River mouth. Water depths adjacent to the shipping channel in the vicinity of the mouth were changed from 7 ft to 4 ft. Furthermore, depths assigned to cells along the shoreline were also reduced from 7 ft to 4 ft. (Water depths assigned to cells composing the channel were unchanged.) As a

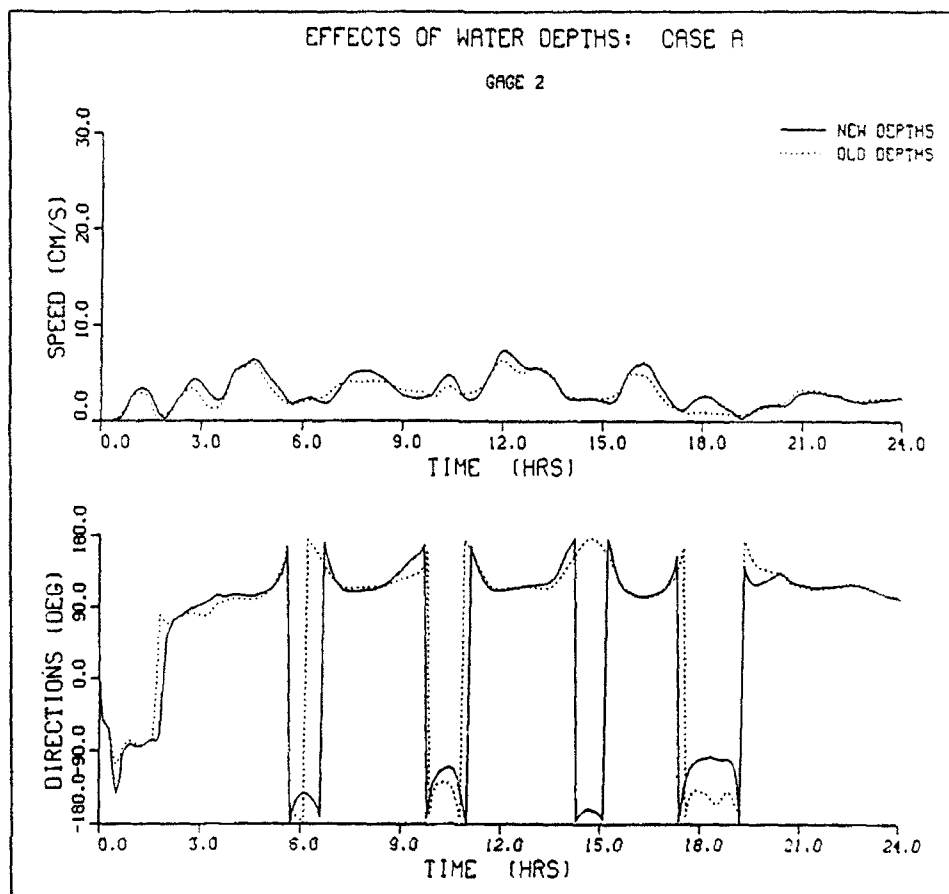


Figure 13. Comparison of water velocities at gauge 2 in depth sensitivity test

result of changing these depths, peak water velocities predicted with the modified depths were as much as 5 cm/sec greater (or 17 percent) than those predicted with the original depths.

Case B, numerical gauge 7, located between Frying Pan Shoals and Grassy Island, also experienced a significant increase in water velocities (Figure 15). These differences approached 7 cm/sec, doubling those velocities computed with the original depth data set. Depths in this area were modified significantly from those presented at the second Technical Review meeting. Furthermore, Frying Pan Shoals and Grassy Island, originally depicted as islands in the original depth data set, were simulated with cells having water depths of 2 ft in the modified data set. Velocity directions were also affected by modifying the depths. During periods of receding water levels, with the circulation at this gauge in roughly the eastern direction, these differences approached approximately 15 deg. The modified depths result in a heading of northeast as opposed to east-northeast. However, the greatest differences in directions occurred during periods when the velocity at this gauge approached zero, and are, therefore, subjected to a greater degree of round-off error in the model.

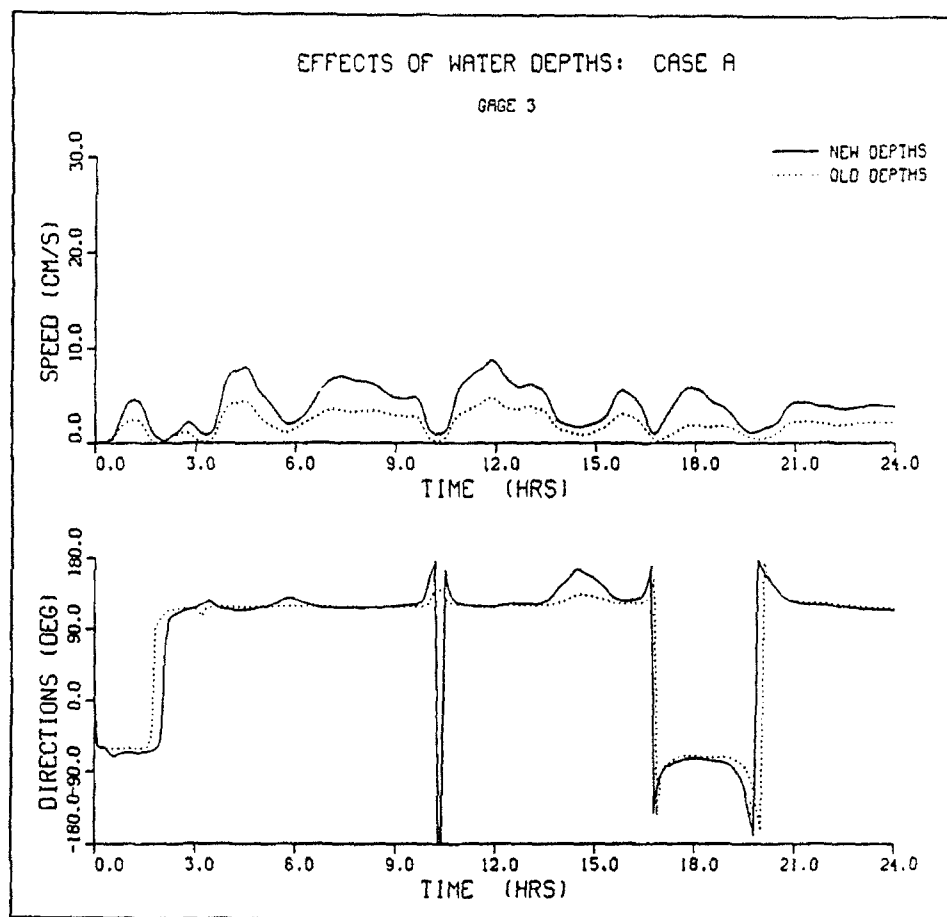


Figure 14. Comparison of water velocities at gauge 3 in depth sensitivity test

Similar deviations in velocity direction were also found at gauge 8, which is located within Dead Horse Bay (Figure 16). During periods of rising water levels, currents predicted with the modified depths had headings of west as opposed to northwest for the simulation using the original depths. Again, the greatest difference occurred during periods when the velocity at this gauge approached zero.

Cases A and B were repeated for purposes of comparing model results produced using the coarse- and fine-resolution grids. Each grid depicts the existing Kidney Island configuration and water depths have been updated to incorporate those suggestions made by Patterson. Furthermore, comparisons of water surface level fluctuations and water velocities and directions are made at the same 15 gauge locations as those presented in the water depth sensitivity tests discussed above. Because of the differing grid resolutions, gauge locations do not match exactly for the two grids. These differences lead to apparent changes in phase and magnitude when comparing time-series output generated using different grids. Gauges that are affected the most are those located in the northern section of the grid, namely gauges 7 through 12. Figure 17 displays the velocities computed at gauge 7.

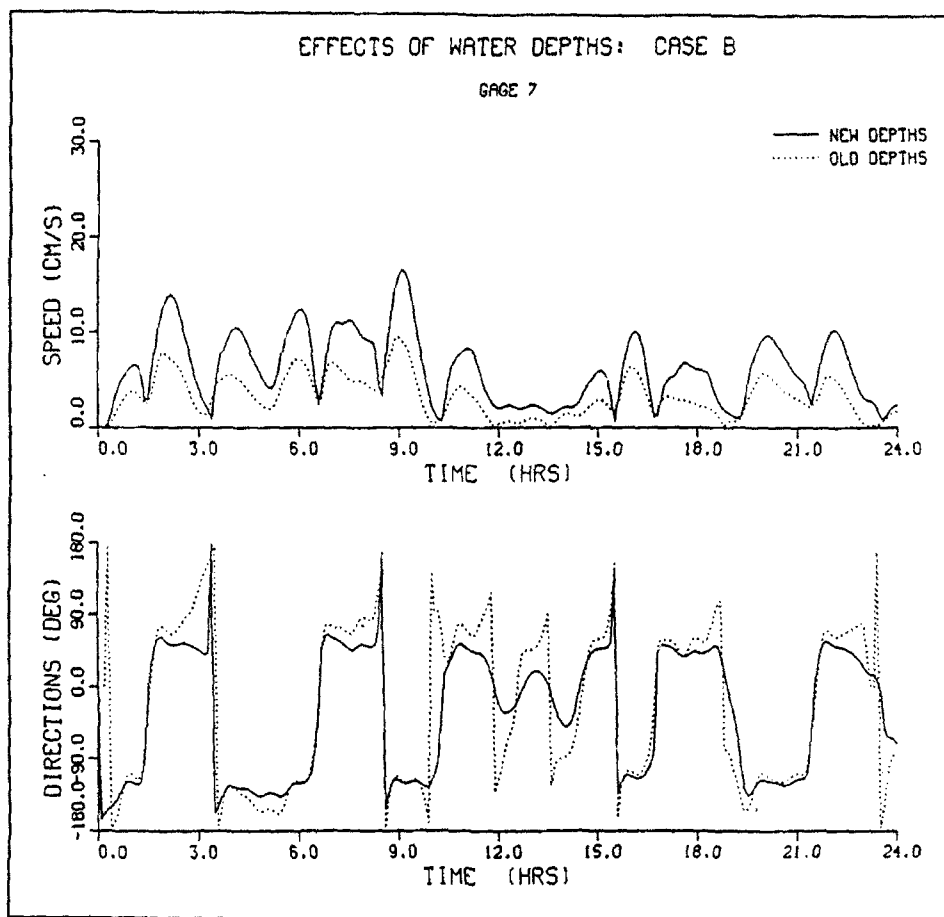


Figure 15. Comparison of water velocities at gauge 7 in depth sensitivity test

As with the water depth sensitivity tests, differences in water surface level fluctuations between the coarse- and fine-resolution grids were negligible. Differences between water velocities were generally small, typically less than 1 cm/sec. The greatest differences in water velocity magnitudes were again computed behind Kidney Island, where differences approached 4 cm/sec (or 40 percent). It is felt that these differences were due, in part, to the increased grid resolution in the eastern portion of the grid. Comparison of gauges located immediately north and west of the island shows minimal differences in magnitudes.

For Case B, velocity directions predicted at numerical gauge 7, located between Frying Pan Shoals and Grassy Island, varied by approximately 10 deg during periods of receding water levels (Figure 18). During these periods, velocity directions computed with the fine-resolution grid had a heading of NE as opposed to ENE for the coarse-resolution grid. This difference is due, in part, to the increased grid/bathymetry resolution within this area.

Similar differences in velocity directions were also found at gauge 8, which is located within Dead Horse Bay (Figure 19). During periods of rising water levels, currents predicted with the finer resolution grid had headings of NW as

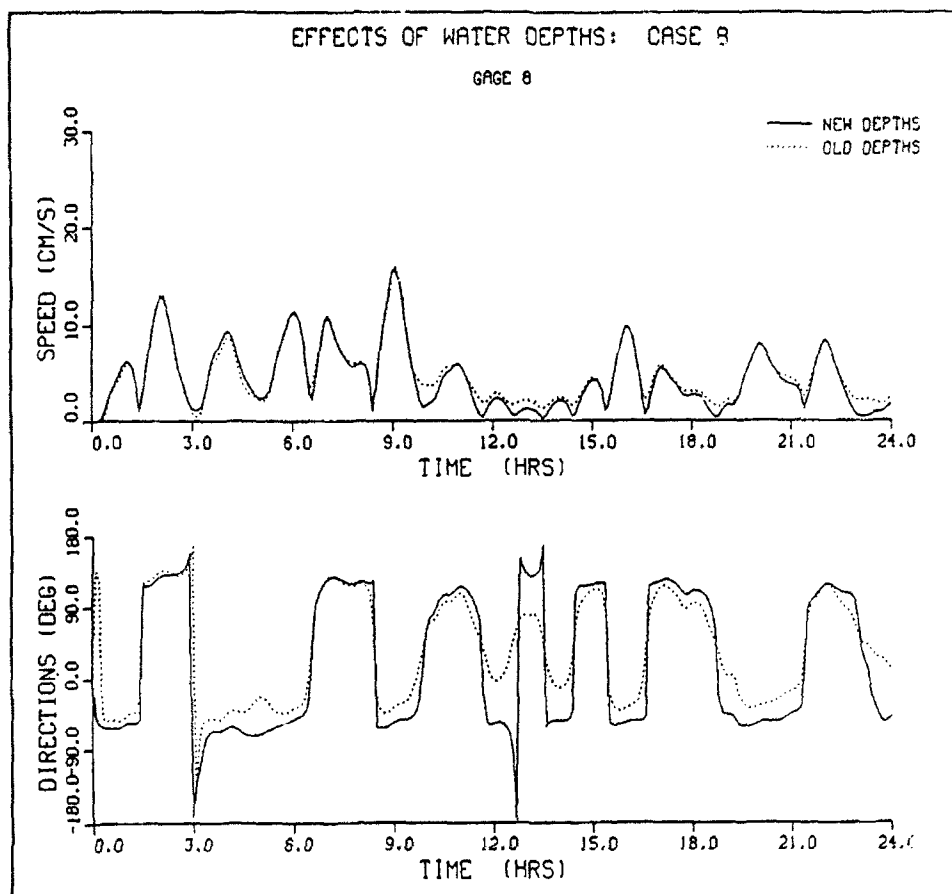


Figure 16. Comparison of water velocities at gauge 8 in depth sensitivity test

opposed to W for the simulation using the coarse grid. Again, this discrepancy is attributed to the increased grid/bathymetry resolution within this area.

Review of both the bathymetry and grid aspect ratio sensitivity tests has shown that the model, in general, is more sensitive to changes in depth than to changes in cell sizes. However, comparisons made at gauges 7 and 8 have shown that water velocities (both magnitudes and directions) are sensitive to the cell sizes within these locales. The lack of change in velocities measured at gauges 9 through 12 suggests that the difference in velocities produced with the coarse and fine grids result from greater grid/bathymetry resolution provided with Dead Horse Bay and within the vicinity of Frying Pan Shoals and Grassy Island.

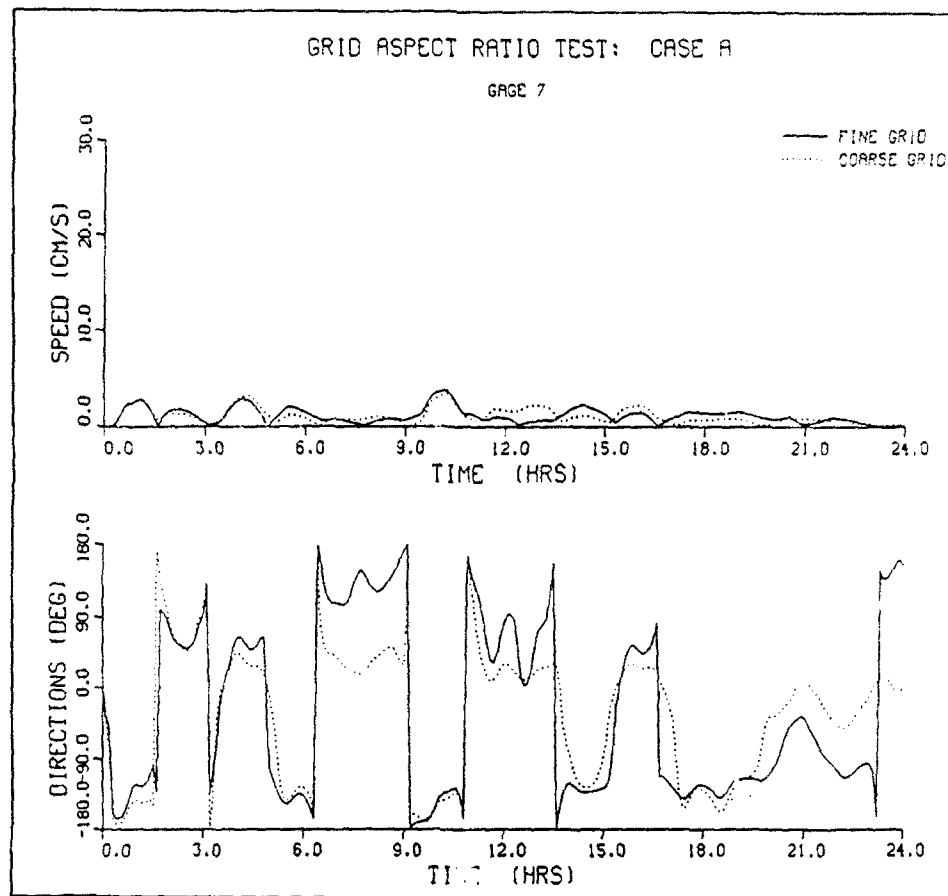


Figure 17. Comparison of water velocities at gauge 7 in grid sensitivity test

Calibration of the Hydrodynamic Model

During the latter stages of constructing a numerical model, the model must undergo calibration and validation to ensure that it accurately predicts hydrodynamic conditions within a given study area. The accuracy of model results is greatly influenced by the accuracy of boundary and forcing conditions, representation of the geometry of the study area (i.e., bathymetry and land/water interface), and to a lesser degree, the choice of certain "calibration" parameters. Calibration is the procedure where certain model parameters, such as the bottom friction coefficient, are adjusted to maximize agreement between model results and measured field data. Once the calibration procedure is completed, then the model undergoes a validation procedure to ensure that the model can replicate differing conditions. In this procedure, the model is applied without adjusting those parameters determined in the calibration procedure. Obtaining a good comparison between model and measured data in the verification procedure provides confidence that the model can accurately simulate hydrodynamics.

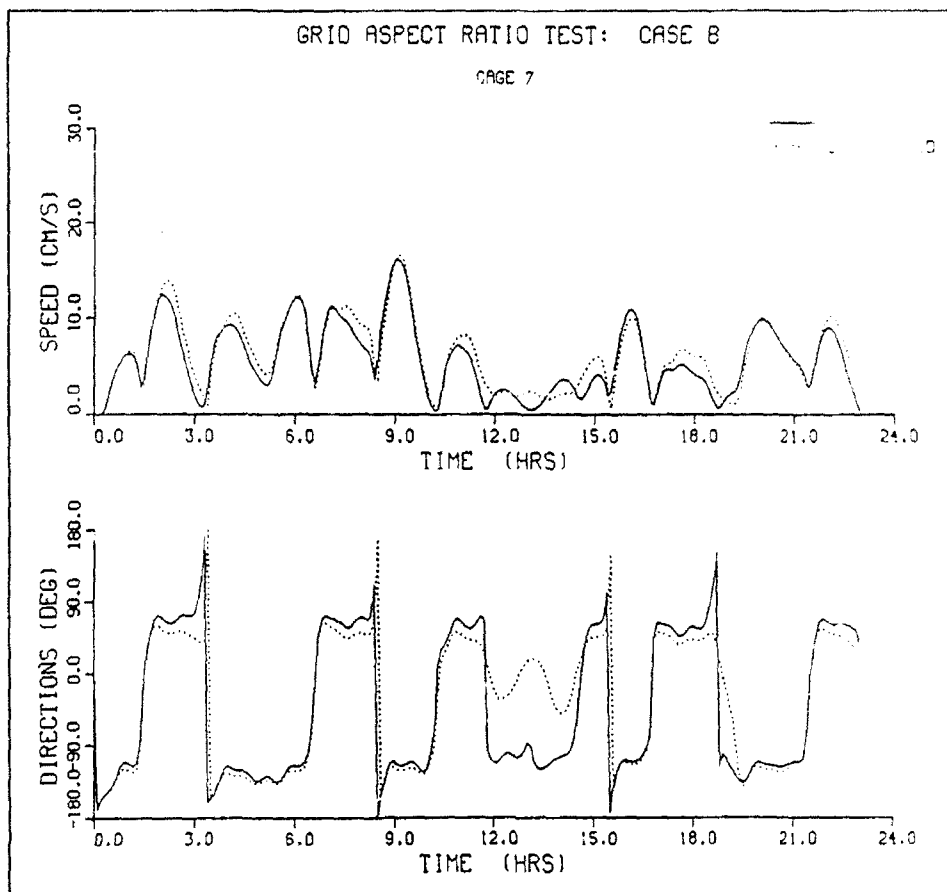


Figure 18. Comparison of water velocities at gauge 7 in grid sensitivity test

The strategy for selecting the time spans over which to calibrate and validate the lower Green Bay model consists of three criteria. First, the selected periods should have the greatest quantity of accurate, synoptic field data available for comparing with model results. Second, these data should be collected over a wide spatial area within the modeling domain to ensure that accurate results are obtained throughout the study area. Third, in order to show that the model can replicate a broad spectrum of events, these periods should reflect both average and extreme events that are commonly experienced in the study area.

In addition, because the hydrodynamic model is subsequently used for supplying flow field parameters to the water-quality model, the hydrodynamic model should be tested over a time span or "loading cycle" consistent with the transport of a contaminant within a bay/river environment. During calm periods, river discharges may lack sufficient momentum in which to flush the loading into open water. Under these conditions, the loading will reside within the river and in the immediate vicinity of the mouth; therefore, diffusion becomes an important process in transporting the loading into open water. For lower Green Bay, loadings normally reside within 0.25 mile of the Fox River

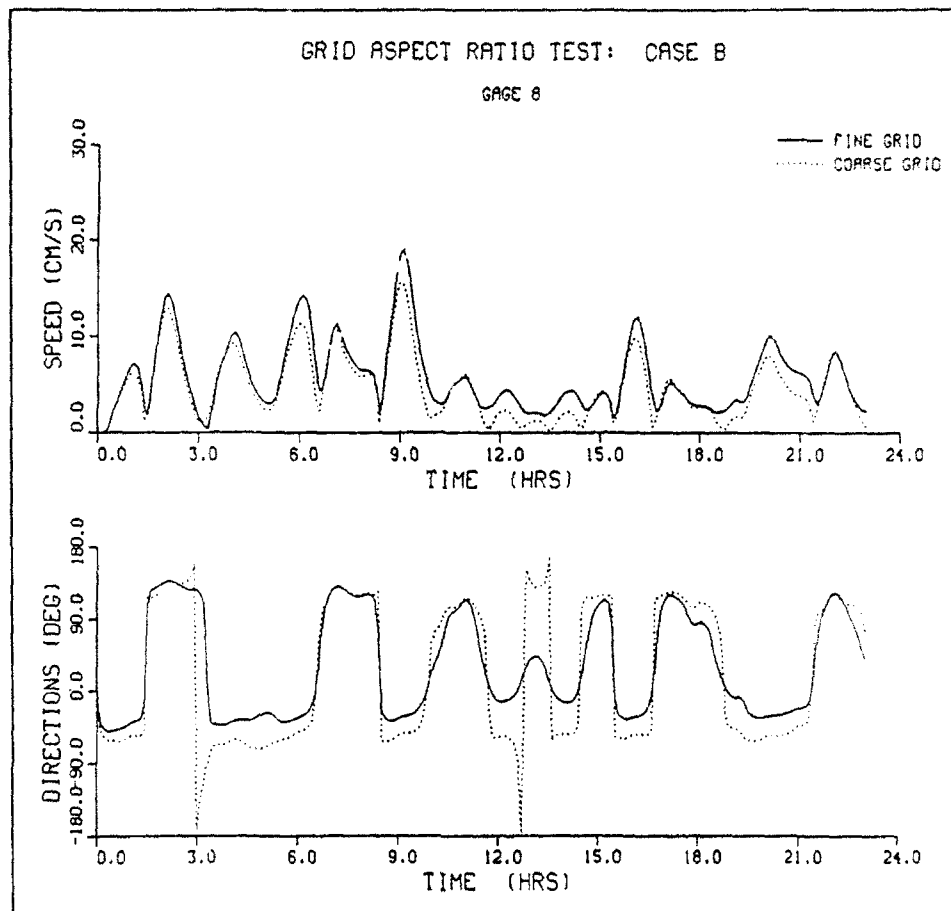


Figure 19. Comparison of water velocities at gauge 8 in grid sensitivity test

mouth (Patterson 1984). During extreme events, seiche action and/or high river discharges can provide sufficient momentum for transporting the loadings into open water. Because of the oscillating nature of a seiche, loading transport will alternately be directed upstream and towards the open water. In summer, a given loading cycle typically consists of a calm period lasting approximately 7 to 10 days, followed by storm conditions lasting for 1 to 2 days. Thus, the lower Green Bay model was calibrated and verified over a multi-week period.

The time span selected for calibrating the hydrodynamic model began on 16 June 1984 at 0000 CST and concluded 14 days later at 2400 CST on 30 June. During this period, the lower bay experienced two relatively high wind events, with one event inducing a maximum range of water level fluctuations of 1.6 ft, or 2.5 times greater than the mean water surface fluctuation range for this area (Patterson 1984).

Overview

Model calibration and validation were performed using the high-resolution grid. Average water levels recorded at the Angle Light gauging station during the latter half of June 1984 were approximately 580.1 ft IGLD. A minimum water level of approximately 579.3 ft IGLD was recorded during the last week of June. Because these water surface levels were above the elevations of the shallow areas described previously, both the single and double crosshatch areas shown in Figure 11 were treated as submerged regions in the model.

The open-water boundary was driven with a time series of water surface levels recorded at the Angle Light gauging station. These data were measured at 15-min intervals. The fine temporal resolution of the data ensures, to a certain degree, that the dominant oscillation modes affecting the lower bay are resolved in the model. Water levels were supplied to the model at the 15-min interval, and water levels were updated via linear interpolation at those time-steps falling between the 15-min intervals. At each time-step, the measured/updated water surface level was assigned uniformly across the open boundary. No water surface level gradient was imposed along this boundary.

Water level data were not adjusted, in phase or amplitude, to account for the distance between the locations of the gauging station and the outer boundary. As a consequence, the water surface levels and velocities computed by the model can be expected to contain phase errors of several minutes. Because the time series is being applied to the model boundary north of the gauge, computed flow field parameters should lag behind the measured data during periods when the net flow is to the south, and the model results should lead the measured data when the net flow has a northerly heading.

Wind speed and direction time histories specified in the model were recorded at the Green Bay Municipal Airport, which is located about 6 miles south-southwest of the bay. Wind data were supplied to the model at 1-hr intervals. Furthermore, these data were updated via linear interpolation at those time-steps falling between the full hour. Wind directions measured at the airport were not altered. Following the procedures presented in Patterson (1984), wind speeds were increased by 31 percent to account for over-land surface friction effects.

Water discharges were specified at the upstream boundaries of the Fox and East Rivers. Because the USGS does not maintain velocity gauges within the modeling area of the Fox River, it was necessary to substitute flow rates measured at Rapid Croche Dam, which is located approximately 9 miles upstream of DePere Dam. No adjustments were made to the flow rates measured at the Rapid Croche gauge.

The USGS does not maintain a discharge gauging station on the East River. Patterson (1984) used flows measured by the USGS on the Kewaunee River as a replacement. The Kewaunee River basin, which is located to the east of lower Green Bay and drains into Lake Michigan, has approximately one fourth the drainage area of the East River basin. Patterson adjusted flow rates

measured on the Kewaunee River to reflect the differences in drainage areas between these two rivers by one fourth. This procedure was adopted in this study.

Discharge data provided by the USGS consist of daily-averaged flow rates. Thus, for each river the model was supplied with one flow rate for each day of the simulation. Flow rates were updated via linear interpolation at each time-step during the simulation. Fox River and adjusted East River flow rates were obtained from Patterson's data sets, bypassing the need for modifying Kewaunee River flows.

Data available for comparison with the model results include time series of water surface levels recorded at the NOAA-operated Pulliam Power Plant gauging station and current speeds and directions from the five current meters. (Because water level data collected at the Angle Light gauging station are used for driving the open water boundary, these data cannot be used for comparison purposes.) The reader is referred to Figure 3 for locations of these gauges and meters.

Water levels were recorded by the Pulliam gauge at 1-hr intervals. Because of the relatively coarse temporal resolution, the measured data do not resolve the higher-frequency oscillations associated with Lake Michigan and Green Bay oscillation modes.

Current data were recorded with Endeco 174 shallow water meters. When new, the meter has a manufacturer-defined speed threshold of 2.57 cm/s. This type of meter employs an impeller that rotates due to current flows. Time-averaged velocity measurements are computed by counting the number of impeller revolutions completed over a user-defined time period. The period at which these meters recorded this information was 10 min. Furthermore, these meters were deployed at an approximate depth of 1 m below the water surface.¹

Of the five meters deployed during the calibration period, only three meters were in continuous operation throughout the entire period. These three meters are the north central, northeast, and southeast meters. The Dead Horse Bay meter was in operation from simulation hour 0 through hour 299. It was not operating for the remaining simulation period. The central channel meter began operation at simulation hour 305 and continued operating for the rest of the period. (It appears that only four meters were deployed in the lower bay, and the same meter was used at the Dead Horse Bay and central channel sites.)

¹ Personal communication, August 1991, Dr. Kwang Lee, Professor, Department of Civil Engineering, University of Wisconsin, Milwaukee, WI.

Calibration procedure

Calibration was performed primarily through adjusting the bottom friction coefficient, Manning's n . Selecting the proper coefficient involved a three-stage procedure. In the first stage, a global coefficient was specified throughout the grid and the model was run over a wide range of values, from 0.020 to 0.045, to determine a "ballpark" coefficient. This value was determined by comparing predicted water surface levels with those measured at the Pulliam gauge station.

With this ballpark coefficient serving as a basis, the model was again run over a range of global values, but in this second stage, a narrower range of coefficients was used for optimizing model-generated velocities. In addition to comparing water levels, this stage also incorporated a comparison of model-generated velocities with those measured by the current meters. This stage yielded a refined friction coefficient, as compared to the ballpark coefficient obtained in the previous stage.

In the third stage, bottom friction coefficients were adjusted in shallower regions in order to better represent the frictional drag of these areas. After completing this task, the model was able to reproduce the water speeds recorded by the meters. However, model-generated water directions were not as accurate. In an effort to improve model results, wind speeds were increased from 31 percent above those recorded at the airport to 50 percent above airport-recorded wind speeds. It was found that once the wind speeds were adjusted, the model reproduced water speeds and directions with a higher degree of accuracy. Current patterns are, in part, dependent on the surface shear stress imposed by wind. In this study, the surface shear stress is represented as a function of the wind speed and wind drag coefficient. In contrast to the wind speed which can be readily measured, wind drag coefficient is represented empirically and is, therefore, more difficult to estimate. Improved model results obtained by increasing the wind speeds are attributed to using a wind drag coefficient that was too low. By increasing the wind speeds, improved accuracy is achieved in predicting the surface shear stress. A discussion of wind drag coefficients is presented in this chapter.

Comparisons between model-generated results and measured data are provided at the end of this chapter. Model results were generated using the 50-percent adjusted wind speeds with a global Manning's n equal to 0.025. Shallow areas having depths less than 3 ft were assigned a Manning's n equal to 0.045, whereas areas whose depths are less than 6 ft but greater than 3 ft were assigned a value of 0.035.

Description of calibration period conditions

The calibration procedure was conducted over a 14-day period beginning at 0000 on 16 June 1984 and ending on 30 June at 2400. In the following discussions, events are referenced relative to simulation time in hours. Thus, this procedure had a simulation time of 336 hr. Comparisons between model

results and measured data are contained in the following package. In these comparisons, separate conventions are used for displaying wind and current directions. Wind directions are defined using the standard meteorological convention; an angle equal to zero defines a wind blowing from north to south, and angles increase in a clockwise direction. Conversely, current directions are displayed with the standard oceanographic convention; an angle equal to zero defines a current traveling from south to north, and angles increase in the clockwise direction.

Average wind speeds experienced during the first 36 hr of the simulation were approximately 3 m/s, with winds blowing primarily from the south-south-west. Wind speeds remained fairly steady from hr 36 to hr 138, but wind directions shifted, with winds coming primarily from the north and varying between the northeast and northwest directions. Water levels fluctuated between 579.8 and 580.7 ft IGLD, or within a maximum range of 0.7 ft. Higher-frequency oscillations were apparent over the 138-hr period, especially around hr 48.

Current speeds were generally less than 5 cm/sec; however, at hr 36, 54, 62, and 80, speeds increased in magnitude to as great as 10 cm/sec. Prior to these times, winds were rapidly shifting directions and began to blow primarily from the north. Current directions occurring at these higher speeds were towards the north, suggesting that the winds experienced in the lower bay differed from those recorded at the airport.

At hr 138, winds began shifting, first blowing from the northeast, then from the east. At hr 154, the prevailing wind direction was from the south-south-east. Mean water levels at hr 150 rose by approximately 0.2 ft and the water levels were fluctuating within a 0.4-ft band. From hr 116 to 182, winds became light and variable, with water levels over this time span oscillating within a 0.7-ft range.

Current speeds recorded from hr 84 through 182 exceeded 15 cm/sec on several occasions, such as at hr 112. Without wind to drive the lower bay after hr 168, however, current magnitudes began decreasing. Lower-frequency oscillations were evident during the simulation period, as were the higher-frequency modes. Currents were directed primarily towards the northeast at the Dead Horse Bay, north central, and southeast meter locations. Currents were directed towards the west at the northeast meter.

Wind speeds began increasing at hr 182 to an average speed of 4 m/sec at hr 186, with wind directions primarily from the west. Over the next 22 hr, with winds remaining steady, water levels dropped by about 1 ft, from 580.6 ft IGLD to 579.6 ft IGLD.

Starting at hr 204, wind speeds increased from 4 m/sec to 9 m/sec at hr 208. During this period, water levels rose by approximately 1 ft, to 580.6 ft IGLD. A corresponding increase in water speeds is also recorded by the north central and northeast meters, where speeds in excess of 24 cm/sec were recorded at the north central meter. The subsequent seiche oscillated for

approximately 24 hr, then quickly died off. From hr 234 to 256, water levels fluctuated within a relatively narrow range of 0.25 ft.

A high wind event was recorded during the period from hr 252 through 264. Over this period, the maximum wind speed was approximately 9 m/sec with prevailing winds coming from the south-southwest. Starting at hour 256, the lower bay experienced significant seiche action with a peak water level change of 1.6 ft, or 2.5 times greater than the mean seiche magnitude of 0.64 ft cited by Patterson (1984). This seiche also produced the greatest current speeds measured during the calibration period. At the north central meter, speeds exceeded 45 cm/sec, while speeds of approximately 40 cm/sec were recorded by the northeast meter. The dominant oscillation period for this seiche was 9.1 hr, which corresponds with the first oscillation mode of Lake Michigan. The die-off time for this seiche was about 2 days.

Another seiche began at hour 299, and the resulting water surface level displacement was approximately 1.1 ft. Average wind velocities during this time span were approximately 5 m/s, with winds blowing from the northwest. Current speeds also increased to as great as 27 cm/sec at the north central meter.

Analysis of calibration results

The model accurately reproduces, in both phase and amplitude, the water surface level time-histories recorded at the Pulliam gauging station throughout the calibration period. However, the model consistently underpredicts measured water levels by approximately 0.1 ft. Because this discrepancy is consistent throughout the calibration period, and also throughout July 1984, it is attributed to errors incurred while establishing benchmark elevations for the Angle Light and/or Pulliam gauge stations. Figure 20 presents a comparison of model-generated and measured Pulliam water surface levels showing this datum shift. Figure 21 presents this comparison after raising the computed water levels by 0.1 ft. Additional figures contained in the package present computed water levels that have been shifted by 0.10 ft.

The model accurately replicates the water surface oscillations, in both phase and amplitude, for the 12- and 9-hr modes of oscillations. However, the 2-hr oscillation period computed by the model is absent from the measured gauge data. One possibility as to why the measured water levels do not exhibit this period is that these water levels are plotted at 1-hr intervals. The process of averaging 1-hr data is not capable of resolving a 2-hr phenomenon.

At the northeast, north central, and southeast current meter locations, the model accurately matched current speeds and directions together with the phases and amplitudes of the lower- and higher-frequency oscillations recorded by these meters. Figure 22 compares water speeds and directions generated with the model to those measured at the north central location.

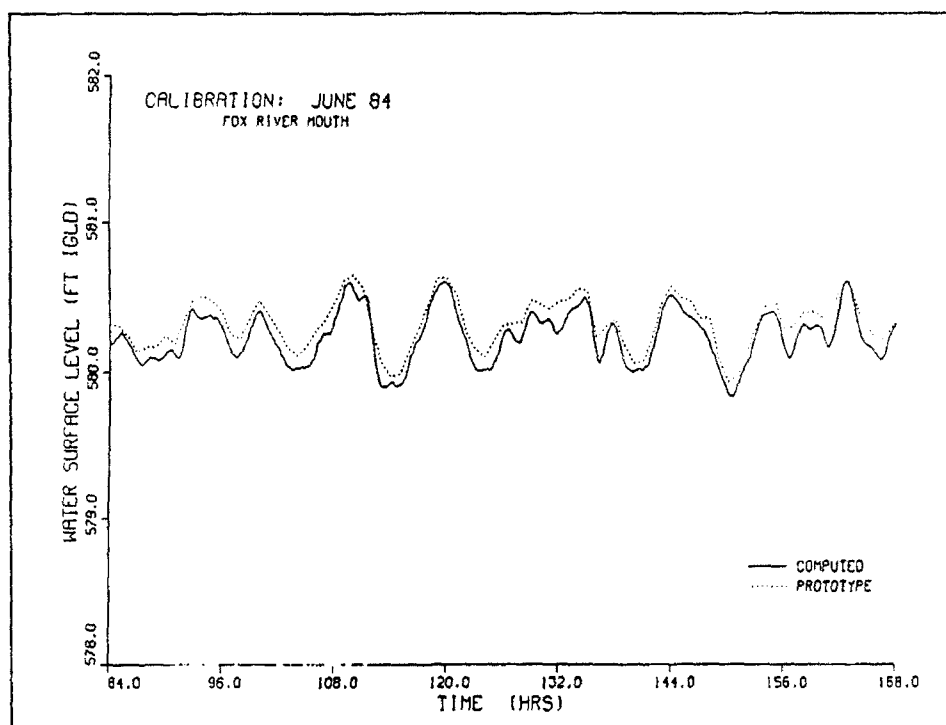


Figure 20. Comparison of water surface levels at Pulliam gauging station

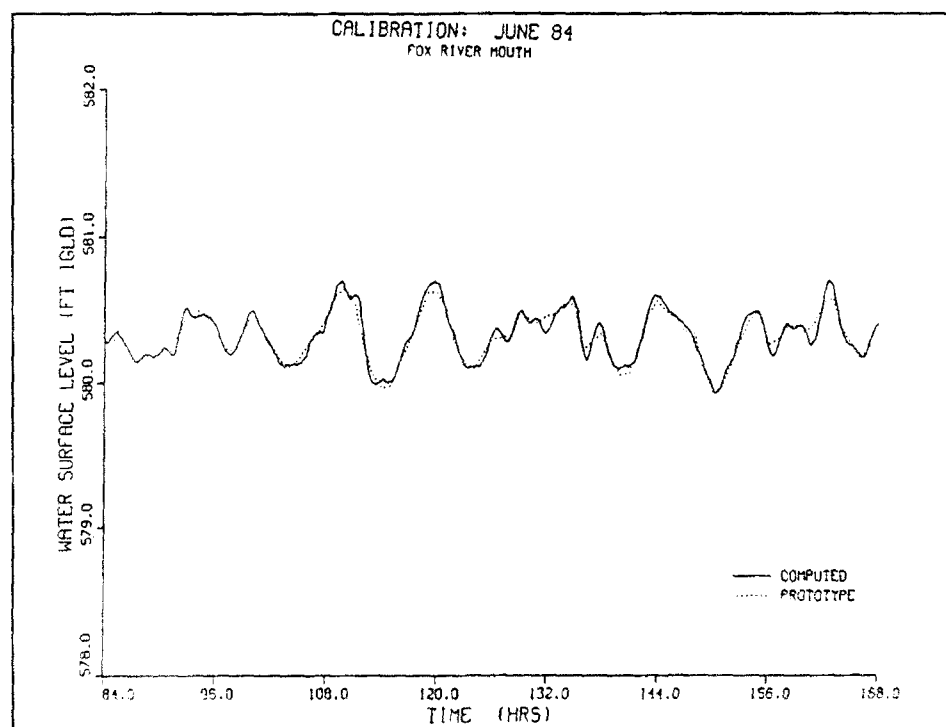


Figure 21. Comparison of water surface levels at Pulliam gauging station with shifted datum

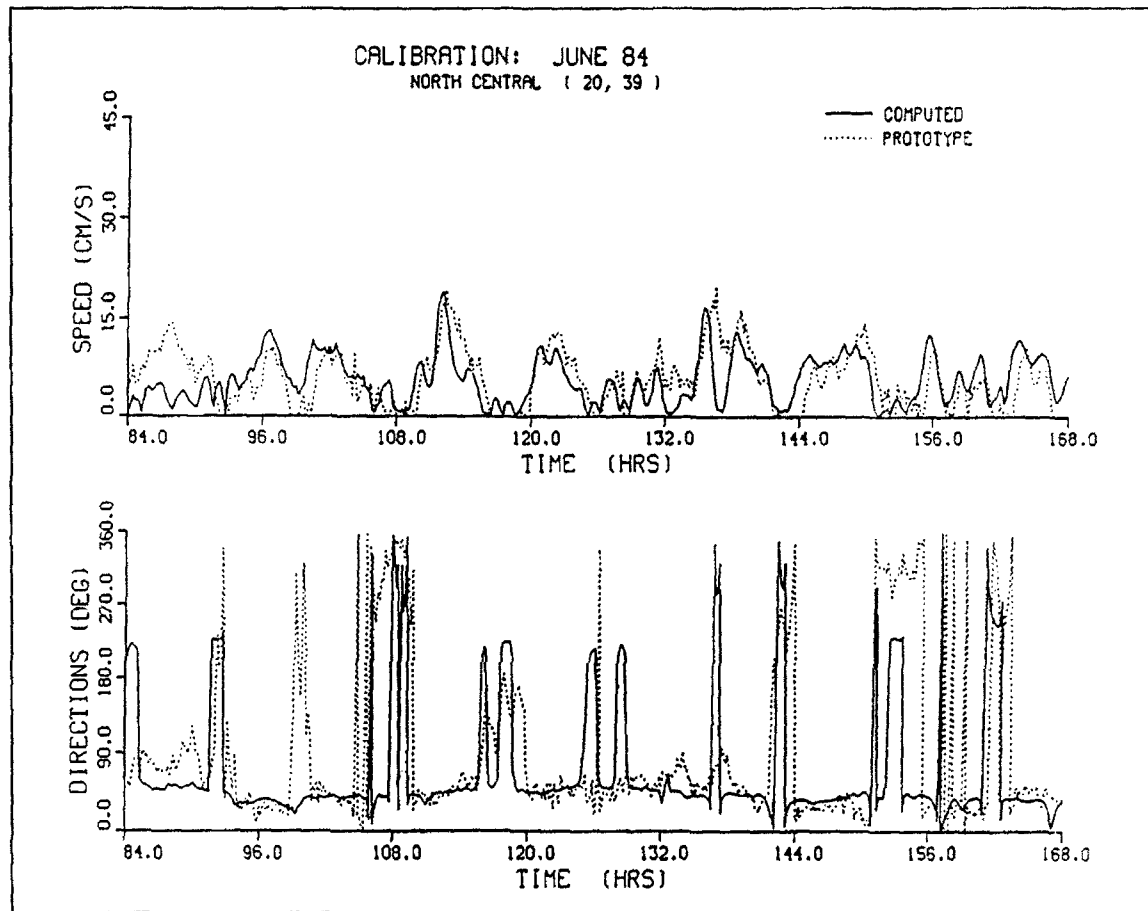


Figure 22. Comparison of water velocities at north central location

Notable exceptions occur during periods, such as at hr 36, when the prevailing winds are from the northeast and water level fluctuations are reduced in amplitude. It appears that during these periods Lake Michigan and/or Green Bay are experiencing a storm surge event where a setup or setdown in water levels reduces the amplitudes in the water surface. Given that the northeast-southwest direction corresponds with the bay's greatest fetch length, wind-generated waves can be generated at lower wind speeds. Because the current meters are deployed close to the water surface, these meters become susceptible to wind-generated waves, degrading the accuracy of the current velocity measurements.

The model generally underestimates current speeds measured at the Dead Horse Bay meter. Furthermore, predicted current directions tend to differ by approximately 90 deg from those recorded by the meter. This discrepancy is attributed to the rotational circulation pattern typically occurring in this area. Model results show that greater velocities can be found along the model's shoreline and surrounding shallow areas as compared with those found at its center. These results are consistent with those found by Swain and Bird (1987).

It is felt that the numerical gauge was placed too close to the center of the bay, thus missing the circular current pattern within Dead Horse Bay. The predicted current direction seems to agree with this assessment because the computed and measured directions tend to differ by a somewhat constant value.

A notable exception to this observation occurs from simulation hr 84 to 144. Neglecting periods when measured current speeds were less than or approximately equal to the threshold of the meter, close agreement exists between the predicted and measured directions. During this period, the lower bay was being driven primarily with wind as opposed to water level fluctuations.

Validation of the Hydrodynamic Model

A 21-day period from 1 July 1984 at 0000 Central Standard Time (CST) to 21 July 1984 at 2400 CST was chosen for model validation. Two large seiche events were recorded during this period. The most significant storm event resulted in a water level displacement of 1.6 ft. In keeping with the purpose of the validation process, model parameters determined in the calibration procedure were not changed for this test. Locations where data were collected, together with their sampling frequencies, are identical to those used in calibrating the model. However, one current meter was not recording over the entire period and two were malfunctioning during parts of this period.

For example, all water speeds and directions contained in the Dead Horse Bay current meter data set were equal to zero. This suggests that this meter, originally deployed in Dead Horse Bay, was moved during the last week of June to the central channel site. Current meters which malfunctioned during July are the northeast and southeast meters. In both cases, water velocity directions remained constant, but speeds did fluctuate. While data from these meters cannot be used for quantifying the accuracy of model-generated current directions, the speeds can aid in understanding the processes occurring in the lower bay.

Description of validation period conditions

Over the first 216 hr of the simulation, wind speeds averaged approximately 3 m/sec, with sustained periods when wind speeds exceeded 7 m/sec. Wind directions varied over this time span, but the primary wind direction was from the west. Water levels fluctuated within a 1.1-ft range during this period, between the extremes of 579.4 and 580.5 ft IGLD. These extremes were reached during the higher, sustained wind periods starting at hr 132 and 60, respectively.

Beginning at hr 212 and lasting until hr 233, wind directions show a high degree of variability, with winds blowing from various directions. At hr 233,

the variability in wind directions decreased as the prevailing winds were primarily from the east and northeast directions. Wind speeds increased at hr 204 from 3 m/sec to 12 m/sec at hr 242. At hr 235, the recorded water level at Angle Light reached an elevation of 581.3 ft IGLD, or 1.6 ft above the 579.7-ft IGLD elevation recorded at hour 229. Again, this displacement is approximately 2.5 times greater than the mean seiche range noted by Patterson. Over the course of the next 48-hr period, the water surface appeared to oscillate, with a period of approximately 12 hr. This oscillation period is approximately equal to the combined Lake Michigan/Huron mode discussed in Mortimer and Fee (1976).

From simulation hr 252 through hr 300, wind speeds remained relatively steady at 3 m/s, with the prevailing winds coming from the west. At hr 300, winds began shifting to the southwest, and wind speeds increased to 6 m/sec at hr 306. Wind speeds decreased to 2 m/sec over the next 12 hr then increased to approximately 9 m/sec at hr 332.

Amplitudes of the water surface fluctuations over this 32-hr period are smaller than those generated by the seiche at hr 235. However, higher-frequency fluctuations in the water surface level are more pronounced during this period. The high wind event that occurred at hr 332 appeared to be a front that activated the seiche at hr 338. This seiche, with a maximum range of 1.4 ft, also appeared to have as its dominant oscillation period the 12-hr Lake Michigan/Huron mode.

From hr 372 to 432, the water surface level fluctuates within a 0.7-ft range from 579.7 ft IGLD to 580.4 ft IGLD. At hr 437, a slight drawdown in water levels to 579.4 ft IGLD, is experienced within the lower bay. Wind direction subsequent to this time is from the northwest. Seven hours later, wind speeds increased from 3 m/sec to 7 m/sec and wind direction was from the southwest. With the increased wind speeds and a shift in wind directions, water levels began oscillating within a 0.5-ft range, from 579.8 ft IGLD to 580.3 ft IGLD. Higher-frequency oscillations are also apparent during this period.

From hr 460 through the end of the simulation at hr 504, average wind speeds are approximately 4 m/sec with wind directions varying from the northeast to the west. Over this period, water levels fluctuated over a 0.6-ft range of 579.9 to 580.5 ft IGLD.

Analysis of validation results

Comparisons between the computed and measured water surface levels at the Pulliam gauge exhibit the same degree of accuracy as those obtained in the calibration procedure (Figure 23). As described in the previous section, measured water surface elevations were adjusted by adding 0.10 ft in the comparisons. The model accurately replicates the water surface oscillations, in both phase and amplitude, for the 12- and 9-hr modes of oscillations. However, the 2-hr oscillation mode depicted in the model is absent from the measured gauge data because of the averaging process.

In general, predicted water levels were within 0.1 ft of the measured water levels with extended periods when the differences were less than 0.05 ft. However, the greatest difference between generated and measured water levels was about 0.5 ft and occurred at approximately simulation hr 242. At this time, the model predicted a water level of approximately 581.1 ft IGLD as opposed to a recorded measurement of 580.6 ft IGLD.

At the north central and central channel current meter locations, the model accurately matched current speeds and directions together with the amplitudes and phases of the lower- and higher-frequency oscillations recorded by these meters. Comparisons of water velocities for the north central and central channel meters are presented in Figures 24 and 25, respectively. Beginning at approximately hr 36, comparisons with the computed and measured velocities at the northeast meter location show a distinctive 2-hr shift in phase. Furthermore, starting at hr 204, a similar shift in phase between computed and measured velocities is evident at the north central site.

No phase shift, relative to the model-generated currents, is exhibited in either the central channel or the southeast current meter data at hr 204. Furthermore, a phase shift is clearly evident when comparing currents measured by either the north central or northeast meter to data collected at the central channel or southeast locations. Therefore, discrepancies in phase at both the northeast and north central locations are attributed to post-measurement processing of the data.

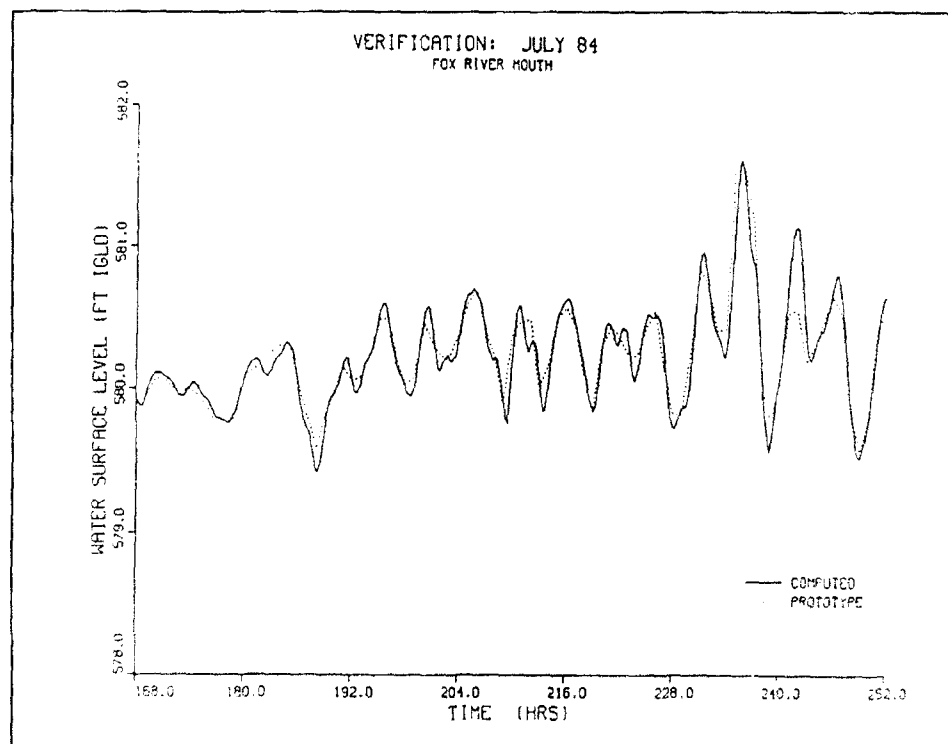


Figure 23. Comparison of water surface levels at Pulliam gauging station

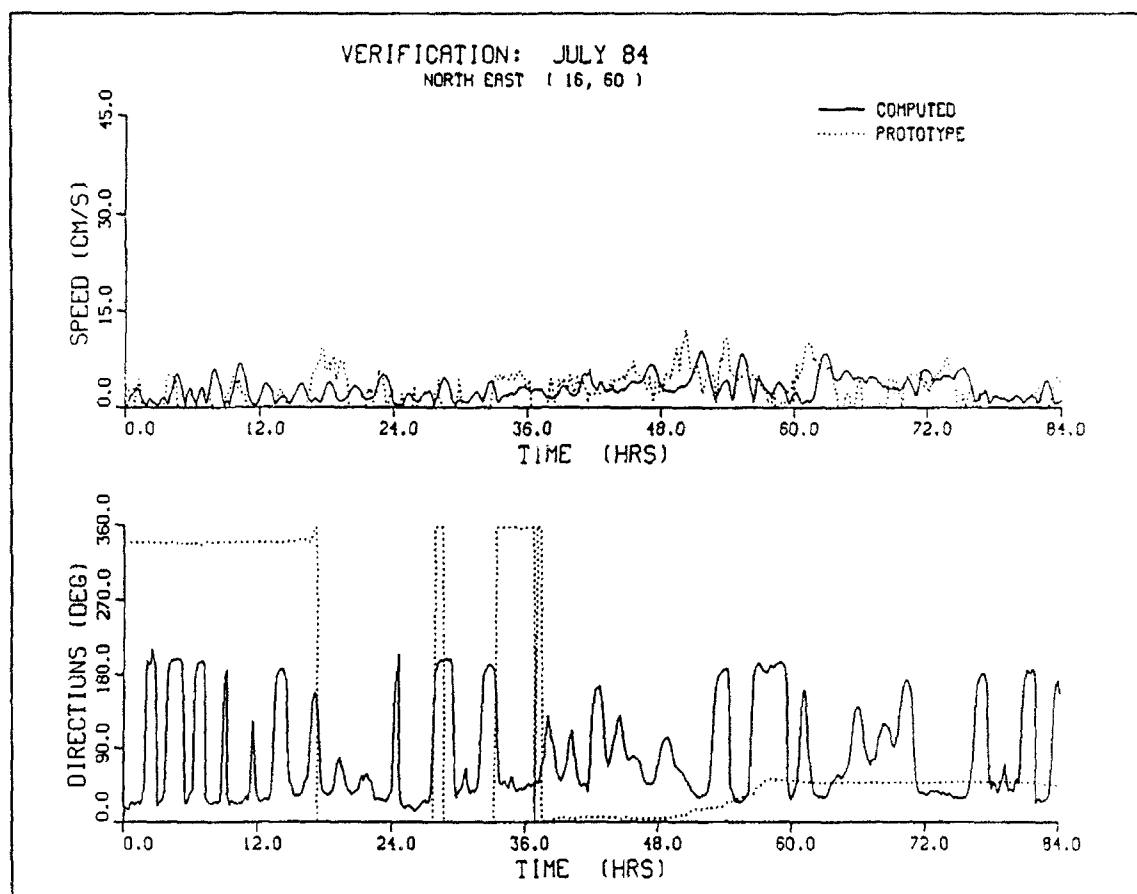


Figure 24. Comparison of water velocities at northeast location

Diagnostic Analyses of Calibration and Validation Results

Several diagnostic analyses were performed, including spectral analysis of water surface level time histories and exceedence distribution comparisons of water velocity time histories. Spectral analyses of water surface level time histories were performed to determine whether the model accurately reproduces the (seiche oscillation) modal structure of lower Green Bay. The spectral analysis tests were performed using a fast-Fourier transformation algorithm, and were applied with water level time histories computed in the calibration and validation simulations at six gauge locations. These locations are the Fox River mouth and the five current meter deployment sites (i.e., north central, northeast, southeast, central channel and Dead Horse Bay locations). In addition, spectral analysis was applied to measured water level data collected at Angle Light gauging station, and results from this analysis serve as a basis for determining whether the model accurately replicates the modal structure of the lower bay.

For the calibration period in June 1984, spectra were calculated with model-generated and measured water surface levels for the 14-day simulation period. A sampling frequency of 15 min was used for both the model and measured water level time series. The measured Angle Light spectrum, presented in Figure 26, shows that the dominant oscillation modes have periods of 9 and 12 hr. These periods correspond to the first Lake Michigan mode and the semidiurnal tidal period, respectively. Green Bay also experiences a combined Lake Michigan/Huron mode, which has a period approximately equal to the 12-hr tidal period. Thus, the energy displayed in Figure 26 for a frequency of about 0.08 hr^{-1} (i.e., 12-hr period) may reflect the combination of lake and tidal oscillations. Less dominant modes were also present and have periods of approximately 5.2, 4.8, and 4.1 hr, which correspond with the second Lake Michigan, and the first and second (independent) Green Bay oscillation periods, respectively.

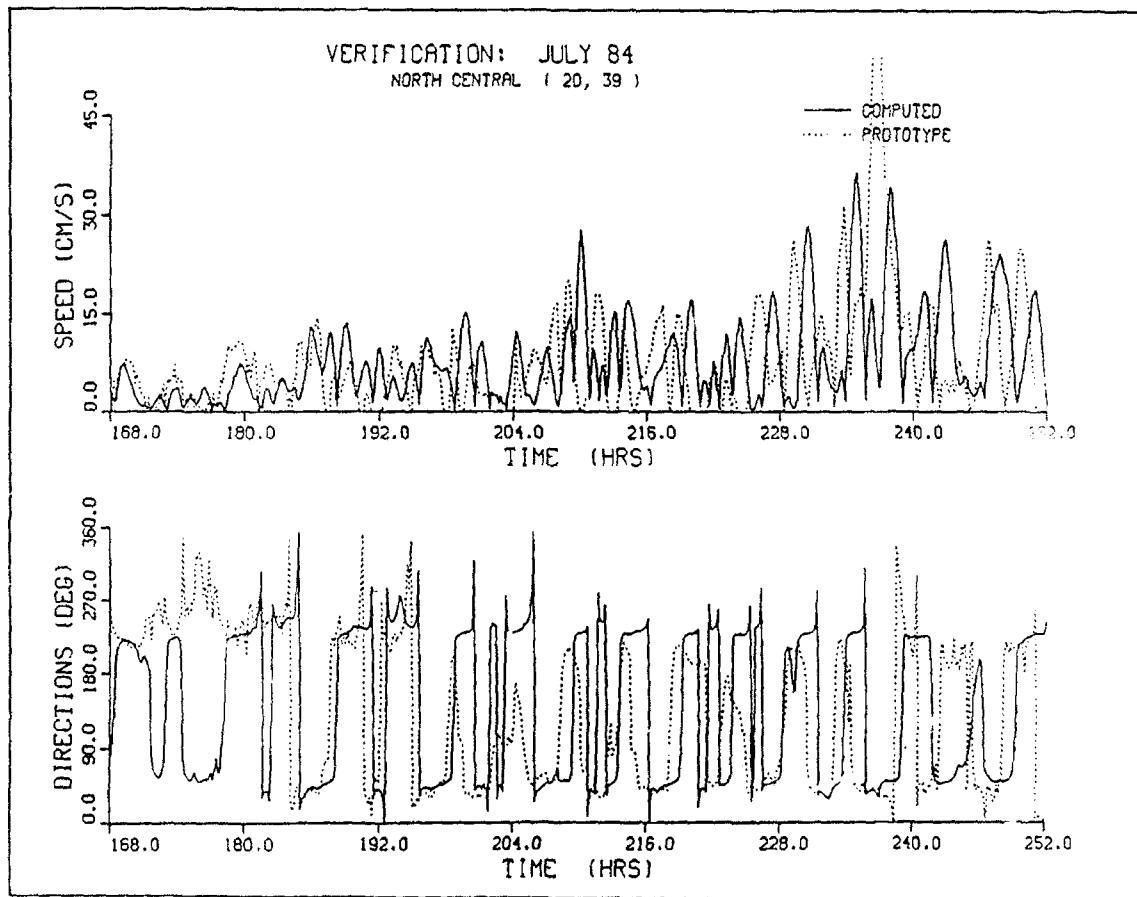


Figure 25. Comparison of water velocities at north-central location

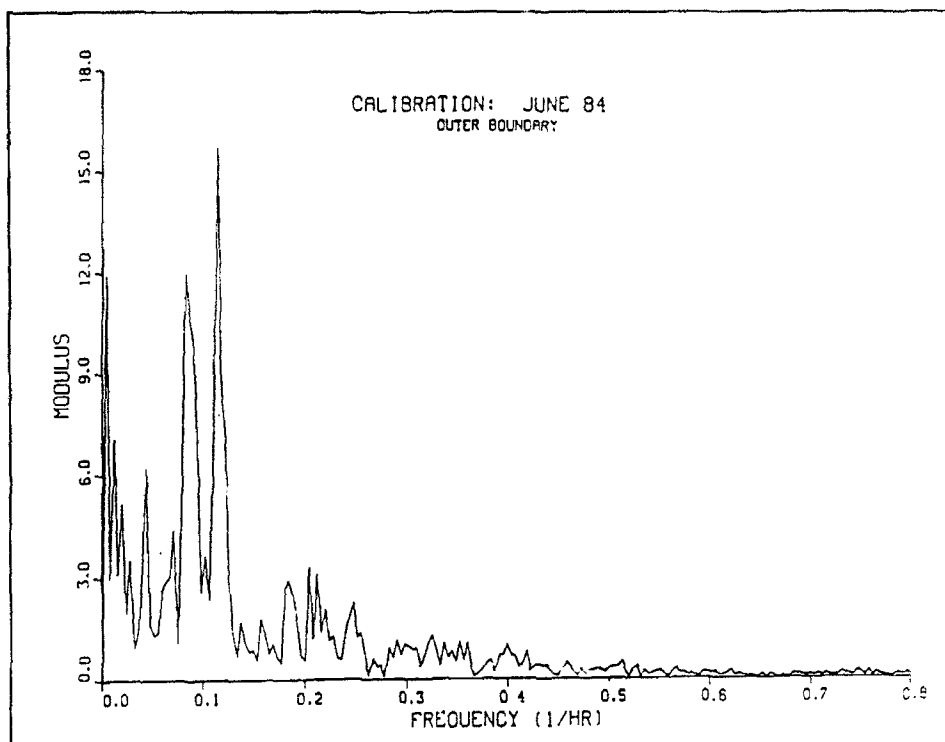


Figure 26. Spectrum of Angle Light water surface level time series for June 1984

Spectra computed with model-generated water levels, presented in Figure 27, were consistent with those oscillation modes described above. Additional model-generated water level spectra are contained in Volume 2. At six locations, the dominant modes had periods of 9 and 12 hr, with less dominant modes having periods of 5.2, 4.8, and 4.1 hr.

For the validation period in July 1984, spectra were calculated at the identical locations as those in the calibration period. A 15-min sampling period was used in defining the time series over the 21-day simulation period. The spectrum produced with water surface levels measured at the Angle Light gauge is presented in Figure 28. Dominant oscillation modes contained in this spectrum appear smeared when compared to those modes contained in the calibration's spectrum. Energy resulting from the first Lake Michigan mode seems divided between the 9.5-hr and 8.8-hr oscillation periods. Furthermore, the 5.2- and 4.8-hr modes are also smeared, resulting in an oscillation mode of 5.0 hr. Spectra produced with model-generated water surface levels are consistent with the spectrum calculated with measured Angle Light water levels (Figure 29).

Parametric and non-parametric statistical tests were performed to quantitatively assess the model's ability to replicate the hydrodynamic processes occurring in lower Green Bay. One test is the root-mean-square (rms) difference calculations of the measured and computed water surfaces level time series. One limitation of the rms difference test is that no information is provided as

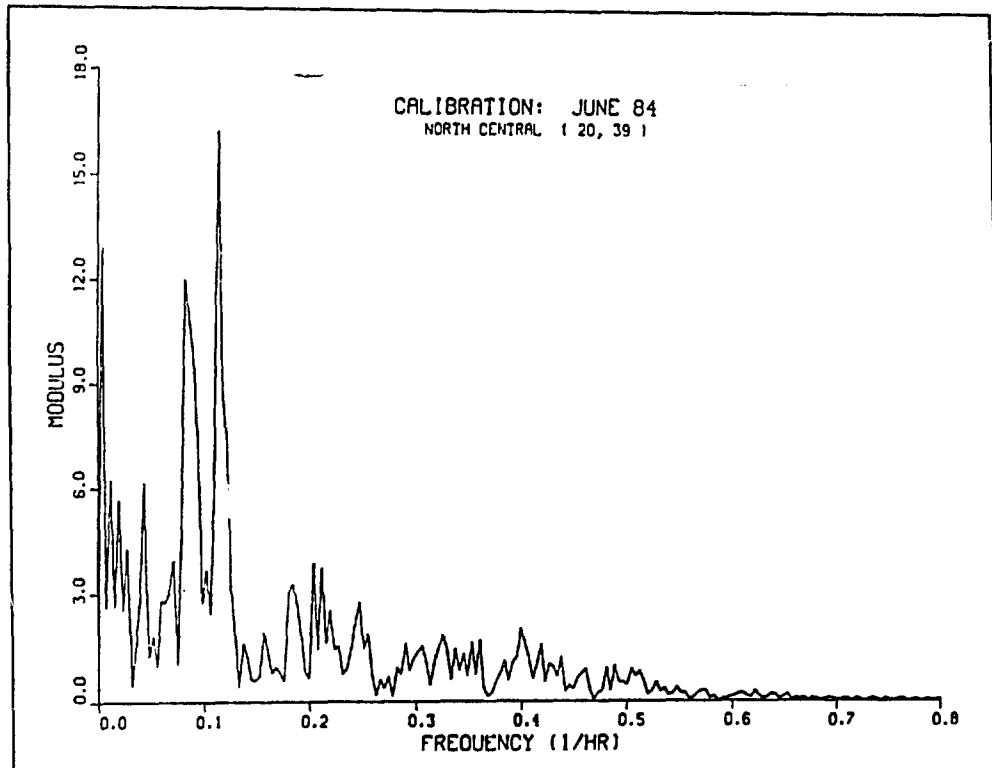


Figure 27. Spectrum of computed water surface level time series at north central location for June 1984

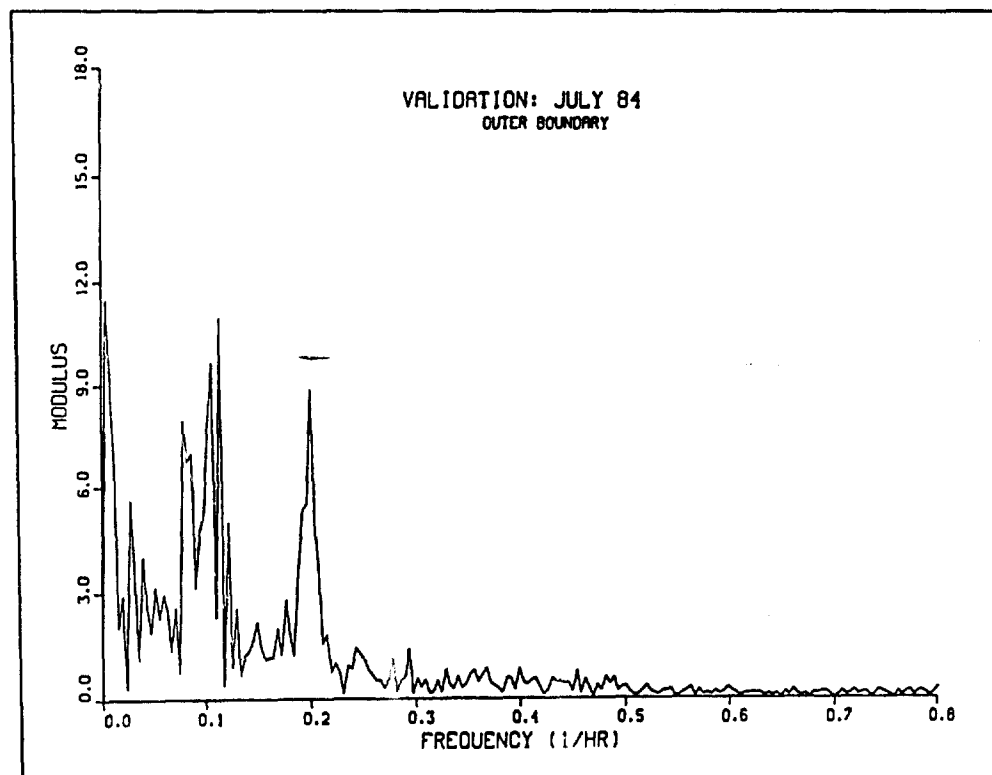


Figure 28. Spectrum of Angle light water surface level time series for July 1984

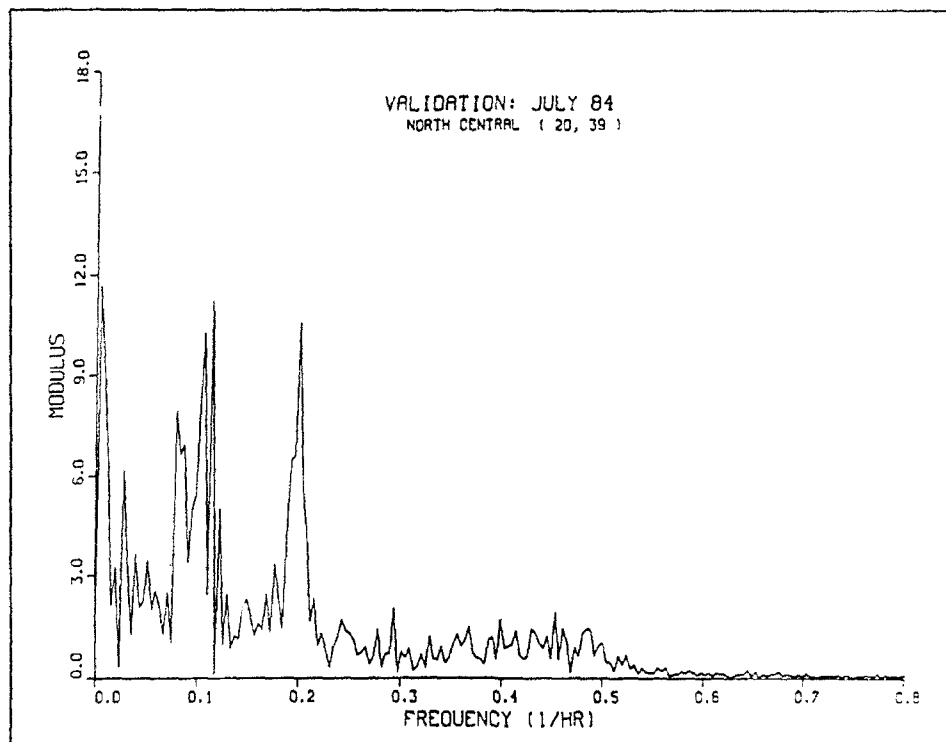


Figure 29. Spectrum of computed water surface level time series at north central location for July 1984

to the source of error being measured. For example, one source of error can be a shift in phase between measured and computed water oscillation periods, whereas a second source could be due to discrepancies in predicted water surface elevations. To overcome this limitation, a series of non-parametric or "skill" tests have been developed to differentiate between phase and magnitude errors (Hess and Bosley 1991).

Skill tests selected for analyzing the lower Green Bay hydrodynamic model include statistical comparisons of the timing and amplitude of local water level extrema (minimum and maximum) contained in the Pulliam Power Plant time series. These tests include the average gain or ratio of predicted to measured extrema, the rms difference in amplitudes, average lag or phase shift between predicted and measured extrema, and the rms difference in lag.

The average gain can be expressed as:

$$G = \frac{1}{N} \left(\frac{Y_c}{Y_m} \right) \quad (13)$$

where G represents the gain, is equal to the number of extrema pairs contained in the time series data, and Y_c and Y_m signify the computed and measured values, respectively.

The rms difference in amplitude has the following formulation:

$$A_{rms} = \left[\frac{1}{V} (Y_c - Y_m)^2 \right]^{1/2} \quad (14)$$

where A_{rms} represents the rms difference in amplitude and the remaining variables have been previously defined.

The average lag between computed and measured extrema can be written as:

$$L_m = \frac{1}{V} (T_c - T_m) \quad (15)$$

where L_m represents the average lag and T_c and T_m signify the time of extrema occurrence in the computed and measured time series, respectively.

The rms difference in lag can be expressed as:

$$L_{rms} = \left[\frac{1}{V} (T_c - T_m)^2 \right]^{1/2} \quad (16)$$

where L_{rms} represents the rms lag.

Model-generated water surface level time series at the Pulliam Power Plant were analyzed with the preceding skills tests to quantify the accuracy in predicted water level amplitudes and oscillation periods. An rms difference was also computed for this analysis. Because the water levels measured at the plant were recorded at hourly intervals, the model-generated time series were analyzed using identical time intervals. Table 8 presents the results of this analysis for the calibration and validation periods.

With values less than 0.01 ft, rms differences resulting from the calibration and validation periods are considered small. The average gain in extrema water surface levels for the calibration and validation procedure was 1.03, which represents a difference of 3 percent between the model-generated extrema and the measured extrema. Because the gain is greater than 1, the model-generated extrema were greater than the measured extrema.

The calibration exercise resulted in an average lag of 0 hr, and the lag rms difference was approximately 30 min over a simulation period of 336 hr. A lag of approximately 15 min was experienced in the validation procedure, with the model-generated water surface oscillations leading the measured oscillations. The lag rms was also higher for the validation exercise than for the calibration, with a cumulative 1-hr error in phase experienced over the course of the 504-hr simulation.

Table 8
Quantification of Model Accuracy in Predicting Water Surface Levels at the Pulliam Power Plant Gauge

Test	Calibration Period	Validation Period
rms Difference (ft)	0.006	0.007
Gain	1.033	1.033
Amplitude rms (ft)	0.009	0.112
Average Lag (hr)	0.000	0.224
Lag rms (hr)	0.471	0.937

In addition to analyzing the accuracy of the predicted water levels, the rms difference test was also performed to quantify the accuracy of the predicted water velocities. The results of this analysis are presented in Tables 9 and 10 for the calibration and validation exercises, respectively.

In general, the differences in rms values, as opposed to the rms differences, between the computed and measured water velocities were within 1 cm/sec. Exceptions are noted for the north central current meter, where the discrepancies of approximately 2.9 cm/sec and 1.1 cm/sec were calculated for the calibration and validation simulations, respectively. For the Dead Horse Bay meter, a difference of 2.4 cm/sec was calculated for the calibration exercise. The rms difference for all meters, however, exceeded 2.5 cm/sec for the calibration and validation procedures. This discrepancy is attributed to phase differences between the computed and measured water velocities. As noted previously, phasing errors and/or discrepancies in magnitudes can have a significant effect on the computed rms difference. In order to determine the primary source of error, distributions in water velocities were computed.

Exceedence or probability distribution comparisons were made in order to determine whether model-generated water velocity magnitudes have the same frequency of occurrence as those measured with the current meters. Together with spectral analysis, which depicts dominant temporal processes, this test aids in defining the integrity of the model-generated water velocity magnitudes. Water velocity distributions were defined with 3-cm/sec intervals (e.g., 0-3 cm/sec, 3-6 cm/sec, etc.). Each time history of water velocities collected at the five current meter locations was analyzed, as were the corresponding model-generated velocities. Comparisons of computed and measured water velocity distributions for the various current meters are presented in Tables 11 through 18.

Of the five current meter locations, the north central meter, followed by the central channel meter, measured the greatest range in water velocity magnitudes. Intuitively, this seems correct since these meters are located in deeper water and in close proximity to the shipping channel. The meter having the least range in magnitudes is the Dead Horse Bay meter. Of the remaining two meters, the northeast and southeast meters exhibited the third and fourth greatest range in magnitudes.

For the measured data collected at the north central, northeast, and central channel sites, approximately one third of the readings were less than or equal to 3 cm/sec, or below the threshold speed of the current meter. Approximately 70 percent of the water speeds recorded by the Dead Horse Bay and southeast meters were below 3 cm/sec. For the northeast, southeast, and Dead Horse Bay sites, approximately 90 percent of the readings were below 6 cm/sec, whereas 60 and 70 percent of the readings were below this speed for the north central and central channel sites, respectively.

Table 9
Skill Test Analysis of Model-Generated Velocities:
Calibration Period

Station	rms Difference (cm/sec)	Gain	Amplitude rms (cm/sec)	Average Lag (hr)	Lag rms (hr)
North Central	7.66	0.74	2.08	0.00	1.07
Northeast	4.64	1.43	4.61	0.43	1.04
Southeast	2.60	0.74	3.63	0.11	0.56
Dead Horse Bay	3.66	0.62	2.91	0.13	1.14
Central Channel	4.45				

Table 10
Skill Test Analysis of Model-Generated Velocities:
Validation Period

Station	rms Difference (cm/sec)	Gain	Amplitude rms (cm/sec)	Average Lag (hr)	Lag rms (hr)
North Central	6.96	0.73	1.67	0.75	0.75
Northeast	4.40	1.06	2.17	0.00	0.49
Southeast	2.78	0.73	1.76	-0.22	0.30
Dead Horse Bay					
Central Channel	4.38	0.82	3.03	0.60	0.92

Table 11
Comparison of Computed and Measured Water Velocity Distributions for June 1984: North Central Current Meter

Velocity Range (cm/sec)	Measured Velocity			Computed Velocity		
	Sample Size	Frequency (percent)	Cumulative Frequency (percent)	Sample Size	Frequency (percent)	Cumulative Frequency (percent)
$0 \leq v < 3$	744	36.9	36.9	633	31.4	31.4
$3 \leq v < 6$	451	22.4	59.3	609	30.2	61.6
$6 \leq v < 9$	256	12.7	72.0	370	18.3	79.9
$9 \leq v < 12$	244	12.1	84.1	220	10.9	90.8
$12 \leq v < 15$	135	6.7	90.8	90	4.5	95.3
$15 \leq v$	187	9.3	100.0	95	4.7	100.0

Table 12
Comparison of Computed and Measured Water Velocity Distributions for July 1984: North Central Current Meter

Velocity Range (cm/sec)	Measured Velocity			Computed Velocity		
	Sample Size	Frequency (percent)	Cumulative Frequency (percent)	Sample Size	Frequency (percent)	Cumulative Frequency (percent)
$0 \leq v < 3$	1143	37.8	37.8	1080	35.7	35.7
$3 \leq v < 6$	783	25.9	63.7	871	28.8	64.5
$6 \leq v < 9$	356	11.8	75.5	481	15.9	80.4
$9 \leq v < 12$	312	10.3	85.8	288	9.5	89.9
$12 \leq v < 15$	196	6.5	92.3	148	4.9	94.8
$15 \leq v$	235	7.8	100.0	157	5.2	100.0

Table 13
Comparison of Computed and Measured Water Velocity Distributions for June 1984: Northeast Current Meter

Velocity Range (cm/sec)	Measured Velocity			Computed Velocity		
	Sample Size	Frequency (percent)	Cumulative Frequency (percent)	Sample Size	Frequency (percent)	Cumulative Frequency (percent)
$0 \leq v < 3$	1276	63.3	37.8	1080	35.7	35.7
$3 \leq v < 6$	507	25.1	63.7	871	28.8	64.5
$6 \leq v < 9$	121	6.0	75.5	48 ⁺	15.9	80.4
$9 \leq v < 12$	68	3.4	85.8	288	9.5	89.9
$12 \leq v < 15$	24	1.2	92.3	148	4.9	94.8
$15 \leq v$	21	1.0	100.0	157	5.2	100.0

Table 14
Comparison of Computed and Measured Water Velocity Distributions for July 1984: Northeast Current Meter

Velocity Range (cm/sec)	Measured Velocity			Computed Velocity		
	Sample Size	Frequency (percent)	Cumulative Frequency (percent)	Sample Size	Frequency (percent)	Cumulative Frequency (percent)
$0 \leq v < 3$	1504	49.7	49.7	1229	40.6	40.6
$3 \leq v < 6$	958	31.7	81.4	1074	35.5	76.1
$6 \leq v < 9$	301	10.0	91.4	477	15.8	91.9
$9 \leq v < 12$	174	5.6	97.0	155	5.1	97.0
$12 \leq v < 15$	51	1.7	98.7	57	1.9	98.9
$15 \leq v$	37	1.2	100.0	33	1.1	100.0

Table 15
Comparison of Computed and Measured Water Velocity Distributions for June 1984: Southeast Current Meter

Velocity Range (cm/sec)	Measured Velocity			Computed Velocity		
	Sample Size	Frequency (percent)	Cumulative Frequency (percent)	Sample Size	Frequency (percent)	Cumulative Frequency (percent)
$0 \leq v < 3$	1409	69.9	69.9	1348	66.8	66.8
$3 \leq v < 6$	454	22.5	92.4	545	27.0	93.8
$6 \leq v < 9$	111	5.5	97.9	98	4.9	98.7
$9 \leq v < 12$	33	1.6	99.5	14	0.7	99.4
$12 \leq v < 15$	10	0.5	100.0	9	0.5	99.9
$15 \leq v$	0	0.0	100.0	3	0.1	100.0

Table 16
Comparison of Computed and Measured Water Velocity Distributions for July 1984: Southeast Current Meter

Velocity Range (cm/sec)	Measured Velocity			Computed Velocity		
	Sample Size	Frequency (percent)	Cumulative Frequency (percent)	Sample Size	Frequency (percent)	Cumulative Frequency (percent)
$0 \leq v < 3$	2255	74.6	74.6	2099	69.4	69.4
$3 \leq v < 6$	606	20.0	94.6	727	24.0	93.4
$6 \leq v < 9$	110	3.6	98.2	149	4.9	98.3
$9 \leq v < 12$	27	0.9	99.1	32	1.1	99.4
$12 \leq v < 15$	10	0.3	99.4	12	0.4	99.8
$15 \leq v$	17	0.6	100.0	6	0.2	100.0

Table 17
Comparison of Computed and Measured Water Velocity Distributions for June 1984: Dead Horse Bay Current Meter

Velocity Range (cm/sec)	Measured Velocity			Computed Velocity		
	Sample Size	Frequency (percent)	Cumulative Frequency (percent)	Sample Size	Frequency (percent)	Cumulative Frequency (percent)
$0 \leq v < 3$	1396	69.2	69.2	1440	71.4	71.4
$3 \leq v < 6$	466	23.1	92.3	528	26.2	97.6
$6 \leq v < 9$	112	5.5	97.8	44	2.2	99.8
$9 \leq v < 12$	34	1.7	99.5	2	0.1	99.9
$12 \leq v < 15$	5	0.3	99.8	3	0.1	100.0
$15 \leq v$	4	0.2	100.0	0	0.0	100.0

Table 18
Comparison of Computed and Measured Water Velocity Distributions for July 1984: Central Channel Current Meter

Velocity Range (cm/sec)	Measured Velocity			Computed Velocity		
	Sample Size	Frequency (percent)	Cumulative Frequency (percent)	Sample Size	Frequency (percent)	Cumulative Frequency (percent)
$0 \leq v < 3$	1398	46.2	46.2	999	33.0	33.0
$3 \leq v < 6$	916	30.3	76.5	1089	36.0	69.0
$6 \leq v < 9$	369	12.2	88.7	528	17.5	86.5
$9 \leq v < 12$	265	8.8	97.5	239	7.9	94.4
$12 \leq v < 15$	43	1.4	98.9	102	3.4	97.8
$15 \leq v$	34	1.1	100.0	68	2.3	100.0

In general, the distributions of model-generated velocities were consistent with those computed with the measured data. At the north central location, for example, 35.7 percent and 28.8 percent of the model-generated velocity data had magnitudes within the ranges of 0-3 cm/sec and 3-6 cm/sec, respectively. These values compare well with the 37.8-percent and 25.9-percent values computed with the measured data for the same intervals.

However, the model underpredicted by approximately 50 percent the number of velocity readings greater than 15 cm/sec, and, by the same percentage, the number of readings within the range of 12 cm/sec to 15 cm/sec. These discrepancies can be attributed to the high velocities being measured at simulation hr 306 and 320 of the calibration period. At these times, velocities exceeding 15 cm/sec are measured for extended periods, some of which have duration greater than 15 hr. Computed velocities during these periods typically range from 6 cm/sec to 9 cm/sec.

Wind Drag Formulation

Drag coefficients

As per the suggestions made by the TRP members, winds recorded at the Green Bay Airport were compared with those measured at the municipal wastewater treatment plant (WWTP). Because of the lack of existing and/or available data collected during the hydrodynamic calibration period, winds recorded from June through August 1986 were used as a substitute. Visual comparisons of the wind speed and direction time series show that both the airport and the WWTP experienced the same major and localized weather patterns. There were, however, some differences between wind speeds and directions measured at these locations.

For both the airport and WWTP data, a statistical analysis was performed where the frequency of occurrence and the corresponding average wind speed were extracted and processed for the eight major compass directions. This information is presented in Table 19. Wind directions presented in this table denote the direction from which winds are coming. Though not noted in this table, light or variable winds and/or periods when no measurements were recorded represent conditions having frequencies of 6.6 and 18.3 percent for the airport and WWTP, respectively.

Wind directions experienced at the Green Bay Airport were primarily from the south, southwest, and west directions; winds from these directions have a combined frequency of approximately 50 percent. Winds recorded at the WWTP for these directions accounted for about 44 percent of the total frequency. Differences between these percentages may be due, in part, to the high number of missing hourly readings in the airport and WWTP data sets. In the airport wind records, a total of 145 hourly readings, out of a total of 2,205 hourly periods, had speeds equal to zero. In the WWTP records, a total of 403 hourly readings had (simultaneously) wind speeds and angles equal to

zero. During periods when the airport recorded zero winds, the WWTP recorded easterly wind directions. During the periods when the WWTP was not recording wind data, the airport recorded winds predominately from the southwest, west, and north.

Northerly winds recorded at the WWTP were approximately 24 percent greater than those measured at the airport. Because winds blowing from this direction have the greatest over-water fetch, it appears logical that the WWTP would record greater wind speeds than the airport, as the WWTP is at the edge of the bay whereas the airport is about 6 miles south-southwest of the bay. For easterly, southeasterly, and westerly winds, average wind speeds recorded at the airport and WWTP are approximately equal. Winds coming from these directions have little, if any, over-water effects and can be expected to be about equal in speed.

Drag formulation

Concern was expressed by members of the TRP committee about the appropriateness of adjusting wind speeds by 50 percent, as opposed to the 32 percent contained in Patterson (1984). The purpose of this type of adjustment is to remove over-land friction effects from wind measurements taken at land-based stations and develop wind speeds which are approximately equal to the actual speeds experienced over open water.

Table 19
Comparison of Average Wind Speeds and Dominant Wind
Directions Recorded at Green Bay Airport and Green
Bay Sewerage District Plant

Wind Direction	Airport		Sewerage District Plant	
	Frequency (percent)	Speed (m/sec)	Frequency (percent)	Speed (m/sec)
North	7.5	4.3	1.1	5.3
Northeast	9.1	4.7	7.1	3.9
East	9.9	3.4	8.0	3.3
Southeast	6.0	3.3	12.9	3.7
South	18.7	4.1	22.1	4.8
Southwest	16.0	4.0	12.3	3.5
West	14.9	3.6	9.2	3.6
Northwest	11.4	3.9	9.0	4.5

Note: Wind directions reflect the direction from which the wind is blowing.

Because current patterns are, in part, dependent on wind speed used for calculating the surface shear stress, selecting the proper wind drag formulation is extremely important for accurate predictions. Wind shear stress computations are particularly sensitive to the magnitude of winds used in a simulation. This is because the shear stress is proportional to the square of the wind speed as shown in the following formulation:

$$\tau = \rho C_d W W \quad (17)$$

where τ is the wind shear stress, ρ represents the atmospheric air density, W is the wind velocity, and C_d is the wind drag coefficient.

The choice of wind drag formulation can also affect calculated current patterns. Typically, wind drag formulations are empirical, being developed from in situ measurements such as time-averaged wind speeds. Schmalz (1986) compared drag coefficients computed with eight formulations. These comparisons were made over a range of wind speeds from 10 to 120 knots at 10-knot increments. Schmalz found that over the entire range of wind speeds, the average difference between coefficients was 30 percent.

Variability of drag coefficients can be attributed to the range and distribution of wind speeds used in developing these formulations. Data used for developing one formula may contain a greater number of samples within a certain range, such as 5 to 10 knots, than a second formula developed primarily of speeds ranging from 20 to 30 knots. It can therefore be assumed that a formulation developed with wind speeds ranging from 5 to 10 knots produces a more reliable coefficient when applied to a 7-knot wind than a second formula developed with winds ranging from 20 to 30 knots.

The lower Green Bay model employs Garratt's wind drag formulation in the wind stress computations. This formulation is:

$$C_d = \frac{(0.75 + 0.067W)}{1000} \quad (18)$$

where C_d is the wind drag coefficient and W is the wind velocity in meters per second. Garratt specified an upper limit of 3.0×10^{-3} for this coefficient. Thus, for wind speeds greater than 65 knots, a constant drag coefficient is applied.

Wind drag laws developed by other researchers are presented in the following equations:

Wu (1980):

$$C_d = \frac{(0.8 + 0.065W)}{1000} \quad (19)$$

Deacon (Rosenthal 1971):

$$C_d = \frac{(1.1+0.04W)}{1000} \quad (20)$$

Powell (1980):

$$C_d = \frac{(1.0236+0.05366W)}{1000} \quad (21)$$

Wang and Conner (1975):

$$C_d = \frac{(1.1+0.0536W)}{1000} \quad (22)$$

The preceding formulas were evaluated to obtain wind drag coefficients for wind speeds ranging from 1 m/sec to 12 m/sec, and these values are presented in Table 20. For a wind speed of 4 m/sec, which is approximately equal to the average speed measured at the Green Bay Airport, Garratt's formulation yields a coefficient equal to 1.018×10^{-3} . The average coefficient at this speed equals 1.178×10^{-3} . Wang and Conner's formulation, producing the greatest value among the different formulations, yields a value equal to 1.314×10^{-3} . Thus, the average drag coefficient is approximately 16 percent greater than the value obtained with Garratt's formulation. Furthermore, Wang and Conner's formulation predicted a coefficient approximately 30 percent greater than Garratt's formulation.

For illustration purposes, the wind shear stress presented in Equation 17 was first evaluated where wind speeds were increased by 32 percent to account for over-land friction effects, and second, where speeds were increased by 50 percent. Assuming identical wind drag coefficients were used in both computations (i.e., neglecting the dependence of the drag coefficient on wind speed, and thereby focusing solely on the square of the wind velocity), the wind shear stress predicted for winds that were increased 50 percent would be approximately 29 percent greater than the stress computed with winds increased by 32 percent. Accounting for the dependence of wind velocity on the wind drag coefficient, the difference in shear stresses is closer to 35 percent.

For a second illustration, wind shear stresses were evaluated with Wang and Conner's formulation and with Garratt's formulation. Assuming a wind speed of 4 m/sec, winds using Wang and Conner's formulation were increased by 32 percent, whereas, for Garratt's formulation, winds were increased by 50 percent. Comparing predicted wind shear stress values, Garratt's formulation produced a stress of 0.0493 N/m^2 . A shear stress equal to 0.0459 N/m^2 was predicted with Wang and Conner's formulation. Whereas an increase in wind shear stress values of 35 percent could be expected due to differing

Table 20
Comparison of Wind Drag Coefficients

Wind Speed (m/sec)	Drag Coefficient					Average ($\times 10^{-3}$)	Std Dev
	Wu ($\times 10^{-3}$)	Powell ($\times 10^{-3}$)	Deacon ($\times 10^{-3}$)	Wang ($\times 10^{-3}$)	Garrat ($\times 10^{-3}$)		
1	0.865	1.077	1.140	1.154	0.817	1.011	0.158
2	0.930	1.131	1.180	1.207	0.884	1.066	0.149
3	0.995	1.185	1.220	1.261	0.951	1.122	0.140
4	1.060	1.238	1.260	1.314	1.018	1.178	0.131
5	1.125	1.292	1.300	1.368	1.085	1.234	0.122
6	1.190	1.346	1.340	1.422	1.152	1.290	0.114
7	1.225	1.399	1.380	1.475	1.219	1.346	0.106
8	1.320	1.453	1.420	1.529	1.286	1.402	0.099
9	1.385	1.507	1.460	1.582	1.353	1.457	0.092
10	1.450	1.560	1.500	1.636	1.420	1.513	0.087
11	1.515	1.614	1.540	1.690	1.487	1.569	0.082
12	1.580	1.688	1.580	1.743	1.554	1.625	0.079

overland correction factors, Garratt's formulation produced a shear stress value only 7 percent greater than Wang and Conner's formula.

In summary, while wind speeds are of primary importance in estimating wind shear stresses, the selected wind drag formulation can also significantly affect shear stress estimates. Given the number of wind drag formulations and the deviation in values they produce at a given wind speed, it can be concluded that there is a level of uncertainty in calculating wind shear stresses. This uncertainty, however, can be reduced, if not eliminated, by including wind speed adjustments in the calibration procedure. In light of the 7-percent difference between wind shear stresses predicted with Garratt's and Wang and Conner's formulations, an increase of 50 percent in wind speeds is appropriate when applying Garratt's formula and is consistent with a 32-percent increase in speeds when applying Wang and Conner's formula.

5 Description of the Water Quality Model

General Structure

The water quality model (WQM) for Lower Green Bay is based on the model CE-QUAL-ICM. CE-QUAL-ICM is a generalized version of the WQM that was developed for Chesapeake Bay (Cерco and Cole 1991). The letters ICM are an abbreviation for integrated compartment methodology, which means that the conservation equations have been integrated over control volumes (i.e., compartments). This approach has also been referred to as a finite volume method and is similar to that used in the U.S. Environmental Protection Agency, Vandergrift, and Wool Water Quality Analysis Simulation Program (WASP) (DiToro, Fitzpatrick, and Thomann 1983; Ambrose 1986).

The ICM is convenient from the standpoint that it allows linking the WQM to any type of hydrodynamic model (HM) (finite difference or finite element) and grid (e.g., one-, two-, and three-dimensional, and mixed dimensions). This convenience is bought with the extra effort required to map the WQM grid to the hydrodynamic model grid. The WQM uses a one-dimensional array for numbering compartments (i.e., grid cells), whereas CH3D uses a three-dimensional array corresponding to the *ijk* coordinate system. Therefore, the unstructured grid of the WQM must be mapped to the structured grid of the HM, as shown in Figure 30.

The WQM is based on the mass conservation equation applied to each control volume in the form

$$\frac{\partial (C_i V_i)}{\partial t} = \sum_j Q_{ij} C_{ij} + \sum_j \frac{D_{ij} A_{ij}}{L_{ij}} (C_j - C_i) \pm \sum_m (SOURCES/SINKS)_{i,m} \quad (23)$$

where

- i = segment index
- j = segment index of adjoining segment
- A_{ij} = facial area of the ij interface
- C_i = segment i concentration
- C_{ij} = concentration at interface of segments i and j
- D_{ij} = eddy diffusion coefficient for ij interface
- L_{ij} = mixing length (segment length) between segments i and j
- Q_{ij} = flow to (positive) or from (negative) segment i from/to segment j
- V_i = segment i volume

and the last term represents the rate of change of mass in segment i from various sources and/or sinks m , e.g., due to loadings and kinetic transformations or transfers. The hydrodynamics (i.e., Q and D at each cell interface) are furnished by hydrodynamic model output that must be linked to the WQM.

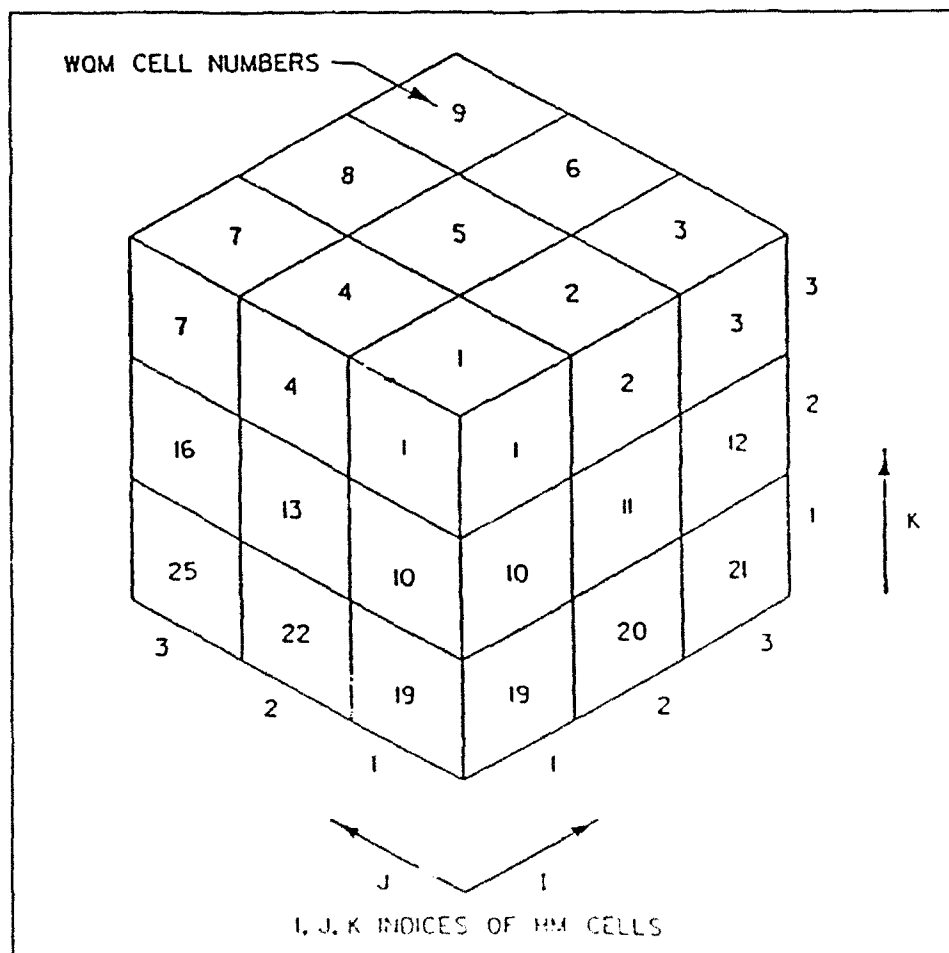


Figure 30. HM - WQM grid structure

Equation 23 is solved for each computational cell and for each water quality state variable, C .

Although CE-QUAL-ICM can be applied for one-, two-, three-, and/or mixed-dimensions, the model was applied in the two-dimensional (depth-averaged) mode throughout the grid for this study. The code is generic, which means it can be and has been applied to other systems. At the time of this study, the model was also being applied to the New York Bight, Indian River-Rehoboth Bay (Delaware coast), and Los Angeles-Long Beach Harbor. Some minor modifications were made to the WQM kinetic routines during this study. For example, carbonaceous biochemical oxygen demand (CBOD) was a modeled state variable rather than organic carbon since the waste-load information is in terms of CBOD. Such modifications are common practice when applying water quality models. Only about half of the total number of state variables were used in this study to keep the model consistent with study needs and data availability. State variables that are not modeled can be easily turned off without having to modify the code.

Solution Schemes

The numerical representations and solution schemes of the WQM are different than those found in the WASP model. The WQM distinguishes between the horizontal and vertical directions. The solutions for horizontal and vertical transport use a split operator. Horizontal advection and diffusion are first computed explicitly for all cells, providing provisional estimates of dependent variables at the new time level. The provisional estimates are then updated for vertical advection and diffusion with an implicit sweep over each vertical column of cells using the Crank-Nicolson scheme. The implicit vertical solution scheme removes time-step restrictions for vertical transport, which can be over-restrictive for multiple layers in shallow regions. Sources and sinks due to loads and kinetic formulations are taken into account at the beginning of each time level update. All kinetic formulations are treated explicitly using information from the previous time level.

Horizontal advective fluxes are normally several orders of magnitude greater than diffusive fluxes in surface waters; thus, it is desirable to accurately resolve advective fluxes without introducing numerical diffusion that may be larger than the real physical diffusion. The use of higher order advection schemes has dramatically reduced or eliminated the concerns associated with numerical diffusion/dissipation in Eulerian transport models. The Quadratic Upstream Interpolation for convective Kinematics with Estimated Streaming Terms (QUICKEST) scheme (Leonard 1979), which is explicit, upstream weighted and third-order accurate in space, was implemented (Chapman 1988) for horizontal advection in the WQM. The QUICKEST scheme is used to obtain the interpolated concentrations at the cell interfaces (i.e., C_{ij} of Equation 23). The scheme is implemented in a fully conservative fashion.

The WQM allows time-varying boundary conditions and hydrodynamic updates. Also, the user can specify a constant model time-step or select the auto-stepping feature, which automatically adjusts the time-step to satisfy the horizontal flow stability restriction. This feature is included to take advantage of potentially larger time-steps during periods with low current velocities.

Linkage to Hydrodynamic Model

An interface processor has been developed and incorporated into the HM (Dortch 1990) that couples the HM and WQM computational grids and processes hydrodynamic information into WQM input data. The interface processor was developed as subroutines within the HM. Therefore, the hydrodynamic information for the WQM is processed and stored while the HM is executing.

Coupling the HM and WQM grids requires generation of map files, which set up a correspondence between the HM and WQM grid formats. Additionally, time-invariant HM geometric information is required to compute distances between cells (i.e., box lengths), initial cell volumes, and cell facial areas. Processing of the time-varying hydrodynamic information can be accomplished in either of two modes, intratidal or intertidal. Although lower Green Bay is not a tidal system in the true sense, it does experience long wave seiches that resemble tides. The interfacing procedures still apply, even if there are no seiches present.

The intratidal model involves processing the hydrodynamics, which are computed in the HM at intervals on the order of minutes, into WQM input at about 1- or 2-hr intervals. The intratidal model simply requires temporal averages of the hydrodynamics (i.e., flows and vertical diffusivities, for three-dimensional grids). The intertidal model involves processing hydrodynamics into WQM input at tidal-period intervals or greater, thus reducing WQM input data storage requirements by an order of magnitude. Intertidal processing requires computation of the Eulerian residuals and Stokes' drifts to obtain a first-order estimate of the Lagrangian residuals (i.e., the correct residual currents). Only Eulerian residuals are required for the intratidal mode. For both modes, processed hydrodynamics are output in a format compatible with the WQM following appropriate scaling. Scaling accounts for the fact that the contravariant velocities in the HM are both nondimensional and defined on a transformed boundary-fitted grid. Thus, these velocities must be converted to dimensional, physical plane flows (m^3/sec). These procedures are explained by Dortch (1990).

For this study, the WQM uses the same grid as the HM; thus, there is one-to-one correspondence or overlay. The total number of computational cells for the HM and WQM varied between 4968 and 4843 for high and low lake levels, respectively. The hydrodynamics were processed and output at 1-hr intervals for all computational cells and for all simulations.

Kinetic Formulations

The central issue in the water quality model is the concentration of DO. DO is necessary to support the life functions of higher organisms and is considered an indicator of the "health" of a water body. DO concentrations are affected by a series of biological and chemical processes, which both supply and utilize DO. The loadings exerted by waste discharges can increase the relative importance of one or more of these processes, resulting in decreases in DO. These processes can be modeled using the appropriate reactions and state variables.

In highly productive systems such as lower Green Bay, primary production has a major impact on nutrients and DO. Variations in DO and nutrient concentrations can not be adequately modeled without including algae, and algae can not be properly modeled without including nutrients. Also, the nitrogen cycle affects DO. Therefore, as a minimum, a reasonable model of lower Green Bay must include temperature, DO, oxygen-demanding substances, major nutrients (nitrogen and phosphorus), and algae. The sources and sinks of DO can be lumped into fewer state variables and parameters, such as total biochemical oxygen demand, but such lumping can result in omission of the correct basic processes. Modeling DO without the components listed above would result in a scientifically indefensible, questionable model. Although the lower Green Bay water quality database is less than ideal, it is considered sufficient for the model with 11 state variables described below and is certainly adequate to address the objectives of this study. The database used in model calibration for this study was also used by Patterson (1985) for development of the water quality model that was used to determine the existing waste-load allocations.

The predominant form of algae found in lower Green Bay during the calibration period is blue-green algae. Blue-green algae are characterized by their bloom-forming characteristics in fresh water. They have lower settling velocities than other forms of algae and are subject to low predation pressure.

Nitrogen is divided into organic and mineral forms. Organic nitrogen is reported as total organic nitrogen (TON). No differentiation is made between dissolved or particulate forms of organic nitrogen. The mineral form is divided into two state variables: ammonium nitrogen ($\text{NH}_4\text{-N}$) and nitrate nitrogen ($\text{NO}_3\text{-N}$). Both forms are utilized to fulfill the nitrogenous nutrient requirements of algae, although ammonium is preferred for thermodynamic reasons. The primary reason for distinguishing between the two is that ammonium is oxidized by nitrifying bacteria into nitrate. Nitrification can be a significant sink of DO. An intermediate in the complete oxidation of ammonium, nitrite, also exists. Nitrite concentrations are usually much less than nitrate, and for modeling purposes, nitrite is combined with nitrate. Hence the nitrate state variable actually represents the sum of nitrate plus nitrite.

Phosphorus is represented in the model as either total organic phosphorus (TOP) or total phosphate (PO_4). Total phosphate exists in the model as

dissolved phosphate and phosphate incorporated in algal cells. Equilibrium partition coefficients are used to distribute the total phosphate between these two states. This approach is used to facilitate modeling the adaptation of algae to phosphorus supply and uptake as discussed later in this section. Algal composition of phosphorus is still maintained.

Carbonaceous biochemical oxygen demand (CBOD) is a measure of the amount of oxygen required for the aerobic stabilization of organics. CBOD is a standard test in environmental engineering for determining the strength of biochemically degradable carbonaceous organic matter and the relative ease of its biodegradation. CBOD is a major sink for dissolved oxygen in the natural environment. In this model, CBOD is expressed in two forms: labile and refractory, i.e., fast and slow reacting, respectively. These distinctions are based on the time frame associated with the organic matter decay.

Dissolved oxygen is required for the existence of higher life forms. Availability of DO affects the distribution of organisms and the flows of nutrients and energy in an ecosystem. DO is a central component of the water quality model.

Temperature (T) is a primary determinant of the rate of biochemical reactions. Reaction rates increase as a function of temperature, although extreme temperatures result in the mortality of organisms. Temperature is a simulated, time- and spatially varying state variable in this model.

A conservative tracer is also included as a state variable. It allows for verification of the transport component of the model and facilitates mass conservation tests. The conservative tracer can also be used to model the behavior of conservative pollutants, such as chlorides.

Therefore, the lower Green Bay WQM has 11 state variables. A schematic of the WQM's state variable interactions is shown in Figure 31. Descriptions of the kinetic formulations affecting each state variable are given in Appendix B. Partial derivatives that are defined in Appendix B describe the changes in state variables due to specific processes. Transport is not considered in these descriptions. Variables and parameters are defined when they first appear and are summarized, along with their units, in Appendix C. Equations are written for a control volume having a volume (V) and cell thickness (H). Since the water quality model is run in a two-dimensional, depth-averaged mode for the lower Green Bay study, the thickness of the control volumes (or cells) is the same as their depth.

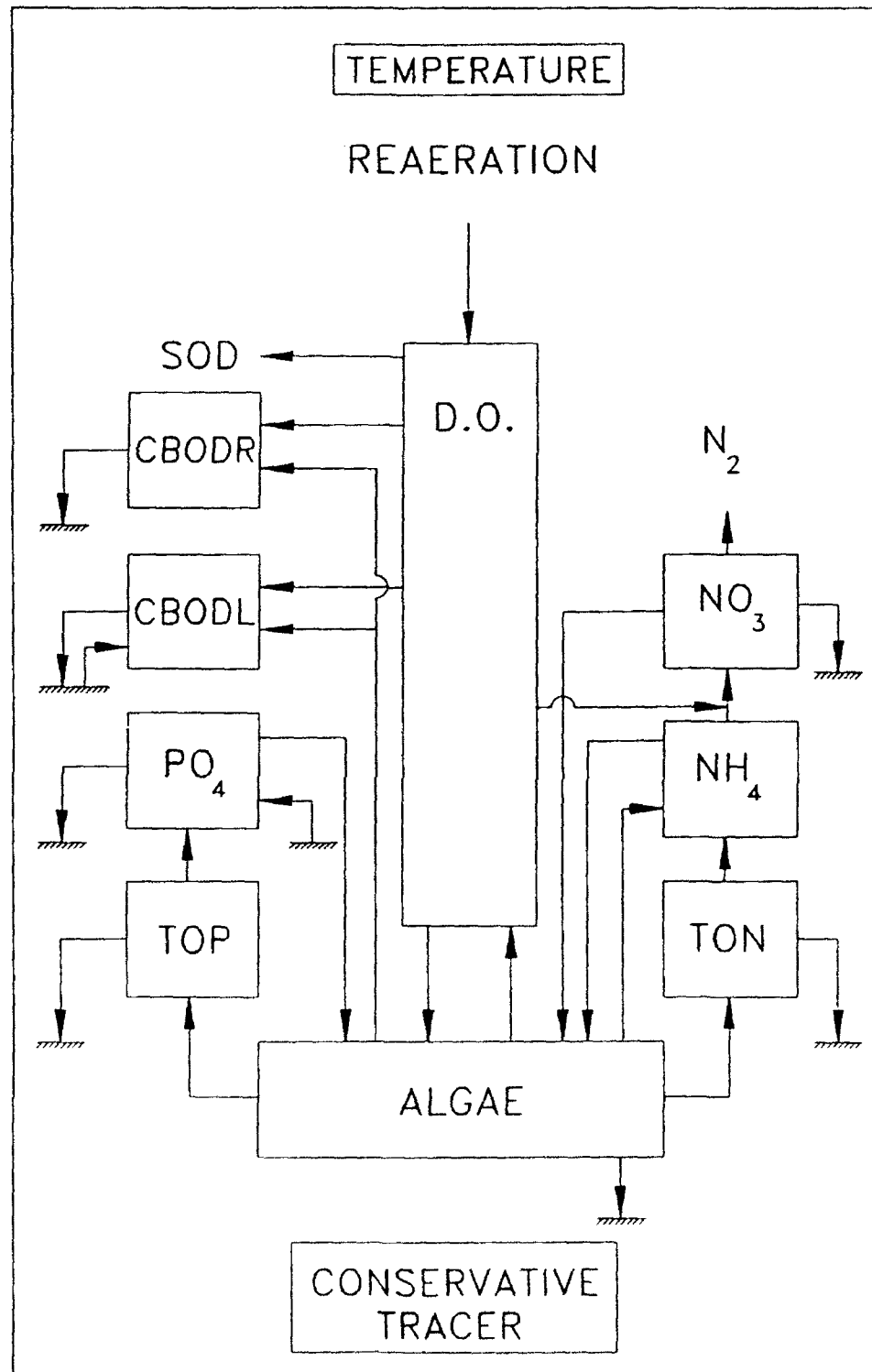


Figure 31. Schematic diagram of WQM

6 Calibration of the Water Quality Model

Transport Verification

The first task in verifying the WQM was to ensure that the transport characteristics of the HM were preserved in the WQM. To accomplish this task, comparisons were made for the transport (i.e., advection and diffusion) of passive (i.e., nonreactive) tracers in both the HM and WQM. These tests were made to verify that the WQM was properly linked to the HM and HM transport was maintained. The model tracer releases were purely hypothetical and do not represent any field data.

Two types of transport comparisons were made, a spot dump and a continuous release of tracer. The spot dump was located about mid-way between Long Tail Point and the mouth of the Fox River in the channel. The continuous release was located about 600 m north of the north shore of Kidney Island. For both tests, 100 units of tracer were introduced into both models. Computed tracer concentrations were output and plotted for the loaded cell in the case of the spot dump and a cell adjacent (north) to the loaded cell in the case of the continuous injection. The results of these two tests are shown in Figures 32 and 33 for the spot dump and the continuous release, respectively. The WQM tracer concentration follows that of the HM closely. Slight differences are attributed to the manner in which the QUICKEST algorithm is implemented in the two models. In the WQM, variations in cell lengths are taken into account for the QUICKEST interpolations, whereas a uniform grid spacing is assumed in the HM.

Another test was run to check mass conservation. All cells were loaded with an initial concentration of 100 units of tracer. Tracer concentrations at the boundaries were set to the same value and all point sources turned off. The WQM was run and the cell tracer concentrations were checked along with the total tracer mass. Results indicated that tracer was conserved throughout the test.

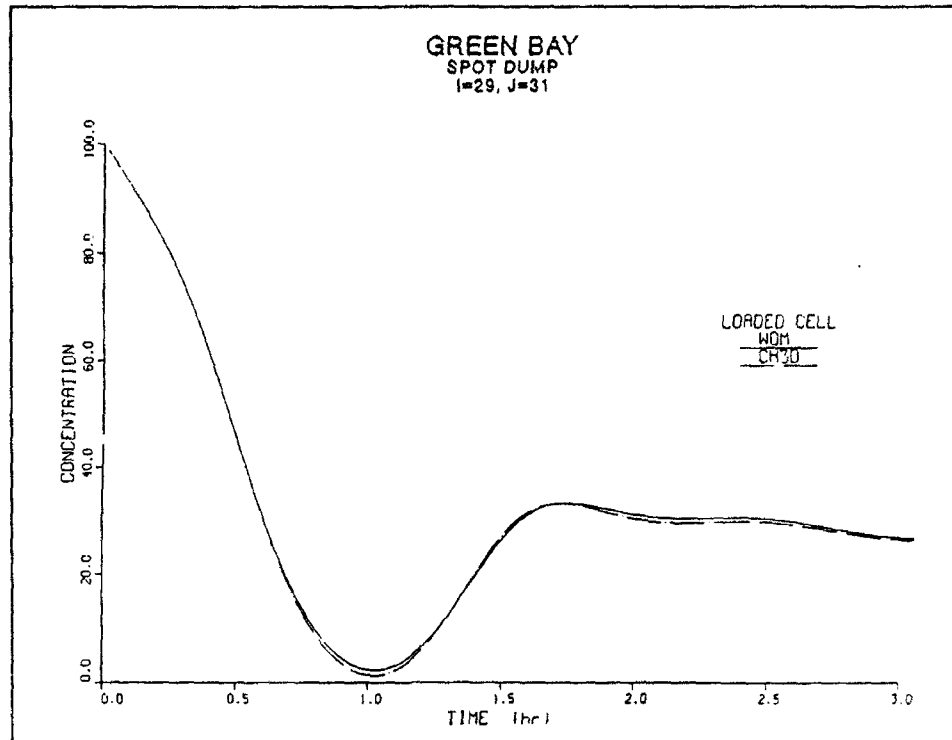


Figure 32. HM - WQM transport spot dump comparison

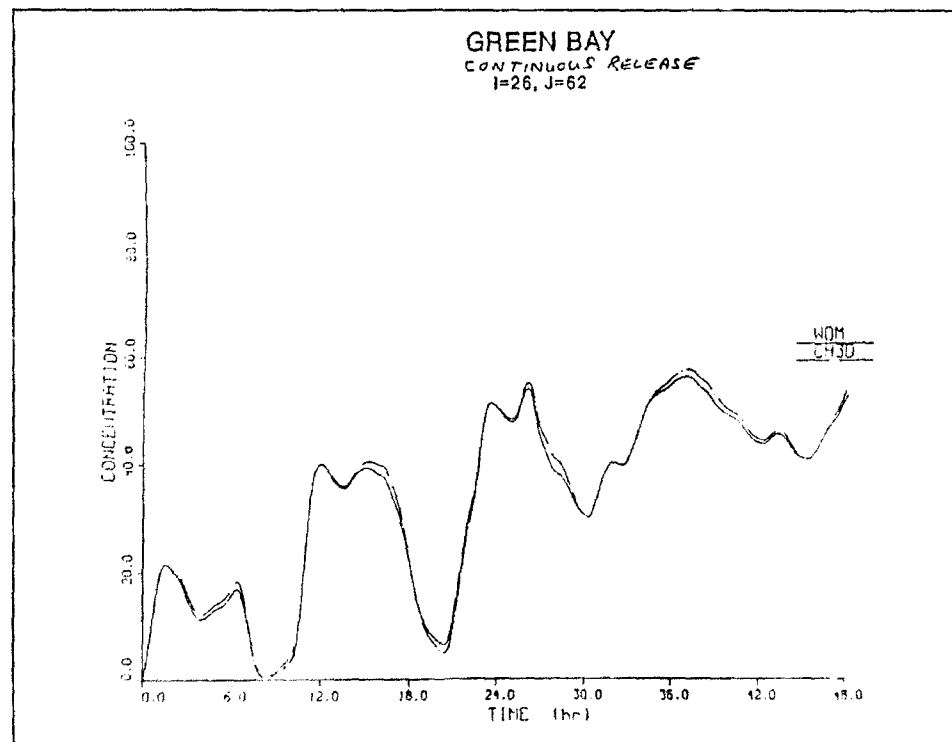


Figure 33. HM - WQM transport comparison, continuous release

Water Quality Calibration

The period beginning July 13, 1983 and ending August 18, 1983 was selected for water quality model calibration. Not as many water quality data were available for 1984, which precluded calibrating the water quality model during the same period used for hydrodynamic model calibration. The WDNR supplied data from their modeling study for the period May through September 1983. July and August were selected as the calibration period, since these months have the highest temperatures, causing higher biological activity and lower dissolved oxygen saturation levels. Conditions in these two months are similar and were modeled together in the WDNR waste-load allocation study (Patterson 1985).

Hydrodynamics for the calibration period were generated using the HM, following HM calibration for lower Green Bay. The HM was allowed to spin up for 1 day (July 12) prior to writing out hydrodynamic data for the water quality model input. Hydrodynamic data were averaged over 60 time-steps (i.e., 1 hr with 1 minute time-steps) and stored for subsequent use in the WQM.

Calibration Input Data

Meteorological data, including dry bulb temperatures, dew point temperatures, wind speeds, and cloud cover were obtained for the Green Bay Airport for the period of record. These data, along with site location and time of year, were used in a pre-processor program to compute daily average values of equilibrium temperature, heat exchange coefficient, and solar radiation. The equilibrium temperature and heat exchange coefficient were used for temperature simulation, and solar radiation was required for algae simulation. Values of daily average wind speed were also computed and stored for use in the reaeration algorithm.

Headwater boundary conditions (i.e., Fox River flows into the system) used during the calibration period were the same as those used by the WDNR during their modeling study. Headwater nutrient, temperature, and CBOD values were updated daily. The values used were based upon actual data interpolated to fill in for any missing days (Patterson 1985). The observed concentrations for algae were converted from $\mu\text{g/L chl-a}$ to $\text{g/m}^3 \text{C}$ since the algal state variable is modeled as carbon. Headwater boundary dissolved oxygen concentrations were based on observed daily maximum and minimum dissolved oxygen concentrations. The minimum dissolved oxygen concentration was fixed at 6:00 a.m. and the maximum at 6:00 p.m. During the remainder of the day, the dissolved oxygen concentration was determined via linear interpolation and the headwater boundary condition was updated hourly. This was the same technique used by WDNR in their waste-load allocation study. The boundary conditions for the outer boundary (i.e., open lake) were fixed to constant values for the duration of the calibration period as were the headwater conditions for

the East River. The values used were based on values used by WDNR in the waste-load allocation runs for the months of July and August.

Eight point sources were included along the Fox River (Figure 34). The loads for each discharger were supplied by the WDNR, who compiled them from discharger monitoring reports. Point loads were updated daily. These loads were distributed uniformly throughout the receiving cell. Daily flows and reported discharge temperatures were used in calculating the heat load from each point source.

Specification of initial conditions was more problematic. The water quality observations were considered to be too sparse to interpolate values for each cell's initial concentration of each state variable. Therefore, it was decided that output from the model would be used to set initial conditions. Initial conditions for all state variables except dissolved oxygen were generated by the model. This was accomplished by setting uniform initial values throughout the grid and running the model to steady-state with constant loadings and boundary conditions. Point source loads for the first day of the calibration period, July 13, 1983, were used for the constant loads. The outer boundary, Fox River, and East River boundary conditions were held constant to the values on the same date. The model was run for 60 days, which was sufficient time to reach dynamic steady-state (i.e., cyclic steady-state, where cycles were caused by the seiche). Hydrodynamics for July 13, 1983 were recycled for

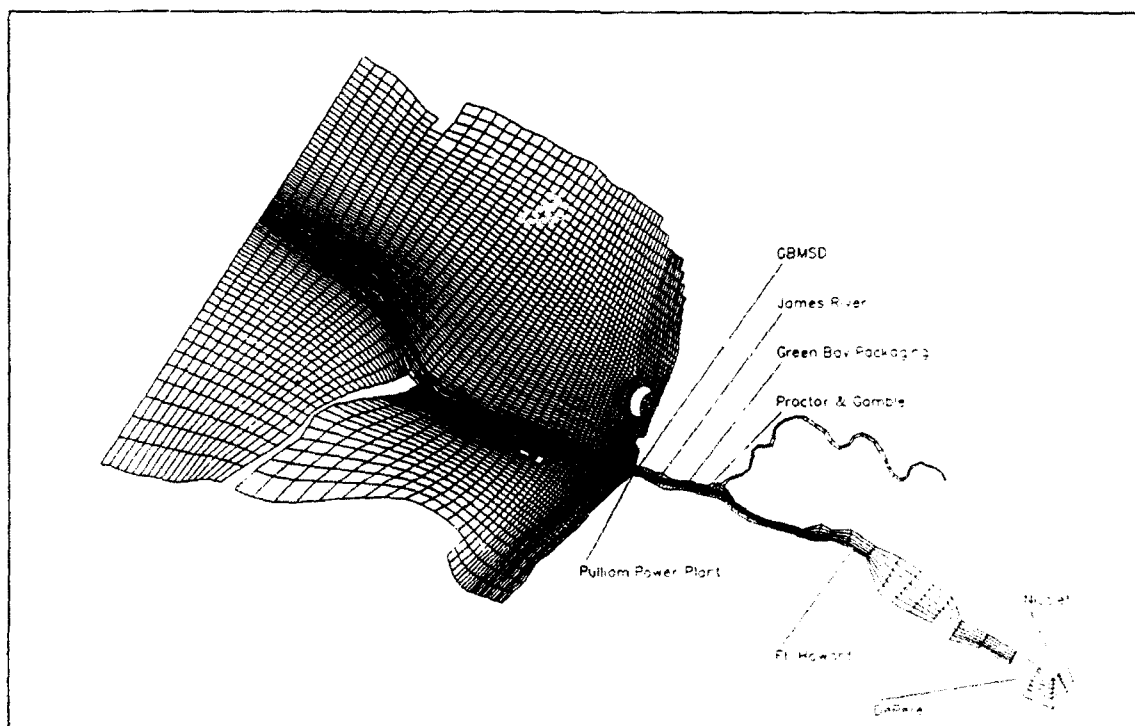


Figure 34. Location of point source dischargers

each day and used for the duration of this run. The results at the end of the steady-state run were used as initial conditions for dynamic runs (i.e., time-varying boundary conditions, loadings, and hydrodynamics).

When the results from the steady-state run were used as initial conditions for the calibration simulation, problems were encountered. The computed initial conditions were too different from the observations on July 13 for use in the calibration. To resolve this problem, the results at the end of the dynamic calibration simulation (where the steady-state results were used for initial conditions) were used as initial conditions for all subsequent calibration simulations and scenario simulations. This approach was more successful than using the steady-state results for initial conditions. This approach was used for all state variables except DO. Initial DO values were assigned based on location. Values for initial DO were set to 9.0 mg/L in the Fox River from Depere Dam to Fort Howard Paper Plant, 5.0 mg/L from the paper plant to the mouth of the Fox River, and 6.0 mg/L in the bay.

Calibration Evaluation Methods

Observed water quality data used for calibration comparisons were obtained from the WDNR. These data consisted of grab samples and continuous DO data. The grab samples were taken for chemical analyses at about weekly intervals at various locations in the Fox River and lower Green Bay. The DO data were obtained from continuous monitors (near surface and near bottom) at stations along the Fox River.

Four methods were used to compare model calibration results against observed water quality data:

- a. Time-averaged transect plots of grab samples.
- b. Time series of grab samples at each station.
- c. Time series of continuous DO data at each station.
- d. Statistical analyses.

Grab sample data at each station were averaged over the calibration period and compared in transect plots to the average values predicted by the model during the calibration period. Only stations that were along or near each transect were used for this type of comparison. Three transects, one longitudinal and two cross-bay, were used for this comparison. The longitudinal transect begins at Depere Dam (km = 0.0) and proceeds down the Fox River and along the ship channel to the outer boundary (Figure 35). The two cross-bay transects begin in Peat's Lake (km = 0.0) and proceed across the bay to the eastern shore (Figure 35). One transect passes between Kidney Island and Grassy Island, while the other passes between Grassy Island and Long Tail Point. This type of comparison also includes the ranges (i.e., minimum and maximum) of the observations and model output.

Grab sample data at each station were plotted with the time series of model output for the cell corresponding to the sampling station. In this case, the observations were not averaged. The stations used for comparing grab sample and model time series are shown in Figure 36.

Similarly, dissolved oxygen data collected at continuous monitoring stations along the lower Fox River were compared against time series of model dissolved oxygen concentrations at the same locations. Locations of these monitors and the corresponding WQM cell are indicated in Figure 37. The DO recorders were deployed for surface and bottom DO readings. The model was compared with the surface recordings. The Grassy Island monitor did not record any data during the calibration period, hence none are available for comparison. The station on Kidney Island was operating during the calibration period but it, like the Grassy Island monitor, required batteries. As indicated in the Data Summary section, the data collected at these battery-operated stations were perceived to be of lower quality than those collected by the stations along the river.

For the statistical analyses, all grab sample data were averaged over the calibration period for each station for comparison with the model calibration results averaged over time at the same stations. Two types of plots are shown in the statistical analyses, scatter plots and cumulative error distribution plots. The scatter plots are simply averages of observations in a cell plotted against model results for that cell with the perfect correlation line (i.e., slope of 1.0 and zero intercept) included. The slope, intercept, and coefficient of the regression (r^2) of these data are also indicated on the plot. The cumulative error plots show cumulative frequency (as percent less than) plotted against error defined as the absolute value of difference in the observation and model result. Mean error, mean absolute error (MAE), root mean square error, and relative error are also indicated on these plots. Relative error is computed as MAE divided by the mean of the observations. Statistical analyses are shown for each water quality variable measured in lower Green Bay.

Calibration process

The WQM was calibrated by brute force, i.e., choosing values for parameters, making the calibration run, and comparing model results to observations using the four methods discussed above. The initial selection of values for parameters was based upon past experience in water quality modeling, literature, and the WDNR model study. Parameters were changed and the process repeated in an attempt to bring the model closer to the observations. However, values for parameters were kept within reasonable limits. Calibration was a slow process since each calibration simulation required about 8 hr on the WES Cray Y-MP. The time-step of the WQM averaged approximately 3.25 min. Plotting and reviewing the results consumed additional time. This process was continued until further adjustments failed to significantly improve the calibration. Over 60 calibration runs were made.

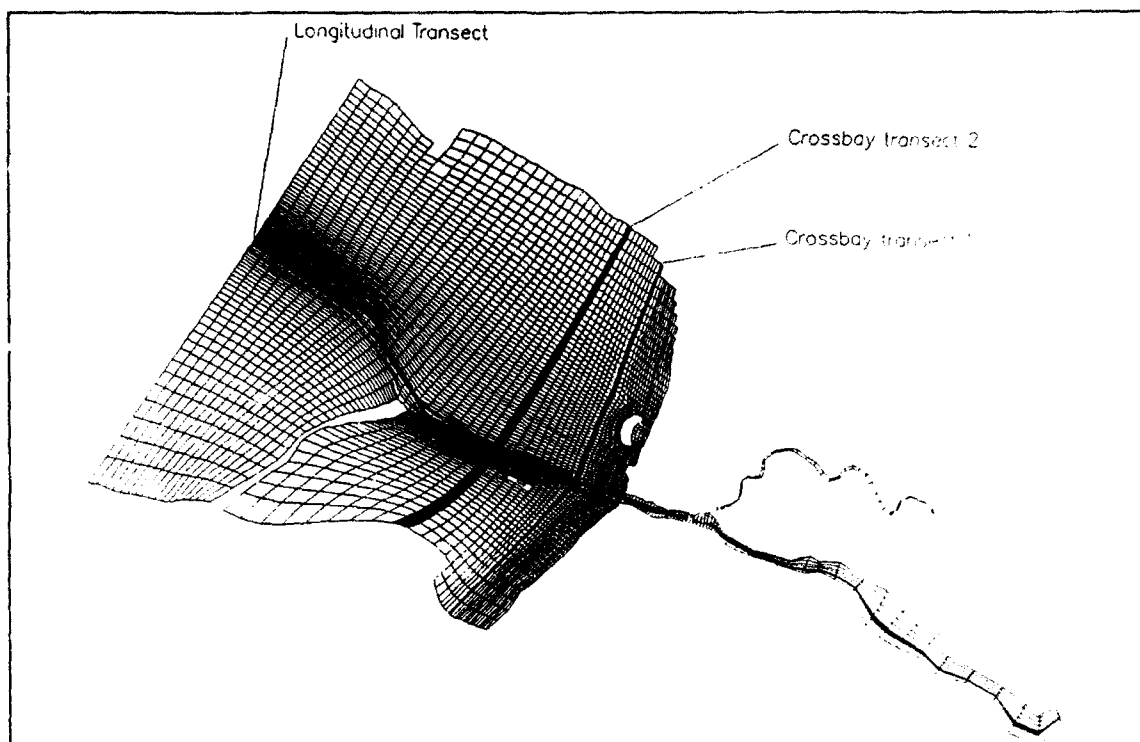


Figure 35. Transect locations for time averaged data - model comparison

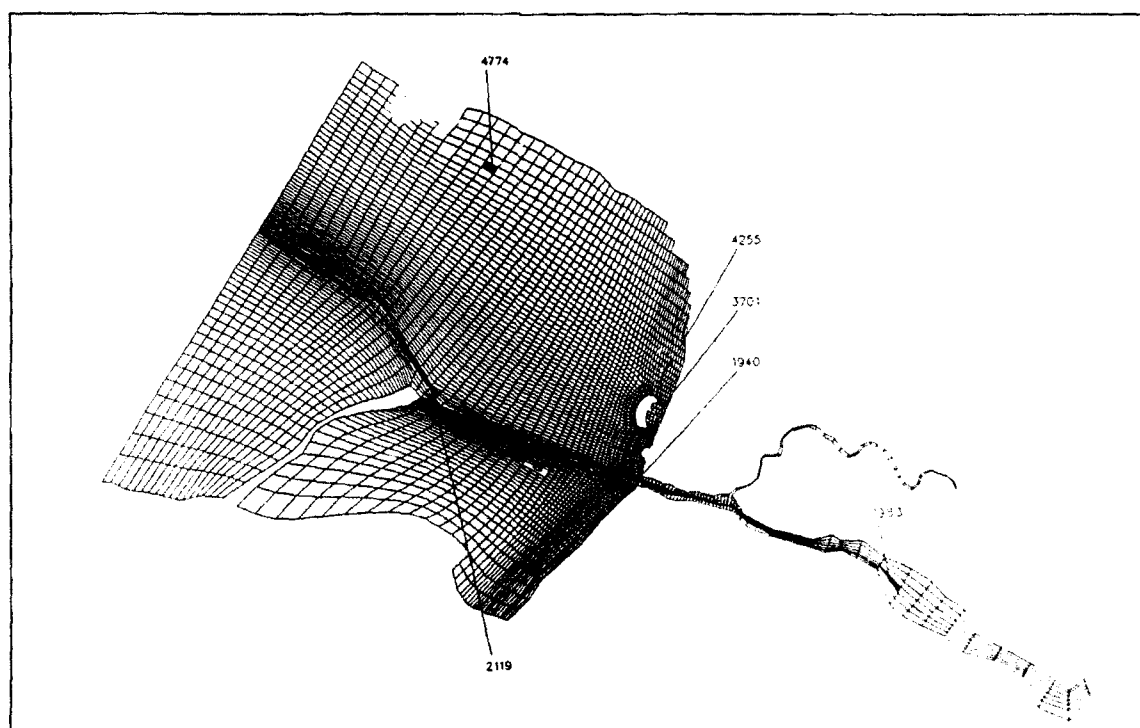


Figure 36. Grab sample locations for time series model - data comparison

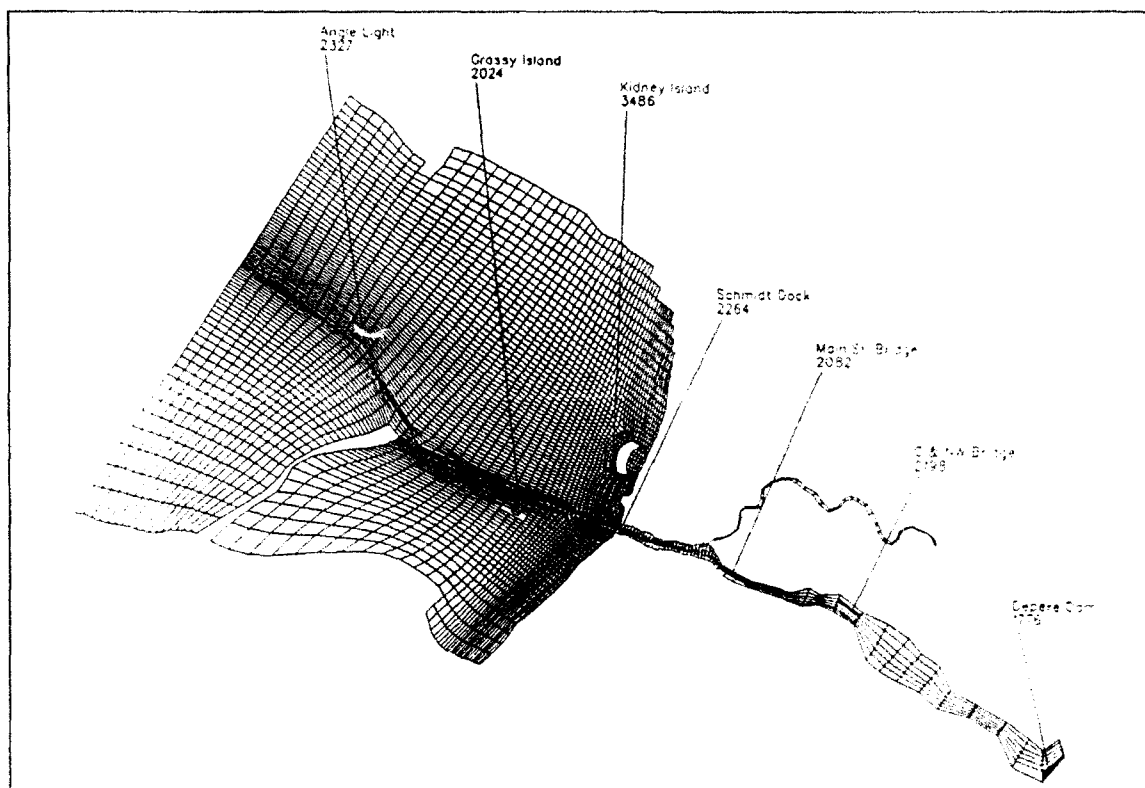


Figure 37. Location of continuous DO monitors used for calibration comparisons

The final calibration values used for WQM parameters are listed in Table 21. Definitions for parameters can be found in Appendix C. With the exception of three parameters, a constant value of each parameter was used over the entire grid throughout the simulation. Time-invariant, but spatially varying parameters were used with regard to sediment oxygen demand (SOD) and wind speed, with different values assigned to the Fox River and open bay. Algal growth rate was varied temporally in the Fox River.

Optimum algal production rate (P_{max}) was decreased in the Fox River for the first 10 days of the calibration period (July 13 through July 23) in an attempt to match the dissolved oxygen sag recorded by the continuous DO monitors. A value of $P_{max} = 0.8 \text{ day}^{-1}$ was used. On July 24 of the calibration, this value was raised to $P_{max} = 3.0 \text{ day}^{-1}$, which was the value used in the bay throughout the calibration period. This action is discussed later in this section.

Three spatially varying values of SOD (i.e., K_{sod}) were used. From Depere Dam to the Fort Howard Paper Plant, a value of $1.5 \text{ g m}^{-2} \text{ d}^{-1}$ was used for K_{sod} . From the Fort Howard Paper Plant to the area of the Fox River mouth, a value of $2.5 \text{ g m}^{-2} \text{ d}^{-1}$ was used; and a value of $0.25 \text{ g m}^{-2} \text{ d}^{-1}$ was used in the bay. It is reasonable to expect that the SOD is higher in the Fox River, where the waste-load discharges are located.

Table 21
Water Quality Model Calibration Parameters

Variable	Parameter Value	Variable	Parameter Value
A_{ca}	60.0 gm C / gm chl	K_{hr}	2.00 gm O_2 m ⁻³
A_{dcr}	2.67 gm O_2 / gm C	K_{min}	0.05 day ⁻¹
A_{nc}	0.167 gm N / gm C	K_{odn}	1.00 gm O_2 m ⁻³
A_{nd}	4.33 gm O_2 / gm N	K_{sco}	1.00 gm O_2 m ⁻³
A_{no}	0.35 gm N / gm O_2	K_{sdn}	0.50 m day ⁻¹
BM_{ref}	0.05 day ⁻¹	K_{sod}	1.50 upper Fox River gm ₂ m ⁻² day ⁻¹ 2.50 lower Fox River 0.25 open bay
F_{in}	0.05	$K1_L$	0.50 day ⁻¹
F_{on}	0.95	$K1_R$	0.14 day ⁻¹
F_{op}	0.50	NR_{max}	0.30 gm N m ⁻³ day ⁻¹
F_{pin}	0.05	pc_1	42.0 gm C / gm P
F_{pon}	0.95	pc_2	0.00 gm C / gm P
F_{pop}	0.50	pc_3	0.00 m ³ / gm P
K_1	0.10 day ⁻¹	P_{max}	0.80 day ⁻¹ Fox River day 1 - 10 3.00 day ⁻¹ Fox River day 11 - 36 3.00 day ⁻¹ open bay day 1 - 36
K_2	0.98 day ⁻¹	PR_{ref}	0.15 day ⁻¹
K_3	0.98 day ⁻¹	SED_p	0.005 g P m ⁻² day ⁻¹
K_4	0.10 day ⁻¹	T_1	10.0 °C
K_{bt}	0.069 °C ⁻¹	T_2	27.0 °C
K_{chl}	17.0 m ² / gm chl	T_3	28.0 °C
$K_{denit} (labile)$	0.50 day ⁻¹	T_4	35.0 °C
$K_{denit} (refractory)$	0.14 day ⁻¹	T_{ref}	20.0 °C
K_{dnalg}	0.50 m ³ / gm C day ⁻¹	W_{saig}	0.05 m day ⁻¹
K_{dnmn}	0.05 day ⁻¹	W_{cl}	0.15 m day ⁻¹
K_{DO}	1.00 gm O_2 m ⁻³	W_{cr}	0.15 m day ⁻¹
K_{dpalg}	1.50 m ³ / gm C day ⁻¹	W_{sn}	0.15 m day ⁻¹
K_{dpmn}	0.10 day ⁻¹	W_{spop}	0.15 m day ⁻¹
K_h	1.00 gm O_2 m ⁻³	z_{optx}	1.00 m
K_{hn}	0.005 gm N m ⁻³	α_L	1.00
K_{hnd}	1.00 gm O_2 m ⁻³	α_{DEN}	1.00
K_{hnn}	1.00 gm N m ⁻³	λ_{na}	1.50 upper Fox River m ⁻¹ 0.80 open bay Eqn. 9 lower Fox River
K_{hp}	0.003 gm P m ⁻³		

The meteorological station is inland, thus sheltered from the wind. As in the HM, the wind speed for the WQM was multiplied by 1.5 for the bay to account for open water effects (i.e., no sheltering). No correction on wind was applied to the river since it is also sheltered.

Calibration results

Time-averaged transect plots are shown in Figures 38-40. Time series plots of grab samples versus model output for select stations are shown in Figures 41-46. Time series plots of continuous observed DO versus model DO at select stations are shown in Figure 47. The statistical results are presented in Figure 48. The six stations chosen for time series plots of grab sample data versus model output (Figures 41-46) were selected based on the amount of data at that station during the calibration period and the proximity of that station to the area of interest, Kidney Island. Plots for the other stations were generated during calibration but are not shown here because of space limitations. The amount of grab sample data for model comparison varied from station to station. The stations with the most data were those that had been sampled by both the WDNR and GBMSD-UWGB sampling programs. Stations such as the Fox River Mouth (WQM cell 1940) and Long Tail Point (WQM cell 2119), which were sampled by both groups, could have 10 or more samples for some state variables depending upon how the sampling programs overlapped. Other state variables at these stations had less, and in some cases, no grab sample data to compare model output with.

The mean, minimum, and maximum for the grab sample data for each state variable were determined for each station. These values were plotted against the model average and extreme values in the transect plots. Since there were a limited number of observed data for each state variable at any station, the extremes probably were not captured in the grab sample data. This is why the range of the grab sample data did not always correspond to that of the WQM output.

In general, the WQM follows the trends in the observed data quite well. It is remarkable how well the model picks up the means and extremes for the transects, considering the complications in the system water quality (as discussed below). Overall, orthophosphate-phosphorus, algae, and DO were under-predicted. Phosphate and algae may have been under-predicted for reasons discussed below. The DO was under-predicted because of the under-prediction of algal production, which tends to super-saturate DO at times. The least error was encountered in the T and DO, while the most error was in algae and nutrients (see Figure 48).

From examination of the observed data, the Fox River and the open bay appear to be entirely different ecosystems. The river experiences high BOD loadings and low DO, while the bay has high algal concentrations and high DO. The shallow regions of the eastern and western shores show very high DO, algae, and nutrient concentrations. These shallow areas are complicated by several potential factors: more pronounced influence of bottom sediments

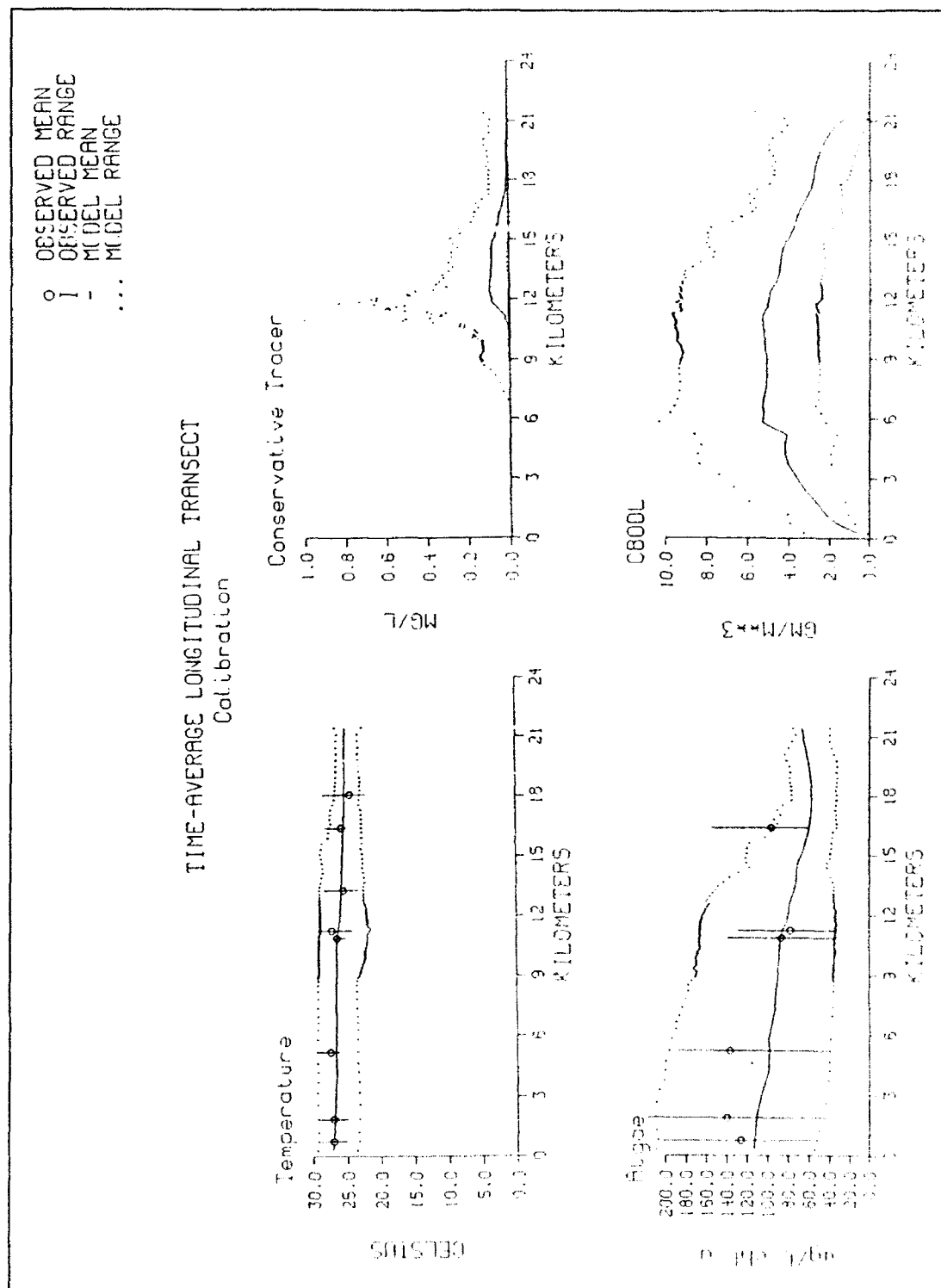


Figure 38. Time-averaged longitudinal transect (Sheet 1 of 4)

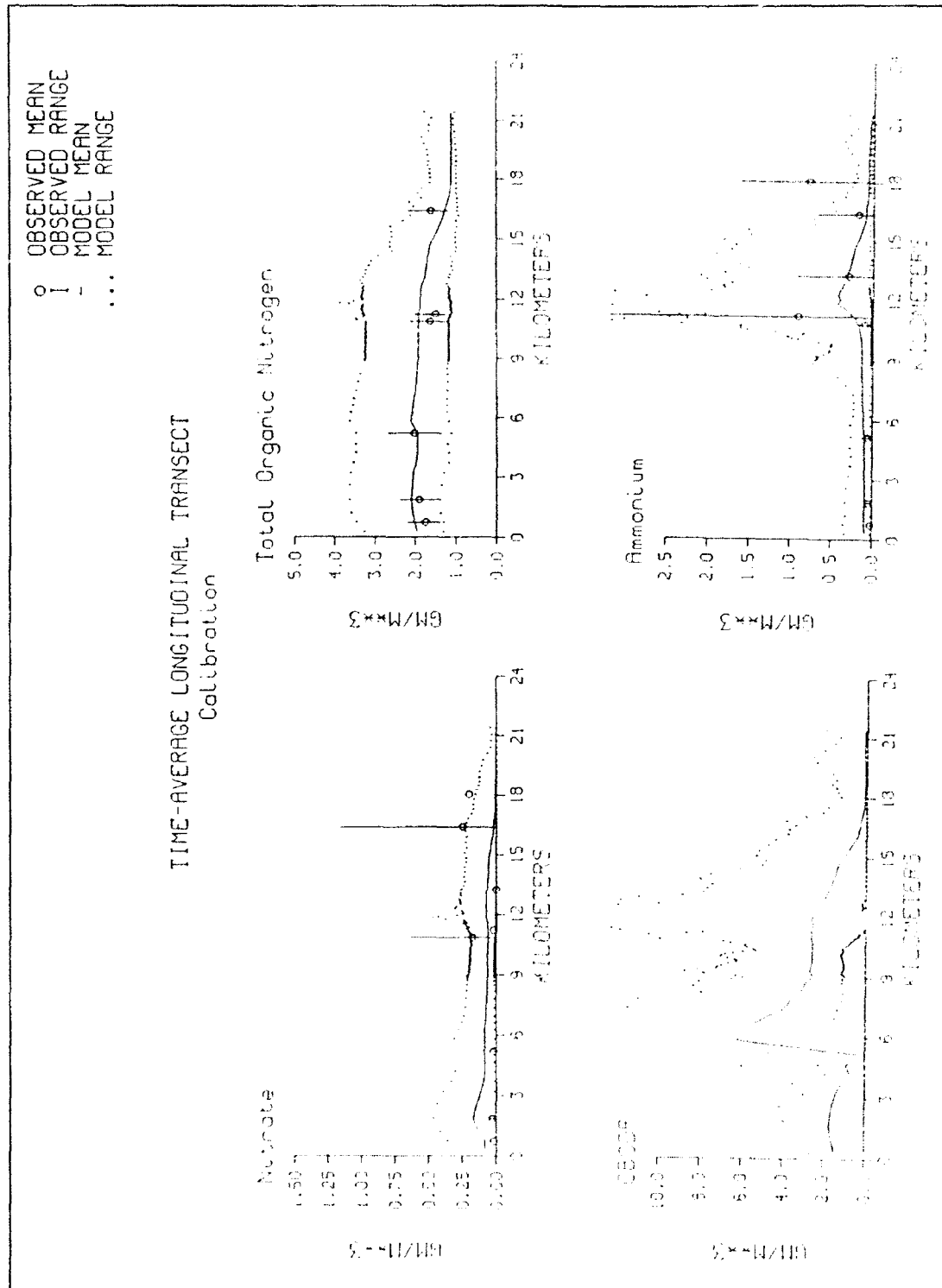


Figure 38. (Sheet 2 of 4)

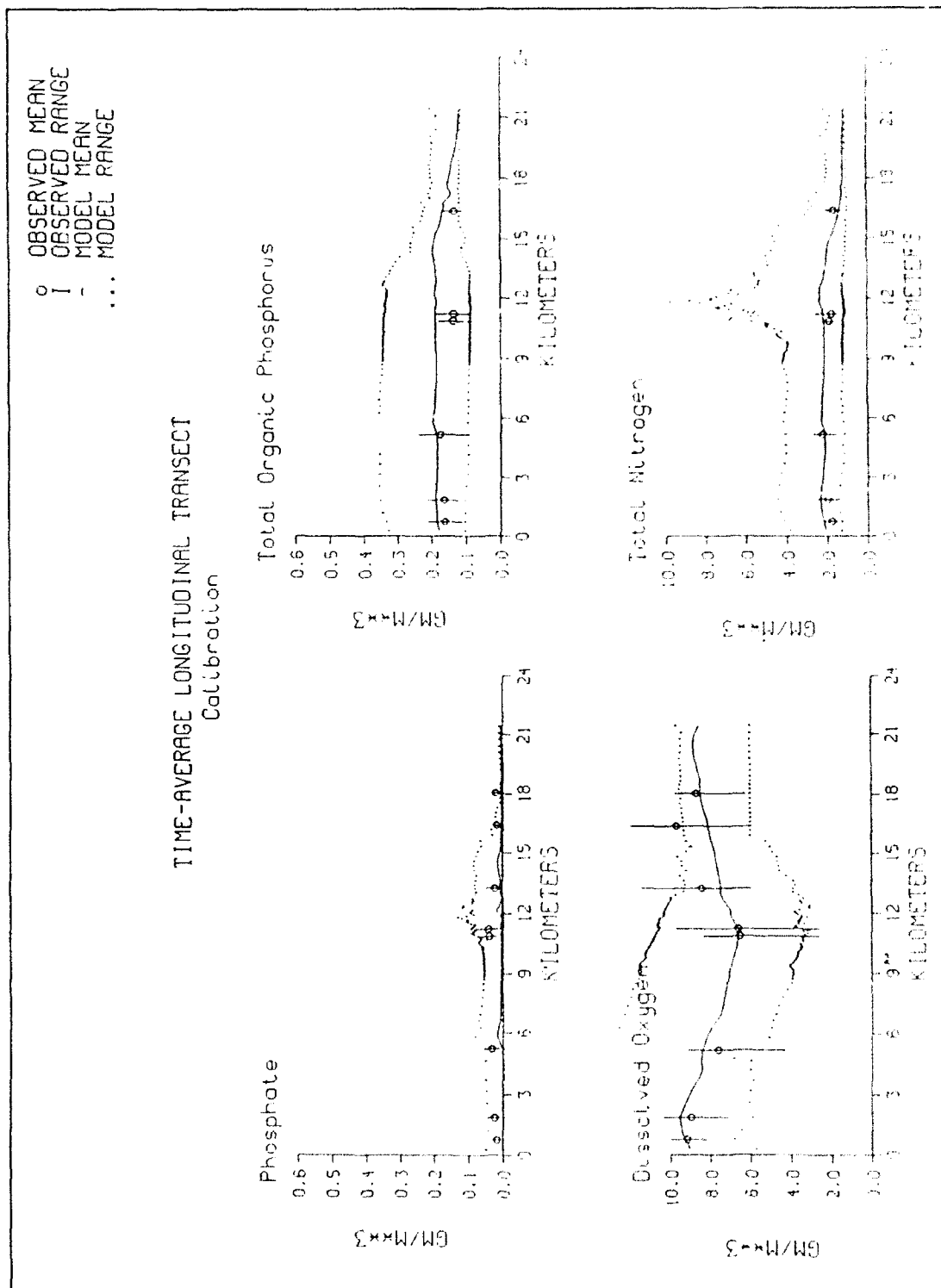


Figure 38. (Sheet 3 of 4)

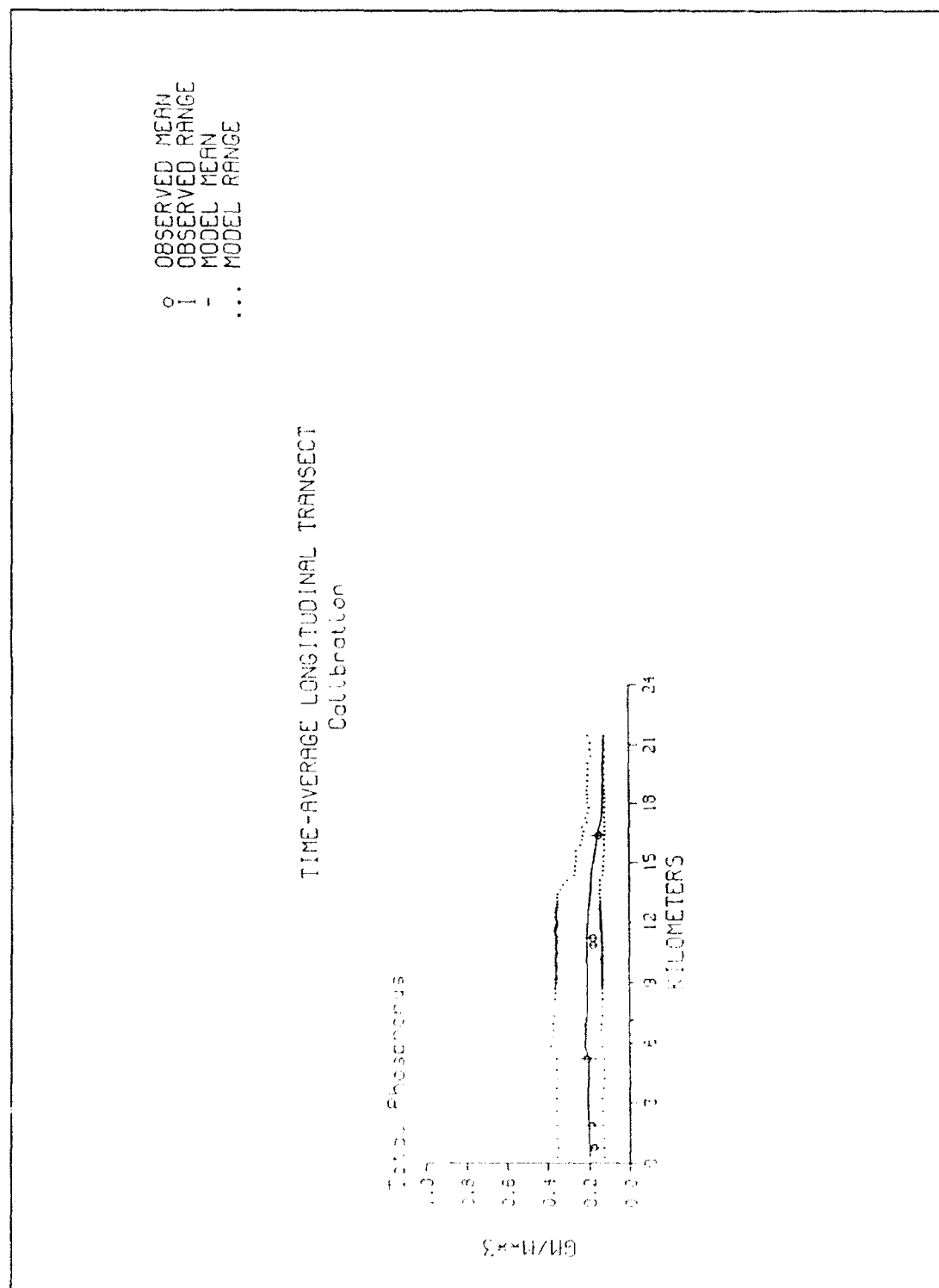


Figure 38. (Sheet 4 of 4)

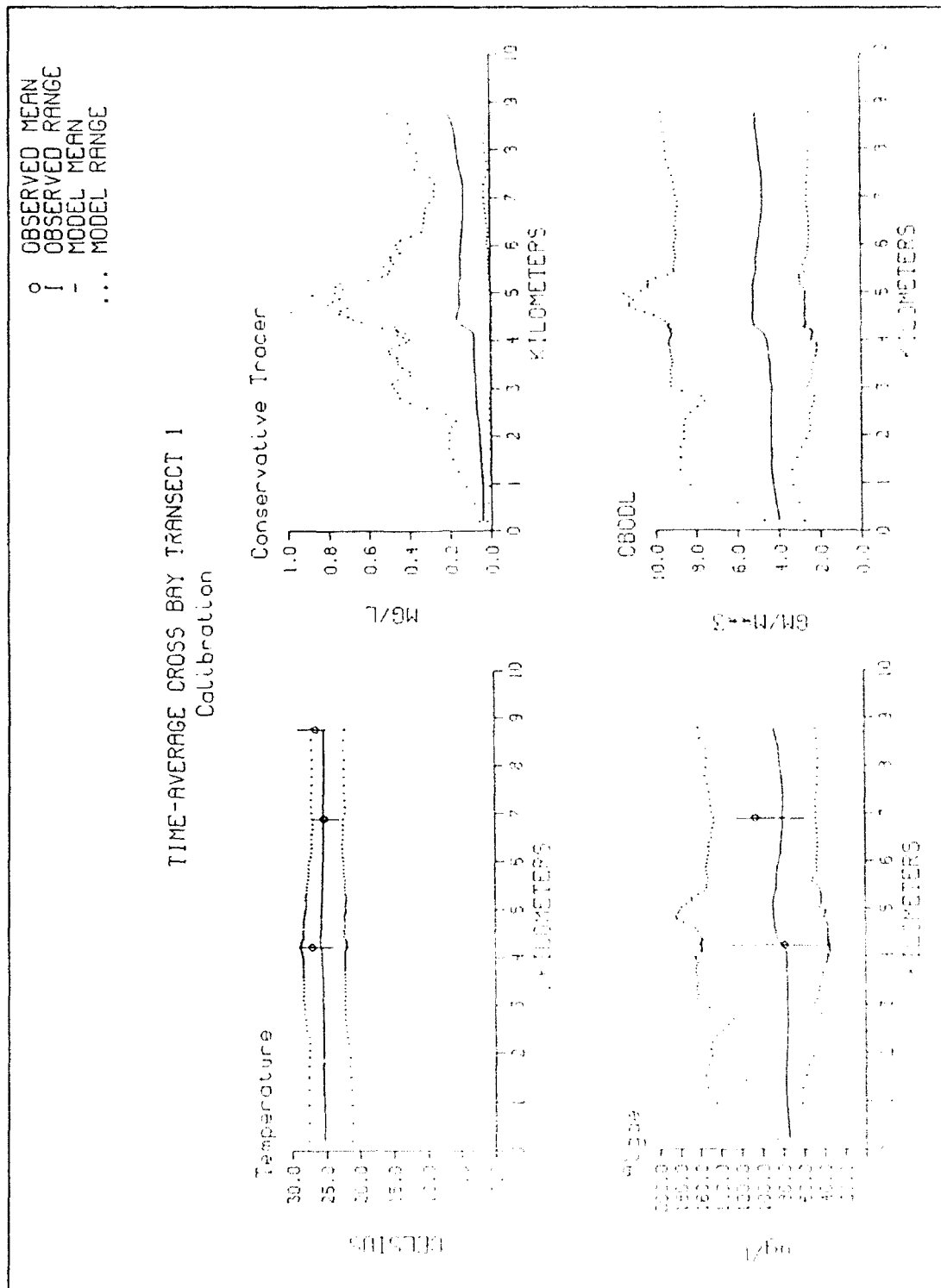


Figure 39. Time-averaged cross-bay transect 1 (Sheet 1 of 4)

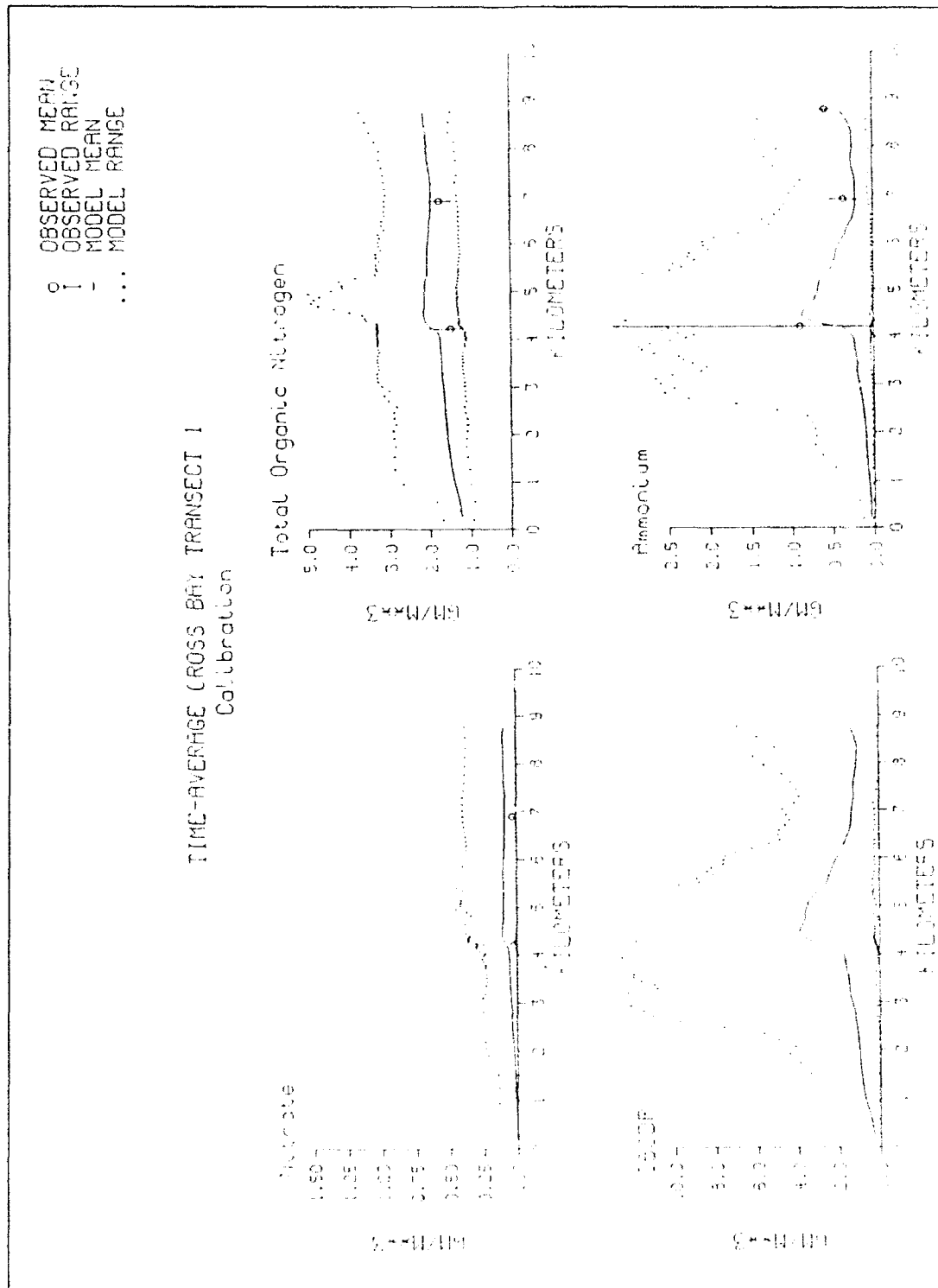


Figure 39. (Sheet 2 of 4)

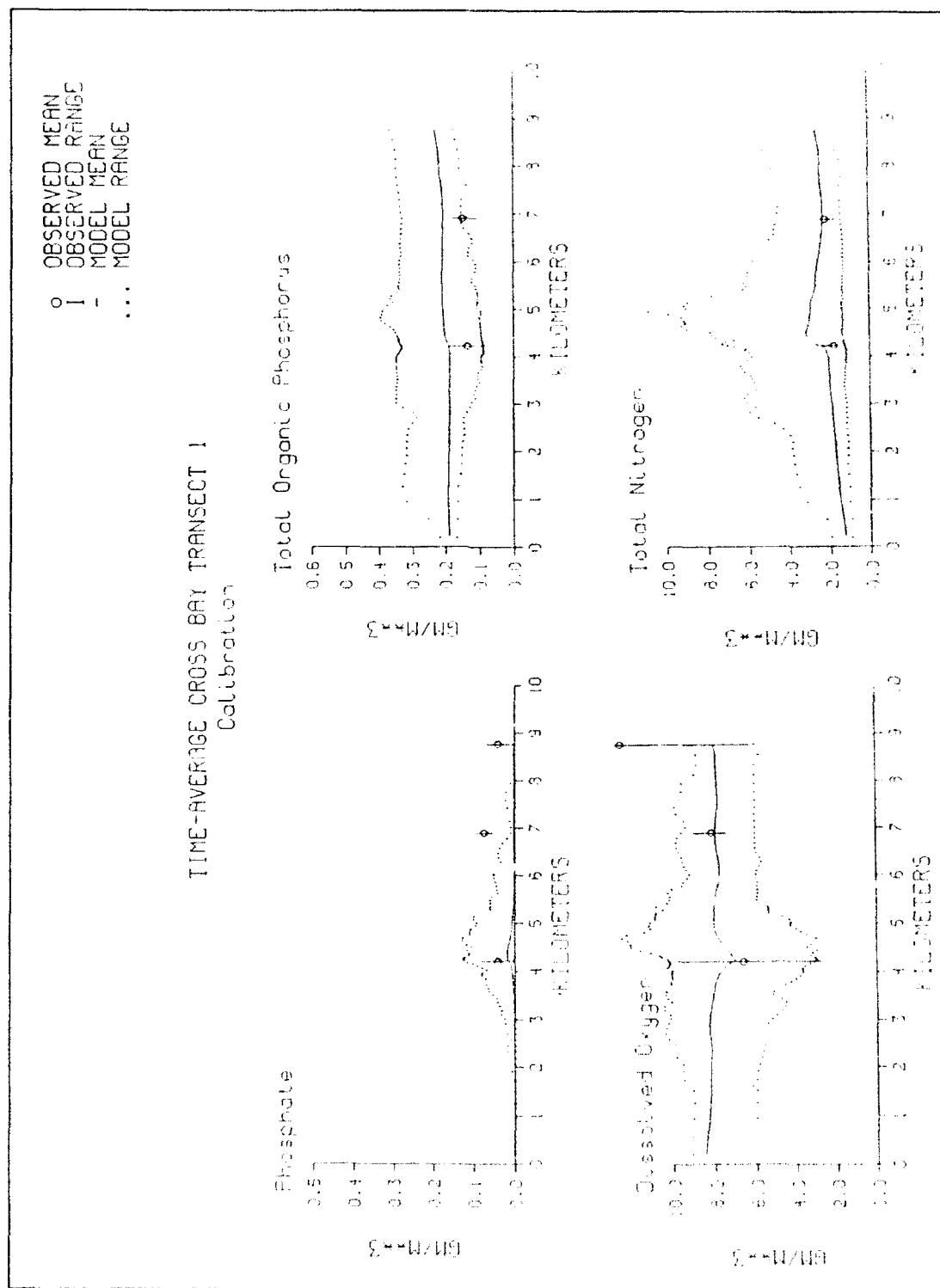


Figure 39. (Sheet 3 of 4)



Figure 39. (Sheet 4 of 4)

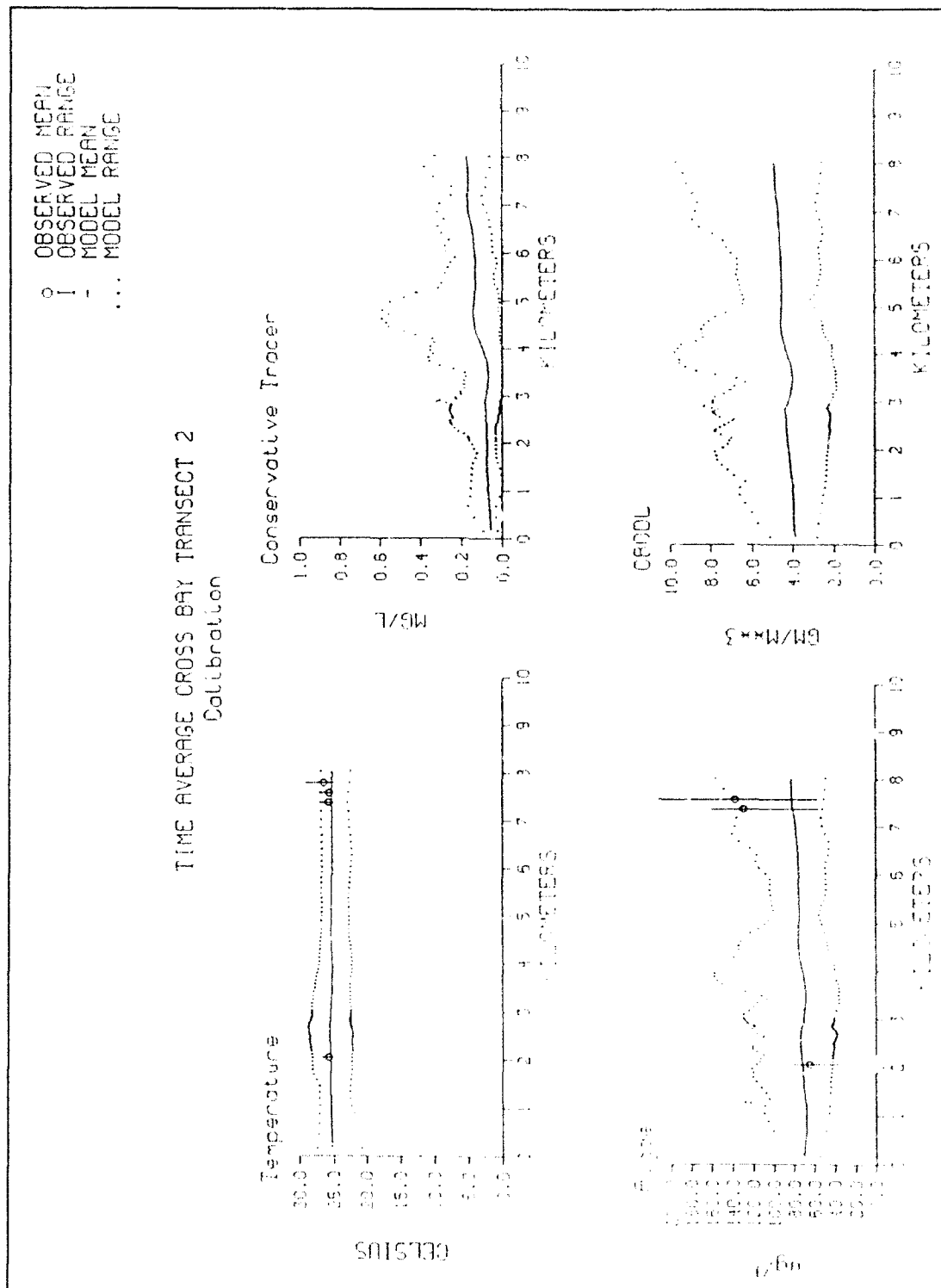
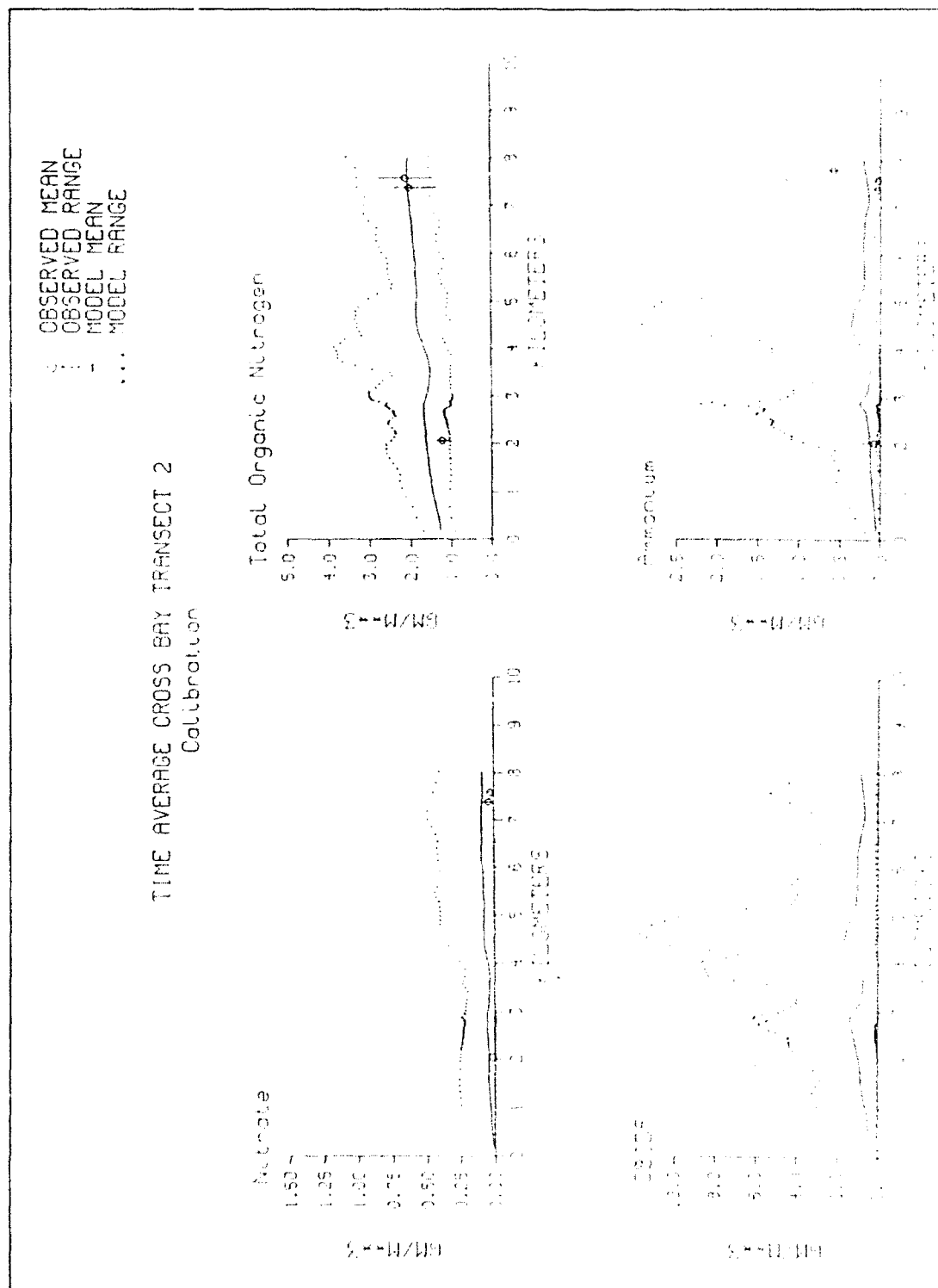


Figure 40. Time-averaged cross-bay transect 2 (Sheet 1 of 4)



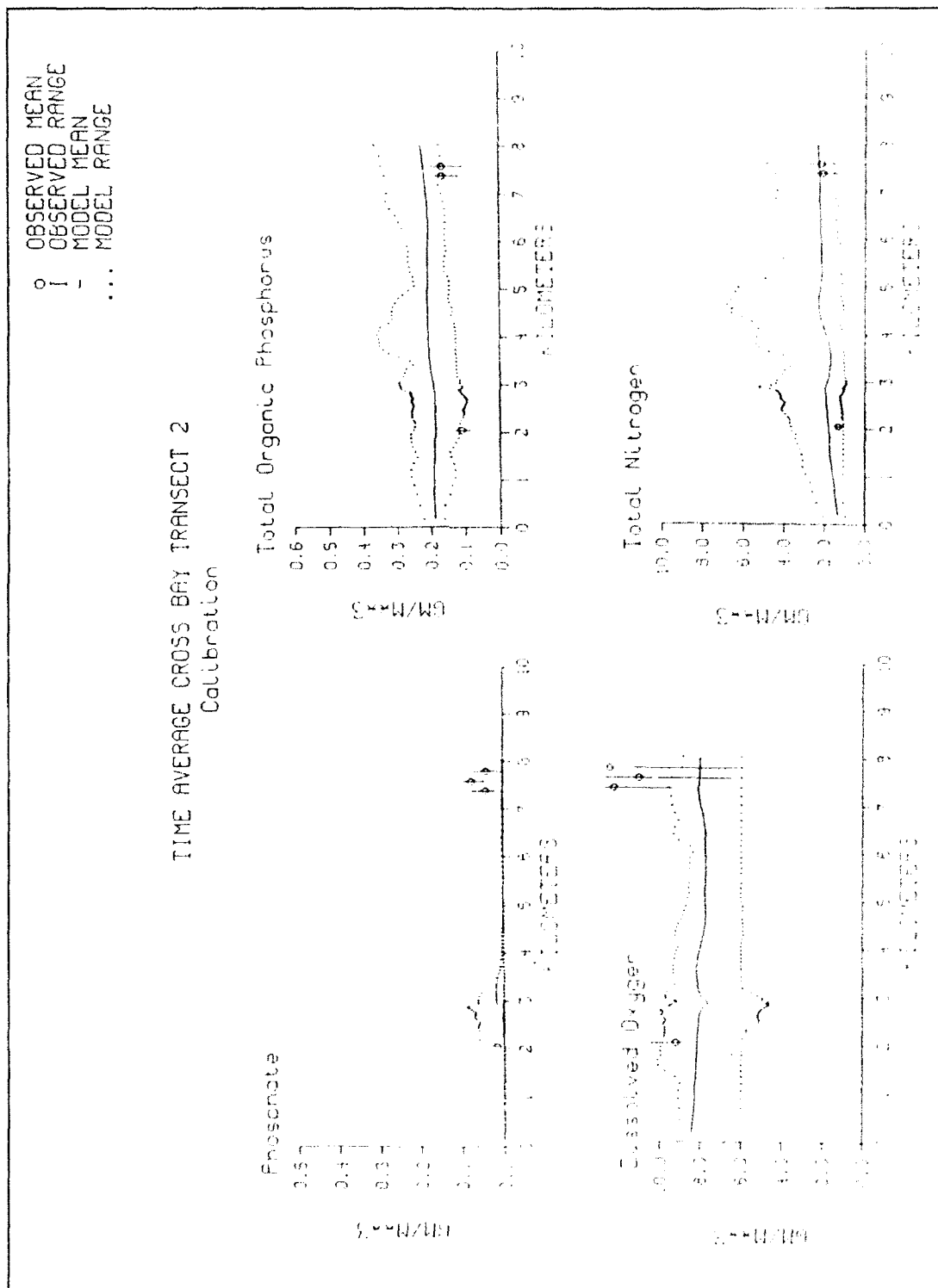


Figure 40. (Sheet 3 of 4)

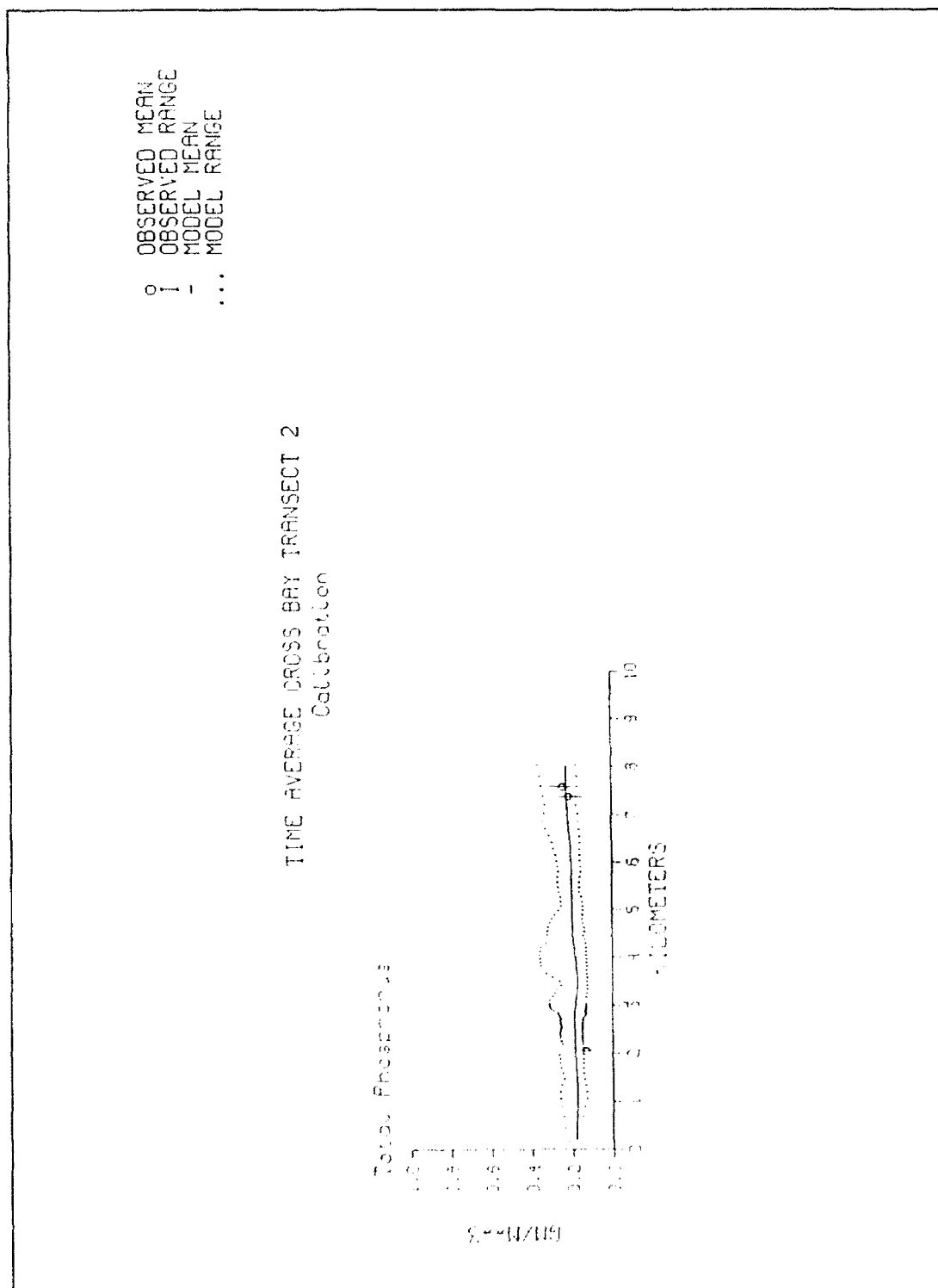


Figure 40. (Sheet 4 of 4)

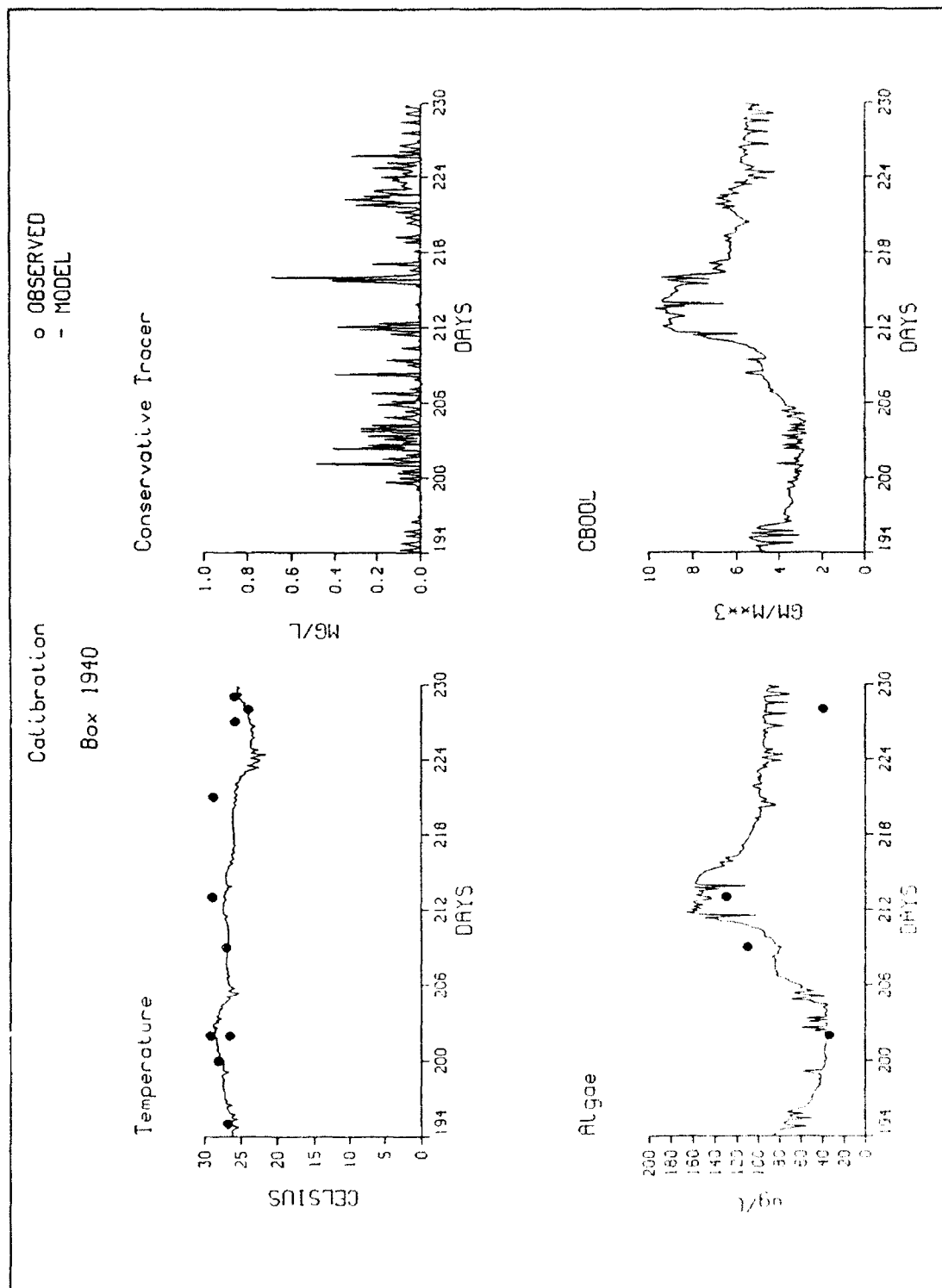


Figure 41. Grab sample, model comparison, cell 1940 (Sheet 1 of 4)

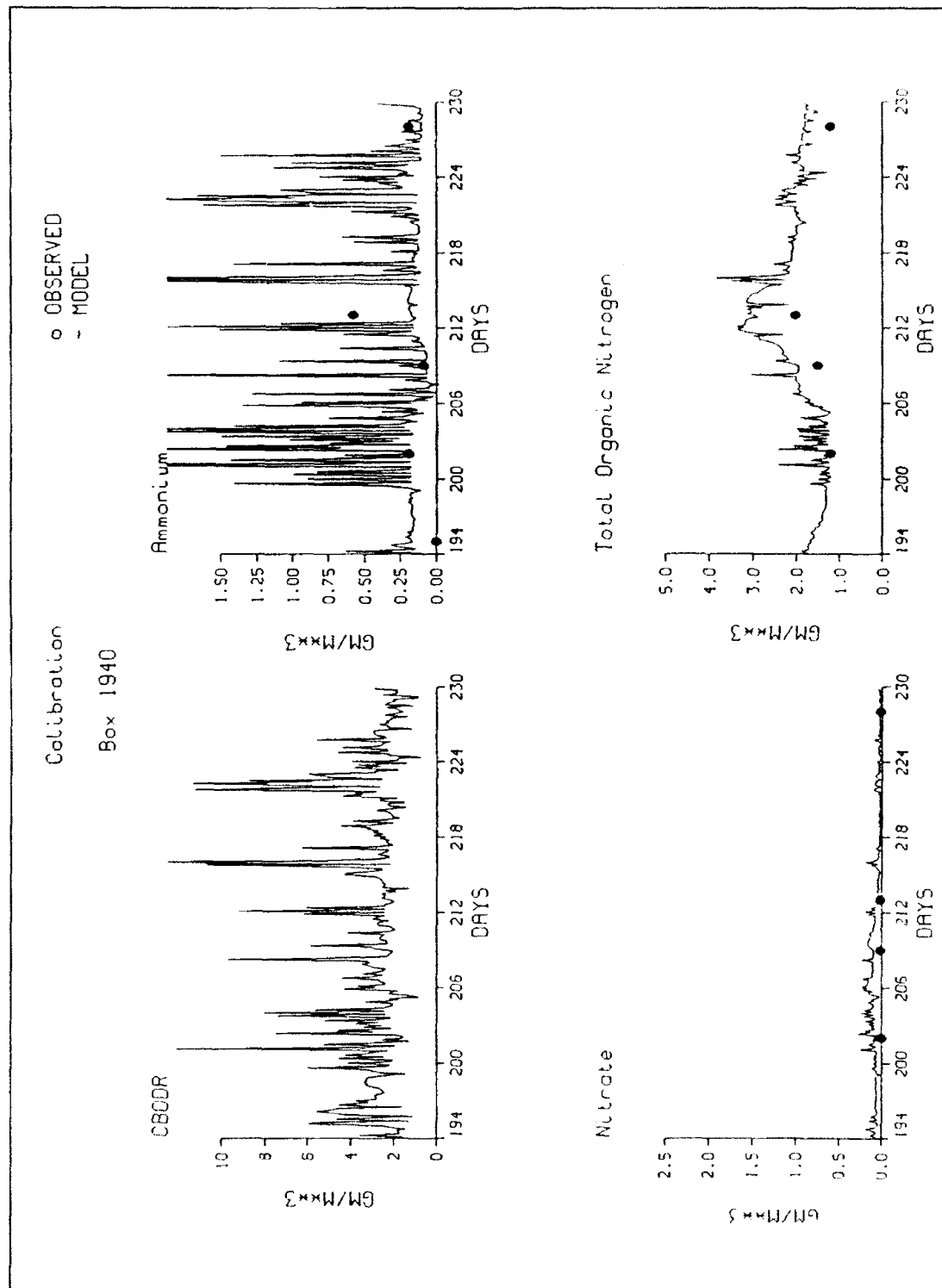


Figure 41. (Sheet 2 of 4)

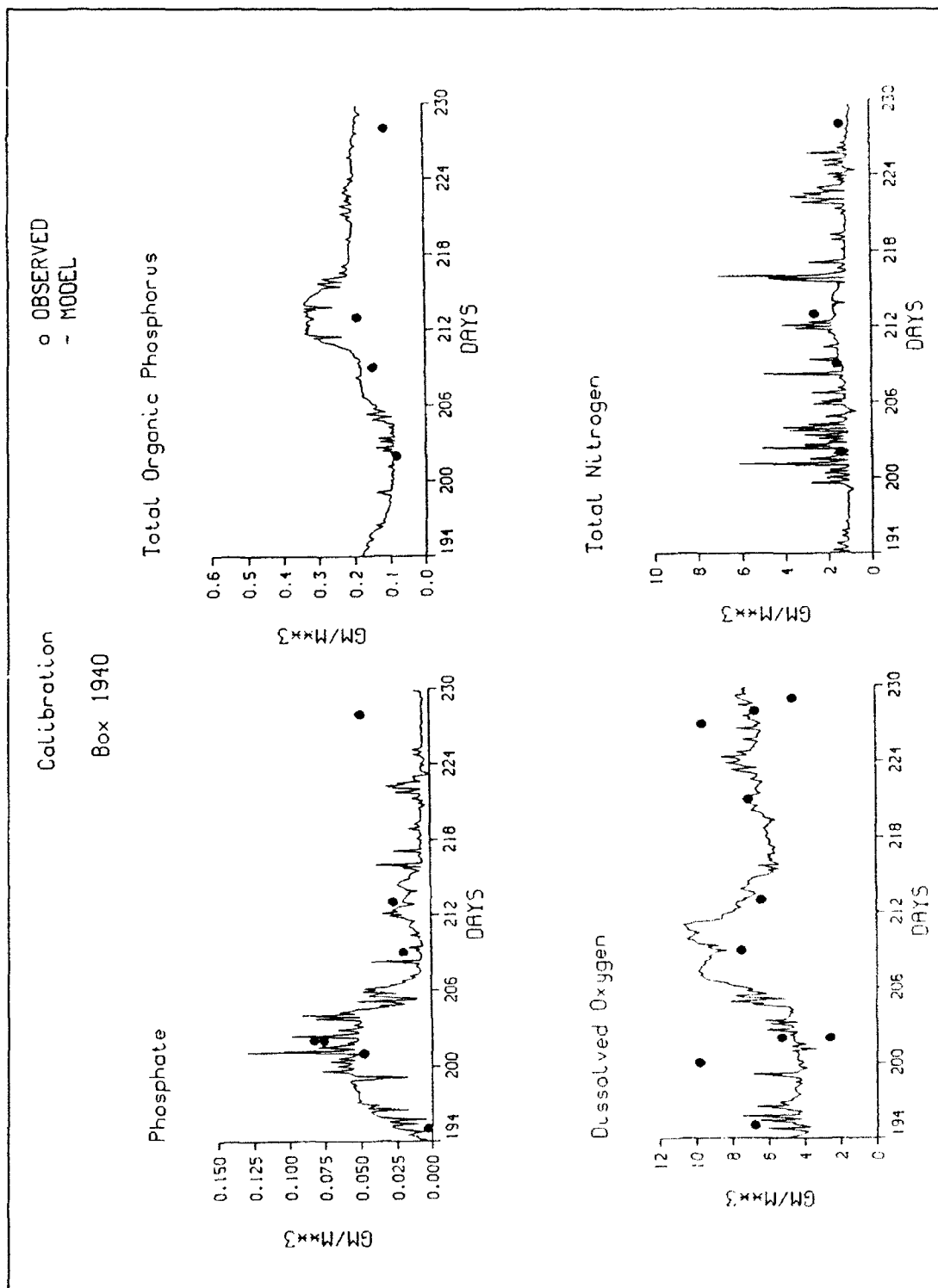


Figure 41. (Sheet 3 of 4)

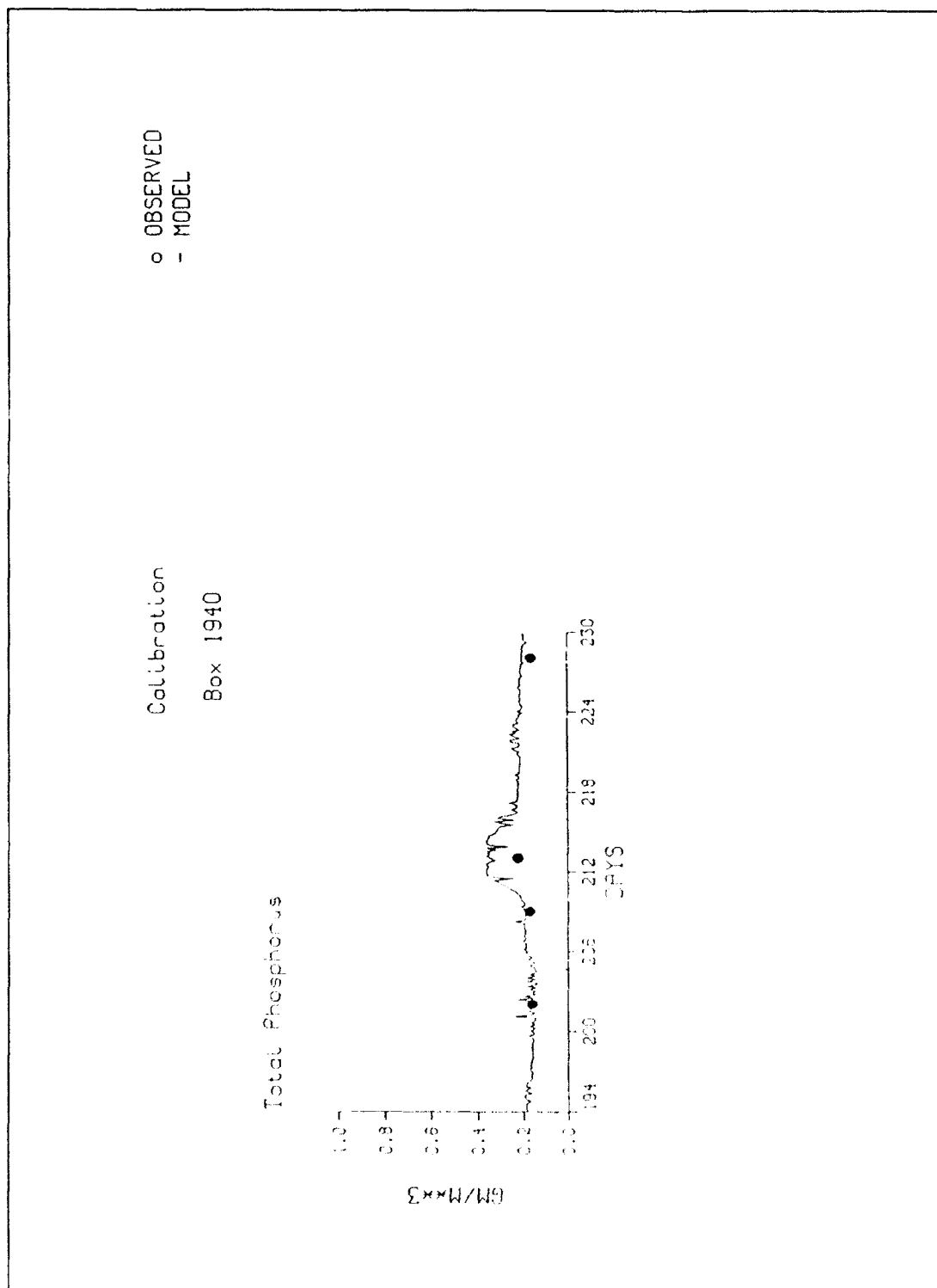


Figure 41. (Sheet 4 of 4)

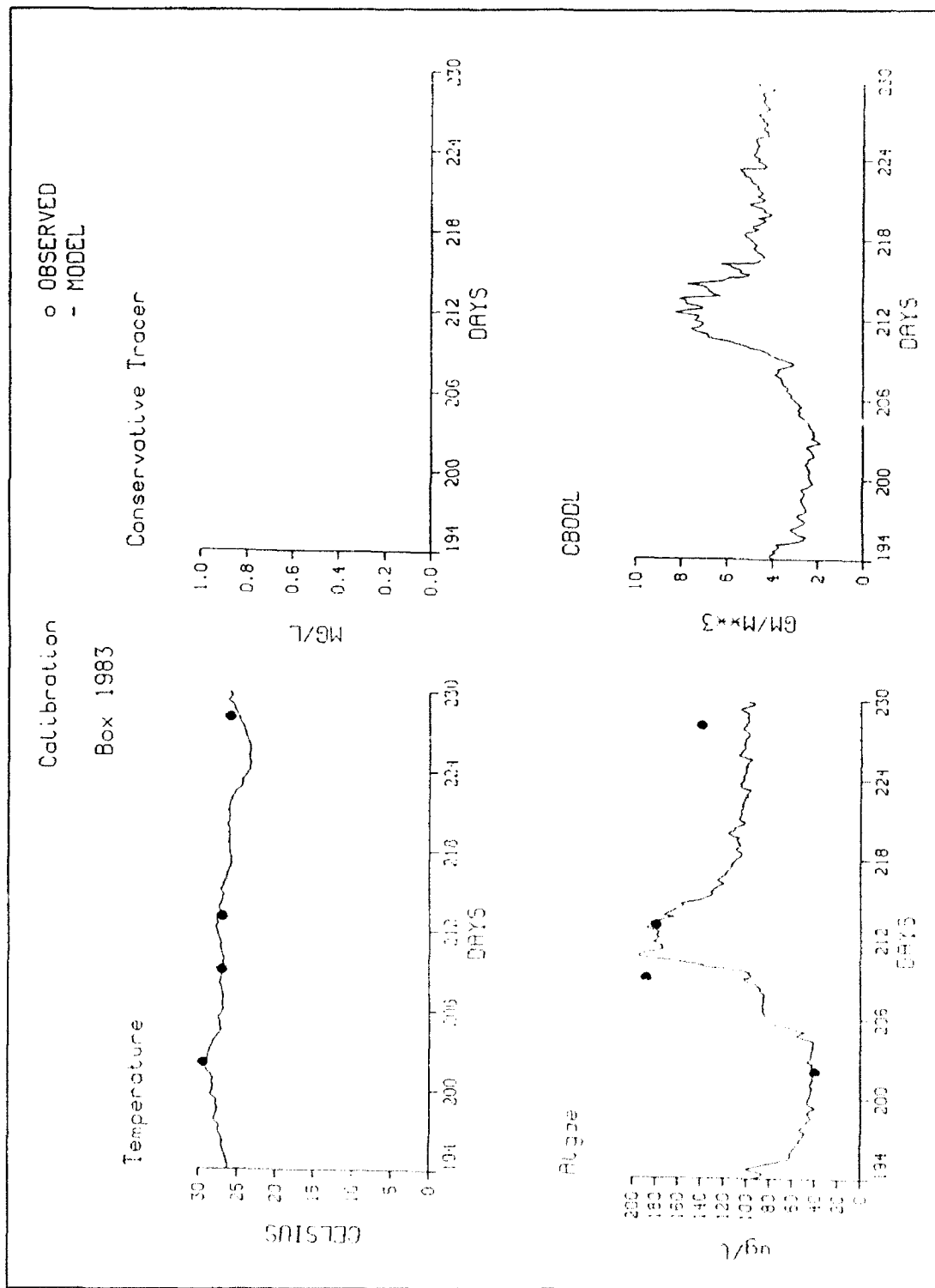


Figure 42. Grab sample, model comparison, cell 1983 (Sheet 1 of 4)

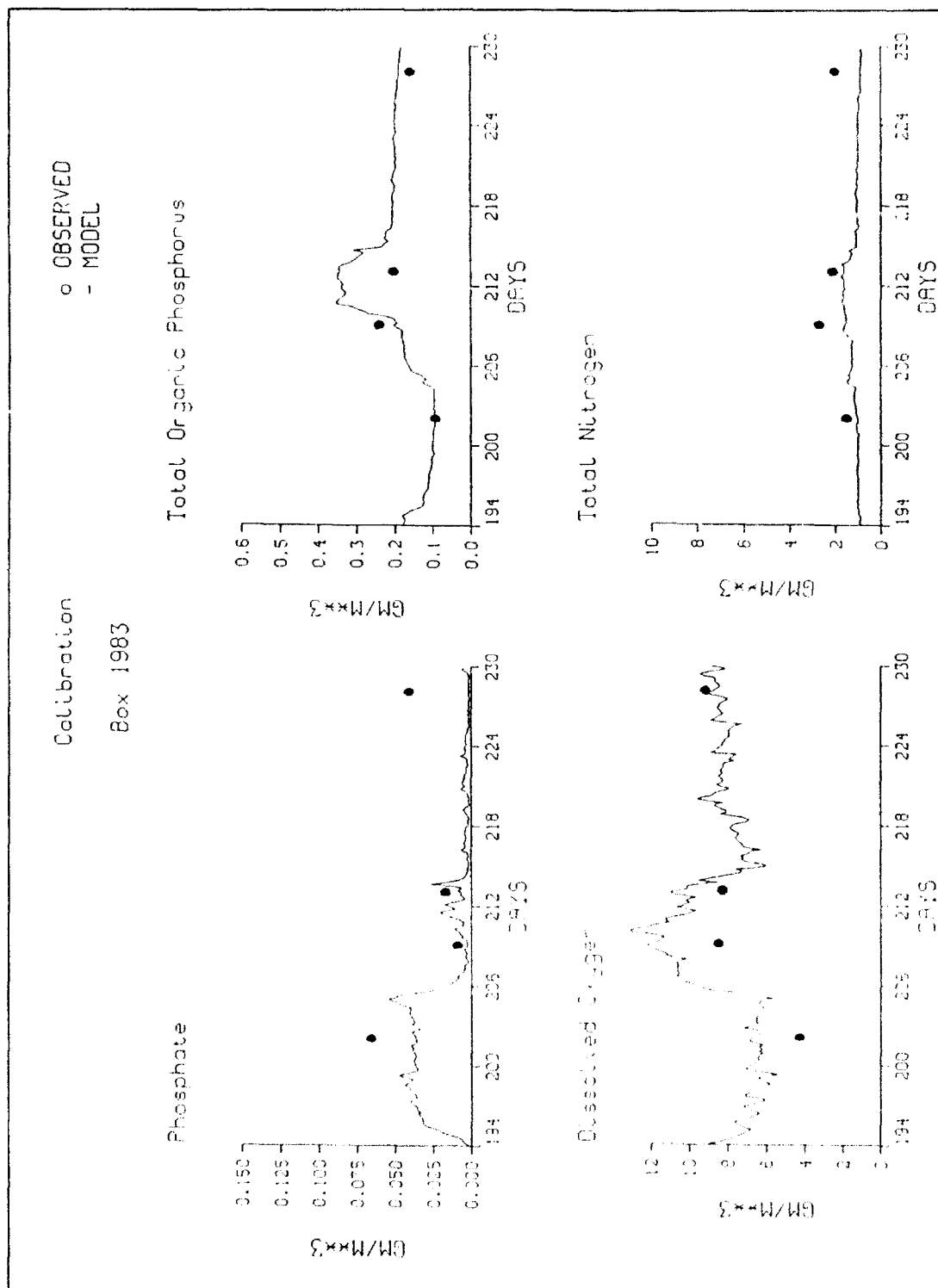


Figure 42. (Sheet 2 of 4)

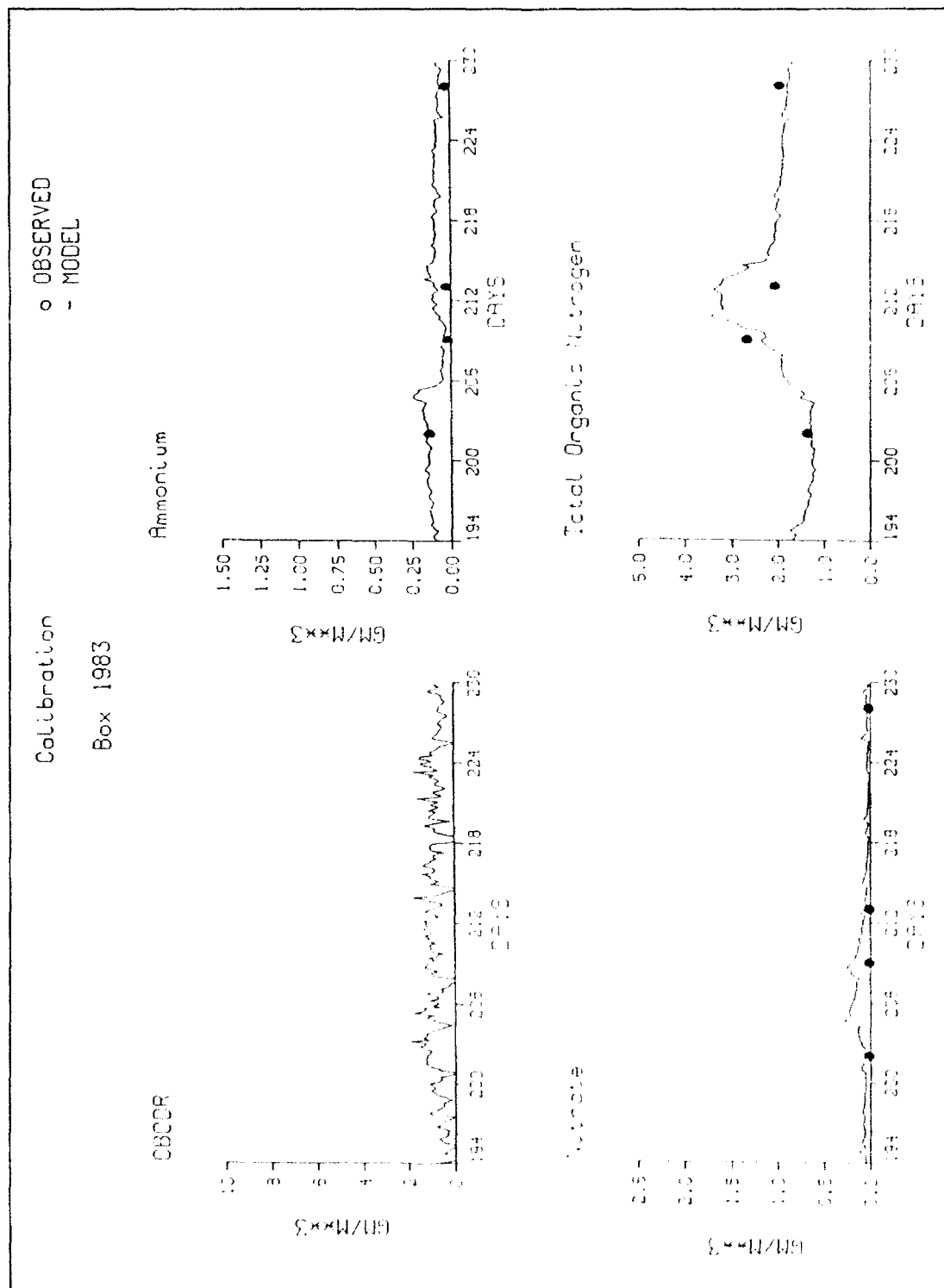


Figure 42. (Sheet 3 of 4)

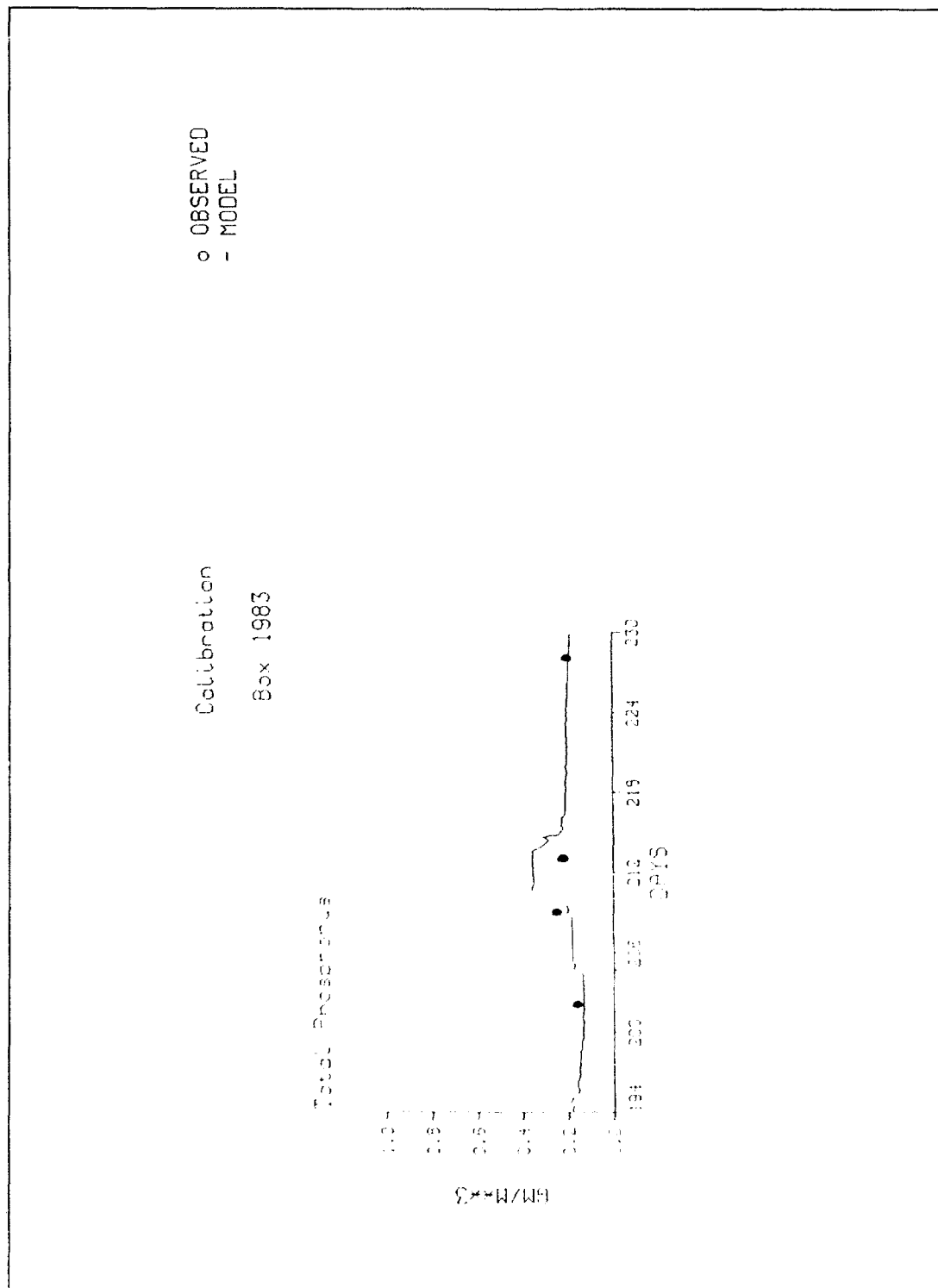


Figure 42. (Sheet 4 of 4)

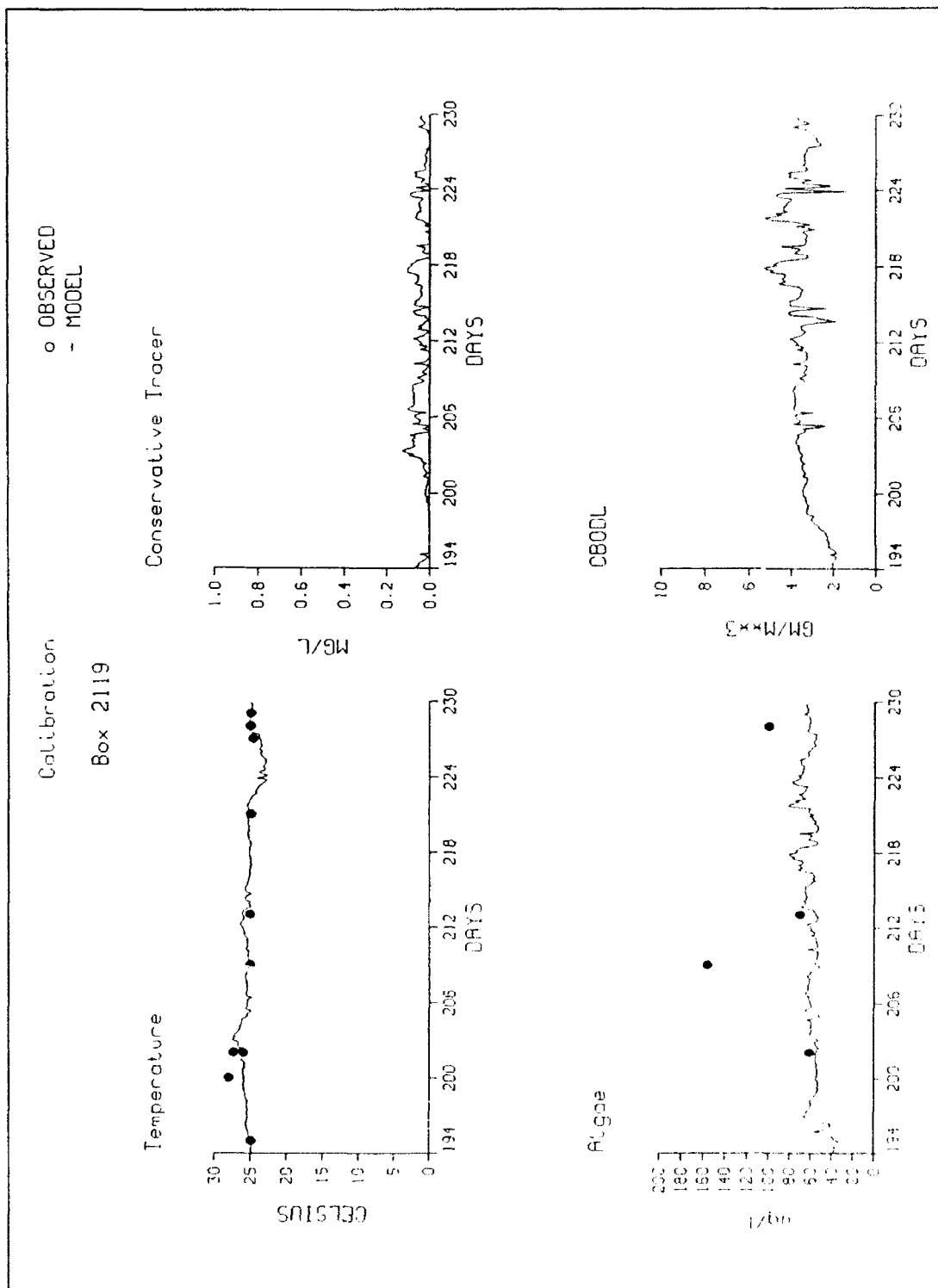


Figure 43. Grab sample, model comparison, cell 2119 (Sheet 1 of 4)

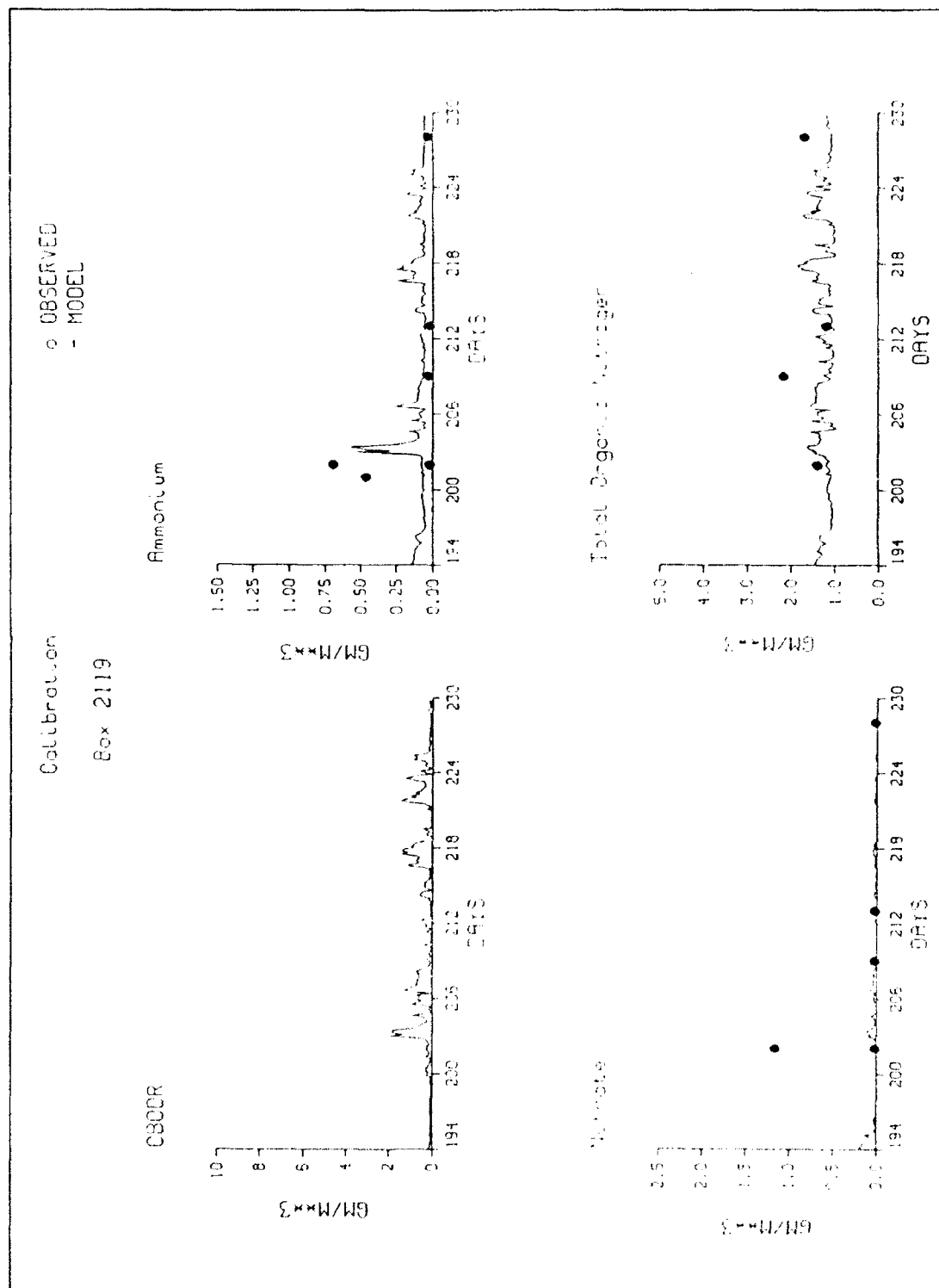


Figure 43. (Sheet 2 of 4)

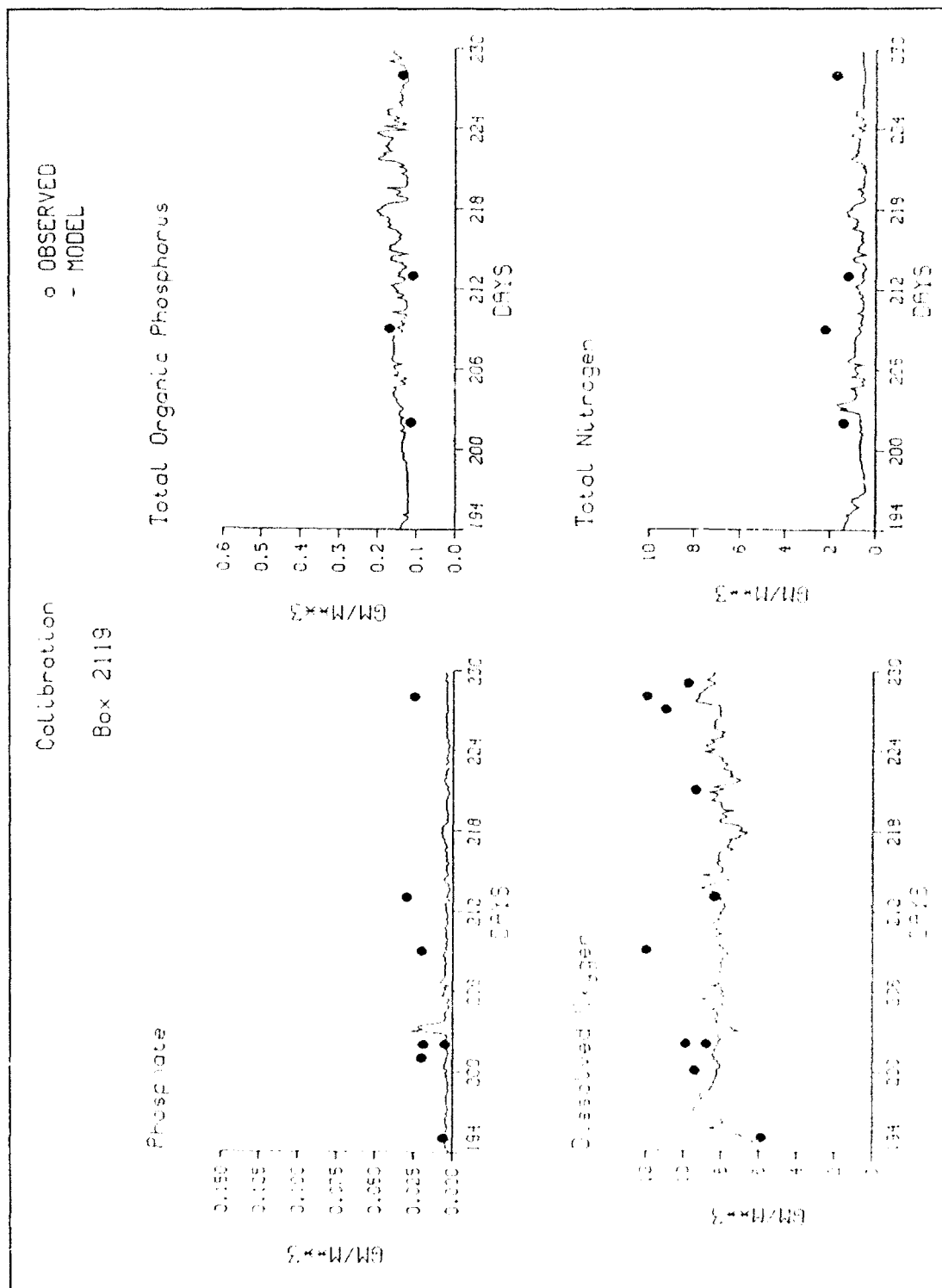


Figure 43. (Sheet 3 of 4)

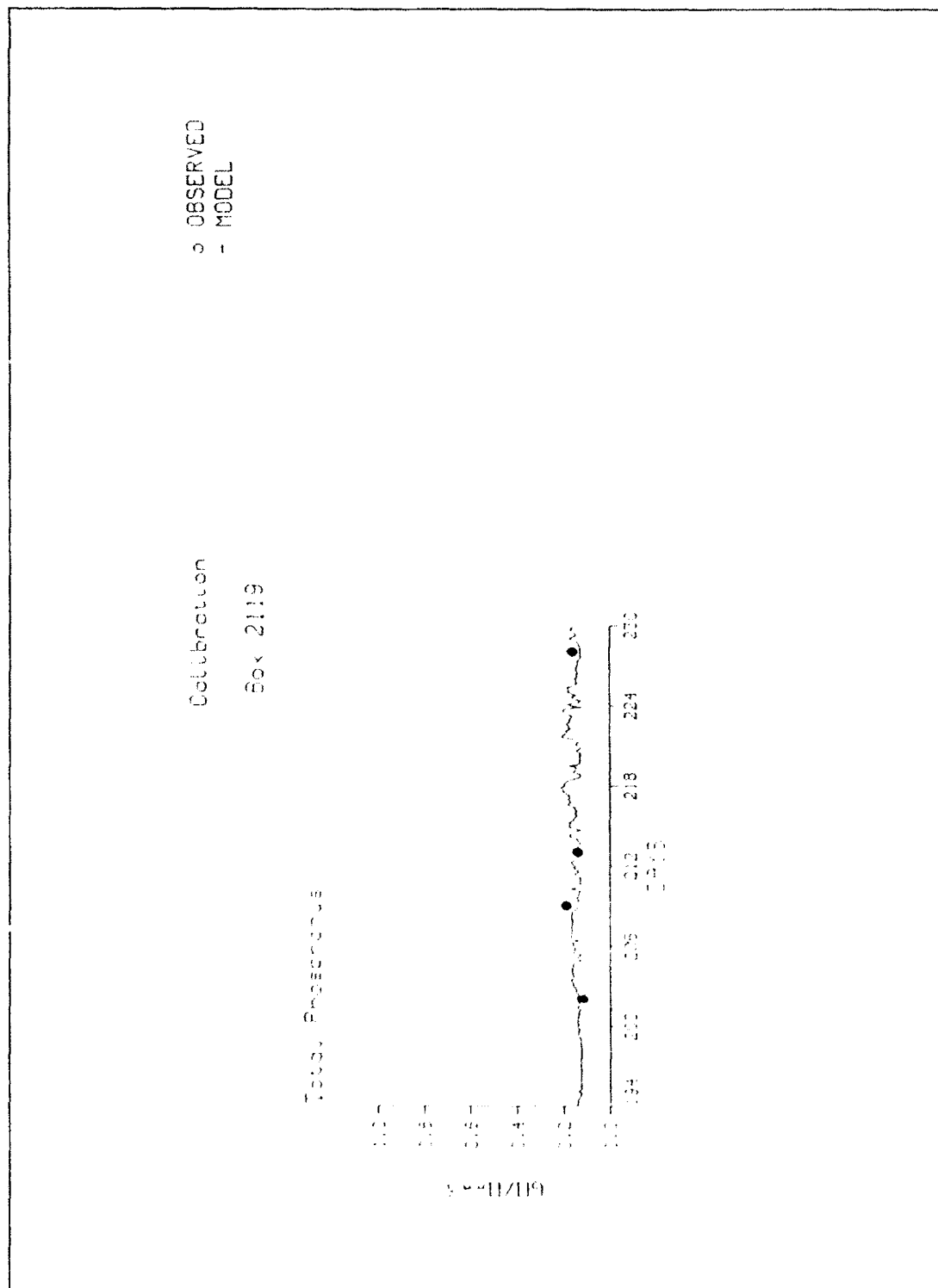


Figure 43. (Sheet 4 of 4)

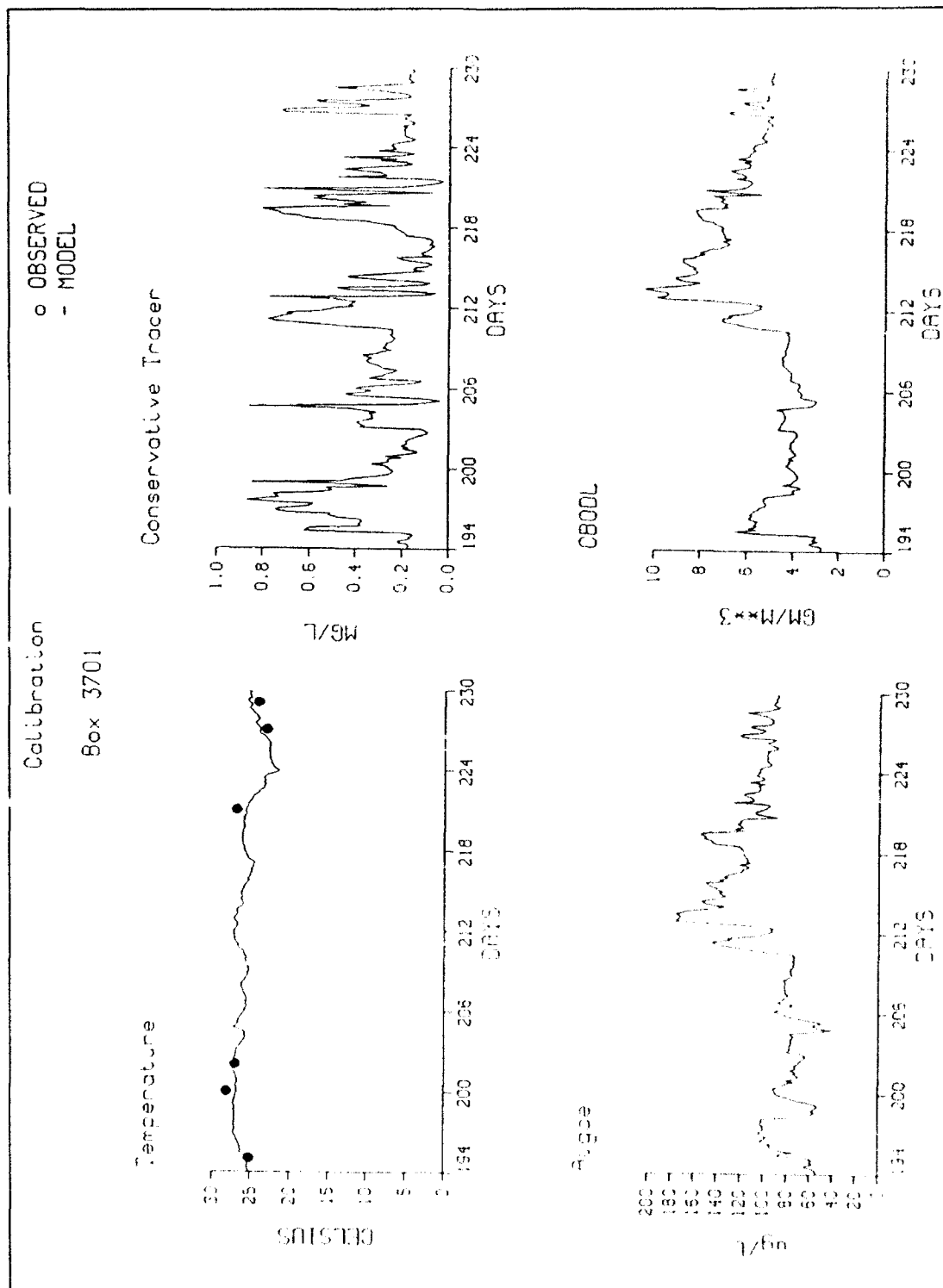


Figure 44. Grab sample, model comparison, cell 3701 (Sheet 1 of 4)

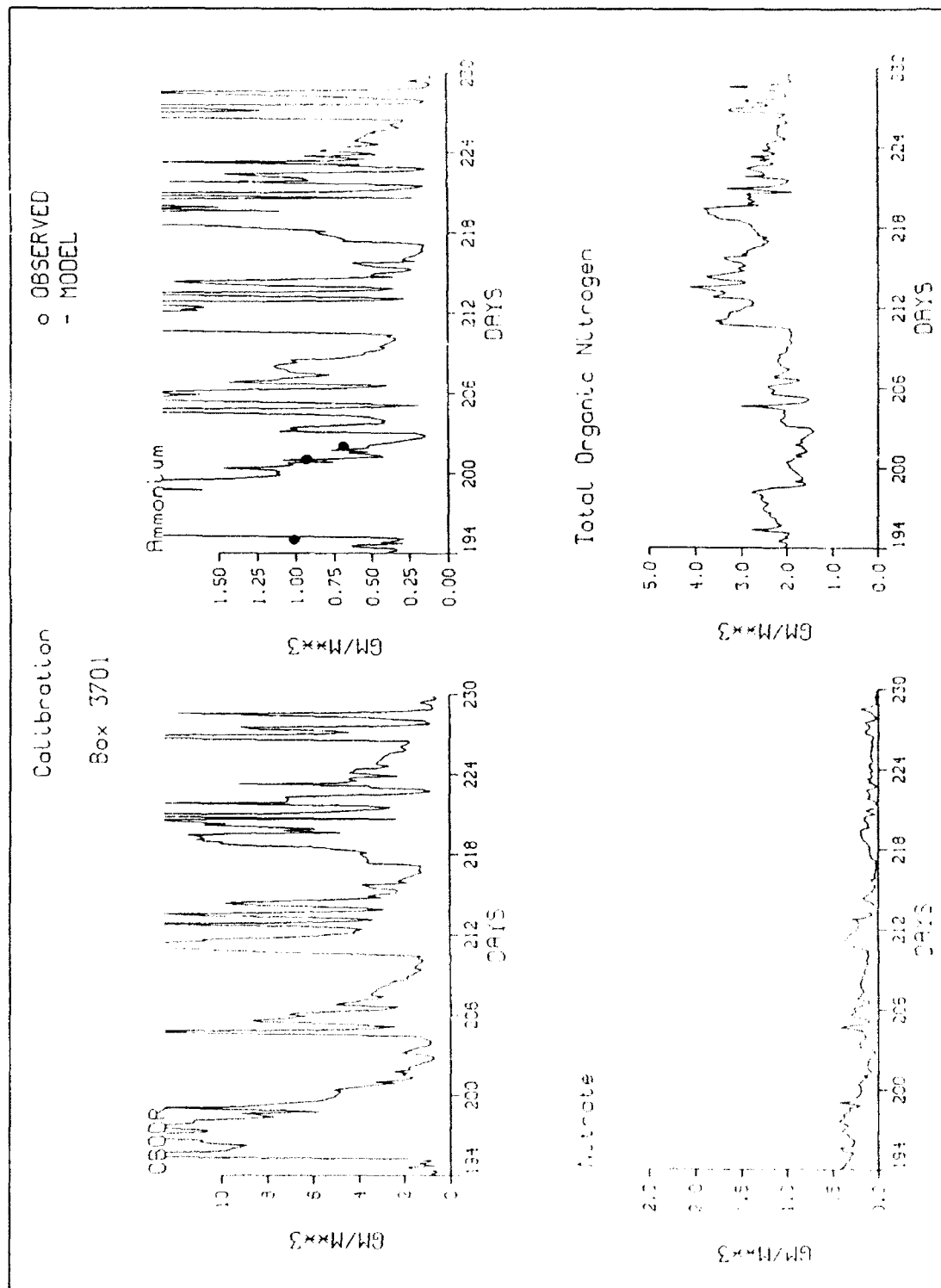


Figure 44. (Sheet 2 of 4)

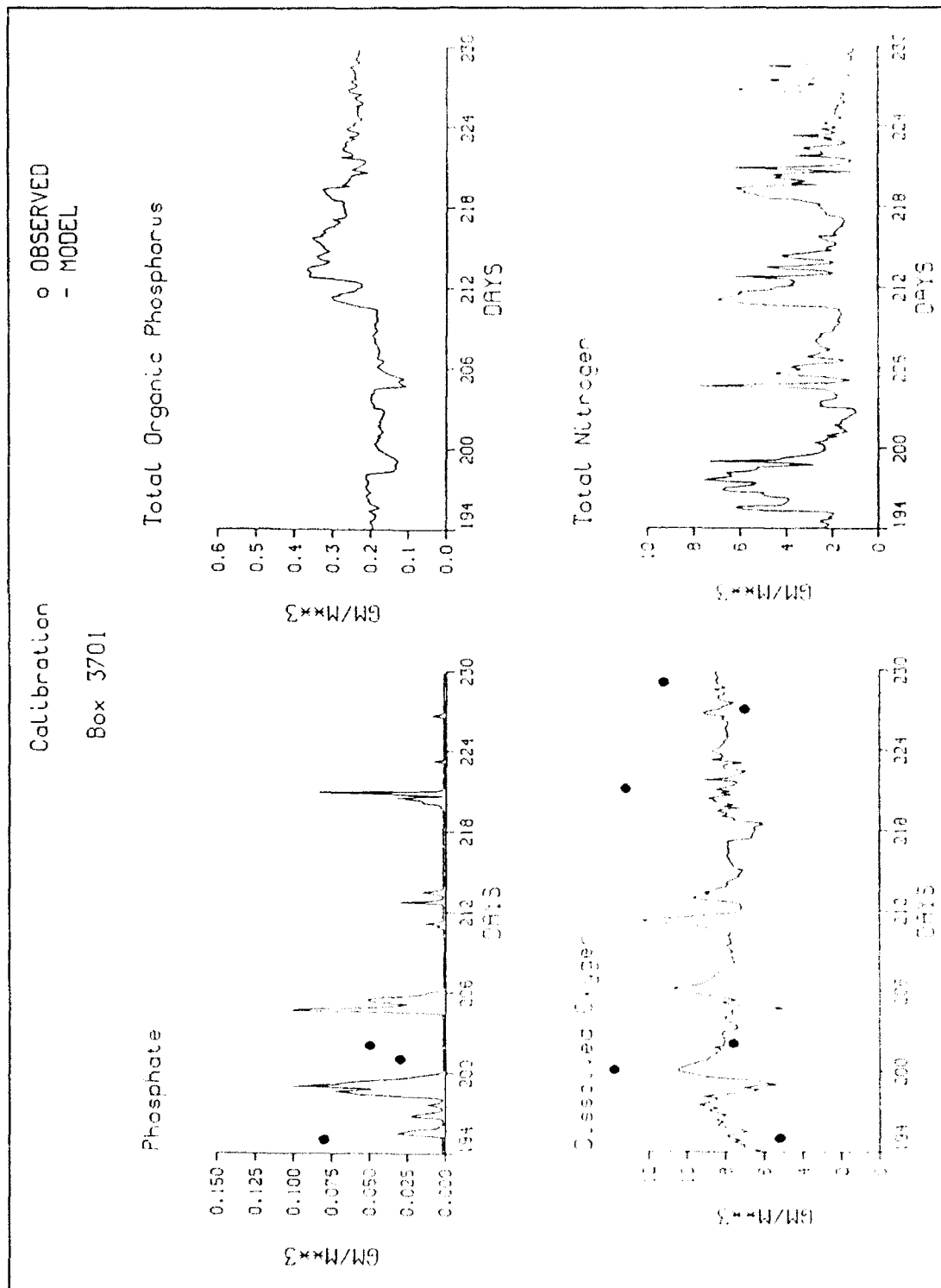


Figure 44. (Sheet 3 of 4)

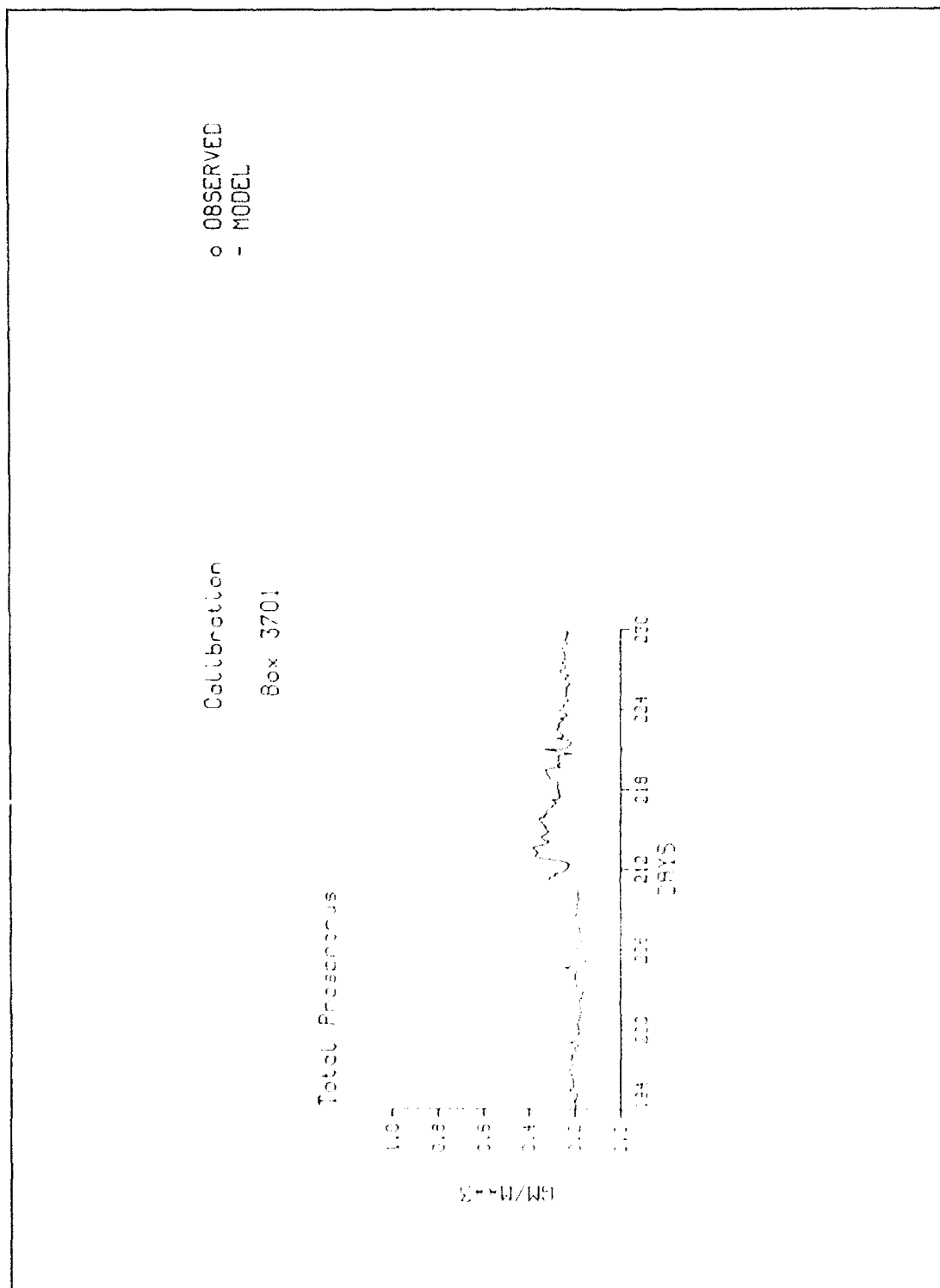


Figure 44. (Sheet 4 of 4)

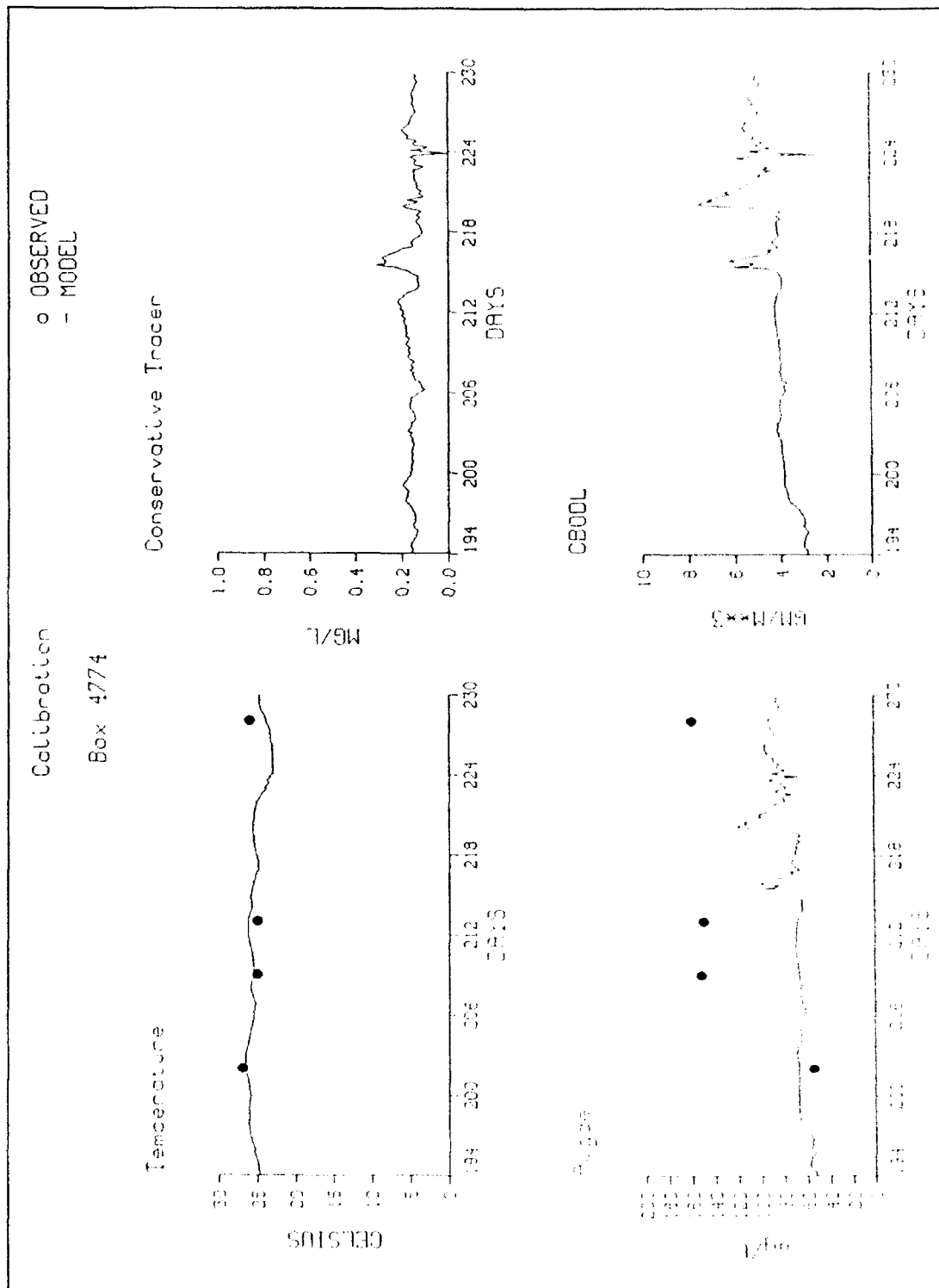


Figure 45. Grab sample, model comparison, cell 4774 (Sheet 1 of 4)

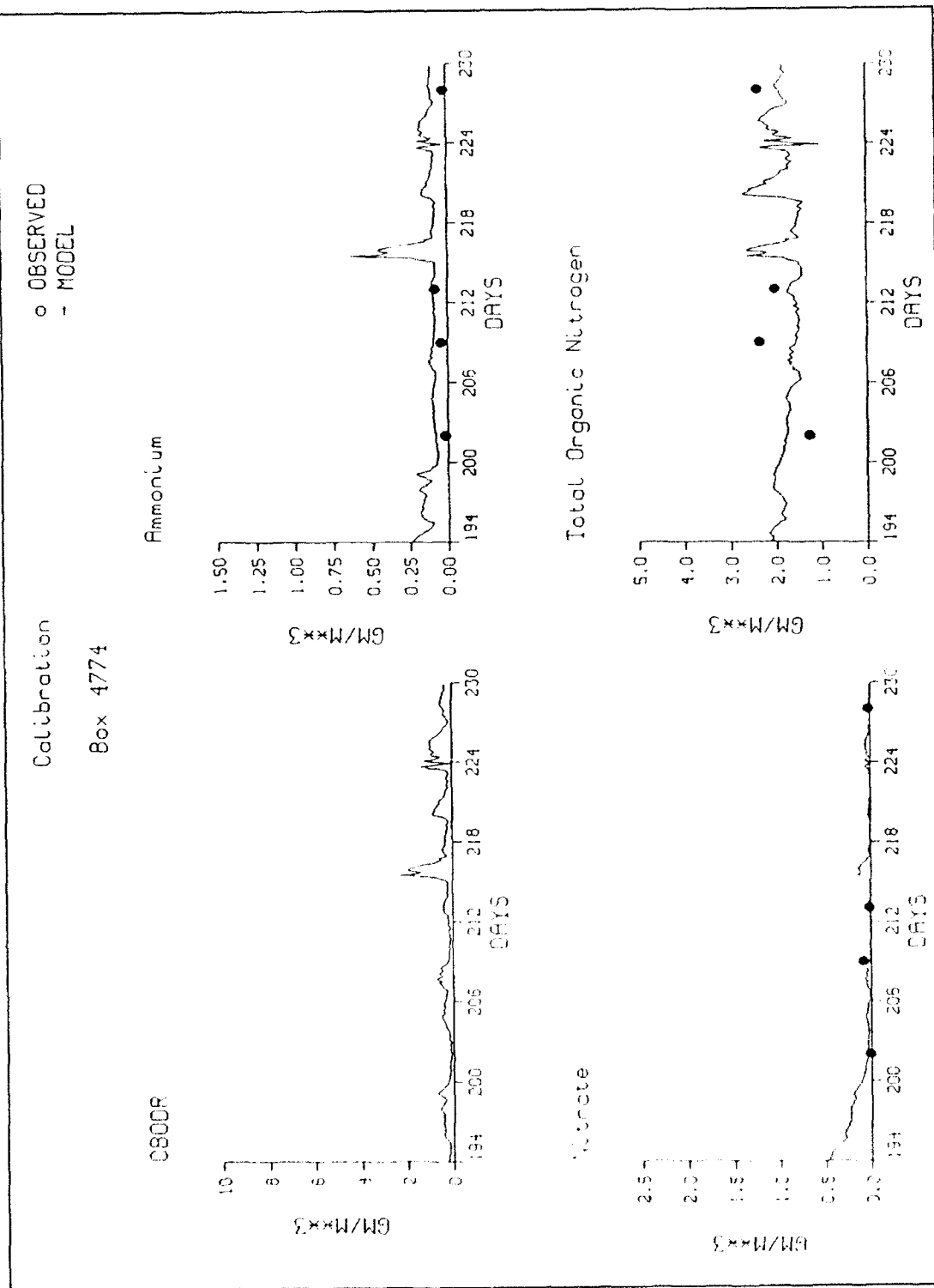


Figure 45. (Sheet 2 of 4)

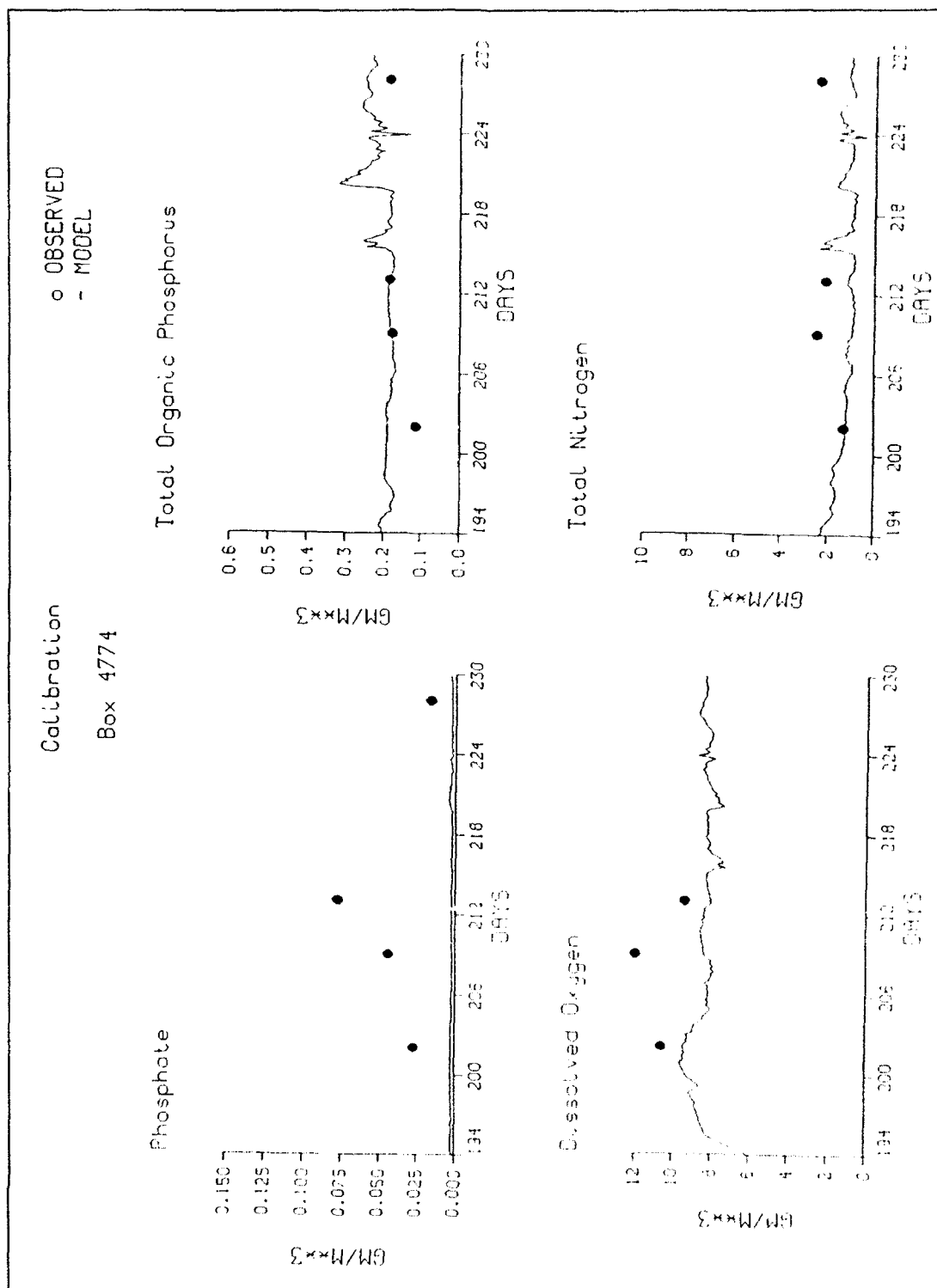


Figure 45. (Sheet 3 of 4)

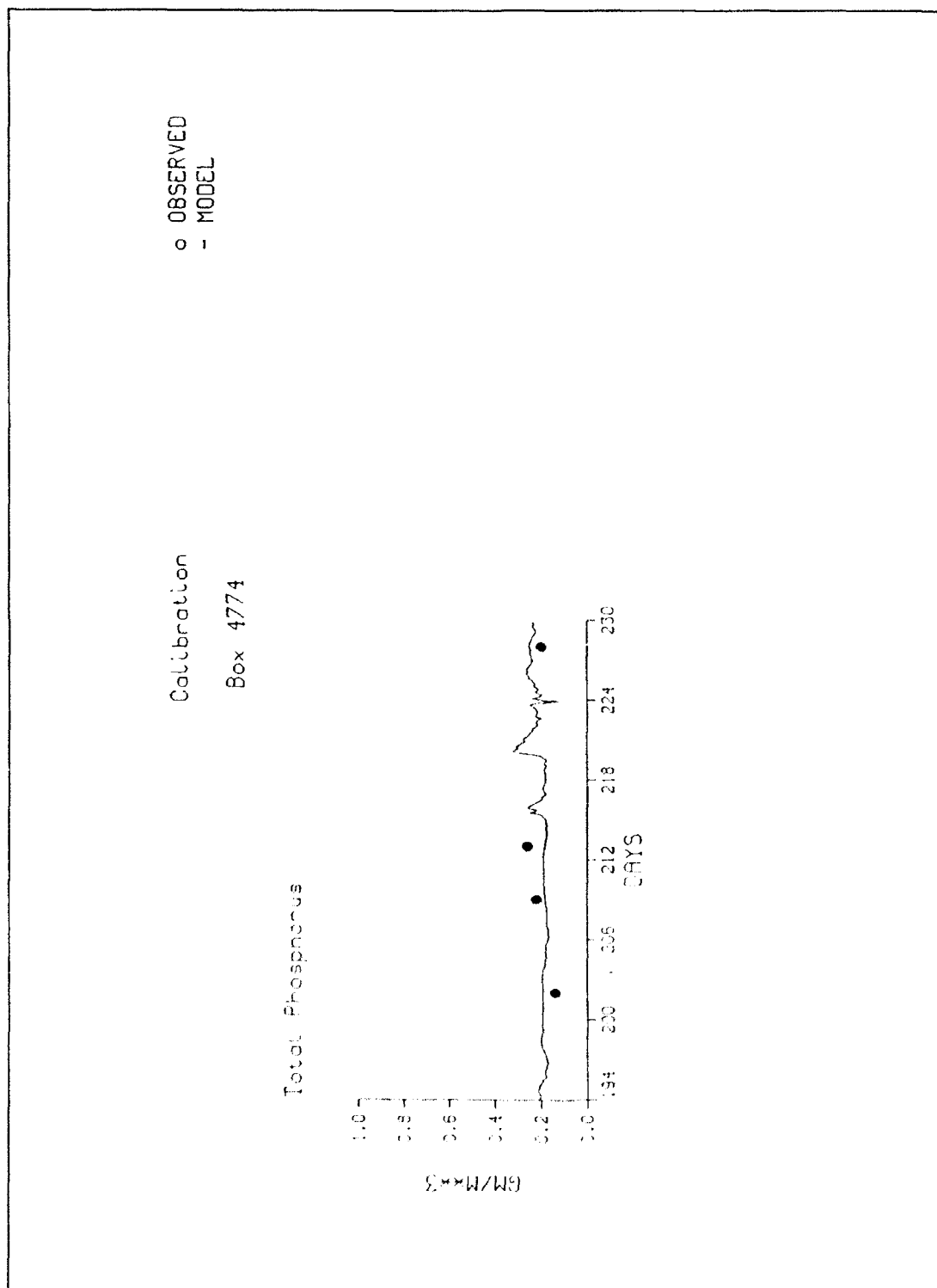


Figure 45. (Sheet 4 of 4)

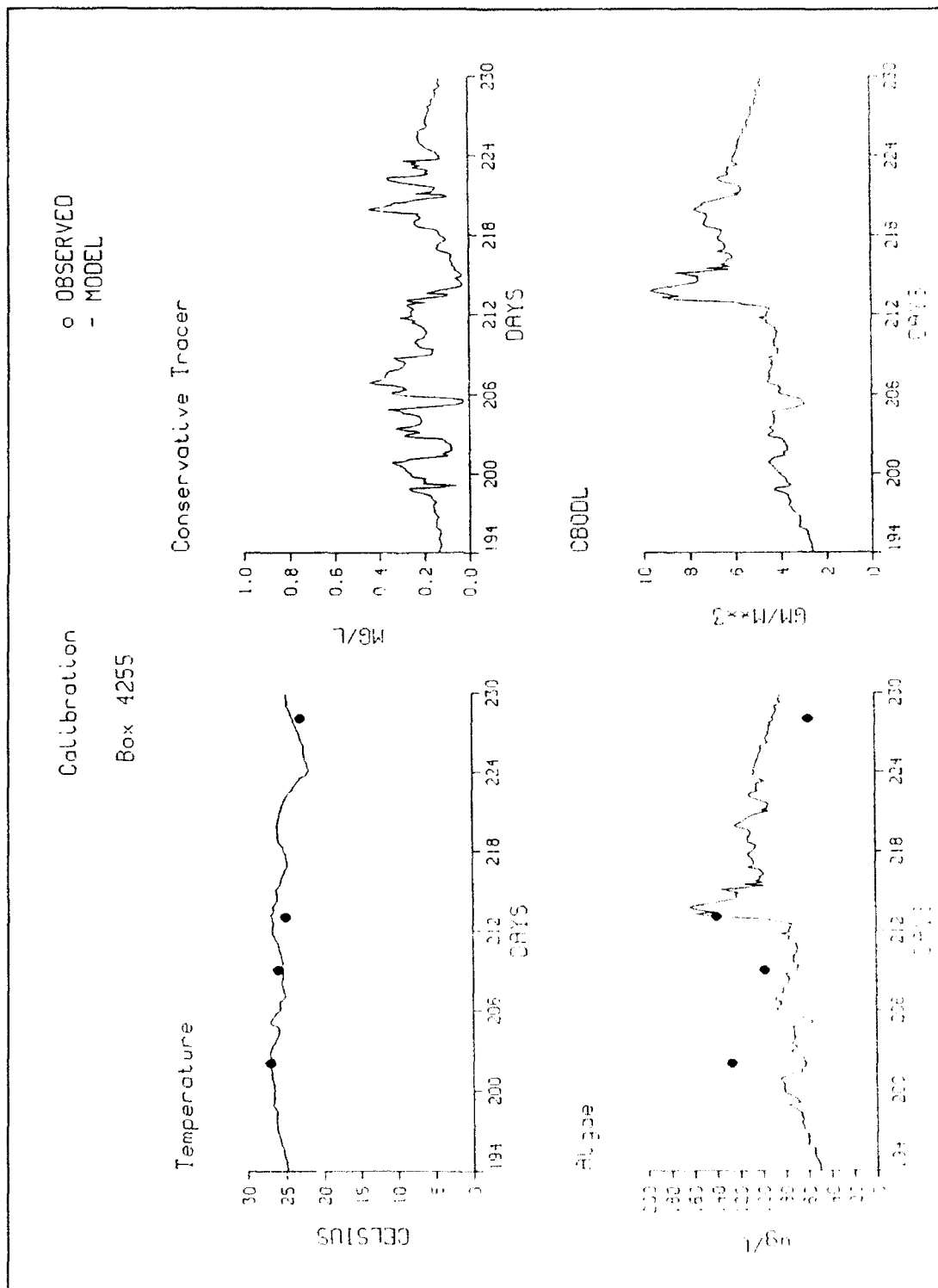


Figure 46. Grab sample, model comparison, cell 4255 (Sheet 1 of 4)

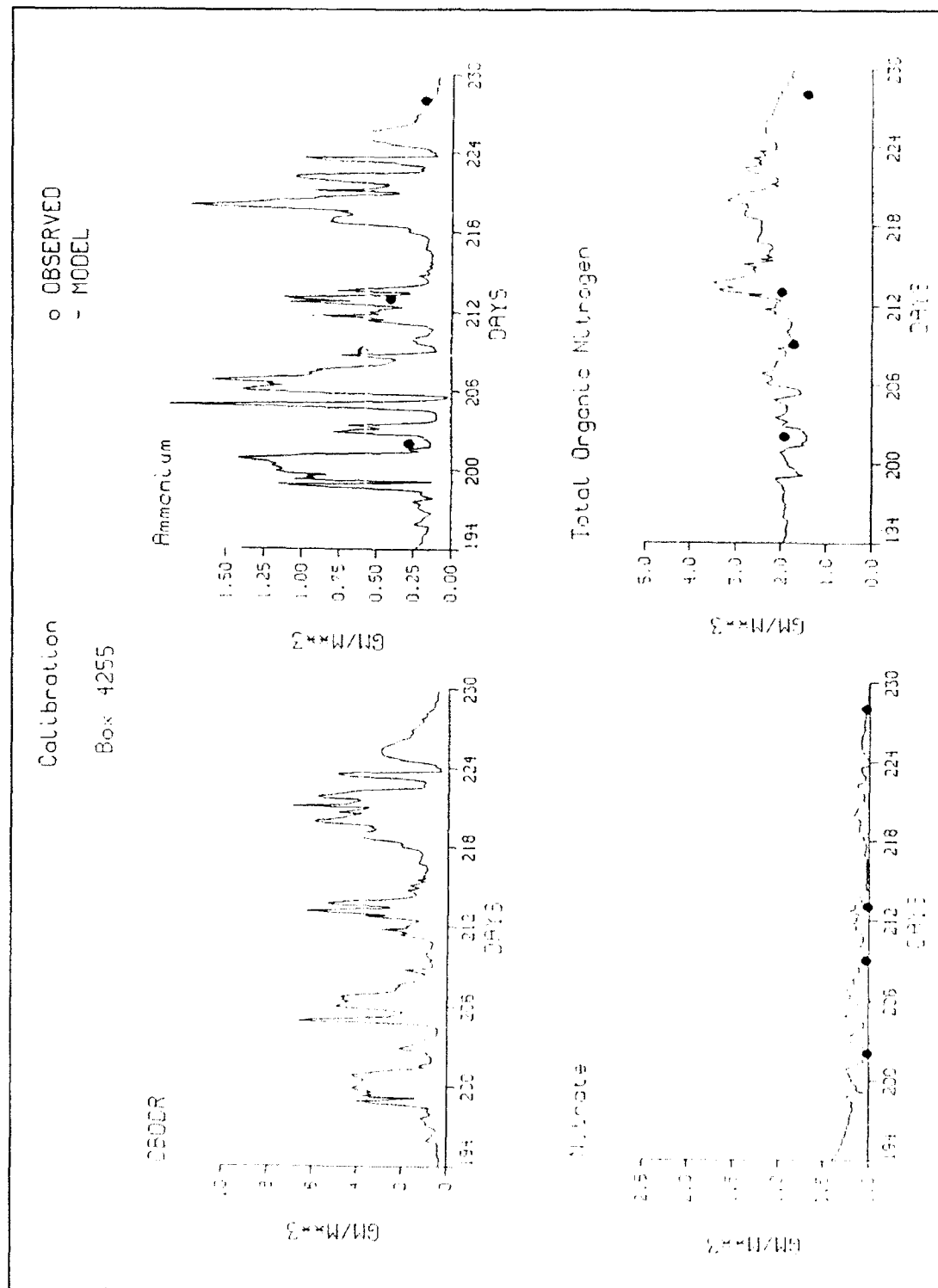


Figure 46. (Sheet 2 of 4)

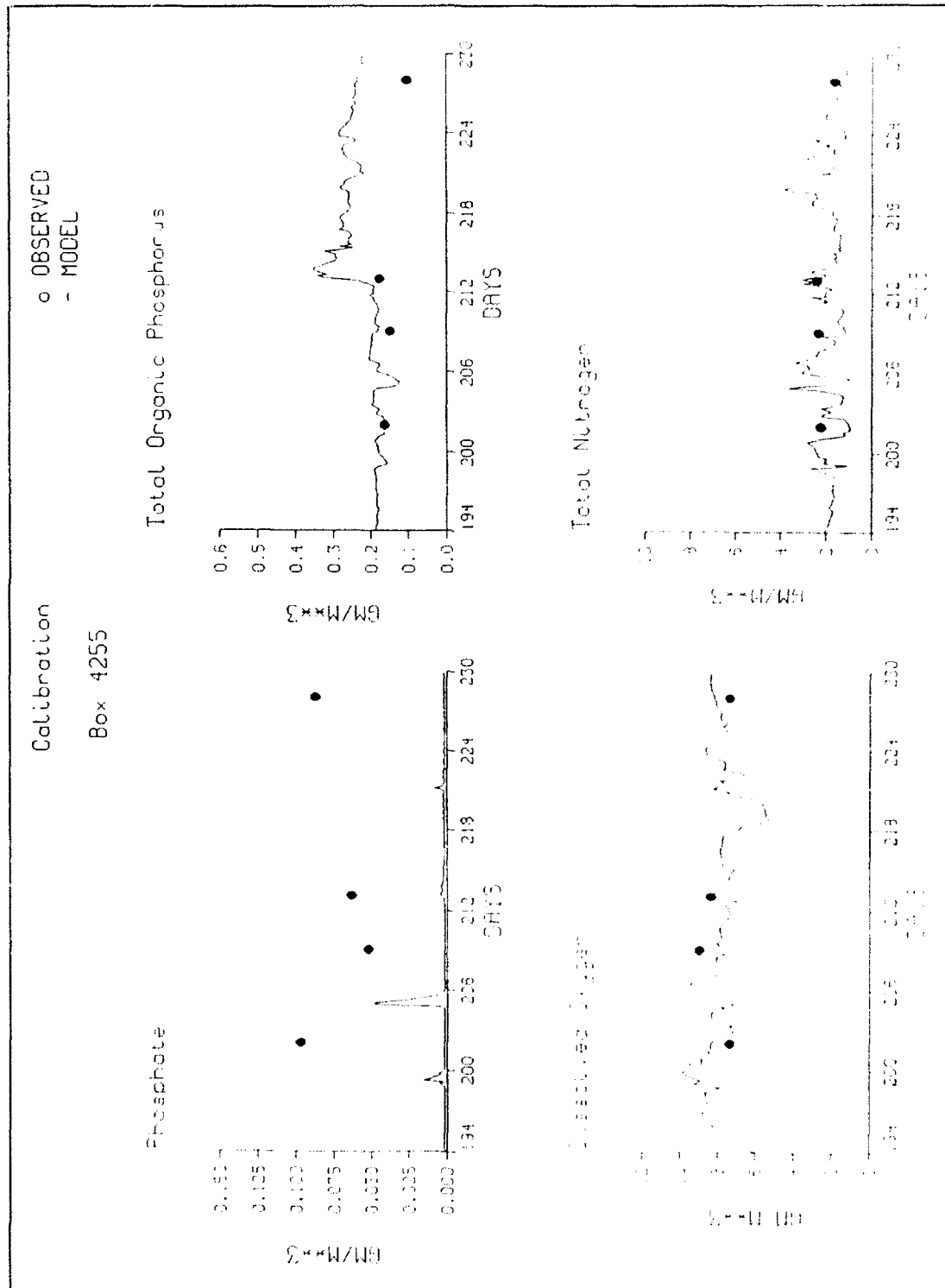


Figure 46. (Sheet 3 of 4)

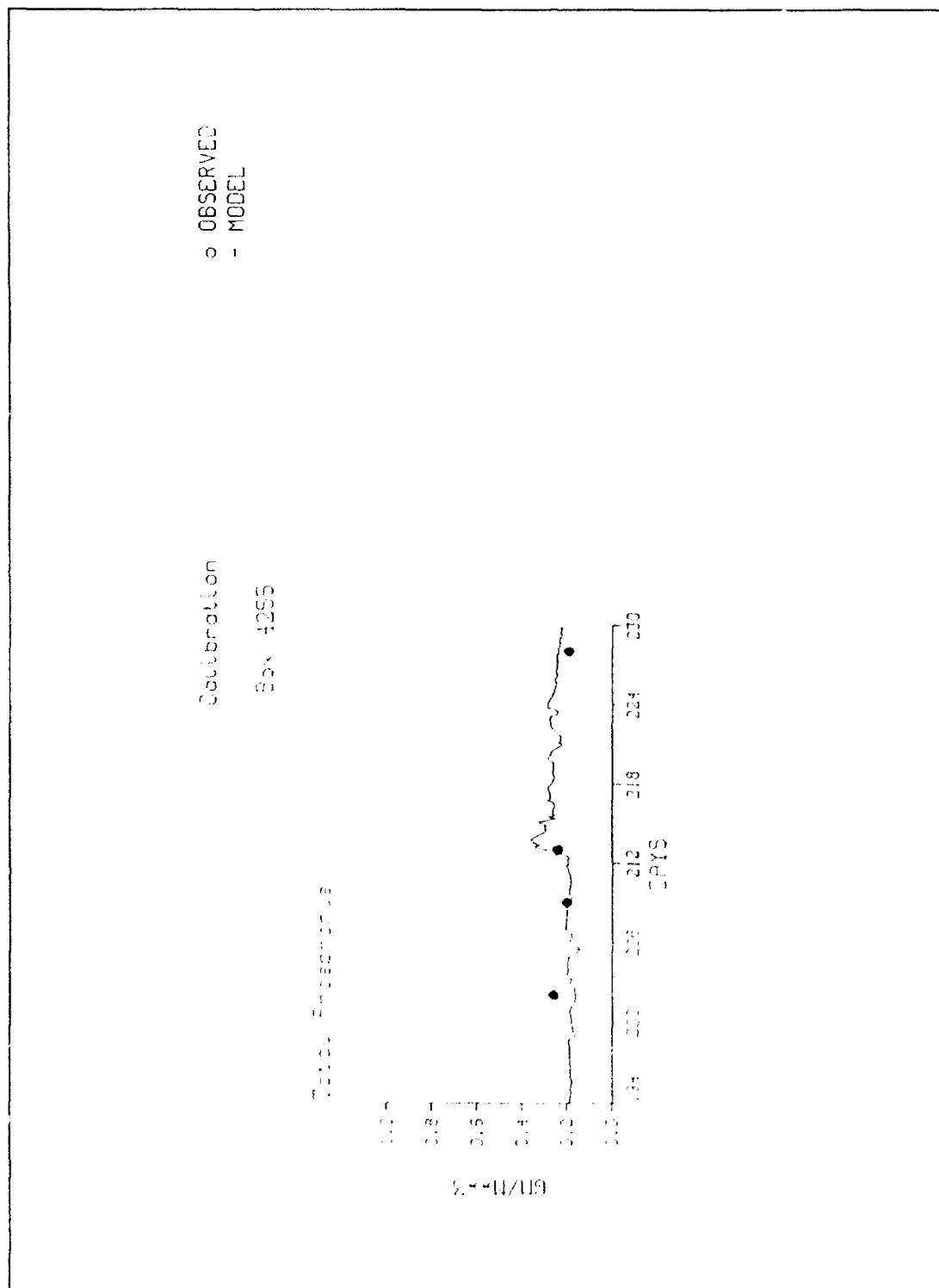


Figure 46. (Sheet 4 of 4)

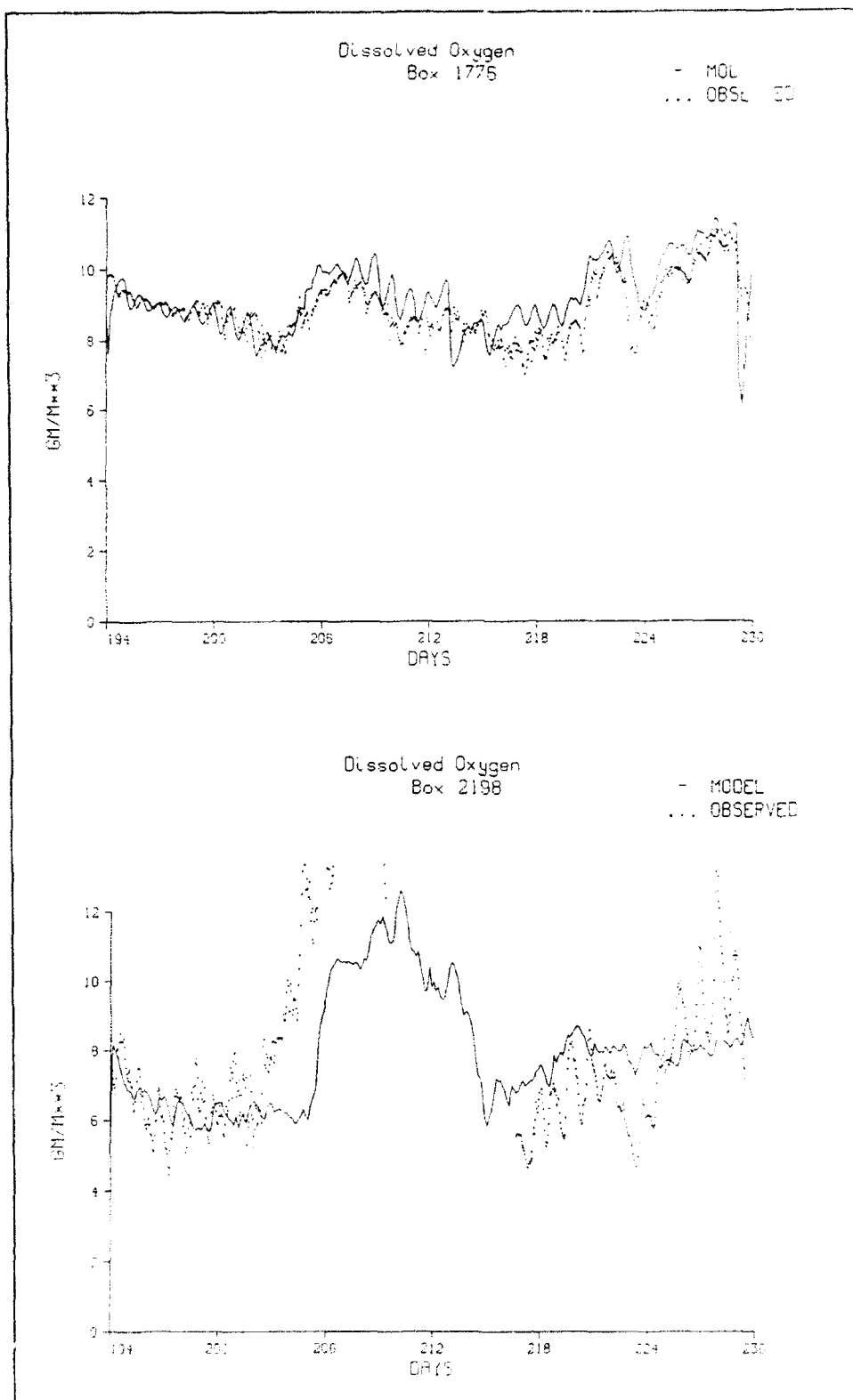


Figure 47. Continuous DO, model comparison (Sheet 1 of 4)

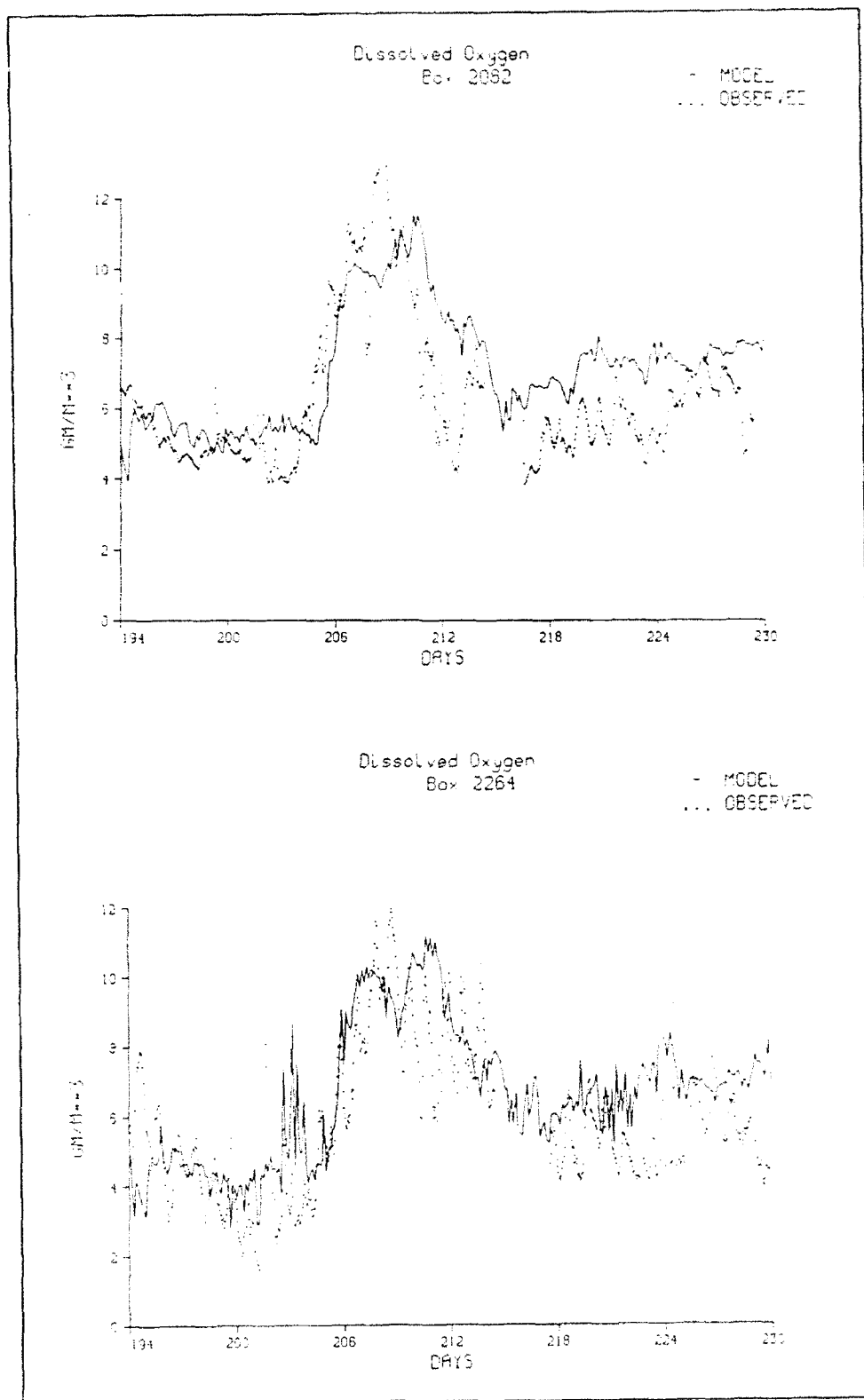


Figure 47. (Sheet 2 of 4)

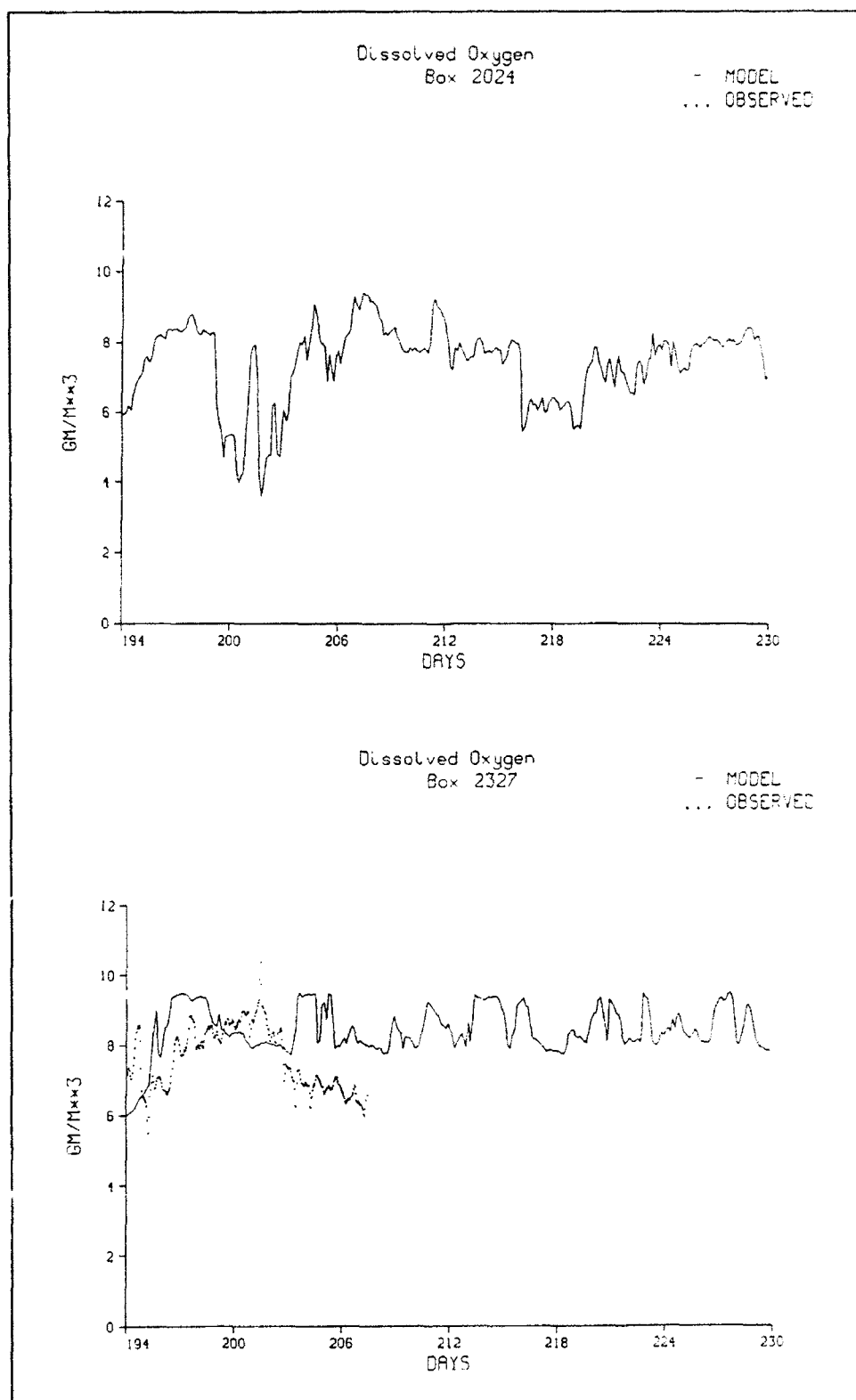


Figure 47. (Sheet 3 of 4)

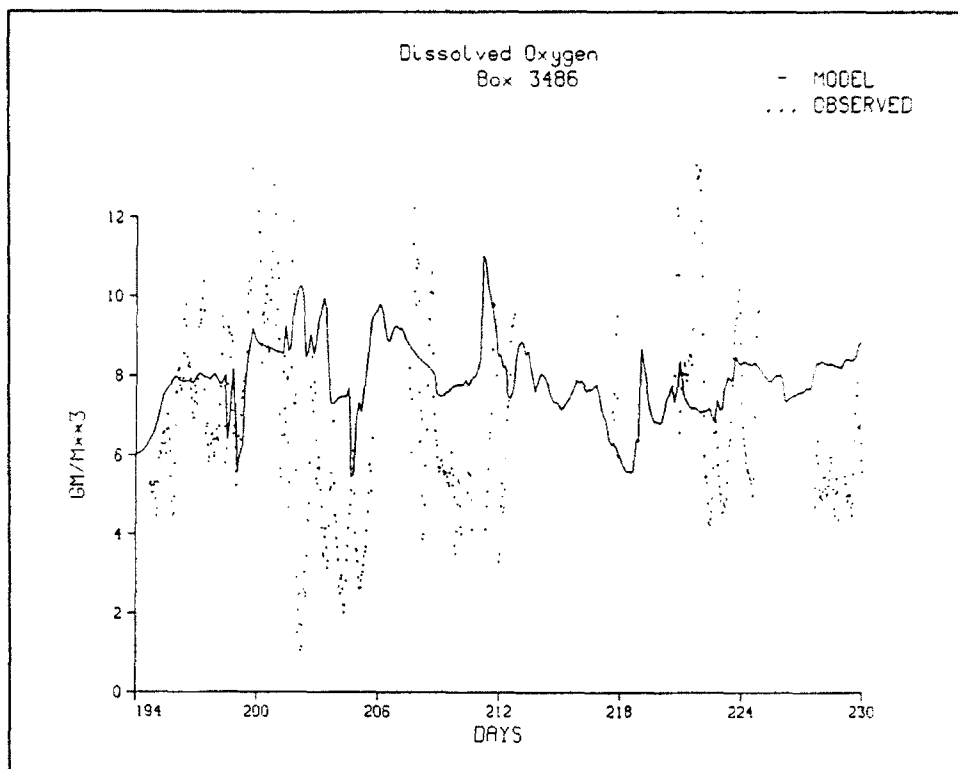


Figure 47. (Sheet 4 of 4)

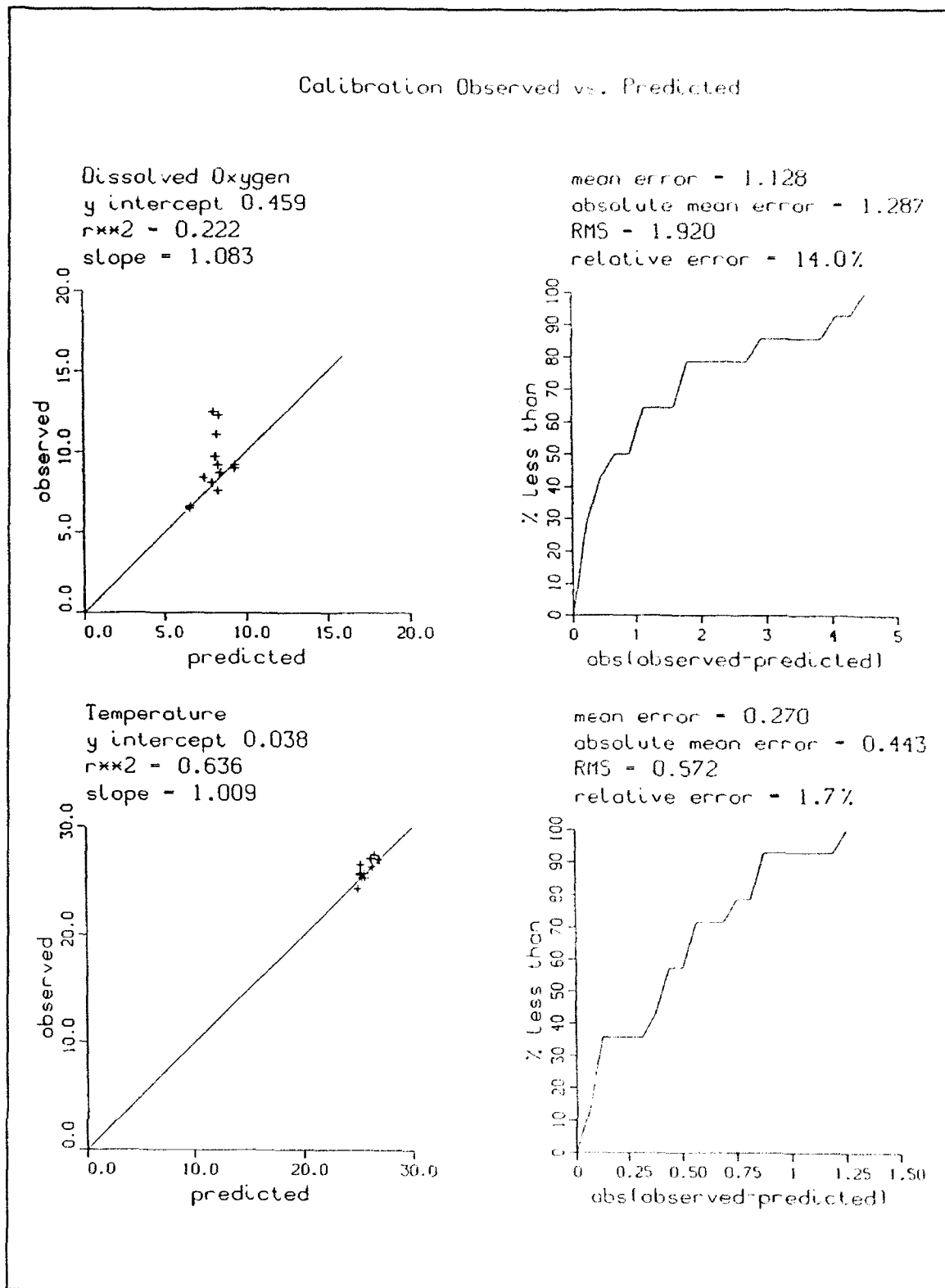
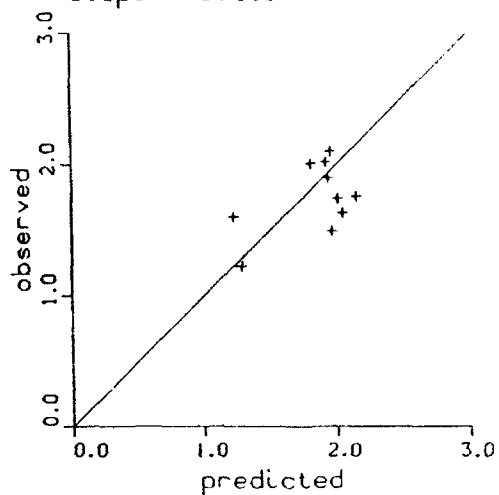


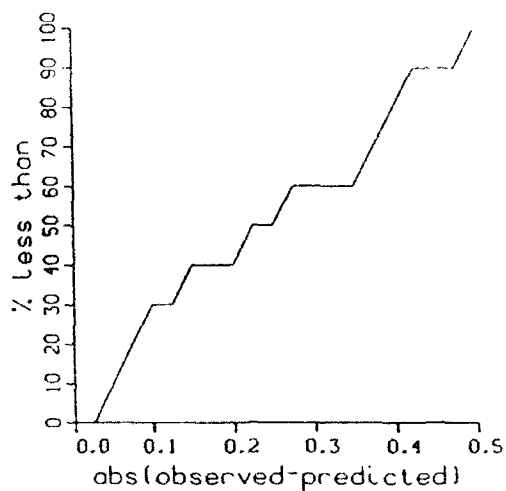
Figure 48. Statistical data, model comparison (Sheet 1 of 5)

Calibration Observed vs. Predicted

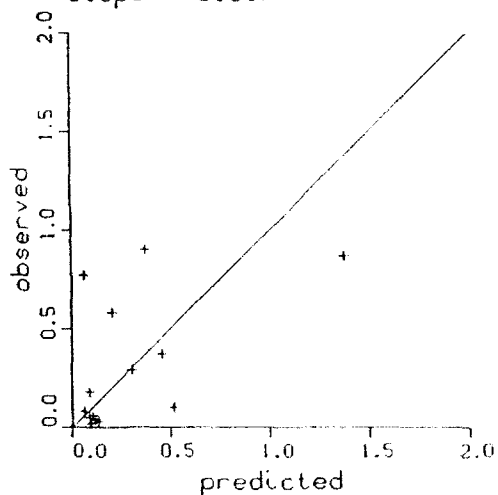
Total Organic Nitrogen
y intercept 0.936
 $r^2 = 0.263$
slope = 0.443



mean error = -0.085
absolute mean error = 0.248
RMS = 0.291
relative error = 14.2%



Ammonium
y intercept 0.162
 $r^2 = 0.295$
slope = 0.517



mean error = 0.024
absolute mean error = 0.220
RMS = 0.314
relative error = 71.0%

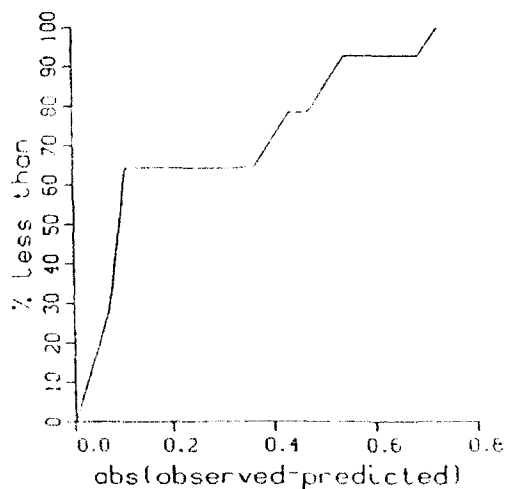
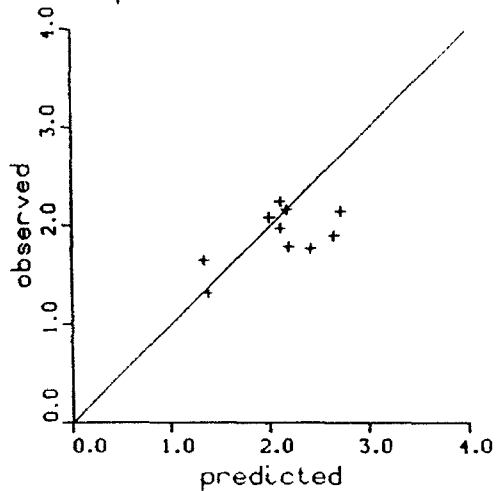


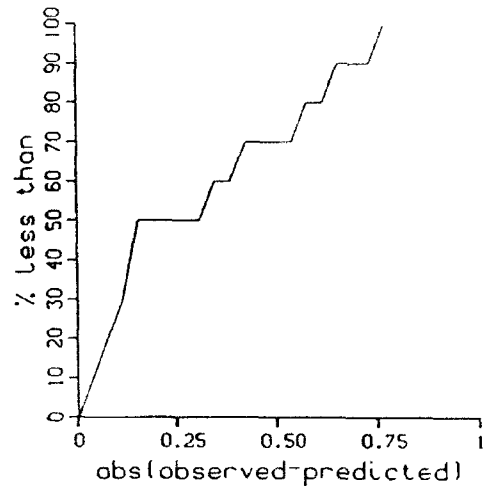
Figure 48. (Sheet 2 of 5)

Calibration Observed vs. Predicted

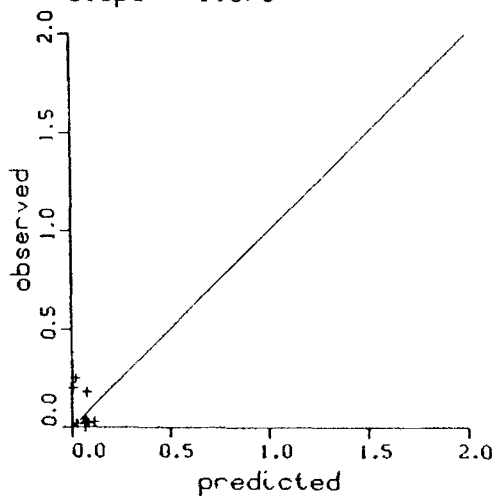
Total Nitrogen
y intercept 1.117
 $r^2 = 0.372$
slope = 0.375



mean error = -0.201
absolute mean error = 0.310
RMS = 0.401
relative error = 16.2%



Nitrate
y intercept 0.173
 $r^2 = 0.335$
slope = -1.579



mean error = 0.005
absolute mean error = 0.082
RMS = 0.103
relative error = 117.3%

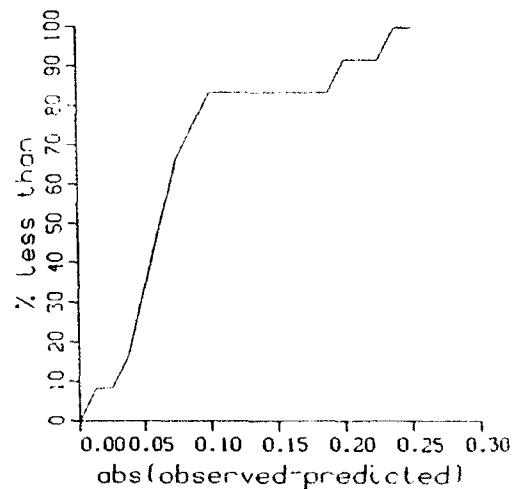
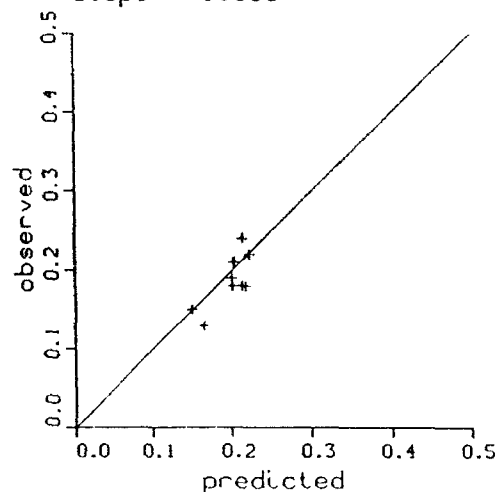


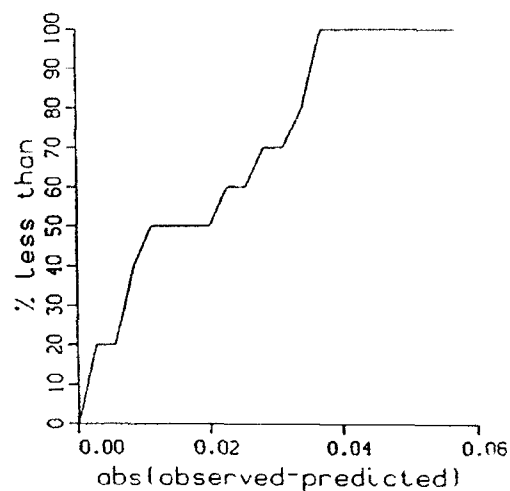
Figure 48. (Sheet 3 of 5)

Calibration Observed vs. Predicted

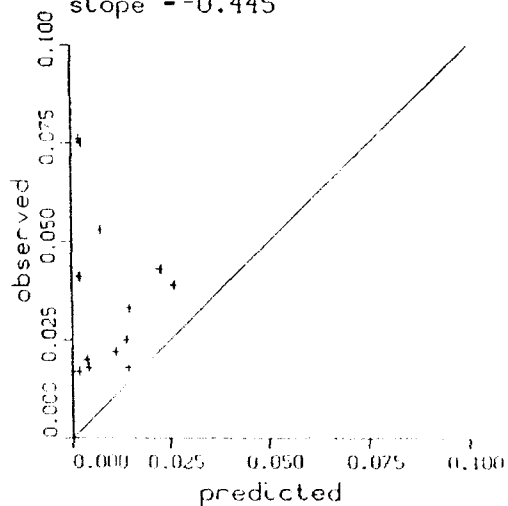
Total Phosphorus
y intercept -0.023
 $r^2 = 0.584$
slope = 1.069



mean error = -0.009
absolute mean error = 0.018
RMS = 0.022
relative error = 9.4%



Phosphate
y intercept 0.041
 $r^2 = 0.034$
slope = -0.445



mean error = 0.028
absolute mean error = 0.028
RMS = 0.036
relative error = 75.2%

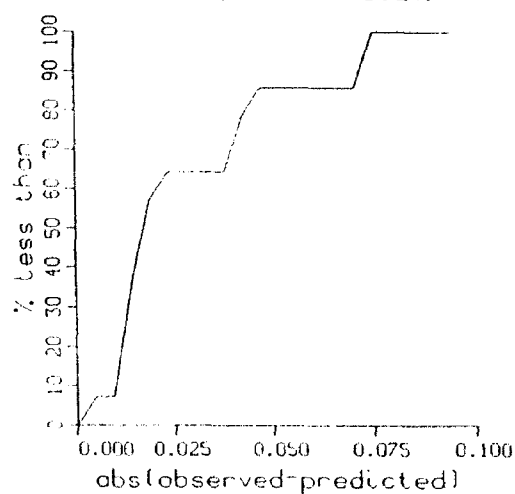
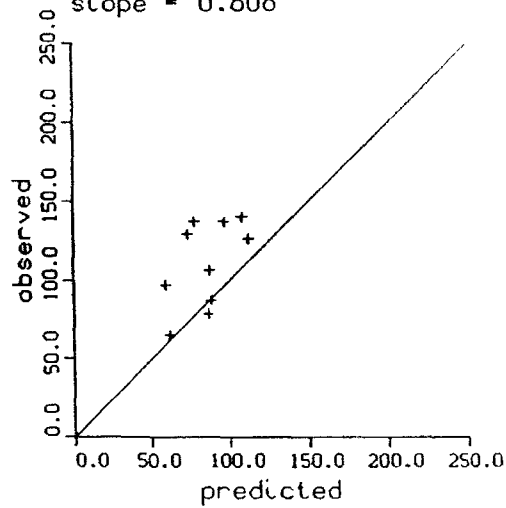


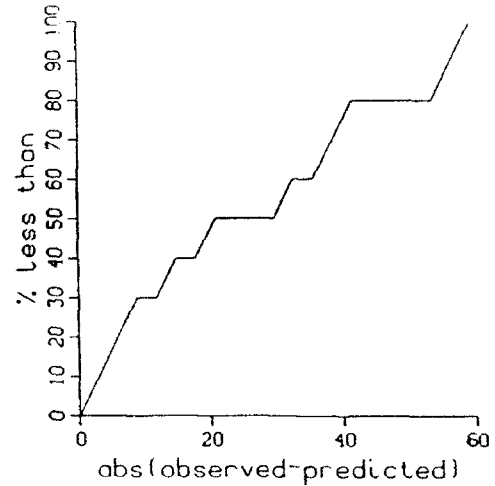
Figure 48. (Sheet 4 of 5)

Calibration Observed vs. Predicted

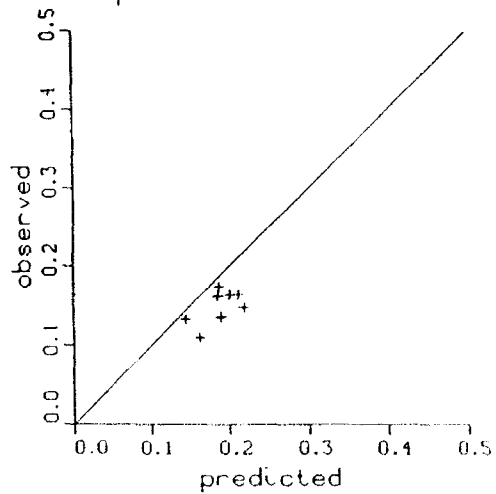
Chlorophyll
y intercept 41.400
 $r^2 = 0.272$
slope = 0.808



mean error = 27.037
absolute mean error = 26.943
RMS = 33.542
relative error = 24.4%



Total Organic Phosphorus
y intercept 0.059
 $r^2 = 0.277$
slope = 0.482



mean error = -0.039
absolute mean error = 0.039
RMS = 0.043
relative error = 26.1%

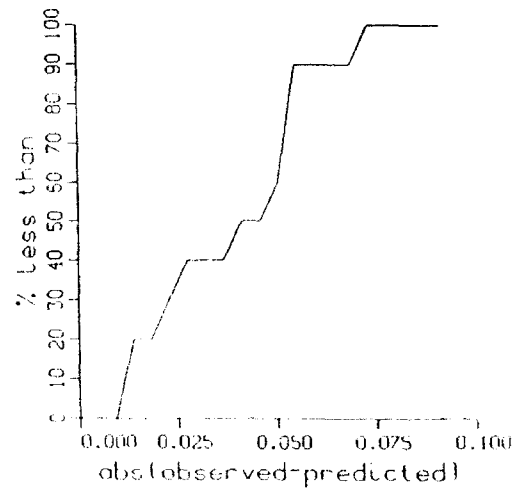


Figure 48. (Sheet 5 of 5)

on water quality in the water column; higher rate of suspension of bottom sediments; higher degree of mixing over a shallow depth that can enhance algal production by providing more opportunity for illumination; and possible existence of aquatic plant beds. The results of these rather complex processes can be quite difficult to predict with a model of limited sophistication, such as the lower Green Bay WQM. For example, the WQM does not include resuspension of bottom sediments, which can be high in phosphorus. High phosphorus concentrations can lead to enhanced algal production and elevated DO. Bottom sediments can be resuspended more easily in the shallow waters of the bay. The model does contain a sediment phosphorus release term to account for these effects.

There are also problems in model-data comparisons that impact the quality of the calibration. The model is depth-averaged, thus, computed algal concentrations are representative of the entire depth, whereas Chl-a measurements were taken near the water surface. It is possible that the algae are not well mixed in the field at times, but are concentrated on the surface. According to the model, the algae are light limited most of the time. Therefore, it is possible that the algae are under-predicted due to the two-dimensional (depth-integrated) assumption of the model, whereas, in the real system, algae can concentrate on the surface, where illumination is greater.

Continuous DO measurements were recorded for near-surface and near-bottom. There can be some amount of vertical DO stratification due to sediment oxygen demand at the bottom and algal production near the surface. Brief periods of DO stratification have been observed (Patterson 1992). Again, the model produces a depth-averaged result. The grab samples, thus Chl-a data, were obtained during the day, when algae are productive. The model uses daily average illumination and does not produce any diel effects that may occur in the field. Finally, there were no observed CBOD data to compare with model CBOD results.

A major emphasis during the calibration phase of this study was matching the data collected at the continuous DO monitors located along the Fox River. These monitors recorded a DO sag over the whole length of the river beginning around day 196 (July 15) and extending to days 204 (July 23) to 206, depending upon location. After this sag, DO increased to concentrations near or exceeding saturation until roughly day 210. Based on the DO monitor data, it appeared that this behavior was limited to the Fox River since the stations in the bay did not exhibit similar behavior. The sag in DO was not evident at Depere Dam either, and the amount of sag increased toward the mouth. Several ideas were put forward in an attempt to explain this behavior. Since the sag was confined to the Fox River, it was thought that it may have been the result of large releases of biodegradable material. The point source loads preceding and during the sag were higher than loads at other times of the calibration but their impact was not enough to cause the observed level of DO depletion. After some investigation, it was determined from the model that DO produced (or not produced) by algae had an appreciable effect on the DO balance of the system.

Other possible causes for the sag were considered. It is possible that toxicity from waste loads could have lowered algal production, thus decreasing oxygen production. Another possible cause of lower algal production may have been an increase in light attenuation as a result of the higher loadings that occurred during the first 10 days of the simulation. Waste loads do increase turbidity, thus increasing light attenuation. One possible cause is wind, where periods of sustained winds from the north can push water into the Fox River, thus impacting flushing rates and DO. Another potential cause is the occurrence of internal seiches that push mid-bay bottom waters with low DO into the lower bay. Review of the data in Patterson (1985) shows that there was DO stratification in the Fox River, especially in the upstream direction, with bottom DO lower than at the surface. However, at Schmidt Dock, no DO stratification was evident, and surface DO values were as low as those observed on the bottom further upstream. The model is compared against surface observations, and there is no mechanism for capturing vertical stratification, since the model is 2D.

Low algal production during the first 10 days of the calibration period is considered to be a reasonable and feasible explanation for the occurrence of the sag. A possible explanation for low algal production follows. Kennedy (1992) indicated that algal production in this system is highly dependent on light availability, which can be impacted by turbidity associated with runoff. This situation is true of other systems. The watershed that drains into the Fox River is predominately agricultural. Thus, turbidity can increase dramatically during summer thunderstorms, even though discharge may not show a significant increase. Rainfall records from the study site indicate 1.64 in. of rain during the period July 11 - July 20, 1983. Following this 10-day period, little rainfall was reported. Therefore, a plausible cause for lower algal production is increased light attenuation resulting from increased non-algal suspended solids, or turbidity, due to rainfall during the first part of the calibration period.

Although light attenuation is related to suspended solids (SS), data were insufficient to model SS. Therefore, the effect of lower algal production was specified directly through P_{max} (the maximum specific algal production rate), rather than through a light attenuation function dependent on SS. A reduction in P_{max} from the initial calibration value of 3.0 day^{-1} to 0.8 day^{-1} , reduced oxygen production and captured most of the sag. Attempts to use a constant value of P_{max} in the Fox River throughout the calibration period either over-predicted DO during the sag or under-predicted DO during the period following the sag, depending on whether the higher or lower value for P_{max} was used. Therefore, the smaller algal production rate ($P_{max} = 0.8 \text{ day}^{-1}$) was used for days 194 through 204 in the Fox River only. For the remainder of the calibration period, days 205 through 230, the higher value ($P_{max} = 3.0 \text{ day}^{-1}$) was used in the Fox River. The value of $P_{max} = 3.0 \text{ day}^{-1}$ was used in the bay throughout the calibration period. The value of 3.0 was used for all scenario runs.

Patterson (1992) indicated that he too had encountered problems modeling July 1983 during the WDNR waste-load allocation study (Patterson 1985) and had to lower the Chl-a/algal biomass ratio and raise the algal respiration rate.

Typically, he used the same Chl-a/algal biomass ratio for May and June and another ratio for the months of July through October. Patterson indicated that the flow and temperature conditions of July 1983 were typical of those observed during May and June, so a Chl-a/algal biomass ratio closer to that of June's was warranted for July 1983 (Patterson 1992). The effect of his modification was that algae growth and oxygen production were lowered.

Although the parameters used to capture the DO sag of July 1983 were different in the Patterson study and in this study, both studies used the same mechanism to produce lower DO values, i.e., less DO production through lower algal production. It is reasonable to expect an increase in light attenuation (thus a decrease in algal production) during rainfall runoff conditions like those that occurred during July 1983.

Calibration conclusions

Overall, the calibration results are judged to be good considering the complexity of the system and the simplicity (i.e., assumptions) of the model. It is recognized that the WQM is simpler than the real system. Even though the model is more comprehensive than the calibration database, the model should not be simplified. Simplifications to the model will lead to loss of resemblance to the real system. It is common practice to include water quality processes through state variables and parameters that may not be completely supported by data. Such practice enables investigation of project impacts to proceed in a timely, cost-effective manner without jeopardizing the integrity of the study.

This calibration and the observed calibration data set are deemed adequate for the purposes of this study; i.e., evaluation of the impact of Kidney Island Expansion on circulation and the resulting impact on dissolved oxygen. If the calibration data set was adequate for the purposes of the study by Patterson (1985), i.e., establishing waste-load allocations, then it is reasonable to expect that the data are sufficient for the purposes of this study.

7 Scenario Descriptions and Results

A series of test simulations have been constructed for modeling lower Green Bay, under both existing and proposed Kidney Island configurations, for assessing possible water quality impacts that result from expanding the CDF. In constructing these tests, lake levels, river flow rates, and seiche action/wind events are treated as independent variables. Seiche action and wind conditions are treated as one independent variable because a seiche is induced by wind and, therefore, these mechanisms cannot be readily uncoupled. Other boundary forcing conditions, such as meteorology, waste loads, and water quality boundary conditions, are treated as dependent variables. For example, meteorology was selected at identical dates as the period selected for seiche conditions.

Each of the three independent variables can be represented by three levels, e.g., high, medium, and low. Thus, a total of 27 simulations can be developed if all combinations of the independent variables are considered. This number can, however, be reduced by judiciously selecting those combinations of variables that would cover the range of expected impacts. One method for reducing the number of scenarios is through the "bracketing" of extreme events. For example, the effects produced by an average seiche, average lake level, and minimum flow conditions can be estimated by investigating two scenarios; one scenario consists of average seiche, minimum flow, and minimum lake level conditions, whereas the second is composed of average seiche, minimum flow, and maximum lake level conditions.

Ten scenarios were selected for assessing possible water quality impacts induced in the lower bay from expanding Kidney Island. All scenario conditions were selected to represent summer periods when water quality conditions are the poorest. Each scenario is composed of two simulations, one where the lower bay is simulated with the proposed CDF configuration, and the second where the lower bay represents existing conditions.

Conditions for the 10 scenario simulations are presented in Table 22. The combination of conditions was selected to bracket the range of expected events. The strategy is to focus on simulating extreme conditions where the higher return period scenarios create conditions that either facilitate or impede

the transport of pollutants into open water. It should be noted that the scenario selections in the tables appear symmetrical.

The logic for this should follow the pattern outlined below. High river flows are expected to occur with extreme seiche condition (i.e., storms). High- and low-water levels could exist for storm conditions; thus, both extreme water levels should be examined as shown in the first table. Water level is important since it impacts flow velocities and the degree of dilution of pollutants.

It is possible for high and low river flows and high and low lake levels to occur with average seiche conditions. Thus, all four conditions should be examined. With these four combinations, all four average conditions (for at least two variables) are bracketed in the table.

Low flows are expected to occur during "no significant seiche" conditions. However, high- and low-water levels may exist; thus, two conditions should be examined as shown in the table.

Scenario Conditions

Duration

Strong wind events associated with the passage of cold fronts through the Great Lakes region occur approximately every 7 to 10 days during the summer. During these storm events, seiche action and/or high river flows can provide sufficient momentum for transporting pollutant loadings into the open water. However, during calm periods river flows may lack sufficient momentum to flush the loadings into the open bay; thus, loadings can reside within the river until they are flushed into the bay with the passage of the next cold front.

The duration of each scenario is consistent with the loading cycle discussed above. Furthermore, because loadings trapped in the river during calm periods will undergo nutrient uptake and biological degradation, each scenario has a duration that is approximately equal to two loading cycles (i.e., 21 days). The first and last 10-day periods of a simulation replicate calm bay conditions. Seiche/storm conditions will be imposed at the midpoint of each simulation. For the prolonged calm period, the same 21-day period is simulated, but without significant seiche action.

The first 10-day period provides the water quality model with sufficient time to spin up and compute reasonable pollutant distributions in the river and in the vicinity of the Fox River mouth. Once an accurate pollutant distribution is developed, the flushing of pollutants by a seiche into shallow areas and open waters can be accurately predicted. Over the last 10-day period, the effects of the flushed pollutants on dissolved oxygen (for a given region) can be reasonably evaluated.

Table 22 Selected Scenario Conditions			
Extreme Seiche Conditions			
River Inflow	Lake Level		
	Minimum	Average	Maximum
Minimum		X	
Average			
Maximum	X		X
Average Seiche Conditions			
River Inflow	Lake Level		
	Minimum	Average	Maximum
Minimum	X		X
Average			
Maximum	X		X
No Significant Seiche Conditions			
River Inflow	Lake Level		
	Minimum	Average	Maximum
Minimum	X		X
Average			
Maximum		X	
Note: X denotes selected seiche, river inflow, and lake level conditions.			

Meteorological Conditions

The important meteorological conditions impacting water quality are temperature, wind speed, and cloud cover. Biological processes are affected by temperature while reaeration is dependent upon both temperature and wind speed. Algal productivity is dependent upon light intensity, which is a function of time and cloud cover.

The meteorological data required for the scenarios consist of cloud cover, wet bulb temperature, dry bulb temperature, and wind speed. Data from the Green Bay Municipal Airport are used for the scenarios. Three sets of 21-day meteorological records corresponding to the periods selected for extreme, average, and no seiche conditions are used. Meteorological data from these periods are used because the reaeration and seiche are both wind-dependent. Since the seiche periods are being selected from the summer months, the temperatures during these times are higher than in other seasons. Higher temperatures

place more stress upon the system because of the increased biological activity and the decreased dissolved oxygen saturation level. It is expected that the calm seiche conditions in the summer occurred with higher temperatures than the other two seiche conditions.

Point loadings and water quality boundary conditions

Each discharger along the lower Fox River has a permit issued by the State of Wisconsin for releasing a maximum allowable BOD₅. The permit loading for each discharger is a function of the water temperature and Fox River flow. These permit loadings are used as the point source loadings during the scenario runs. Point source loadings are generated based on the flow time series selected for the flow scenarios. BOD₅ loadings are varied according to river flow and the previous day's water temperature. Average values for nitrogen and phosphorus loadings for these dischargers are used during the scenario runs.

Headwater nutrient boundary conditions for the scenario runs are held constant for the duration of the simulation. Average nutrient concentrations used in the scenario runs are the same as those used by the WDNR in its waste-load allocation runs. Constant headwater dissolved oxygen concentrations are used with a diurnal fluctuation superimposed upon them. Headwater BOD₅ concentrations are varied with flow and temperature in the same manner as was done in the waste-load allocation simulations by the WDNR. Outer boundary conditions will be held constant throughout the scenario runs.

Initial conditions

Initial conditions for WQM calibration were generated with constant loadings, meteorological conditions, and hydrodynamic input. The input conditions corresponded to the beginning of the calibration period, i.e., 13 July 1983. The model was run to steady-state conditions. The steady-state concentrations for the state variables were subsequently used as the initial conditions for a model calibration run. The final concentrations from this calibration run were used as initial conditions for all subsequent calibration and scenario runs.

Selection of Seiche/Wind Events

Two seiche events and one prolonged calm period were selected for representing the three seiche/wind conditions used in the scenarios. One seiche represents extreme storm conditions, whereas the other reflects "average storm" conditions typically encountered on Green Bay. Time series of water surface levels for depicting these scenarios were taken from the Angle Light gauge data sets collected by the USGS during the summers of 1982, 1983, and 1984. Time series of wind speeds and directions recorded at the Green Bay

Municipal Airport were used in simulating the scenarios and these data correspond to the identical time periods as the water level time series data.

The time series of water surface levels selected for depicting the extreme seiche condition began on 27 August 1982 at 0000 CST and concluded 21 days later at 2400 CST on 17 September. The maximum water surface level displacement (i.e., range) occurred on 6 September and measured 2.2 ft. Wind directions at this time were primarily from the south-southwest and had speeds of approximately 7 m/s. Figures 49 and 50 illustrate the water level and wind time histories measured during this period, respectively. Although measured wind speeds were increased 50 percent in the model, speeds displayed in Figure 50 depict those measured at the airport.

A distribution of water level displacements was calculated with Angle Light data to aid in defining the "average storm" seiche condition. Average displacements for the summers (i.e., June through September) of years 1982 through 1984 were 0.55 ft, 0.57 ft, and 0.53 ft, respectively. Tables 23 through 25 summarize the distribution of displacements for the summers of 1982 through 1984.

The seiche occurring on 27 June 1984 was selected to represent the "average storm" seiche condition. This storm produced a maximum water level displacement of approximately 1.5 ft, or approximately 2.7 times greater than the mean seiche range. Furthermore, a displacement of this magnitude occurs

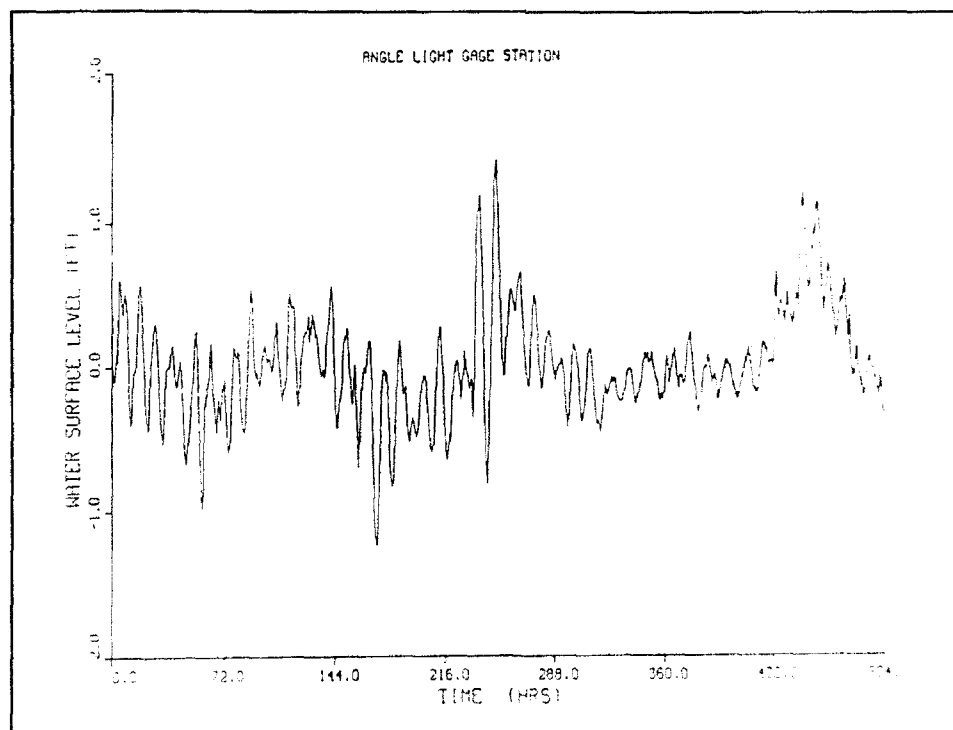


Figure 49. Time series of water surface levels for extreme seiche condition

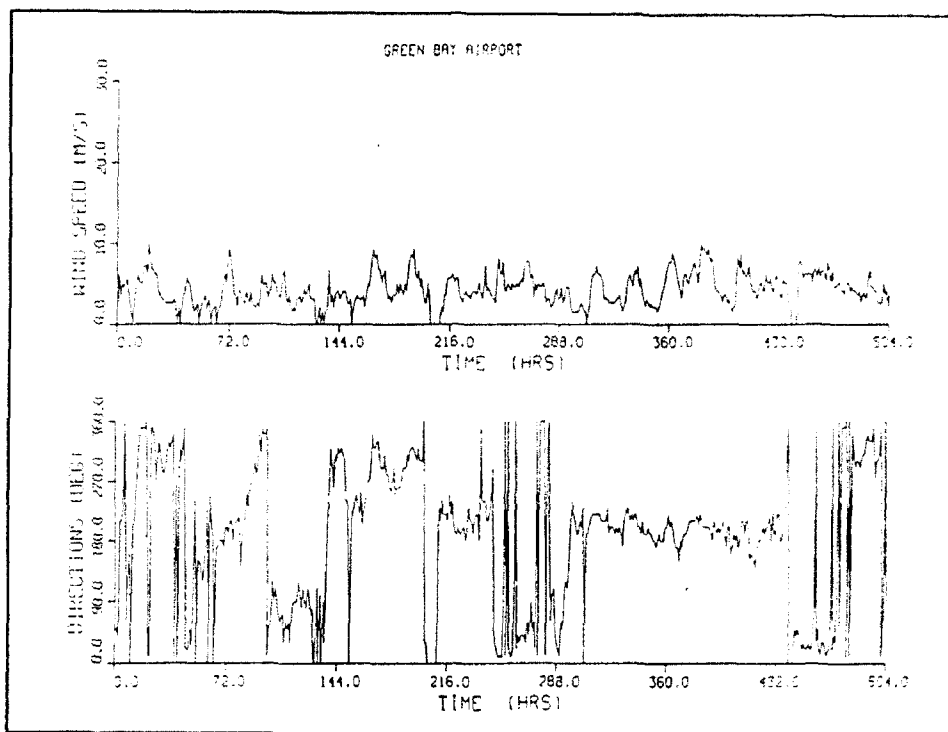


Figure 50. Time series of wind speeds and directions for extreme seiche condition

approximately four times per summer. The period chosen for depicting this condition began on 17 June 1984 at 0000 CST and concluded at 2400 CST on 7 July.

Winds preceding the maximum water surface displacement were from the west and had speeds of approximately 4 m/sec. The time series of water surface levels and wind speeds and directions are presented in Figures 51 and 52, respectively.

The period 16 June through 6 July 1982 was chosen to represent the calm seiche condition. Over this 21-day period, the average water level displacement was approximately equal to 0.49 ft, and corresponds to the longest sustained period without significant storm conditions. The time series of water surface levels and wind speeds and directions are presented in Figures 53 and 54, respectively.

Selection of River Flow Rates

Historical time series for high flow, "average storm," and low flow conditions were selected from the USGS records of daily averaged flow rates for the Fox and Kewaunee Rivers. Records for the Fox River discharges measured at

Table 23
Distribution of Water Surface Level Displacements Recorded at
Angle Light in Summer 1982

Displacement Range (ft)	Sample Size	Frequency (percent)	Cumulative Frequency (percent)
0.00 - 0.25	39	9.1	9.1
0.25 - 0.50	171	39.9	50.0
0.50 - 0.75	122	28.4	78.4
0.75 - 1.00	74	17.2	94.6
1.00 - 1.25	15	3.5	98.1
1.25 - 1.50	7	1.6	99.7
1.50 - 1.75	0	0.0	99.7
1.75 - 2.00	0	0.0	99.7
2.00 - 2.25	1	0.2	100.0

Table 24
Distribution of Water Surface Level Displacements Recorded at
Angle Light in Summer 1983

Displacement Range (ft)	Sample Size	Frequency (percent)	Cumulative Frequency (percent)
0.00 - 0.25	50	10.8	10.8
0.25 - 0.50	165	35.7	46.5
0.50 - 0.75	141	30.5	77.0
0.75 - 1.00	61	13.2	90.2
1.00 - 1.25	29	6.3	96.5
1.25 - 1.50	11	2.4	98.9
1.50 - 1.75	5	1.1	100.0
1.75 - 2.00	0	0.0	100.0
2.00 - 2.25	0	0.0	100.0

Table 25
Distribution of Water Surface Level Displacements Recorded at
Angle Light In Summer 1984

Displacement Range (ft)	Sample Size	Frequency (percent)	Cumulative Frequency (percent)
0.00 - 0.25	64	12.9	12.9
0.25 - 0.50	181	36.6	49.5
0.50 - 0.75	169	34.1	83.6
0.75 - 1.00	54	10.9	94.5
1.00 - 1.25	16	3.2	97.7
1.25 - 1.50	8	1.6	99.3
1.50 - 1.75	3	0.7	100.0
1.75 - 2.00	0	0.0	100.0
2.00 - 2.25	0	0.0	100.0

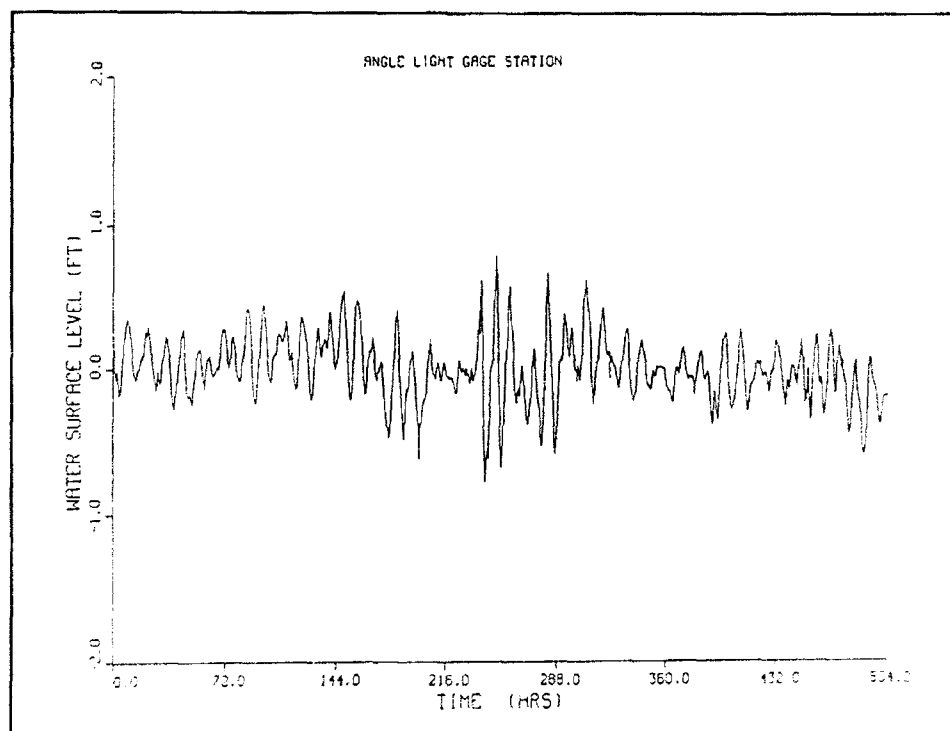


Figure 51. Time series of water surface levels for average storm seiche condition

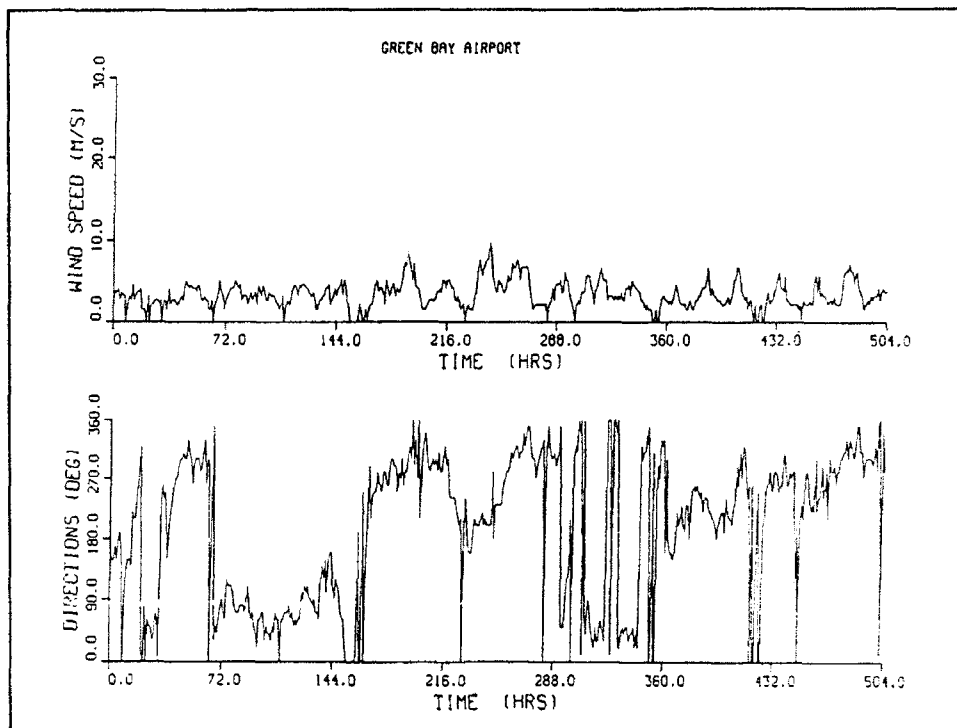


Figure 52. Time series of wind speeds and directions for average storm seiche condition

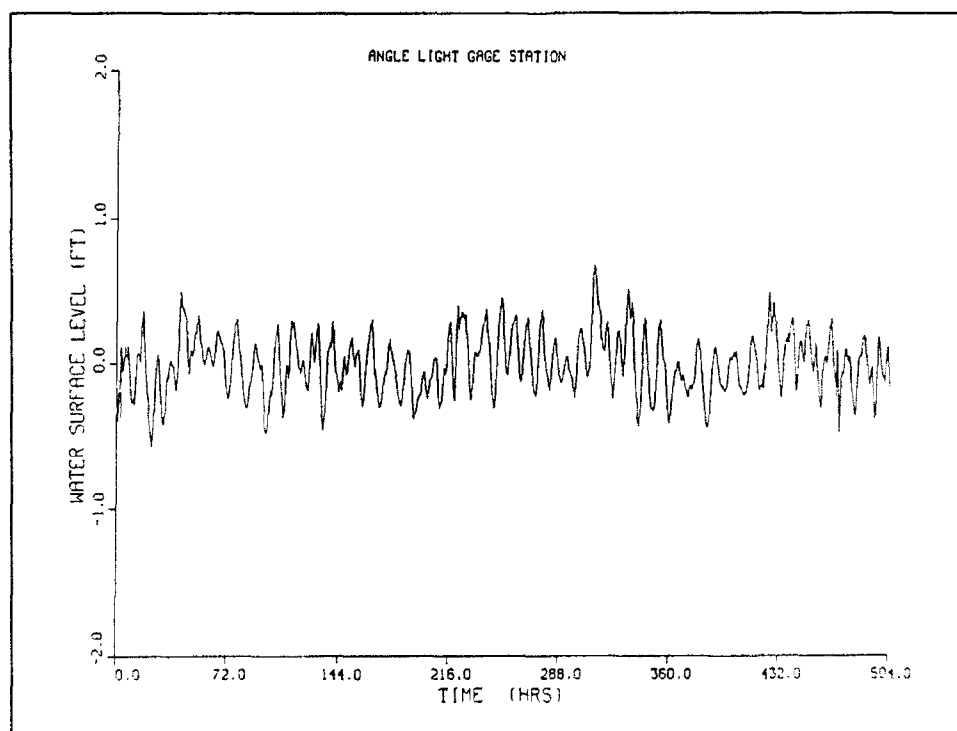


Figure 53. Time series of water surface levels for calm seiche condition

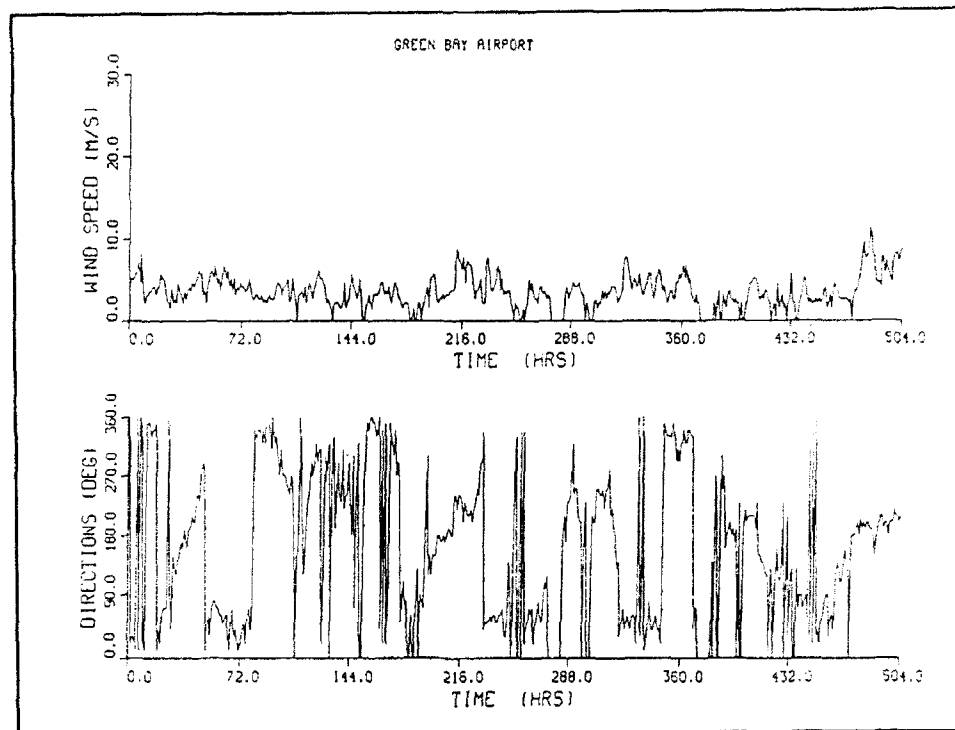


Figure 54. Time series of wind speeds and directions for calm seiche condition

the Rapid Croche Dam begin in 1917, and 71 years of daily data are available. Beginning in 1961, the Kewaunee River records contain 29 years of daily flow rates. In constructing the Fox and East River discharge data sets, it was assumed that flood flows and seiche action are in temporal phase. Thus, the first day of rising flood waters corresponds with the day of peak seiche action (i.e., the middle of the 21-day period).

This assumption aids in preserving the hydrodynamic and hydrologic phasing between the storm-induced bay and river events. Furthermore, using historical time series data ensures, to a certain degree, that the hydrologic response of the Fox River is maintained or replicated in the scenarios. The selected time series, which are discussed below, represent summer flow conditions only.

The historical flows for the months of June through September were analyzed for selecting the appropriate time series. Concerning the high and average storm conditions, the highest daily average flow for June through September of each year of record was recorded, along with its date of occurrence. These peak flows were ranked and the frequency of occurrence was determined using a Log-Pearson Type III analysis procedure. Table 26 provides the frequency of flood flows derived from this analysis.

A flood having a 20-year return period was selected for depicting the high flow condition. As shown in Table 26, a flood with this return period has a peak discharge of approximately 16,000 cfs. Reviewing the dates of

occurrence, which were assembled during the flood analysis procedure, a 21-day period starting on 1 September 1986 and ending on 21 September was chosen to represent the high flow condition. Figure 55 illustrates the hydrograph of Fox River flow rates.

Inspection of Figure 55 shows that, during the 21-day period, the Fox River has a peak discharge of approximately 12,000 cfs. This apparent discrepancy in peak flows results from the 12 dams within the Fox River drainage basin attenuating the flood. With this high number of dams along the river, the Fox River becomes a highly regulated system, and is capable of attenuating flood discharges for extended periods of time. Concerning the flood beginning on 11 September 1986, the peak flow was measured on 13 October 1986, or 33 days after the flood began. Flow rates exceeding 10,000 cfs were measured at the Rapid Croche Dam for over 60 consecutive days. A cursory review of other extreme flood events shows that these floods also have long durations, and that the duration of the 11 September 1986 flood is consistent with other high flow events.

The time series of river flows beginning on 25 June 1978 and extending through 16 July 1978 was selected to represent the "average storm" flow condition. During this period, the Fox River experienced a peak discharge of 6,980 cfs, which represents a flood having a 2-year return period. Figure 56 presents the river flow time series selected for this condition.

A 21-day summer period containing the 7Q10 flow (i.e., 7-day average low-flow event that has a frequency of occurrence once every 10 years) was selected to represent the low river flow condition. The procedure used for determining the 7Q10 is similar to that used in selecting high flow events. Fox River daily average flow data were analyzed to determine the minimum 7-day average flow rate during June through September for each year of record. This information was saved for each of the 71 years of record. These data were ranked and analyzed using a Log-Pearson Type III procedure to determine the flow having a 10-year return period. From this analysis, it was determined that the 7Q10 has a magnitude of 990 cfs.

Given the magnitude of the 7Q10, the yearly minimum flow data were inspected to select an appropriate flow event. For this condition, the period starting on 25 July 1937 and concluding on 15 August 1937 was selected. Figure 57 illustrates the river flow time series for this condition.

For higher flow events, time series of Kewaunee River flows were selected having the identical dates as those for the Fox River flows. However, for the period selected to represent the low-flow condition, no discharge records exist for the Kewaunee River for the year 1937. Therefore, a second analysis was performed to determine the 7Q10 for this river. The period of 22 July 1988 through 11 August 1988 was selected for representing the low-flow condition.

Table 26
Return Periods of Fox River Flood Discharges

Return Period (yr)	Discharge (cfs)
1.01	1,689.0
1.25	4,228.0
2.00	6,970.0
5.00	11,343.0
10.00	14,548.0
25.00	18,900.0
50.00	22,327.0
100.00	25,855.0

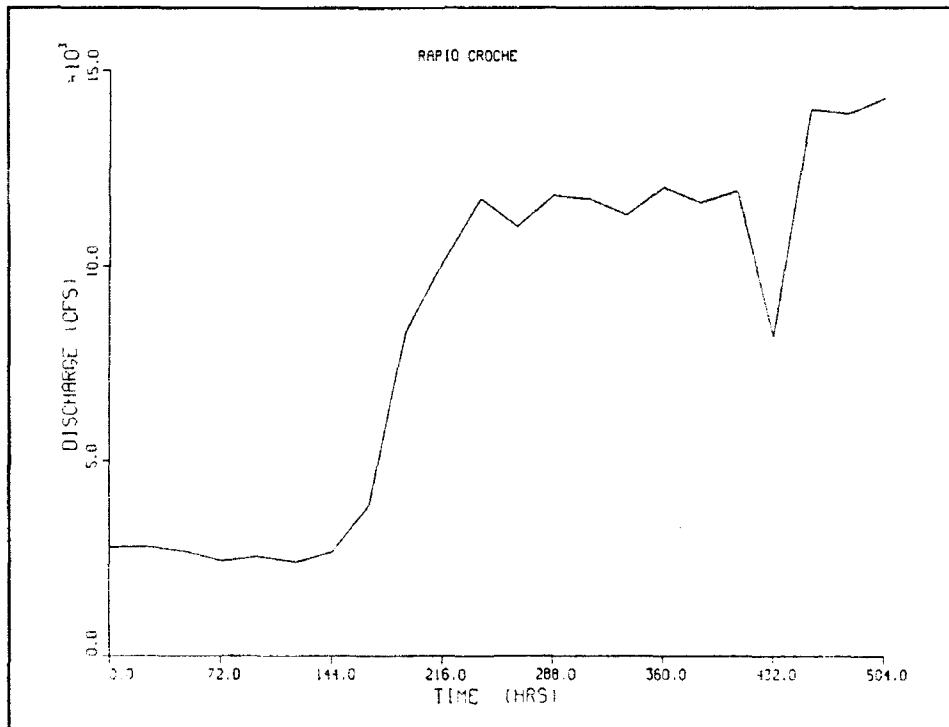


Figure 55. Time series of maximum Fox River flow condition

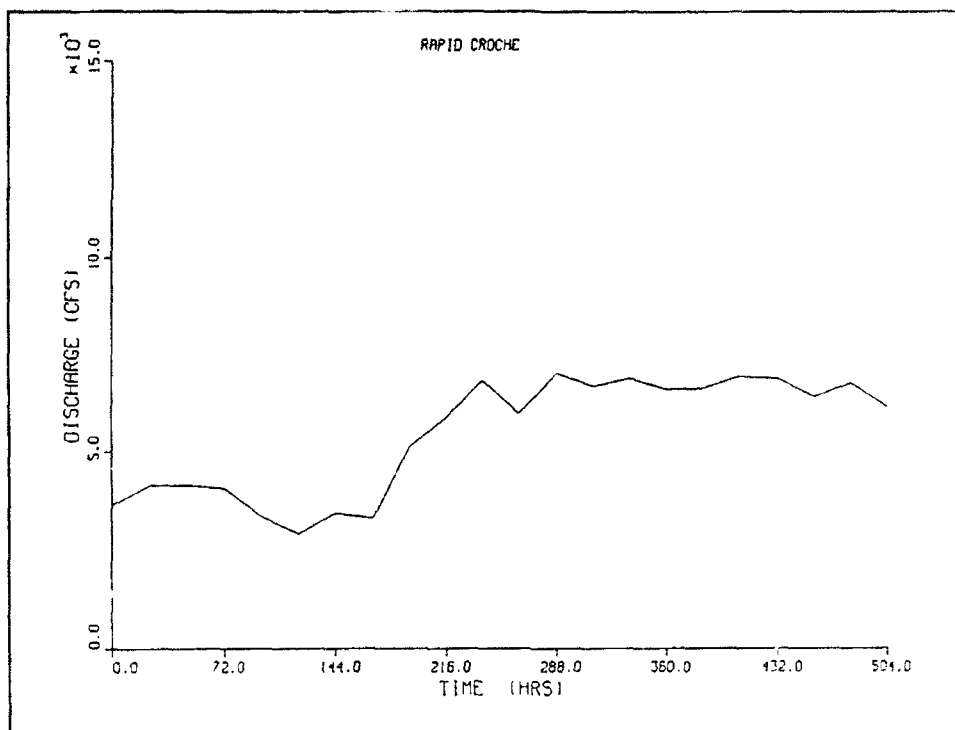


Figure 56. Time series of average storm Fox River flow condition

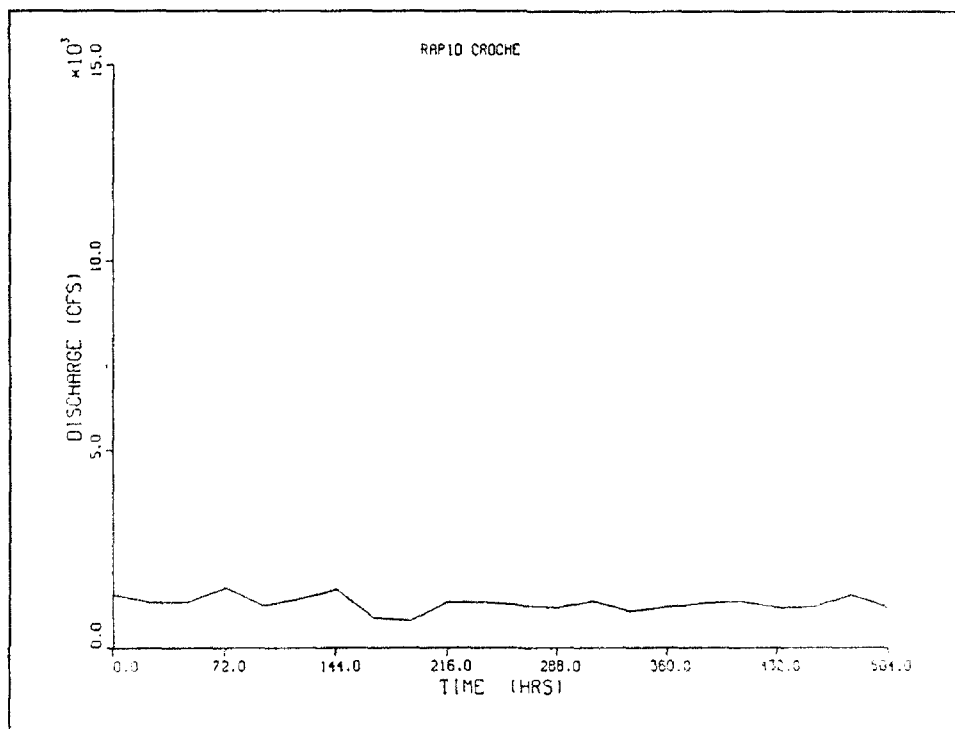


Figure 57. Time series of low Fox River flow condition

Selection of Long-Term Lake Levels

Monthly mean water levels for lower Green Bay were compiled by the NOAA for the years 1955 through 1980. Furthermore, these records span the time periods in which historical minimum and maximum water levels were measured on the upper Great Lakes. For the summer months, the minimum monthly mean water level was recorded in May 1964 at a level of 575.9 ft IGLD, whereas the maximum monthly mean water level of 581.1 ft IGLD was experienced in June 1974. The average, summer mean water level for this 26-year period was approximately 578.81 ft IGLD.

Lake levels selected for the scenario simulations consist of the average summer mean water level presented in the above paragraph, whereas the high and low lake levels are 580.50 ft IGLD and 576.93 ft IGLD, respectively. Elevations for the high and low lake levels are equal to the average summer mean water level ± 1.5 times the standard deviation (i.e., 1,367 ft) in lake levels over this 26-year period.

Several areas within the lower bay become exposed at the selected average and low lake levels. These areas, such as portions of Grassy Island, are denoted in Figure 11 with double crosshatch shading. Consequently, the exposed areas were specified as land in the model.

In trial simulations, it was found that the extreme and average seiche conditions would lower the water level such that those areas denoted with a single crosshatch in Figure 11 would become dry. This phenomenon only occurs during periods of significant drawdown. Therefore, as opposed to removing these cells from the model, cell depths were increased by 0.6 ft.

Analysis of Hydrodynamic Impacts Resulting from CDF Expansion

For each scenario, flow rates were computed across several transects within the study area. Transect positions are presented in Figure 58. Figures 59 through 64 provide a comparison of flow rates between the existing and proposed CDF configurations for the extreme seiche, extreme river flow, and minimum lake level scenarios. Furthermore, the figures display the discharges during the period of extreme seiche action. Flow directions are referenced relative to the grid axes; negative flows represent flows in the negative x- and y-directions, whereas positive flows represent flows in the positive grid directions. In other words, flows directed towards the south and east are defined as positive values, whereas northerly and westerly directed flows are defined as negative.

Of those transects placed in the vicinity of the Fox River mouth, the greatest change in flows was measured at transect 11, which extends from the CDF to Grassy Island. Because the expansion reduces the conveyance through this

reach, it can be expected that this transect would experience a reduction in flows. As shown in Figure 59, the proposed CDF reduces the discharges, in both the east and west directions, across this transect.

With a reduction in flow across transect 11, increased flows should be experienced across transects 3, 4, 9, and 12. (Changes in flow across transect 1 should be negligible during periods of bay-directed flows due to the momentum induced by the river.) The greatest change in flows can be seen for this period across transect 3. Negligible changes in flows are displayed at transects 4, 9, and 12.

Transects shown in the above figures form a "closed box" around the critical area at the confluence of the Fox River. For the expansion to adversely impact water quality conditions in regions that are presently and relatively unaffected, greater quantities of pollutants must be transported into these regions. To a certain degree, those areas affected by the expansion can be identified by a change in flow across a given transect. However, conclusions concerning water quality impacts derived solely from changing flow rates can be misleading because of several factors which the hydrodynamic model does not measure. These factors include pollutant concentrations, residence time, and mixing of bay and river waters. Analysis of the hydrodynamic model results can be used, however, to identify changes in current patterns, which influence the transport of pollutants through the lower bay.

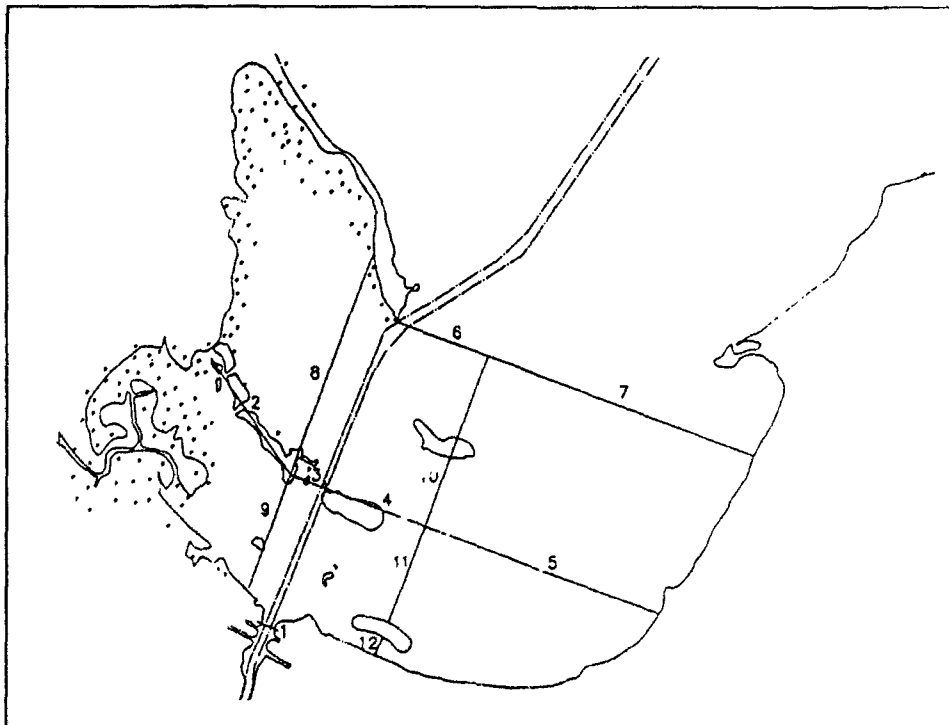


Figure 58. Location of transects in lower Green Bay

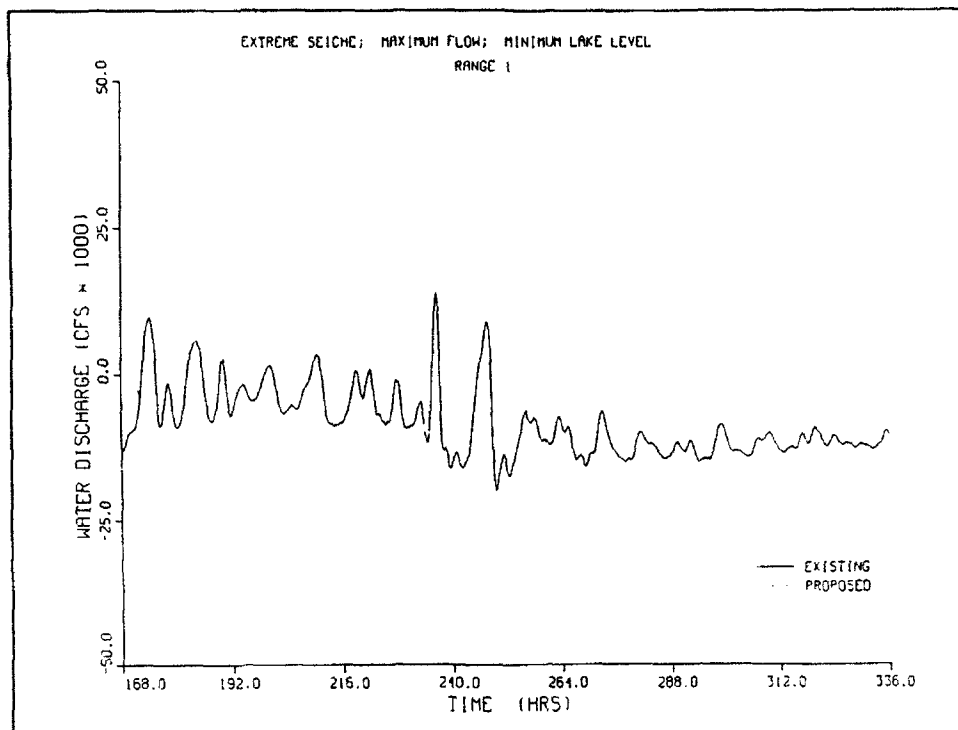


Figure 59. Comparison of discharge computed at transect 1

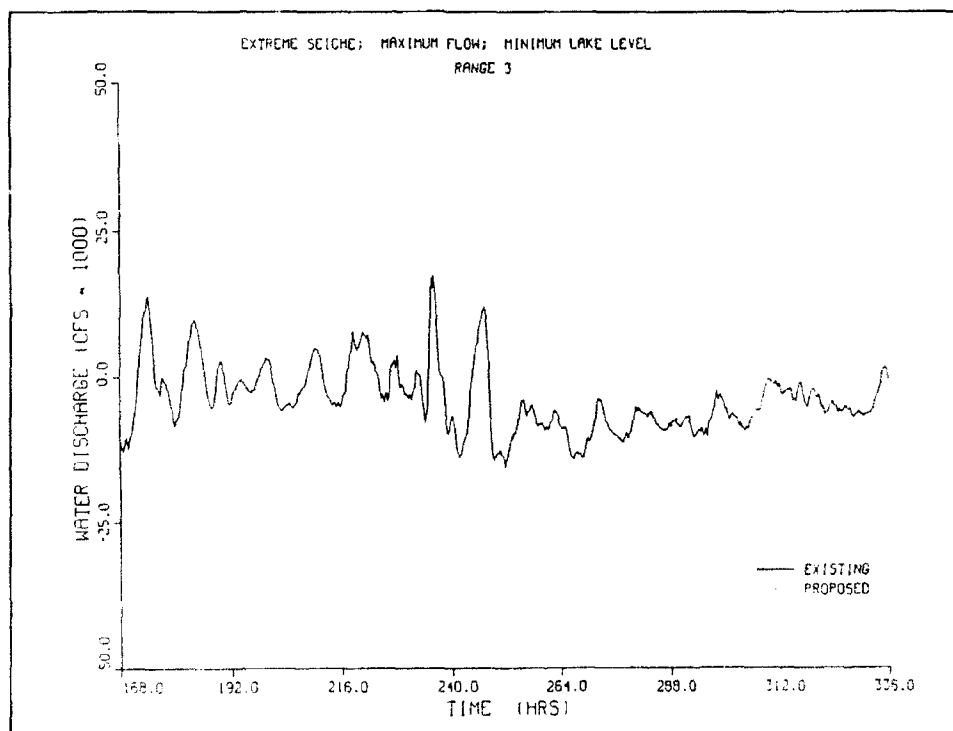


Figure 60. Comparison of discharge computed at transect 3

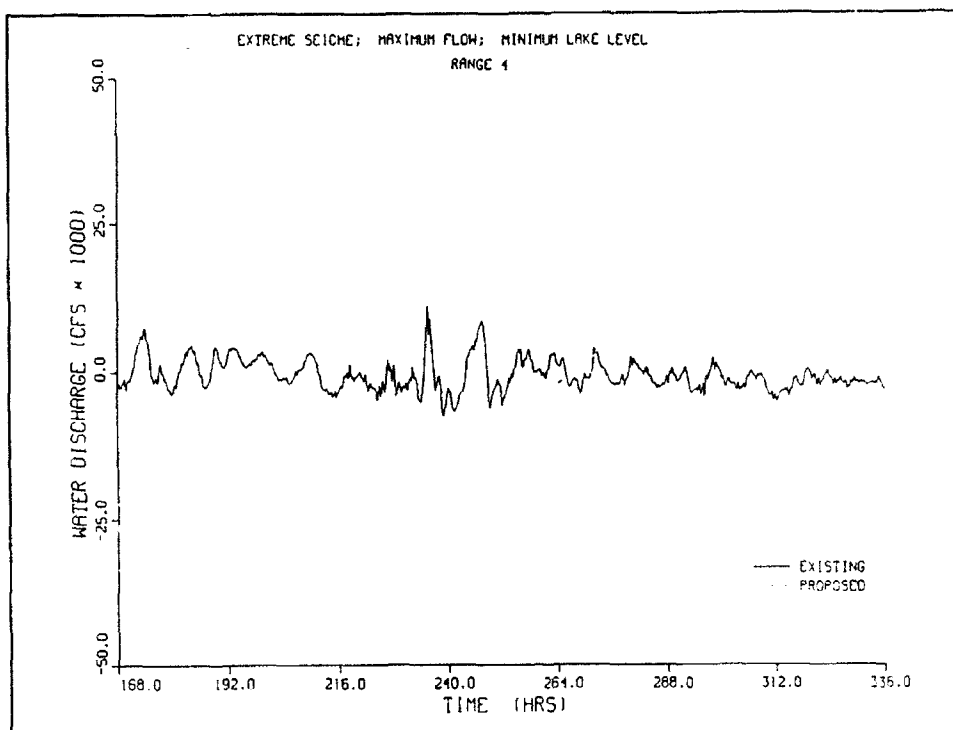


Figure 61. Comparison of discharge computed at transect 4

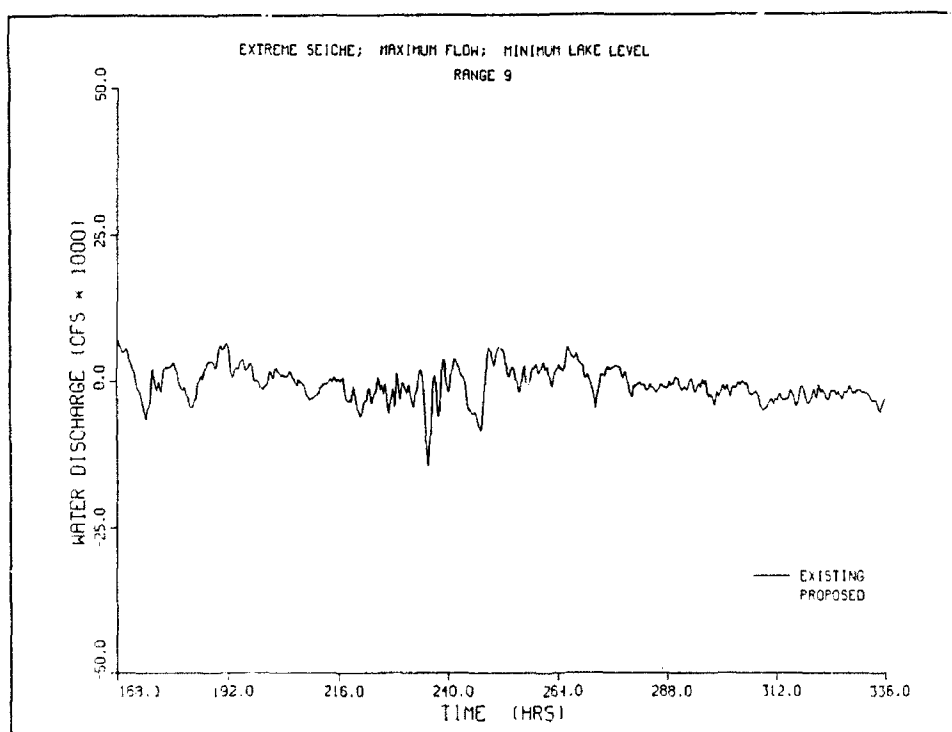


Figure 62. Comparison of discharge computed at transect 9

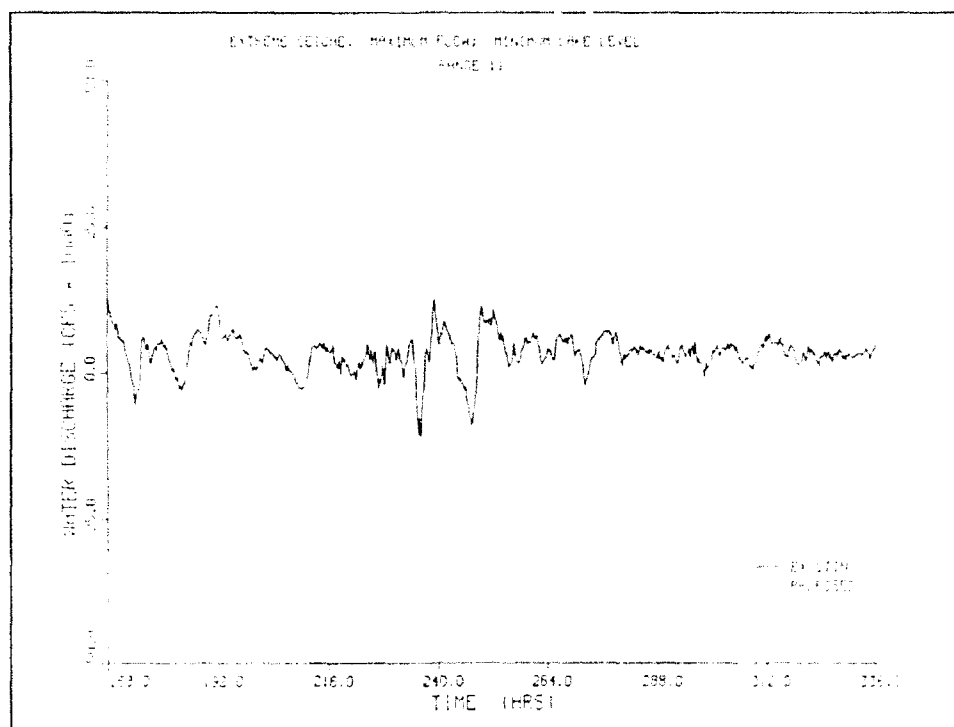


Figure 63. Comparison of discharge computed at transect 11

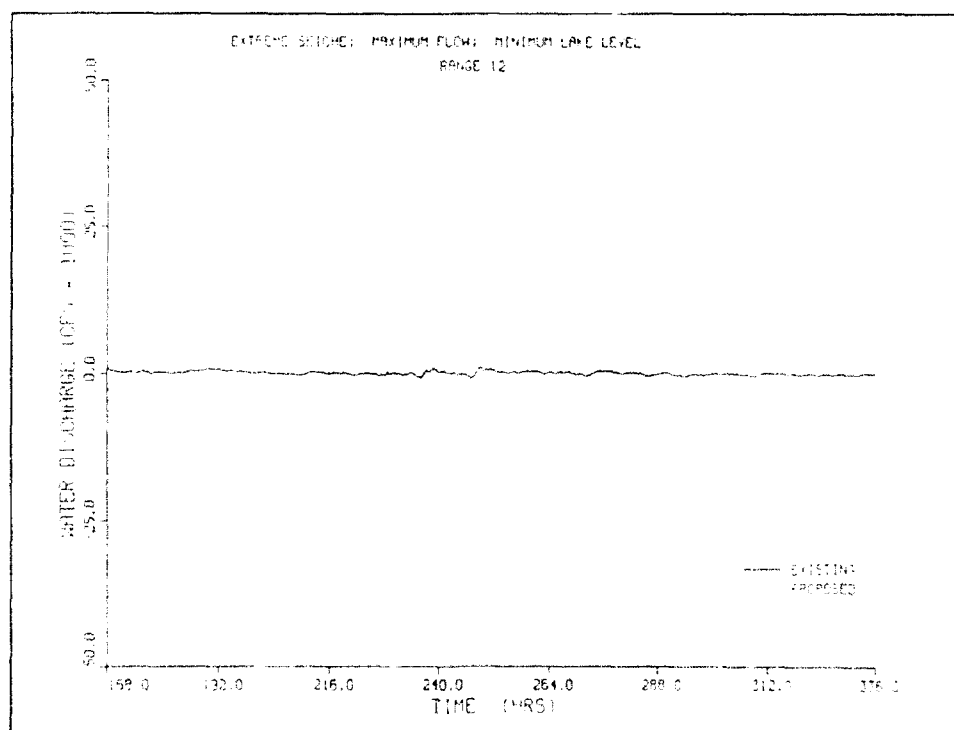


Figure 64. Comparison of discharge computed at transect 12

One means of quantifying the change in current patterns is through a statistical averaging of flows at each transect. Tables 27 and 28 summarize the net flow entering/exiting the critical area for the 10 scenarios. Table 27 presents the net flows computed with the existing CDF configuration, whereas net flows computed with the proposed configuration are given in Table 28.

Flows have been normalized and are expressed as a percentage of the total net flow entering the critical area. Furthermore, values quoted in brackets represent the fraction of total net flow entering the critical area, whereas values without brackets represent that fraction exiting this area.

The minimum seiche, minimum river flow, and minimum lake level scenarios reflect a condition that is dominated by calm water level fluctuations. For the existing CDF configuration simulation, 48.4 percent of the net river flow exits the critical area through the channel (i.e., transect 3). The second greatest proportion of net river flow, 33.9 percent, exits through transect 11, or that transect most affected by the CDF expansion. For the remaining transects, 10.3, 7.3, and 0.2 percent of the net river flow exits through transects 4, 9, and 12, respectively.

With the proposed configuration, net river flow exiting through transect 11 will decrease from 33.9 percent to 31.4 percent, or a reduction of 2.5 percent of the net flow. A decrease of 0.8 percent is also exhibited at transect 4. The bulk of the change, or 2.3 percent of the net flow, will be transported through the channel. The remaining fraction, 0.3 percent, will be transported into Peats Lake (i.e., transect 9), and 0.6 percent will pass behind Kidney Island (transect 12).

Other tendencies in the lower bay's current patterns can be discerned by comparing the proportion of net river flows between the various scenarios. For example, the bulk of the net flow exits the critical area via the channel. At minimum lake levels, flow exiting through the channel for the different scenarios ranges from 24.6 percent to 51.5 percent of the net river flow. This proportion is reduced, however, at higher lake levels. At maximum lake levels, between 16.3 percent and 33.6 percent of the net river flows exit the area through the channel. This phenomenon is attributed to lower bottom friction effects due to deeper water depths. With deeper water depths, less impedance is imposed on flows by the bottom friction, permitting greater flow volumes to enter shallower areas.

Lake levels also have a large impact on the net flow through transect 4, which is located along Grassy Island. At lower lake levels, portions of Grassy Island become exposed, thus reducing the conveyance of water through this area. At higher water levels, greater water volumes pass through this transect. Similarly, the proportion of net river flow increases for transect 12, or behind Kidney Island. A portion of these increases is reflected in the decrease in net flow through the channel.

Table 27
Proportion of Net River Flow Exiting Critical Area: Existing CDF Configuration

Scenario Conditions			Transect Number								
Seiche	River	Lake	1 (percent)	3 (percent)	4 (percent)	9 (percent)	11 (percent)	12 (percent)			
Extreme	Extreme	Minimum	(100.0)	43.7	9.6	8.1	37.5	1.3			
Extreme	Extreme	Extreme	(100.0)	16.3	22.2	16.5	42.1	3.1			
Average	Minimum	Minimum	(77.8)	24.6	(10.7)	(11.5)	70.6	5.0			
Average	Minimum	Extreme	(54.6)	10.2	(3.6)	(41.8)	78.9	11.0			
Average	Extreme	Minimum	(100.0)	51.5	6.1	5.2	35.6	1.5			
Average	Extreme	Extreme	(100.0)	36.6	10.3	4.4	44.7	4.1			
Minimum	Minimum	Minimum	(100.0)	48.4	10.3	7.3	33.9	0.2			
Minimum	Minimum	Extreme	(89.1)	33.6	26.2	(9.2)	40.3	(1.7)			
Extreme	Minimum	Average	(78.0)	(22.0)	19.8	11.1	63.0	6.0			
Minimum	Extreme	Average	(100.0)	43.9	9.8	12.5	33.0	0.9			

Note: Values quoted within brackets represent the fraction, in percent, of total flow entering critical area, whereas values without brackets represent the percent of total flow exiting this area.

Table 28 Proportion of Net River Flow Exiting Critical Area: Proposed CDF Configuration											
Scenario Conditions			Transect Number								
Seiche	River	Lake	1 (percent)	3 (percent)	4 (percent)	9 (percent)	11 (percent)	12 (percent)			
Extreme	Extreme	Minimum	(100.0)	45.2	10.1	8.4	34.5	1.9			
Extreme	Extreme	Extreme	(100.0)	18.3	23.0	17.7	36.9	4.3			
Average	Minimum	Minimum	(79.3)	28.5	(9.4)	(11.3)	65.8	5.7			
Average	Minimum	Extreme	(56.3)	14.1	(2.1)	(41.6)	74.0	12.1			
Average	Extreme	Minimum	(100.0)	52.8	6.9	5.5	32.8	2.0			
Average	Extreme	Extreme	(100.0)	38.3	11.1	5.5	40.4	4.9			
Minimum	Minimum	Minimum	(100.0)	50.7	9.5	7.6	31.4	0.8			
Minimum	Minimum	Extreme	(92.2)	37.8	25.2	(7.7)	37.0	(0.1)			
Extreme	Minimum	Average	(83.8)	(16.2)	20.7	12.9	58.8	7.6			
Minimum	Extreme	Average	(100.0)	45.1	10.1	13.2	30.0	1.7			
Note: Values quoted within brackets represent the fraction, in percent, of total flow entering critical area, whereas values without brackets represent the percent of total flow exiting this area.											

As shown in Table 29, which summarizes the change in net river flow due to the expansion for the 10 scenarios, decreasing net flows across transect 11 are experienced in each scenario. This decrease is attributed to the reduction in conveyance through this transect. The decrease in net flows ranges from 3.0 percent to 5.2 percent of the net river flow. The average reduction is 3.8 percent. As is to be expected, the decrease in flows through transect 11 increases the net river flow through the remaining transects which surround the critical area.

Comparing changes in net flow, the greatest increase in net flows occurs through transect 3, or the channel. Neglecting the extreme seiche, minimum river flow, and average lake level condition, the averaged net flow through the channel increases by a proportion equal to 2.4 percent of the net river flow. Averaged increases in flows across transects 4 and 9 are approximately equal. However, transect 4 appears to be more sensitive to changing scenario conditions. Flows behind Kidney Island also exhibit sensitivity between the various scenarios.

Input Description for Water Quality Scenario Analyses

As discussed earlier, the conditions for the scenarios are intended to provide an extreme range of expected forcing conditions (i.e., flows, seiches, and lake levels) that could occur in the lower Green Bay. Each scenario evaluation consisted of two water quality simulations. One simulation was made with existing conditions and another with the planned Kidney Island expansion in place. Concentrations of all state variables for all cells were output on a 3-hr basis over the duration of the run. Other than the difference in the grids resulting from the expansion of Kidney Island, everything else about the two runs was identical.

Three additional HM grid linkage (map) files were generated for the high-lake-level expanded island case and for the low-lake-level existing and expanded island cases. Map files used for the calibration period were used for the high-water existing case. Map files for the low-water cases were used for the average-lake-level scenarios. Two sets of hydrodynamics (i.e., existing and planned expansion) were generated for each scenario using the appropriate map files. The HM was allowed to spin up for two days before generating hydrodynamic output for the WQM. Thus duration of each water quality scenario simulation was 19 days.

Meteorological data corresponding to the time frame of the seiche condition were used to generate daily equilibrium temperatures and heat exchange coefficients, fractional day lengths, daily solar radiation, and daily average wind speeds for the scenarios. Point source loads, except for CBOD_l and CBOD_r , were set to the levels used in the WDNR waste-load allocation study and held constant during the scenario runs. CBOD_l and CBOD_r were allowed to vary but were always set to the maximum permitted load for each discharger. The

Table 29
Proportion of Net River Flow Exiting Critical Area: Change in Net Flows

Scenario Conditions			Transect Number								
Seiche	River	Lake	1 (percent)	3 (percent)	4 (percent)	9 (percent)	11 (percent)	12 (percent)			
Extreme	Extreme	Minimum	(0.0)	1.5	0.5	0.3	-3.0	0.6			
Extreme	Extreme	Extreme	(0.0)	2.0	0.8	0.7	-5.2	1.2			
Average	Minimum	Minimum	(1.5)	3.9	(-1.3)	(-0.2)	-4.8	0.7			
Average	Minimum	Extreme	(1.7)	3.9	(-1.5)	(-0.2)	-4.9	1.1			
Average	Extreme	Minimum	(0.0)	1.3	0.8	0.3	-2.8	0.5			
Average	Extreme	Extreme	(0.0)	1.7	0.8	1.1	-4.3	0.8			
Minimum	Minimum	Minimum	(0.0)	2.3	-0.8	0.3	-2.5	0.6			
Minimum	Minimum	Extreme	(3.1)	4.2	-1.0	(-1.5)	-3.3	(-1.6)			
Extreme	Minimum	Average	(5.8)	(-5.8)	0.9	1.8	-4.2	1.6			
Minimum	Extreme	Average	(0.0)	1.2	0.3	0.7	-3.0	0.8			

Note: Values quoted within brackets represent the fraction, in percent, of total flow entering critical area, whereas values without brackets represent the percent of total flows exiting this area.

total CBOD₅ that could be discharged by all point sources varied as a function of temperature and the average of the preceding four days flow at Rapid Croche Dam. The relationship between average flow and temperature and allowable total CBOD₅ load for all discharges is indicated in the WDNR waste-load allocation report (Patterson 1985). Once the total CBOD₅ that could be discharged was determined, it was divided among the various dischargers, converted to CBOD_u, and then separated into CBOD_L and CBOD_R.

Maximum permit loads were used so that the worst case dissolved oxygen conditions for each scenario would be simulated and any difference in DO resulting from expansion would be more evident. This approach resulted in a rigorous test for violation of the 5.0-mg/L state DO standard. The maximum allowable CBOD loading is directly related to flow. As flow changed, the CBOD loadings changed so that the maximum allowable CBOD load was always being applied. In reality, industrial loads are a function of production schedules and domestic loads are a function of population and per capita usage. It is very doubtful that industrial production would follow the fluctuations in flow, especially in the high water scenario, that the scenario loads did. The permit loads are far above the loadings used in the calibration period and reflect a worst case condition since several dischargers currently operate well below the permitted levels.

Headwater boundary conditions were held constant over the duration of each scenario except for CBOD_L, CBOD_R, and dissolved oxygen. CBOD_L and CBOD_R were varied as a function of flow and temperature. Relationships among temperature, flow, and CBOD for the lower Fox River are indicated in the WDNR waste-load allocation report (Patterson 1985). The headwater temperature was held constant at 27 °C, which was the average temperature during the calibration period. Headwater dissolved oxygen concentrations were based on saturation at 27 °C with a 1.7-mg/L diurnal swing. The same boundary conditions were used for the outer boundary and East River headwater boundary conditions that were used in the calibration runs. The same initial conditions were used during the scenarios as during calibration. All scenarios were run using a constant algal production rate ($P_{max}=3.0 \text{ day}^{-1}$) in the Fox River.

In order to observe flow pattern variation resulting from expansion of Kidney Island, a conservative tracer was injected into the same cell that GBMSD point load was applied in. This tracer was injected at a rate of 1,000 kg/day. Tracer concentrations were monitored in all cells and output was monitored at 3-hr intervals.

Methods of Scenario Analysis

Ten water quality scenarios were run in order to determine the impact of Kidney Island expansion upon water quality (Table 22). For ease of referring to a specific scenario, a three-letter nomenclature is used, as indicated in Table 30. Each scenario consisted of a WQM run with existing conditions and a WQM run with the Kidney Island expansion in place. For each WQM run,

results were saved every 3 hr for all computational cells and for all state variables. These results were archived to tape. Results were saved at 3-hr intervals to reduce output files to a reasonable and manageable size. Three-hour output is considered frequent enough to determine impacts, and for practical purposes can be considered as "instantaneous." The saved scenario results were post-processed and analyzed for various measures of change as explained below.

Maximum changes (i.e., maximum instantaneous and average decrease from existing to plan conditions) in *DO* and the respective locations were determined for each scenario simulation. Maximum instantaneous (i.e., 3-hr interval) *DO* decrease was determined by comparing the change in *DO*, from existing to plan, every 3 hr for all computational cells and retaining the largest decrease and its respective cell location. The maximum decrease in average *DO* was determined by computing the average *DO* for the entire scenario simulation (existing and plan simulations), for each computational cell, and searching for the maximum decrease and its respective location.

Four plotting methods were used to further evaluate the scenario results. These plots are grouped by scenario and are shown for select scenarios in Appendix D. The first four of the five scenarios (AEE, EEE, EEM, AEM, and MMM) selected for inclusion in Appendix D (Figures D1 through D36, respectively) exhibited the greatest impact in terms of decrease in *DO* from existing to expanded island. Scenario MMM was added to exhibit the effects of minimum seiche, flow, and lake level. The plots in Appendix D consist of:

- a. Time series plots of $CBOD_L$, conservative tracer, and *DO* concentrations at selected stations for existing and plan conditions.

Table 30
Water Quality Scenarios

Scenario	Description
EEE	Extreme Seiche
	Extreme River Flows
	Extreme Lake Level
EEM	Extreme Seiche
	Extreme River Flows
	Minimum Lake Level
EMA	Extreme Seiche
	Minimum River Flows
	Average Lake Level
AEE	Average Seiche
	Extreme River Flows
	Extreme Lake Level
AEM	Average Seiche
	Extreme River Flows
	Minimum Lake Level
AME	Average Seiche
	Minimum River Flows
	Extreme Lake Level
AMM	Average Seiche
	Minimum River Flows
	Minimum Lake Level
MEA	Minimum Seiche
	Extreme River Flows
	Average Lake Level
MME	Minimum Seiche
	Minimum River Flows
	Extreme Lake Level
MMM	Minimum Seiche
	Minimum River Flows
	Minimum Lake Level

- b. Time series plots of the differences in plan and existing (i.e., plan minus existing) concentration for CBOD_L , conservative tracer, and DO at selected stations.
- c. A plan view of bay shading plots of average conservative tracer concentrations for existing and plan conditions.
- d. A plan view of bay shading plots of the differences in average conservative tracer and average DO concentrations between existing and plan conditions.
- e. A plan view of bay shading plots of lowest instantaneous DO concentrations for existing and plan conditions.

Time series plots of DO , CBOD_L , and conservative tracer were generated for existing and plan conditions at selected stations. The conservative tracer was injected at the mouth of the Fox River at the same location as the GBMSD discharge. Time series were plotted for nine stations for each scenario. Six of these stations are common to all scenarios. These six stations, which are shown on a map for each scenario in Appendix D, were positioned as follows:

Station 1 - About 250 m north of the expanded Kidney Island.

Station 2 - Between Kidney Island and the eastern shore.

Station 3 - About 1,700 m north of the expanded Kidney Island.

Station 4 - Between Kidney Island and the western shore.

Station 5 - Between Kidney Island and the southern shore.

Station 6 - At the mouth of Fox River.

The location of the seventh station varies from scenario to scenario. The seventh station is the cell that has the largest instantaneous decrease in dissolved oxygen between existing and plan conditions at any time during the scenario simulation. The location of the eighth station is the cell which had the largest decrease in average DO . The ninth station is composed of two cells, one located on the north face of the existing island and one on the face of the expanded island at approximately the same east-west location of the first cell (i.e., existing island shore). The locations of all stations are indicated on a map for each scenario in Appendix D (Figures D1, D8, D15, D22, and D29).

Shading plots of scenario average values were generated by determining the simulation time-average value of DO and conservative tracer in each cell based upon the values output at 3-hr intervals. Shading plots of the changes in average conservative tracer and DO levels were generated by determining the differences in the average concentration of each cell. Shading contrasts corresponding to the concentration ranges are shown on the shading plots.

A number of analyses were performed to evaluate the effect of the expansion on the violation of the state minimum *DO* standard (5.0 mg/L). These included determination of the number of *DO* standard violations, minimum *DO* concentration, and the *DO* volume-days of violation. The procedures used to determine each are detailed later.

Water Quality Scenario Results

Changes in dissolved oxygen

A summary of *DO* changes for all 10 scenarios is presented in Table 31. This summary is presented in order of decreasing maximum instantaneous *DO* decrease. It is noted that scenario AEE resulted in the maximum instantaneous decrease in *DO*, while scenario AEM had the maximum decrease in average *DO* of 0.891 mg/L. The first five scenarios caused the greatest decreases in *DO* for both measures of change. The maximum instantaneous decreases in *DO* are much larger than the maximum decrease in the average *DO* because slight phase shifts (in time) of *DO* fluctuations can reflect rather large *DO* changes for short periods of time. The large differences in *DO* seem to occur when a sudden increase in concentration in the plan lags the same increase in the existing case. The time series plots of *DO* that follow illustrate this. When the maximum decrease in average *DO* is calculated, it is evident that the overall decrease in *DO* in all cells resulting from expansion is minor.

Time series plots

The locations of stations selected for time series plots are shown in Figures D1, D8, D15, D22, and D29 for the five scenarios presented. Time series plots of *DO* (Figures D2, D9, D16, D23, and D30) indicate that the maximum instantaneous *DO* differences listed in Table 31 were short-term events. In most cases, the time series for *DO* were very similar for plan and existing conditions throughout the scenario. As discussed above, most differences are due to time phase shifts, where differences generally resulted from the increase in *DO* in the plan lagging slightly behind the increase in *DO* in the existing case. Since model concentrations were output on a 3-hr basis, slight time phase differences between the existing and proposed cases were amplified and could contribute to the magnitude of the differences.

Time series for station 1 in scenario EEM (Figure D16) indicate slight increases in CBOD_L and the conservative tracer after expansion. The period of the most significant increase in CBOD_L corresponds to the largest decrease in *DO* at that station. The increased levels of tracer and CBOD_L are indicative of the waste plume passing across the face of Kidney Island being displaced outward by the expansion. Slight increases in conservative tracer concentrations and CBOD_L were observed at station 5 behind Kidney Island. A period of slightly decreased *DO* levels around day 12 occurred at this station. This period occurred under both existing and plan conditions but was of slightly

Table 31
Summary of Changes in Dissolved Oxygen

Scenario	Maximum Inst. DO Decrease (mg/L)	Location WQM Cell No., HM Cell(I,J)	Maximum Decrease in Average DO (mg/L)	Location WQM Cell No., HM Cell(I,J)
AEE	5.504	4196 (49,72)	0.591	3913 (51,67)
EFE	4.210	3692 (42,63)	0.616	3534 (43,60)
MEA	3.895	3436 (43,59)	0.517	3327 (43,57)
EEM	3.812	4090 (45,71)	0.579	3595 (43,62)
AEM	3.717	3489 (43,60)	0.891	3489 (43,60)
EMA	3.293	2997 (46,51)	0.074	3701 (43,64)
AMM	2.484	2945 (47,50)	0.080	3913 (39,68)
AME	2.646	3638 (41,62)	0.320	3799 (43,65)
MME	2.494	3147 (47,53)	0.265	3379 (51,57)
MMM	2.008	3868 (51,67)	0.119	3701 (43,64)

longer duration under plan conditions. Although island expansion did affect concentrations of CBOD_L, tracer, and DO somewhat at these two stations, overall the same trends were followed and the post-expansion conditions are similar to the pre-expansion conditions. At station 2 located east of Kidney Island and station 3 located north of Kidney Island, the differences in pre- and post-expansion simulations were minimal. At station 6 at the mouth of the Fox River there were no differences, as would be expected due to the high flow conditions. Differences in concentrations at station 4 near Peats Lake were imperceptible. Therefore, it is evident that, for this scenario, expansion did not redistribute flow to the western portion of the bay.

The results at stations 1-6 for scenario EEM discussed above are typical of the pattern observed in the other scenarios. The largest deviation from existing conditions occurred at the stations closest to the island, station 1 and station 5. Minor, almost imperceptible, differences between existing and plan conditions occurred at stations 2, 3, and 6. Practically no differences can be detected at the station near Peats Lake (station 4). Therefore, it appears that the expansion has no impact upon the area surrounding station 4. The impact of expansion upon DO, CBOD_L, and conservative tracer is clearly demonstrated in the time series plots of concentration differences (Figures D3, D10, D17, D24, and D31).

Time series plots for the stations experiencing the largest instantaneous DO change at any time during the scenario are shown at station 7. The locations of these stations for all scenarios are shown in Figure 65 and in Figures D1, D8, D15, D22, and D29. Existing and post-expansion concentrations of DO, tracer, and CBOD_L are generally very similar at station 7 for all scenarios.

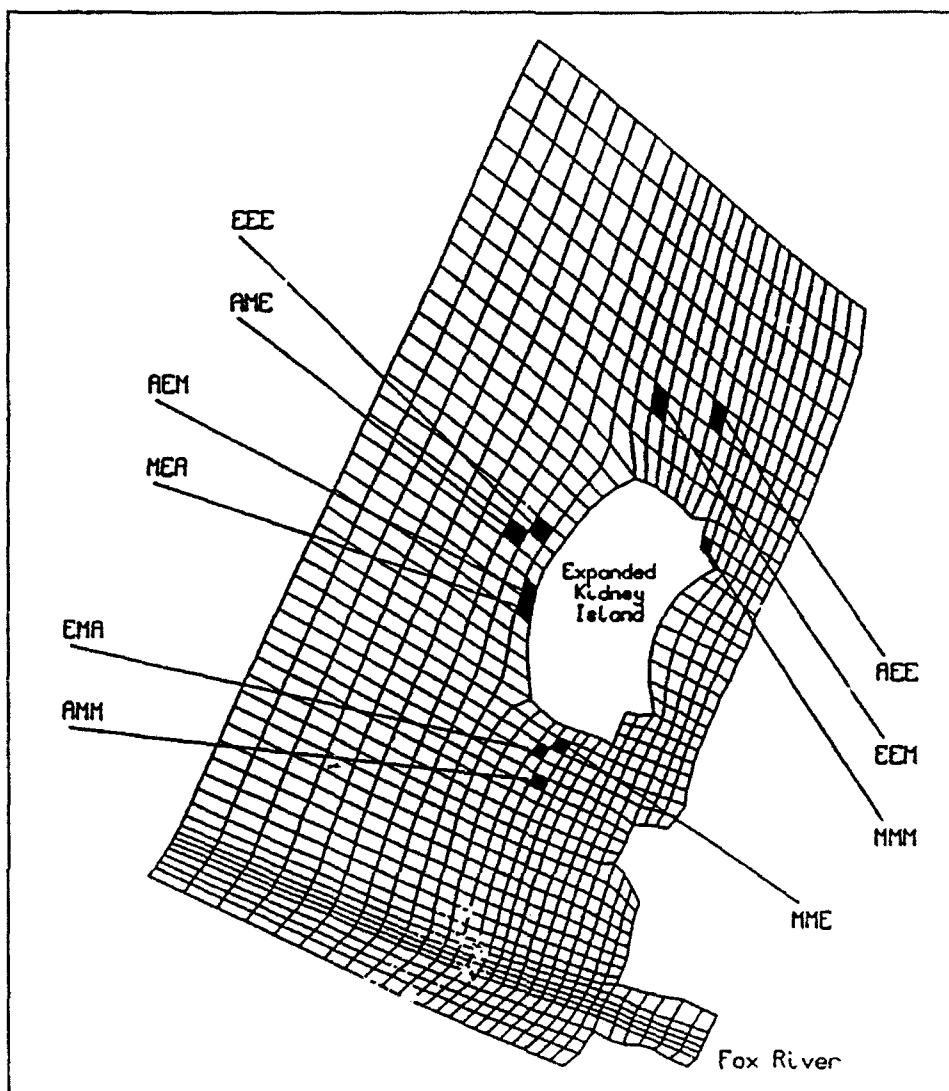


Figure 65. Cells with largest instantaneous decrease in DO for all scenarios

The large instantaneous differences in *DO* at station 7 (listed in Table 31 for each scenario) are short-term events. Only in scenario AEM (Figures D23 and D24) are there significant differences in *DO* for a sustained period of the simulation. This same cell in scenario AEM had the largest decrease in average *DO*. All cells that had the largest instantaneous decrease in *DO* were located in the vicinity of Kidney Island. These cells were actually next to the island in three scenarios. For the other scenarios, they were close to the island (in its "shadow").

Station 8 is the location of the cells that experienced the maximum decrease in average *DO* and is shown in Figure 66 and Figures D1, D8, D15, D22, and D29 for all scenarios. For nine of the ten scenarios, this cell was adjacent to Kidney Island. These cells next to the expanded island experienced the largest change in circulation. Conditions prior to expansion for these cells

were more representative of open water. After expansion, these cells were along the boundary of Kidney Island where velocity gradients are greatest. Expansion simply pushes water that is near the existing boundary further out.

Time series plots for station 9 (Figures D2, D9, etc.) are actually a comparison of two different cells. One cell is adjacent to the north face of the existing Kidney Island. The second cell is on the face of the expanded Kidney Island in the same row as the first cell (i.e., immediately north of the first cell). Agreement between pre- and post-expansion conditions at these cells is much better than agreement at station 8. Concentrations in the cells that compose station 9 are similar throughout each scenario and follow the same patterns within a scenario. This indicates that similar conditions exist along the shore of Kidney Island before and after expansion. Therefore, the differences predicted along the boundary of the island are due primarily to comparison of post-expansion boundary conditions to pre-expansion open-water conditions.

Conservative tracer shading plots

Bay-wide, plan view shading plots of conservative tracer were used to determine the spatial extent of Kidney Island expansion impact on pollutant transport. In the plots of average concentration (Figures D4, D11, D18, D25, and D32), darker areas indicate higher average concentrations. Scenarios with high Fox River flows experienced the highest conservative tracer concentrations in the area stretching from the Fox River mouth eastward along the shore. It appears that a portion of the Fox River flow passes between Kidney Island and the shore or along the front face of Kidney Island between Kidney Island and Grassy Island. In scenarios EEE and AEE, the highest average tracer concentrations were between Kidney Island and the shore. The area along the front face of Kidney Island has elevated tracer concentrations, but not as high as the area behind the island. Scenarios AEM and EEM also have high average tracer concentrations behind the island but have higher tracer concentrations along the front of Kidney Island than in EEE and AEE. This area of higher tracer concentrations ($>0.20 \text{ g/m}^3$) forms a narrow (2-3 cell) band along the north boundary of the island. Scenarios AEM and EEM are minimum water level scenarios, while EEE and AEE are extreme (high) water level scenarios. It appears that the higher concentrations along the north boundary in scenarios AEM and EEM are due to shallow water between the island and shore that forces more water north of the island. The above results are very similar for both existing and plan conditions.

Scenario AEM and AEE results indicate higher tracer concentrations in the western portion of the bay, Peats Lake, than do scenarios EEE and EEM. Scenarios AEM and AEE are average seiche condition scenarios, while EEE and EEM are extreme (high) seiche scenarios. All other conditions are the same; thus, the difference in seiche conditions must affect the amount of flow entering Peats Lake.

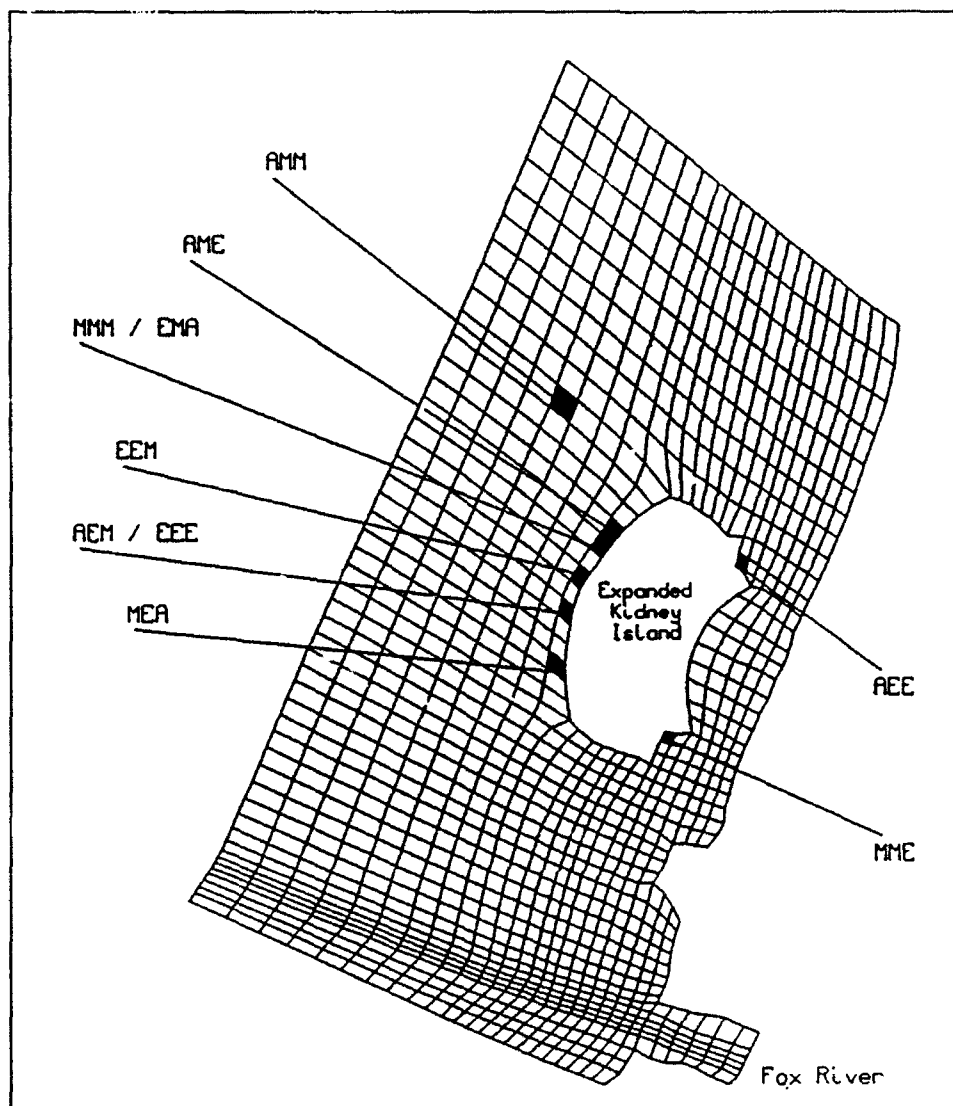


Figure 66. Cells with the largest decrease in average DO for all scenarios

To better assess the impact of expansion upon tracer concentrations, the differences in the average tracer concentrations need to be viewed (Figures D5, D12, D19, D26, and D33). Darker areas indicate increased average tracer concentration after the expansion. It is important to note that a change in the shading intensity of a cell between the existing and plan cases does not necessarily signal a dramatic increase in tracer concentrations. Instead it indicates that the average concentration of conservative tracer in that cell increased until it exceeded the threshold of the next shading range.

Shading plots of differences in average tracer concentrations between existing and plan conditions indicated that tracer concentration throughout the bay remained relatively unchanged between existing and plan cases for each scenario. Increases in average tracer concentration were limited to the region surrounding Kidney Island, mostly on the northern side. No increases in tracer

concentration between existing and plan configurations are indicated in the western portion of the bay. The degree to which tracer concentrations change around Kidney Island varied among scenarios.

Scenarios AEM and AEE had the largest increases in average tracer concentrations, which occurred along the north boundary of expanded Kidney Island. These increases occurred when flow passing the north boundary was displaced by expansion. Prior to expansion, a plume of water containing high tracer concentrations passed along the north boundary of the island. Concentrations in this plume decreased with distance out from the boundary. After expansion, this plume still followed the boundary of the expanded island, but the cells bordering the face of the expanded island were in open water prior to expansion. Prior to expansion, average tracer concentrations in these cells were lower than concentrations after expansion because of the repositioning of this plume. Scenarios EEE and EEM also registered increases in average tracer concentrations along the boundary of Kidney Island for the same reasons. The magnitude of the increases was less than those of AEM and AEE, which is attributed to differences in seiche conditions.

In all scenarios, no increases in average tracer concentrations were indicated except for the area immediately around Kidney Island. Therefore, expansion does not have any effect on transport over large portions of the bay, including Peats Lake.

DO shading plots

Bay-wide, plan view shading plots of the differences in simulation average *DO* concentrations indicate that the effects of expansion are localized around Kidney Island (see Figures D.1.6, D.2.6, D.3.6, D.4.6, and D.5.6). The locations of the regions around Kidney Island which experienced decreases in average *DO* after expansion were generally the same regions which experienced increases in average tracer concentrations (mostly on the northern side). One reason why these areas do not match exactly can be attributed to the fact that the increments used for *DO* and tracer shading do not correspond.

In most cases, the cell with the maximum decrease in average *DO* was adjacent to the Kidney Island expansion. Prior to expansion these cells were not adjacent to Kidney Island. Expansion of Kidney Island brought the island out to these cells. Comparison of existing and post-expansion conditions in the cells next to the expansion amounts to comparison of conditions in a cell away from the island (existing conditions) and a cell next to the island (expanded conditions). The poorer water quality found along the edge of the existing island was displaced to the edge of the expanded island. Thus, decreases in *DO* around the expansion result from displacement rather than degradation. Little or no degradation in *DO* occurs between the island and south shore as a result of expansion. This is due to the increased flow (i.e., flushing rate) in this area as noted under the HM results.

In two scenarios, AEE and MME, the cells with the largest decreases in average *DO* were located on the right and left sides of Kidney Island where the expansion connects with the existing island. These cells are in the corners created by the connection of the expansion to the existing island and experienced significant changes in circulation after expansion compared to pre-expansion conditions. In scenario AEE, the cell with the largest decrease in average *DO* was located on the eastern side of Kidney Island (side away from the Fox River mouth). This scenario was a high-flow scenario and conservative tracer plots indicated that this region was in the wake of the flow passing around the island. In scenario MME, a low-flow, minimum-seiche scenario, the cell with the largest decrease in average *DO* was on the western side of Kidney Island (side closest to the Fox River mouth). The hydrodynamic conditions of this scenario resulted in little flushing of this corner. Prior to expansion the flow could follow the boundary of Kidney Island around the island. After expansion, the flow along the southwestern edge of Kidney Island was partially blocked by the expansion and there wasn't enough energy in this scenario to keep the cell in the corner flushed.

Figures D7, D14, D21, D28, and D35 are bay-wide, plan view shading plots of lowest (throughout the scenario simulation) instantaneous *DO* concentrations for existing and plan conditions. Each cell is shaded according to the lowest *DO* predicted for that cell without regard for when it may have occurred. The regions which are shaded vary from scenario to scenario. However, for a given scenario, the same regions are shaded to the same degree in both pre- and post-expansion conditions. This indicates how similar the minimum *DO* concentrations are throughout the bay.

Violations of minimum *DO* standards

In this section, comparisons are made between the pre- and post-expansion *DO* conditions as related to the state minimum *DO* standards (5.0 mg/L). In these comparisons the first day's data (day 0.0 to day 1.0) were omitted and only data from days 1 through 19 used. The first day was omitted from these comparisons to decrease the impact of initial conditions upon the interpretation of the WQM results.

Dissolved oxygen concentrations for all cells were output in 3-hr intervals for all cells during the water quality scenarios. The number of these 3-hr outputs that the *DO* was below 5.0 mg/L were determined with and without the expansion in place for all cells and for all scenarios. It must be remembered that when the *DO* was below 5.0 mg/L by any amount, no matter how small, it was counted. It is pointed out, however, that the waste-load allocations were based on 24-hr average values of *DO*.

The cells in which the *DO* fell below 5.0 mg/L the most are summarized in Table 32 for each scenario. In seven of the scenarios, the cells which had the most *DO* concentrations below 5.0 mg/L after expansion were the same cell or adjacent to the cells which had the most *DO*s below 5.0 mg/L before expansion (see Figures 67 and 68).

The lowest *DO* concentration for each scenario was determined for both pre- and post-expansion conditions (Table 33). The *DO* concentrations, which were output at 3-hr intervals, were searched and the lowest *DO* that occurred in any cell was determined. Locations of these cells are shown in Figures 69 and 70.

The total number of occurrences of violation of the state *DO* standard (5.0 mg/L) for the entire study area were determined for each scenario as shown in Table 34. This value is the sum of the number of total violations of the state *DO* standard for all cells. The data contained in Tables 33 and 34 demonstrate that the pre- and post-expansion *DO* conditions are very similar.

Figures 68 and 70 demonstrate that the expansion does not cause *DO* degradation upstream of the Fox River mouth, which is critical for existing wasteload allocations. The same three scenarios experienced their maximum number of *DO* violations within the Fox River for both pre- and post-expansion conditions (see Figure 68). The lowest *DO* occurred within the Fox River for three pre-expansion scenarios, whereas only one post-expansion scenario had the lowest *DO* within the Fox River, at the same location as the pre-expansion condition (see Figure 70).

The determination of the number of state *DO* standard violations did not indicate the degree of these violations. Any *DO* concentration below 5.0 mg/L was counted as a violation without regard to its magnitude. While it is important to know how far the *DO* falls below the state standard, it is also important to determine the volume of water to which this condition applies. The *DO* deficit was determined for the cells in which violations occurred by multiplying the cell volume by the difference between 5.0 mg/L and the predicted *DO* concentration. Since *DO* concentrations were output at 3-hr intervals, these deficits were assumed to last until the next *DO* output, at which time new deficits were calculated. The deficit was multiplied by the 3-hr interval to yield *DO* deficit-days. *DO* deficit-days (g O₂-days) are computed from

$$DO\text{-deficit-day} = V * (5.0 - DO) * (3/24)$$

where

$$V = \text{cell volume (m}^3\text{)}$$

The deficit-days were summed for all cells to arrive at one value for both pre- and post-expansion conditions for each scenario (Table 35).

If all cells in the grid maintained the state standard of 5.0 mg/L throughout the 18 days of scenario used for comparisons, the total *DO* mass duration required would be 3.042×10^{10} g O₂-days. Therefore, the largest *DO* deficit days of 0.31×10^8 g O₂-days (Table 35) represents about 0.10 percent of the total *DO* mass duration required for state standards throughout the simulation.

Table 32 Cells (WQM No. and HM I,J) with Maximum Number of 3-hr DO Outputs Below 5.0 mg/L							
Scenario	Cell Before Expansion	Number of Violations Before Expansion	Number of Violations After Expansion	Cell After Expansion	Number of Violations Before Expansion	Number of Violations After Expansion	
AEE	4945 13.87	22	19	4867 15.87	21	22	
EEE	2592 50.43	2	2	2535 50.42	0	2	
MEA	4263 47.74	23	10	4012 47.71	11	16	
EEM*	2738 57.46	38	39	2682 57.45	38	39	
AEM*	3764 57.65	73	69	3008 57.51	72	72	
EMA**	2043 68.36	20	20	2042 67.36	19	21	
AMM*	2738 57.46	81	83	2738 57.46	81	83	
AME**	2161 62.37	98	96	2052 61.36	96	97	
MME**	2056 65.36	79	79	2056 65.36	79	79	
MMM*	2682 57.45	56	55	2738 57.46	56	56	

* Cell is along shore between Fox River mouth and eastern end of Kidney Island.

** Cell is in Fox River slightly upstream of the mouth

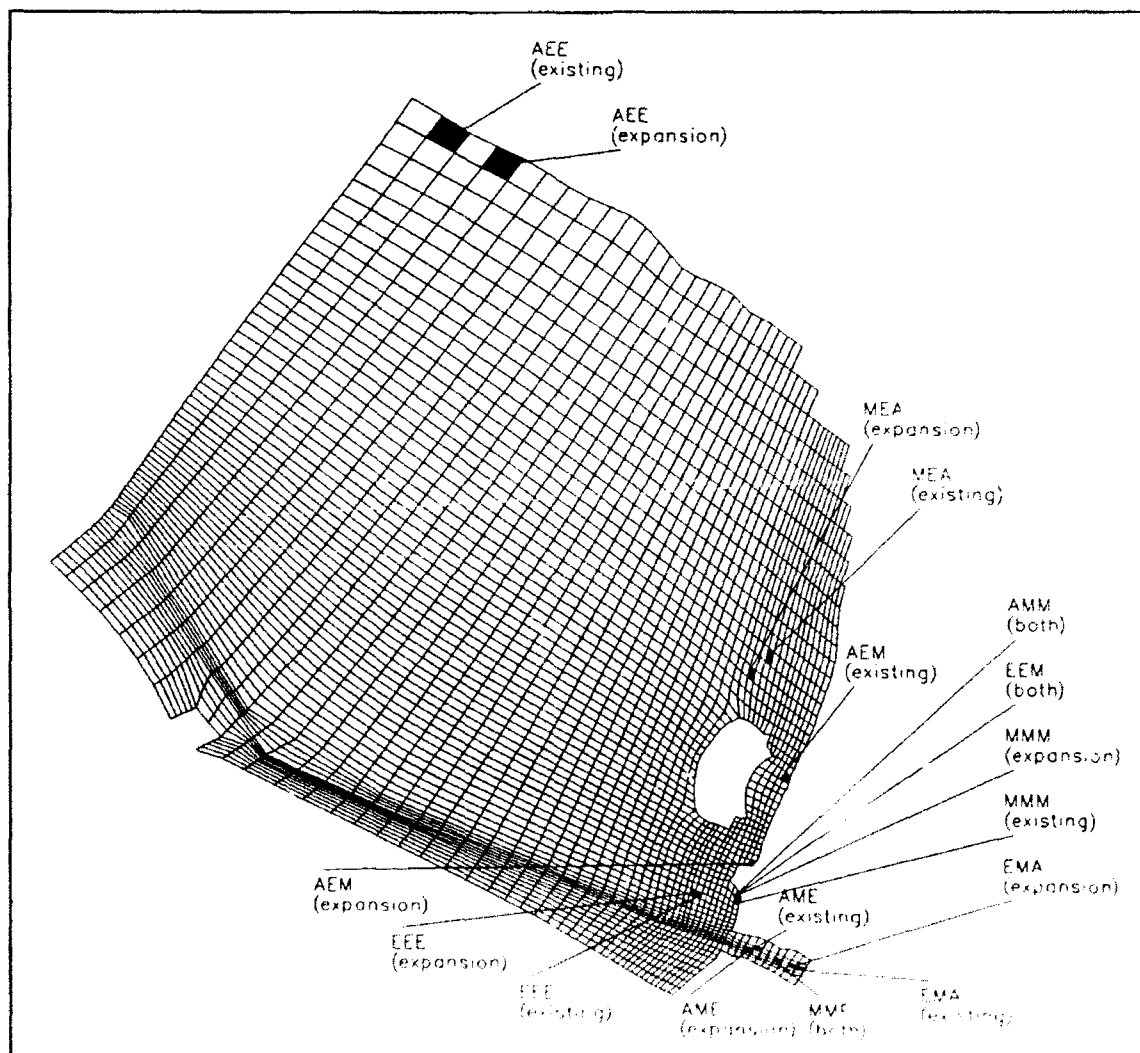


Figure 67. Cells with most *DO* violations

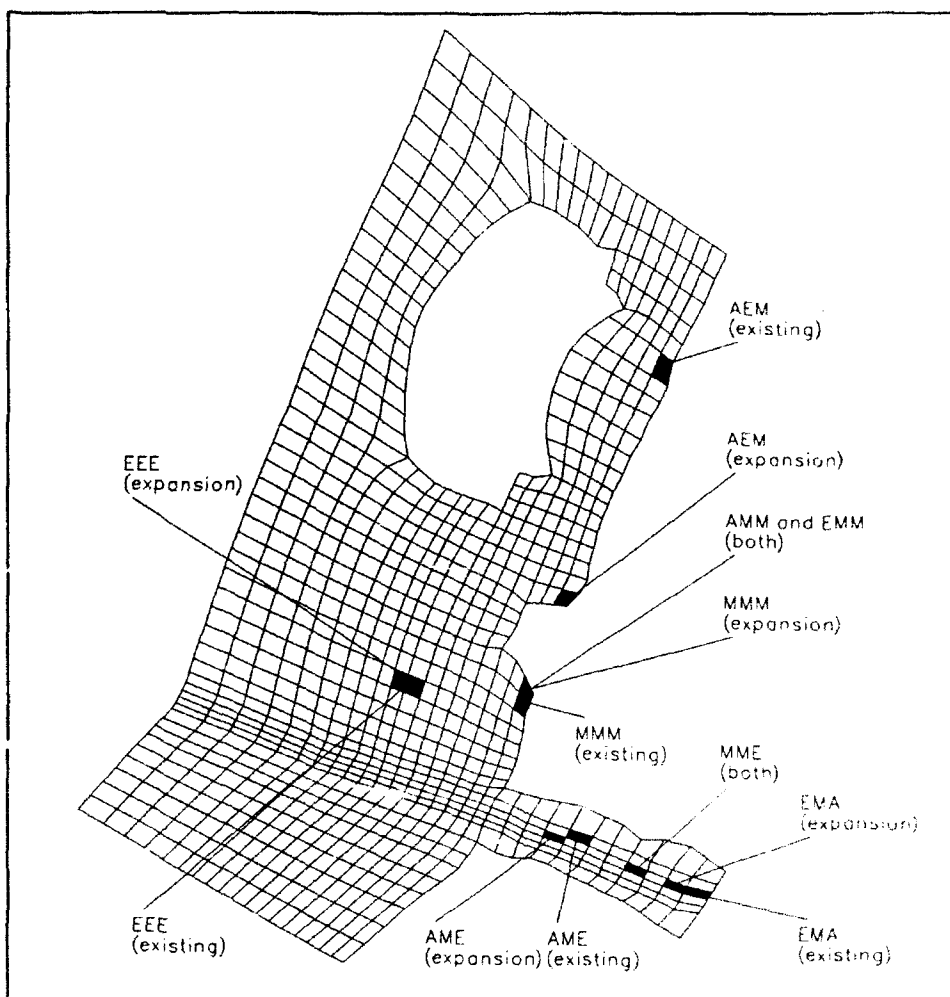


Figure 68. Cells with most DO violations, Fox River mouth vicinity

Table 33
Lowest DO Concentration and its Location (day 0-1 omitted)

Scenario	Existing Conditions		Expanded Conditions	
	DO (mg/L)	Cell	DO (mg/L)	Cell
AEE	3.63	4924 23,86	3.61	2532 47,42
EEE	3.89	1383 48,27	3.90	1383 48,27
MEA	2.56	4428 43,77	3.04	4285 36,76
EEM	2.92	2682 57,45	2.86	2626 57,44
AEM	1.73	2249 59,38	1.66	2738 57,46
EMA	3.16	2253 63,68	3.25	2253 63,38
AMM	1.25	2249 59,38	1.26	2738 57,46
AME	1.61	2150 51,37	1.55	2150 31,37
MME	2.32	2042 51,36	2.30	1930 47,35
MMM	2.25	2404 55,40	2.24	2404 55,40

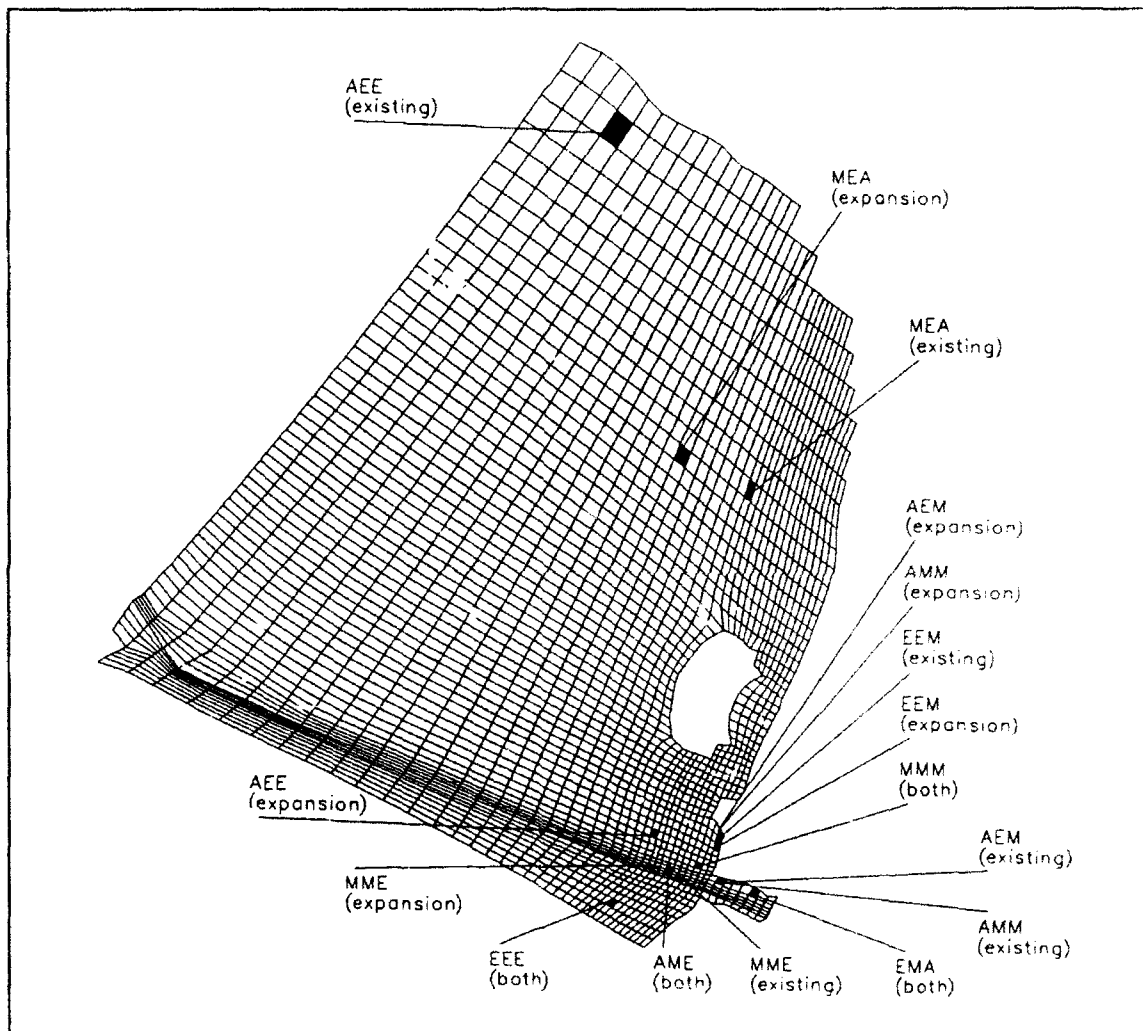


Figure 69. Cells with lowest *DO*

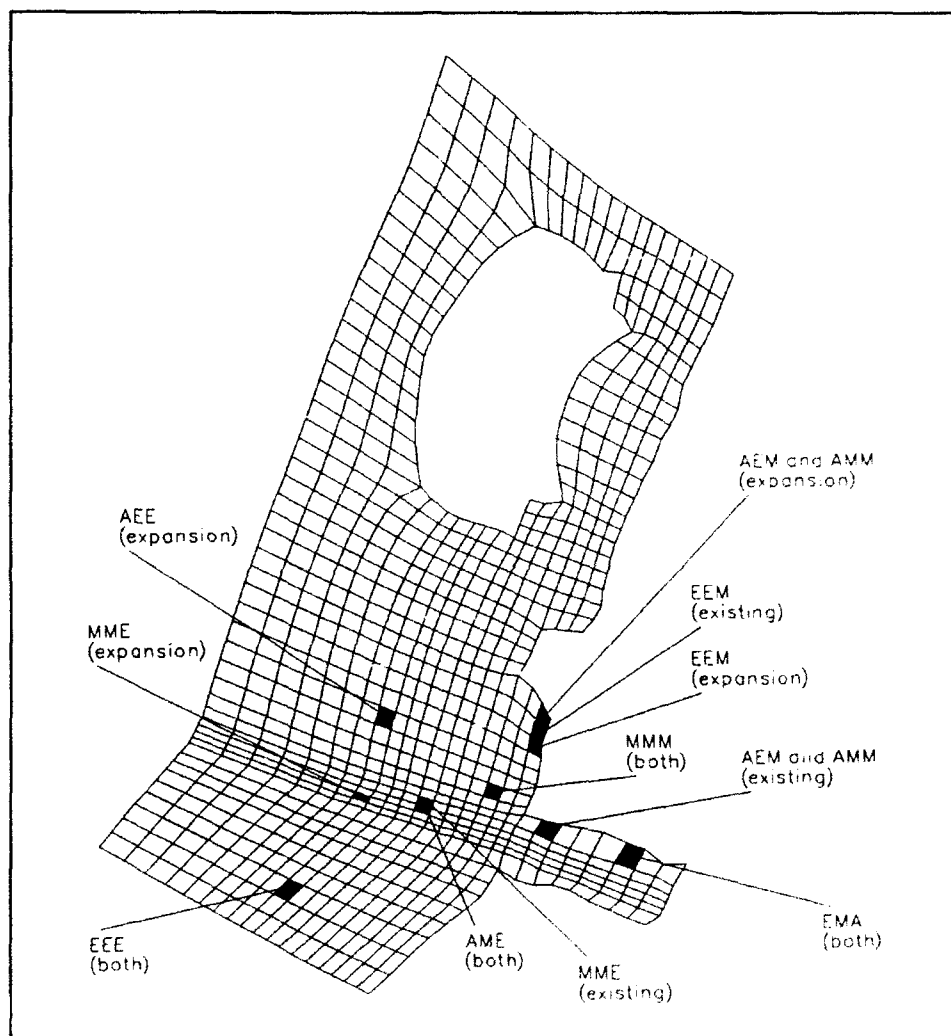


Figure 70. Cells with lowest *DO*, Fox River mouth vicinity

Table 34
Number of Occurrences of DO Below 5.0 mg/L During Each Scenario
(day 0 - 1 omitted)

Scenario	Before Expansion	Expansion in Place
AEE	3060	3684
EEE	219	224
MEA	3516	3178
EEM	1174	1487
AEM	9047	9399
EMA	3709	3665
AMM	18248	18290
AME	25870	25894
MME	19319	19395
MMM	7684	7709

Table 35
DO-volume-days of violation (cell volume)*(5.0-DO)*(3hr/24hr)
(day 0-1 omitted)

Scenario	Before Expansion (g-day)	After Expansion (g-day)
AEE	0.118×10^8	0.144×10^8
EEE	0.959×10^5	0.968×10^5
MEA	0.127×10^8	0.122×10^8
EEM	0.105×10^8	0.145×10^8
AEM	0.150×10^8	0.161×10^8
EMA	0.167×10^7	0.166×10^7
AMM	0.108×10^8	0.109×10^8
AME	0.313×10^8	0.314×10^8
MME	0.223×10^8	0.225×10^8
MMM	0.487×10^7	0.494×10^7

Statistical Analysis of Violations of Minimum *DO* Standards

Statistical significance tests were conducted on the results of Tables 32-35. Five sets of paired data were tested to determine if there were differences between pre- and post-expansion *DO* violations in LGB. The five sets of paired data are:

- a. Number of pre- and post-expansion *DO* violations in the cell which had the most *DO* violations before expansion for each scenario (see Table 32).
- b. Number of pre- and post-expansion *DO* violations in the cell which had the most *DO* violations after expansion for each scenario (see Table 32).
- c. Lowest pre- and post-expansion *DO* concentration for each scenario (see Table 33);
- d. Total number of *DO* violations for all cells before and after expansion for each scenario (see Table 34).
- e. *DO*-volume-days of violation before and after expansion for each scenario (see Table 35).

For each of the above five comparisons, there are 10 independent data samples (i.e., 10 scenarios) with paired results (i.e., pre- and post-expansion) for each sample. All samples were obtained from model results.

The Wilcoxon signed rank test was used to test the null hypothesis, i.e., the means for pre- and post-expansion observations are equal. The Wilcoxon test is a nonparametric analog to the paired difference *t* test. This test was used since it does not require the normal distribution assumption, which the *t* test requires. Using both one- and two-tailed tests with $\alpha = 0.05$, the null hypothesis could not be rejected for all of the above comparisons except (2). The number of post-expansion *DO* violations for test 2 either remained the same or slightly increased for each scenario (see right side of Table 32), thus causing the null hypothesis to be rejected. In summary, the statistical analysis indicates that there is no significant difference in pre- and post-expansion *DO* violations for four of the five types of *DO* violation comparisons conducted.

8 Investigation of Sediment Resuspension Potential

One possible consequence of expanding Kidney Island is the increase in water nutrient and toxin levels within the lower bay. This potential increase could be induced by higher current velocities and the associated resuspension of cohesive sediment, such as clays and silts, which had adsorbed pollutants prior to deposition. Because the chemical bond attaching the nutrient to a sediment particle may not be permanent, it can dissociate from the clay particle and be reintroduced into the water column, should resuspension occur. This pollutant may then enter the aquatic life-cycle process (i.e., food chain) or again be adsorbed by sediment and remain in the sediment deposition/resuspension cycle.

Development of a rigorous modeling procedure to investigate and quantify sediment transport is not in the scope of this study. However, a qualitative assessment is made by determining those areas in the lower bay where the potential for sediment resuspension will increase due to expanding Kidney Island. This qualitative assessment focuses on delineating those areas which can be expected to experience an increase in bottom shear stress, the process controlling resuspension of sediment.

Description of Modeling Algorithm

In shallow areas, such as lower Green Bay, sediment resuspension is a function of the orbital velocities associated with short wave fields together with the shear stress imparted by the depth-averaged flow. In order to account for this coupled process, an effective increase in the bed shear stress is used in the modeling algorithm. This modification, based on the concepts developed by Bijker (1967), states that an effective shear stress, including both waves and currents, can be written as a function of a wave-induced increase in the bed shear stress produced by currents only. This function can be expressed as:

$$\tau_{wc} = \tau_c \left[1 + \frac{1}{2} \left(\xi \frac{u_0}{u_c} \right)^2 \right] \quad (24)$$

where τ_{wc} is the entrained bottom shear stress incorporating both orbital and current velocities, τ_c represents the bottom shear stress due only to currents, u_c is the current speed, u_0 is the amplitude of the wave orbital velocity, and ξ is an entrainment coefficient.

The bottom shear stress formulation for currents is:

$$\tau_c = \frac{\rho g \bar{u}_c^2}{C_z^2} \quad (25)$$

where ρ is the water density, g is the gravitational acceleration, and C_z is the Chezy friction factor.

The wave orbital velocity defined in the first equation can be written:

$$u_0 = \frac{HgDT}{4\pi} \frac{1}{\cosh(kD)} \quad (26)$$

where H is the wave height, D is the water depth, and T and k represent the wave period and wave number, respectively.

The entrainment coefficient is:

$$\xi = C \left(\frac{f_w}{2g} \right)^{1/2} \quad (27)$$

where f_w is the wave friction factor (Jonsson 1966). C is a coefficient accounting for bottom friction effects and has the form:

$$C = 18 \log \left(\frac{12D}{r} \right) \quad (28)$$

where r represents the bed roughness.

The wave friction factor can be approximated by (Swart 1974):

$$f_w = \exp \left[-5.977 + 5.213 \left(\frac{r}{a_0} \right)^{0.194} \right] \quad (29)$$

The quantity a_0 is the maximum orbital excursion length and is defined as:

$$a_0 = \frac{H}{2} \frac{1}{\sinh(kD)}$$

The modeling procedure described above provides a spatial distribution of areas subject to erosion as a function of local depth, sediment size, wave fields, and hydrodynamic forcing. Because cohesive sediment deposition patterns give an indication of sediment-adsorbed substance concentrations, this approach provides a qualitative insight into the potential effects of the proposed CDF on the distribution of toxic materials.

Application of Modeling Approach

In order to evaluate potential sediment resuspension patterns over a wide range of hydrodynamic conditions, the algorithm discussed above was applied to each of the 10 scenarios described in the previous chapter. To identify areas subject to changing sediment resuspension potentials, bottom shear stresses computed with the proposed Kidney Island configuration were compared to those stresses computed with the existing configuration. Bed shear stresses were computed as a function of local rms velocity magnitudes and local wind wave conditions. The hydrodynamic model results were used to compute the root-mean-square velocities for each cell in the grid.

The procedures presented in the *Shore Protection Manual* (1984) were followed for estimating significant wave height and period for fetch-limited and shallow-water conditions. The significant wave height and period were estimated to be equal to 1.3 ft and 2.2 sec, respectively. A fetch length of 3 miles, a water depth of 10 ft, and a wind speed of 7 m/sec were used to predict these values. The selected wind speed represents the maximum sustained wind speed measured at the Green Bay Airport. This speed was increased by 50 percent to correct for overland friction effects. The wave period was assumed constant throughout the grid; however, the wave height was adjusted to account for depth-limited wave conditions (e.g., breaking waves). Figures 71 and 72 illustrate the computed bottom shear stresses for the existing and proposed CDF configurations, respectively, under extreme seiche, extreme river flow, and minimum lake level conditions. Figure 73 depicts the

departure, or relative change in bottom shear stress, resulting from expanding Kidney Island.

Figures 71 and 72 show a correlation between water depth and bottom shear stress, where greater shear stresses are typically experienced in shallower water. For example, in Peats Lake, where depths are generally less than 4 ft, stresses exceed 50 dynes/cm², whereas, having depths exceeding 20 ft, the navigation channel experiences stresses below 10 dynes/cm².

At each cell in the grid, the departure in bottom shear stresses is computed as the difference in bottom shear stresses resulting from expanding Kidney Island. The existing CDF configuration serves as the basis of comparison. Thus, a positive change reflects an increase in stresses (due to expanding Kidney Island), whereas a negative change depicts a decrease in stresses. In Figure 73, departures are expressed in percent. Furthermore, a threshold value of 5 dynes/cm² was specified as the critical stress required to induce movement of cohesive sediment. Thus, no sediment movement will occur when stresses are below this threshold value.

In Peats Lake and Dead Horse Bay, bottom shear stresses are most sensitive to the variation in lake levels. For example, at minimum lake levels, stresses vary between 10 dynes/cm² and 50 dynes/cm², whereas stresses range from 10-40 dynes/cm² and 0-30 dynes/cm² for the average and maximum lake levels, respectively. A negligible change in stress patterns is noted for the extreme and average storm seiche conditions, and also between differing flow rates. A small change is noted, however, between extreme and minimum seiche conditions. A negligible change in stress departure is noted in these areas.

In the southeast section of the lower bay, which is defined as that area east of Kidney Island and south of Frying Pan Shoal, high shear stress areas predominately reside along the shoreline. For the extreme seiche, extreme river flow, and minimum lake level condition, stresses ranged between 30 dynes/cm² and 50 dynes/cm². For average and maximum lake levels, stresses were typically in the 20-30 dynes/cm² range along the shoreline.

For the minimum lake level scenarios, large portions in the southeast section have stresses in the 10-20 dynes/cm² range. Towards the center of this section, stresses are lower and vary up to 10 dynes/cm². Interestingly, the center of a large eddy typically exists in this area. For average and maximum lake levels, stresses are reduced and fall within the 0-10 dynes/cm² range. No dependence is noted on river flow rates, and a negligible change in stresses occurs between pre- and post-expansion CDF configurations.

Because of its depth, bottom shear stresses within the channel are predominately small and vary up to 10 dynes/cm². However, for minimum lake level conditions, greater stresses are experienced in the shallower areas adjacent to the channel and these stresses can range from 10 dynes/cm² to 20 dynes/cm². The departures in stresses in areas adjacent to the channel are most sensitive

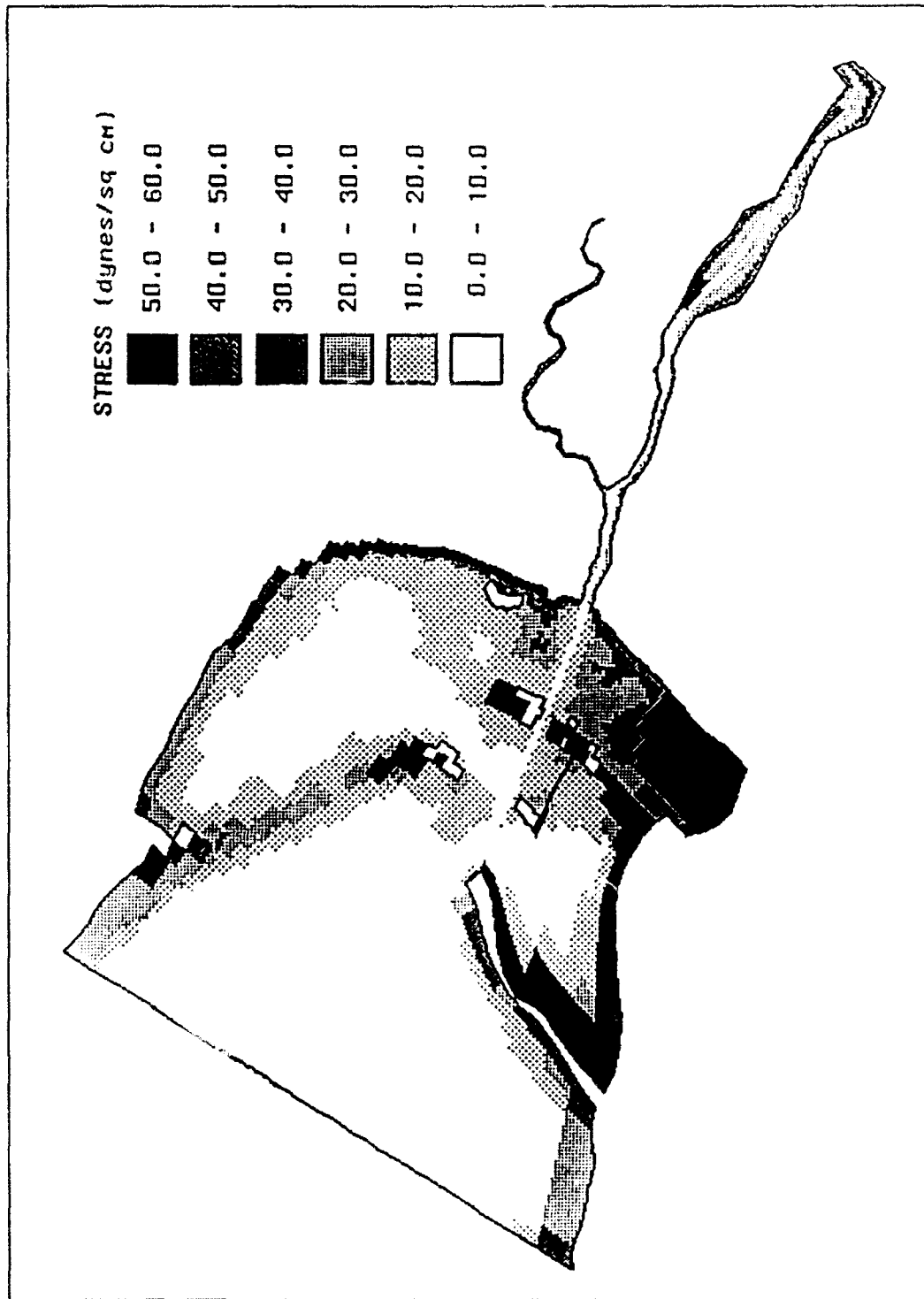


Figure 71. Location map of bottom shear stresses, with existing CDF configuration, produced under extreme seiche, extreme flow, and minimum lake level conditions

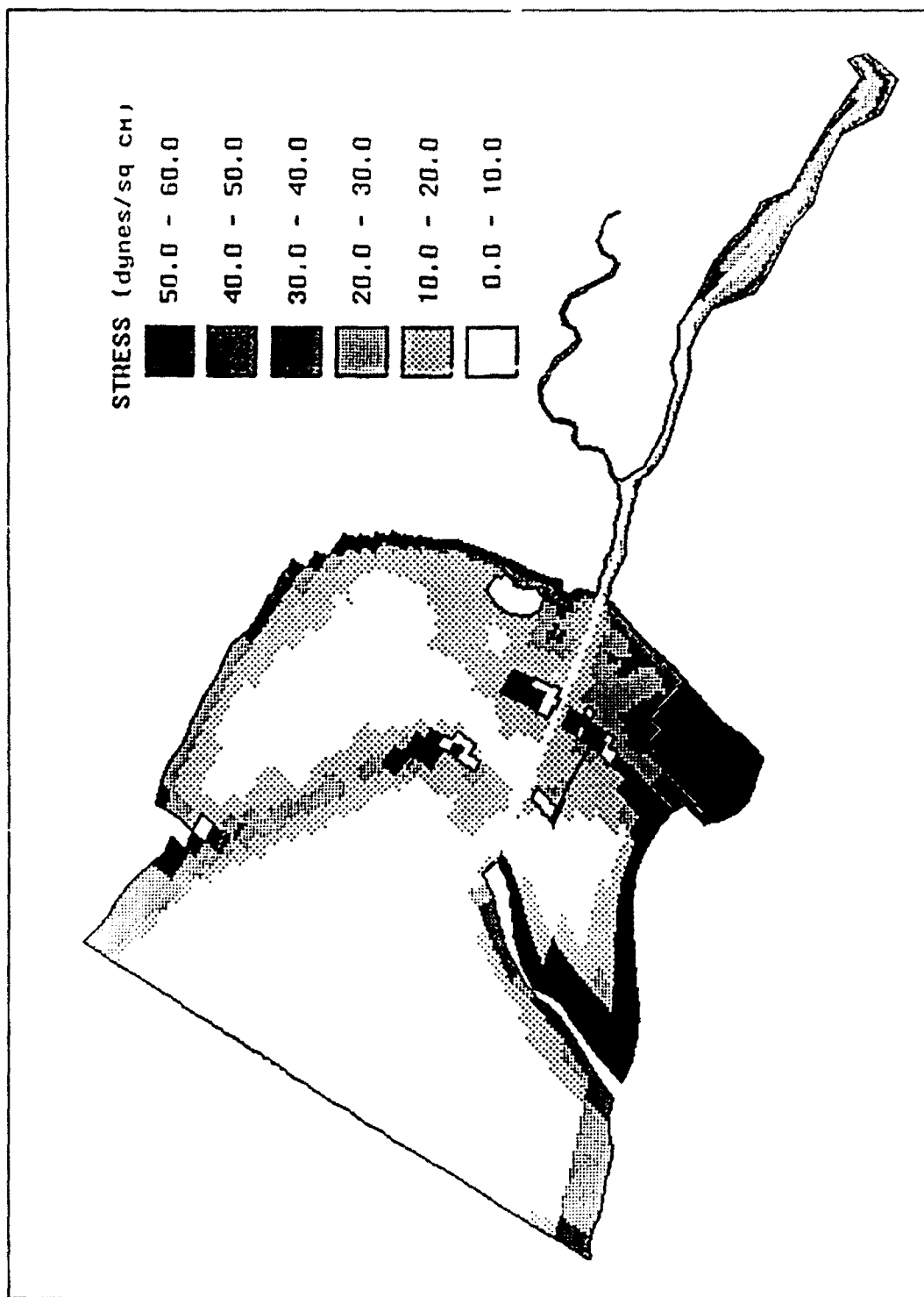


Figure 72. Location map of bottom shear stresses, with proposed CDF configuration, produced under extreme seiche, extreme flow, and minimum lake level conditions

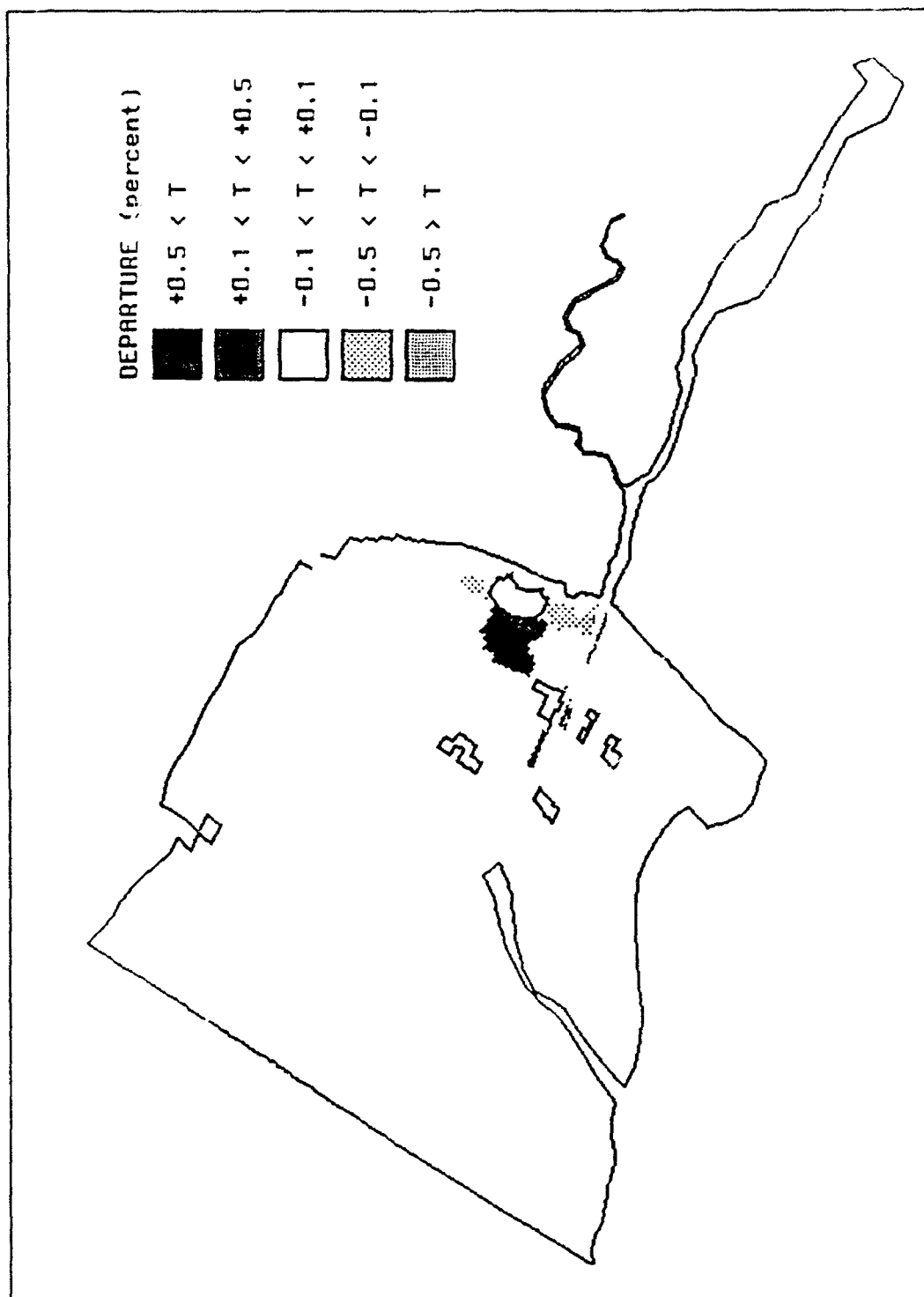


Figure 73. Location map of bottom shear stress departures produced under extreme seiche, extreme flow, and minimum lake level conditions

to the combined effects of maximum river flows, together with average and low lake levels. A negligible departure is noted at maximum lake levels. Seiche action slightly increases the area subject to resuspension, and the greatest effect is experienced in the zone adjacent to Grassy Island.

For Kidney Island, bottom shear stresses around the island can approach 40 dynes/cm². At maximum lake levels, stresses to the north of the island are typically in the 0-10 dynes/cm² range. Behind the CDF, stresses approach 30 dynes/cm² along the shoreline, but decrease to the 10-20 dynes/cm² range along the island. This difference in stresses is attributed to the fact that a small change in water depth, especially in shallower water, can have a significant impact on shear stresses.

At average lake level conditions, stresses in front of Kidney Island do not exceed 10 dynes/cm², whereas stresses can range from 20-40 dynes/cm² behind the CDF. The higher stresses behind the CDF occur along the shoreline. To the east of Kidney Island, stresses vary up to 10 dynes/cm². To its west and northwest, stresses in the vicinity of the CDF are in the range of 10-30 dynes/cm², with the higher stresses occurring in areas of shallower depths, such as along the shoreline.

In the vicinity of Kidney Island, shear stresses generated with minimum water level conditions are, in general, approximately 10 dynes/cm² greater than those calculated with average lake levels. Behind the island, maximum shear stresses increased from approximately 45 dynes/cm² to 55 dynes/cm², and stresses in front of the island increased from approximately 7 dynes/cm² to 15 dynes/cm². A commensurate increase in stresses also occurred in the regions west and east of the island.

For maximum lake level conditions, departures in bottom shear stresses show a potential increase in sediment resuspension in the vicinity of the unnamed shoal area located west-northwest of the CDF. This increase varies from 0.1 to 0.5 percent. In addition, areas behind Kidney Island also exhibit increased resuspension potential for extreme and average seiche conditions occurring in conjunction with maximum river flows. The spatial extent of these areas decreases under minimum river flow conditions. A decrease in resuspension potential can be found to the west of the CDF. This decrease is attributed to the sheltering effect caused by enlarging the island. Compared to the existing configuration, the proposed CDF impedes the flow of water through this region, thus reducing the water velocities, and, therefore, the shear stresses.

Whereas the area in front of Kidney Island exhibits a tendency of increasing bottom shear stress departures with decreasing lake levels, the departures for areas behind the island appear to increase with increases in lake levels. This phenomenon is attributed to the increased flows behind Kidney Island resulting from seiche action.

Compared with departures resulting from maximum lake level conditions, a greater spatial extent becomes susceptible to possible erosion during periods of

average lake levels. This increase in resuspension potential is primarily in the region extending north from Kidney Island to Grassy Island. Increases range from 0.1 to 0.5 percent. An increase of 4 percent is computed, however, immediately adjacent to the northwest section of the island. The spatial extent of this area is greater under extreme seiche and minimum river flow conditions than with minimum seiche and extreme river flow conditions. This suggests that seiche action will have a greater impact on possible erosion patterns than high river flows. In addition, sheltering effects can be found to the west and east of Kidney Island.

In summary, only those areas in the immediate vicinity of Kidney Island will experience a change in sediment resuspension potential. To the east and west of Kidney Island, the potential for sediment resuspension is reduced. This phenomenon can be attributed to the sheltering effect caused by enlarging the island. Compared to the existing CDF configuration, the expanded island impedes the flow of water through these areas, thus reducing the water velocities, and, therefore, the shear stresses. The overall decrease in stresses is generally small, ranging from -0.5 to -1.0 percent.

An increase in resuspension potential exists to the north of Kidney Island. This increase is attributed to constricting the cross-sectional area between the CDF and Grassy Island, resulting in slightly higher velocities in this region. As a result, increases in stresses range from 0.5 to 1.0 percent, with the greatest increase shown in the area immediately adjacent to the northwest face of the island. Several areas along the navigation channel also show an increase in resuspension potential. This increase results from the increased flows exiting through the channel.

9 Summary and Conclusions

The conclusions presented in this chapter were drawn by WES from an analysis of the hydrodynamic and water quality modeling results. These conclusions, however, do not necessarily reflect those drawn by the TRP.

This study was conducted to assess potential redistribution of current patterns and subsequent impacts on water quality (e.g., dissolved oxygen) resulting from a planned expansion of a CDF located in lower Green Bay, Wisconsin. Two-dimensional, vertically averaged hydrodynamic and water quality models were applied to make this assessment. Because most bay processes can be adequately represented using a two-dimensional modeling approach and because of the absence of data for validating a three-dimensional model, assessing potential impacts using depth-integrated hydrodynamic and water quality models was accepted as a reasonable approach by the U.S. Army Corps of Engineers, both WES and NCE, WDNR, and the PIO. The hydrodynamic model, CH3D, was used for computing water surface levels and velocity fields which were subsequently used by the water quality model, CE-QUAL-ICM, for predicting the transport and fate of water quality constituents.

The CH3D model incorporated all of the dominant physical processes affecting currents in the lower bay, including water surface level fluctuations (e.g. seiches), river inflows, surface and bottom shear stresses, and Coriolis effect. Time series of water surface elevations collected at the Angle Light gauging station were used as boundary conditions at the northern or open water boundary. Daily-averaged river discharges were specified at the Fox and East River boundaries. Time series of wind speed and direction data collected at the Green Bay Municipal Airport were used for input to the model.

The water quality model is comprised of 11 state variables, including dissolved oxygen (DO), and their associated kinetic processes. In addition to DO, modeled constituents include algae, labile and refractory carbonaceous biochemical oxygen demand (CBOD), temperature, nitrate-nitrogen, ammonium-nitrogen, total organic nitrogen, total organic phosphorus, orthophosphate-phosphorous, and a conservative tracer. Sediment oxygen demand is specified as a benthic boundary condition, and reaeration is simulated using a wind-driven, gas transfer formulation.

The lower Green Bay grid was constructed such that coordinate lines smoothly followed the irregular landforms in the study area, including the

shoreline, Kidney Island, and Long Tail Point, as well as the navigation channel. The final grid included improved spatial resolution in regions to the north and to the east of Kidney Island as suggested by members of the TRP. Excluding the Fox and East Rivers, this improvement increased the total number of cells by 44 percent. The grid's finest resolution was placed within the critical zone encompassing the Fox River mouth where significant mixing of the Fox River discharge and the bay water occurs. Cells in this area measure approximately 75 ft by 125 ft in the east-west and north-south directions, respectively.

Measured water surface level and water velocity time series data were used in calibrating and validating the hydrodynamic model. Parametric and non-parametric statistical tests, comparing model-generated to measured time series data, were performed to quantify model accuracy. Furthermore, the model was calibrated and validated over multi-week periods, during which the lower bay experienced a variety of conditions, reflecting both calm and storm events typically encountered in summer.

The hydrodynamic model was calibrated over a 14-day period in June 1984 with time series data collected at one water surface elevation gauge station and four current meter stations. During this period, Green Bay experienced two relatively high wind events, with one event inducing a maximum range of water level fluctuations of 1.6 ft, or 2.5 times greater than the mean fluctuation for this area. Model validation was performed over a 21-day period in July 1984. Data used in this procedure consisted of time series of water surface elevations collected at one gauge and water velocities collected with four current meters. (Of the four current meters, only two meters were in continuous operation over the validation period and the remaining two were operational approximately 50 percent of the time.) Two significant seiche events were recorded during the validation period.

The water quality model was calibrated with data from a 36-day period during July and August 1983. Grab sample data collected in the Fox River and throughout lower Green Bay and records from continuous *DO* monitoring stations located along the Fox River were used for calibration comparisons. These data were supplied by the WDNR, and had been used in their waste-load allocation study. Model output was compared to observed data in time series, transect, and scatter plots. At the beginning of the calibration period, a sustained *DO* sag was recorded by the continuous *DO* monitors along the lower Fox River but not in Green Bay. Although this period experienced higher waste loadings than the latter part of the calibration period, oxygen uptake associated with the waste loads was insufficient to cause the sag. To capture this sag, the algal production rate was lowered for the first 10 days of the calibration period in the Fox River only. The justification for this action was that algal production can decrease as light attenuation increases during periods of high turbidity associated with rainfall runoff.

A series of test simulations or scenarios were performed to assess possible water quality impacts resulting from the CDF expansion. This assessment was made by comparing simulated spatial and temporal variations in dissolved

oxygen and conservative tracer concentrations. Two simulations were conducted for each scenario; one simulation depicts the lower bay with the existing Kidney Island configuration, whereas the second simulation portrays the lower bay with the proposed configuration.

In constructing the scenario tests, lake levels, river flow rates, and seiche action/wind events were treated as independent variables. A statistical analysis was conducted to determine the range of values that are representative of these variables. Furthermore, three values were selected for each variable. One value represents the average condition, whereas the remaining two values represent high and low conditions. A series of tests were constructed by interchanging the values assigned to each independent variable. Thus, a given test portrays a particular hydrodynamic/hydrologic condition or event. Evaluation of ranges of conditions provides a broad spectrum of plausible events to accurately evaluate water quality impacts incurred by expanding Kidney Island and increases the reliability of conclusions drawn. Of the 27 possible permutations of conditions (i.e., wind/seiche, river flow, and lake level), 10 conditions were selected for scenario testing. These 10 conditions should sufficiently bracket the range of expected conditions and corresponding impacts.

To analyze hydrodynamic impacts imposed by expanding Kidney Island, several transects were placed within the study area. Flow across these transects was used to define the distribution of flow adjacent to the study area. Time series of flow rates were computed for each scenario. Averaged flows for each transect were computed for each scenario and pre- and post-expansion flow rates were compared to quantify changes in current patterns. Six transects were placed to form a "closed box" around the critical zone located at the confluence of the Fox River and the bay in order to quantify changes in flow distribution resulting from the expansion.

Comparing flows computed with pre- and post-expansion conditions, the expansion resulted in a slight decrease in flows at the transect extending from the CDF to Grassy Island. This decrease in flow is attributed to the CDF expansion reducing the conveyance through this transect. The average decrease in flow is equal to 3.8 percent of the net river flow. As a consequence of reducing the flow across this transect, increased flows were simulated across the remaining transects situated in the bay. (A negligible change in flows was found at the transect measuring Fox River discharges.)

The greatest increase in net flows exists in the critical zone through the channel. The average net flow through the channel increased by a proportion equal to 2.8 percent of the net river flow. The average flow entering Peats Lake increased by a proportion equal to 0.7 percent of the net river flow, whereas northerly flow in the vicinity of Grassy Island was increased by 0.9 percent of the net river flow. The net flow between the south shore of the bay and the CDF increased 0.9 percent of the net river flow.

Results from the WQM scenarios were analyzed to determine the temporal and spatial impacts of expansion upon water quality. Analysis of differences in average *DO* and average tracer concentrations between existing island and

expanded island conditions, for all 10 scenarios, indicated that the impacts of expansion were in the immediate vicinity of Kidney Island (mostly north of the island). The locations of the largest decreases in average *DO* in nine of the ten scenarios were in cells along the boundary of the expanded CDF. These cells experienced the largest changes in circulation between pre- and post-expansion conditions. Conditions near the island boundary are displaced northward to what was open water prior to expansion. Thus, comparisons of pre- and post-expansion conditions show differences along the post-expansion boundary.

Time series plots revealed that water quality was very similar at all locations, for all scenarios, for existing and plan conditions. Decreases in *DO* (from existing to plan conditions) were very short-term and were generally the result of slight time-phase shifts (from existing to plan) in *DO* during periods when *DO* was changing. These phase shifts resulted from slight changes in circulation around the island. Additionally, the boundary displacement effect discussed in the previous paragraph caused some of the differences north of the island. At stations removed from Kidney Island, there were only slight (practically imperceptible) differences between pre- and post-expansion *DO*, *CBOD_L*, and tracer concentrations. The expansion had no detectable impact on the water quality in Peats Lake for all scenarios.

Examination of tracer results revealed that a considerable portion of the Fox River waste loads pass between Kidney Island and the south shore of the bay. Thus, it is reasonable to expect that water quality conditions can be more degraded in this area for both pre- and post-expansion conditions, although the expansion does force slightly more flow (possibly increasing the flushing rate) between the island and the shore. The expansion does not degrade water quality from existing conditions in the area between the island and the south shore.

Using the maximum waste-load allocations, the water quality model indicated that there can be violations in the minimum *DO* standard of 5.0 mg/L for short periods of time for both the existing and plan conditions. Most violations were just below 5.0 mg/L and their locations were similar for existing and plan conditions for all scenarios. In seven of the ten scenarios, the cells that had the most violations after the expansion were either adjacent to or the same cell that had the most violations prior to expansion. In all scenarios, expansion only slightly changed the number of violations. Expansion did not degrade the *DO* in the Fox River mouth, which is a critical region for the purpose of waste-load allocations. A statistical analysis indicated that there was no significant difference in pre- and post-expansion *DO* violations for four of the five types of *DO* violation comparisons conducted.

Data collection and analysis in support of this modeling study were not within the scope of work set forth at the beginning of the study. However, at the last TRP meeting, a suggestion was made to collect some data in the vicinity of Kidney Island to determine the existing conditions around the island. During August 1992, *DO* measurements were made at five locations in the vicinity of Kidney Island. The *DO* was measured 1 ft below the surface and 1 ft above the bottom at each station three times daily for five days. The data,

along with a brief discussion, are in Appendix E. These data indicate that the *DO* in waters immediately adjacent to the north face of Kidney Island is lower than the *DO* in waters further out. These data support the model results of this study, which indicate that *DO* is lower near the Kidney Island boundary and that there is a gradient of increasing *DO* from the island boundary toward the north (i.e., bayward).

In summary, the WQM indicates that the planned CDF expansion should not adversely impact water quality conditions (e.g., *DO*). The only substantial differences in water quality (between pre- and post-expansion conditions) are in the immediate vicinity of Kidney Island, with the greatest decreases in *DO* usually along the north face of the island. Differences are due to changes in circulation around the island resulting from the CDF's retaining wall being extended into open water.

Potential changes in sediment resuspension patterns resulting from the CDF expansion were investigated. A qualitative assessment was made to delineate those areas in the lower bay that can be expected to experience an increase in bottom shear stress, the process controlling resuspension of sediment. Because cohesive sediment deposition patterns give an indication of sediment-adsorbed nutrient concentrations, this approach provides insight into the potential distribution of this material. The modeling algorithm used in this task is based on the concepts developed by Bijker, which estimate an effective bottom shear stress accounting for the combined effects of short wave orbital velocities and currents.

Local wind wave conditions were used for approximating the short wave effects in the lower bay. Significant wave height and period were estimated for fetch-limited and shallow-water conditions, and the maximum sustained wind speed and direction measured during the summer of 1984 were used to depict wind conditions. Root-mean-square water velocities were used to estimate current speeds.

The above algorithm was applied to each of the 10 scenarios previously discussed. Test results show that changes in sediment resuspension potential are limited to areas in the immediate vicinity of Kidney Island. An increase in resuspension potential is noted to the north of the expansion, whereas a reduction was found to the east and west of the expanded island. The increase in resuspension potential to the north of Kidney Island is attributed to the increased flow passing through this area. The decrease in resuspension potential to the west and east of the island is attributed to a sheltering effect caused by expanding the island. In all areas, changes in sediment resuspension potential are generally small, ranging from 0.5 to 1.0 percent. It is therefore concluded that the expansion will have a negligible effect on sediment resuspension within the lower bay.

References

- Ambrose, R. B., Vandergrift, S. B., and Wool, T. A. (1986). "WASP3, a hydrodynamic and water quality model - model theory, user's manual, and programmer's guide," Report No. EPA/600/3-86/034, U.S. Environmental Protection Agency, Environmental Research Laboratory, Athens, GA.
- Ammerman, J. F., and Azam, F. (1985). "Bacterial 5'-nucleotidase in aquatic ecosystems: A novel mechanism of phosphorus regeneration," *Science* 227, 1338-1340.
- Bijker, E. W. (1967). "Some considerations about scales for coastal models with movable bed," Delft Hydraulics Laboratory, Publication No. 50, Delft, The Netherlands.
- Bird, D. F., and Kalff, J. (1984). "Empirical relationships between bacterial abundance and chlorophyll concentration in fresh marine waters," *Canadian Journal of Fish and Aquatic Science* 44, 1015-1023.
- Boni, L., Carpent, E., Wynne, D., and Reti, M. (1989). "Alkaline phosphate activity in *Protonyaulax tamarensis*," *Journal of Plankton Research* 11, 879-885.
- Cerco, C. F. (1991). "Overview the Chesapeake Bay water quality," paper presented and submitted to the State of the Estuary Conference, San Francisco Estuary Project, May 30 - June 1, 1991, Berkeley, CA.
- Cerco, C. F., and Cole, T. M. (1989). "Calibrating the Chesapeake Bay water quality model," *Proceedings of Estuarine and Coastal Modeling*, Newport, RI.
- _____. (1993). "Verification of the time-varying, three-dimensional model of Chesapeake Bay," U.S. Army Engineer Waterways Experiment Station, Vicksburg, MS.
- Chapman, R. S. (1988). "Analysis and improvement of the numerical and physical mixing characteristics of the WASP box model," Contract Report submitted to the U.S. Army Engineer Waterways Experiment Station, Vicksburg, MS.

- Chrost, R. J., and Overbeck, J. (1987). "Kinetics of alkaline activity and phosphorus availability for phytoplankton and bacterioplankton in Lake Plubsee (North German Eutrophic Lake)." *Microbial Ecology* 13, 229-248.
- Cole, J. J., Findlay, S., and Pace, M. L. (1988). "Bacterial production in fresh and saltwater ecosystems: A cross system-overview," *Marine Ecology - Progress Series* 43, 1-10.
- DiToro, D. M., Fitzpatrick, J., and Thomann, R. V. (1983). "Documentation for Water Quality Analysis Simulation Program (WASP) and Model Verification Program (MVP)," EPA 600/3-81-044, U.S. Environmental Protection Agency, Environmental Research Laboratory, Athens, GA.
- DiToro, D., O'Connor, D. J., and Thomann, R. V. (1971). "A dynamic model of the phytoplankton population in the Sacramento-San Joaquin Delta," *Nonequilibrium Systems in Natural Water Chemistry*, Advances in Chemistry Series 106, American Chemical Society, Washington, DC, 131-180.
- Dortch, M. S. (1990). "Three-dimensional, Lagrangian residual transport computed from an intratidal hydrodynamic model," Technical Report EL-90-11, U.S. Army Engineer Waterways Experiment Station, Vicksburg, MS.
- Edinger, J. E., Brady, D. K., and Geyer, J. C. (1974). "Heat exchange and transport in the environment," Report No. 14, EPRI Publication No. 74-049-00-3, prepared for the Electric Power Research Institute, Palo Alto, CA.
- Edinger, J. E., Duttweiler, D., and Geyer, J. (1968). "The response of water temperatures to meteorological conditions," *Water Resources Research* 4(5).
- Garratt, J. R. (1977). "Review of drag coefficients over oceans and continents," *Monthly Weather Review* 105, 915-929.
- Hess, K., and Bosley, K. (1991). "Validation of a Tampa Bay circulation model," *2nd International Conference on Estuarine and Coastal Modeling*, Tampa, FL, 13-15 November 1991.
- Johnson, B. H., Heath, R. E., Hsieh, B. B., Kim, K. W., and Butler, H. L. (1991). "User's guide for a three-dimensional numerical hydrodynamic, salinity, and temperature model of Chesapeake Bay," Technical Report HL-91-20, U.S. Army Engineer Waterways Experiment Station, Hydraulics Laboratory, Vicksburg, MS.
- Jonsson, I. G. (1966). "Wave boundary layers and friction factors," *Proceedings 10th Coastal Engineering Conference*, ASCE, 127-148.
- Kennedy, J. A. (1991). "Long-term water quality monitoring of the lower Fox River and Green Bay: The first five years," *Program and Abstracts of 34th Conference on Great Lakes Research*, Buffalo, NY.

- Kremer, J. N., and Nixon, S. W. (1978). *A Coastal Marine Ecosystem*, Springer-Verlag, NY.
- Lauria, J. M., and Pimie, M. (1986). "Measurement of sediment interstitial water COD gradient for estimating the sediment oxygen demand," *Sediment Oxygen Demand: Processes, Modeling, and Measurement*, K. J. Hatcher, ed., Inst. Nat. Res., University of Georgia, Athens, GA, 367-388.
- Lee, K. K. (1984). "Lower Green Bay and Fox River currents and mass transports hydrodynamics study for two proposed confined disposal facilities," U.S. Army Engineer District, Detroit, Detroit, MI.
- Leonard, B. P. (1979). "A stable and accurate convection modelling procedure based on quadratic upstream interpolation," *Computer Methods in Applied Mechanics and Engineering* 19, 59-98.
- Matavulj, M., and Flint, K. P. (1987). "A model for acid and alkaline phosphatase activity in a small pond," *Microbial Ecology* 13, 141-158.
- Monod, J. (1949). "The Growth of Bacterial Cultures," *Annual Review of Microbiology* III, 371-394.
- Morel, F. M. M. (1983). *Principles of Aquatic Chemistry*, John Wiley and Sons, New York.
- Mortimer, C. H., and Fee, E. J. (1976). "Free surface oscillations and tides of Lakes Michigan and Superior," *Philosophical Transactions of the Royal Society of London* 281, 1-51.
- O'Connor, D. J. (1983). "Wind effects on gas-liquid transfer coefficients," *Journal, Environmental Engineering Division*, American Society of Civil Engineers 109, 731-752.
- Parsons, T., Takahasi, M. and Hargrave, B. (1984). "Chemical composition, the primary formation of particulate materials," *Biological Oceanographic Processes*, 3rd ed., Pergamon Press, Oxford, 37-114.
- Palenik, B., and Morel, F. M. (1990). "Amino acid utilization by marine phytoplankton: A novel mechanism," *Limnological Oceanography* 35, 260-269.
- Patterson, D. (1984). "Water quality modeling of the lower Fox River for wasteload allocation development: Cluster III - hydrodynamic modeling," Wisconsin Department of Natural Resources, Madison, WI.
- _____. (1985). "Water quality modeling of the lower Fox River for wasteload allocation development," PUBL-WR-123-86, Wisconsin Dept. of Nat. Res., Madison, WI.

- Powell, M. D. (1980). "Evaluation of diagnostic marine boundary-layer models applied of hurricane," *Monthly Weather Review*, pp 757-766.
- Rao, D. B., Mortimer, C. H., and Schwab, D. J. (1976). "Surface normal modes of Lake Michigan: Calculations compared with spectra of observer water level fluctuations," *Journal of Physical Oceanography* 6, 575-588.
- Roache, P. J. (1976). "Computational Fluid Dynamics," Hermosa Publishers, Albuquerque, NM.
- Rosenthal, S. L. (1971). "The response of a tropical cyclone model to variations in boundary layer parameters, initial conditions, lateral boundary conditions, and domain size," *Monthly Weather Review*, 99, 767-777.
- Schmalz, R. A. (1986). "A numerical investigation of hurricane induced water level fluctuations in Lake Okeechobee," Miscellaneous Paper CERC-86-12, U.S. Army Engineer Waterways Experiment Station, Vicksburg, MS.
- Sheng, Y. P. (1986). "A three-dimensional mathematical model of coastal, estuarine, and lake currents using boundary fitted grid," Report No. 585, A.R.A.P. Group Titan Systems, Princeton, NJ.
- Shore Protection Manual*. (1984). 4th ed., 2 Vols, U.S. Army Engineer Waterways Experiment Station, Coastal Engineering Research Center, U.S. Government Printing Office, Washington, D.C.
- Steele, J. H., and Menzel, D. W. (1962). "Conditions for maximum primary productivity in the mixed layer," *Deep Sea Research* 9, 39-49.
- Swain, A., and Bird, S. (1987). "Lower Green Bay hydrodynamic and mass transport," Miscellaneous Paper CERC-87-19, U.S. Army Engineer Waterways Experiment Station, Vicksburg, MS.
- Swart, D. H. (1974). "Offshore sediment transport and equilibrium beach profiles," Delft Hydraulics Lab. Pub. 131, Delft Univ., Delft, The Netherlands.
- Thomann, R. V., and Fitzpatrick, J. J. (1982). "Calibration and verification of a mathematical model of the eutrophication of the Potomac Estuary," Department of Environmental Services, Government of the District of Columbia, HydroQual, Inc., Mahwah, NJ.
- Thorton, K. W., and Lessum, A. S. (1978). "A temperature algorithm for modifying biological rates," *Transactions of the American Fisheries Society* 107, 284-287.
- Wang, J. D., and Connor, J. J. (1975). "Mathematical modelling of near coastal circulation," Report No. 200, Ralph M. Parsons Laboratory, Massachusetts Institute of Technology, Cambridge, MA.

Wezernak, C. T., and Gannon, J. J. (1968). "Evaluation of nitrification in streams," *Journal of the Sanitary Engineering Division*, ASCE SA5, 883-895.

Wu, J. (1980). "Wind-stress coefficients over sea surface near neutral conditions - a revisit," *Monthly Weather Review* 10, 727-740.

Appendix A

Charter of the Technical Review Panel

Lower Green Bay Hydrodynamic and Water Quality Model to Evaluate Expansion of Kidney Island

I. As set forth in Scope-of-Work, Lower Green Bay Hydrodynamic and Water Quality Model to Evaluate Expansion of Kidney Island, date 10 October 1990, a Technical Review Panel (TRP) is being established for the purpose of providing expert review and guidance on model development and application. The U.S. Army Engineer Waterways Experiment Station (WES) will conduct a model study to evaluate the impact of a proposed expansion of an existing Confined Disposal Facility on water quality within lower Green Bay. The TRP will provide technical oversight, review, and guidance for this study effort.

II. The TRP will function in a technical advisory capacity and will be responsible for a) providing technical review and guidance concerning work program execution and results, b) review of interim documents as work proceeds, and c) providing written comments following meetings and in response to request for review of interim study documents. A senior member of the WES staff will be the facilitator for the TRP, which will operate by consensus. Every attempt shall be made to respond to issues and concerns raised by TRP members; however, unanimity from all members will not be required. All unresolved issues and differences of opinion are to be documented.

III. Four meetings of the TRP are proposed during the course of the study as follows:

- 1) Project initiation meeting to review and provide guidance on the study approach and methodology.
- 2) First progress meeting to review study progress and to adjust study approach and methodology if necessary.
- 3) Second progress meeting to review study progress and results to date and to provide direction for study completion.
- 4) Final report meeting to achieve consensus on study results.

Meetings will be scheduled in advance at locations to facilitate travel (accessibility and reduced costs) for all members. The TRP may add or delete meetings as necessary as the study progresses.

Appendix B

Water Quality Model Kinetic Formulations

Algae

The Green Bay model contains one form of algae, blue-green. Blue-green algae are the predominant form of algae during the summer (Patterson 1985),¹ the period selected for model calibration and scenario evaluations. Sources and sinks of algae are:

Sources

Growth (production)

Sinks

Settling

Basal metabolism (e.g., respiration)

Predation

The last two sinks of algae are temporarily grouped here under the heading mortality. The governing equation for algal biomass is:

$$\frac{\partial B}{\partial t} = P_{GRO} B - MB - \frac{W_{salg}}{H} B \quad (B1)$$

where

B = biomass of algae, expressed as carbon (gm C m^{-3})

t = time (day)

P_{GRO} = rate constant for production of algae (day^{-1})

¹ See References at the end of the main text.

M = rate constant for mortality of algae (day^{-1})

W_{alg} = settling velocity of algae (m day^{-1})

H = water depth (m)

Production

Production by phytoplankton is determined by the availability of nutrients, by the intensity of light, and by the ambient temperature. The effects of each are considered to be multiplicative:

$$P_{\text{GRO}} = P_{\text{max}} f(N) f(I) f(T) \quad (\text{B2})$$

where

P_{max} = production rate under optimal conditions (day^{-1})

$f(N)$ = effect of suboptimal nutrient concentration ($0 \leq f(N) \leq 1$)

$f(I)$ = effect of suboptimal illumination ($0 \leq f(I) \leq 1$)

$f(T)$ = effect of suboptimal temperature ($0 \leq f(T) \leq 1$)

Carbon, nitrogen, and phosphorus are the primary nutrients required for algal growth. Carbon is usually available in excess and is not considered. The effects of nutrients on growth are described by the formulation commonly referred to as "Monod kinetics" (Monod 1949) in which growth is dependent upon nutrient availability at low nutrient concentrations but independent of nutrients at high concentrations. Liebig's "law of the minimum" is invoked so that growth is determined by the nutrient in least supply:

$$f(N) = \text{minimum} \left[\frac{\frac{NH_4 + NO_3}{K_{hn} + NH_4 + NO_3}}{\frac{PO_4}{K_{hp} + PO_4}} \right] \quad (\text{B3})$$

where

NH_4 = ammonium concentration, as nitrogen (gm N m^{-3})

NO_3 = nitrate plus nitrite concentration, as nitrogen (gm N m^{-3})

K_{hn} = half-saturation concentration for nitrogen uptake (gm N m^{-3})

PO_4 = dissolved phosphate concentration, as phosphorus (gm P m^{-3})

K_{hp} = half-saturation concentration for phosphorus uptake (gm P m^{-3})

Some blue-green algae, notably the bloom-forming genus *Anabaena*, are capable of fixing atmospheric nitrogen. The nitrogen limitation expressed in Equation 3 does not apply to nitrogen fixers.

Algal production increases as a function of light intensity until an optimal intensity is reached. Beyond the optimal intensity, production declines as intensity increases. Steele's equation (DiToro, O'Connor, and Thomann 1971) describes this phenomenon:

$$f(I) = \frac{I}{I_s} \exp \left[1 - \frac{I}{I_s} \right] \quad (\text{B4})$$

where

I = illumination rate (langley day^{-1})

I_s = optimal illumination rate (langley day^{-1})

Steele's equation describes the effect of light intensity upon algae at a specific point. Light intensity is not uniform throughout a body of water, but instead decreases exponentially with increasing depth according to

$$I = I_o e^{-\lambda z} \quad (\text{B5})$$

where

I_o = illumination at water surface (langley day^{-1})

λ = light attenuation coefficient (m^{-1})

z = depth (m)

Steele's equation is for the instantaneous light limitation and must be integrated over a period of time for model use. In this study, Steele's equation is integrated over the period of a day. Substituting Equation 5 into Equation 4 and integrating with respect to depth (for depth averaging) and time yields

$$f(I) = \frac{2.72 f_{day}}{\lambda H} (e^{ab} - e^{at}) \quad (\text{B6})$$

where

$$\alpha b = - \frac{I_o}{f_{day} I_s} e^{-\lambda H}$$

$$\alpha x = - \frac{I_o}{f_{day} I_s}$$

and where

$$f_{day} = \text{fractional daylength, i.e., length of day with sunlight,} \\ (0 \leq f_{day} \leq 1)$$

Now all light intensity variables of Equation 6 are daily average values. Optimal illumination I_s for photosynthesis depends on algal taxonomy, duration of exposure, temperature, nutritional status, and previous acclimation. Variations in optimal illumination are largely due to adaptations by algae intended to maximize production in a variable environment. Steele and Menzel (1962) noted the result of adaptations is that optimal illumination is a consistent fraction ($\approx 50\%$) of daily illumination. Kremer and Nixon (1978) reported an analogous finding that maximum algal production occurs at a constant depth (≈ 1 m) in the water column. Their approach is adopted here so that optimal illumination is expressed

$$I_s = I_a e^{-\lambda z_{optx}} \quad (B7)$$

where

$$I_a = \text{time-weighted average daily illumination (langley day}^{-1}\text{)}$$

$$z_{optx} = \text{depth of maximum algal production (m)}$$

A minimum I_s is specified for optimal illumination so that algae do not thrive at extremely low light levels. The time required for algae to adapt to changes in illumination is recognized by computing I_s based on a time-weighted average of daily illumination, i.e.,

$$I_a = 0.7 I_o + 0.2 I_1 + 0.1 I_2 \quad (B8)$$

where

$$I_1 = \text{daily illumination one day preceding model day (langley day}^{-1}\text{)}$$

$$I_2 = \text{daily illumination two days preceding model day (langley day}^{-1}\text{)}$$

Light attenuation is the sum of two forms: non-algal light attenuation (λ_{na}) and algal self shading (λ_{as}). The non-algal form of light attenuation is the light attenuation due to water color and suspended solids. Often the effluent from a wastewater discharge is high in color or suspended solids and exerts a carbonaceous biochemical oxygen demand (*CBOD*). Therefore non-algal shading is expressed as a function of *CBOD* in regions containing point source discharges as follows:

$$\lambda_{na} = 0.8 + 0.02(CBODL + CBODR) \quad (B9)$$

Equation 9, which relates non-algal shading to *CBOD*, was developed from observed secchi depths and model *CBOD* values. In other regions, such as the upper Fox River and open bays, non-algal shading is set to a constant value.

Algal self-shading is the light attenuation resulting from light adsorption by chlorophyll. It is expressed as a function of algal biomass.

$$\lambda_{as} = K_{chl} \frac{B}{A_{ca}} \quad (B10)$$

where

K_{chl} = light attenuation coefficient for chlorophyll ($m^2/gm\ chl$)

A_{ca} = algal carbon to chlorophyll ratio ($gm\ C/gm\ chl$)

Algal production is temperature (*T*) dependent. The influence of temperature upon algal growth can be represented by the function shown in Figure B1. Optimum growth occurs for a limited temperature range. Growth diminishes for temperatures above and below that range. The mathematical representation of Figure 1 (Thorton and Lessem 1978) is expressed as

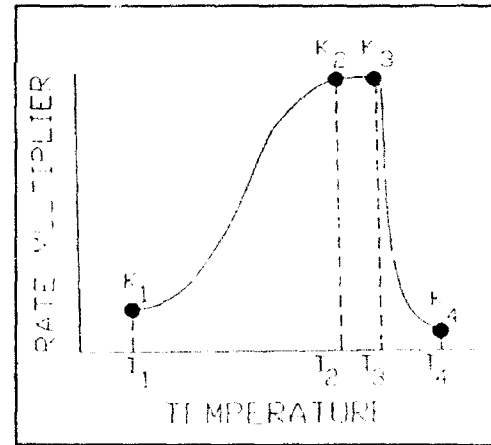


Figure B1. Rate multipliers for algal growth

$$f(T) = \begin{bmatrix} 0 & T < T_1 \\ \frac{K_1 e^{\lambda_1(T-T_1)}}{1 + K_1 [e^{\lambda_1(T-T_1)} - 1]} & T_1 < T < T_4 \\ \frac{K_4 e^{\lambda_2(T_4-T)}}{1 + K_4 [e^{\lambda_2(T_4-T)} - 1]} & T_1 < T < T_4 \\ 0 & T_4 < T \end{bmatrix} \quad (B'1)$$

where

$$\lambda_1 = \frac{1}{T_2 - T_1} \ln \left[\frac{K_2(1-K_1)}{K_1(1-K_2)} \right]$$

$$\lambda_2 = \frac{1}{T_4 - T_3} \ln \left[\frac{K_3(1-K_4)}{K_4(1-K_3)} \right]$$

Maximum growth rates are multiplied by Equation 11 to determine the growth rate at a specific temperature. Values for T_1 through T_4 , temperature parameters ($^{\circ}\text{C}$), along with values for the rate multiplier parameters K_1 through K_4 are user specified. The values of K_2 and K_3 are set equal to 0.98. T is the local water temperature.

Mortality

Mortality of phytoplankton results from basal metabolism and predation, or

$$M = BM + PR \quad (\text{B12})$$

where

BM = basal metabolic rate of algae (day^{-1})

PR = predation rate on algae (day^{-1})

As employed here, basal metabolism is the sum of all internal processes that decrease algal biomass. A portion of the metabolism is respiration and may be viewed as a reversal of production. In respiration, carbon and nutrients are returned to the environment accompanied by the consumption of dissolved oxygen (DO). A second internal sink of biomass is excretion (exudation), which is modeled as a return of $CBOD$ to the water column.

Respiration cannot proceed in the absence of DO . Basal metabolism cannot decrease in proportion to decreasing oxygen, however, or algae would approach immortality under anoxic conditions. To solve this dilemma, basal metabolism is considered to be independent of DO , but the distribution of metabolism between respiration and excretion is DO -dependent. When oxygen is freely available, respiration is a large fraction of the total. When oxygen is restricted, excretion becomes dominant.

BM is commonly considered to be an exponentially increasing function of temperature:

$$BM = BM_{ref} e^{K_{bt}(T-T_{ref})} \quad (B13)$$

where

BM_{ref} = metabolic rate of algae at T_{ref} (day^{-1})

K_{bt} = effect of temperature on algae metabolism ($^{\circ}\text{C}^{-1}$)

T_{ref} = reference temperature for algae metabolism ($^{\circ}\text{C}$)

The PR is identical to basal metabolism, or

$$PR = PR_{ref} e^{K_{bt}(T-T_{ref})} \quad (B14)$$

where

PR_{ref} = predation rate on algae at T_{ref} (day^{-1})

The difference in predation and basal metabolism lies in the distribution of the end products of these processes.

Effect of algae on nitrogen

Algae take up NH_4 and NO_3 during production and release NH_4 and organic nitrogen through mortality. No attempt is made to model the preference of algae for either NO_3 or NH_4 . Instead, algal uptake of nitrogen is partitioned in proportion to the concentrations of NO_3 and NH_4 according to

$$Pa = \text{NH}_4 \left[\frac{\text{NO}_3}{(K_{hn} + \text{NH}_4)(K_{hn} + \text{NO}_3)} + \frac{K_{hn}}{(\text{NH}_4 + \text{NO}_3)(K_{hn} + \text{NO}_3)} \right] \quad (B15)$$

where

Pa = algal preference for NH_4 ($0 \leq Pa \leq 1$)

Algal biomass is expressed in units of carbon. Algal uptake and release of nitrogen are quantified through a proportionality constant that represents the average ratio of nitrogen to carbon in algal biomass. As with algal uptake, the

preference of algal nitrogen through mortality is represented by distribution coefficients. The effects of algae on the nitrogen state variables are expressed as

$$\frac{\partial NH_4}{\partial t} = BM F_{in} A_{nc} B + PR F_{pin} A_{nc} B - Pa P_{GRO} A_{nc} B \quad (B16)$$

$$\frac{\partial NO_3}{\partial t} = - (1 - Pa) P_{GRO} A_{nc} B \quad (B17)$$

$$\frac{\partial TON}{\partial t} = BM F_{on} A_{nc} B + PR F_{pon} A_{nc} B \quad (B18)$$

where

A_{nc} = nitrogen-to-carbon ratio of algae (gm N / gm C)

F_{in} = fraction of inorganic nitrogen produced by metabolism
($0 \leq F_{in} \leq 1$)

F_{on} = fraction of organic nitrogen produced by metabolism ($0 \leq F_{on} \leq 1$)

F_{pin} = fraction of inorganic nitrogen produced by predation
($0 \leq F_{pin} \leq 1$)

F_{pon} = fraction of organic nitrogen produced by predation ($0 \leq F_{pon} \leq 1$)

TON = concentration of total organic nitrogen (gm N m⁻³)

The sums of the metabolism fractions and the predation fractions must each equal unity.

Effect of algae on phosphorus

Algae utilize PO_4 during production and release PO_4 and organic phosphorus through mortality. Since the total phosphate state variable includes both intra- and extracellular PO_4 , no explicit representation of the effect of algae on PO_4 is necessary. Distribution of total phosphate is determined by partition coefficients as detailed in the "Phosphorus" section. The equations that express the effects of algae on organic phosphorus closely follow the equations for nitrogen

$$\frac{\partial TOP}{\partial t} = BM F_{op} A_{pc} B + PR F_{pop} A_{pc} B \quad (B19)$$

where

A_{pc} = phosphorus-to-carbon ratio of algae (gm P / gm C)

F_{op} = fraction of organic phosphorus produced by metabolism
($0 \leq F_{op} \leq 1$)

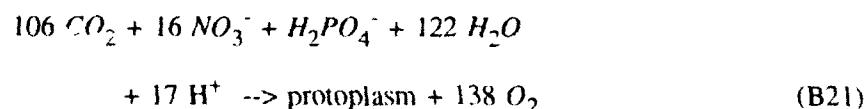
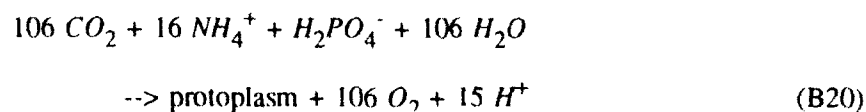
F_{pop} = fraction of organic phosphorus produced by predation
($0 \leq F_{pop} \leq 1$)

TOP = concentration of total organic phosphorus (gm P m⁻³)

The sums of the metabolism and respiration fractions must equal unity.

Effect of algae on dissolved oxygen

Algae produce oxygen during photosynthesis and consume oxygen through respiration. The quantity produced depends on the form of nitrogen taken up. Since oxygen is released in the reduction of NO_3 , more oxygen is produced per unit of carbon fixed when NO_3 is the algal nitrogen source than when NH_4 is the algal nitrogen source. Equations describing algal uptake of carbon and nitrogen and production of DO are (Morel 1983):



From the above equations, it is evident that when NH_4 is the nitrogen source, 1 mole of oxygen is produced per mole of carbon dioxide fixed. When NO_3 is the nitrogen source, 1.3 moles of oxygen are produced per mole of carbon dioxide fixed. When both NO_3 and NH_4 are present, the moles of oxygen produced by photosynthesis vary linearly between 1 and 1.3 in relation to the algal preference for NH_4 . This variation is modeled as $(1.3 - 0.3 Pa)$.

The equation that describes the effect of algae upon *DO* in the model is

$$\frac{\partial DO}{\partial t} = (1.3 - 0.3 Pa) P_{GRO} A_{dcr} B - \frac{DO}{K_{hr} + DO} BM A_{dcr} B \quad (B22)$$

where

A_{dcr} = dissolved oxygen-to-carbon ratio of algae (gm O₂ / gm C)

K_{hr} = oxygen half-saturation concentration for respiration (gm O₂ m⁻³)

Effect of algae on *CBOD*

Algal predation/death causes a release of organic carbon that can exert an oxygen demand. This oxygen demand is expressed as *CBOD*. Excretion (i.e., that portion of algal metabolism that does not exert a direct oxygen demand, as respiration does, contributes to *CBOD*. The effect of algae on *CBOD* is expressed as

$$\frac{\partial CBOD}{\partial t} = A_{dcr} PR B + \frac{K_{hr}}{K_{hr} + DO} BM A_{dcr} B \quad (B23)$$

The other sources and sinks of *CBOD* are not shown in Equation 23, but will be added in the section on *CBOD* below. Additionally, Equation 23 does not distinguish between labile and refractory *CBOD*, but this distinction will be shown in the latter section.

Nitrogen

The following processes affect nitrogen in this model: algal production, metabolism, and predation; mineralization of organic nitrogen to ammonium; settling; nitrification; and denitrification. Effects on nitrogen resulting from algal production, metabolism, and predation have already been detailed. Descriptions of mineralization, nitrification, denitrification, and settling follow.

Mineralization

For purposes of this model, mineralization is defined as the process by which total organic nitrogen (*TON*) is converted to *NH₄*. Conversion of *TON* to *NH₄* proceeds through the sequence of hydrolysis and mineralization. The formulation for mineralization is based on the following assumptions: (a) rate

of mineralization is proportional to available substrate; (b) rate of mineralization is proportional to algal biomass; and (c) mineralization is accelerated when inorganic nitrogen is insufficient to supply algal demand.

Assumption (a) states that mineralization cannot proceed in the absence of TON. The assumption is in agreement with first-order kinetics that are used here. Assumption (b) recognizes that nitrogen transformation rates are influenced by the biomass of heterotrophic organisms that mediate the transformations. While bacteria and zooplankton are not quantified in the model, observations in numerous systems (Bird and Kalff 1984; Cole, Findlay, and Pace 1988) indicate their biomass is proportional to algal biomass. Consequently, algal biomass is an indicator of heterotrophic biomass and the relation of nitrogen transformations to algal biomass is appropriate. Assumption (c) is based largely on the analogy to phosphorus mineralization for which the rationale will be clearly stated. The assumption is partially justified, however, by noting that algae can supply their nitrogen needs through the utilization of urea and amino acids (Palenik and Morel 1990), compounds that are classified as a dissolved form of TON in the model system. Parsons, Takanashi, and Hargrave (1984) indicate that urea is utilized after NH_4 is exhausted and amino acids are utilized after inorganic nitrogen and urea are exhausted. Formulation of the mineralization rate, consistent with these assumptions, is

$$K_{\min} = K_{d\min} + \frac{K_{hn}}{K_{hn} + NH_4 + NO_3} K_{dnalg} B \quad (B24)$$

where

K_{\min} = mineralization rate of TON (day^{-1})

$K_{d\min}$ = minimum mineralization rate of TON (day^{-1})

K_{dnalg} = constant that relates mineralization of TON to algal biomass ($\text{m}^3 / \text{gm C day}^{-1}$)

Mineralization rates are temperature-dependent. Changes in these rates due to temperature are indicated by

$$K_{\min}(T) = K_{\min} f(T) = K_{\min}(20^\circ\text{C}) \theta^{(T-20)} \quad (B25)$$

where

$f(T)$ = temperature correction term for rates, dimensionless

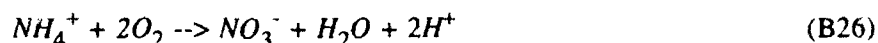
$K_{\min}(T)$ = mineralization rate at temperature T (day^{-1})

$K_{\min}(20^{\circ}\text{C}) = \text{mineralization rate at } 20^{\circ}\text{C (day}^{-1}\text{)}$

$\theta = \text{dimensionless temperature correction factor}$

Nitrification

Nitrification is a process mediated by specialized groups of autotrophic bacteria that obtain energy through the oxidation of ammonium to nitrite and oxidation of nitrite to nitrate. A simplified expression for complete nitrification is



Equation B24 indicates that 2 moles of oxygen are required to nitrify one mole of ammonium into nitrate. This simplified equation is not strictly true, however. Cell synthesis by nitrifying bacteria is accomplished by the fixation of carbon dioxide so that less than 2 moles of oxygen are consumed per mole of ammonium utilized (Wezernak and Gannon 1968). Nitrification is modeled as a complete Monod function rather than first order kinetics. At low concentrations of NH_4 , the Monod kinetics approach first order kinetics. The Monod function depends on temperature and the amount of available ammonium and dissolved oxygen according to

$$NR = \frac{DO}{K_{hnd} + DO} \frac{NH_4}{K_{hnn} + NH_4} f(T) NR_{\max} \quad (\text{B27})$$

where

$NR = \text{nitrification rate (gm N m}^{-3} \text{ day}^{-1}\text{)}$

$NR_{\max} = \text{maximum nitrification rate at optimal temperature (gm N m}^{-3} \text{ day}^{-1}\text{)}$

$K_{hnd} = \text{half-saturation concentration of DO required for nitrification (gm O}_2 \text{ m}^{-3}\text{)}$

$K_{hnn} = \text{half-saturation concentration of NH}_4 \text{ required for nitrification (gm N m}^{-3}\text{)}$

The effect of temperature is given by Equation 25, with appropriate changes in notation and the value for θ . The effect of nitrification on ammonium is expressed as

$$\frac{\partial NH_4}{\partial t} = -NR \quad (B28)$$

Thus, the effect of nitrification on nitrate is expressed as

$$\frac{\partial NO_3}{\partial t} = NR \quad (B29)$$

The effect of nitrification on dissolved oxygen is expressed as

$$\frac{\partial DO}{\partial t} = -A_{nd} NR \quad (B30)$$

where

A_{nd} = mass DO consumed per mass NH_4-N nitrified ($gm\ O_2 / gm\ N$)

Denitrification

Denitrification is a process in which bacteria use NO_3 instead of O_2 while they utilize organics (i.e., $CBOD$). NO_3 is converted to N_2 in this process. The effects of denitrification in the water column are negligible except during periods of very low DO and depend on the availability of nitrate. At low DO levels, the bacteria stop using O_2 and begin using NO_3 (Thomann and Fitzpatrick 1982). Denitrification can also occur in bottom sediments. As nitrate in the sediments is reduced, nitrate in the overlying water column can diffuse into the sediments. Therefore, denitrification is modeled as an NO_3 sink for the water column and sediments. Water column denitrification is modeled as

$$DEN = A_{no} K_{denit} f(T) \frac{NO_3}{NO_3 + K_{ndn}} \frac{K_{odn}}{K_{odn} + DO} CBOD \quad (B31)$$

where

DEN = water column denitrification rate ($gm\ N\ m^{-3}\ day^{-1}$)

A_{no} = mass of nitrate nitrogen consumed per mass of $CBOD$ (as oxygen) removed by denitrification ($gm\ N / gm\ O_2$)

K_{denit} = denitrification rate at 20°C (day⁻¹)

K_{odn} = half-saturation concentration of *DO* for denitrification
(gm O₂ m⁻³)

K_{ndn} = half-saturation concentration of nitrate for denitrification
(gm N m⁻³)

Water column denitrification results in a decrease in *CBOD* due to the decrease in organics. The change in *CBOD* resulting from water column denitrification is

$$\frac{\partial CBOD}{\partial t} = - \frac{DEN}{A_{no}} \quad (B32)$$

The removal of nitrate from the water column as a result of bottom sediment denitrification is modeled as a mass transfer process where nitrate is transferred from the water column to the sediments according to

$$SDEN = \frac{K_{sdn}}{H} NO_3 \quad (B33)$$

where

$SDEN$ = nitrate removal rate through sediment denitrification
(gm N m⁻³ day⁻¹)

K_{sdn} = water column-to-sediment mass transfer rate for nitrate
(m day⁻¹)

Equation 33 actually represents the diffusion of nitrate into the sediments where the water column concentration is much higher than the sediment concentration of nitrate; thus, the mass transfer rate is multiplied by the nitrate gradient, which is simply the water concentration. Equation 33 must be divided by water depth for proper representation.

Settling

TON represents both dissolved and particulate forms of organic nitrogen. No differentiation between these forms is made in this model, but settling of the particulate form is accomplished by allowing a fraction of the *TON* to settle. This fraction is not specified explicitly, rather it is reflected through the value selected for the settling velocity. Removal of *TON* by settling is modeled as

$$\frac{\partial TON}{\partial t} = - \frac{W_{sn}}{H} TON \quad (B34)$$

where

W_{sn} = effective settling velocity of TON (m day⁻¹)

Summary of nitrogen equations

The equations for NH_4-N , TON , and NO_3-N are written by summing all previously described sources and sinks:

$$\begin{aligned} \frac{\partial NH_4}{\partial t} = & BM F_{in} A_{nc} B + PR F_{pin} A_{nc} B - Pa P_{GRO} A_{nc} B \\ & + K_{min} f(T) TON - NR \end{aligned} \quad (B35)$$

$$\begin{aligned} \frac{\partial TON}{\partial t} = & BM F_{on} A_{nc} B + PR F_{pon} A_{nc} B - K_{min} f(T) TON \\ & - \frac{W_{sn}}{H} TON \end{aligned} \quad (B36)$$

$$\frac{\partial NO_3}{\partial t} = -(1-p_a) P_{GRO} A_{nc} B - DEN + NR - SDEN \quad (B37)$$

Phosphorus

Processes in the phosphorus system are largely analogous to the nitrogen system. Phosphorus sources and sinks include algal production, metabolism, and predation; mineralization of organic phosphorus; settling; and sediment release. Effects on phosphorus of algal production, metabolism, and predation have already been detailed. Descriptions of mineralization, settling, and sediment release follow.

Mineralization

Analogous to nitrogen, mineralization is defined as the process by which *TOP* is converted to PO_4 . Conversion of *TOP* to PO_4 proceeds through the sequence of hydrolysis and mineralization. The formulation for mineralization is based on the three assumptions detailed for nitrogen.

A brief review of mineralization of *TOP* clarifies the representations of mineralization employed in the model. Although zooplankton excretion is of fundamental importance in phosphorus recycling, a second pathway for mineralization is through the release of nucleotidase and phosphatase enzymes by bacteria (Ammerman and Azam 1985, Chrost and Overbeck 1987) and algae (Matavulj and Flint 1987, Chrost and Overbeck 1987, Boni et al. 1989). Since the algae themselves release the enzyme and since zooplankton and bacterial abundance are related to algal biomass, the *TOP* mineralization rate may be rationally related to algal biomass. A most remarkable property of the enzyme process is that alkaline phosphatase activity is inversely proportional to ambient PO_4 concentration (Chrost and Overbeck 1987, Boni et al. 1989). Put in different terms, when PO_4 is scarce, algae stimulate production of an enzyme that mineralizes *TOP* to PO_4 . Simulation of this process in the model is obtained by relating mineralization to the algal phosphorus nutrient limitation. By this relationship, mineralization is highest when algae are strongly phosphorus-limited and is relatively low when no limitation occurs.

The expression for the mineralization rate is

$$K_{pmin} = K_{dpmn} + \frac{K_{hp}}{K_{hp} + PO_4} K_{dpalg} B \quad (B38)$$

where

K_{pmin} = mineralization rate of *TOP* (day^{-1})

K_{dpmn} = minimum mineralization rate of *TOP* (day^{-1})

K_{dpalg} = constant that relates *TOP* mineralization rate to algal biomass ($\text{m}^3 / \text{gm C day}^{-1}$)

The mineralization rate is a function of temperature as expressed by Equation 25 with appropriate changes in notation.

Phosphate partitioning

One fraction of total phosphorus in the water column is phosphorus incorporated in algal biomass. This fraction is computed in the model as the product of algal biomass and A_{pc} , the phosphorus-to-carbon ratio. In the

environment, algae adjust their phosphorus content in response to external conditions. Algal phosphorus content is high when external phosphorus is abundant and phosphorus content is low when phosphorus is scarce. The adaptation of algae to their environment indicates A_{pc} should be a variable in the model. Treatment of A_{pc} as a variable, however, complicates specifications and computation of phosphorus kinetics. The complication is avoided if intracellular and extracellular phosphorus are treated and transported as a single state variable. Intracellular and extracellular concentrations are determined by equilibrium partitioning of their sum.

The phosphorus-to-carbon ratio can be calculated by an empirical function (Cерco and Cole 1992)

$$A_{pc} = \frac{1}{pc_1 + pc_2 e^{-pc_3 PO_4}} \quad (B39)$$

where

pc_1 = parameter that determines maximum algal phosphorus-to-carbon ratio (gm C / gm P)

pc_2 = parameter that determines minimum algal phosphorus to carbon ratio (gm C / gm P)

pc_3 = parameter that expresses the effect of PO_4 on algal phosphorus to carbon ratio (m^3 / gm P)

Meaning is assigned to the parameters in Equation 39 by examining limiting cases. When dissolved PO_4 is available in excess, $A_{pc} = 1/pc_1$, the maximum phosphorus-to-carbon ratio. When dissolved PO_4 is scarce, $A_{pc} = 1/(pc_1 + pc_2)$, the minimum phosphorus-to-carbon ratio. Parameter pc_3 determines the PO_4 range over which limiting values of A_{pc} are attained.

Settling and sediment release

The PO_4 incorporated in algal biomass settles at the same rate as the algae. A portion of the TOP is particulate and is also allowed to settle.

A constant, zero-order sediment release rate is implemented to account for the PO_4 that may diffuse or be resuspended from the sediments to the water column.

Summary of phosphorus equations

The PO_4 balance is written by summing the previously described sources and sinks.

$$\frac{\partial PO_4}{\partial t} = - \frac{W_{salg}}{H} A_{pc} B + K_{pmin} f(T) TOP + \frac{SED_p}{H} \quad (B40)$$

where

SED_p = sediment release rate of PO_4 ($g P m^{-2} day^{-1}$)

Algal uptake and release of PO_4 represents an exchange of PO_4 fractions rather than a source or sink of PO_4 . Consequently, no algal source or sink terms are included in the PO_4 kinetics equation.

The equation for TOP is written as

$$\begin{aligned} \frac{\partial TOP}{\partial t} = & BM F_{op} A_{pc} B + PR F_{pop} A_{pc} B - K_{pmin} f(T) TOP \\ & - \frac{W_{sop}}{H} TOP \end{aligned} \quad (B41)$$

where

W_{sop} = effective settling velocity for TOP ($m day^{-1}$)

CBOD

CBOD is fractioned into two variables, labile (fast) and refractory (slow) biodegradation. Terms are included for removal of **CBOD** by biological activity (i.e., biodegradation), settling, and denitrification. Algal predation (i.e., mortality) is a source of labile and refractory **CBOD**. During periods of low DO , algal excretion contributes to labile **CBOD** to be exerted as an oxygen demand upon DO recovery. Additionally, sediment oxygen demand (SOD) contributes to labile **CBOD** if the water column DO is low. All of these processes have been discussed previously, except for biodegradation and SOD.

Biodegradation of CBOD

First-order labile and refractory biodegradation, modified by DO -dependent Monod functions, are modeled as

$$DECAY_L = K_{I_L} f(T) \frac{DO}{DO + K_{DO}} CBOD_L \quad (B42)$$

$$DECAY_R = K_{I_R} f(T) \frac{DO}{DO + K_{DO}} CBOD_R \quad (B43)$$

where

$DECAY_L$ = labile $CBOD$ decay ($\text{gm O}_2 \text{ m}^{-3} \text{ day}^{-1}$) 100/100

$DECAY_R$ = refractory $CBOD$ decay ($\text{gm O}_2 \text{ m}^{-3} \text{ day}^{-1}$)

$CBOD_L$ = ultimate labile $CBOD$ ($\text{gm O}_2 \text{ m}^{-3}$)

$CBOD_R$ = ultimate refractory $CBOD$ ($\text{gm O}_2 \text{ m}^{-3}$)

K_{I_L} = aerobic labile $CBOD$ decay rate at 20°C (day^{-1})

K_{I_R} = aerobic refractory $CBOD$ decay rate at 20°C (day^{-1})

K_{DO} = oxygen half-saturation concentration required for aerobic $CBOD$ decay ($\text{gm O}_2 \text{ m}^{-3}$)

Temperature dependence in the above equations is according to Equation B25.

SOD Source of $CBOD$

Sediment diagenesis (i.e., decay and mineralization) occurs even when the water column DO is low. However, rather than exerting an oxygen demand in the absence of DO , other substances are reduced (such as iron, manganese, nitrate, sulfate) thus exerting a chemical oxygen demand (COD) (Lauria and Pirmie 1986). The COD that is released during low DO conditions is added to the $CBOD$ pool as follows:

$$SED_{CBOD} = SOD f(T) \frac{K_{sco}}{K_{sco} + DO} \quad (B44)$$

where

SED_{CBOD} = sediment source of $CBOD$ ($\text{gm O}_2 \text{ m}^{-3} \text{ day}^{-1}$)

SOD = sediment oxygen demand ($\text{gm O m}^{-3} \text{ day}^{-1}$)

K_{sco} = oxygen half-saturation concentration for SOD release of $CBOD$ ($\text{gm O}_2 \text{ m}^{-3}$)

Summary of *CBOD* equations

The sources and sinks of labile and refractory *CBOD* are summarized as

$$\begin{aligned} \frac{\partial CBOD_L}{\partial t} = & - DECA Y_L - \frac{W_{cl}}{H} CBOD_L + \alpha_L A_{dcr} PR B \\ & + A_{dcr} BM \frac{K_{hr}}{K_{hr} + DO} B - \alpha_{DEN} \frac{DEN}{A_{no}} + SED_{CBOD} \end{aligned} \quad (B45)$$

$$\begin{aligned} \frac{\partial CBOD_R}{\partial t} = & - DECA Y_R - \frac{W_{cr}}{H} CBOD_R + (1 - \alpha_L) A_{dcr} PR B \\ & - (1 - \alpha_{DEN}) \frac{DEN}{A_{no}} \end{aligned} \quad (B46)$$

where

W_{cl} = labile *CBOD* settling velocity (m day⁻¹)

W_{cr} = refractory *CBOD* settling velocity (m day⁻¹)

α_L = fraction of algal *CBOD* contribution that is labile

α_{DEN} = fraction of *CBOD* decrease resulting from water column denitrification that is labile

Both labile and refractory *CBOD* are computed as ultimate values. However, measurements for *CBOD* are usually values at the end of five days. The conversions between ultimate and five-day labile and refractory *CBOD* are:

$$CBOD_{L5} = CBOD_L (1 - e^{-5 K I_L}) \quad (B47)$$

$$CBOD_{R5} = CBOD_R (1 - e^{-5 K I_R}) \quad (B48)$$

where

$CBOD_{L5}$ = 5-day labile *CBOD* (gm O₂ m⁻³)

$CBOD_{R5}$ = 5-day refractory *CBOD* (gm O₂ m⁻³)

Dissolved Oxygen

Sources of *DO* in the water column include algal photosynthesis and atmospheric reaeration; sinks include algal respiration, nitrification, carbonaceous biochemical oxygen demand, and sediment oxygen demand. Algal interactions and the effects of *CBOD* and nitrification were presented earlier. The effects of reaeration and sediment oxygen demand are discussed below.

Reaeration

The effect of reaeration is modeled as

$$\frac{\partial DO}{\partial t} = \frac{K_r}{H} (DO_s - DO) \quad (B49)$$

where

K_r = *DO* reaeration coefficient (m day⁻¹)

DO_s = dissolved oxygen saturation concentration (gm O₂ m⁻³)

The reaeration coefficient is calculated using the O'Connor formulation (1983) for wind-driven gas transfer. This approach was selected since it is believed that reaeration is dominated by wind stress more so than bottom stress in lower Green Bay. Local wind speeds are used to compute K_r .

Sediment Oxygen Demand

SOD represents oxygen demand exerted by benthic sediments. The *SOD* rate coefficient is specified by the user as a flux. This rate is divided by the water depth in order to distribute the *SOD* throughout the water column. A Monod term is included, which accounts for the effect of *DO* concentrations on limiting *SOD* exertion on *DO*. Temperature dependence is also included. The equation for *SOD* is

$$SOD = \frac{DO}{DO + K_h} f(T) \frac{K_{sd}}{H} \quad (B50)$$

where

K_{sod} = sediment oxygen demand rate ($\text{gm O}_2 \text{ m}^{-2} \text{ day}^{-1}$)

K_h = oxygen half-saturation concentration for sediment oxygen demand exertion on DO ($\text{gm O}_2 \text{ m}^{-3}$)

Summary of DO sources and sinks

The complete kinetics for DO are:

$$\begin{aligned} \frac{\partial DO}{\partial t} = & (1.3 - 0.3 Pa) P_{GRO} A_{dcr} B - \frac{DO}{K_{hr} + DO} BM A_{dcr} B \\ & - A_{nd} NR - DECA Y_L - DECA Y_R \quad (B51) \\ & - SOD + \frac{K_r}{H} (DO_s - DO) \end{aligned}$$

Temperature

There are several sources and sinks of heat that affect the overall heat balance and temperature of a water body. These can be described by

$$H_N = H_S + H_L - H_E - H_B \pm H_C \quad (B52)$$

where

H_N = net heat flux (W m^{-2})

H_S = net short-wave radiation

H_L = net long-wave radiation

H_E = heat loss due to evaporation

H_B = heat loss due to back radiation of water

H_C = heat loss due to conduction at water surface

The temperature change with respect to time is computed as

$$\frac{\partial T}{\partial t} = \frac{H_N}{\rho C_p H} \quad (\text{B53})$$

where

C_p = specific heat of water, .0486 W day Kg⁻¹ °C⁻¹

ρ = density of water, 1,000 Kg m⁻³

Water temperature is calculated using the equilibrium temperature approach (Edinger, Duttweiler, and Geyer 1968), which accounts for the effects of surface heating and radiation. The equilibrium temperature T_E is defined as the water temperature at which the net heat exchange H_N is zero. Several of the terms on the right side of Equation 52 are functions of surface water temperature, T . With $H_N = 0$ in Equation 52, substituting T_E for T , and applying some linearization, the terms on the right side of Equation 52 can be solved iteratively for T_E and a heat exchange coefficient K_E . Therefore, the equilibrium temperature and heat exchange coefficient can be computed a priori from meteorological data without knowledge of the water temperature. Additionally, net short wave radiation is computed using cloud cover, site location, and time of year. This information is used for illumination in algal growth.

The net heat transfer rate is computed as

$$H_N = K_E (T_E - T) \quad (\text{B54})$$

where

K_E = heat exchange coefficient (W m⁻² °C⁻¹)

T_E and K_E are calculated using meteorological data (i.e., air temperature, dew-point temperature, cloud cover, and wind speed) independently from the simulation. Edinger, Brady, and Geyer (1974) present a detailed explanation of the calculation of T_E and K_E . The water temperature on the right side of Equation 54 is treated explicitly, i.e., taken from the previous time-step.

Heat sources from discharges, such as power plants, are computed as

$$H_p = \rho C_p Q_p \Delta T \quad (\text{B55})$$

where

H_p = heat transfer rate from power plant discharge (W)

Q_p = discharge rate from power plant ($\text{m}^3 \text{ day}^{-1}$)

ΔT = temperature difference between power plant discharge and ambient (intake) water ($^{\circ}\text{C}$)

Equation B55 must be divided by $\rho C_p V$ to convert to a rate of temperature change, where V is the volume of the computational cell where the power plant discharge enters. Combining Equations B54 and B55, Equation B53 becomes

$$\frac{\partial T}{\partial t} = \frac{K_E (T_E - T)}{\rho C_p H} + \frac{Q_p \Delta T}{V} \quad (\text{B56})$$

Conservative Tracer

A conservative tracer is included in the suite of variables simulated by the WQM. This tracer is used to check mass conservation and study transport. It can also be used to simulate the transport of conservative substances found in the water column. The only loss for this conservative tracer is transport through the outer boundary of the model.

Appendix C

Water Quality Model Kinetic Notation and Units

A_{ca}	Algal carbon-to-chlorophyll ratio (gm C / gm chl)
A_{dcr}	Dissolved oxygen-to-carbon ratio of algae (gm O ₂ / gm C)
A_{nc}	Nitrogen-to-carbon ratio of algae (gm N / gm C)
A_{nd}	Mass DO consumed per mass ammonium nitrogen nitrified (gm O ₂ / gm N)
A_{no}	Mass of nitrate nitrogen consumed per mass of CBOD (as oxygen) removed by denitrification (gm N / gm O ₂)
A_{pc}	Phosphorus-to-carbon ratio of algae (gm P / gm C)
B	Biomass of algae, as carbon (gm C m ⁻³)
BM	Basal metabolic rate of algae (day ⁻¹)
BM_{ref}	Metabolic rate of algae at reference temperature (day ⁻¹)
$CBOD_L$	Ultimate labile CBOD (gm O ₂ m ⁻³)
$CBOD_{L5}$	Five-day labile CBOD (gm O ₂ m ⁻³)
$CBOD_R$	Ultimate refractory CBOD (gm O ₂ m ⁻³)
$CBOD_{R5}$	Five-day refractory CBOD (gm O ₂ m ⁻³)
C_p	Specific heat of water (0.0486 watt day kg ⁻¹ °C ⁻¹)
$DECAY_L$	Labile CBOD decay (gm O ₂ m ⁻³ day ⁻¹)
$DECAY_R$	Refractory CBOD decay (gm O ₂ m ⁻³ day ⁻¹)

DEN	Water column denitrification rate ($\text{gm N m}^{-3} \text{ day}^{-1}$)
DO	Dissolved oxygen ($\text{gm O}_2 \text{ m}^{-3}$)
DO_s	Dissolved oxygen saturation concentration ($\text{gm O}_2 \text{ m}^{-3}$)
f_{day}	Fractional daylength ($0 \leq f_{day} \leq 1$)
$f(I)$	Effect of suboptimal illumination on algal production ($0 \leq f(I) \leq 1$)
$f(N)$	Effect of suboptimal nutrient concentration on algal production ($0 \leq f(N) \leq 1$)
$f(T)$	Effect of suboptimal temperature on algal production ($0 \leq f(T) \leq 1$). Also temperature correction term for other rates.
F_{in}	Fraction of inorganic nitrogen produced by algal metabolism ($0 \leq F_{in} \leq 1$)
F_{on}	Fraction of organic nitrogen produced by algal metabolism pool ($0 \leq F_{on} \leq 1$)
F_{op}	Fraction of organic phosphorus produced by algal metabolism ($0 \leq F_{op} \leq 1$)
F_{pin}	Fraction of inorganic nitrogen produced by algal predation ($0 \leq F_{pin} \leq 1$)
F_{pon}	Fraction of organic nitrogen produced by algal predation ($0 \leq F_{pon} \leq 1$)
F_{pop}	Fraction of organic phosphorus produced by algal predation ($0 \leq F_{pop} \leq 1$)
H	Water depth (m)
H_B	Heat loss due to back radiation of water
H_C	Heat loss due to conduction at water surface
H_E	Heat loss due to evaporation
H_L	Net long-wave radiation
H_N	Net heat flux (W m^{-2})
H_p	Heat transfer rate from power plant discharge (W)
H_S	Net short-wave radiation

I	Illumination rate (langley day ⁻¹)
I_a	Time-weighted average daily illumination (langley day ⁻¹)
I_o	Daily illumination at water surface (langley day ⁻¹)
I_s	Optimal illumination rate (langley day ⁻¹)
I_1	Daily illumination one day preceding model day (langley day ⁻¹)
I_2	Daily illumination two days preceding model day (langley day ⁻¹)
K_1 -- K_4	Rate multiplier parameters in algal rate multiplier equation (day ⁻¹)
K_{bt}	Effect of temperature on metabolism of algae (°C ⁻¹)
K_{chl}	Light attenuation coefficient for chlorophyll (m ² / gm chl)
K_{denit}	Denitrification rate at 20 °C (day ⁻¹)
K_{dnalg}	Constant that relates <i>TON</i> mineralization rate to algae biomass (m ³ / gm C day ⁻¹)
K_{dmin}	Minimum mineralization rate of <i>TON</i> (day ⁻¹)
K_{DO}	Oxygen half-saturation concentration required for aerobic <i>CBOD</i> decay (gm O ₂ m ⁻³)
K_{dpalg}	Constant that relates <i>TOP</i> mineralization rate to algae biomass (m ³ / gm C day ⁻¹)
K_{dpmn}	Minimum mineralization rate of <i>TOP</i> (day ⁻¹)
K_E	Heat exchange coefficient (W m ⁻² °C ⁻¹)
K_h	Oxygen half-saturation concentration for sediment oxygen demand (gm O ₂ m ⁻³)
K_{hn}	Nitrogen half-saturation concentration for nitrogen uptake by algae (gm N m ⁻³)
K_{hnd}	Half-saturation concentration of <i>DO</i> required for nitrification (gm O ₂ m ⁻³)
K_{hnn}	Half-saturation concentration of <i>NH₄</i> required for nitrification (gm N m ⁻³)
K_{hp}	Half-saturation concentration of phosphorus for uptake by algae (gm P m ⁻³)

K_{hr}	Oxygen half-saturation concentration for respiration ($\text{gm O}_2 \text{ m}^{-3}$)
K_{min}	Mineralization rate of <i>TON</i> (day^{-1})
K_{ndn}	Half-saturation concentration of nitrate for denitrification (gm N m^{-3})
K_{odn}	Half-saturation concentration of <i>DO</i> for denitrification ($\text{gm O}_2 \text{ m}^{-3}$)
K_{pmin}	Mineralization rate of <i>TOP</i> (day^{-1})
K_r	<i>DO</i> reaeration coefficient (m day^{-1})
K_{sco}	Oxygen half-saturation concentration for <i>SOD</i> release of <i>CBOD</i> ($\text{gm O}_2 \text{ m}^{-3}$)
K_{sdn}	Water column-to-sediment mass transfer rate for nitrate (m day^{-1})
K_{sod}	Sediment oxygen demand rate ($\text{gm O}_2 \text{ m}^{-2} \text{ day}^{-1}$)
Kl_L	Aerobic labile <i>CBOD</i> decay rate at 20 °C (day^{-1})
Kl_R	Aerobic refractory <i>CBOD</i> decay rate at 20 °C (day^{-1})
M	Rate constant for mortality of algae (day^{-1})
NH_4	Ammonium concentration, as nitrogen (gm N m^{-3})
NO_3	Nitrate plus nitrite concentration, as nitrogen (gm N m^{-3})
NR	Nitrification rate ($\text{gm N m}^{-3} \text{ day}^{-1}$)
NR_{max}	Nitrification rate under optimal temperature conditions ($\text{gm N m}^{-3} \text{ day}^{-1}$)
Pa	Preference of algae for NH_4 uptake ($0 \leq Pa \leq 1$)
pc_1	Parameter that determines maximum algal phosphorus-to-carbon ratio ($\text{gm C} / \text{gm P}$)
pc_2	Parameter that determines minimum algal phosphorus-to-carbon ratio ($\text{gm C} / \text{gm P}$)
pc_3	Parameter that expresses effect of PO_4 on algal phosphorus-to-carbon ratio ($\text{m}^3 / \text{gm P}$)
P_{GRO}	Production rate of algae (day^{-1})
P_{max}	Production rate of algae under optimal conditions (day^{-1})

PO_4	Total or dissolved phosphate concentration, as phosphorus (gm P m ⁻³)
PR	Predation rate on algae (day ⁻¹)
PR_{ref}	Predation rate on algae at T_{ref} (day ⁻¹)
Q_p	Discharge rate from power plant (m ³ day ⁻¹)
$SDEN$	Nitrate removal rate through sediment denitrification (gm N m ⁻³ day ⁻¹)
SED_{CBOD}	Sediment source of $CBOD$ (gm O ₂ m ⁻³ day ⁻¹)
SED_p	Sediment release rate of PO_4 (g P m ⁻² day ⁻¹)
SOD	Sediment oxygen demand (gm O m ⁻³ day ⁻¹)
T	Water temperature (C°)
T_I--T_4	Temperature parameters in algal rate multiplier equation (°C)
t	Time (day)
T_E	Equilibrium temperature (°C)
TON	Total organic nitrogen concentration (gm N m ⁻³)
TOP	Total organic phosphorus concentration (gm P m ⁻³)
T_{ref}	Reference temperature for metabolism of algae (°C)
V	Volume of model computational cell (m ³)
W_{salg}	Settling velocity of algae (m day ⁻¹)
W_{cl}	Settling velocity of labile $CBOD$ (m day ⁻¹)
W_{cr}	Settling velocity of refractory $CBOD$ (m day ⁻¹)
W_{sn}	Effective settling velocity of TON (m day ⁻¹)
W_{spop}	Effective settling velocity of TOP (m day ⁻¹)
z	Depth (m)
z_{optx}	Depth of maximum algal production (m)
α_L	Fraction of algal $CBOD$ contribution that is labile

α_{DEN}	Fraction of <i>CBOD</i> decrease resulting from denitrification that is labile
ΔT	Temperature difference between power plant discharge and ambient (intake) water ($^{\circ}\text{C}$)
λ	Light attenuation coefficient (m^{-1})
λ_{as}	Algal self-shading light attenuation coefficient (m^{-1})
λ_{na}	Non-algal light attenuation coefficient (m^{-1})
ρ	Density of water ($\approx 1,000 \text{ kg m}^{-3}$)
θ	Dimensionless temperature correction factor

Appendix D

Water Quality Model Scenario Figures

Results from selected water quality model scenarios presented in this appendix are in the form of time series plots and shading plots. Also presented for each scenario is a map to indicate the location of stations used for pre- and post-expansion comparisons. Results are grouped by scenario and presented in the following order: AEE, EEE, EEM, AEM, and MMM.

The results are organized for each scenario as follows:

- a. Map of lower Green Bay indicating the location of the selected pre- and post-expansion comparison stations.
- b. Time series plots for ultimate labile carbonaceous biochemical oxygen demand ($CBOD_L$), dissolved oxygen (DO), and conservative tracer at comparison stations.
- c. Time difference plots for $CBOD_L$, DO, and conservative tracer at comparison stations.
- d. Shading plots of average conservative tracer concentrations for pre- and post-expansion conditions.
- e. Shading plot of the increases in average conservative tracer concentrations occurring after expansion.
- f. Shading plot of decreases in average DO concentrations occurring after expansion.
- g. Shading plots of the lowest instantaneous DO predicted at any time during the scenario for pre- and post-expansion conditions.

SCENARIO AEE

**(Average Seiche, Extreme River Flows,
Extreme Lake Level)**

Figures D1 - D7

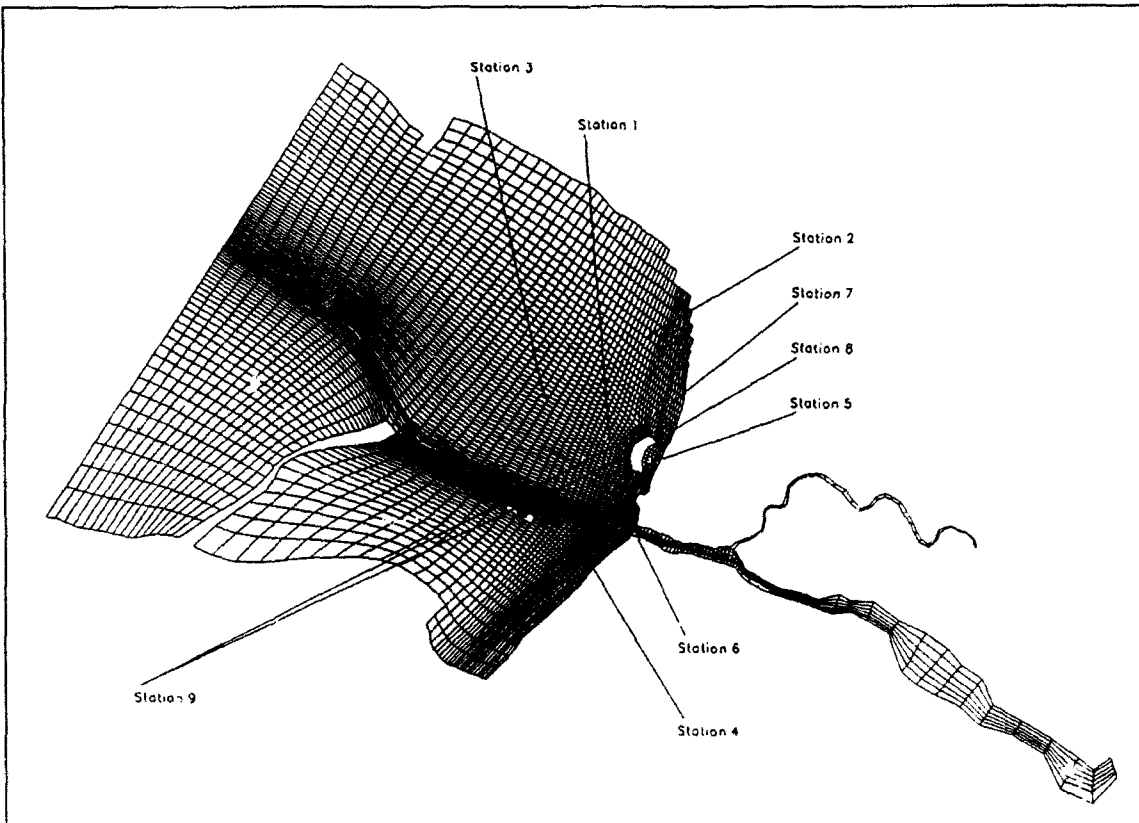


Figure D1. Pre- and post-expansion comparison stations, Scenario AEE

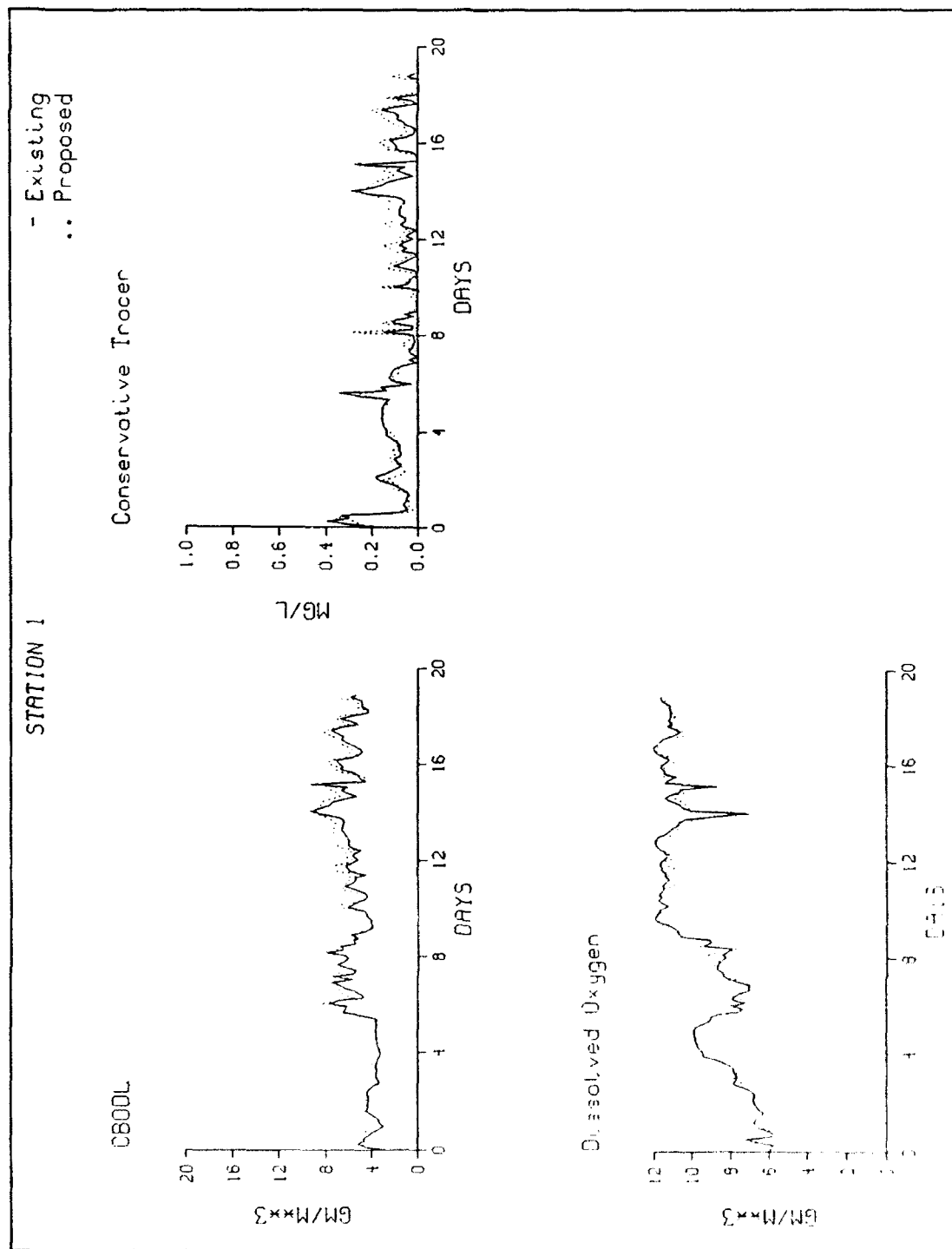


Figure D2. Time series for comparison stations, Scenario AEE (Sheet 1 of 9)

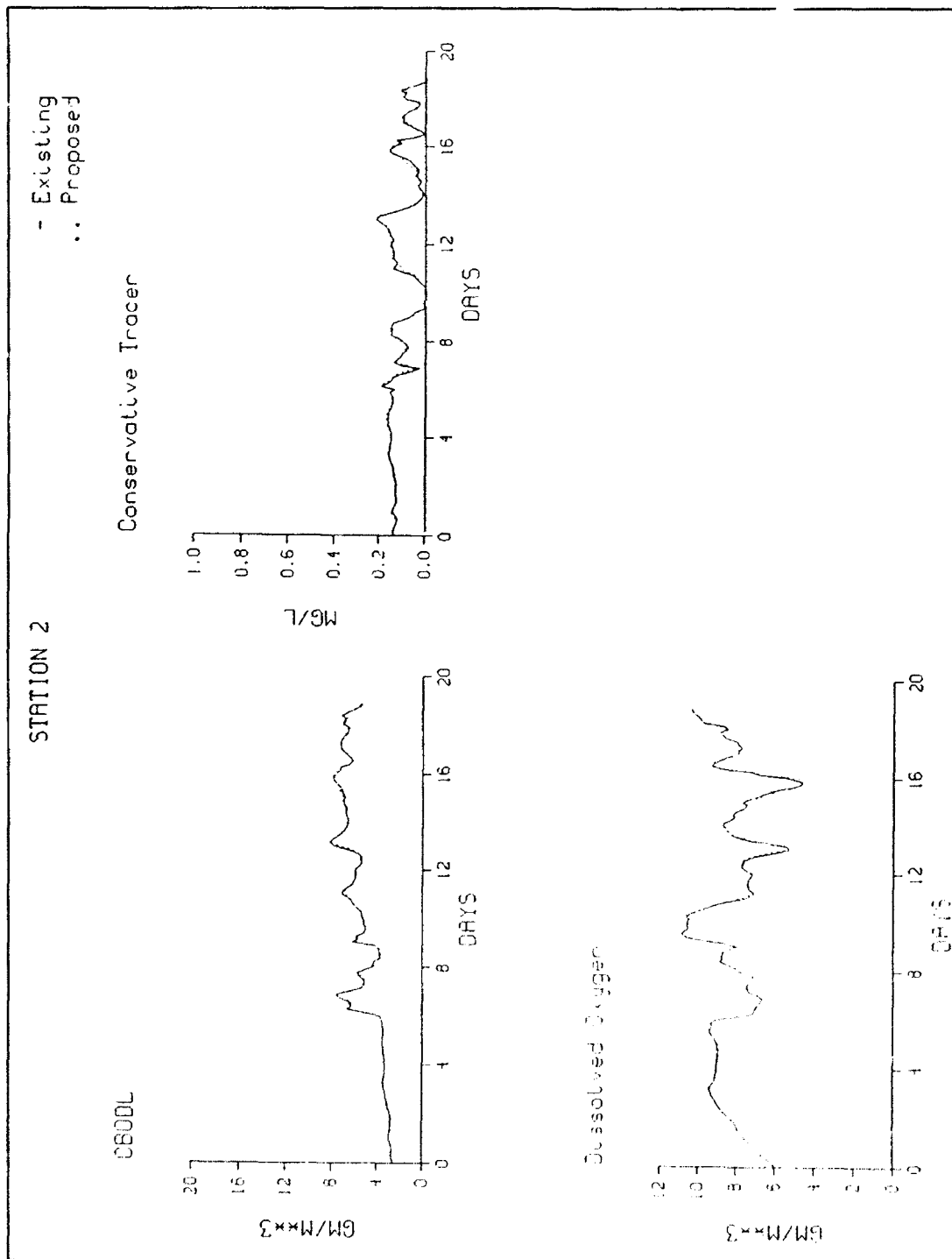


Figure D2. (Sheet 2 of 9)

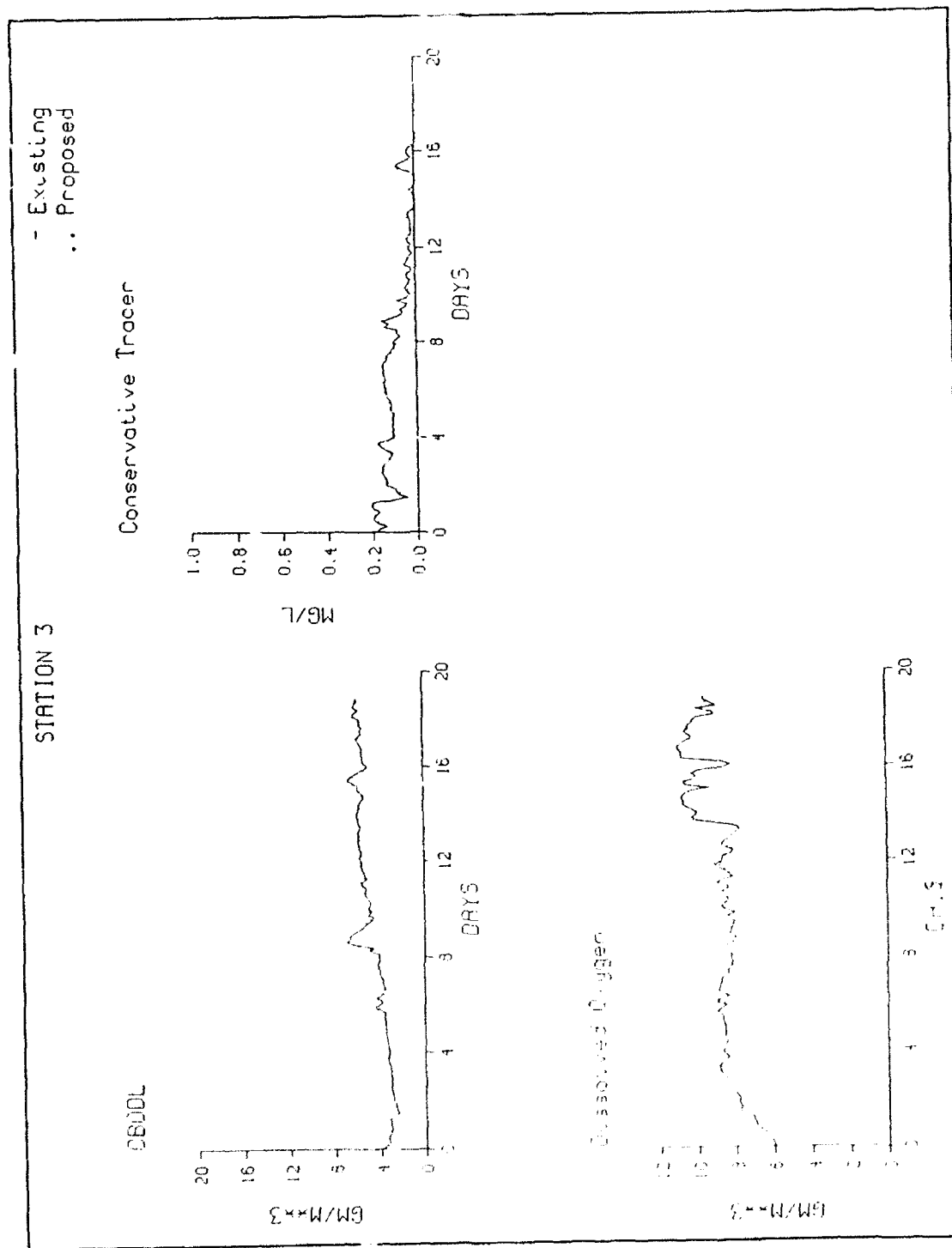


Figure D2. (Sheet 3 of 9)

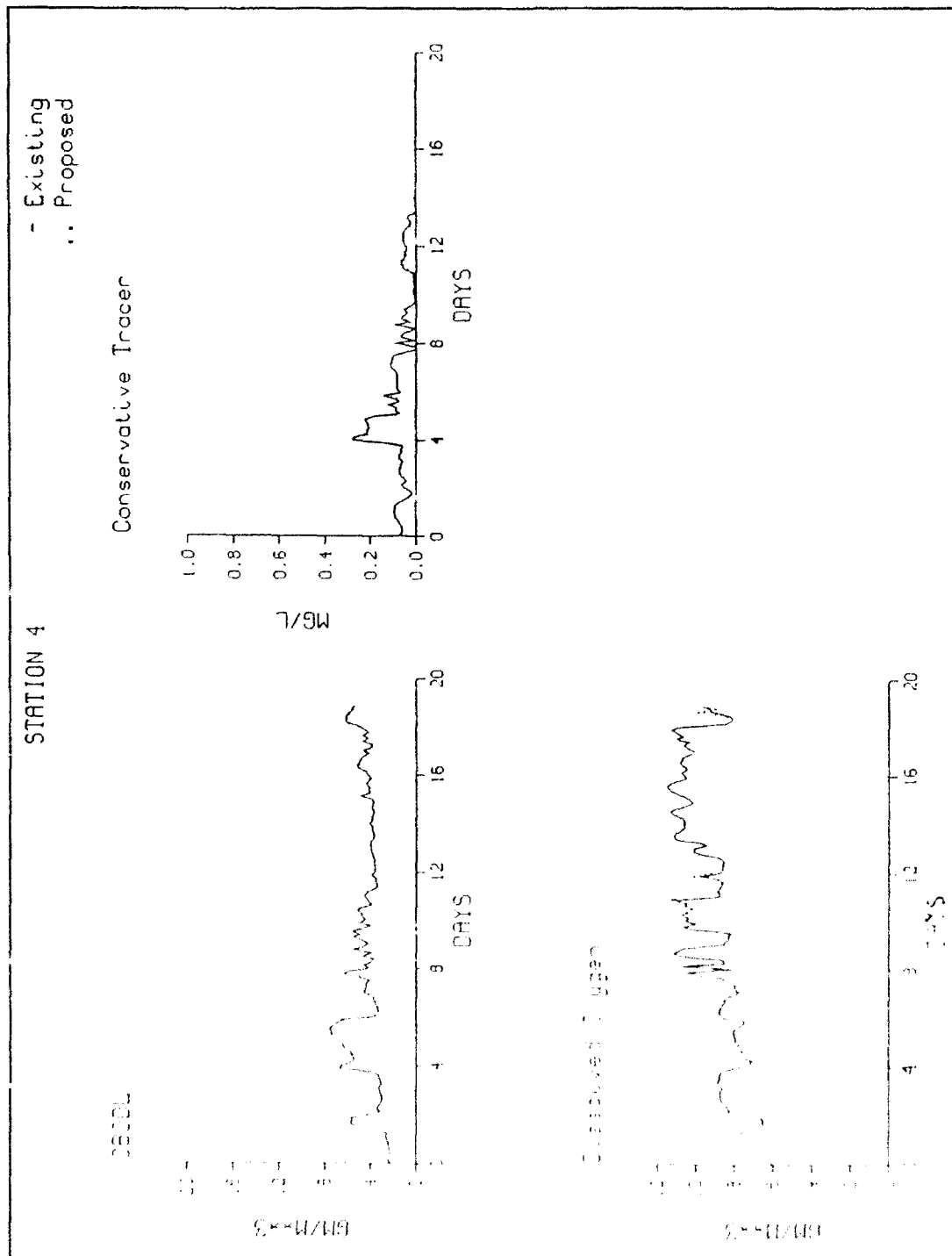


Figure D2. (Sheet 4 of 9)

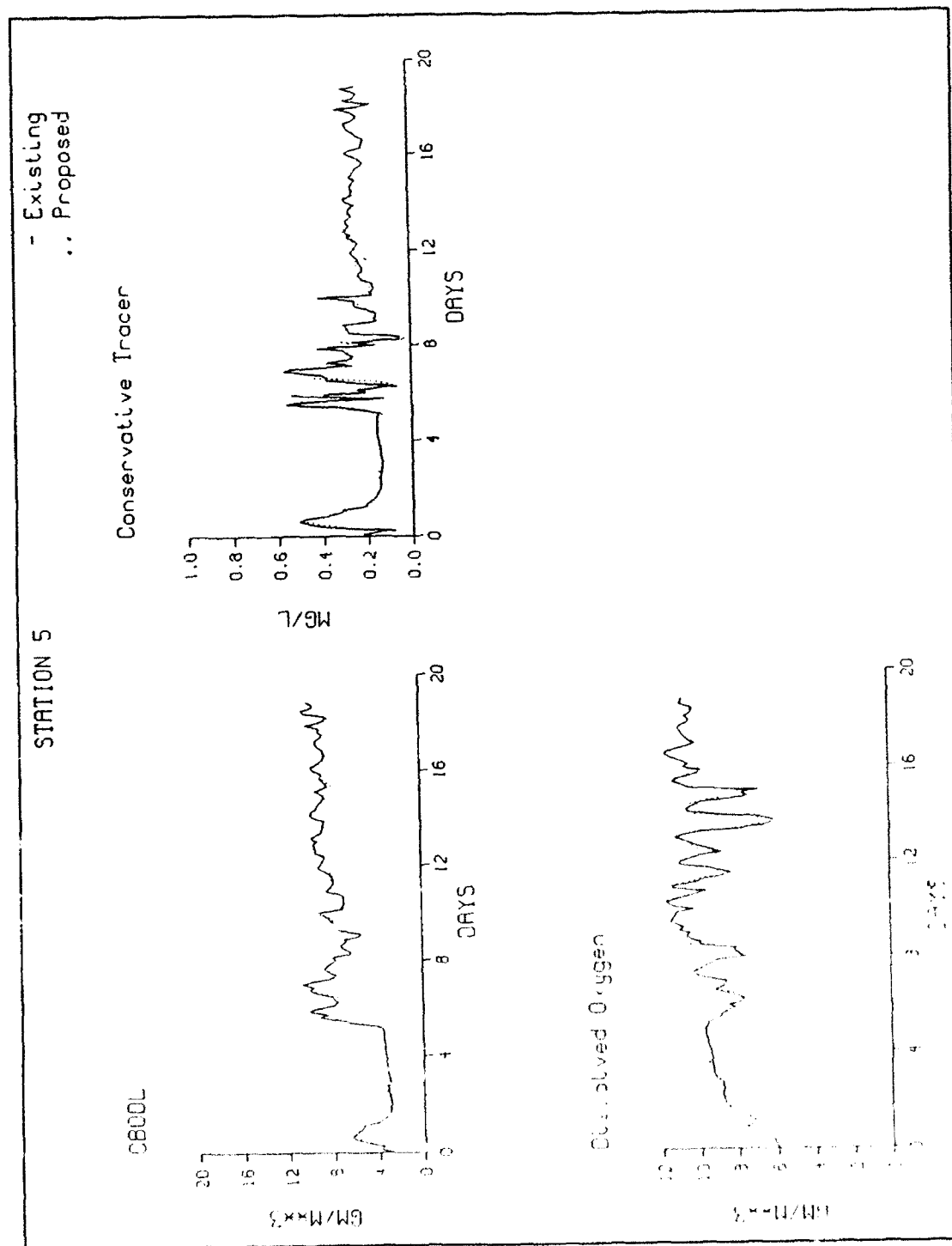


Figure D2. (Sheet 5 of 9)

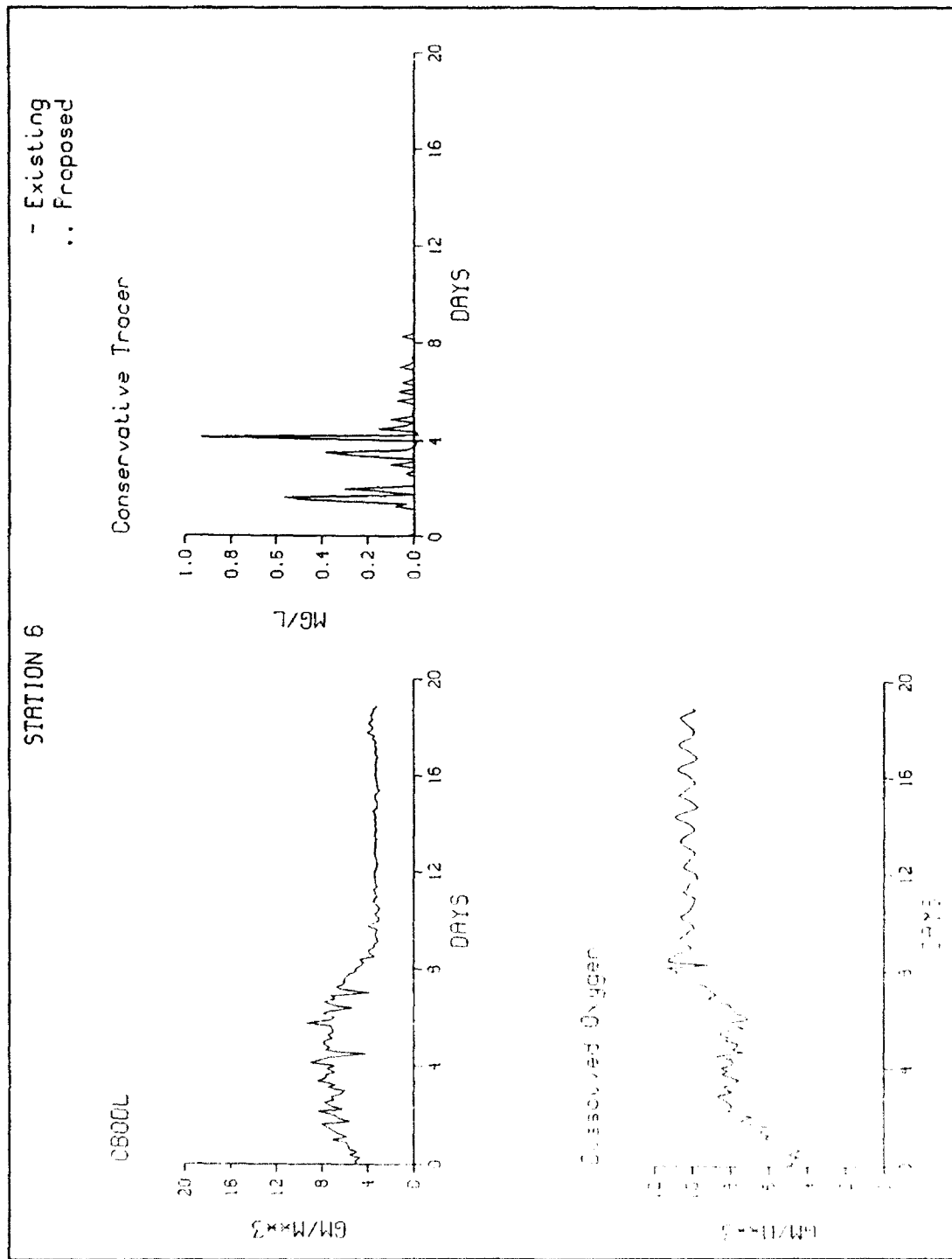


Figure D2. (Sheet 6 of 9)

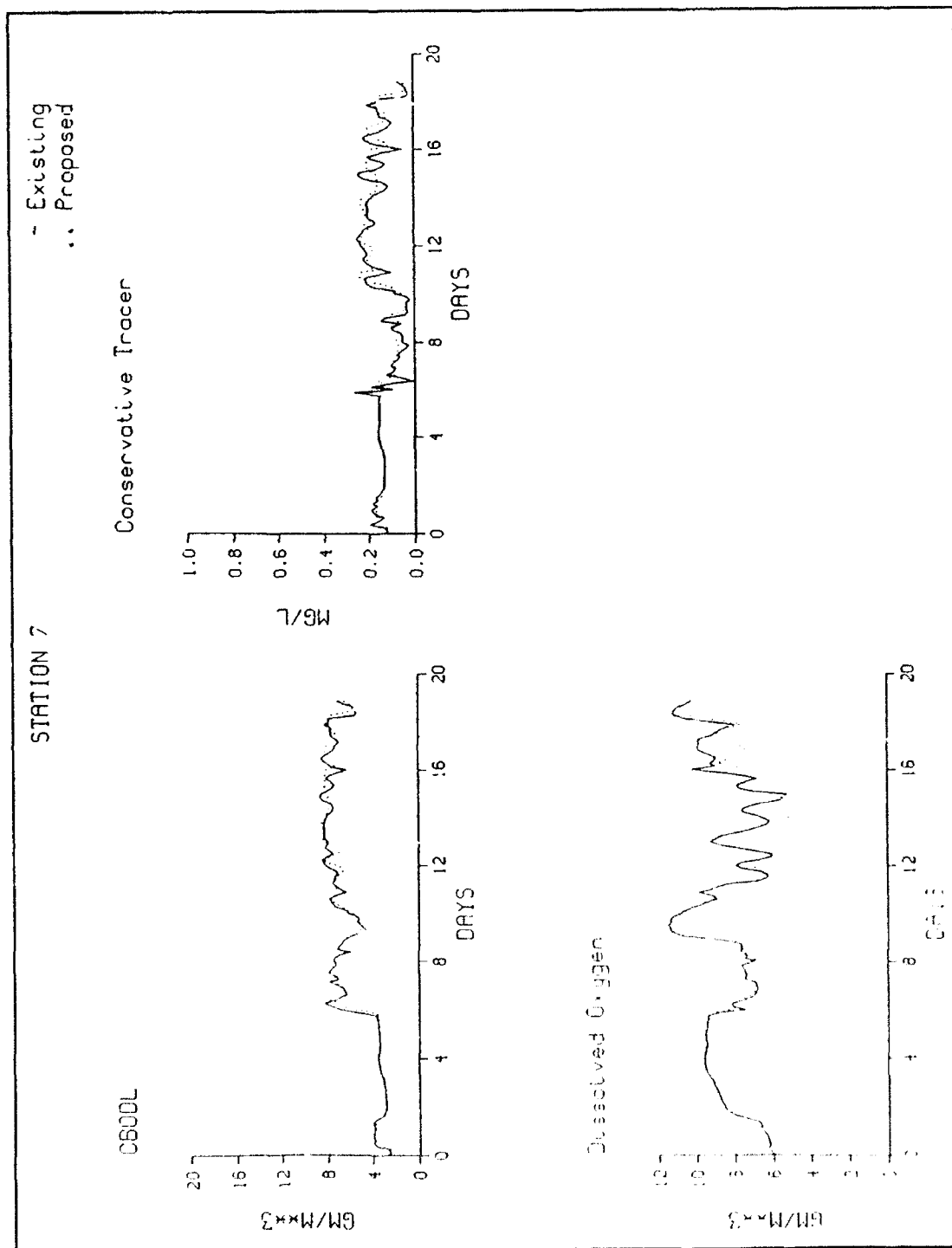
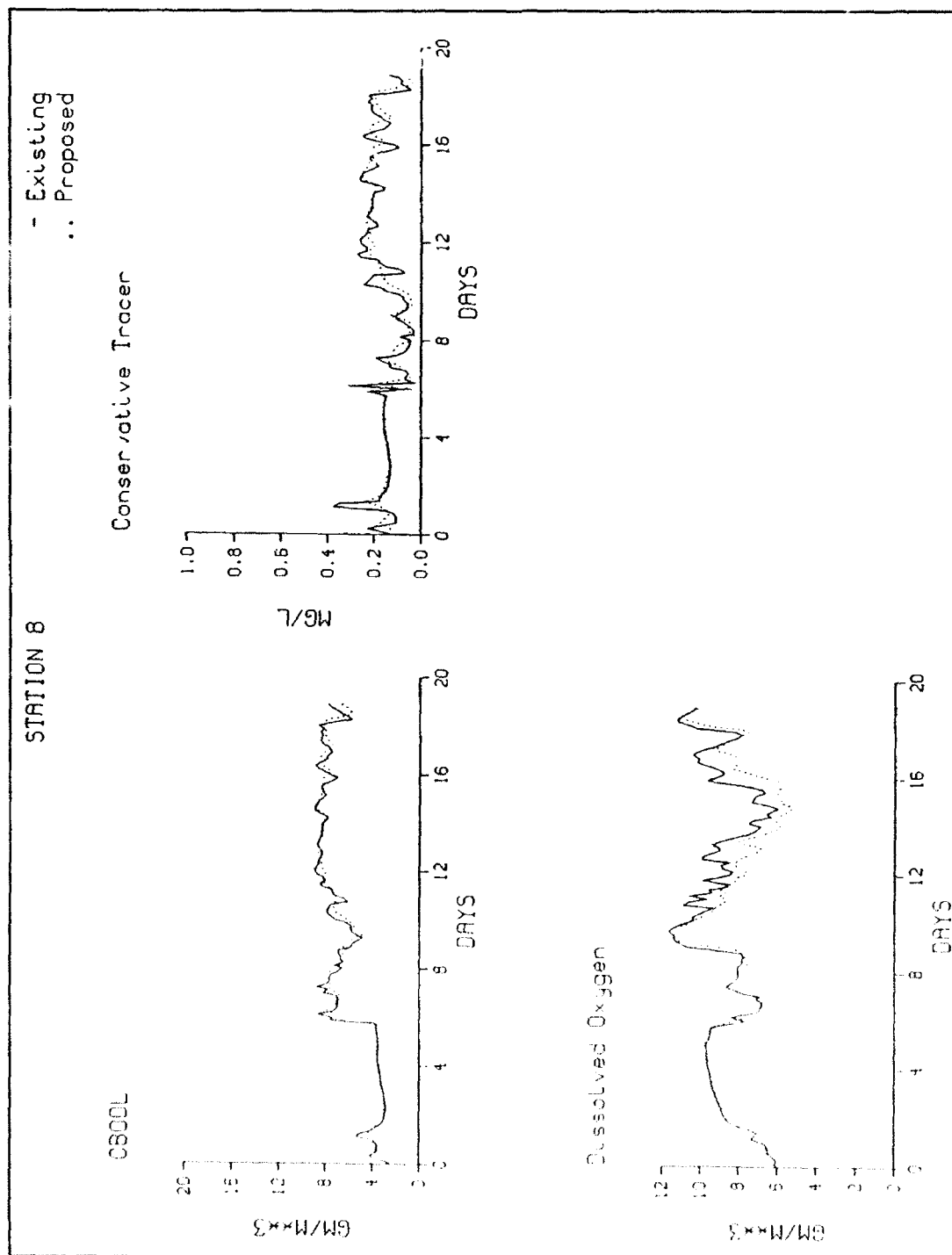


Figure D2. (Sheet 7 of 9)



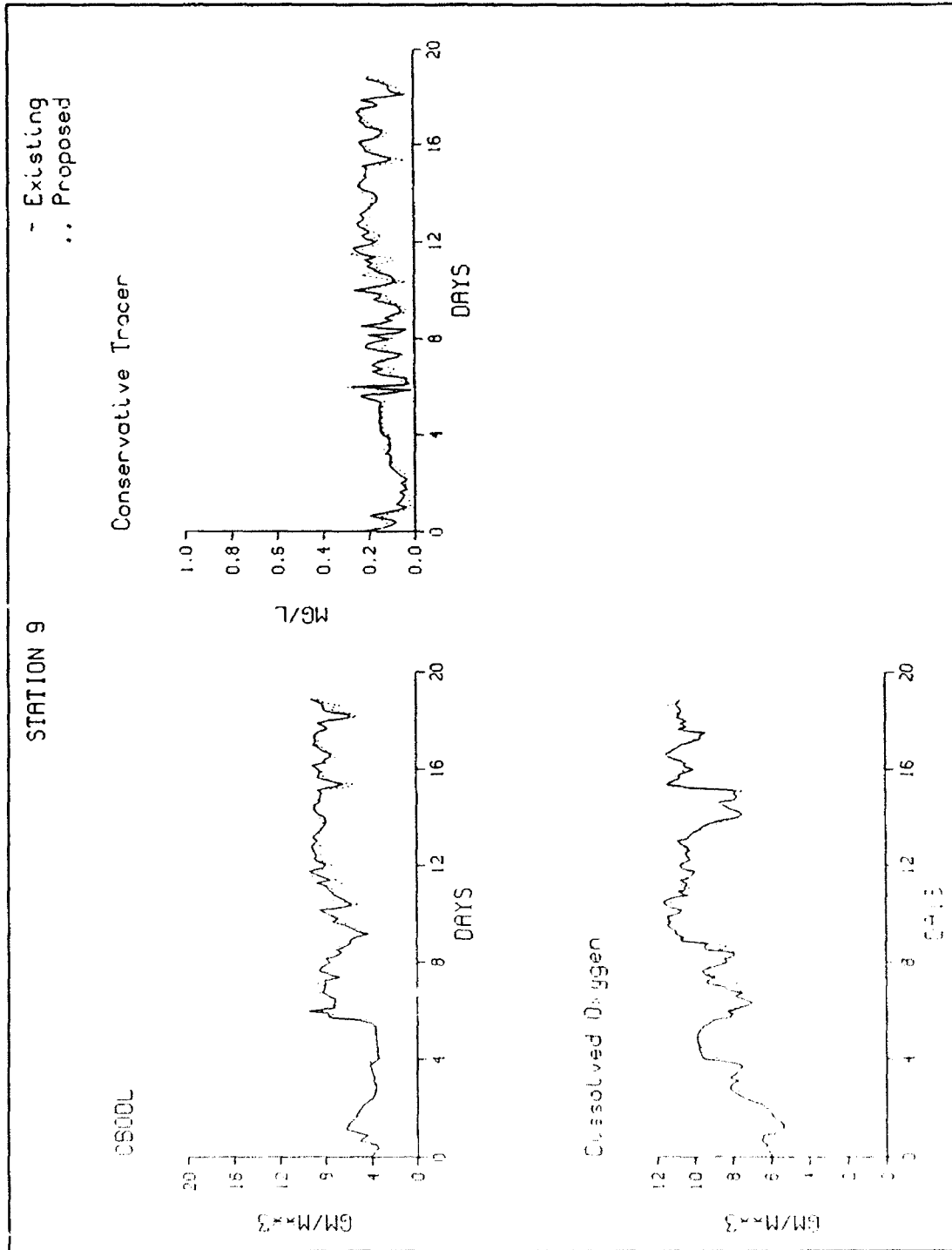


Figure D2. (Sheet 9 of 9)

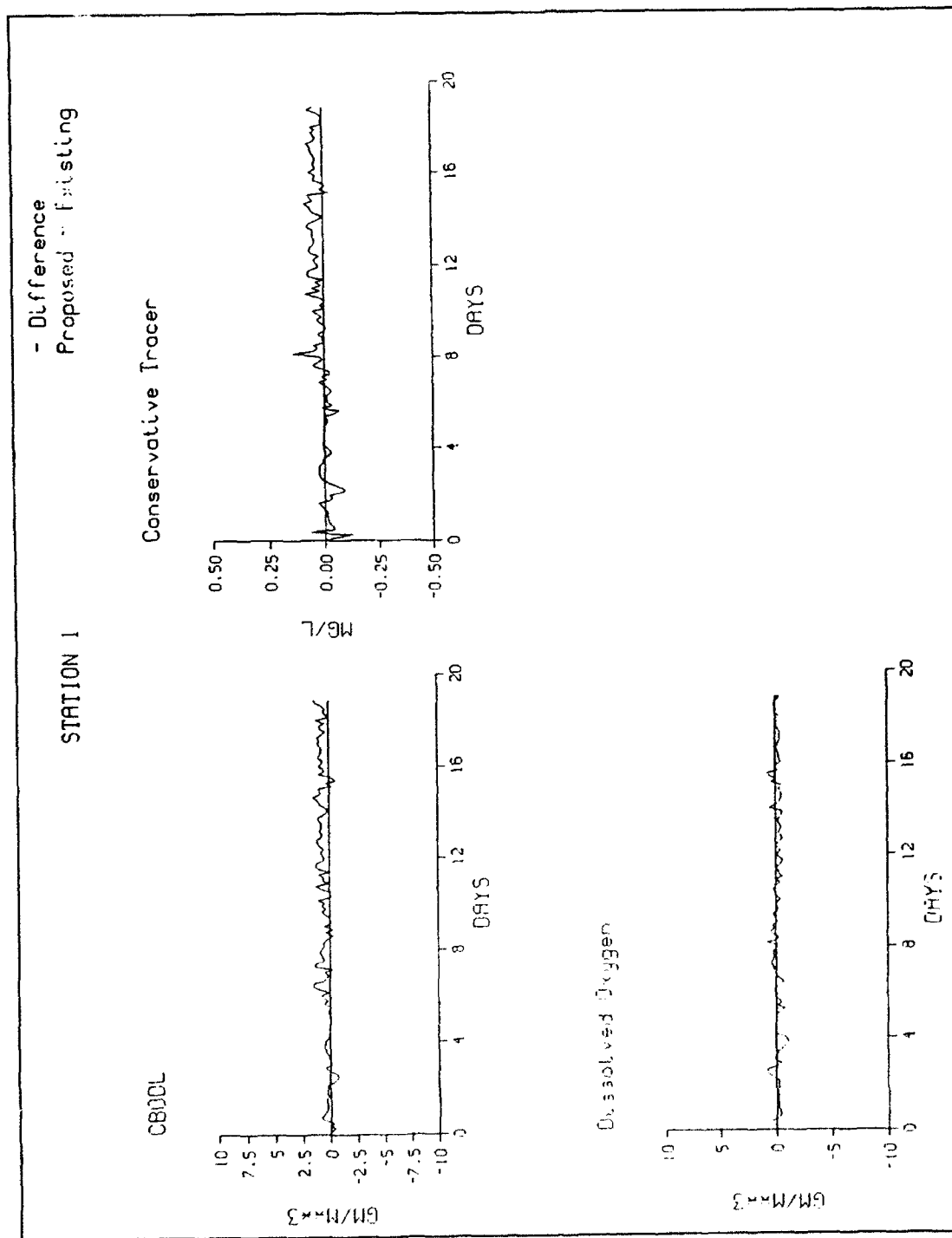


Figure D3. Time series differences for comparison stations, Scenario AEE (Sheet 1 of 8)

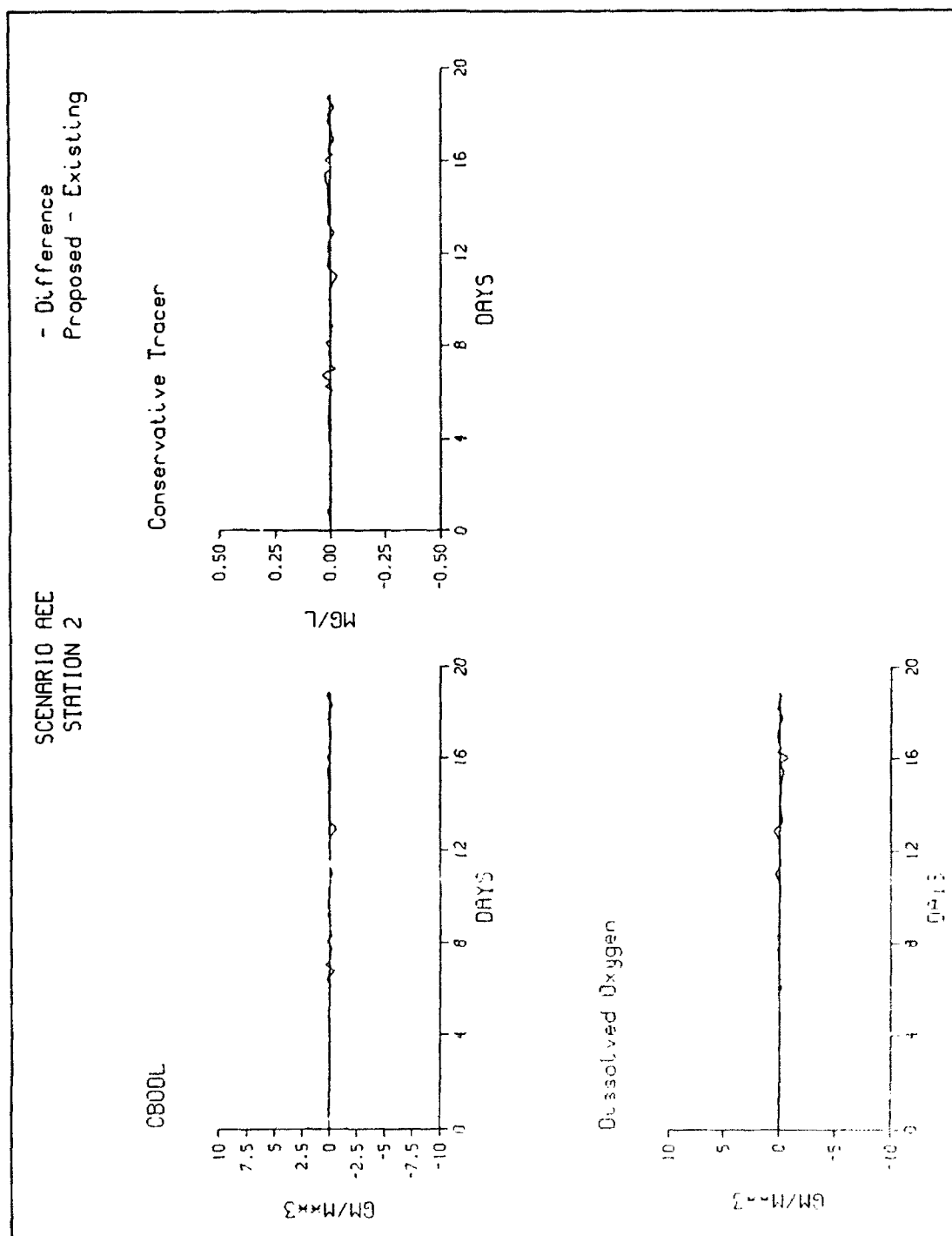


Figure D3. (Sheet 2 of 8)

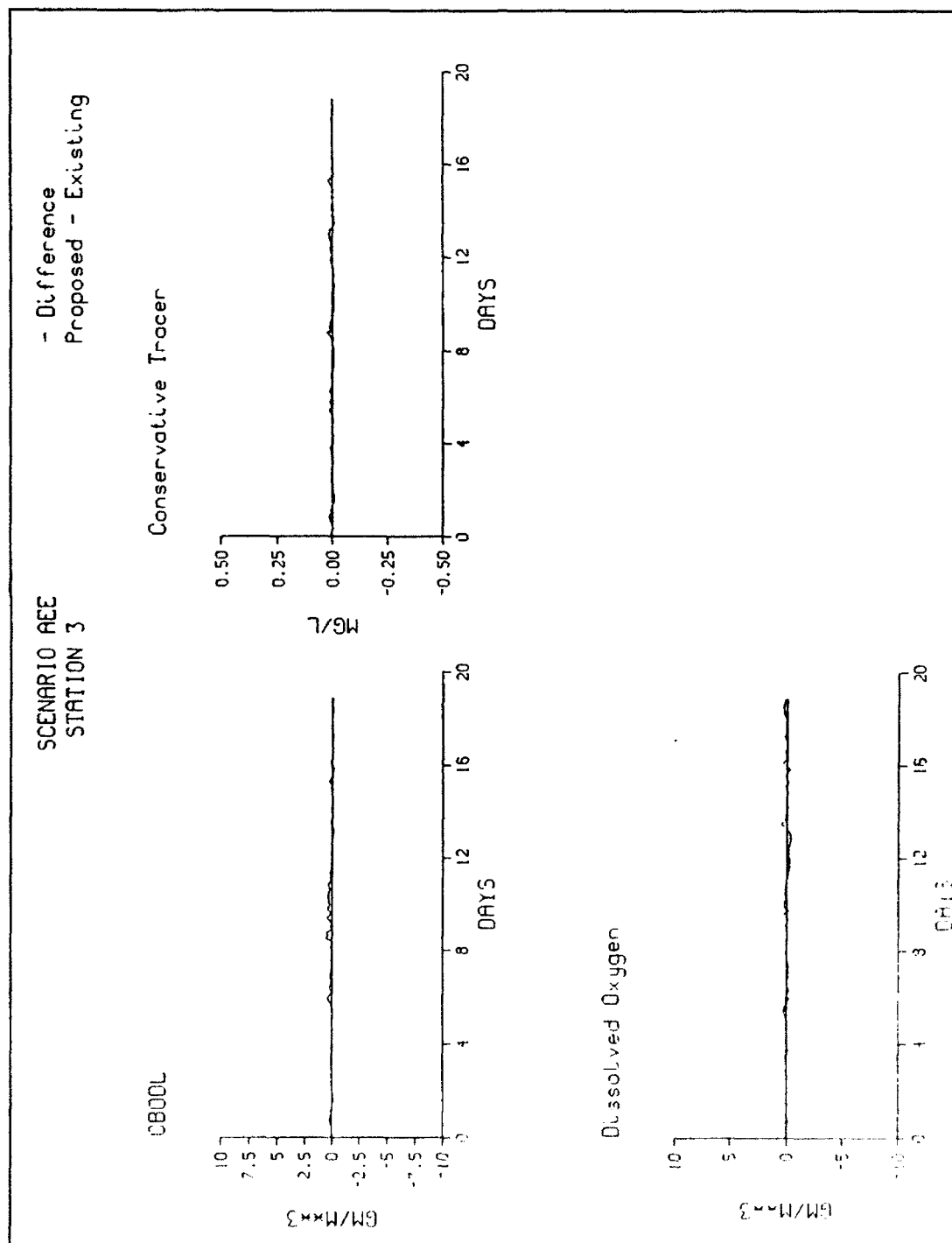


Figure D3. (Sheet 3 of 8)

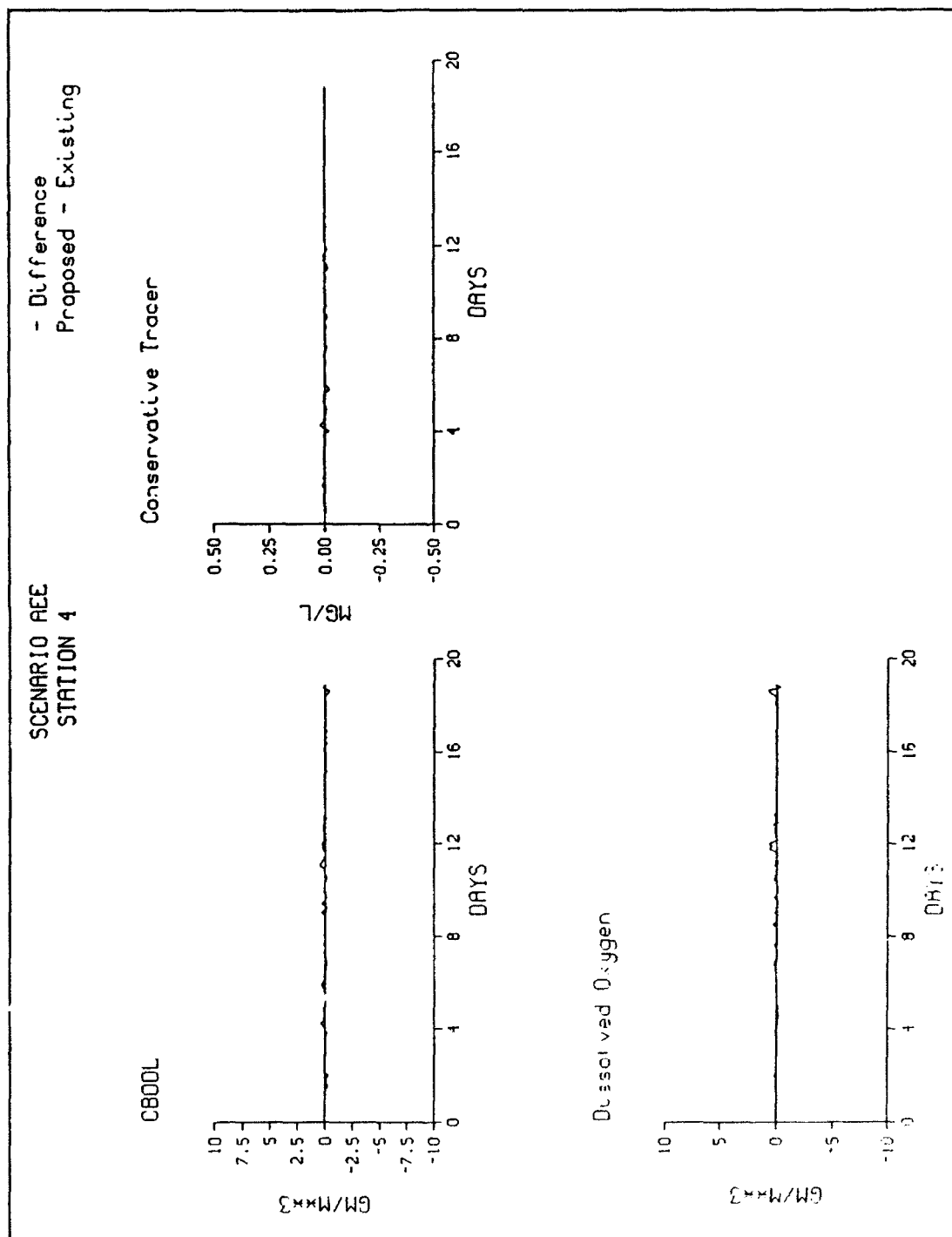


Figure D3. (Sheet 4 of 8)

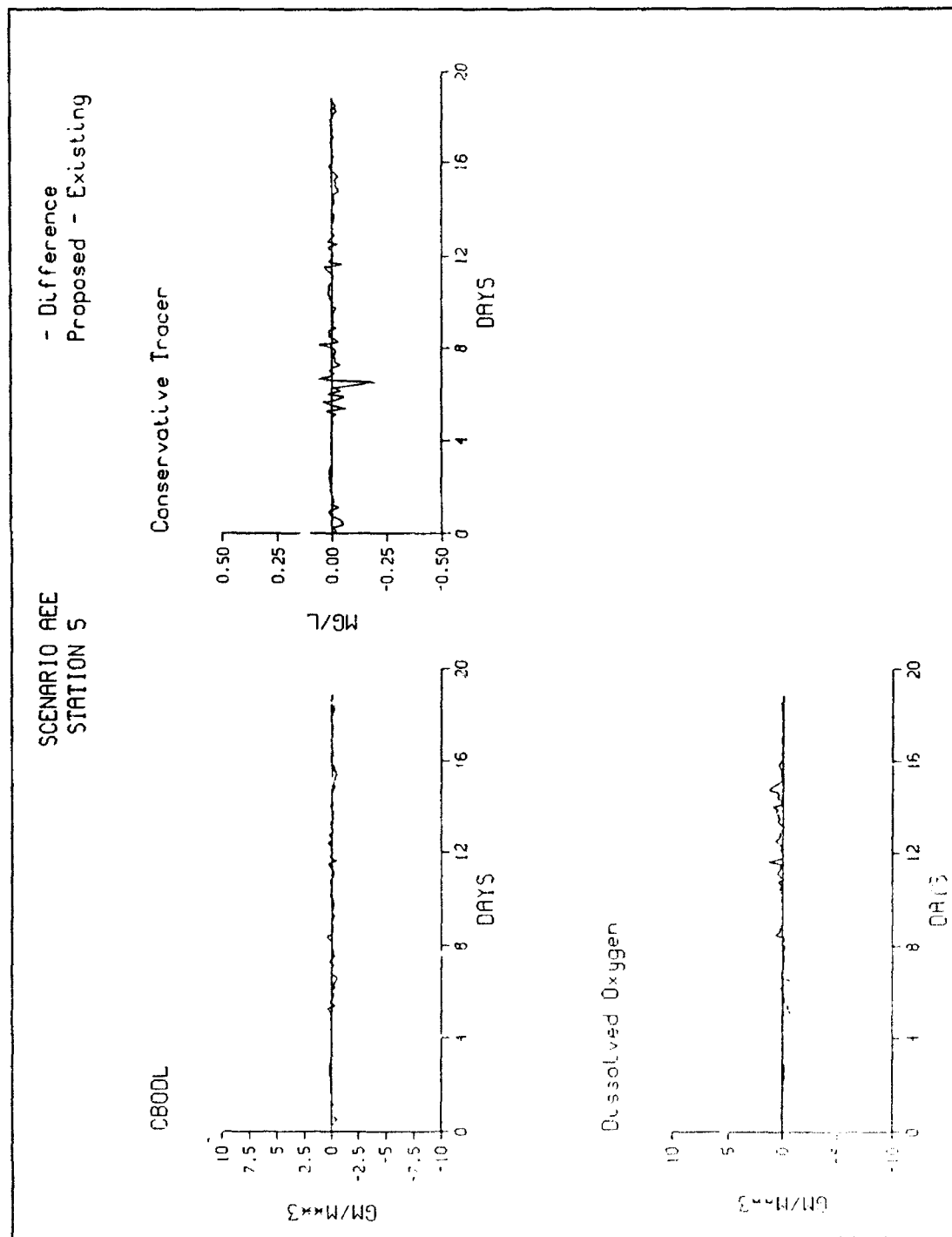


Figure D3. (Sheet 5 of 8)

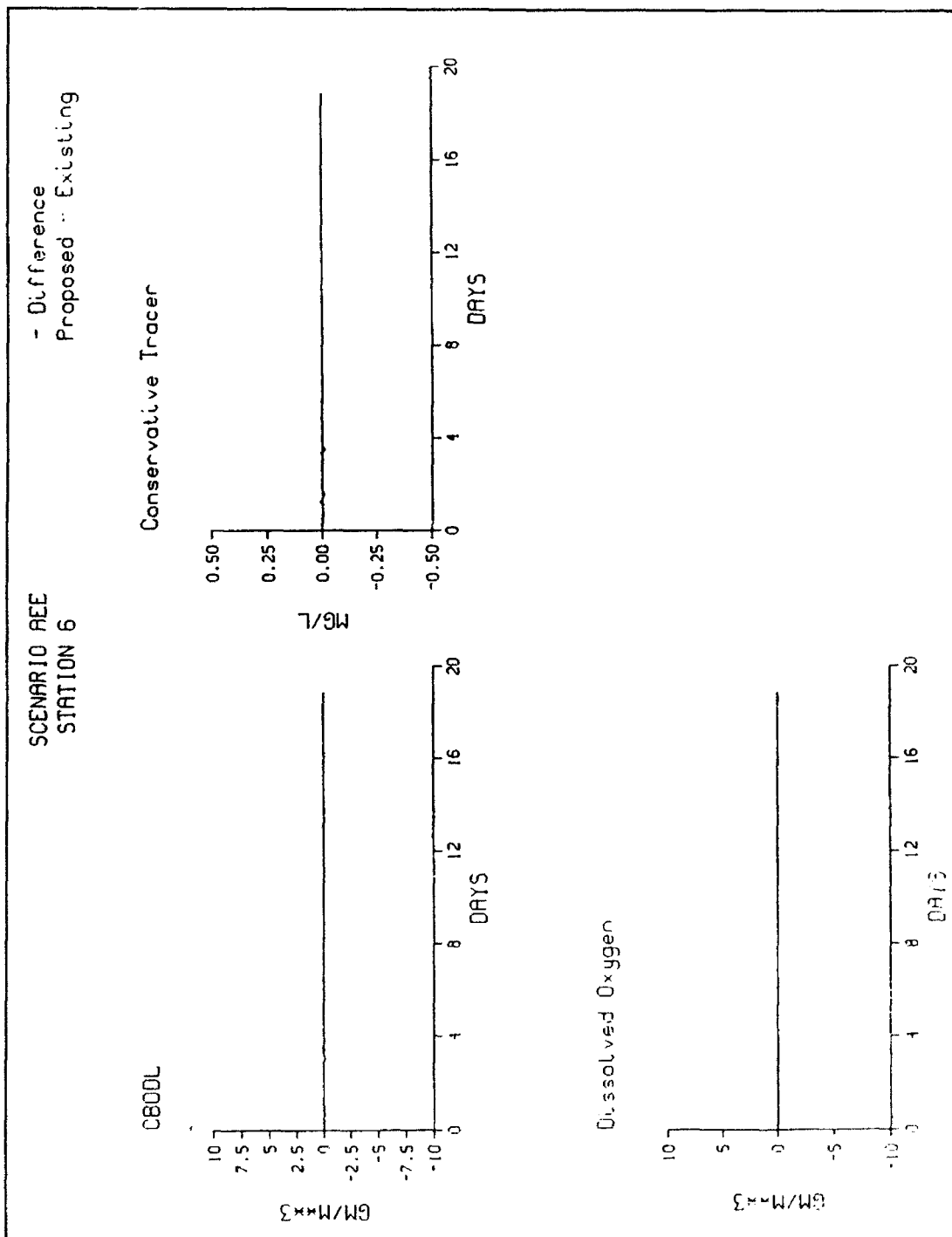


Figure D3. (Sheet 6 of 8)

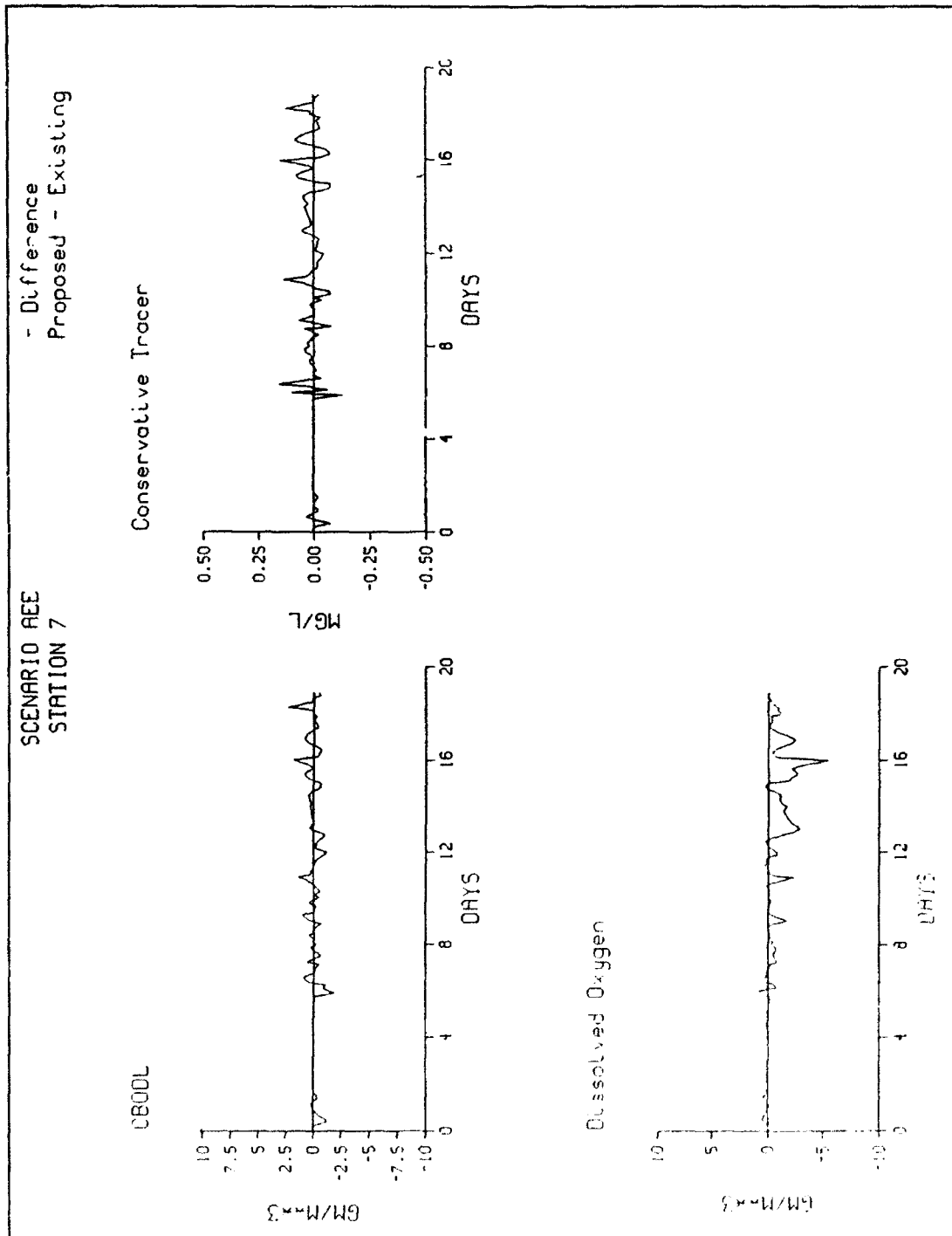


Figure D3. (Sheet 7 of 8)

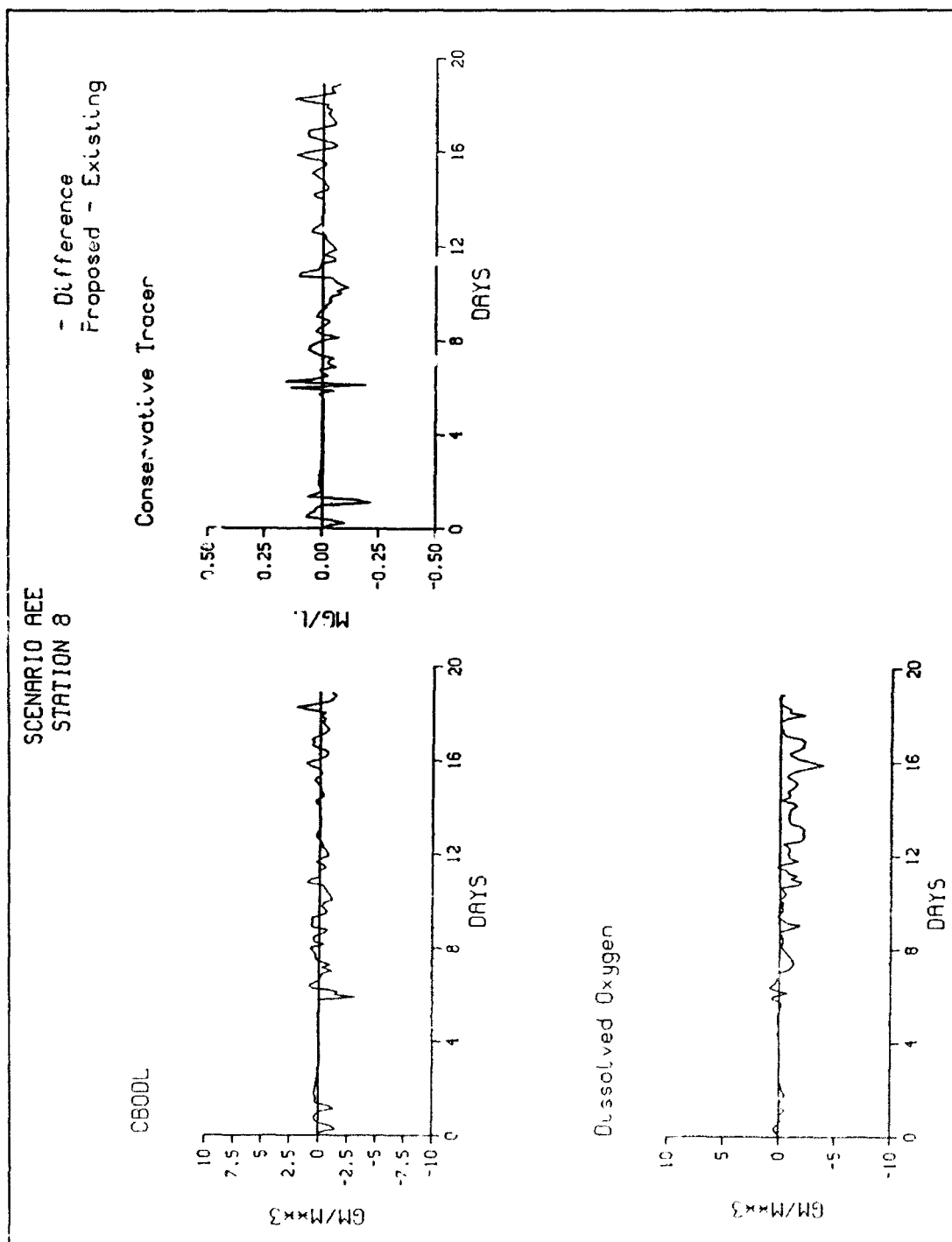


Figure D3. (Sheet 9 of 8)

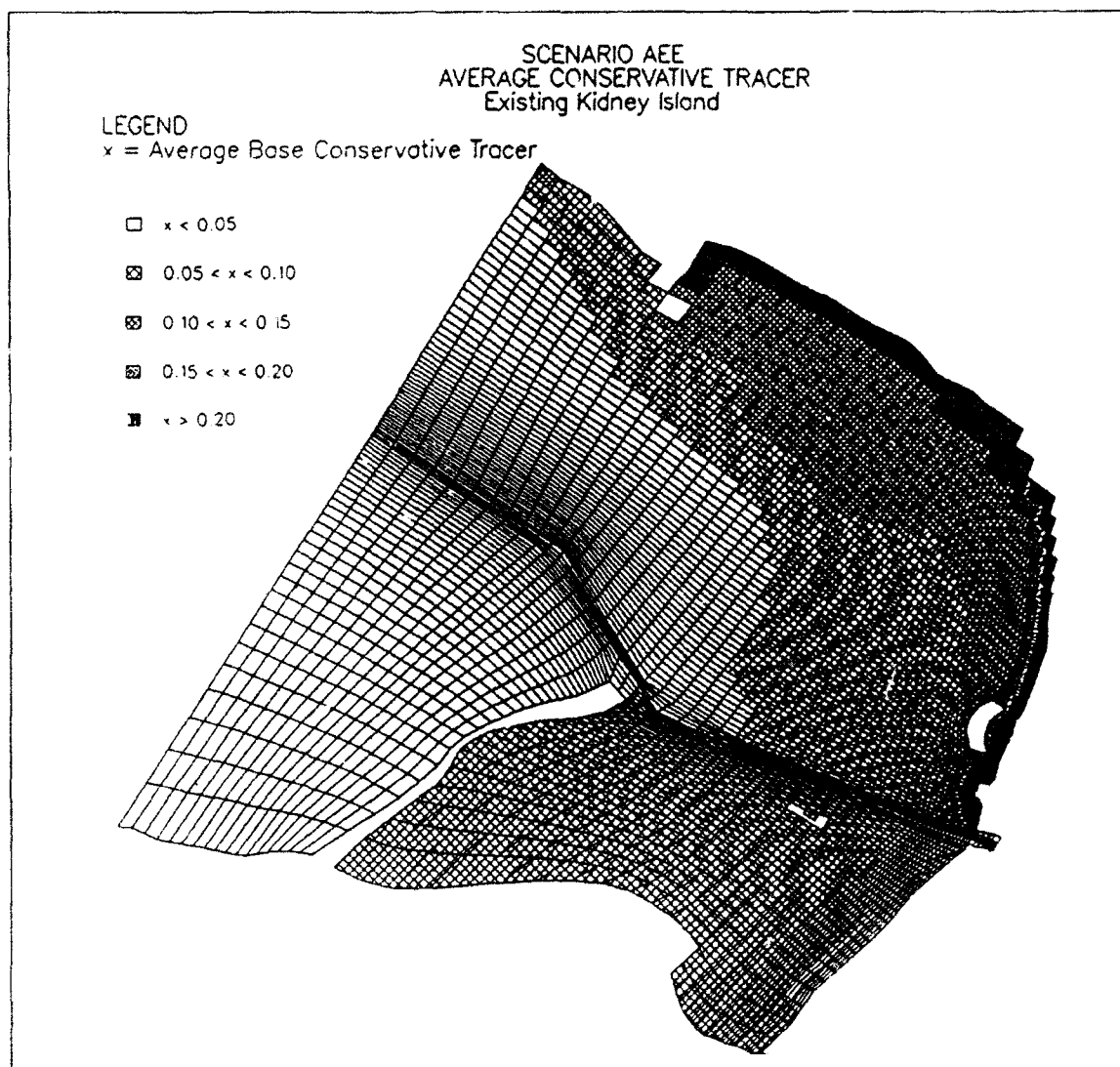


Figure D4. Average conservative tracer concentrations, Scenario AEE (Continued)

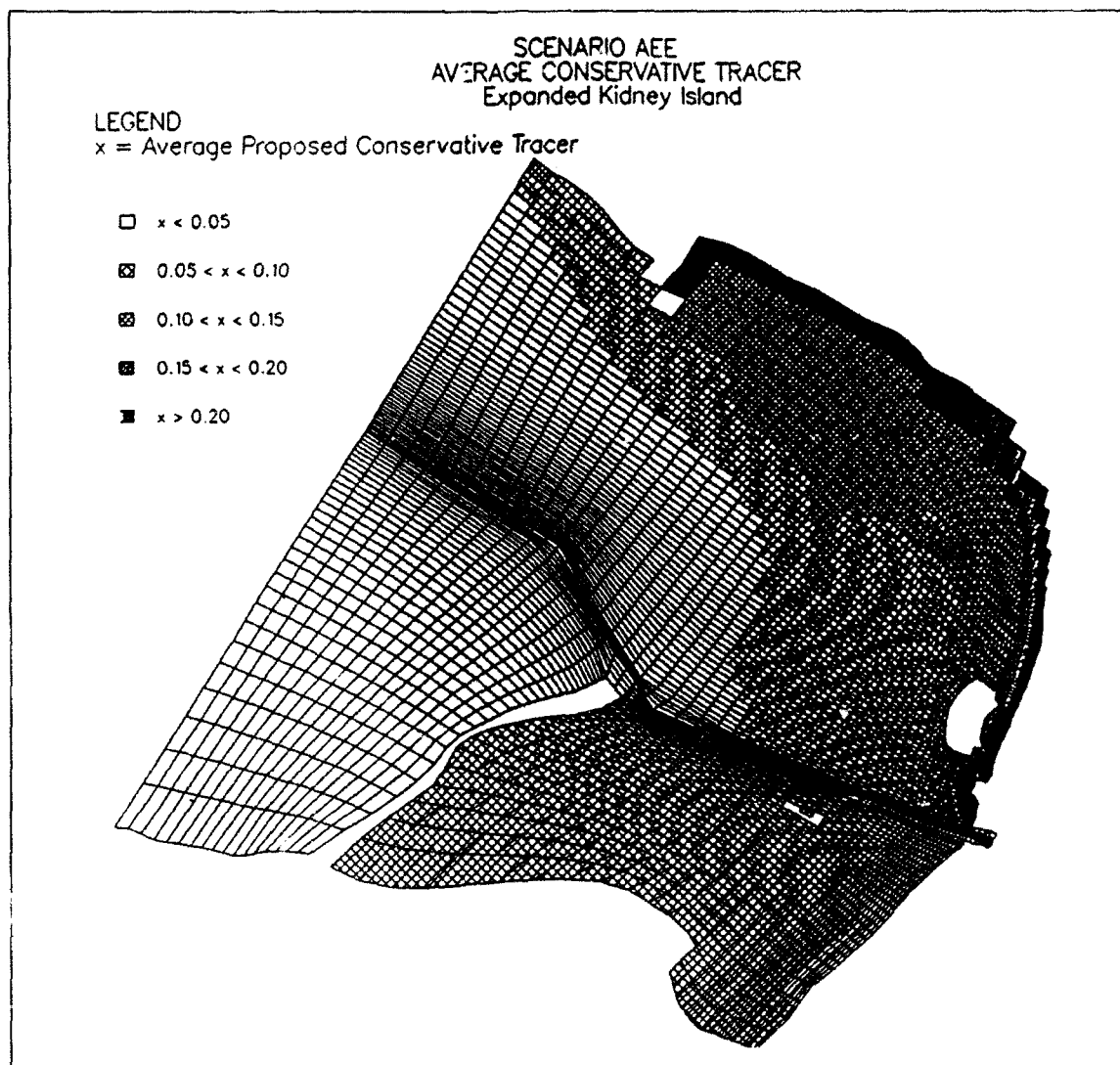


Figure D4. (Concluded)

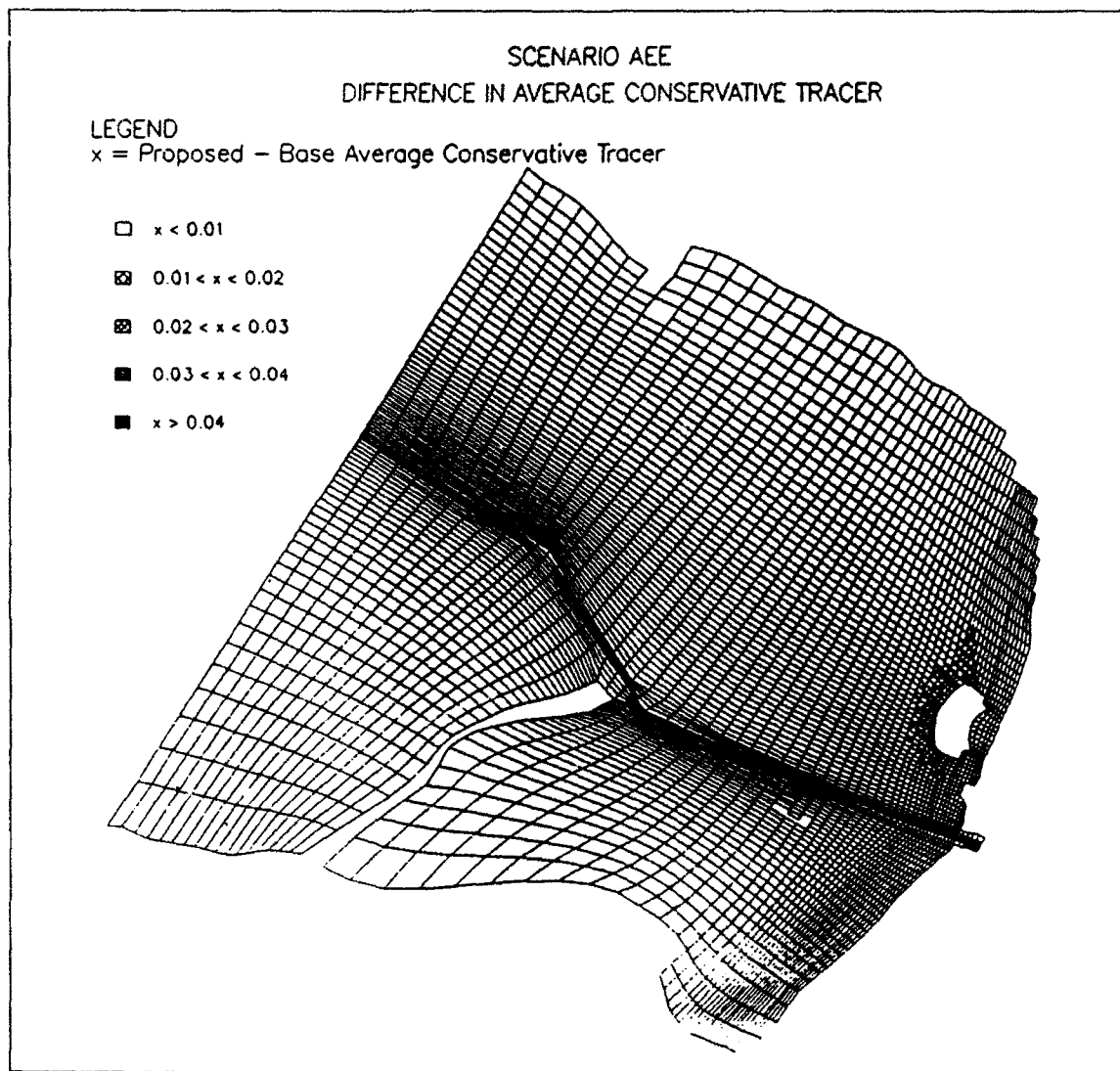


Figure D5. Difference in average conservative tracer, Scenario AEE

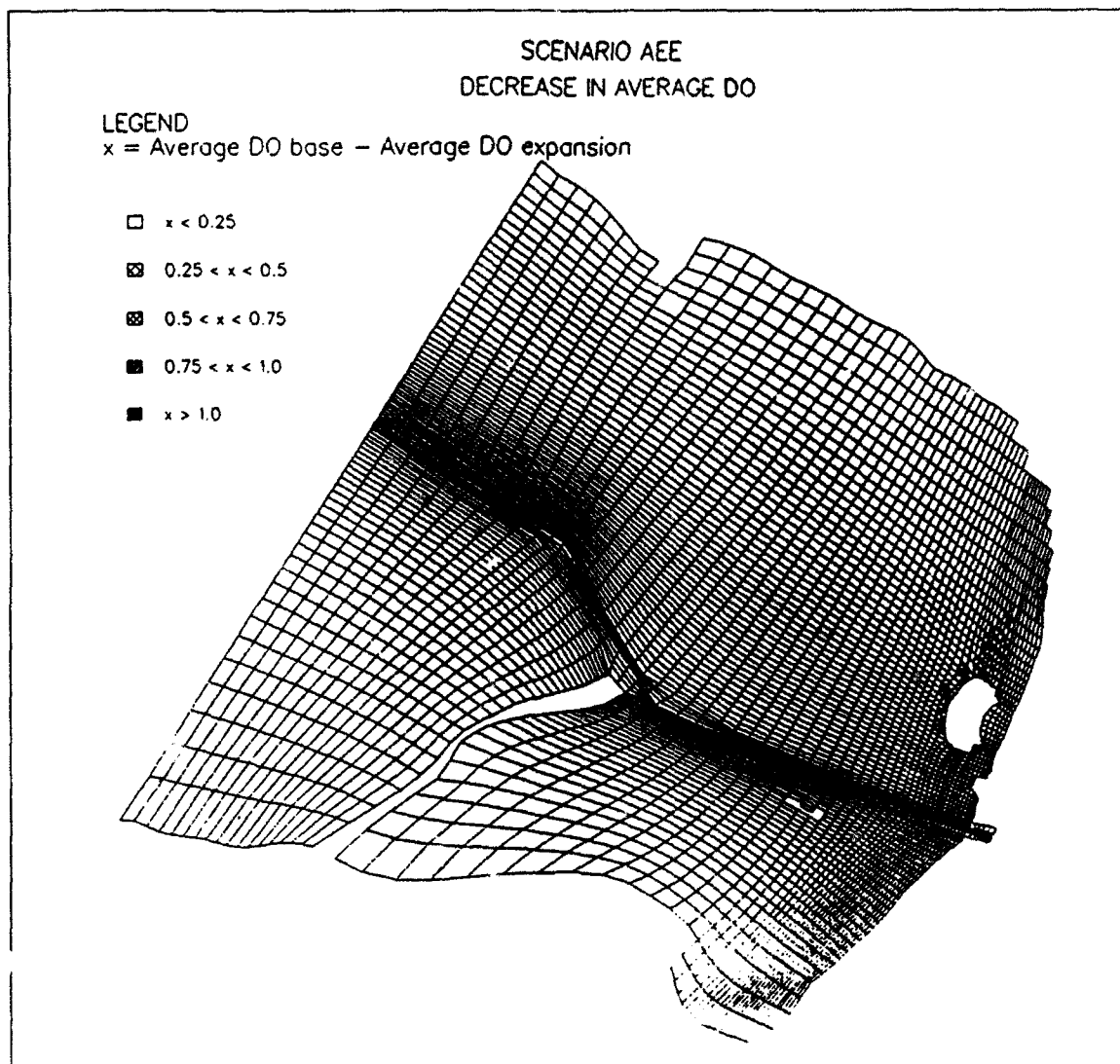


Figure D6. Decrease in average DO concentrations, Scenario AEE

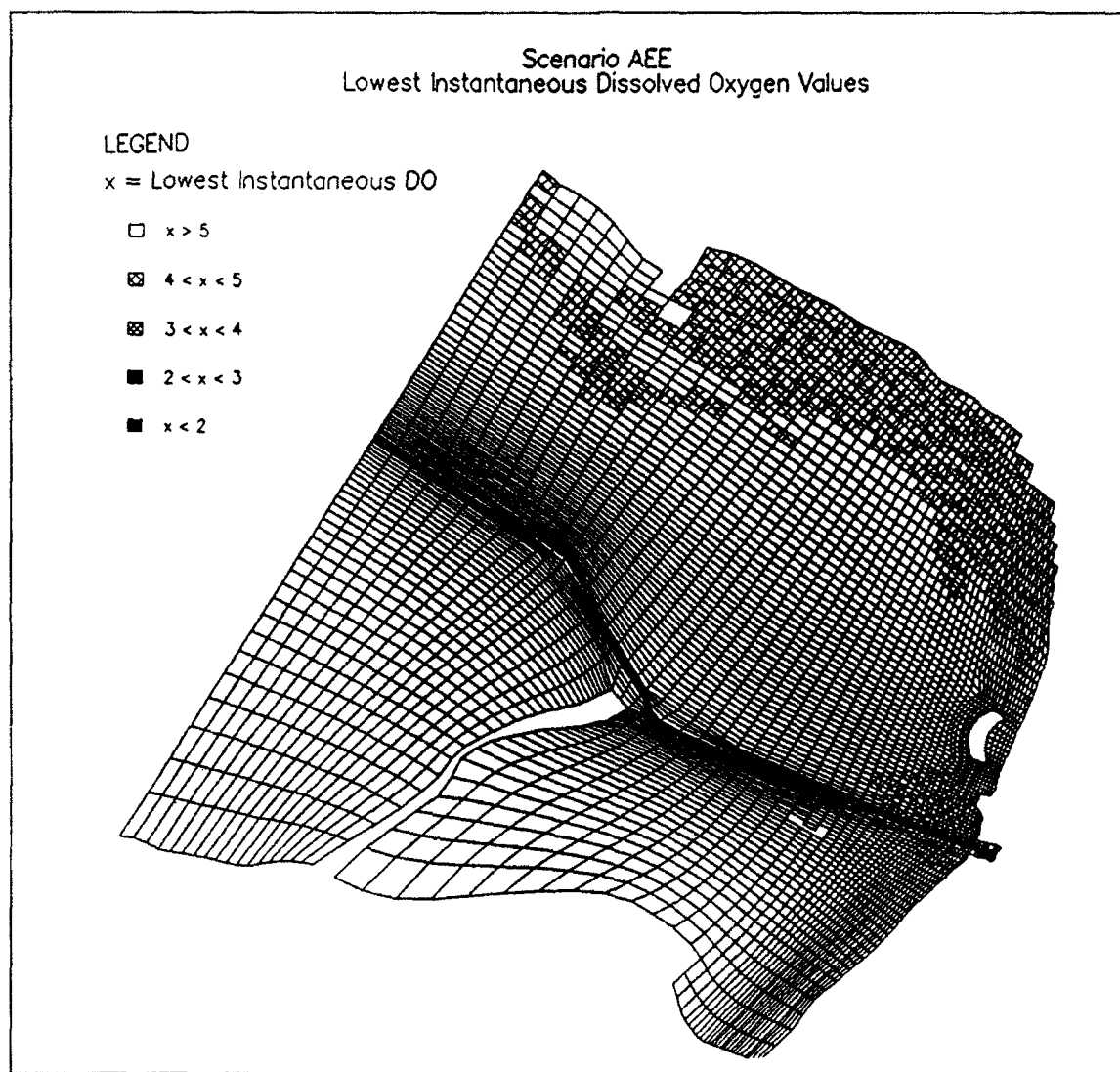


Figure D7. Lowest instantaneous DO, Scenario AEE (Continued)

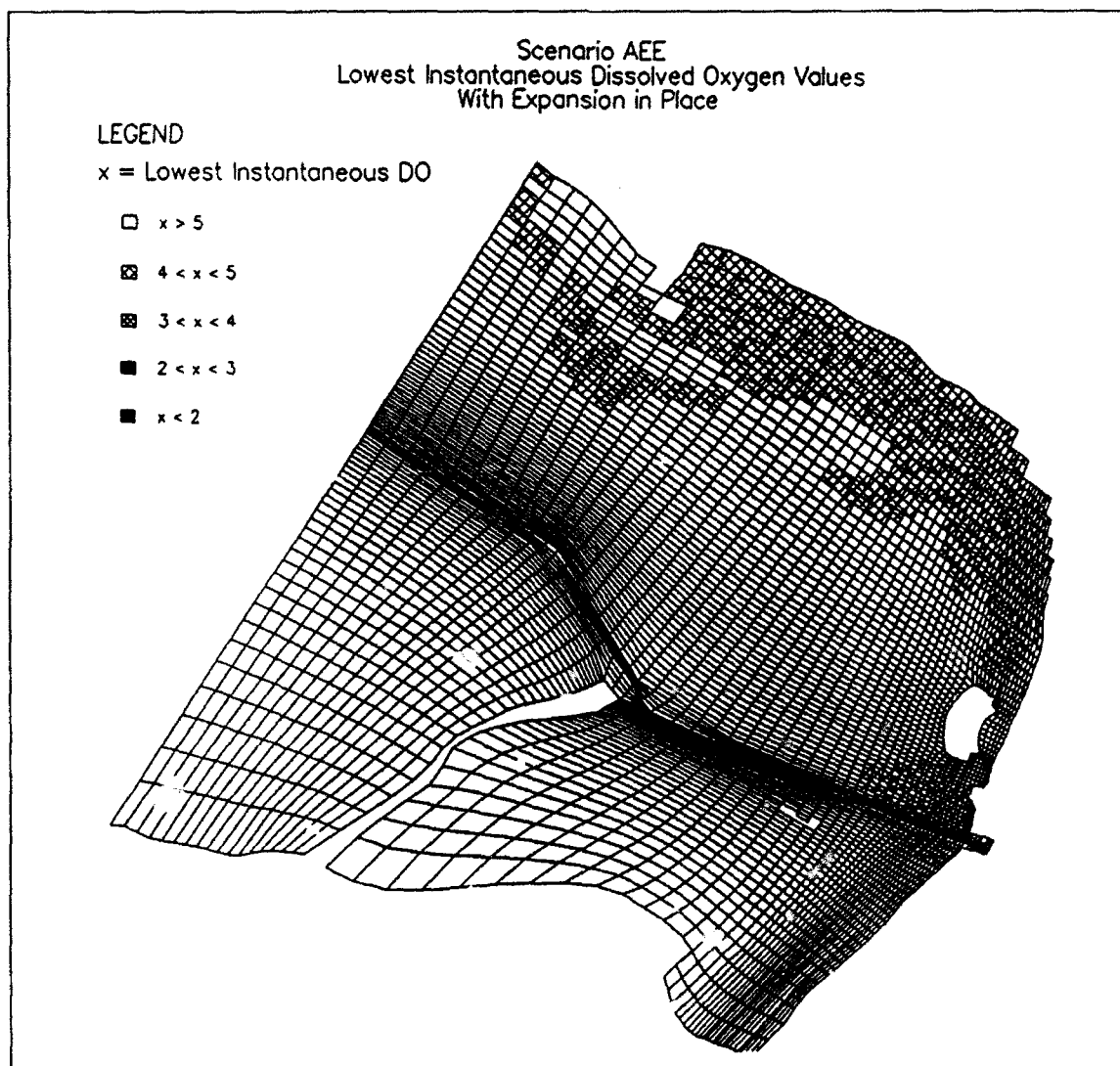


Figure D7. (Concluded)

SCENARIO EEE

**(Extreme Seiche, Extreme River Flows,
Extreme Lake Level)**

Figures D8 - D14

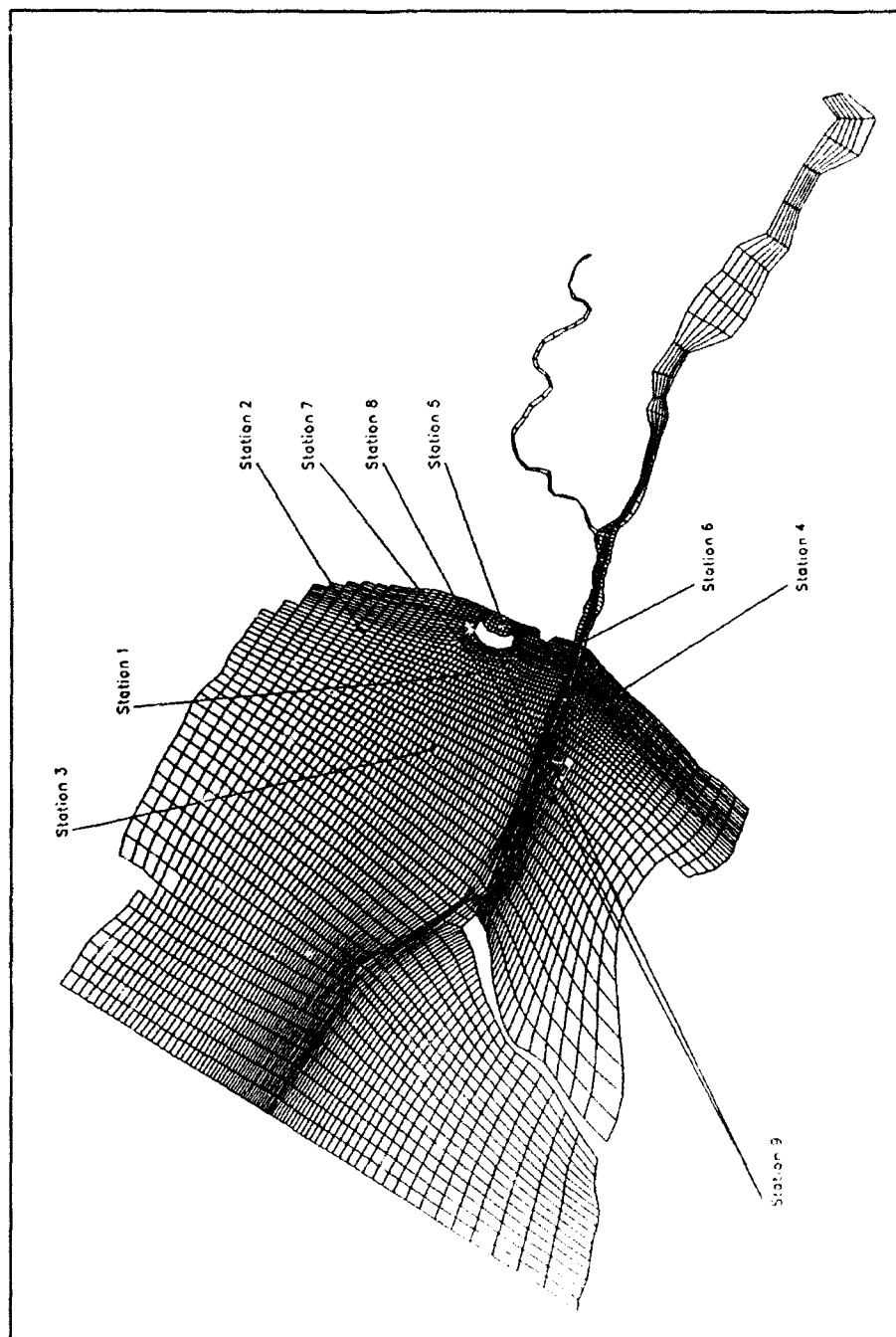


Figure D8. Pre- and post-expansion comparison stations, Scenario EEE

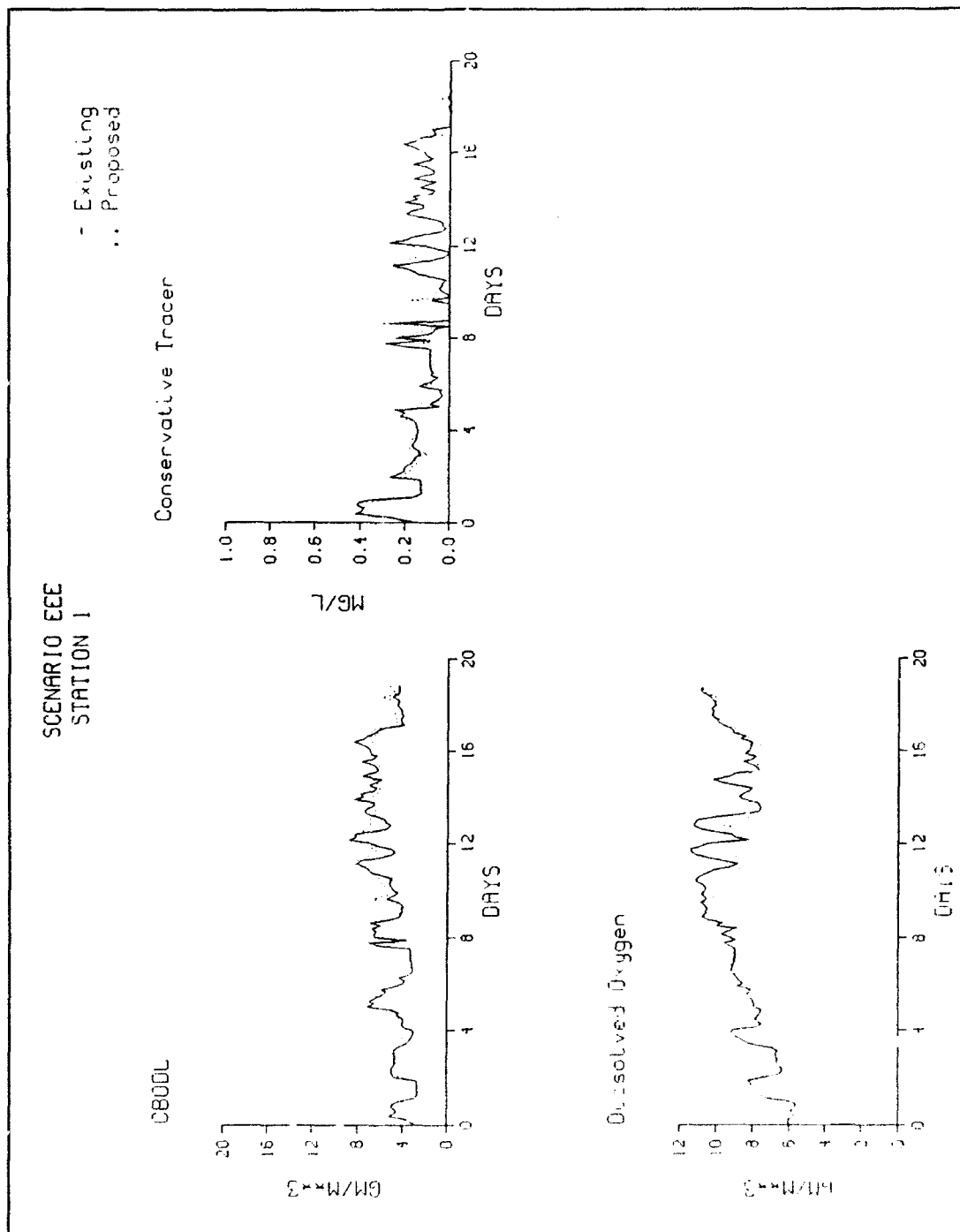


Figure D9. Time series for comparison stations, Scenario EEE (Sheet 1 of 9)

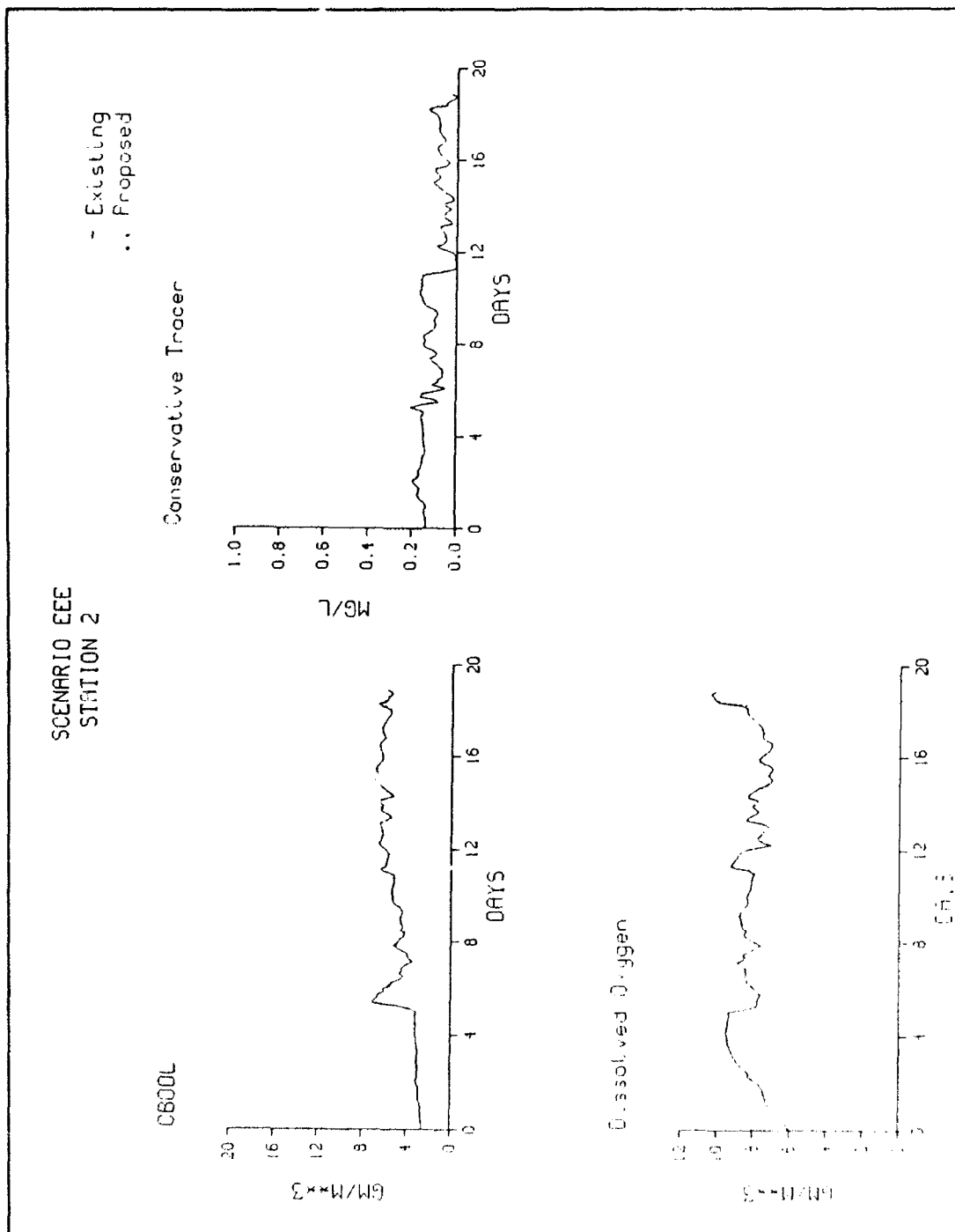


Figure D9. (Sheet 2 of 9)

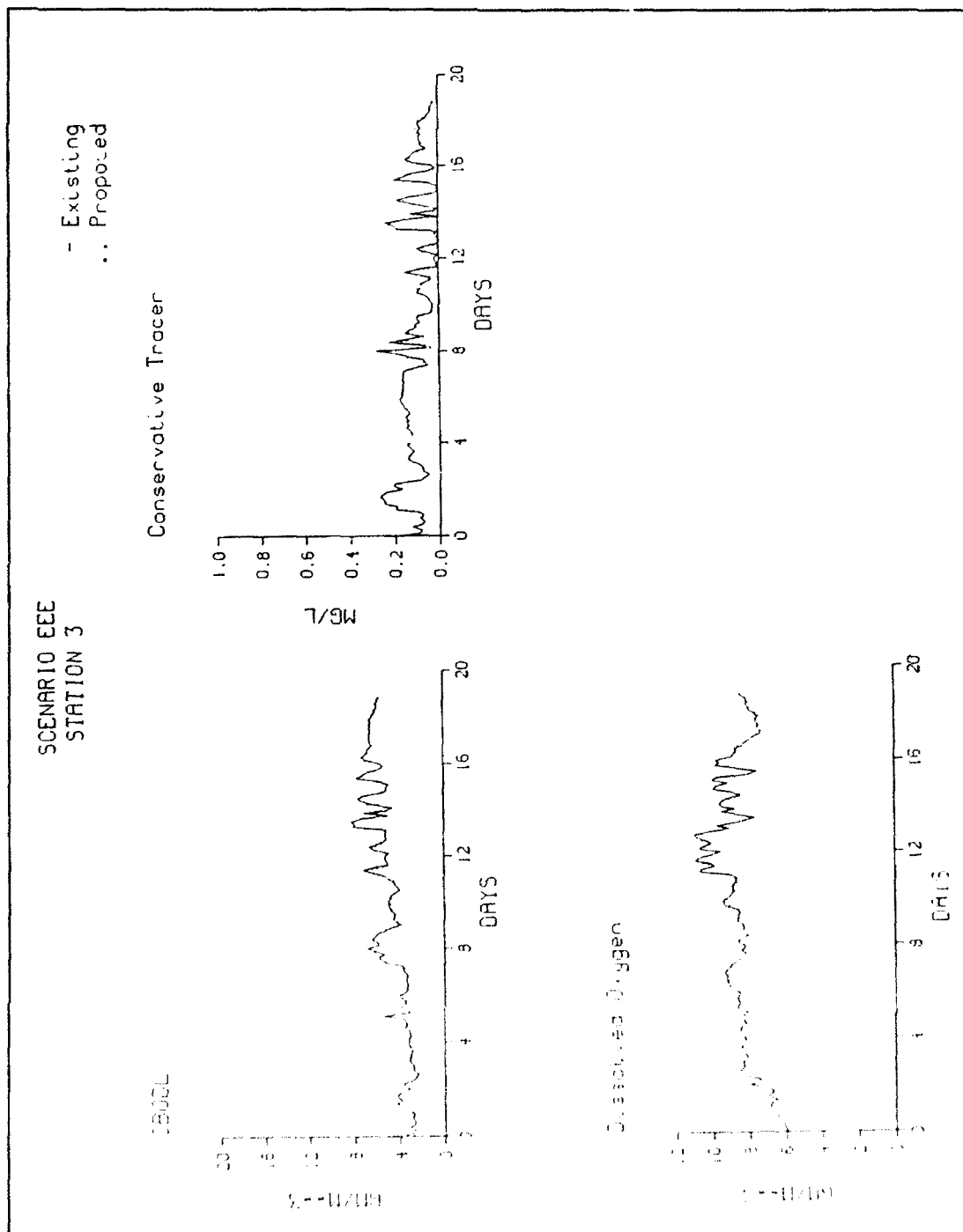


Figure D9. (Sheet 3 of 9)

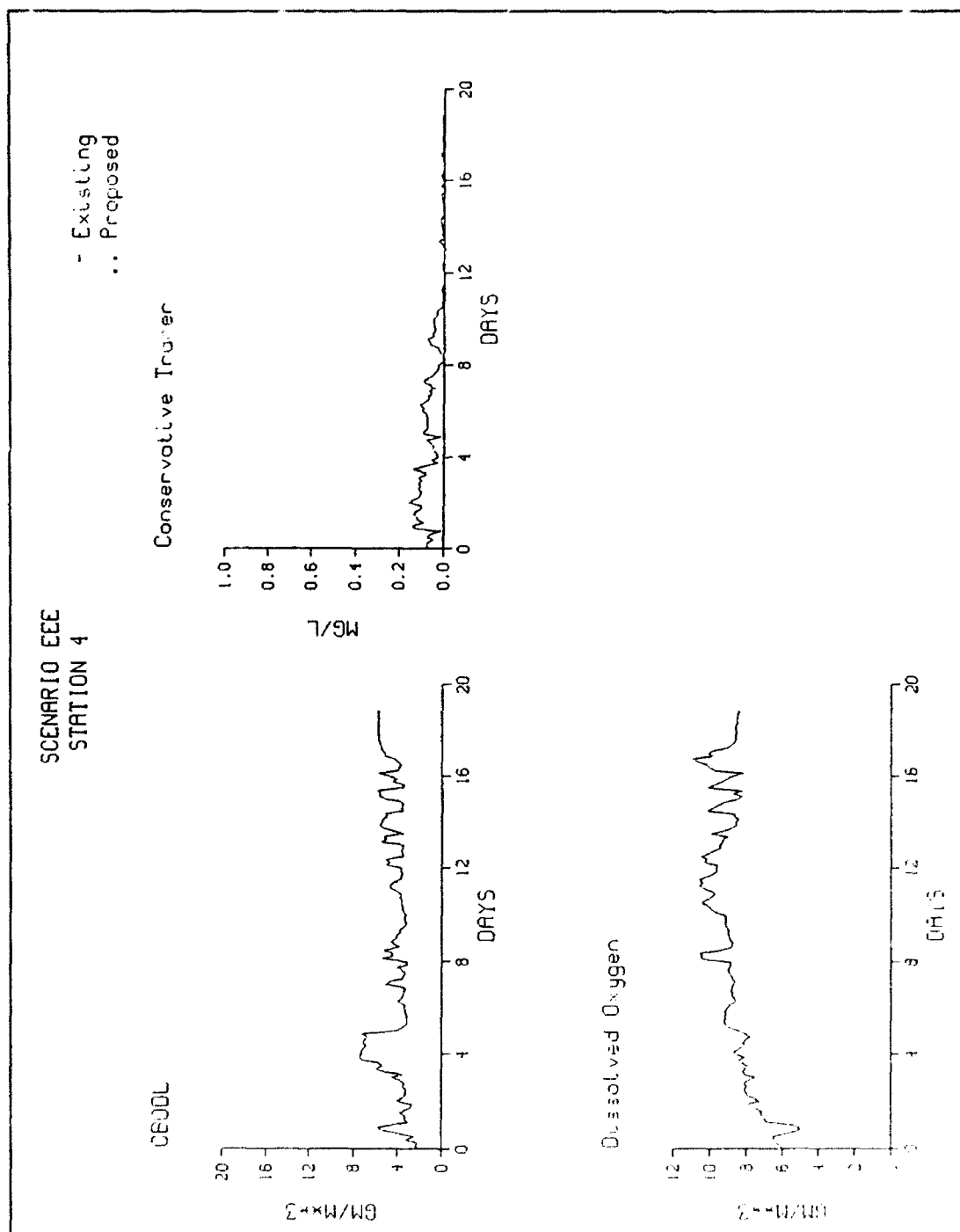


Figure D9. (Sheet 4 of 9)

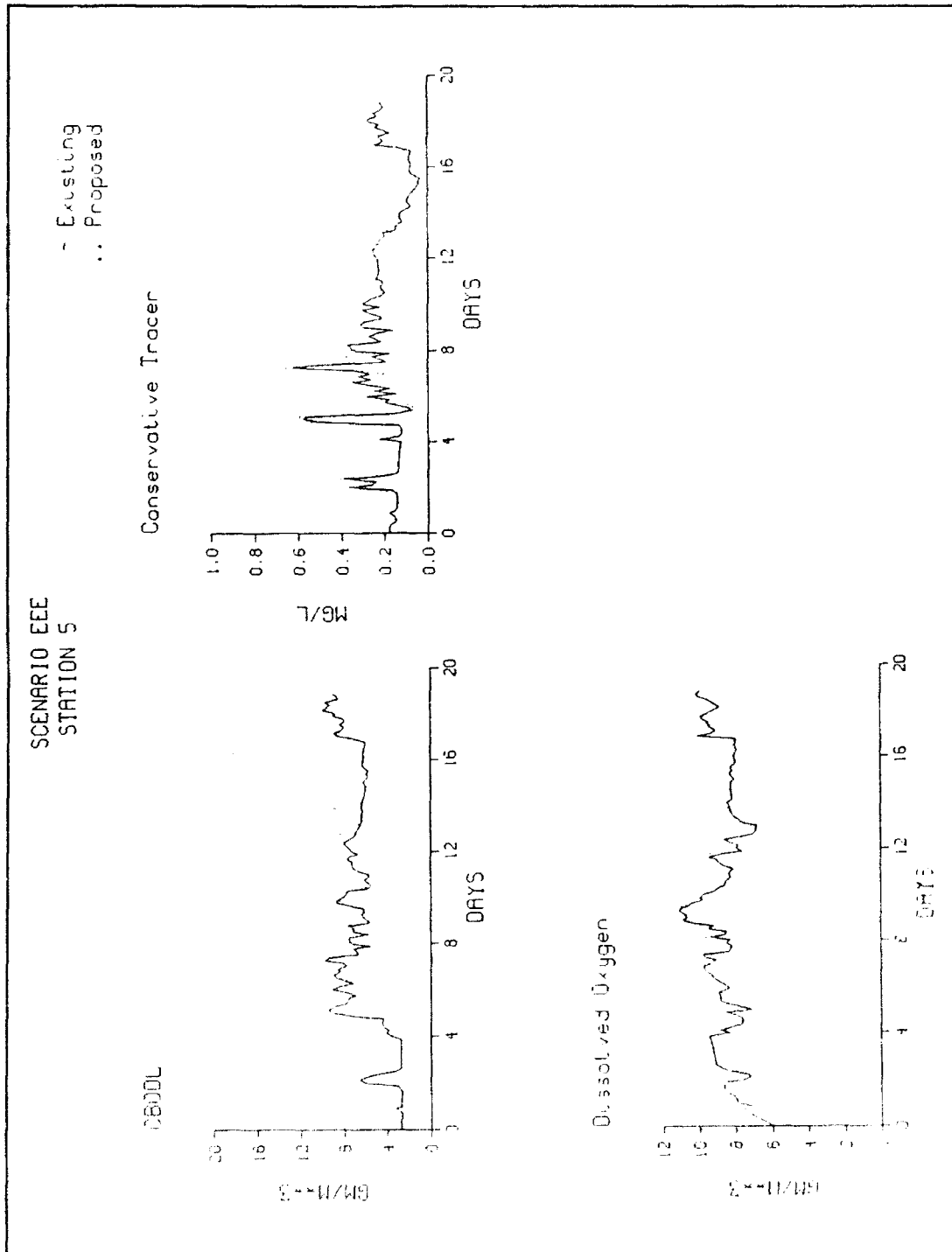


Figure D2. (Sheet 5 of 9)

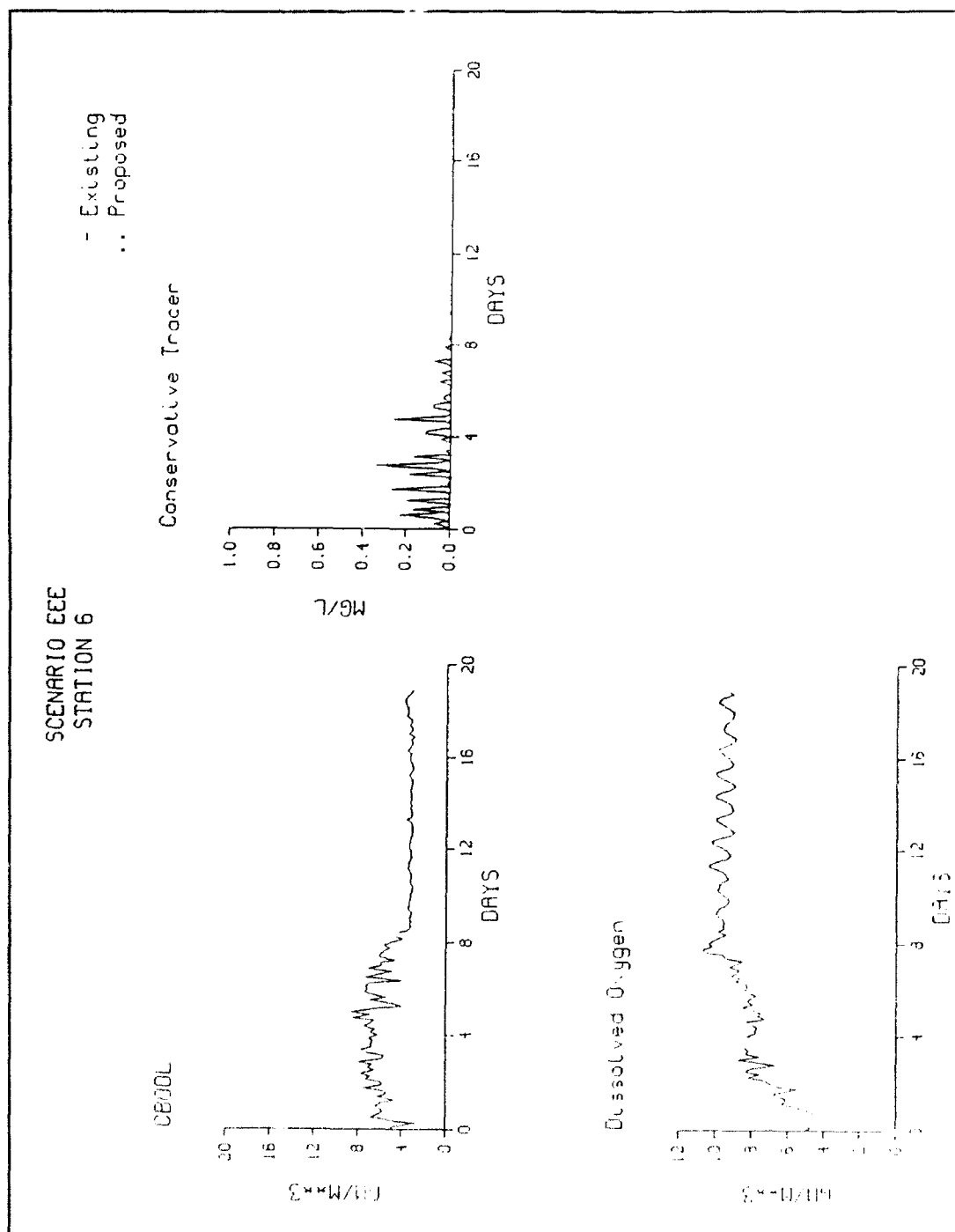


Figure D9. (Sheet 6 of 9)

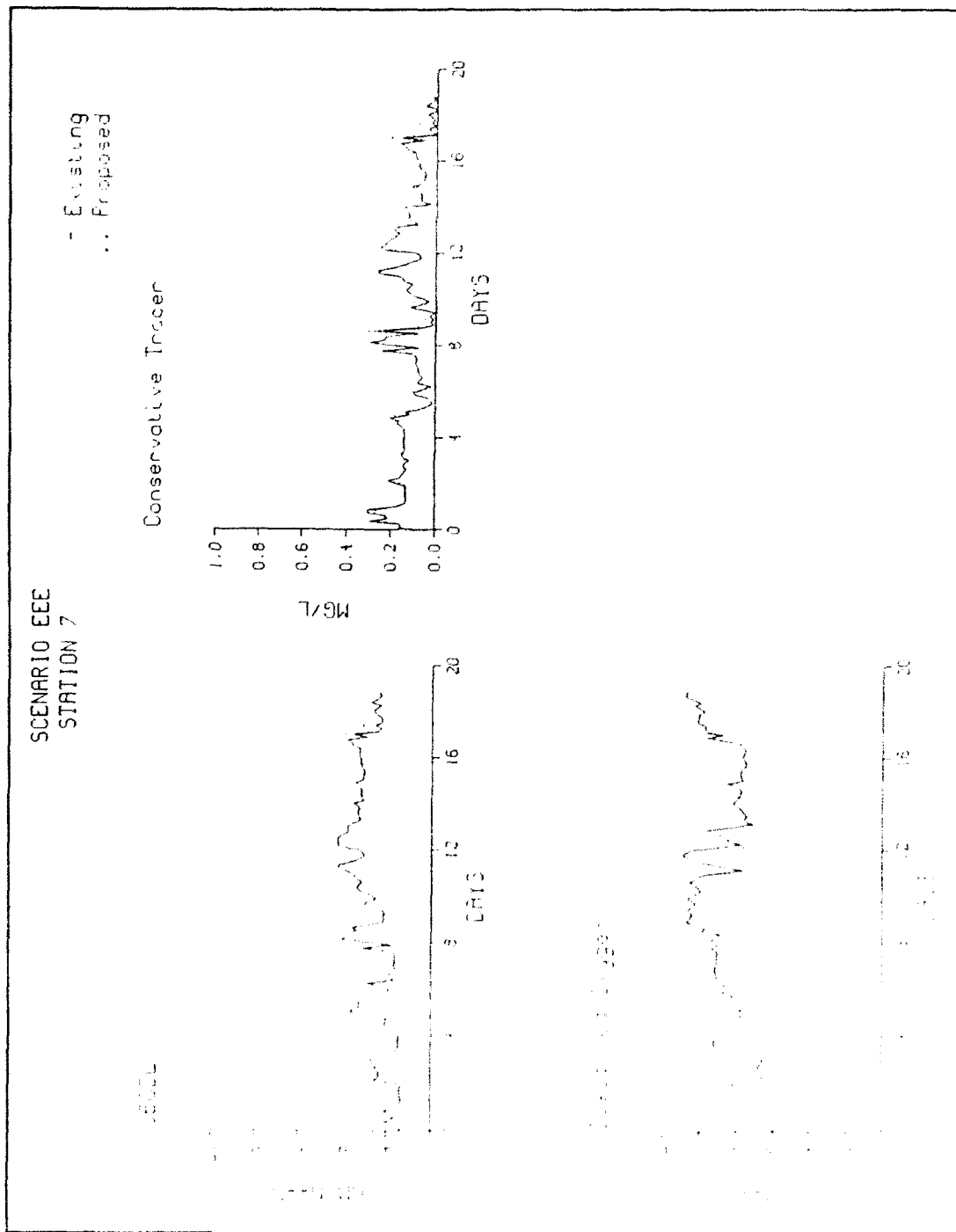


Figure D9. (Sheet 7 of 9)

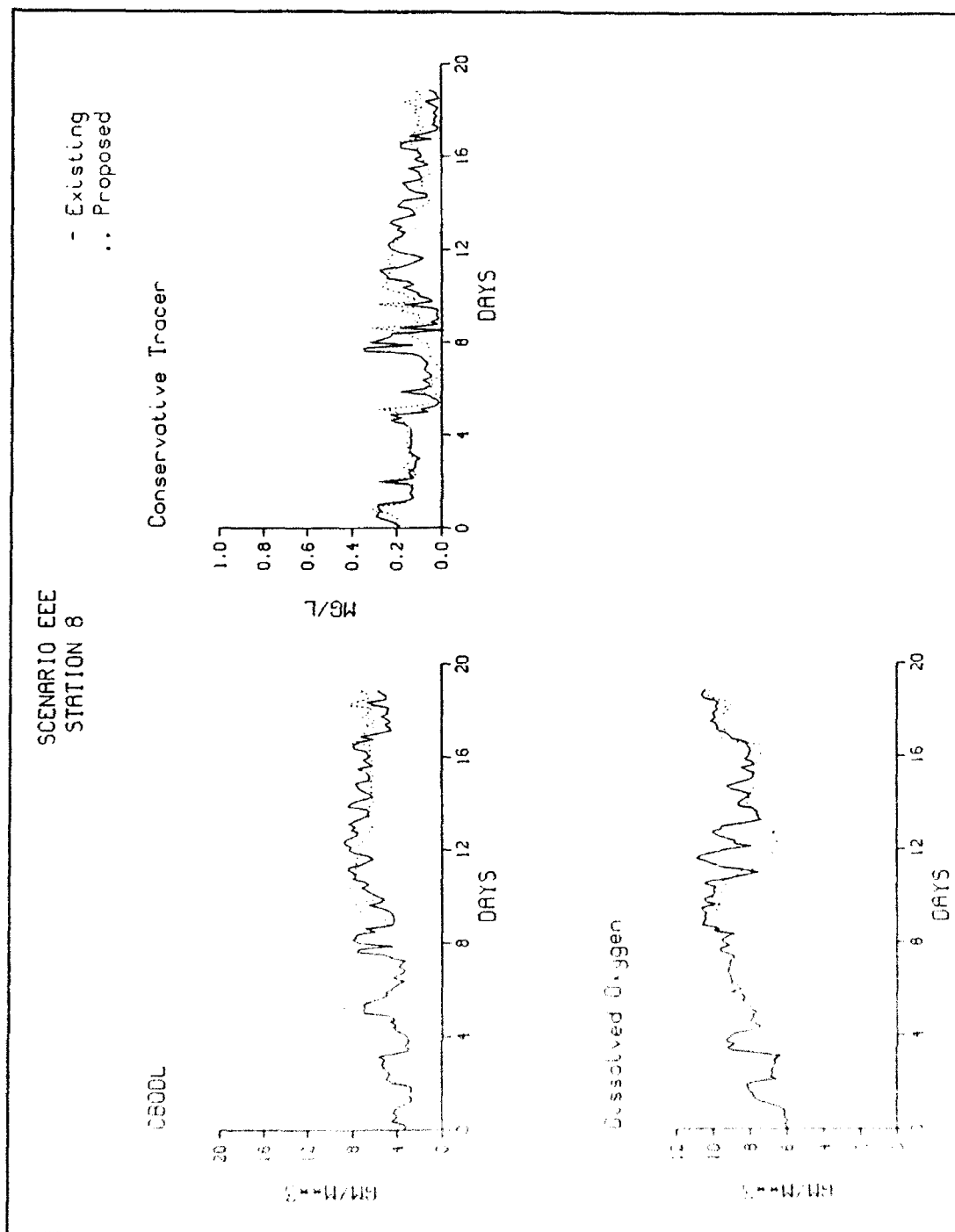


Figure D9. (Sheet 8 of 9)

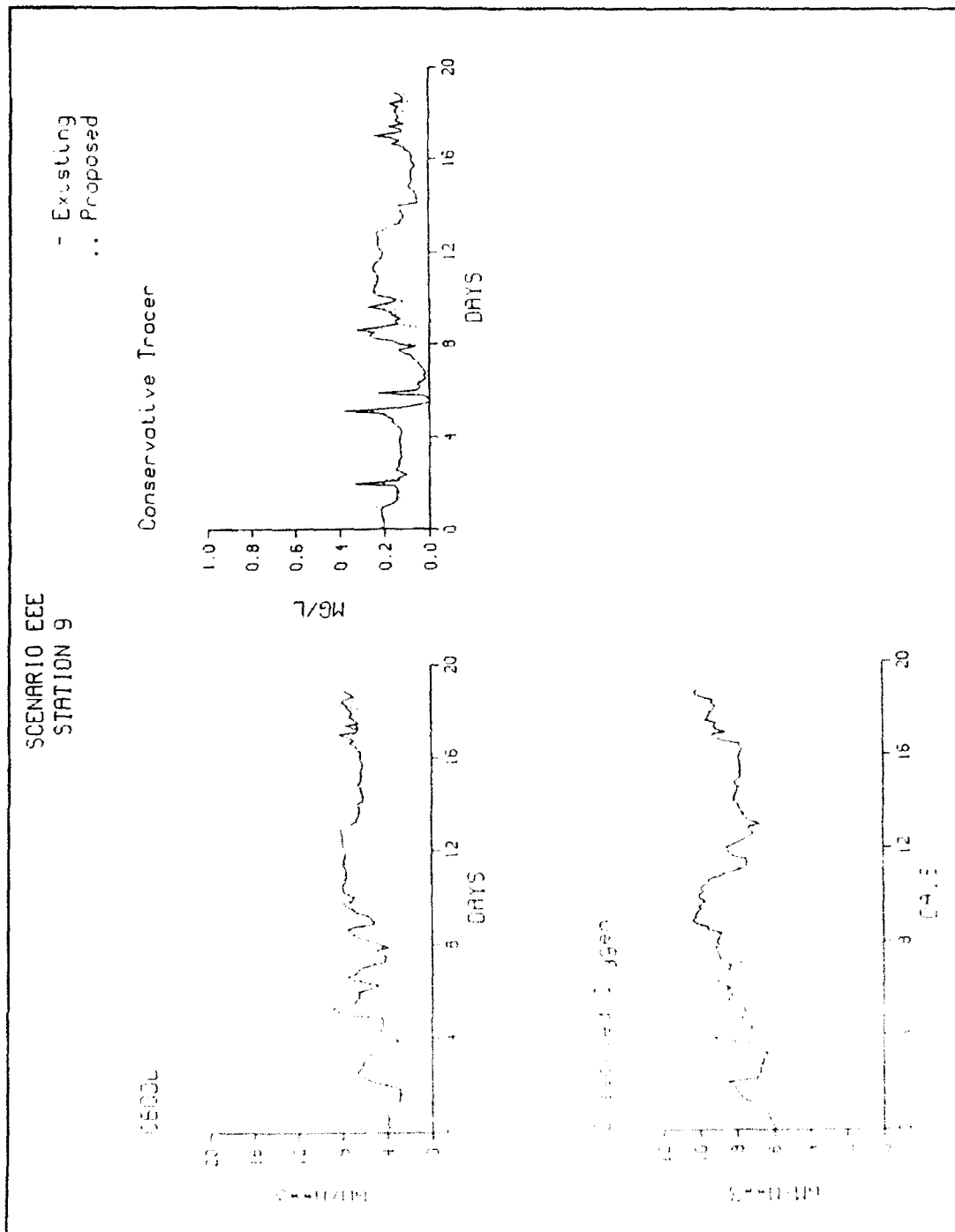


Figure D9. (Sheet 9 of 9)

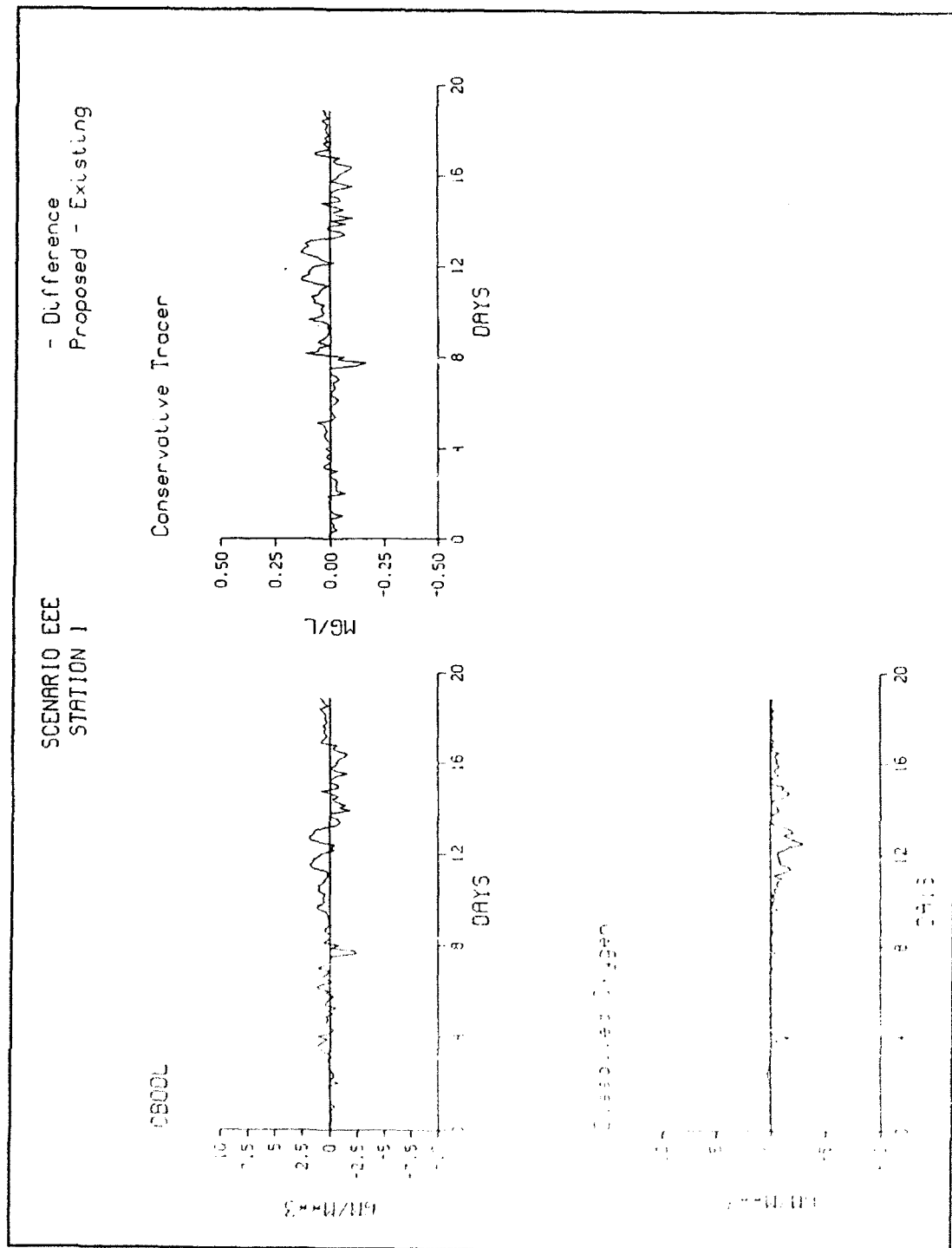


Figure D10. Time series differences for comparison stations, Scenario EEE (Sheet 1 of 8)

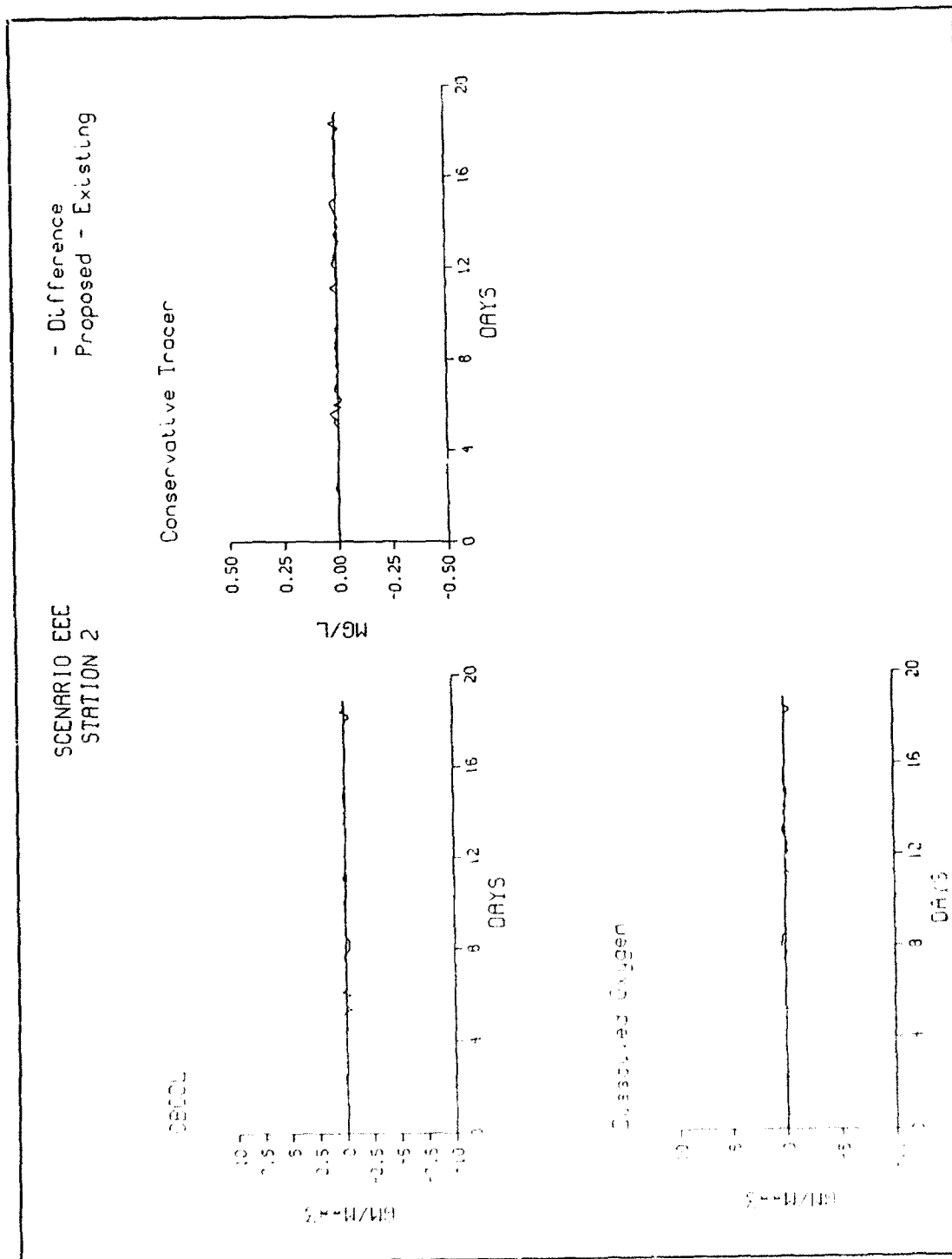


Figure D10. (Sheet 2 of 8)

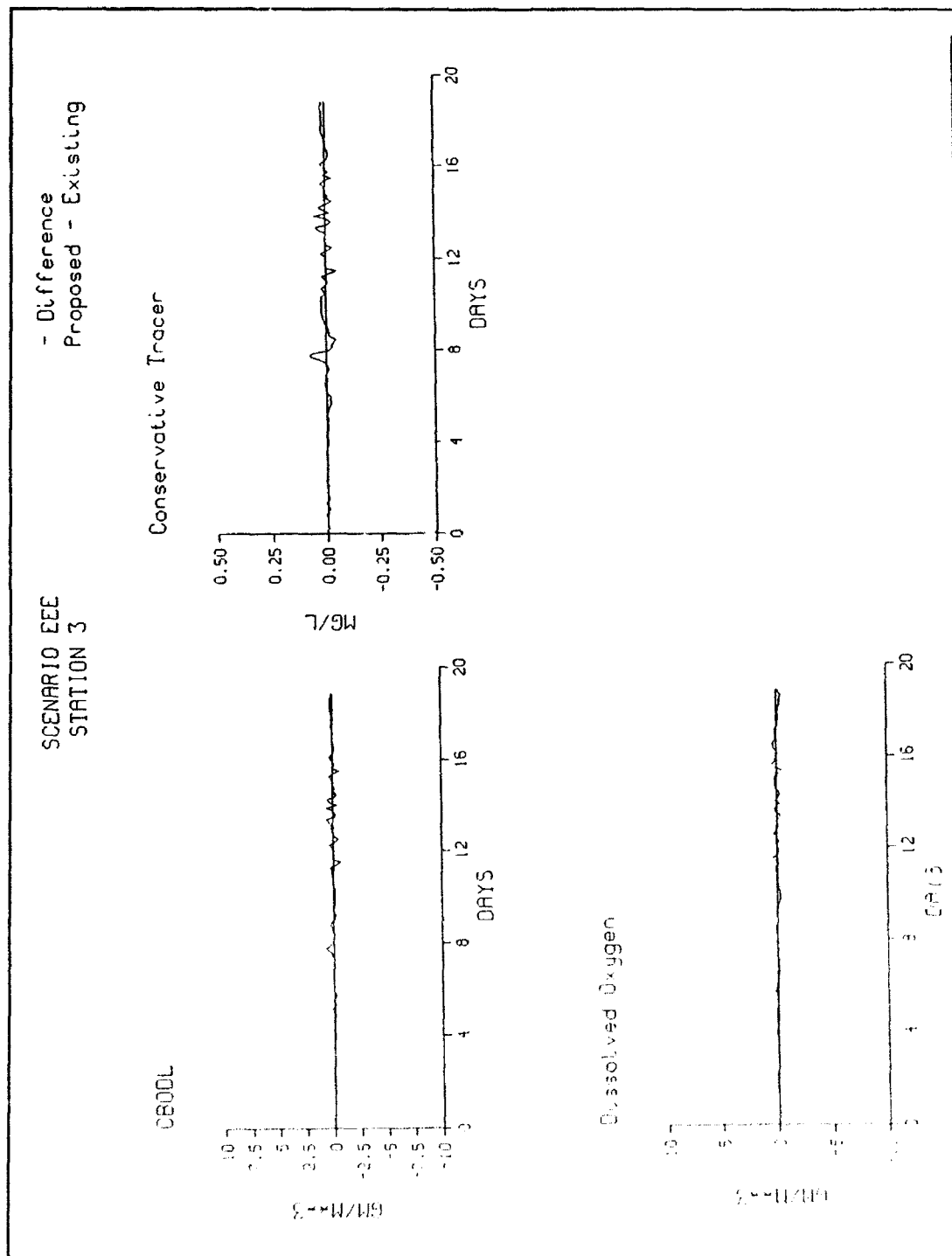


Figure D10: (Sheet 3 of 8)

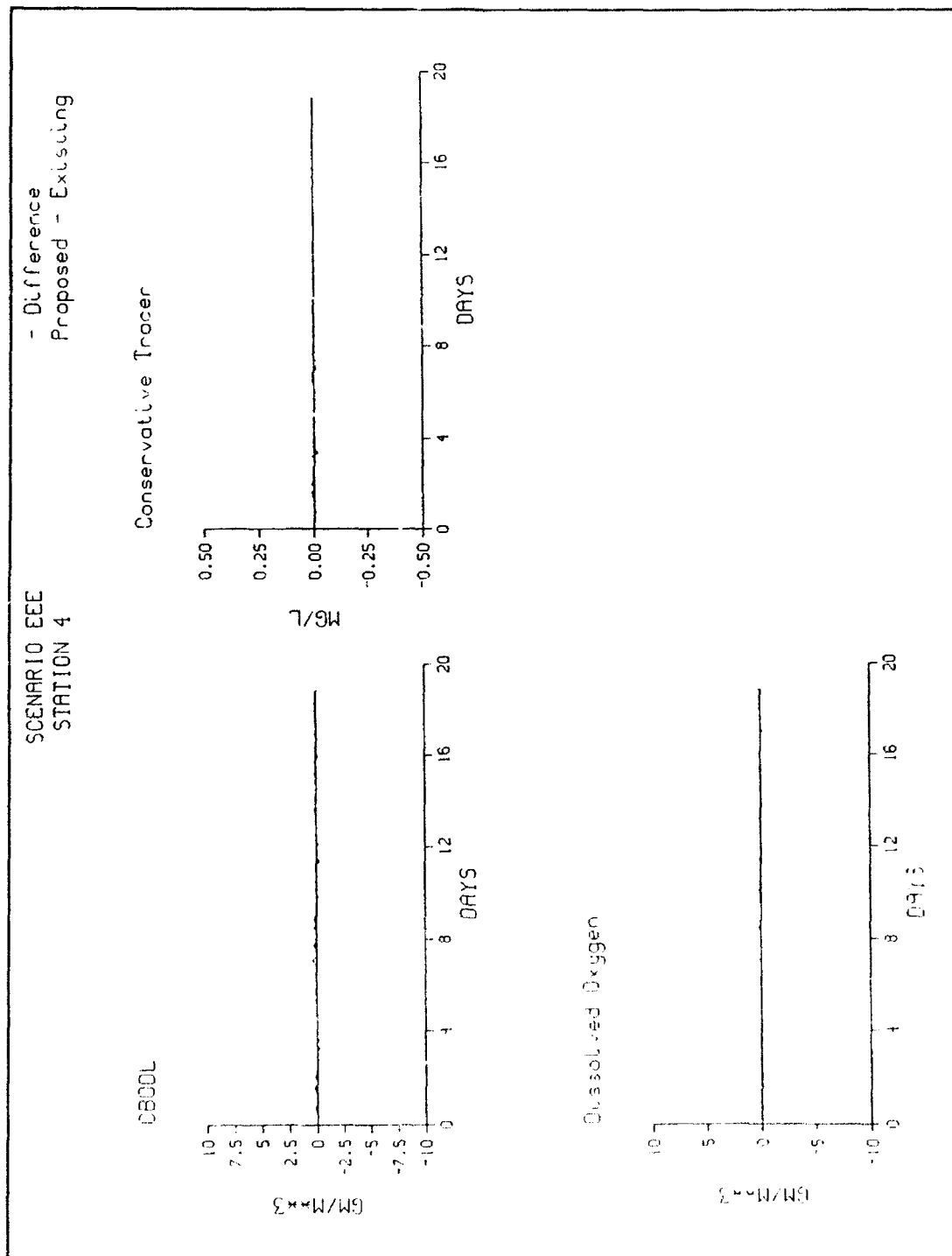


Figure D10. (Sheet 4 of 8)

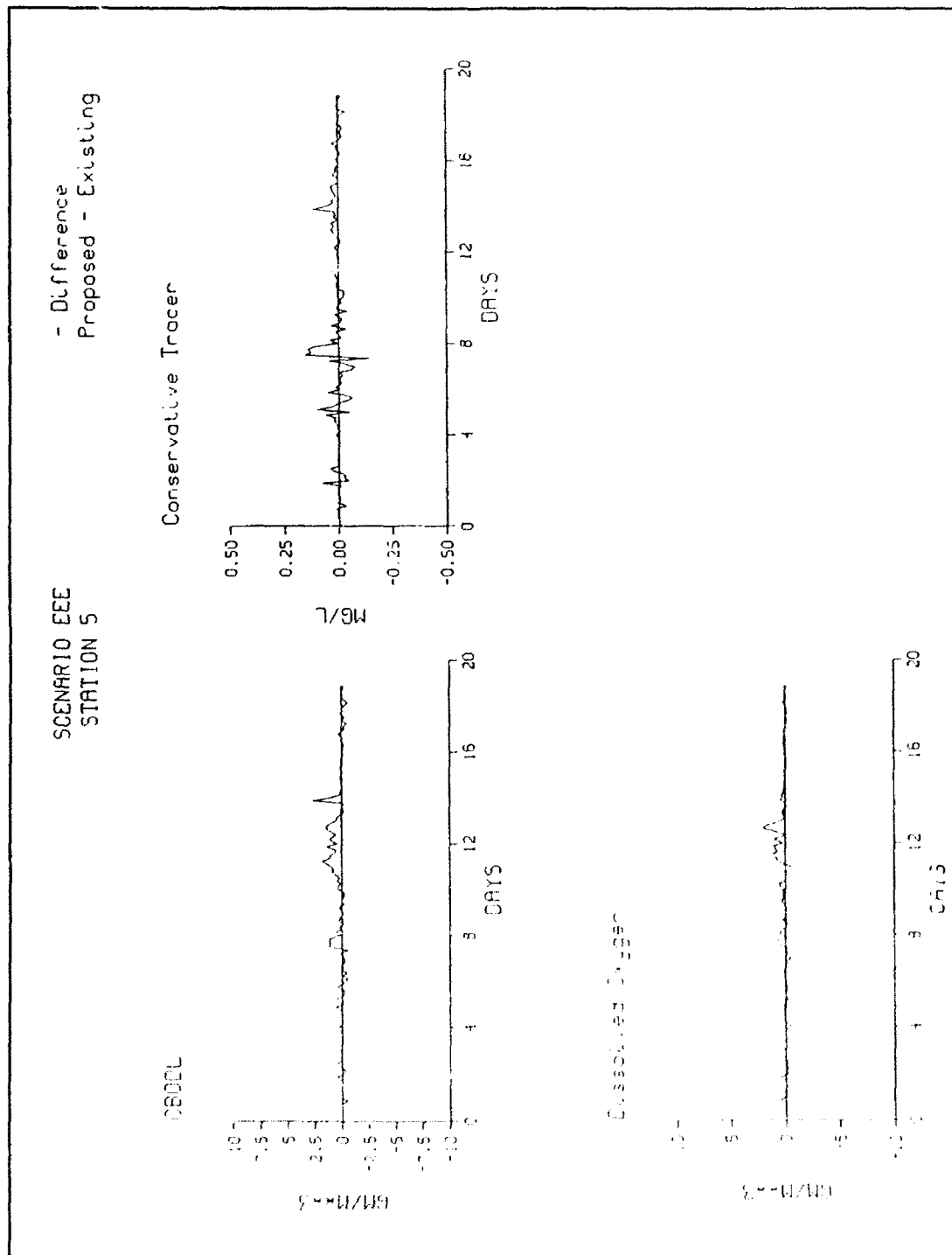


Figure D10. (Sheet 5 of 8)

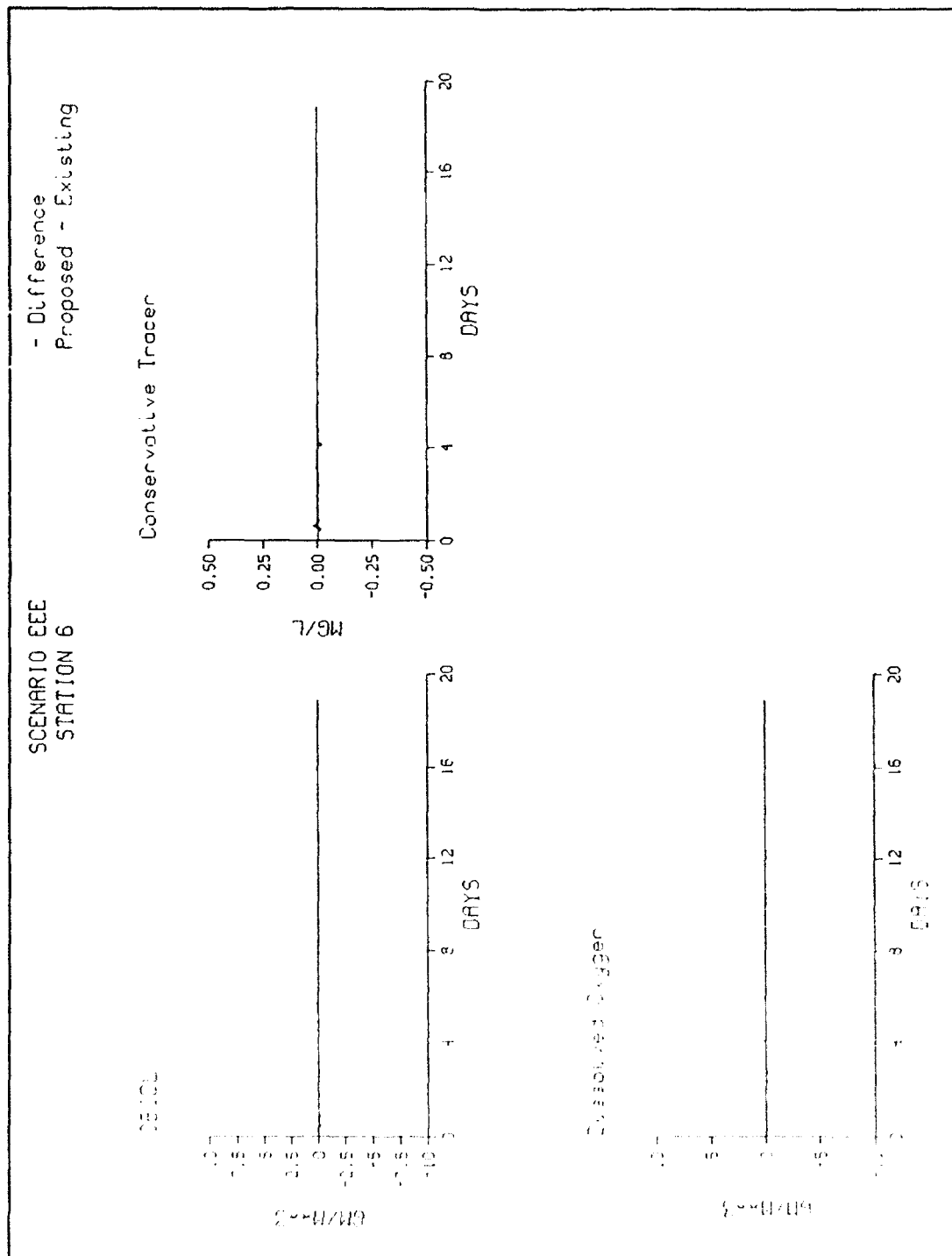


Figure D10. (Sheet 6 of 8)

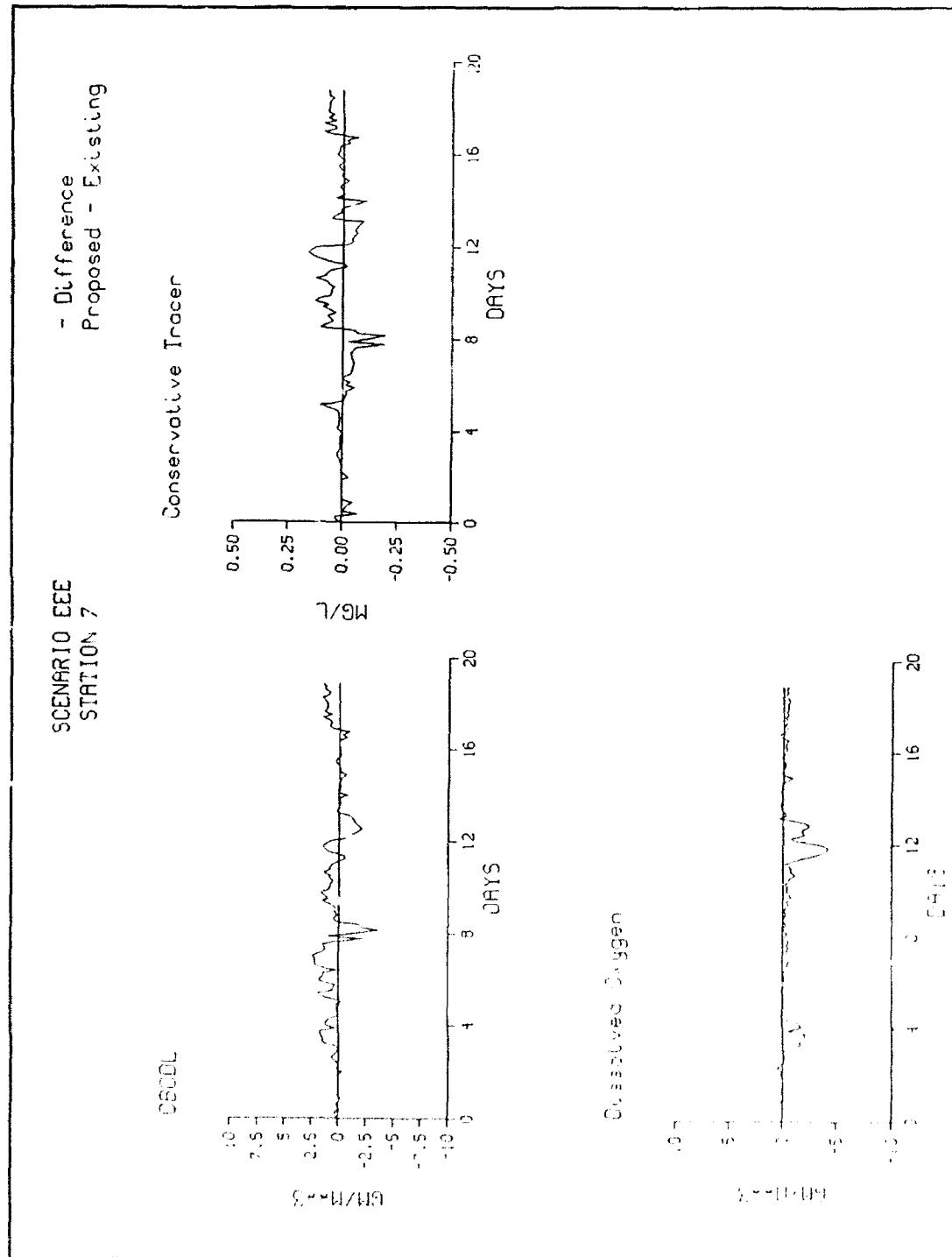


Figure D10. (Sheet 7 of 8)

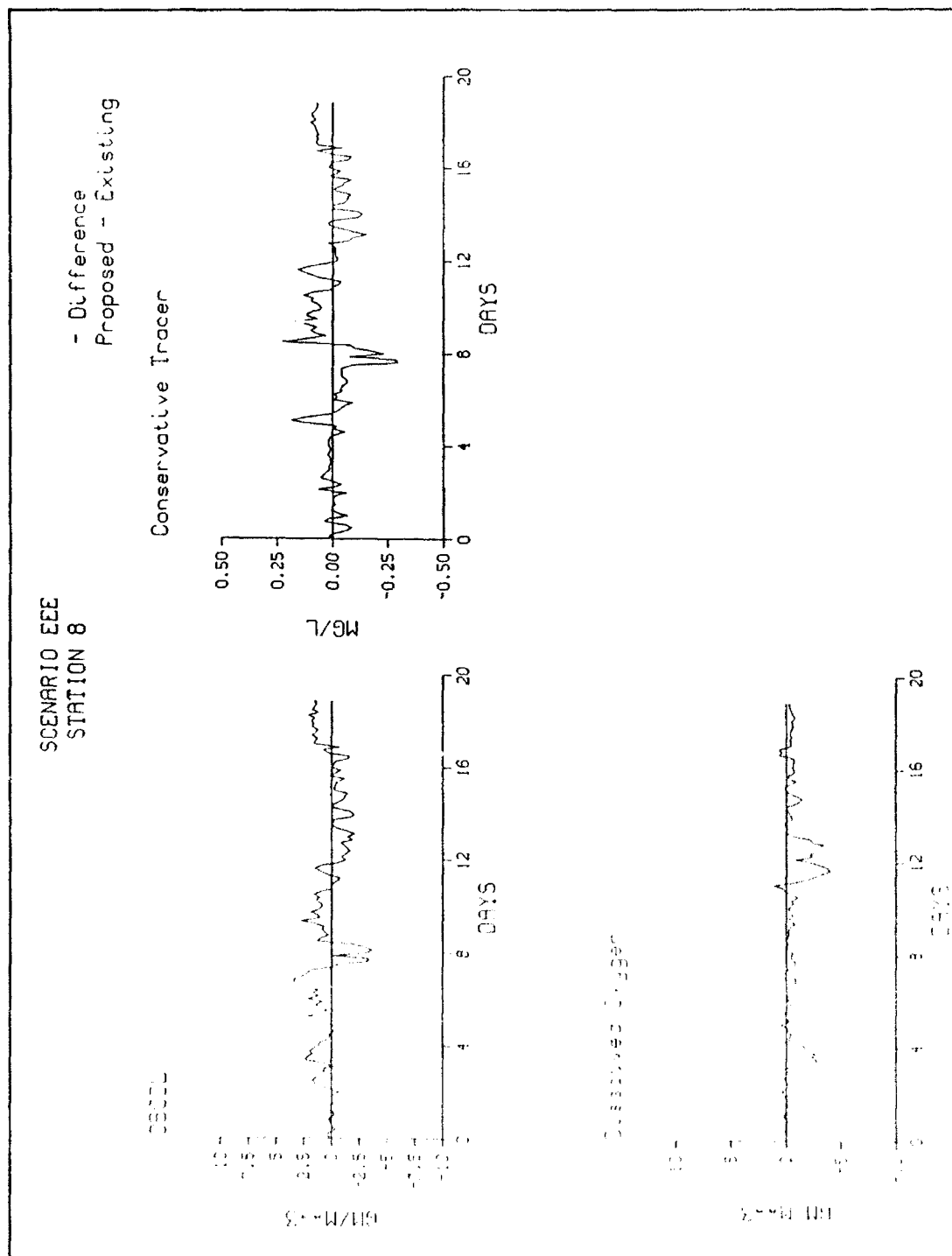


Figure D10. (Sheet 8 of 8)

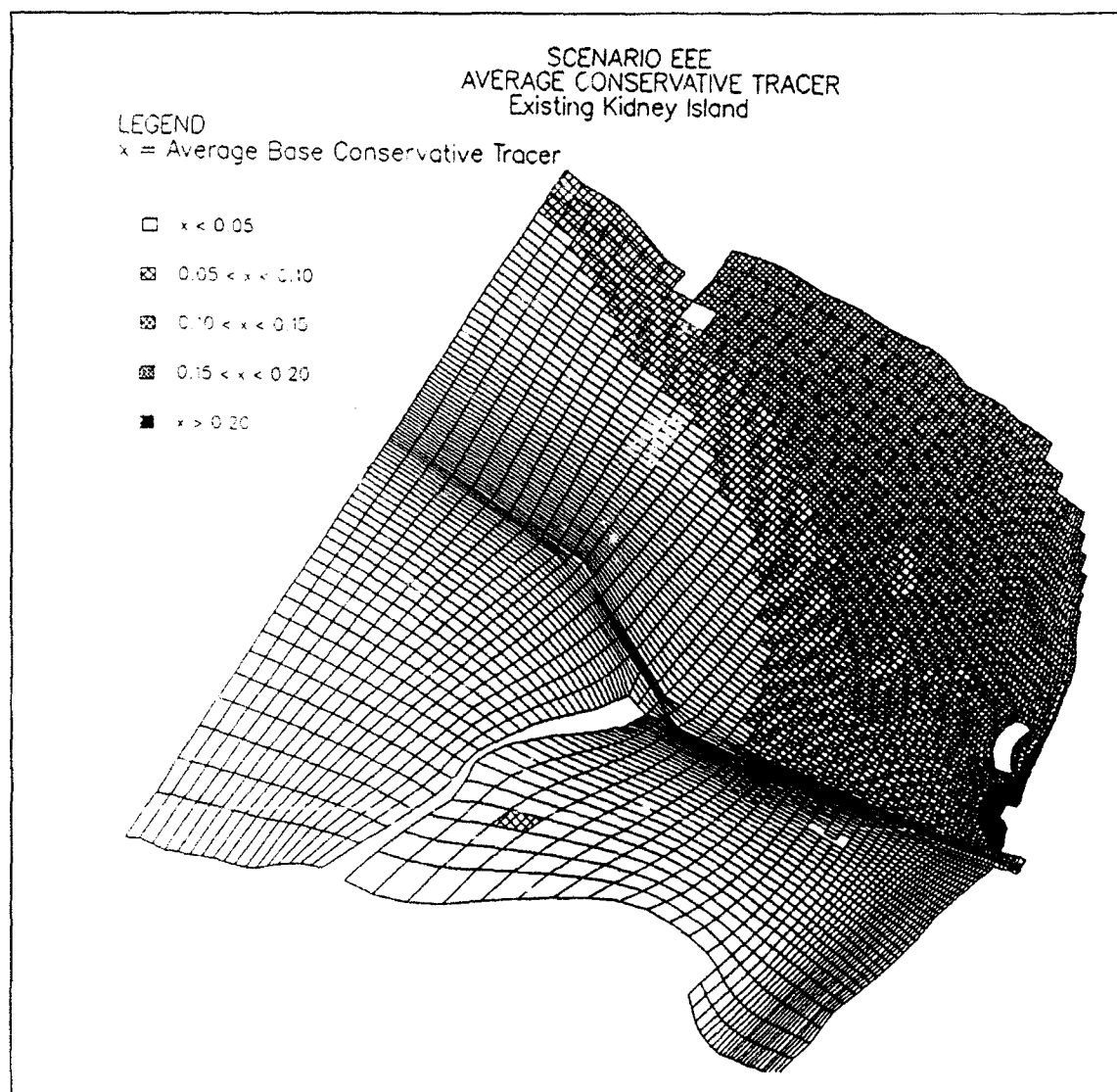


Figure D11. Average conservative tracer concentrations, Scenario EEE (Continued)

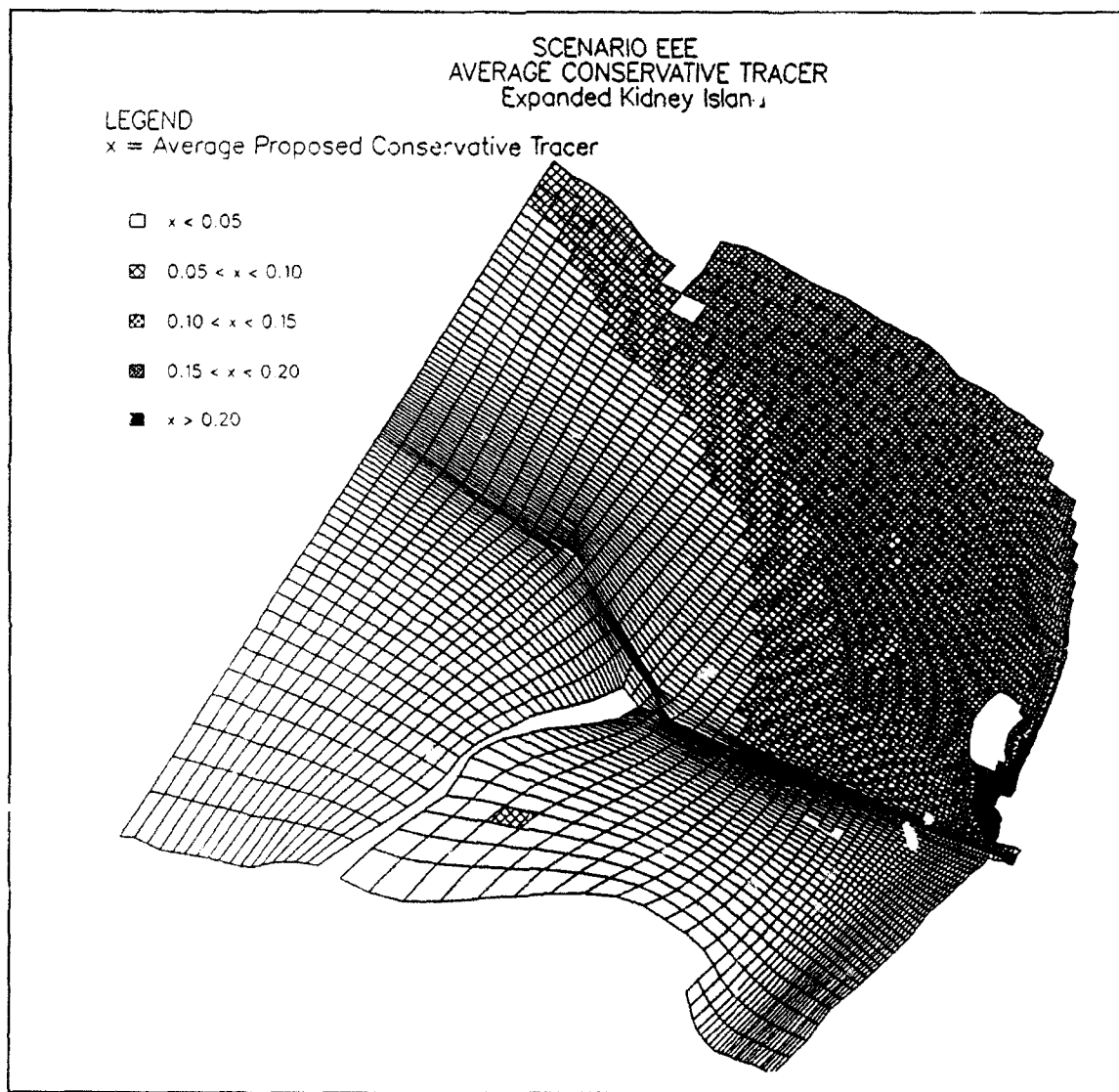


Figure D11. (Concluded)

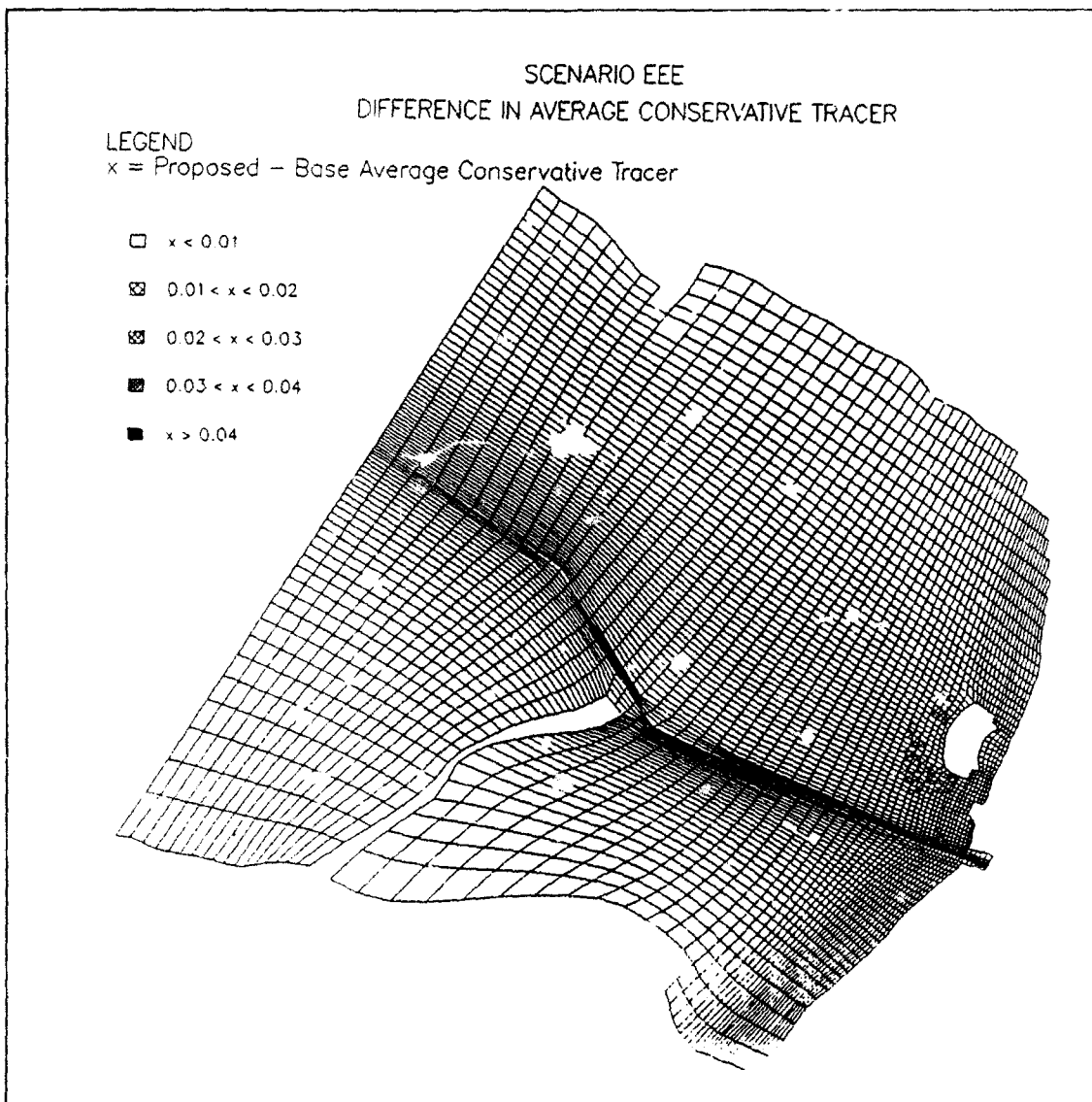


Figure D12. Difference in average conservative tracer, Scenario EEE

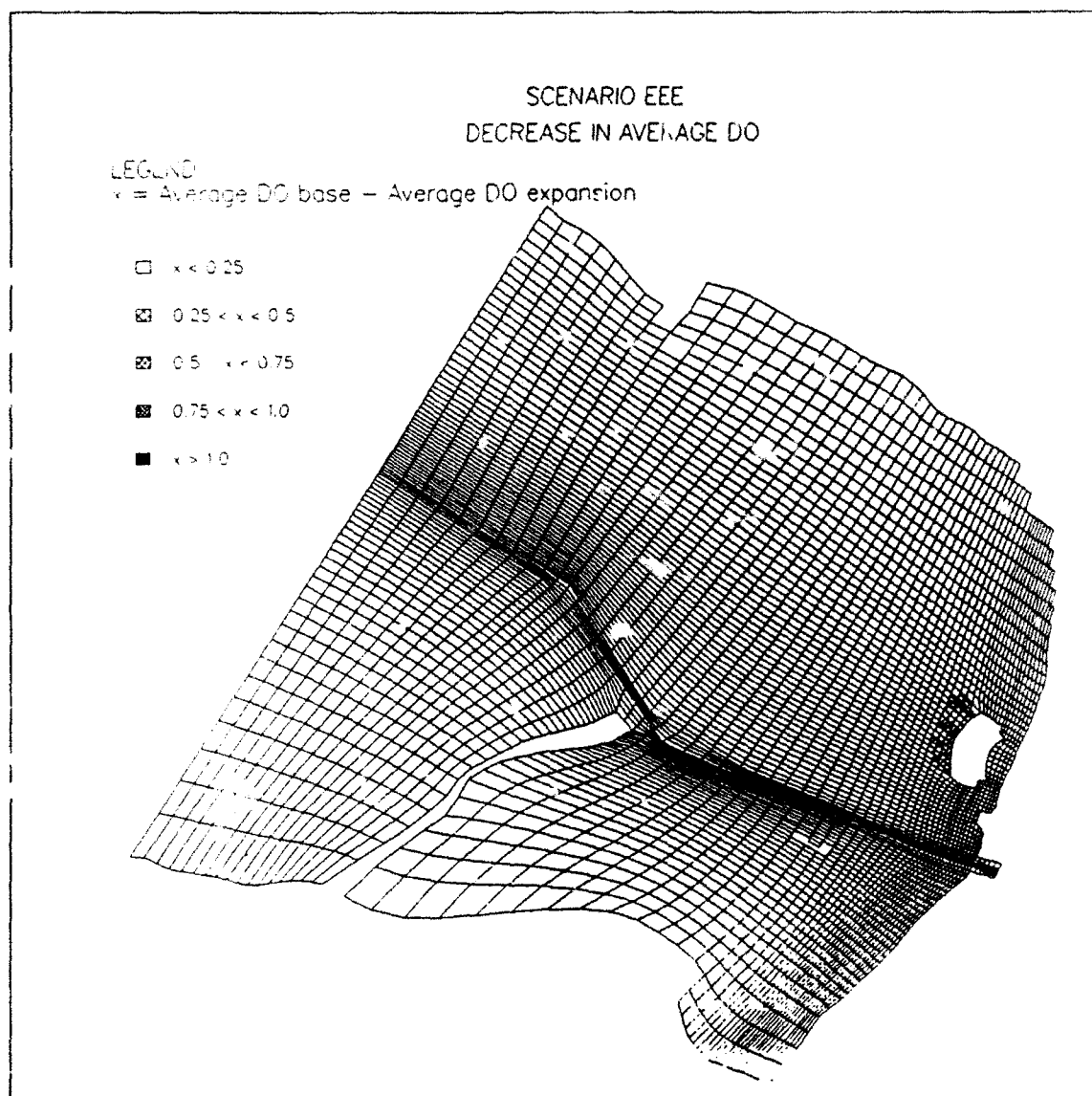


Figure D13. Decrease in average DO concentrations, Scenario EEE

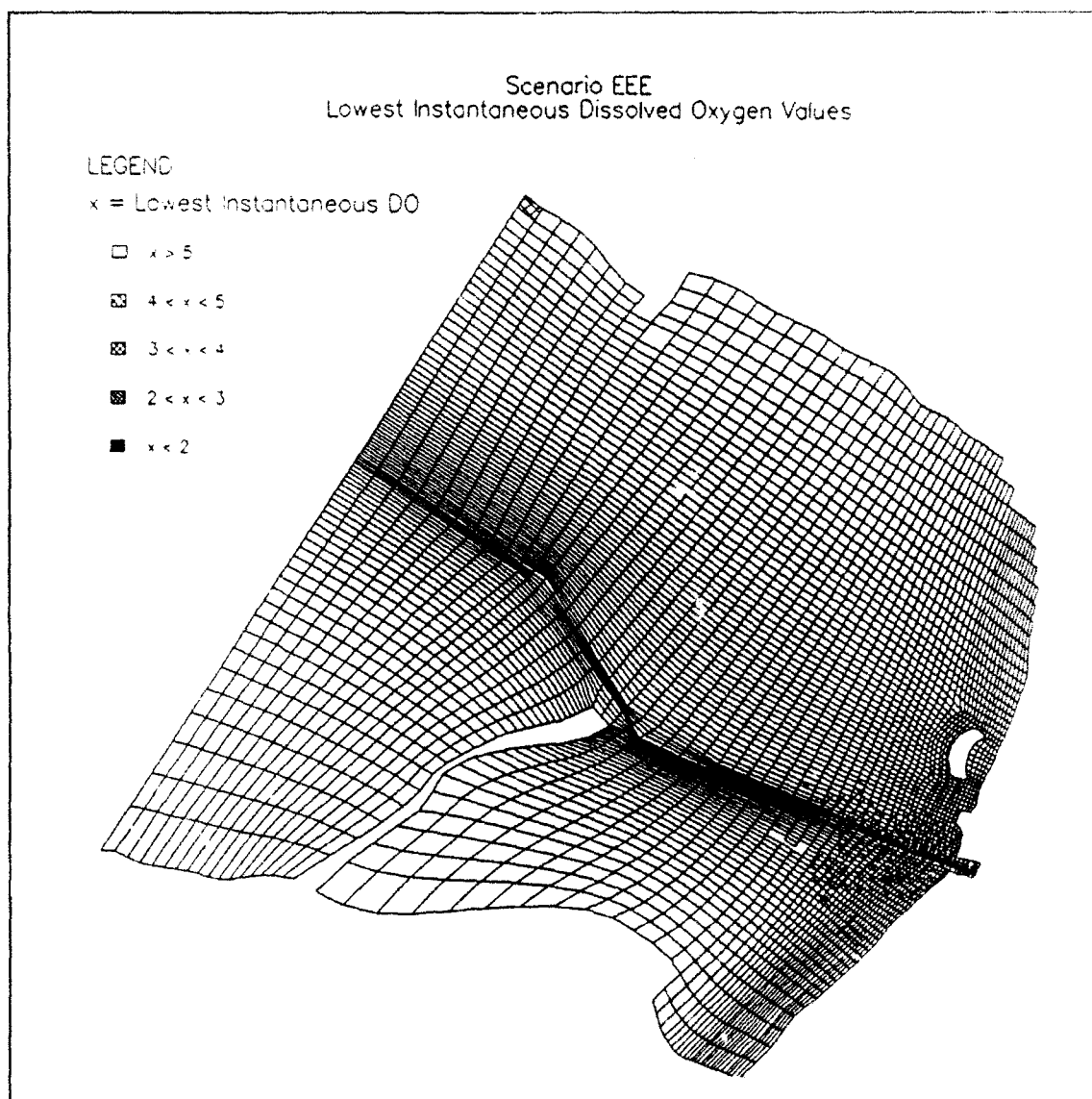


Figure D14. Lowest instantaneous DO, Scenario EEE (Continued)

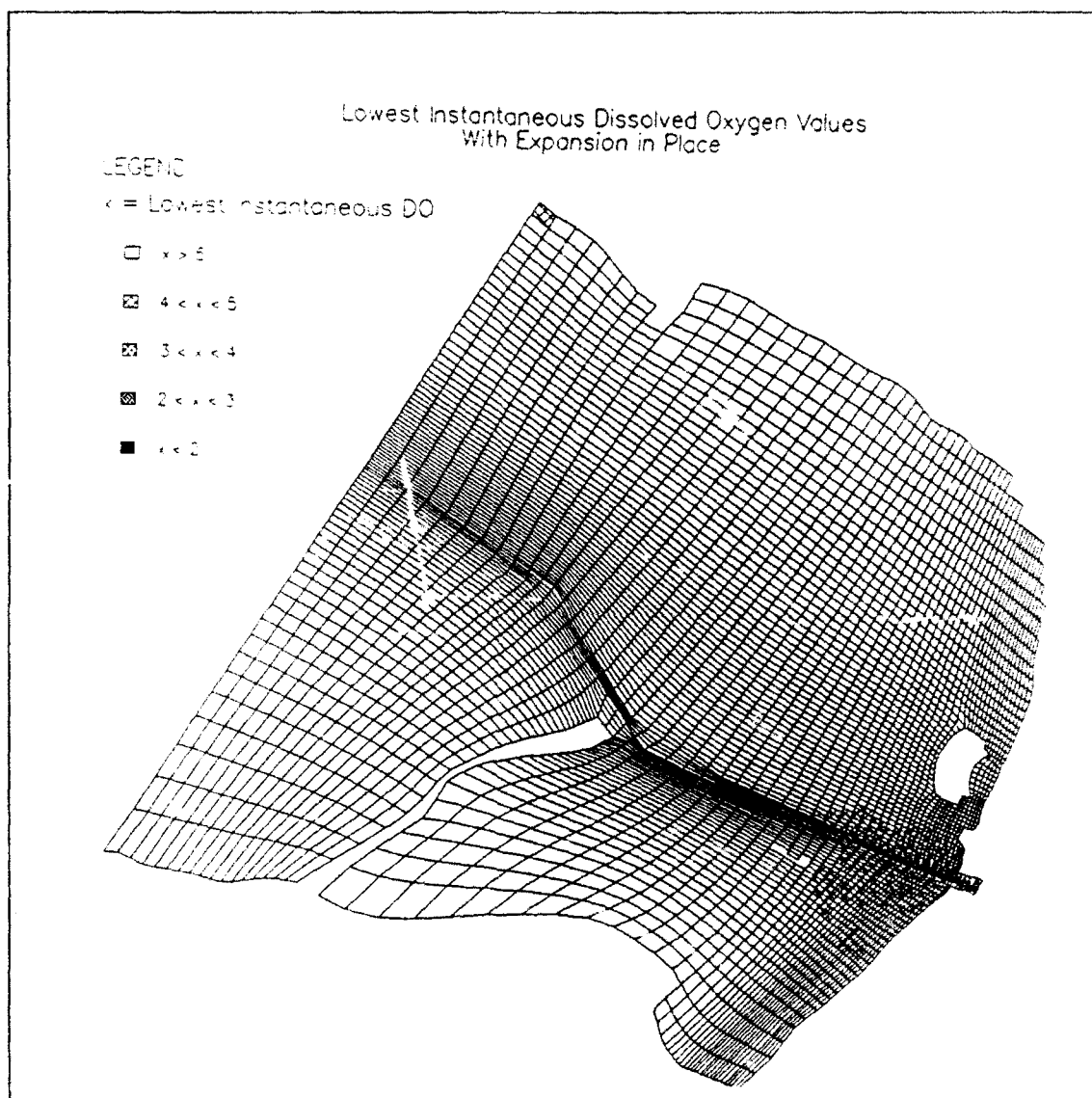


Figure D14. (Concluded)

SCENARIO EEM

**(Extreme Seiche, Extreme River Flows,
Minimum Lake Level)**

Figures D15 - D21

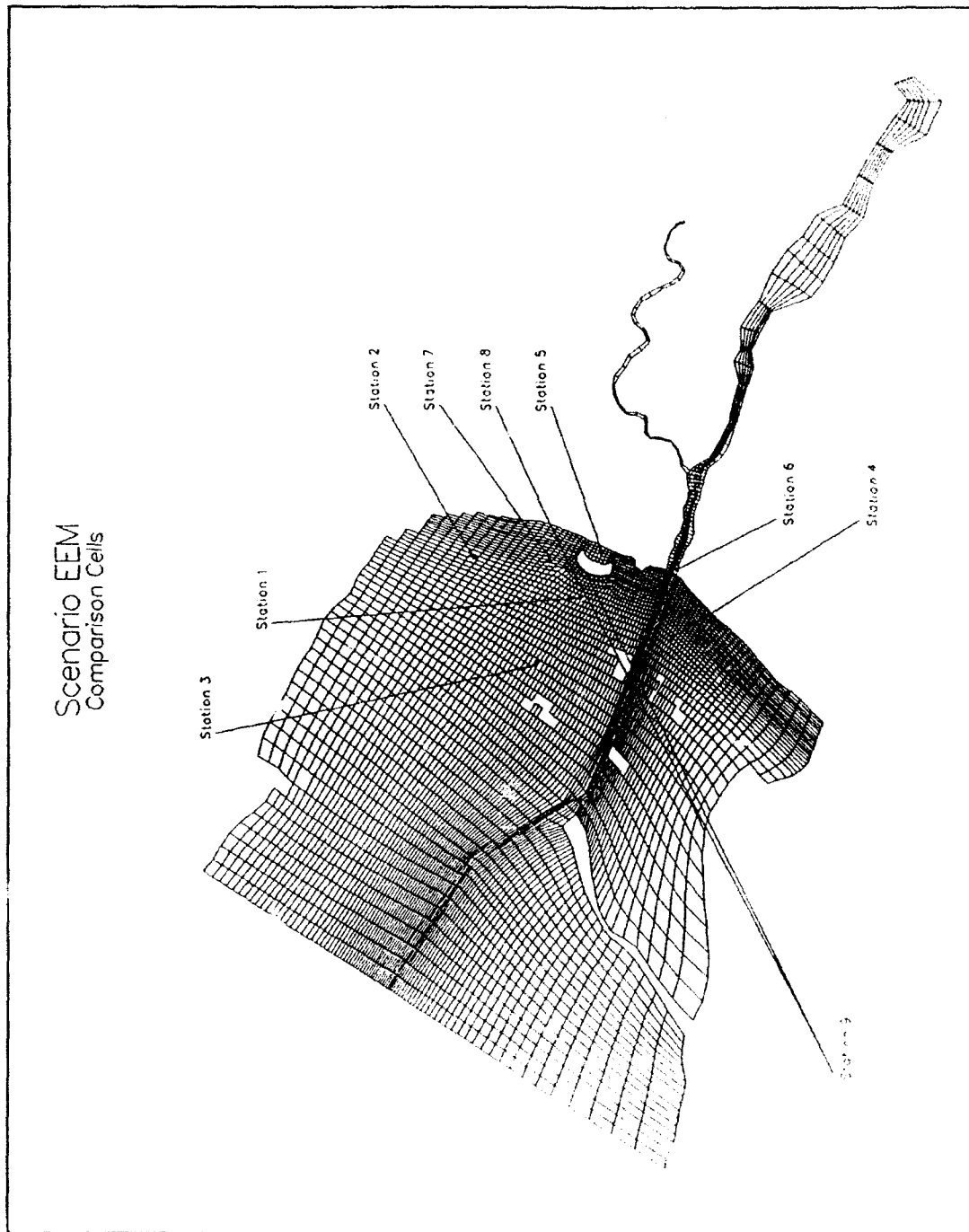


Figure D15. Pre-and post-expansion comparison stations, Scenario EEM

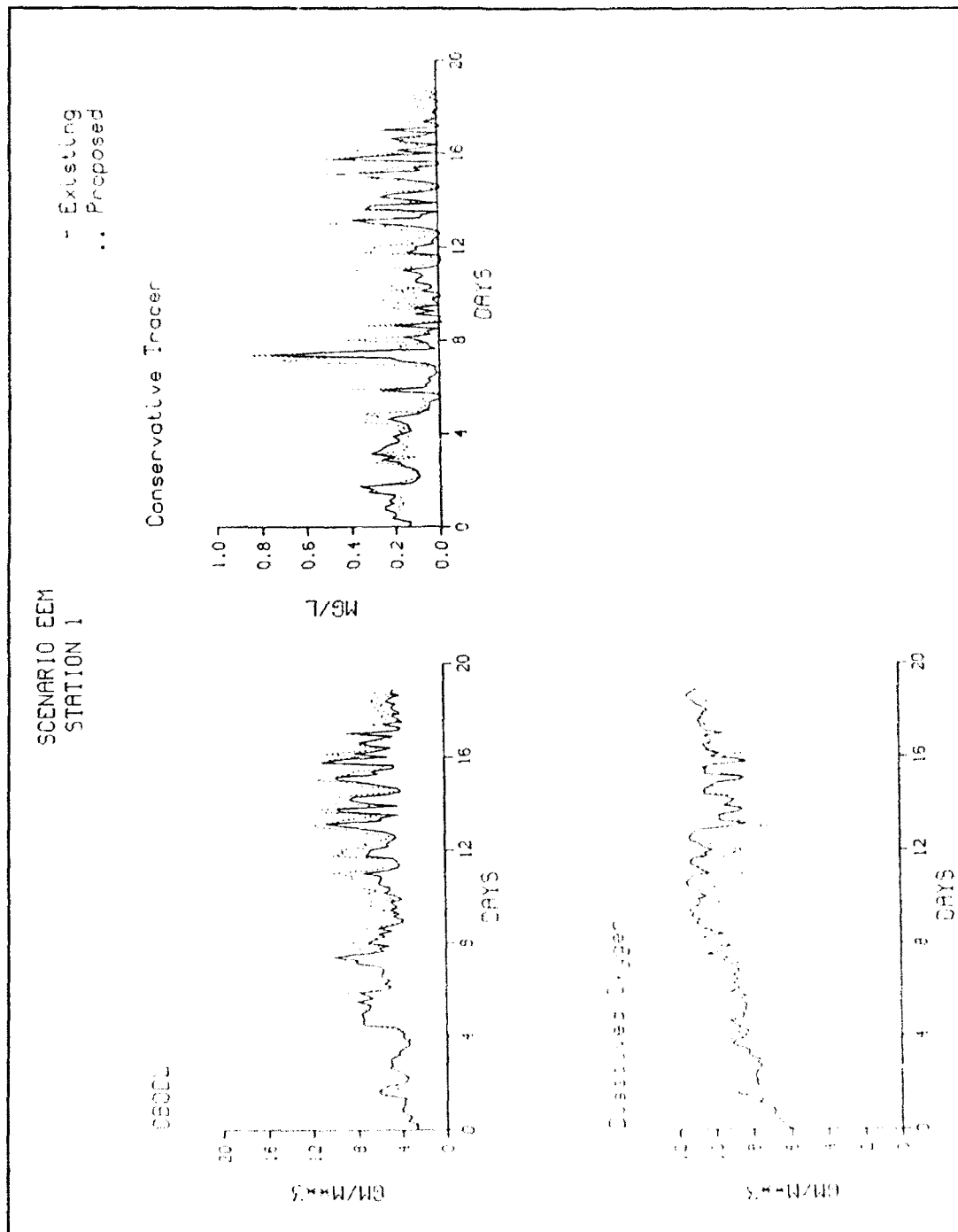


Figure D16. Time series for comparison stations, Scenario EEM (Sheet 1 of 9)

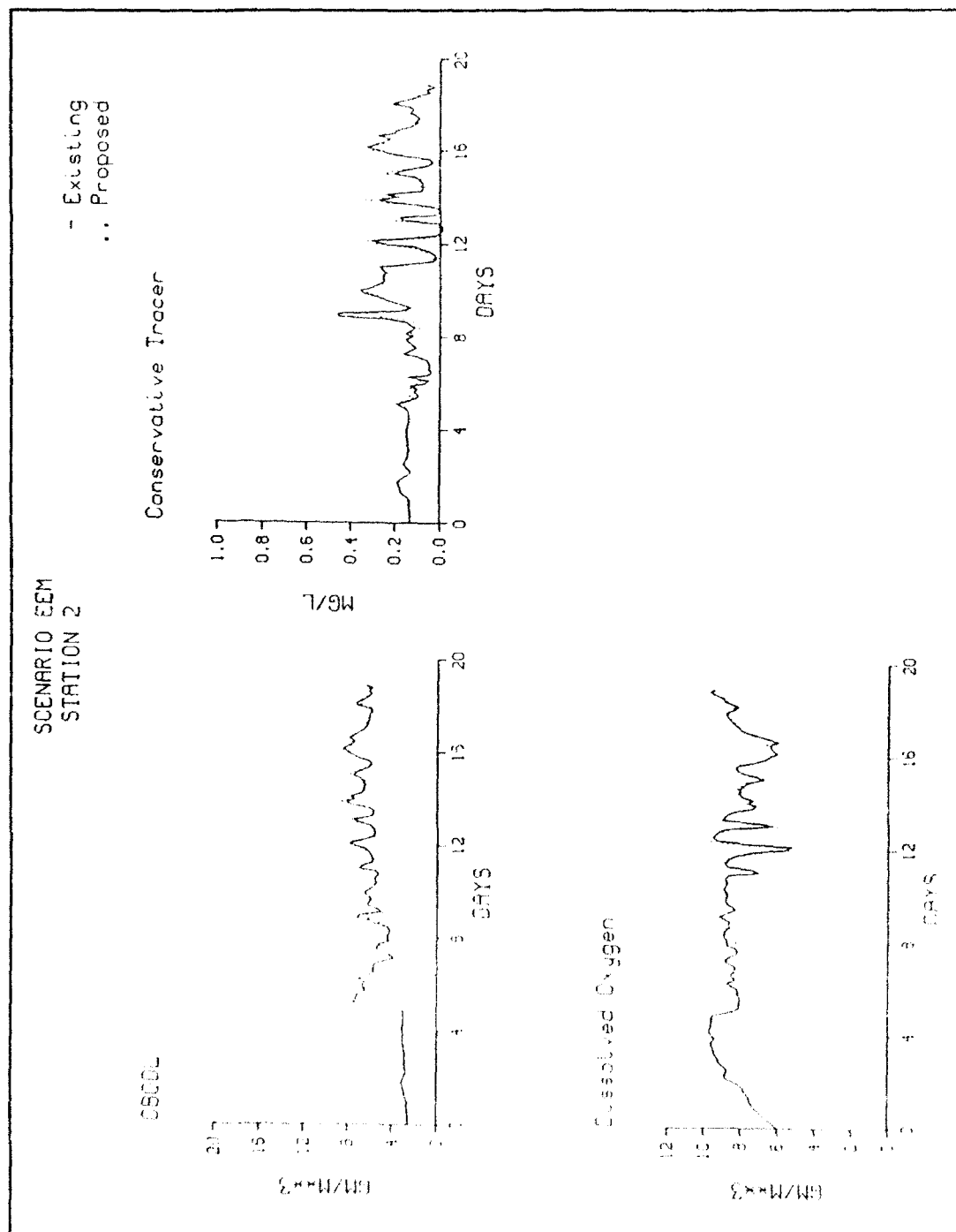


Figure D16. (Sheet 2 of 9)

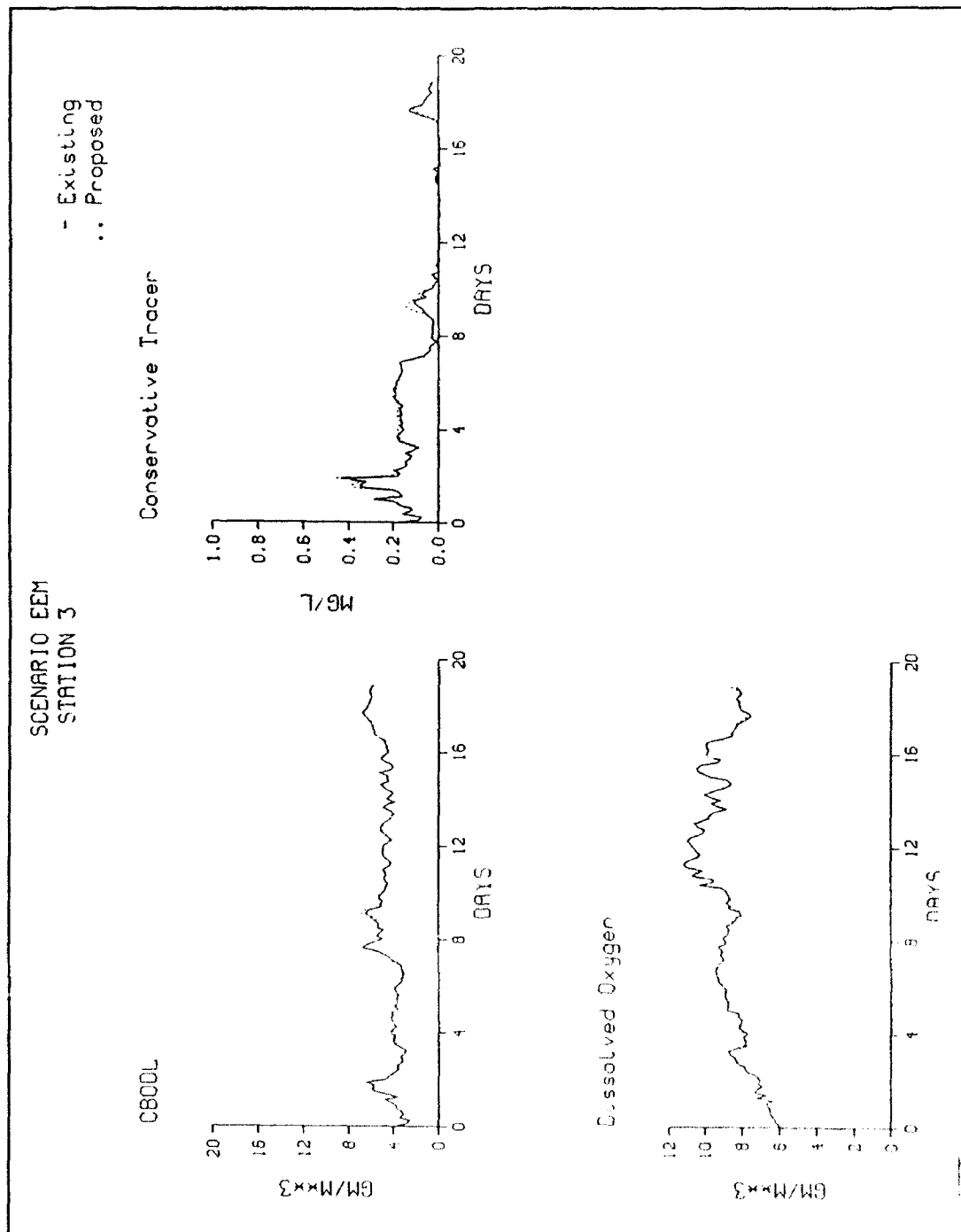


Figure D16. (Sheet 3 of 9)

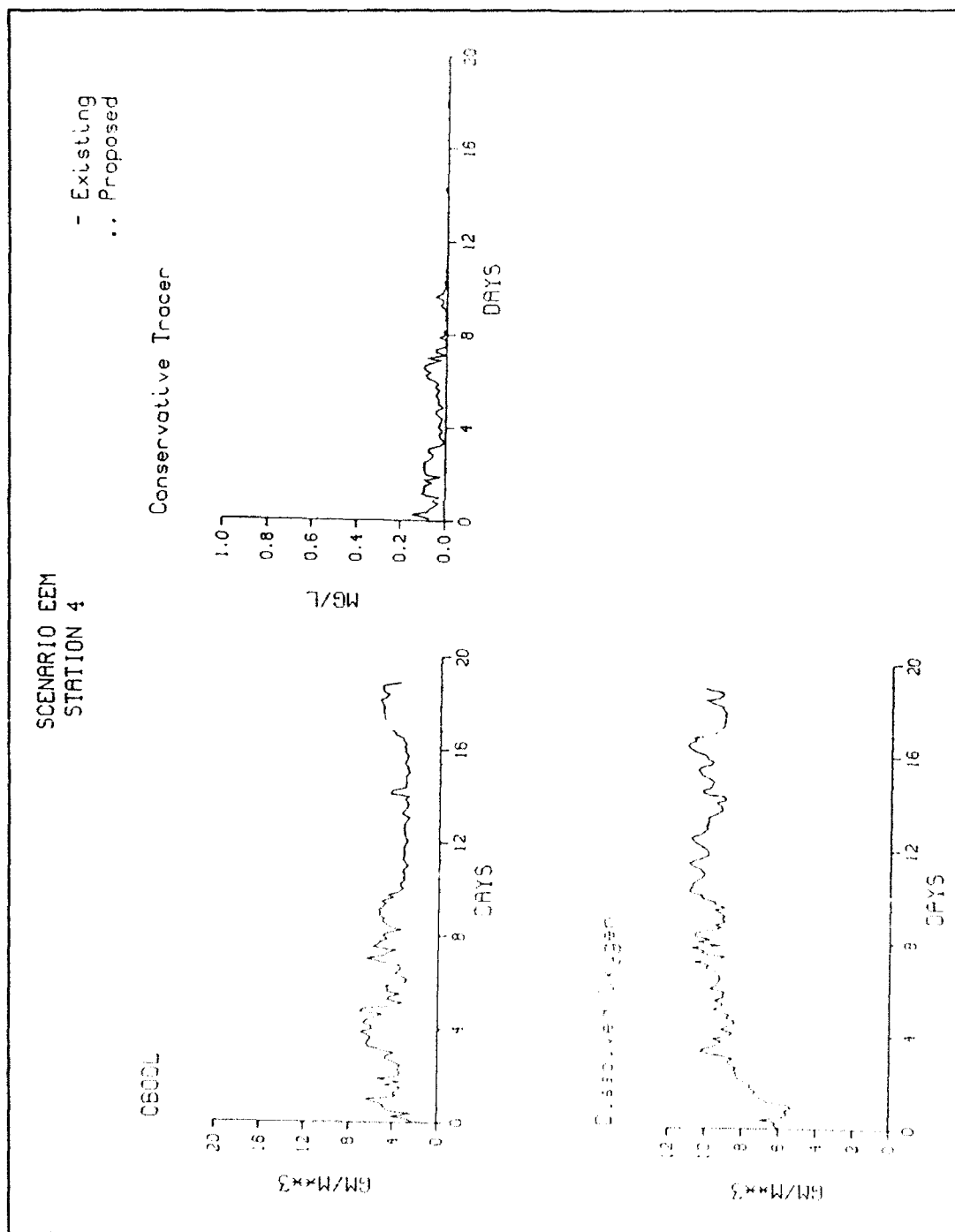


Figure D16. (Sheet 4 of 9)

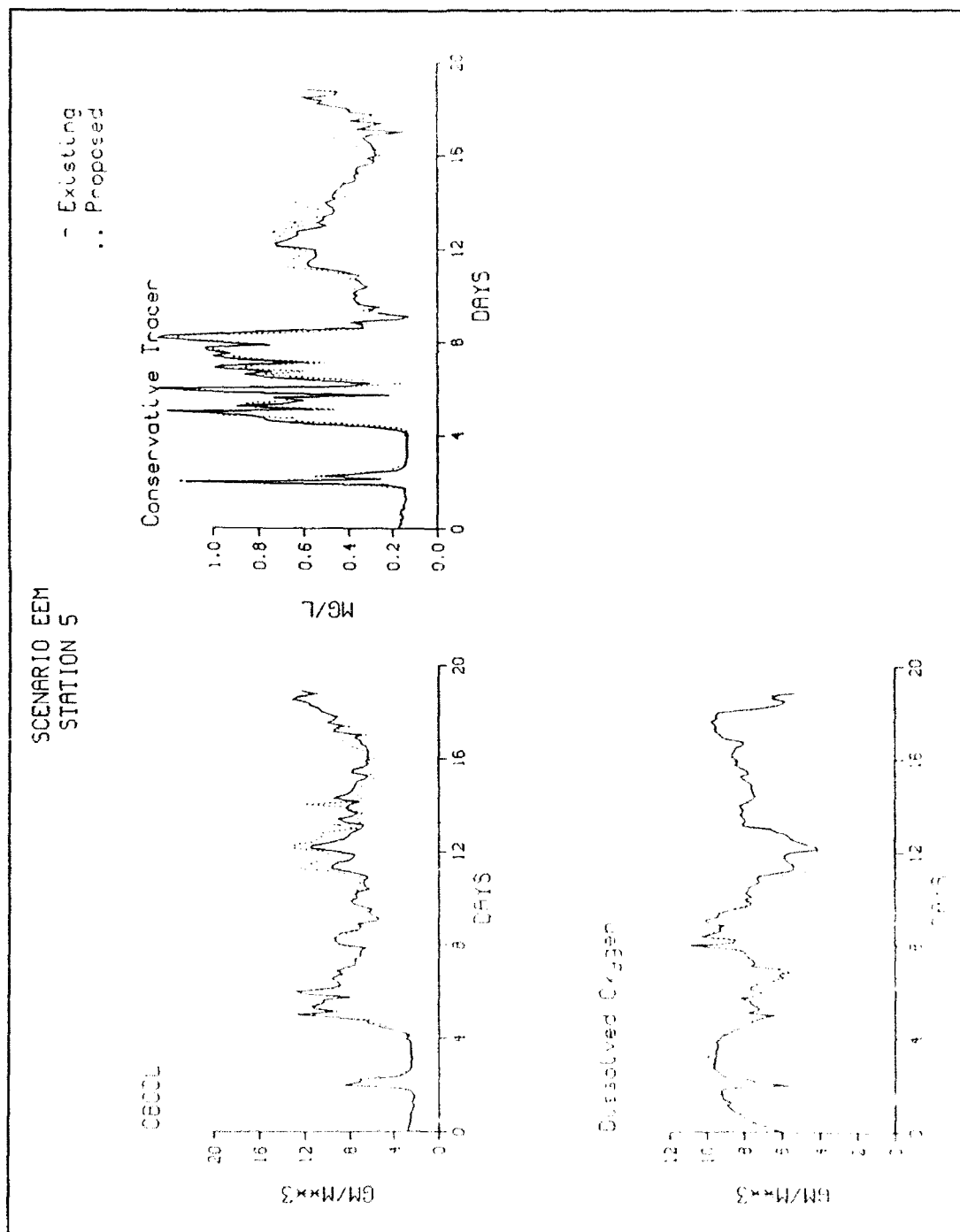


Figure D16. (Sheet 5 of 9)

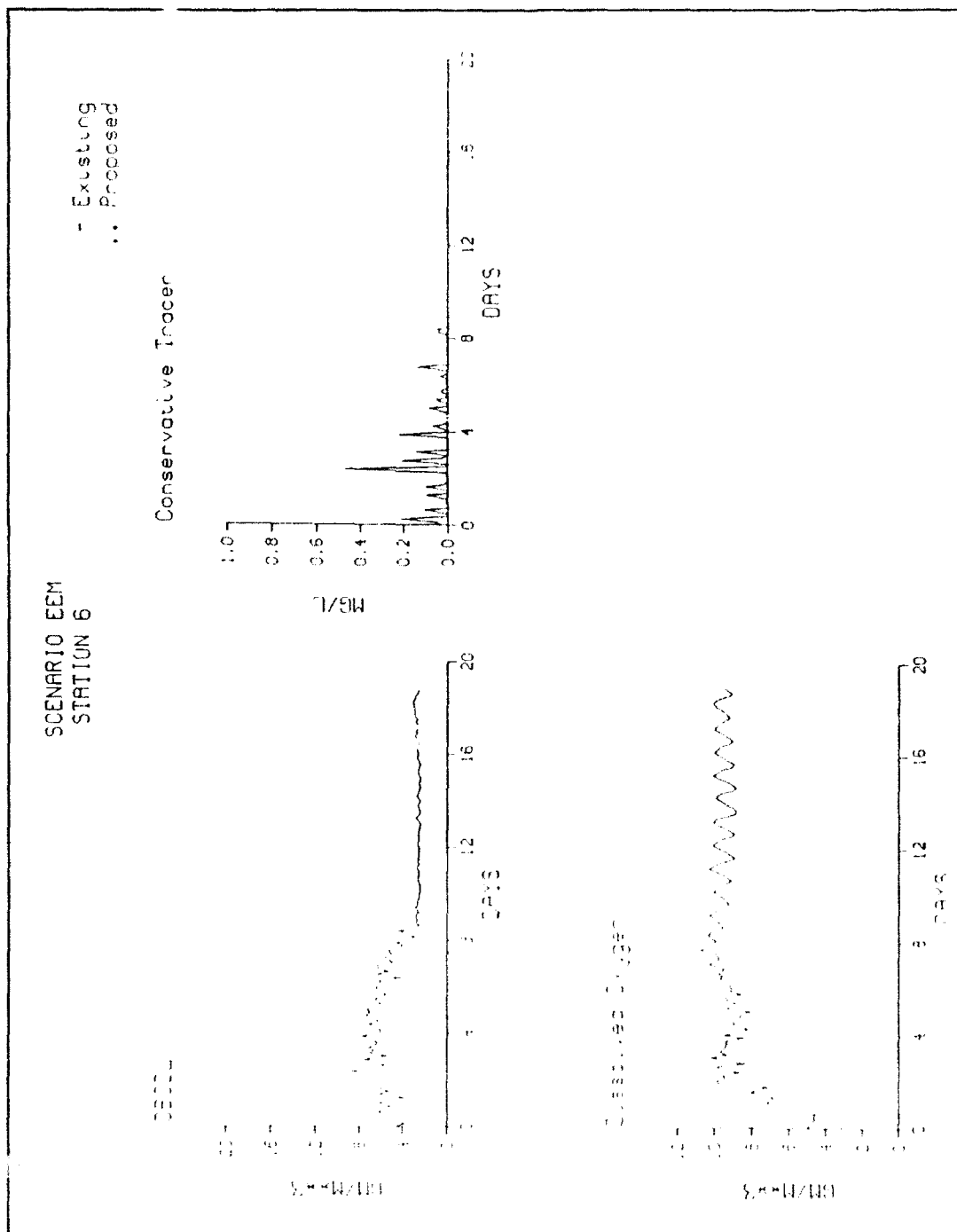


Figure D16. (Sheet 6 of 9)

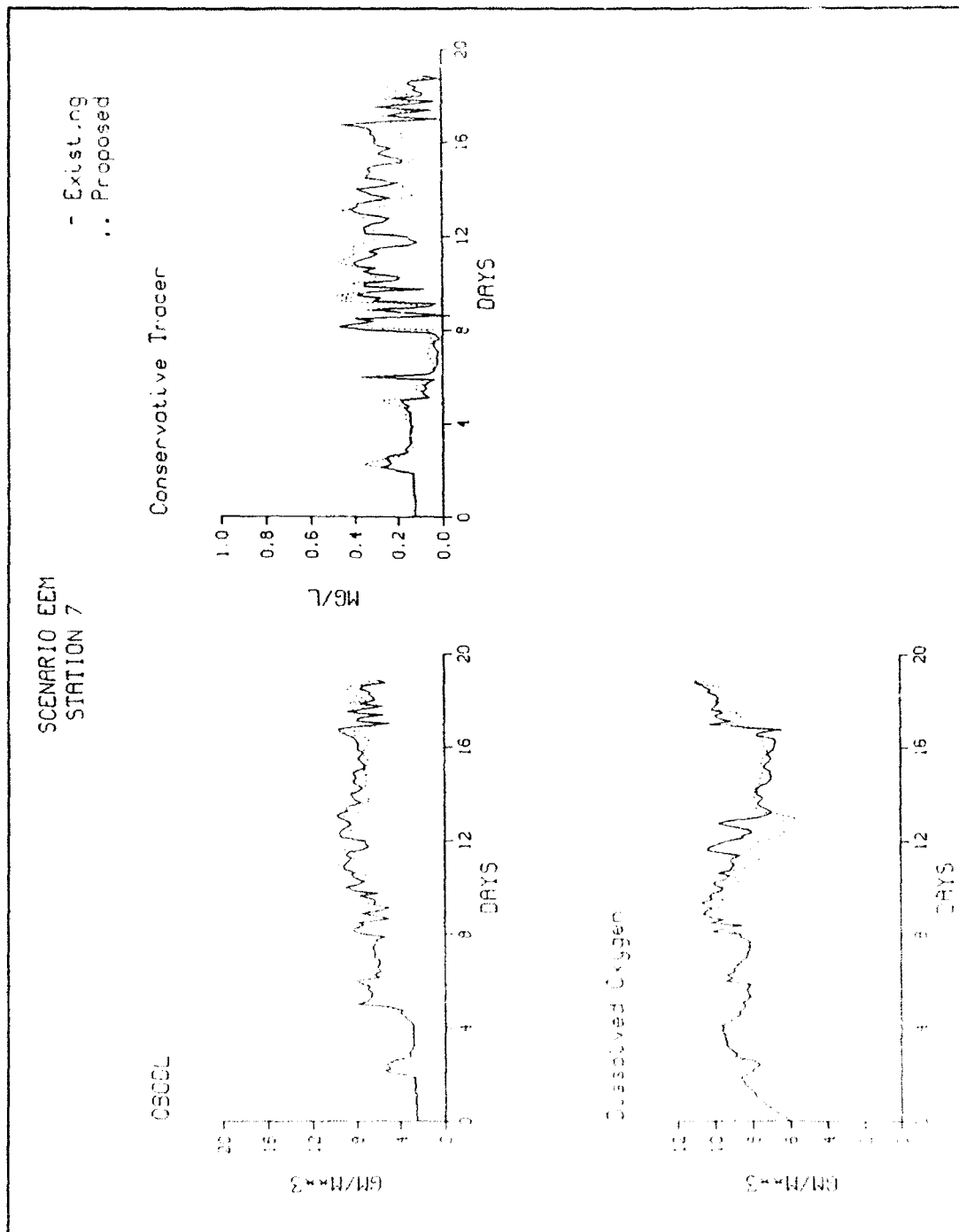


Figure D16. (Sheet 7 of 9)

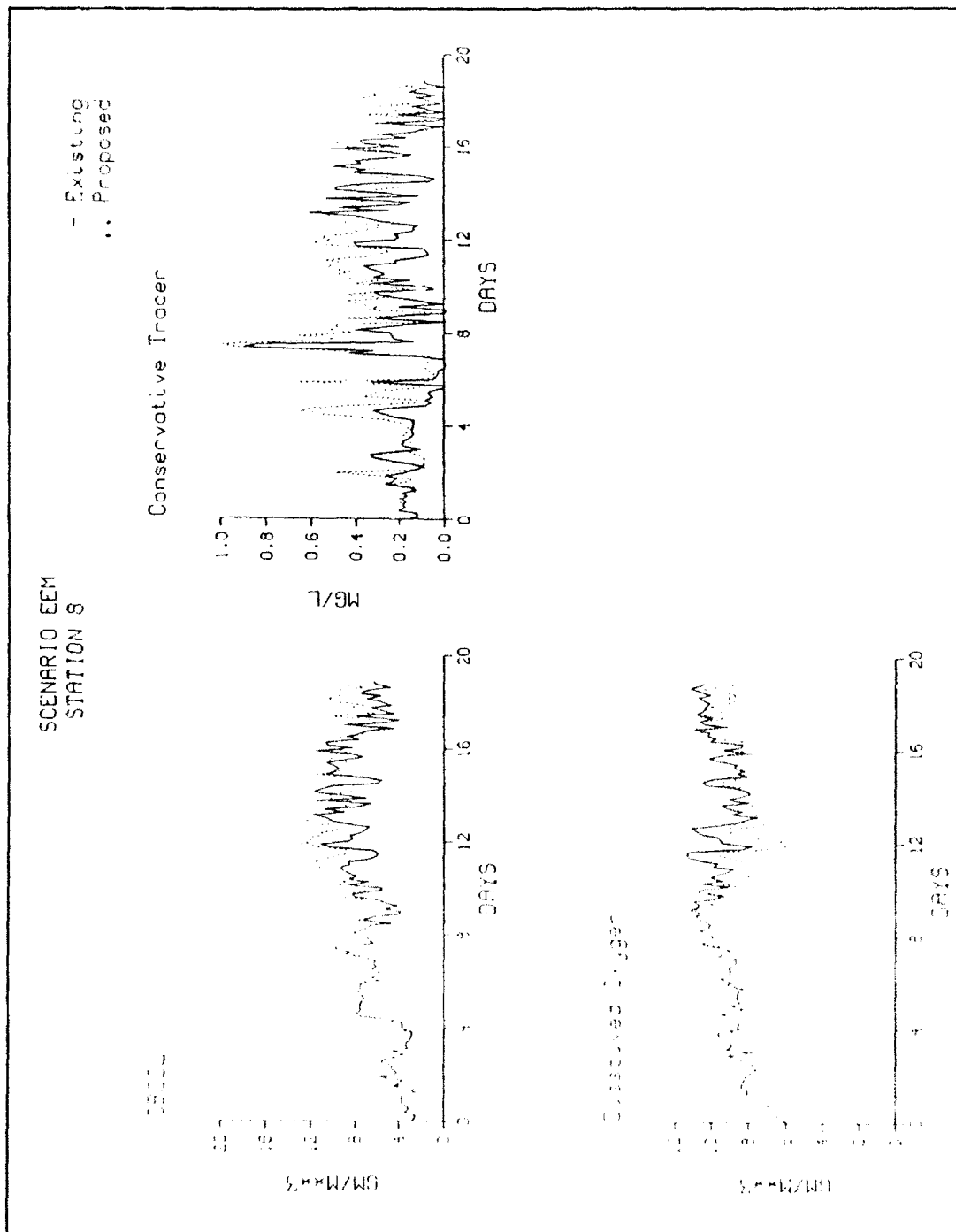


Figure D16. (Sheet 8 of 9)

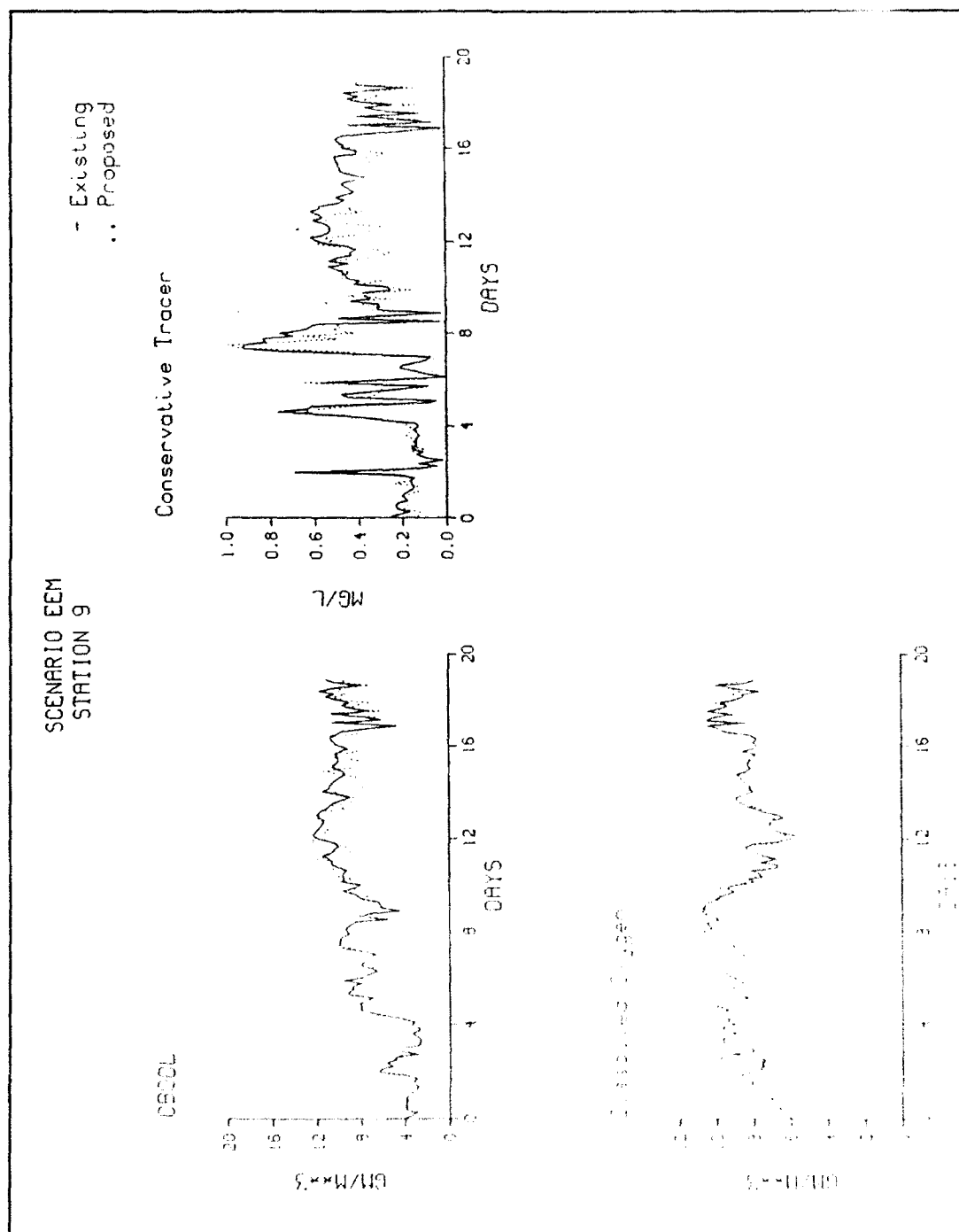


Figure D16. (Sheet 9 of 9)

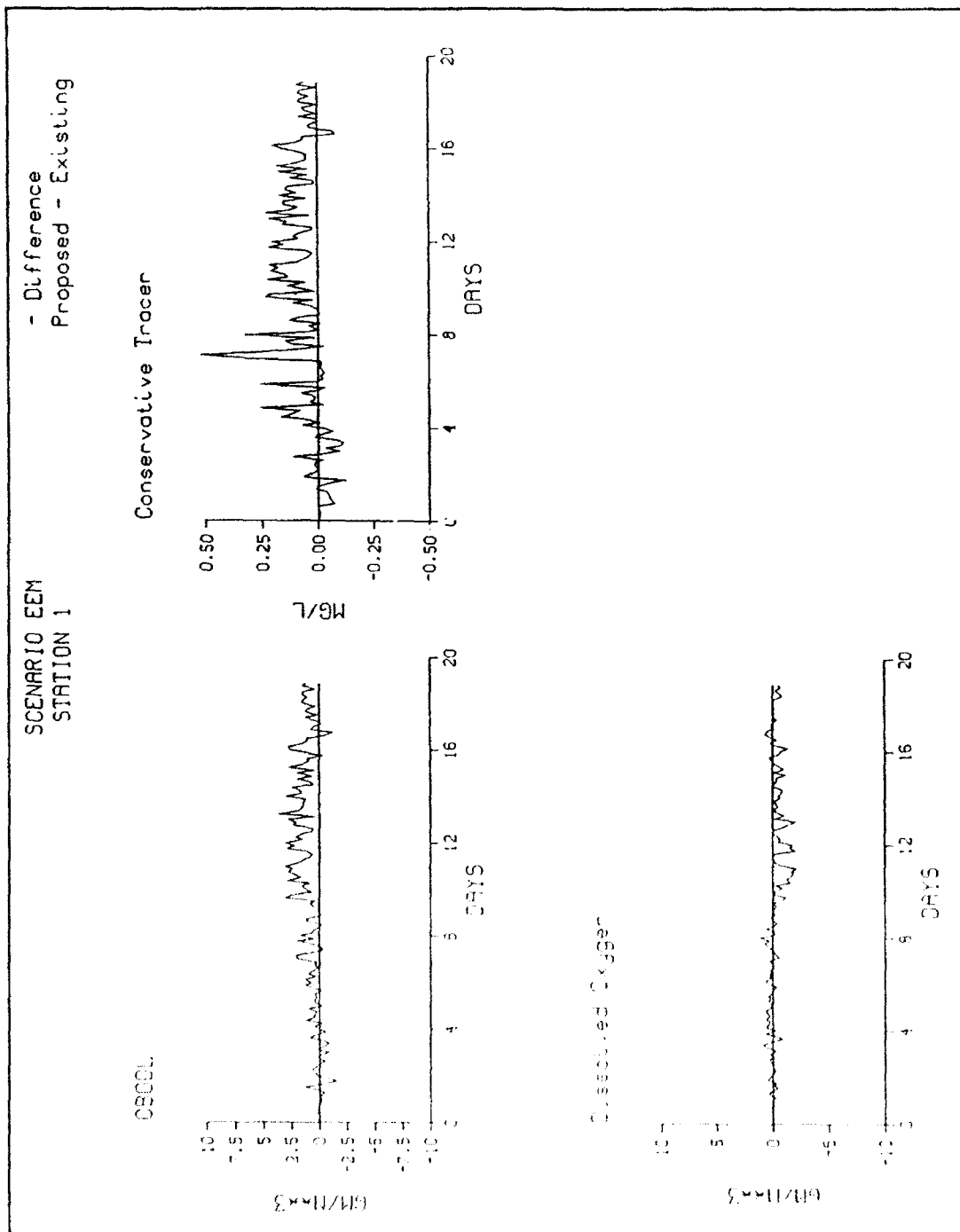


Figure D17. Time series differences for comparison stations, Senario EEM (Sheet 1 of 8)

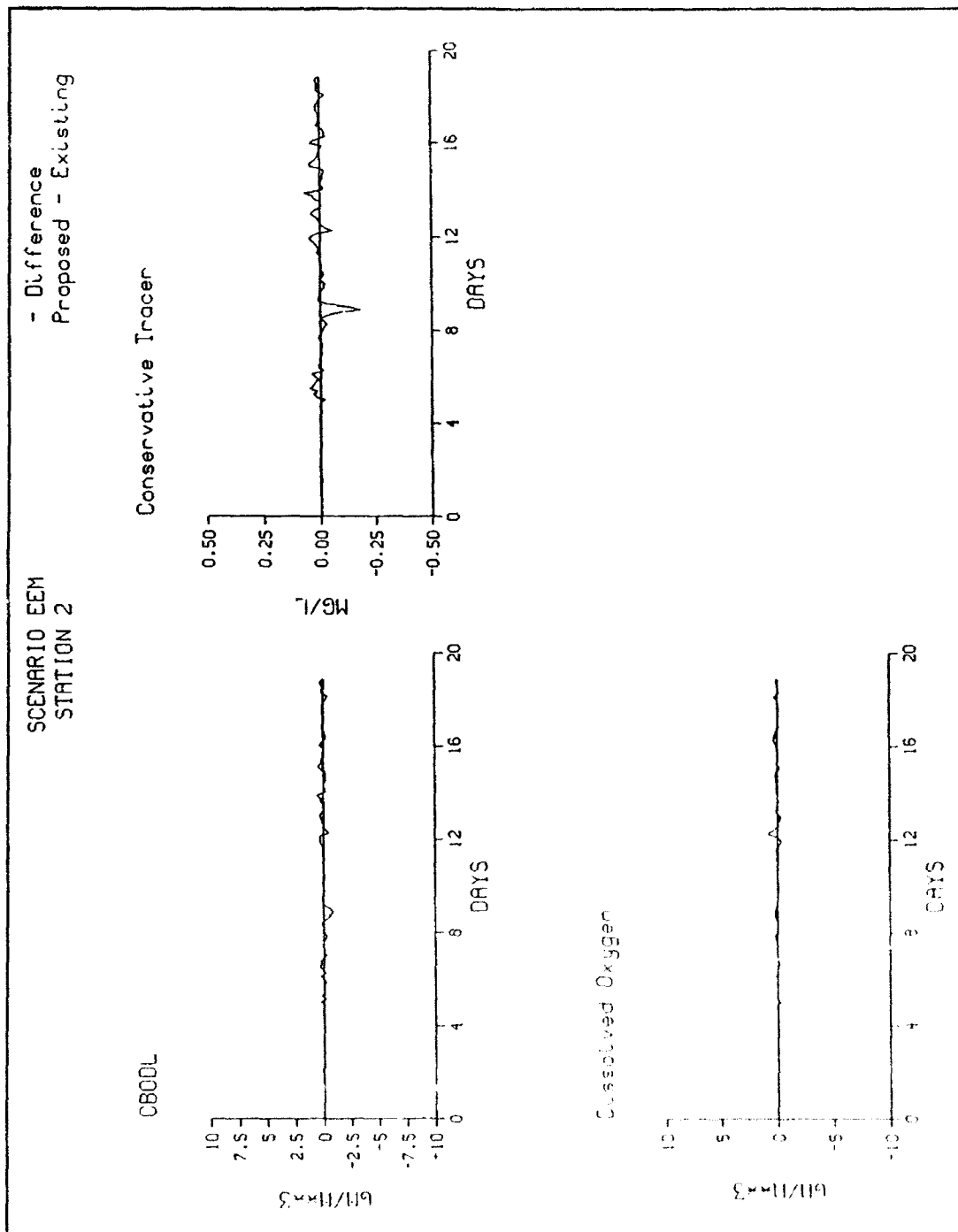


Figure D17. (Sheet 2 of 8)

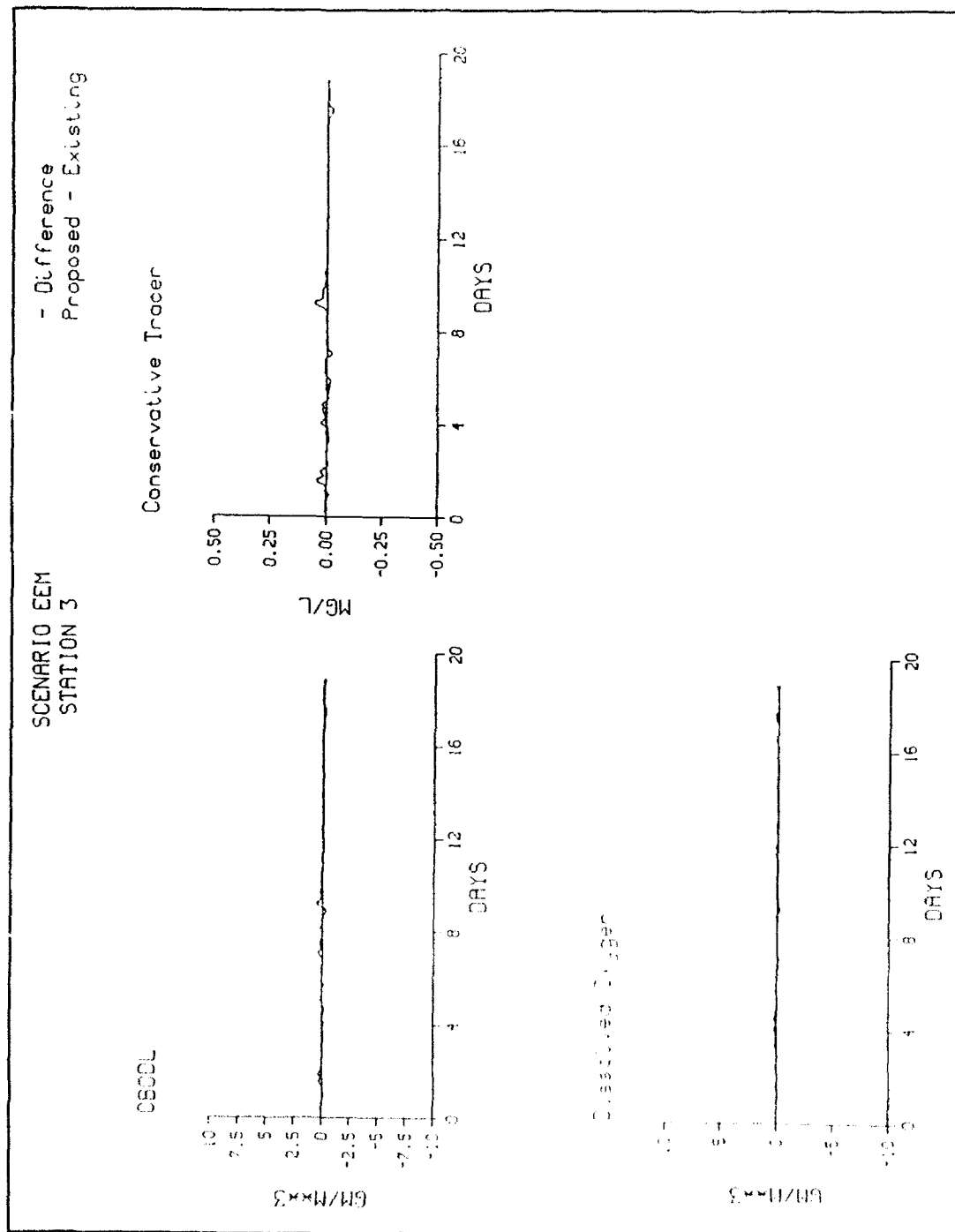


Figure D17. (Sheet 3 of 8)

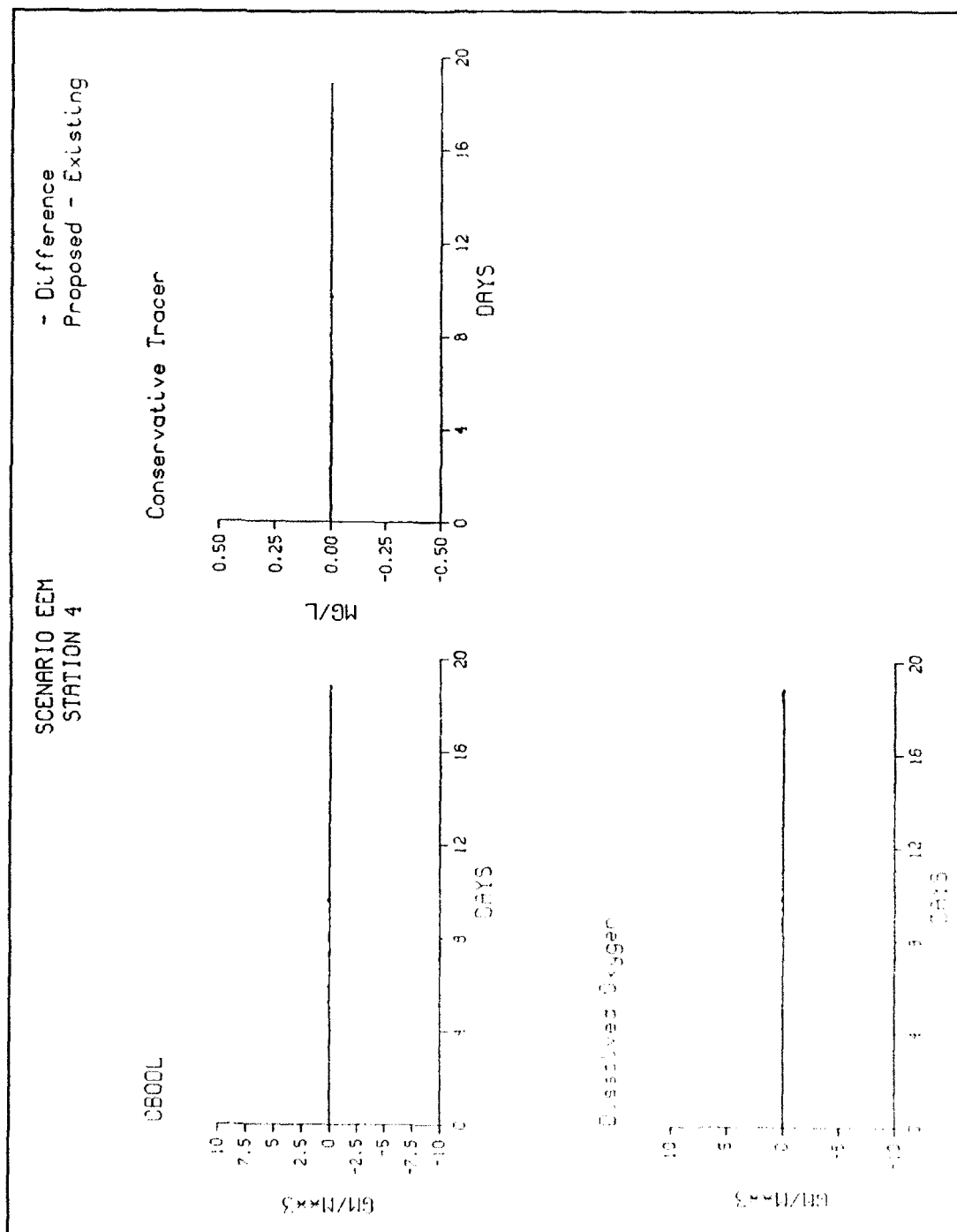


Figure D17. (Sheet 4 of 8)

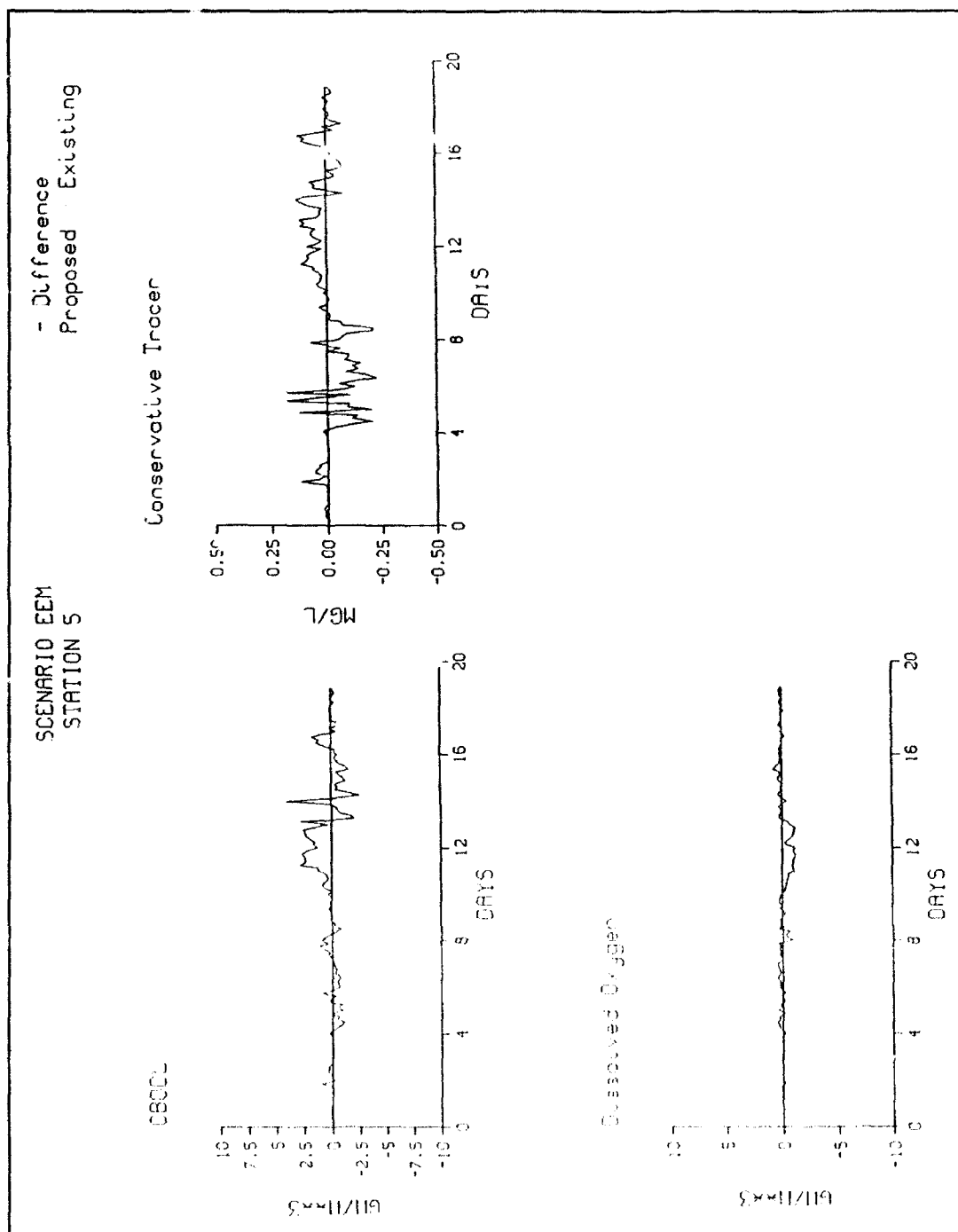


Figure D17. (Sheet 5 of 8)

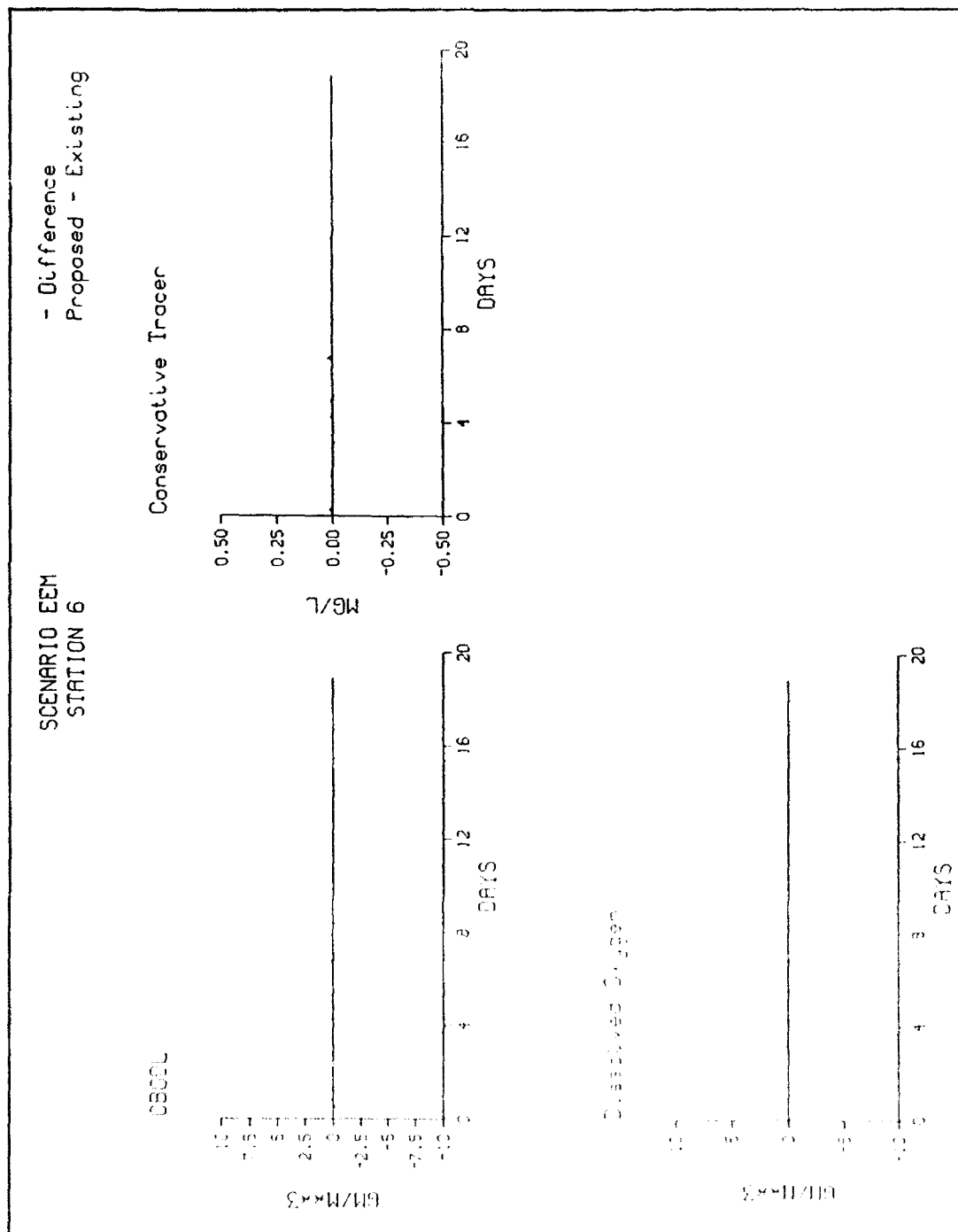


Figure D17. (Sheet 6 of 8)

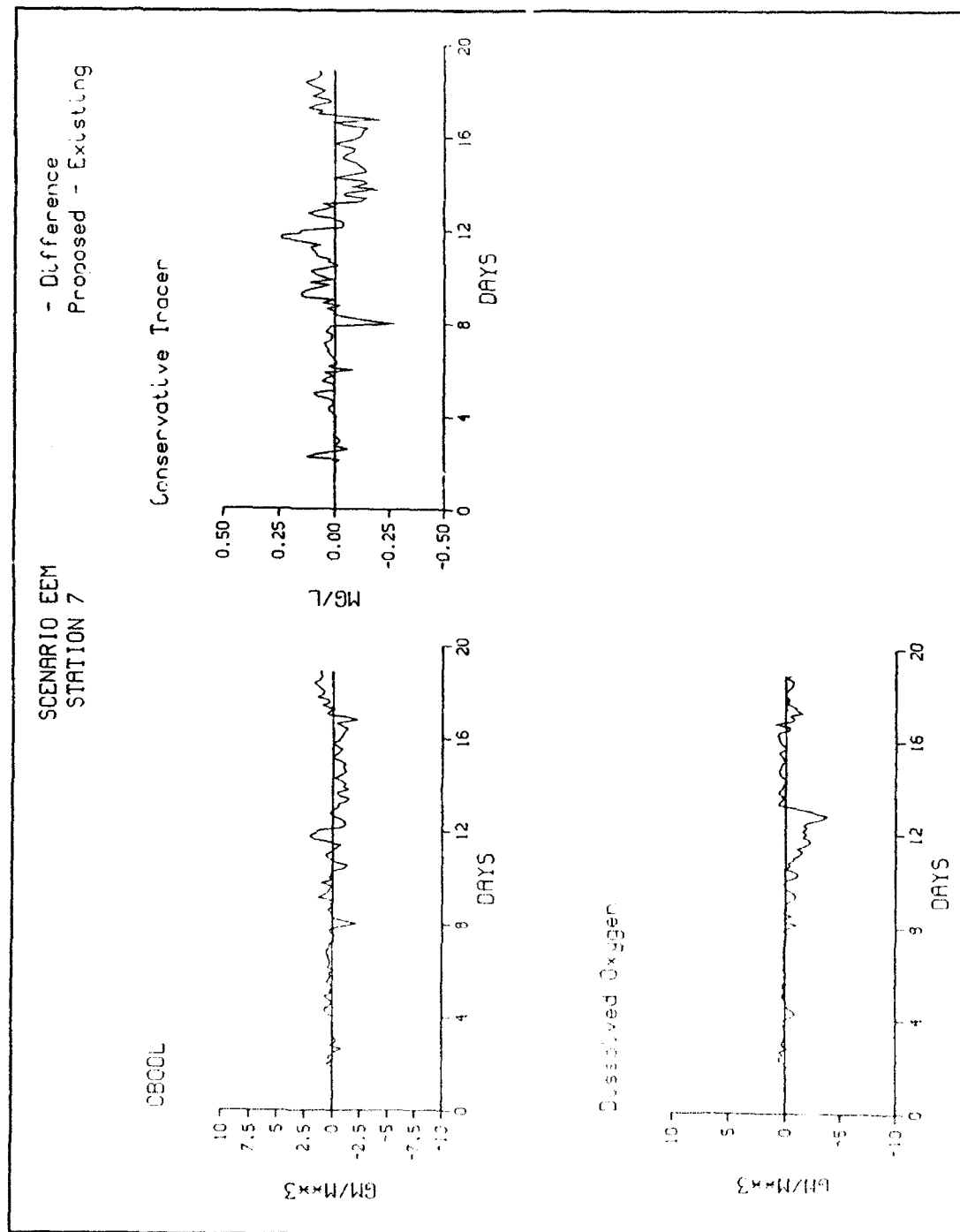


Figure D17. (Sheet 7 of 8)

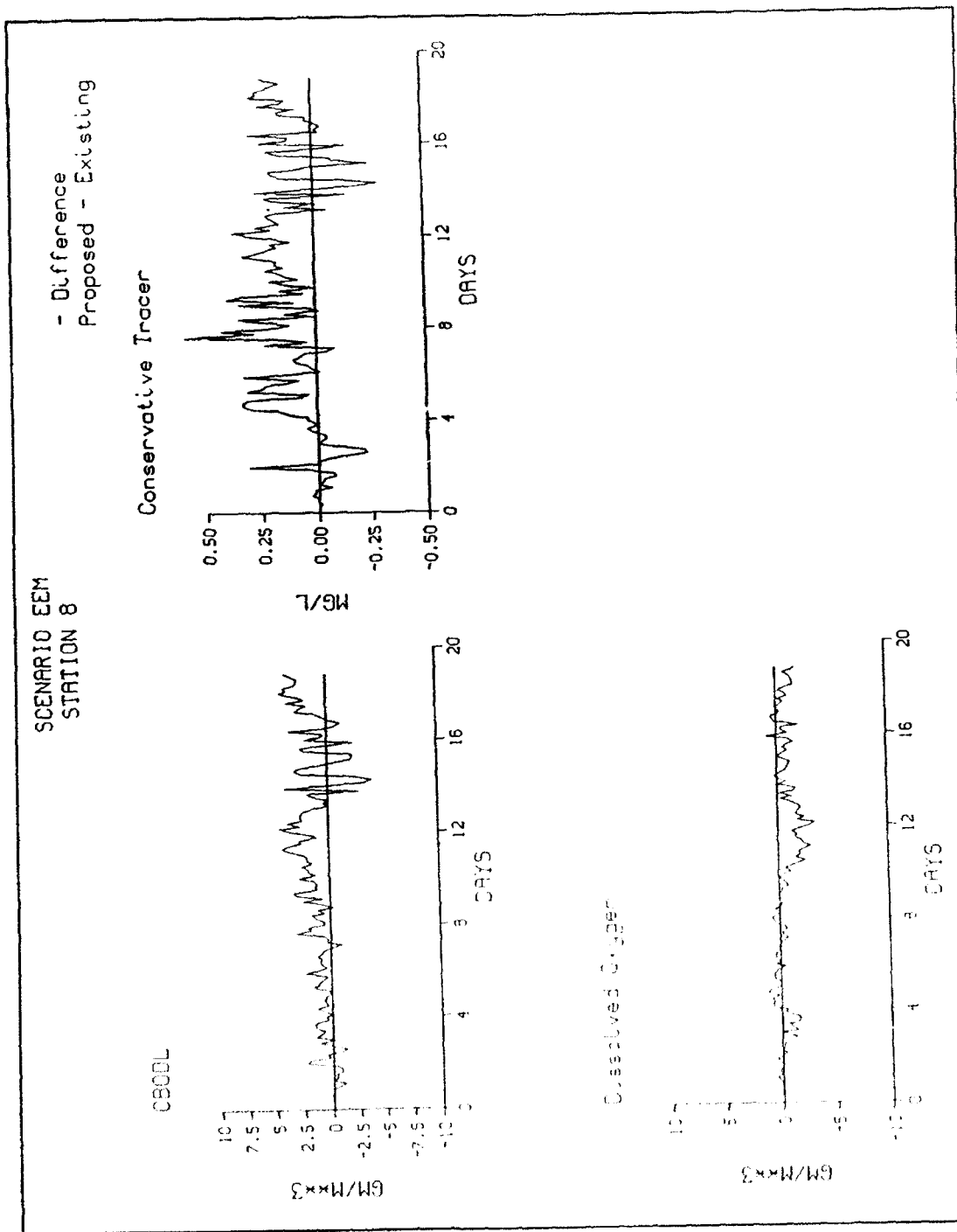


Figure D17. (Sheet 8 of 8)

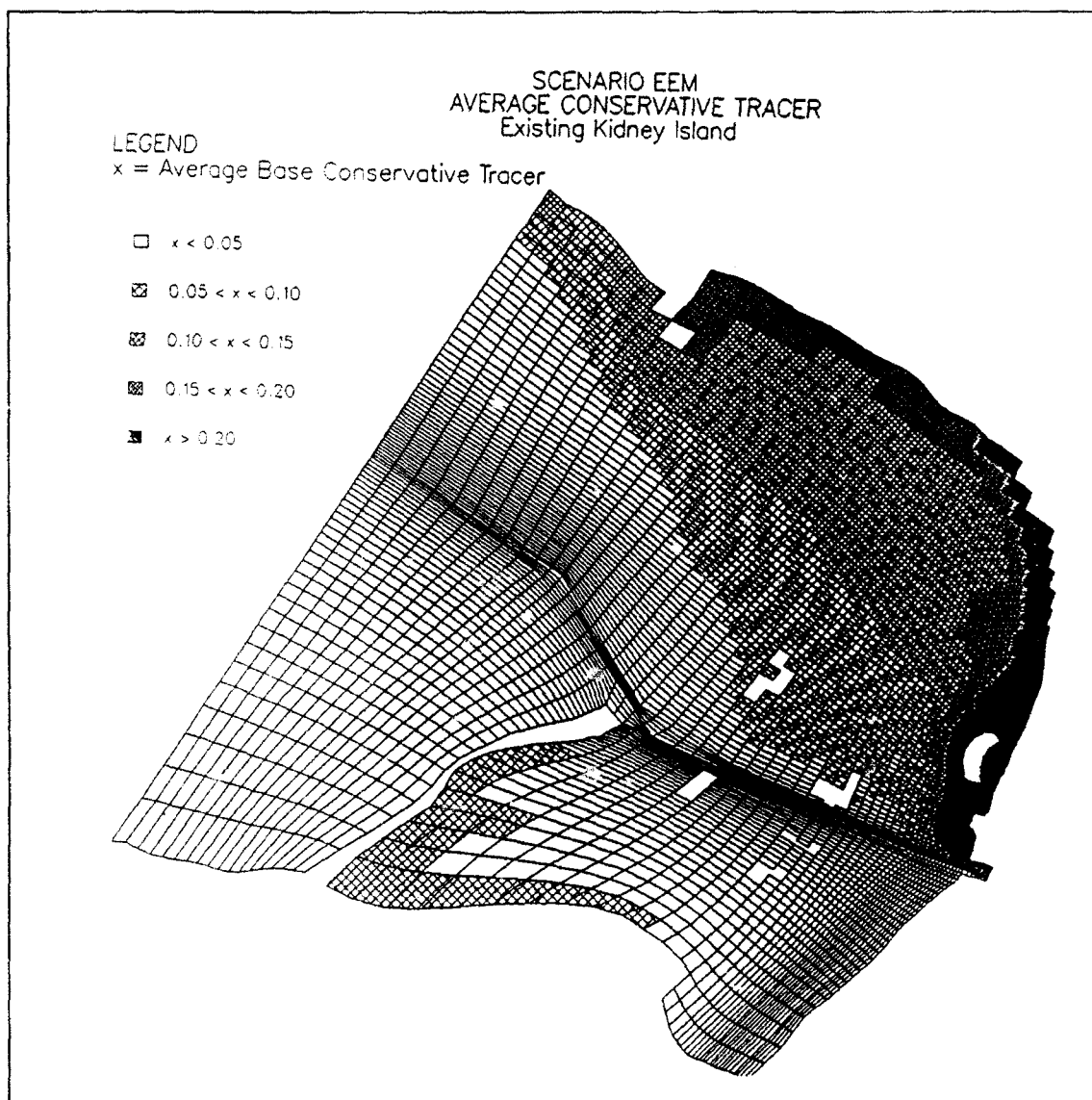


Figure D18. Average conservative tracer concentrations, Scenario EEM (Continued)

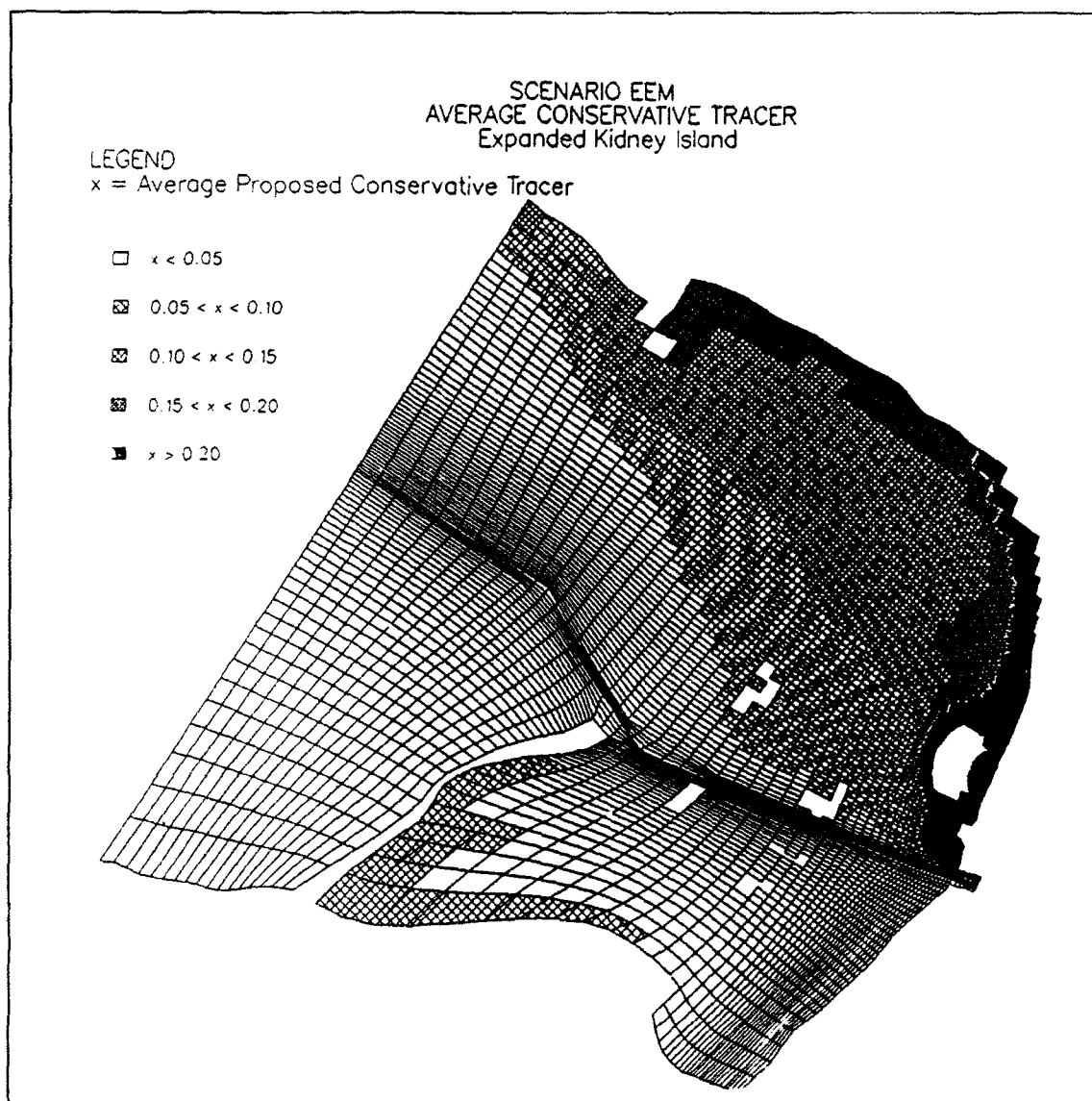


Figure D18. (Concluded)

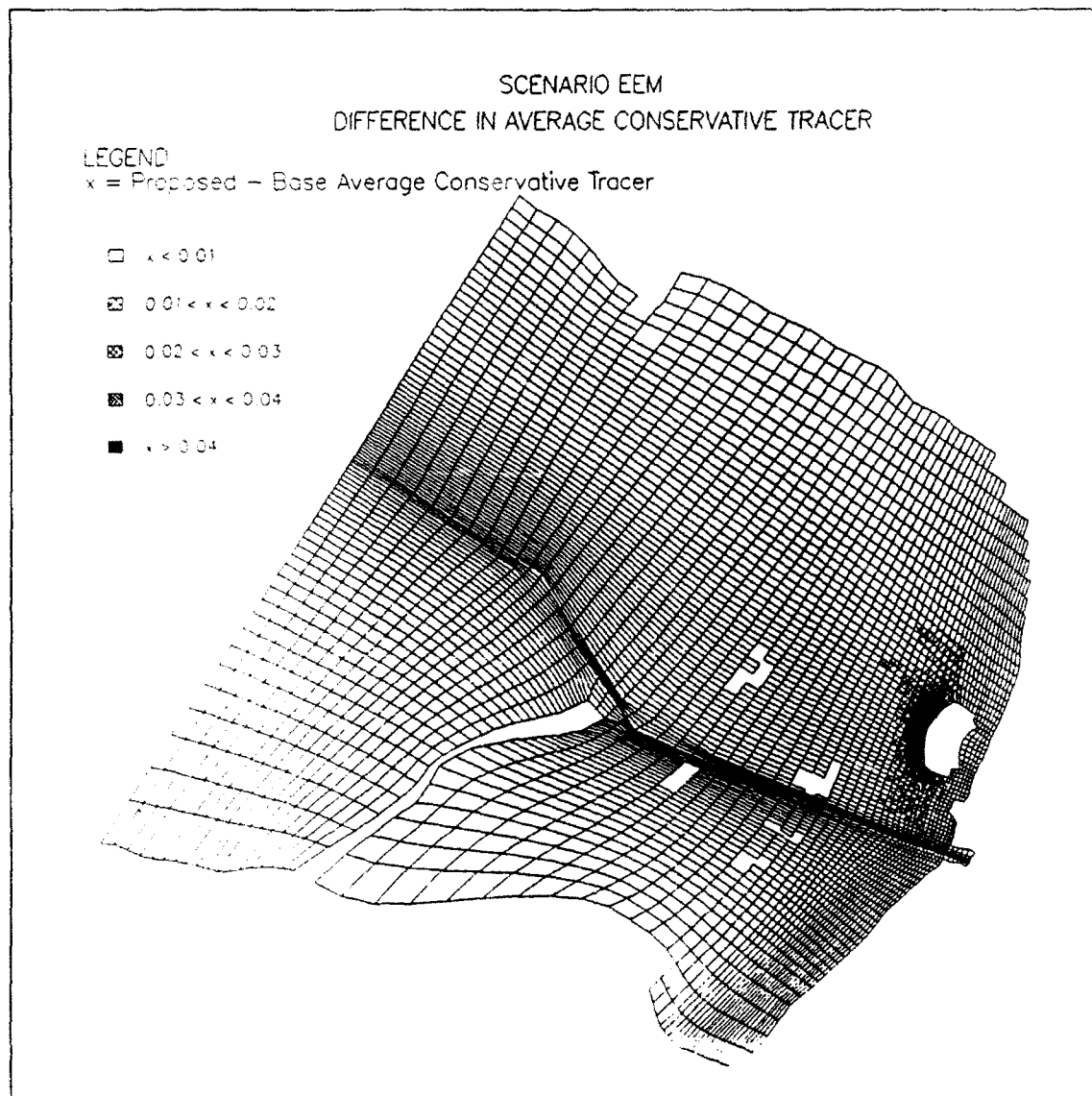


Figure D19. Difference in average conservative tracer, Scenario EEM

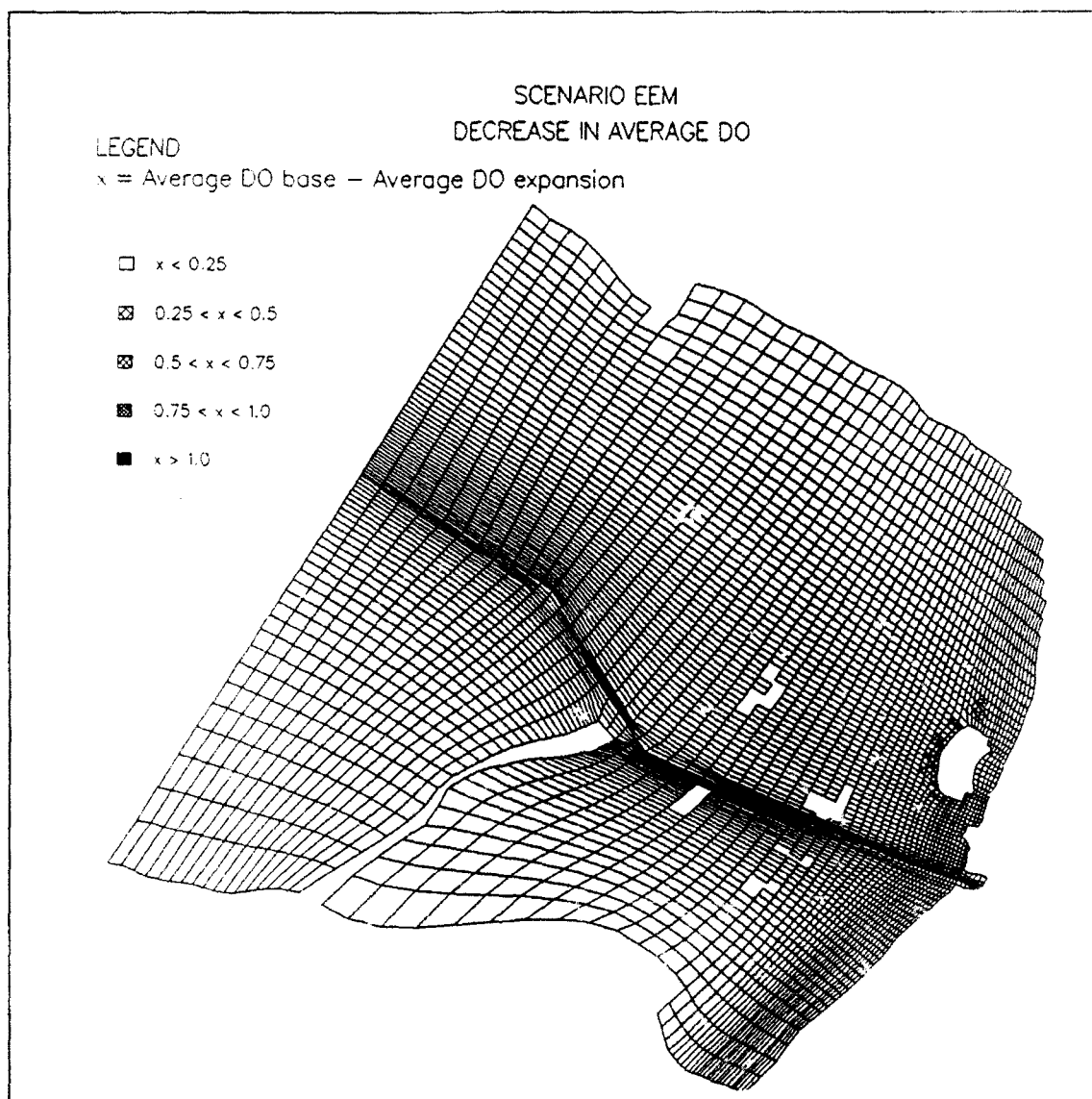


Figure D20. Decrease in average DO concentrations, Scenario EEM

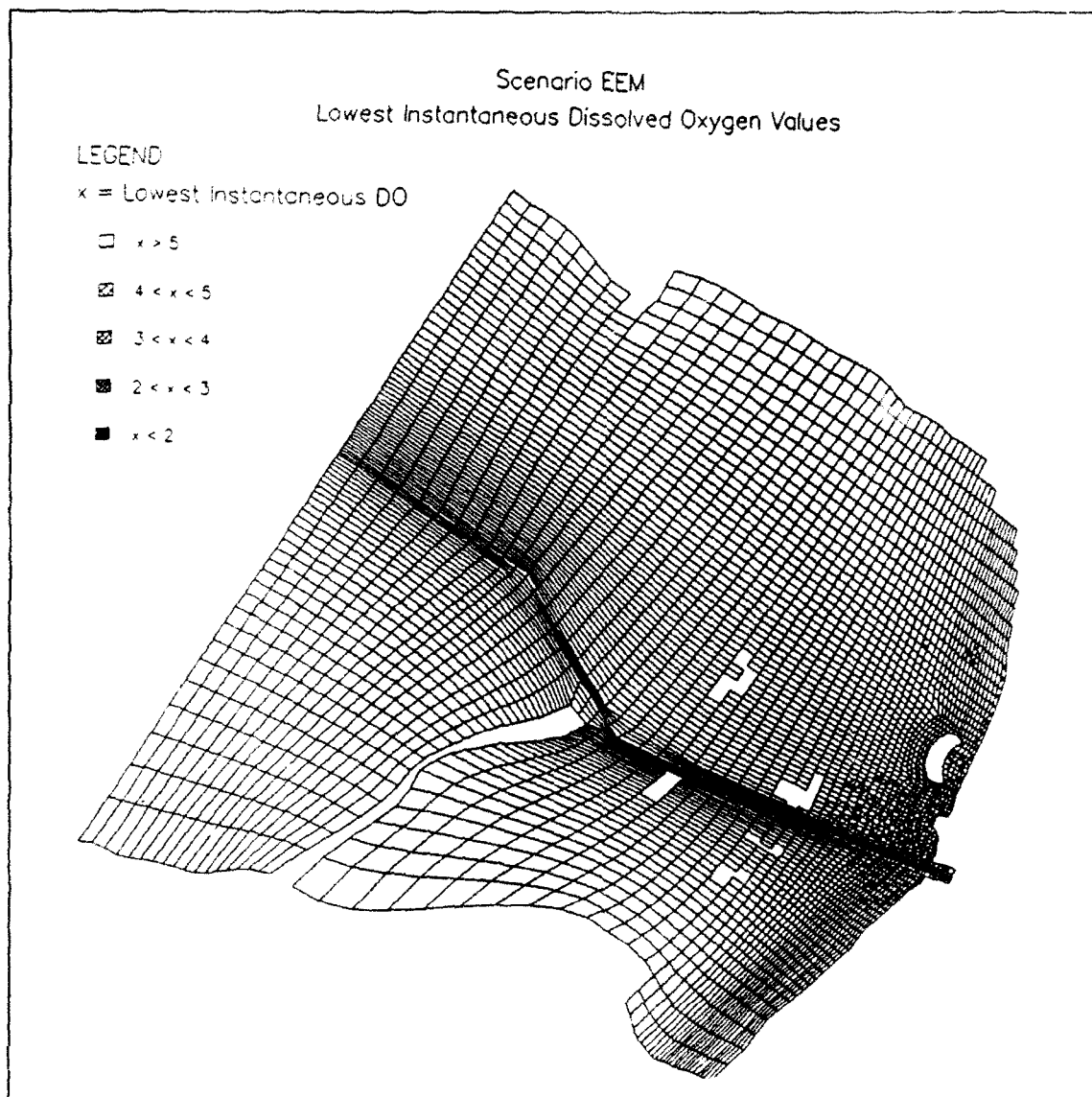


Figure D21. Lowest instantaneous DO, Scenario EEM (Continued)

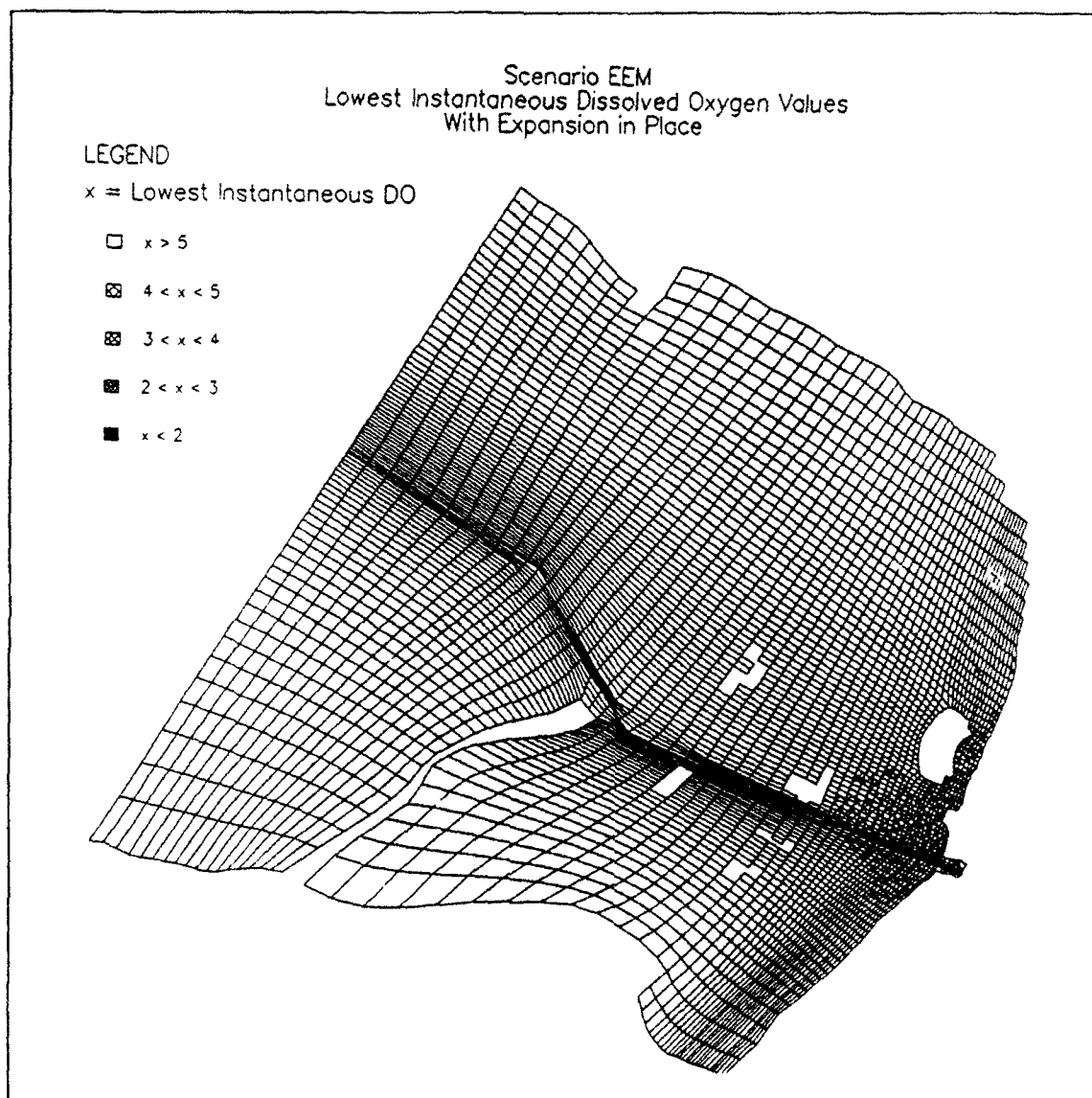


Figure D21. (Concluded)

SCENARIO AEM

**(Average Seiche, Extreme River Flows,
Minimum Lake Level)**

Figures D22 - D28

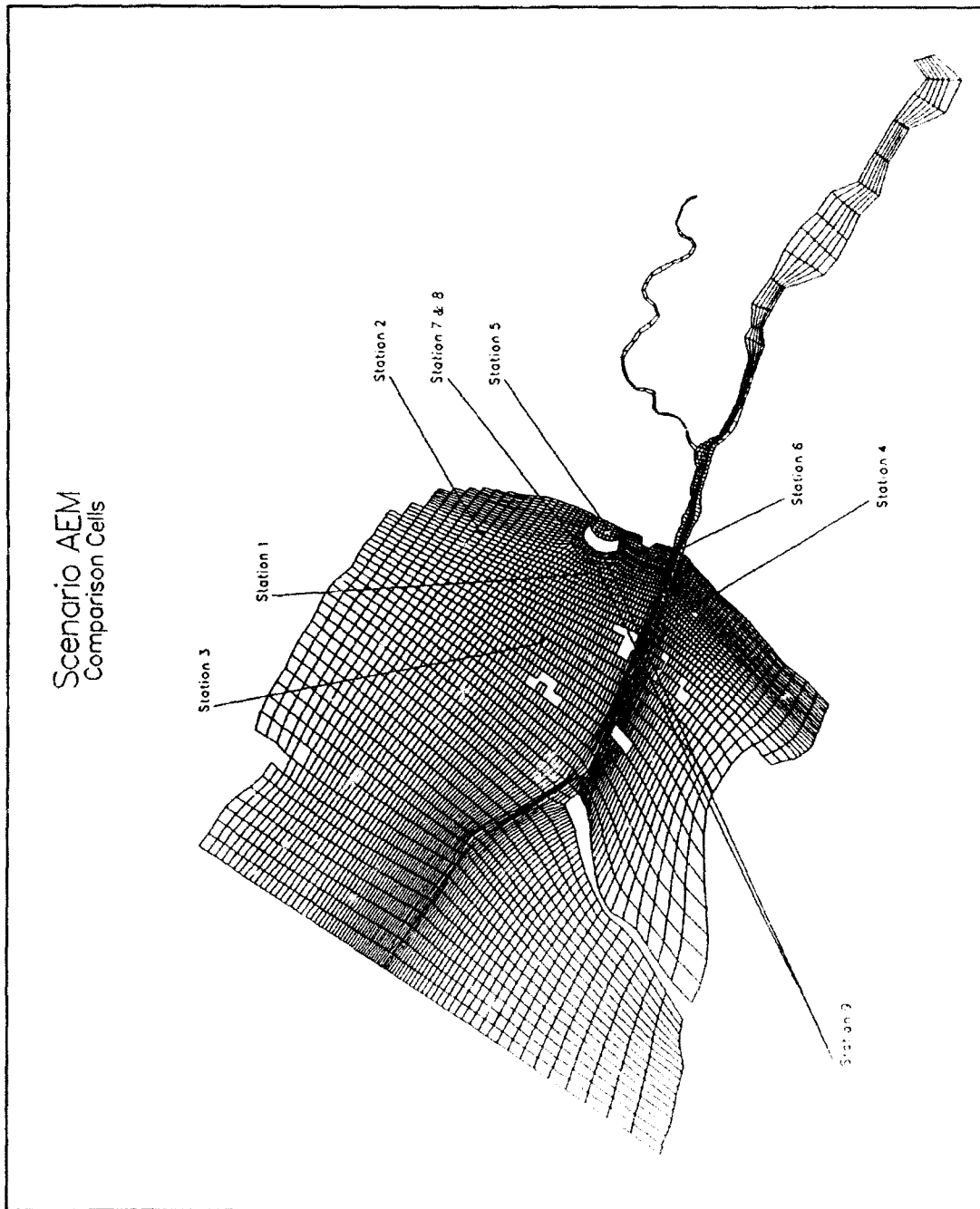


Figure D22. Pre and post-expansion comparison stations, Scenario AEM

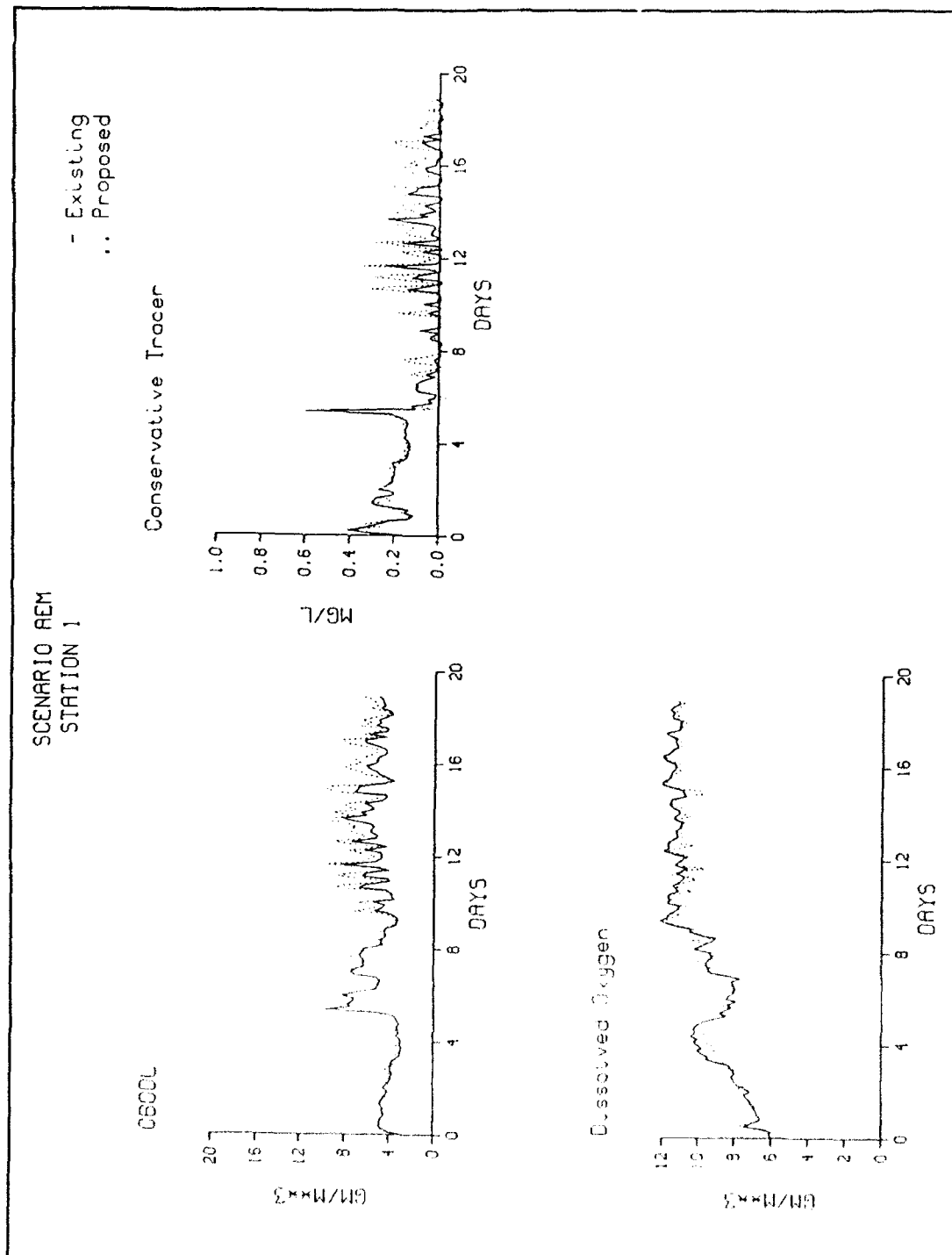


Figure D23. Time series for comparison stations, Scenario AEM (Sheet 1 of 9)

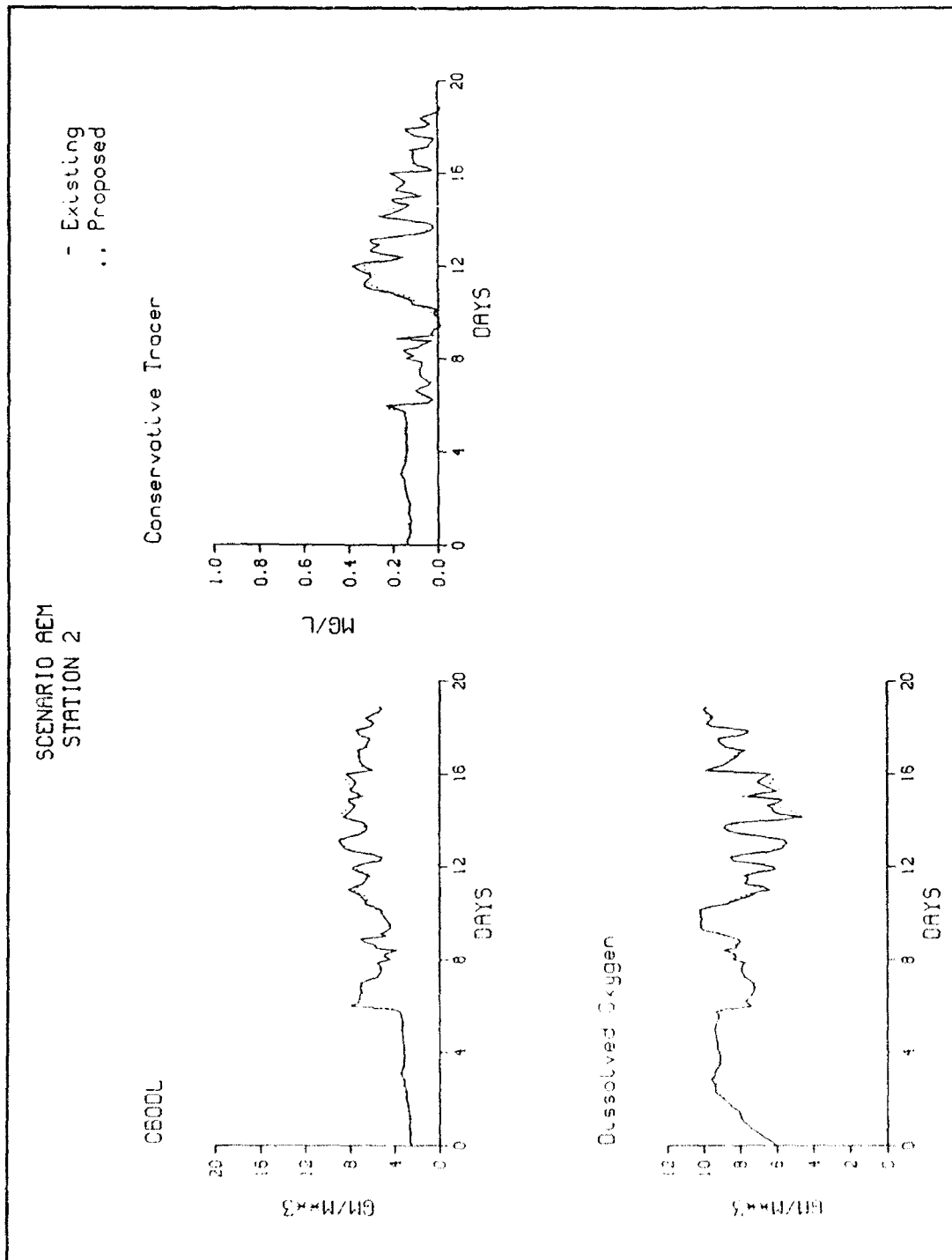


Figure D23. (Sheet 2 of 9)

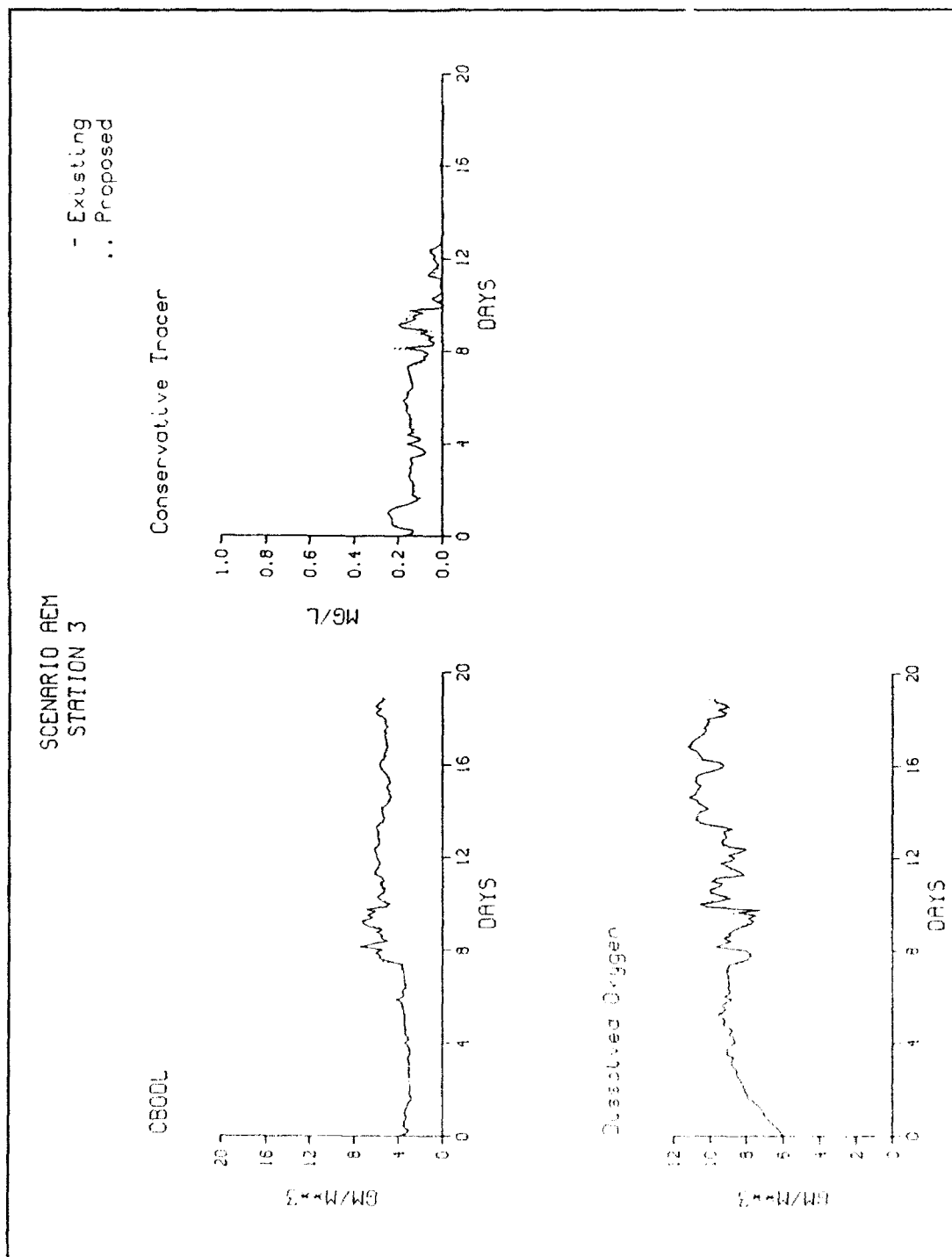


Figure D23. (Sheet 3 of 9)

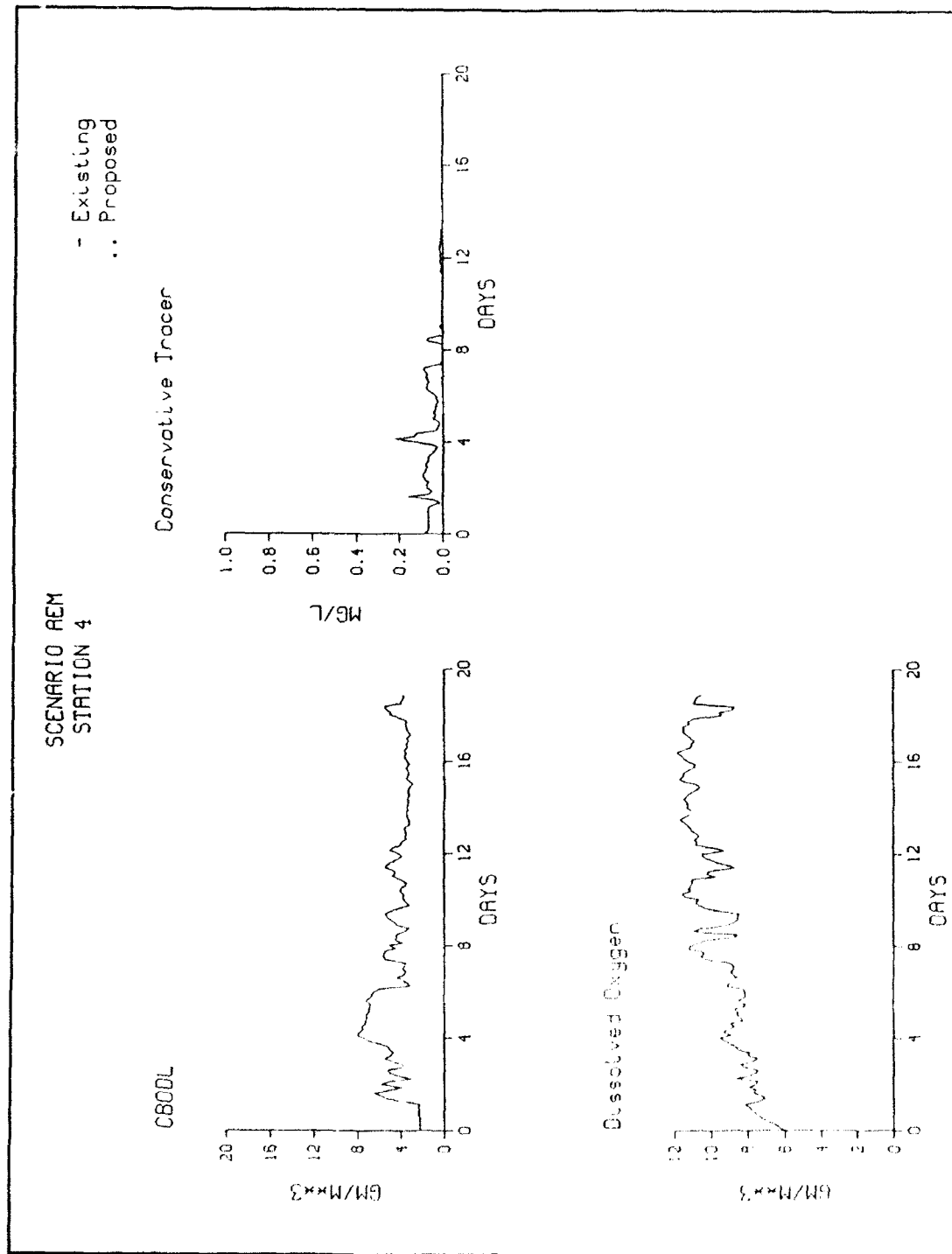


Figure D23. (Sheet 4 of 9)

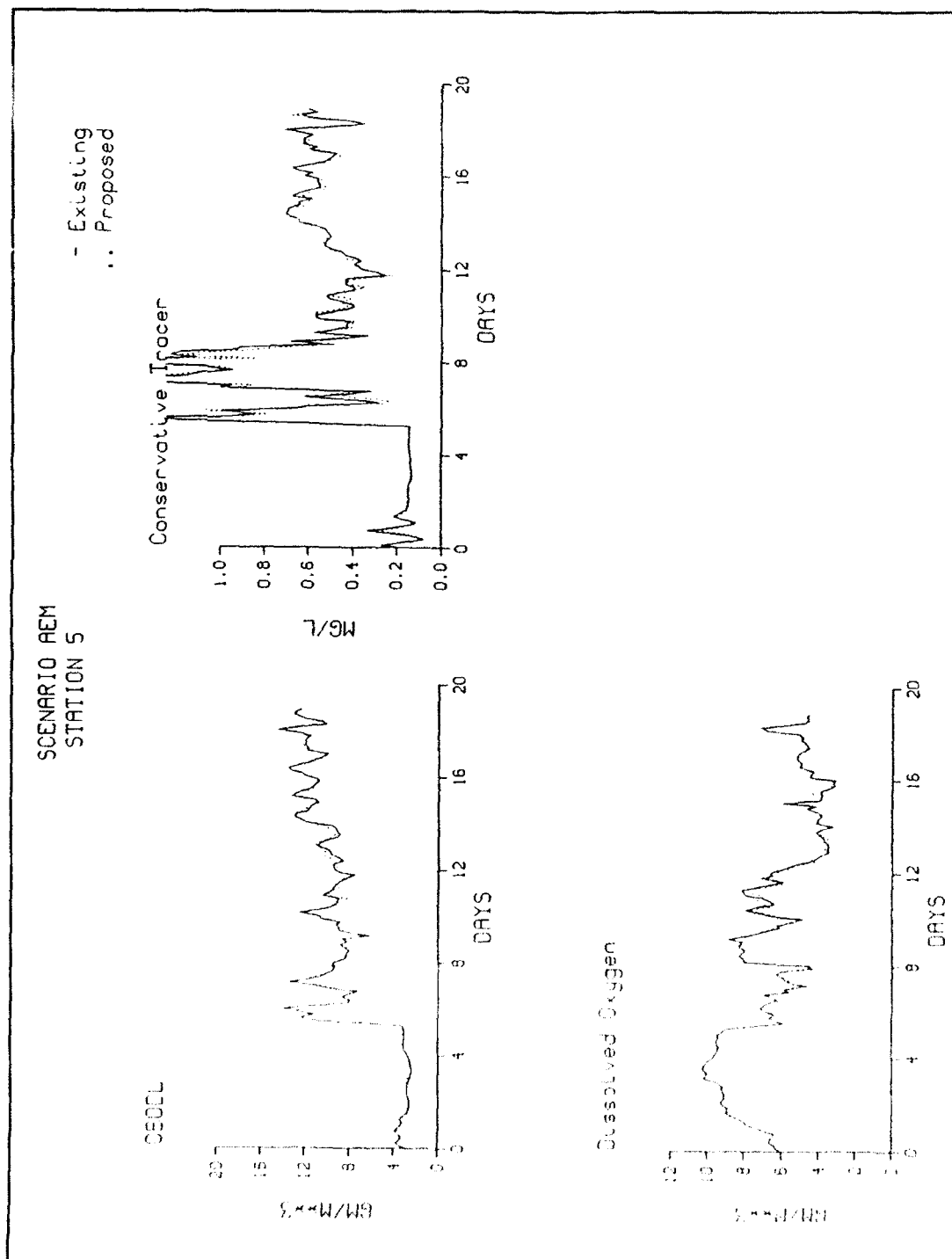


Figure D23. (Sheet 5 of 9)

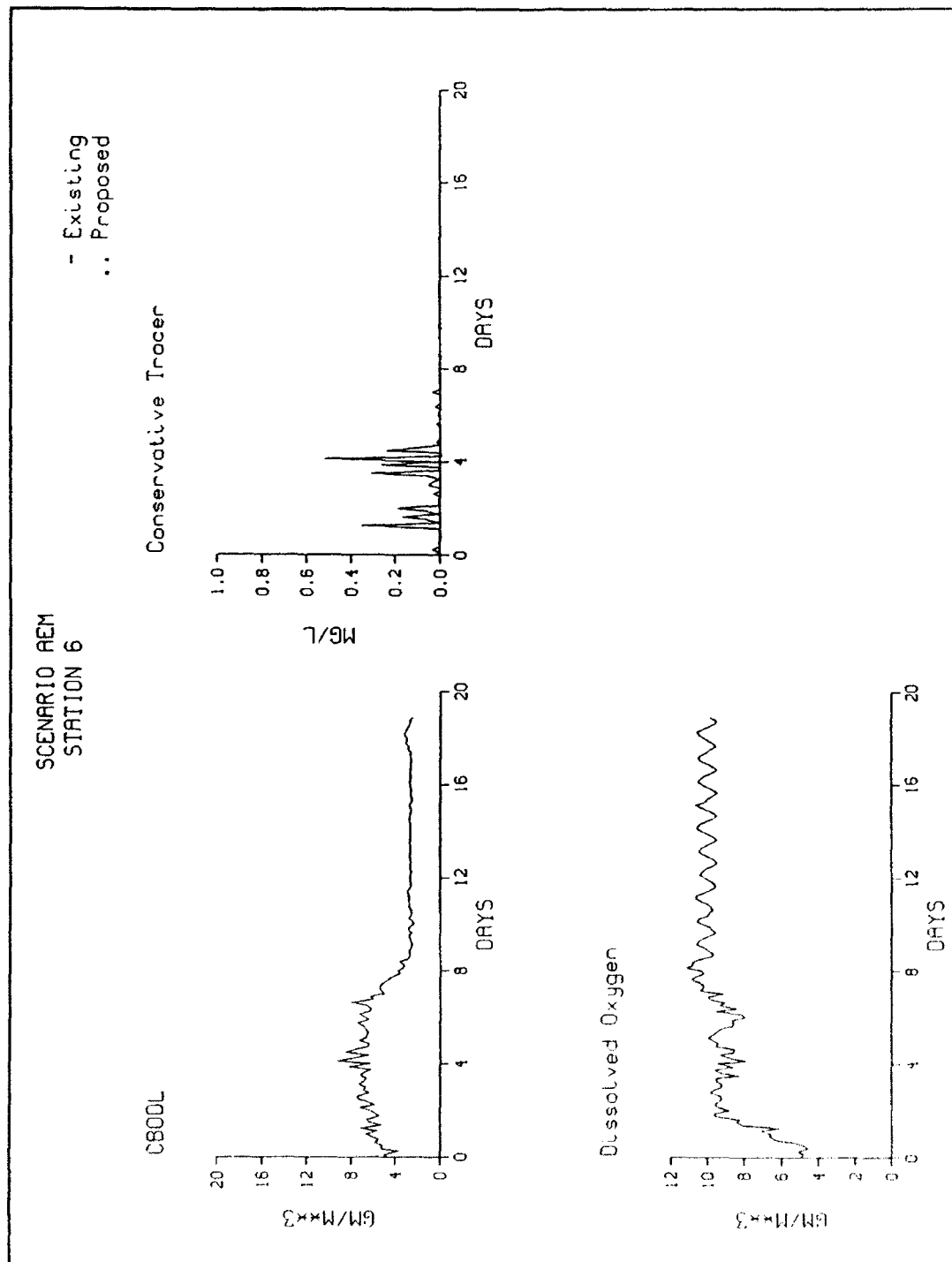


Figure D23. (Sheet 6 of 9)

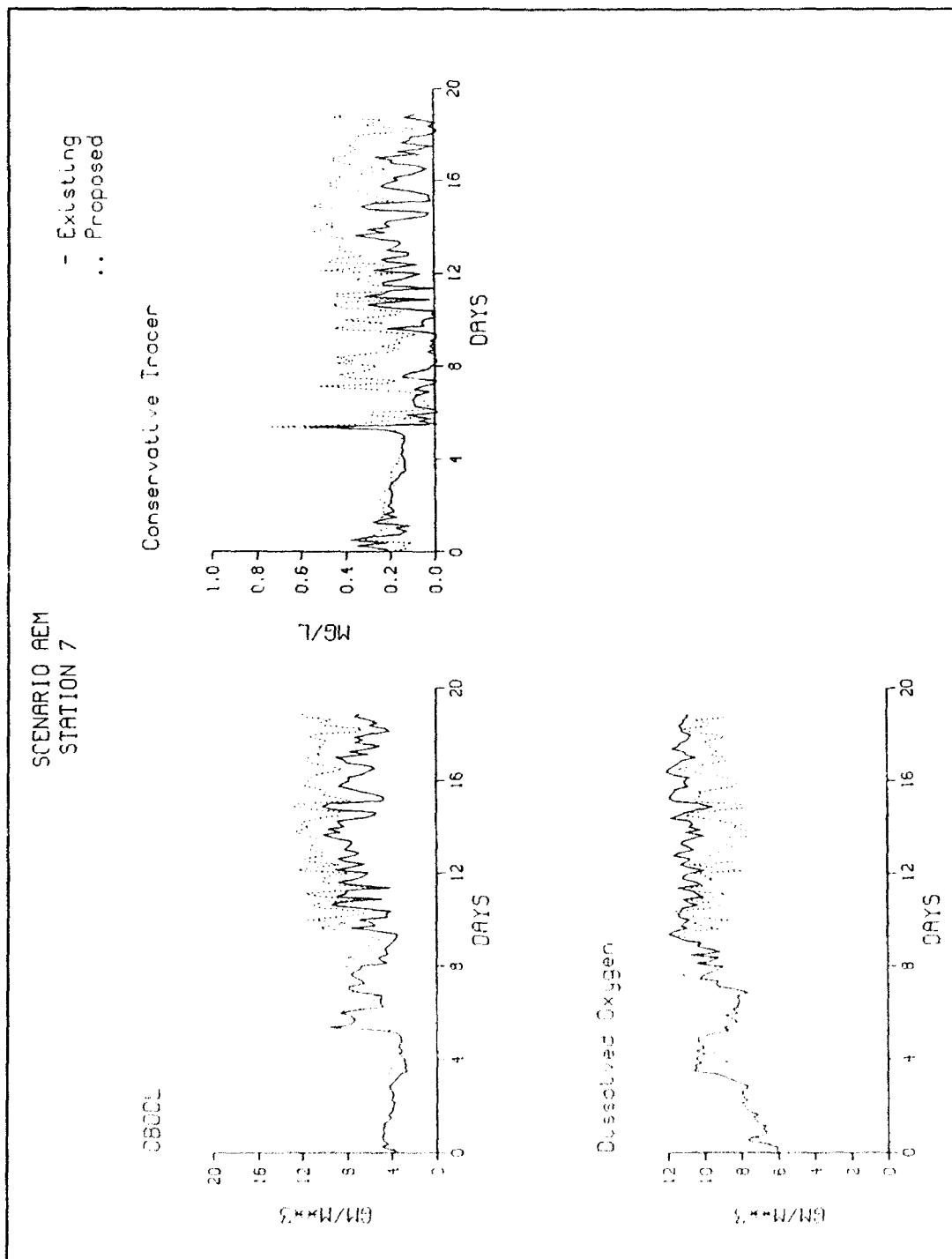


Figure D23. (Sheet 7 of 9)

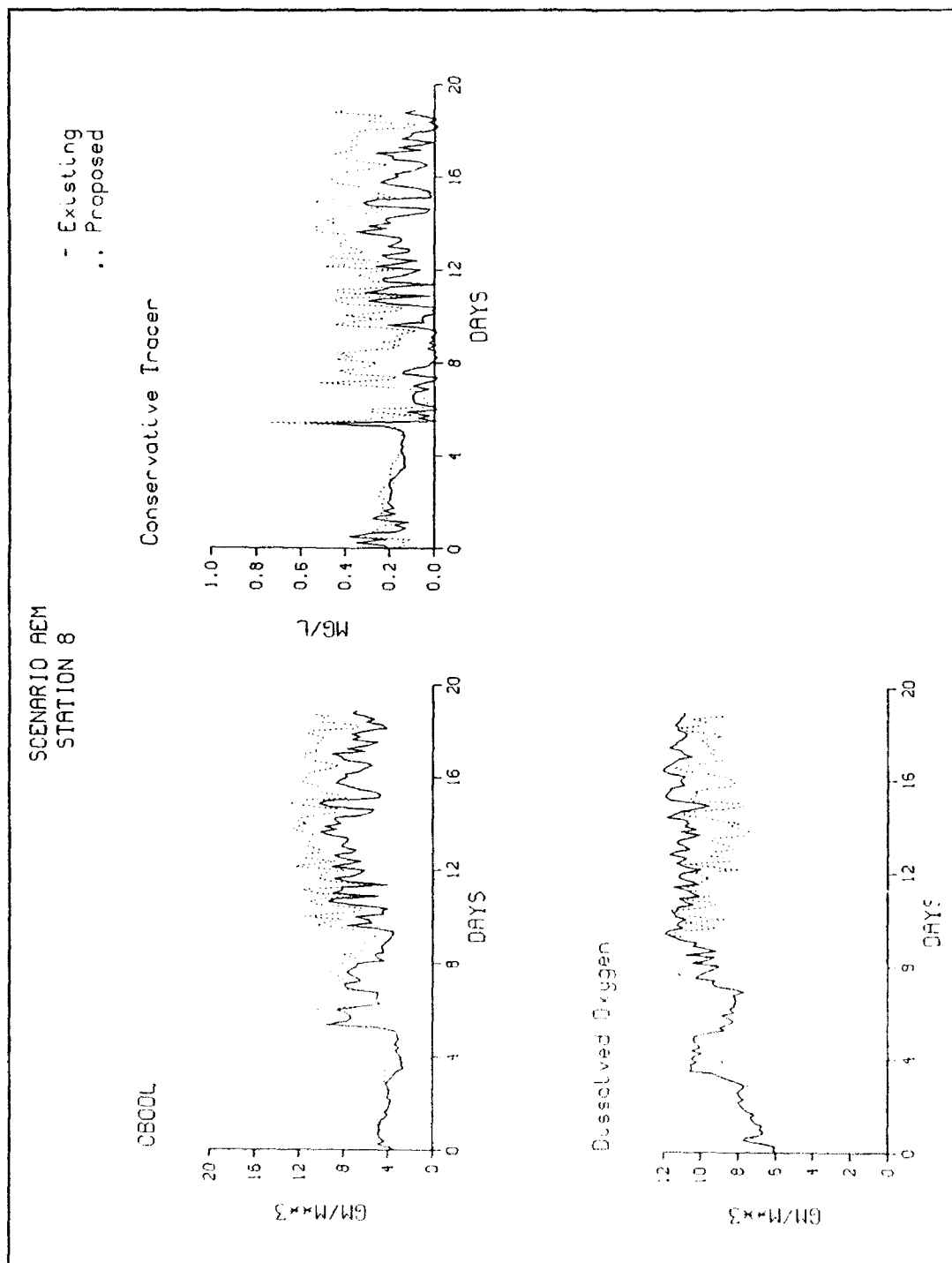


Figure D23. (Sheet 8 of 9)

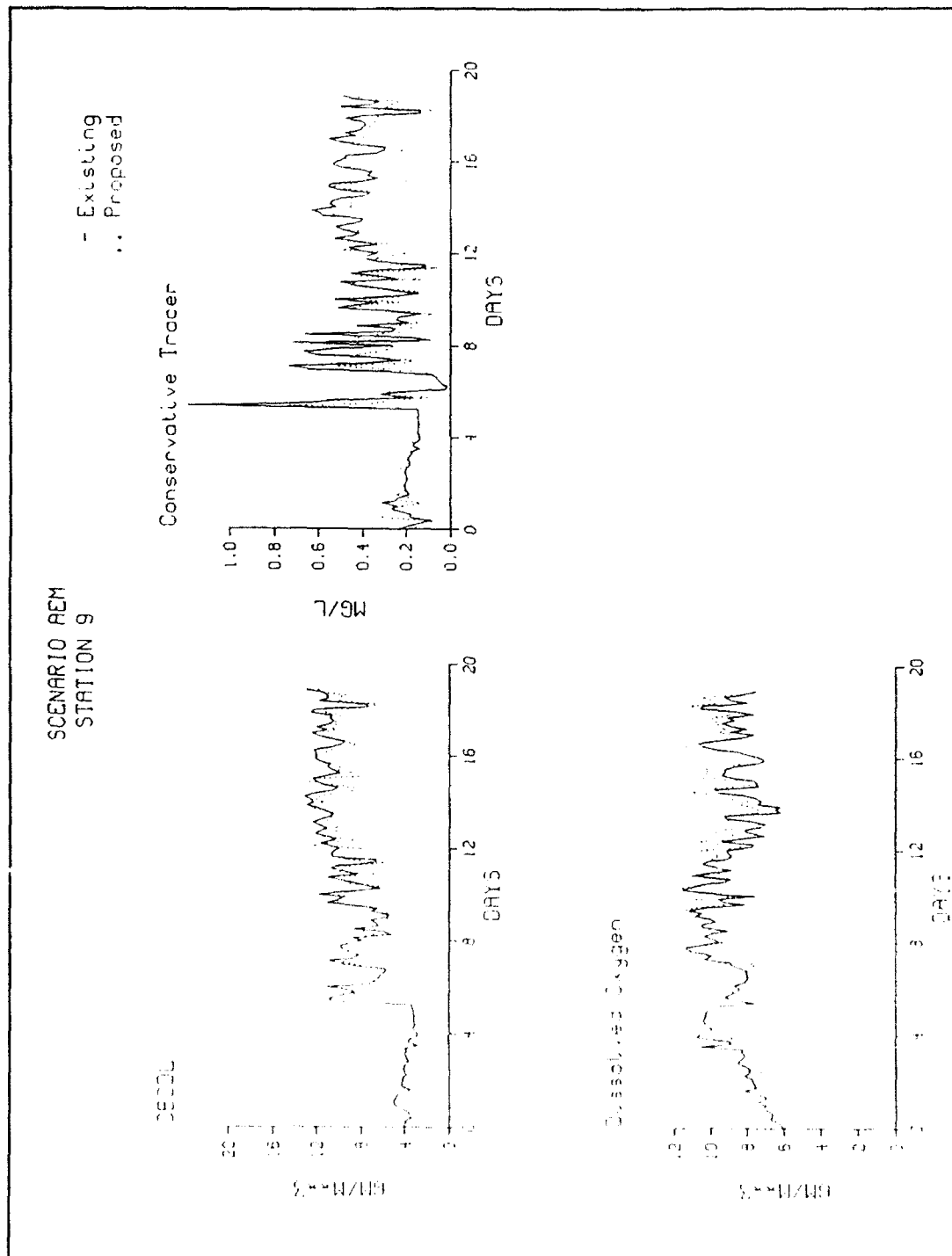


Figure D23. (Sheet 9 of 9)

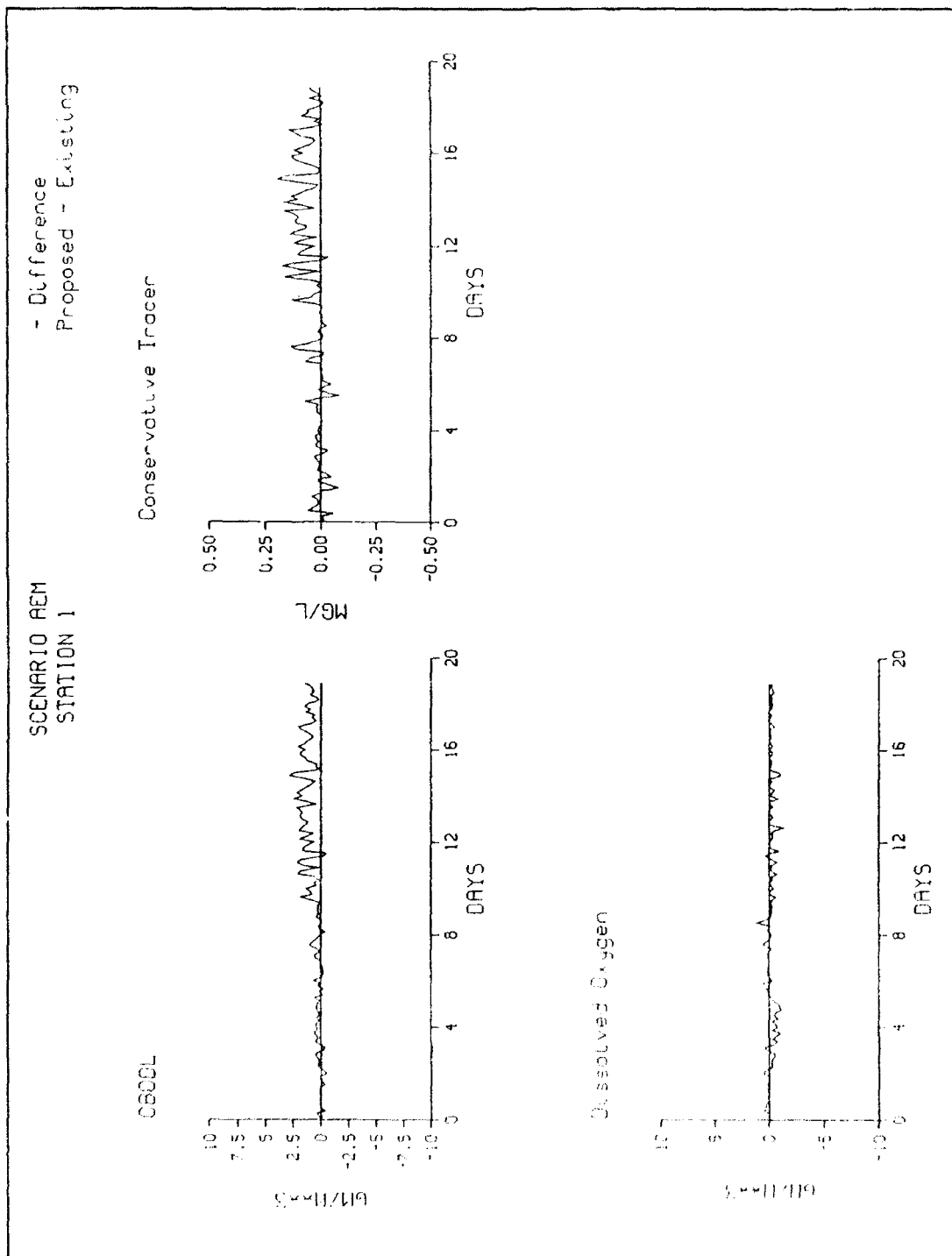


Figure D24. Time series differences for comparison stations, Scenario AEM (Sheet 1 of 8)

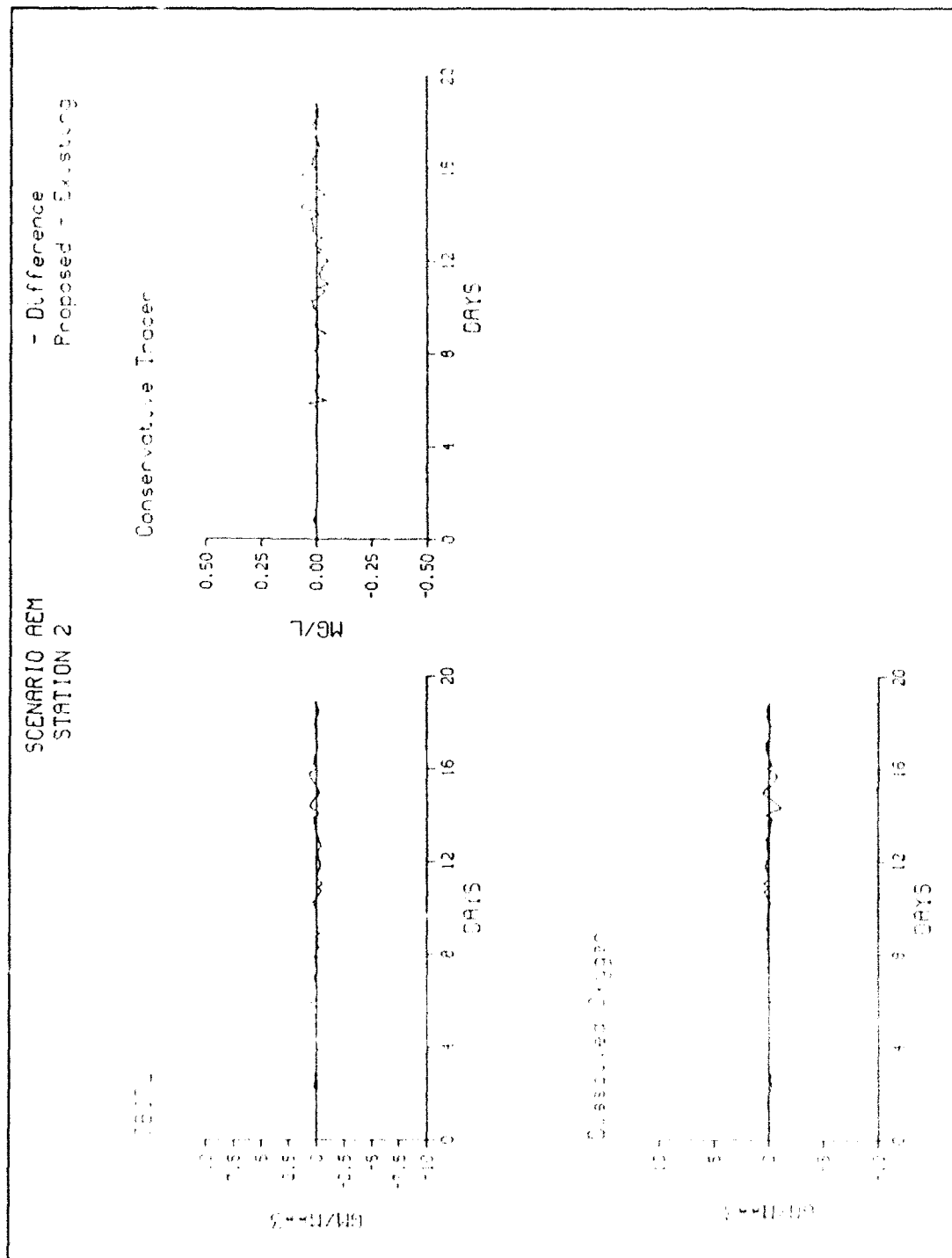


Figure D24. (Sheet 2 of 8)

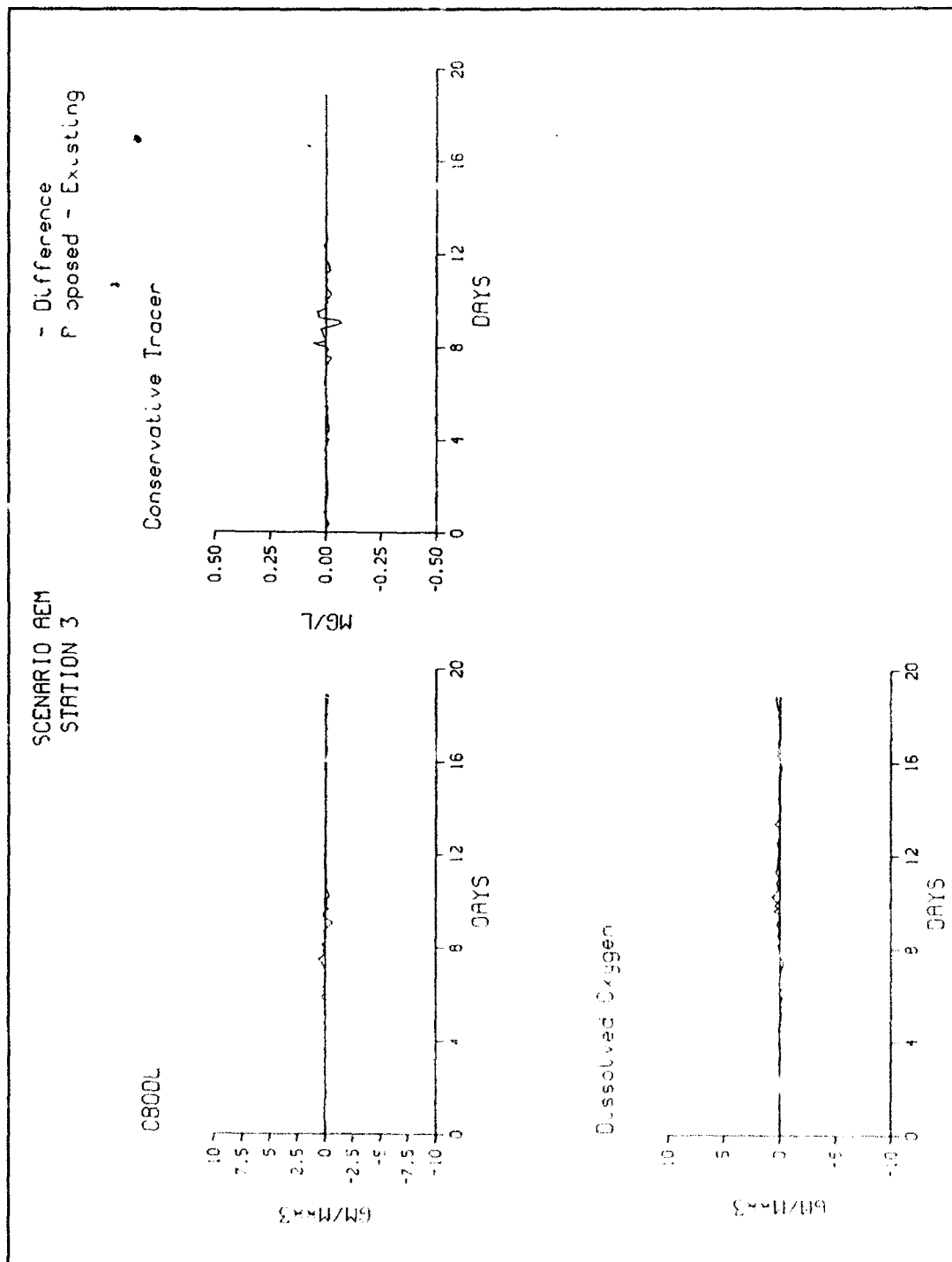


Figure D24. (Sheet 3 of 8)

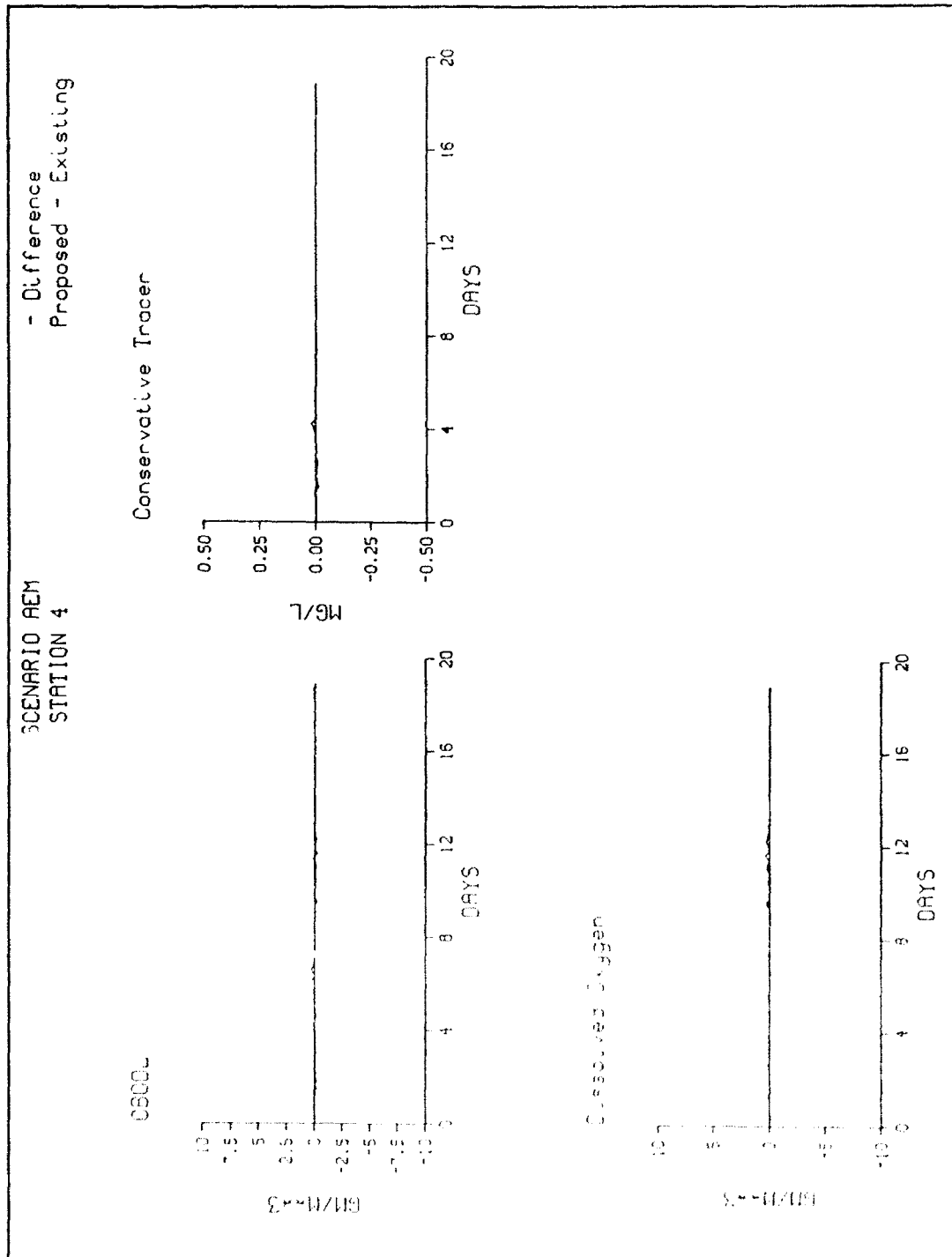


Figure D24. (Sheet 4 of 8)

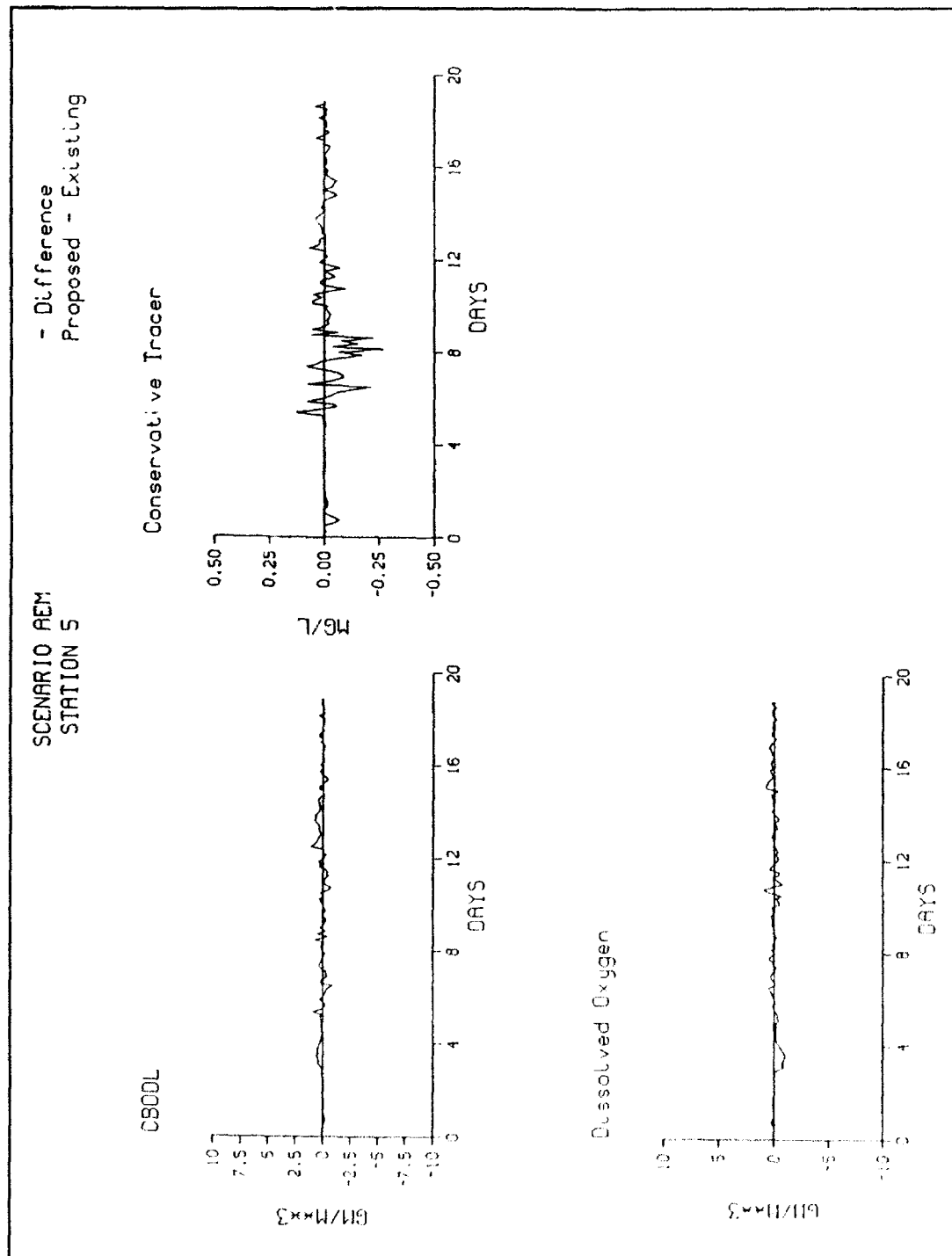


Figure D24. (Sheet 5 of 8)

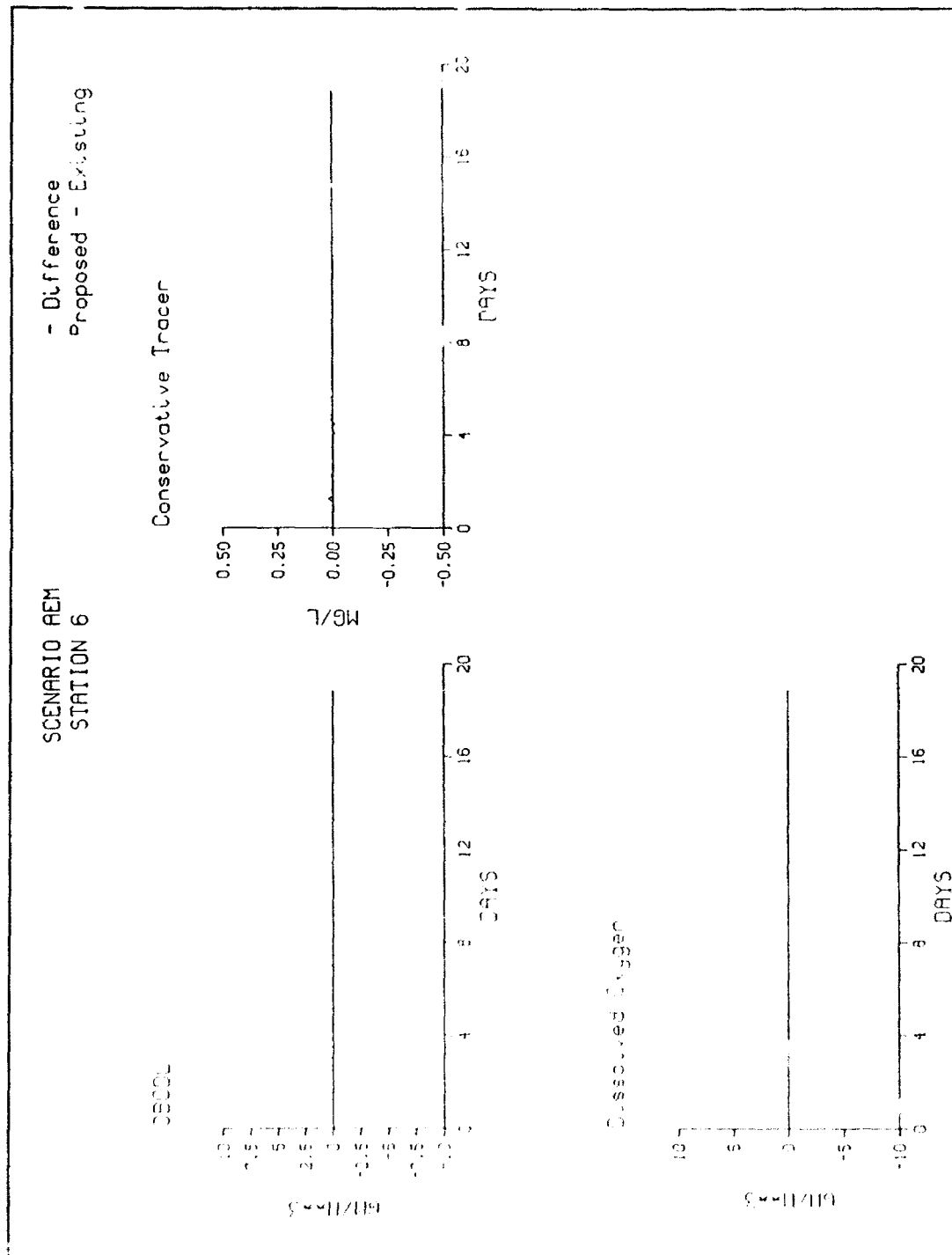


Figure D24. (Sheet 6 of 8)

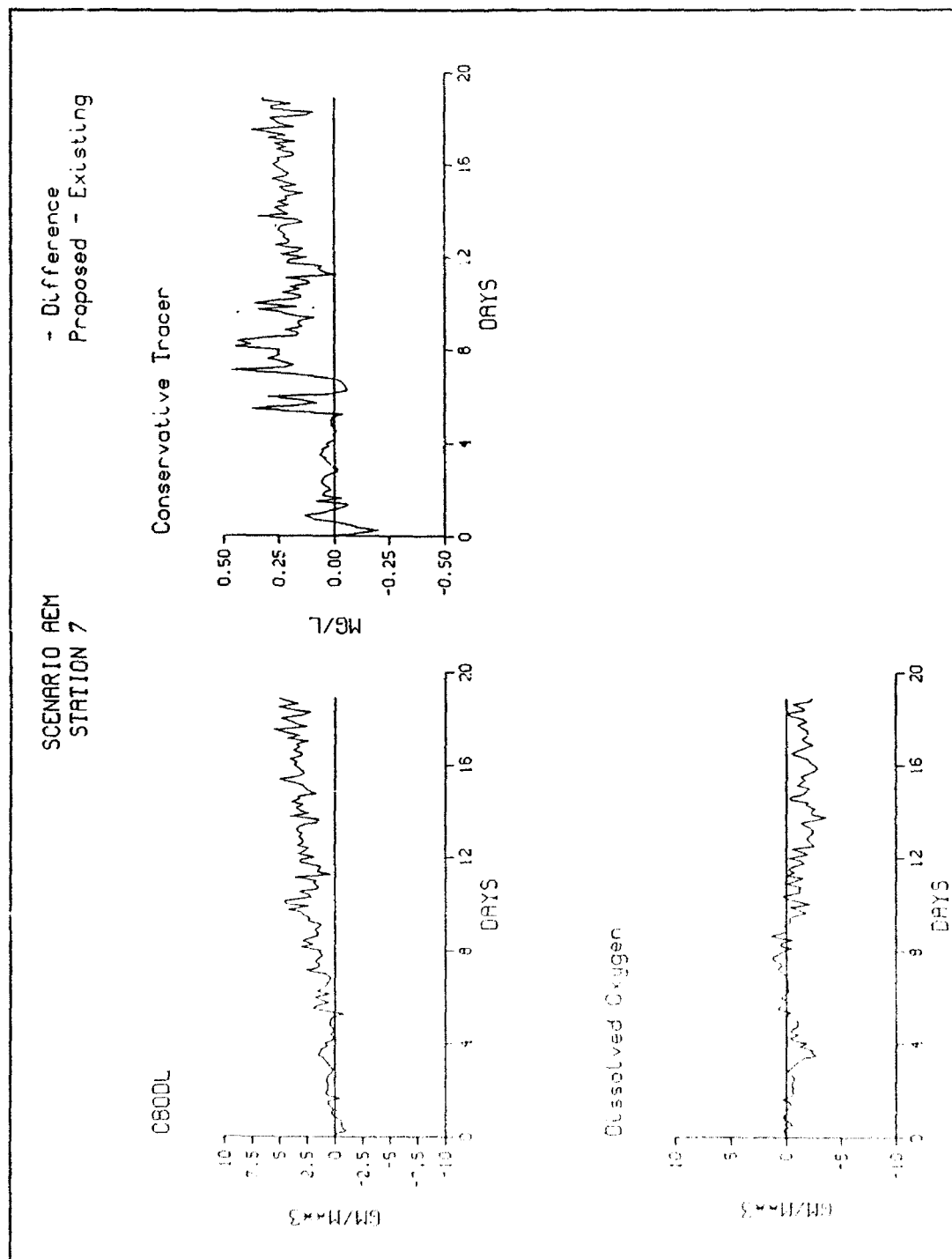


Figure D24. (Sheet 7 of 8)

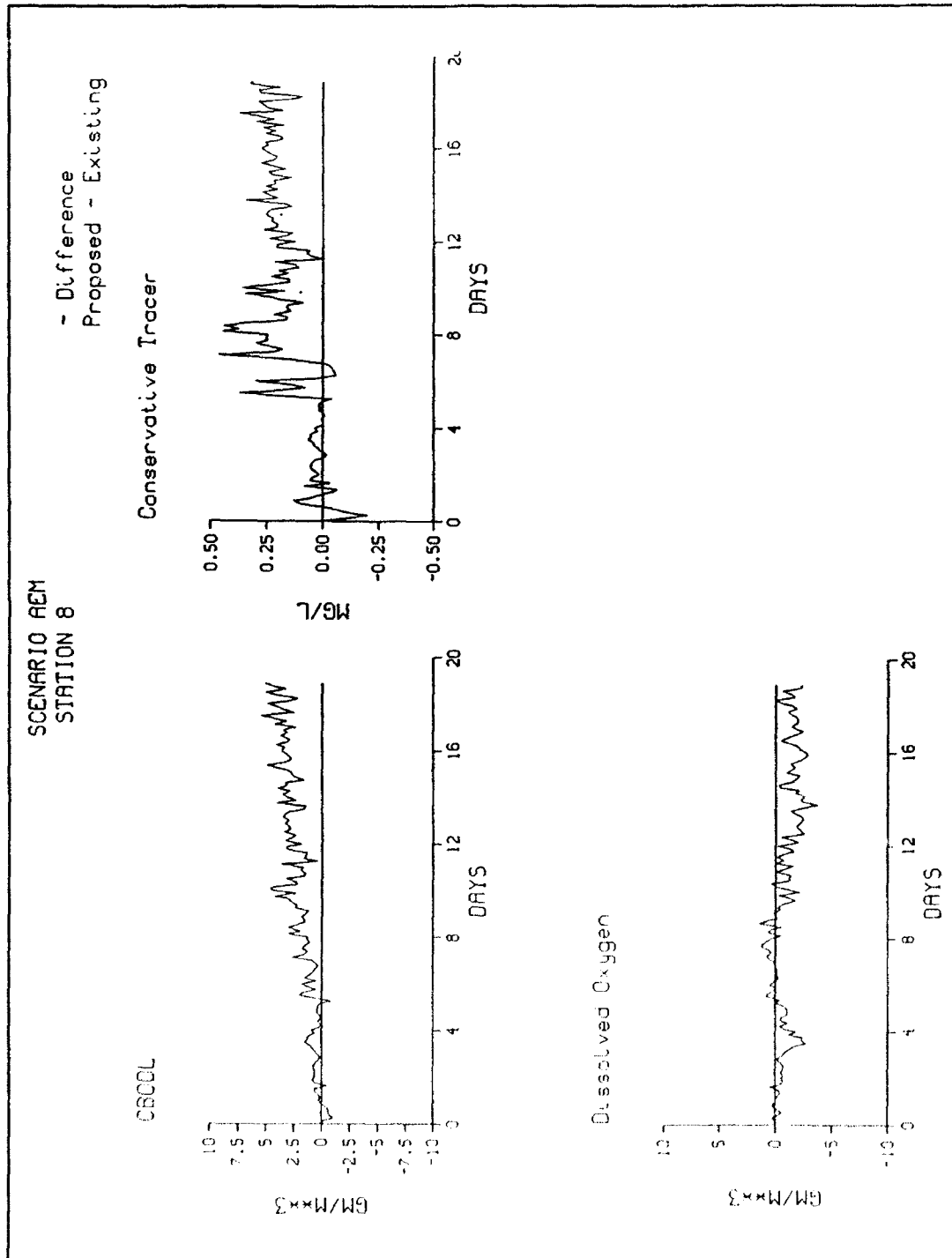


Figure D24. (Sheet 8 of 8)

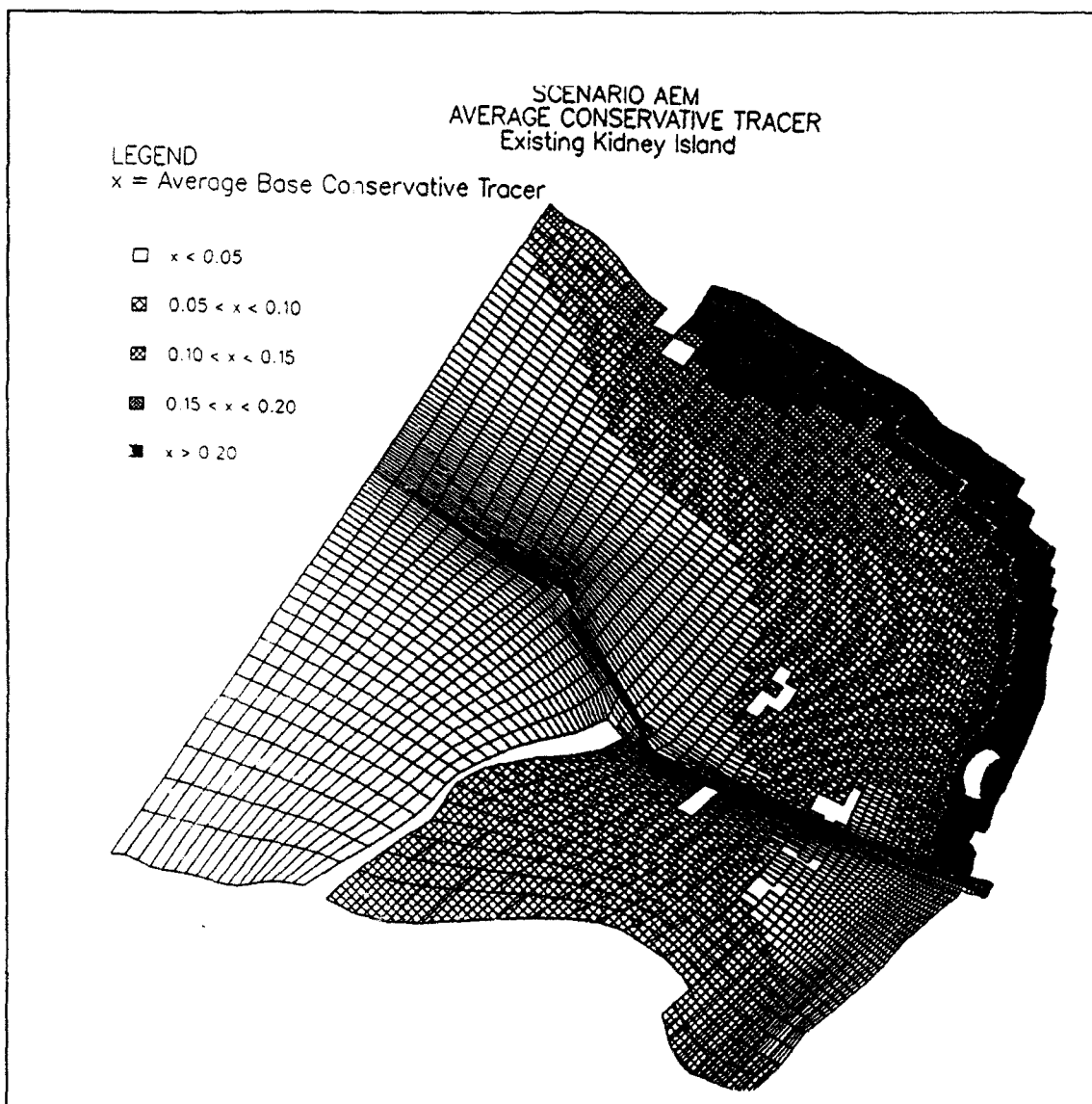


Figure D25. Average conservative tracer concentrations, Scenario AEM (Continued)

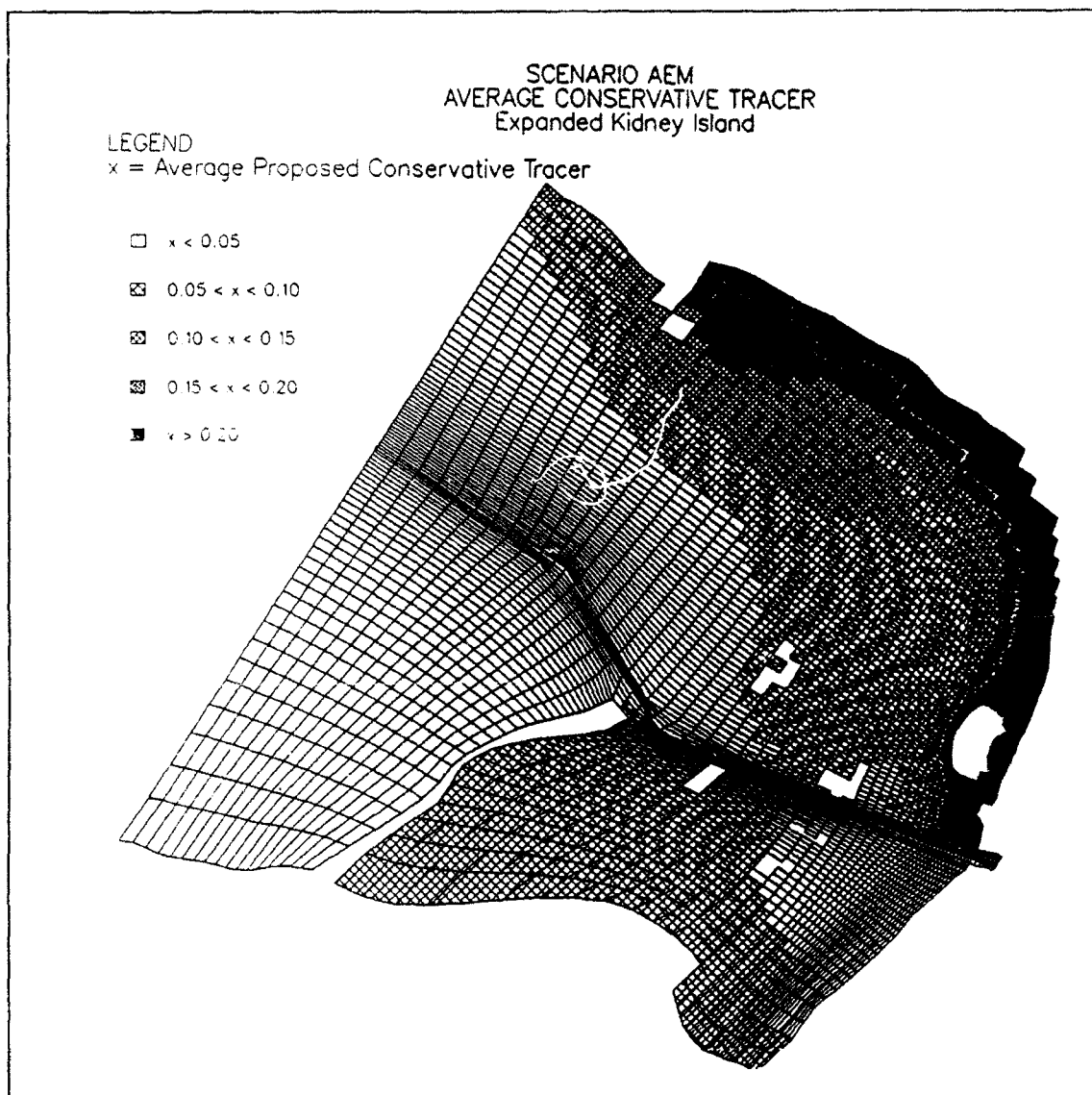


Figure D25. (Concluded)

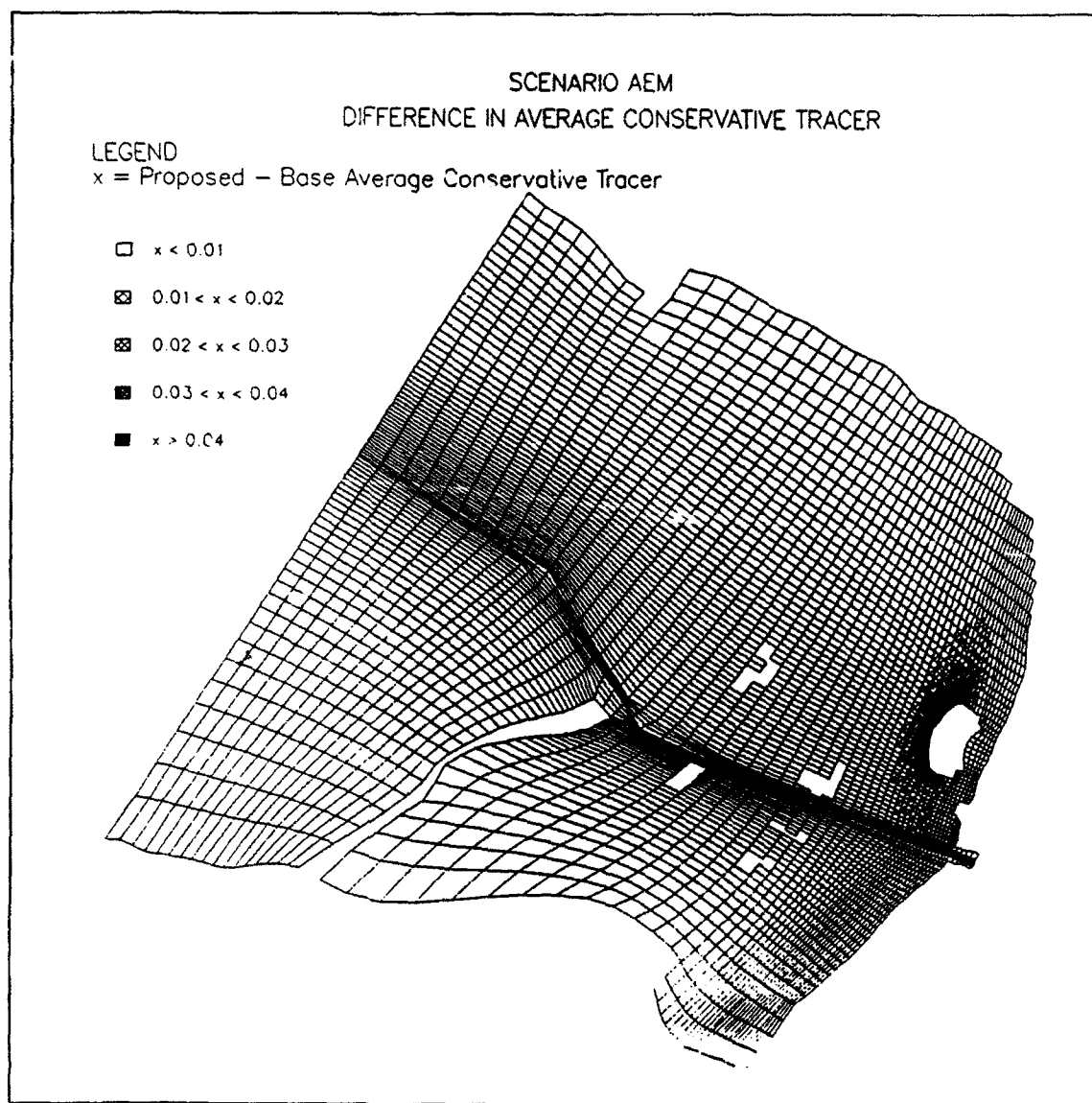


Figure D26. Difference in average conservative tracer, Scenario AEM

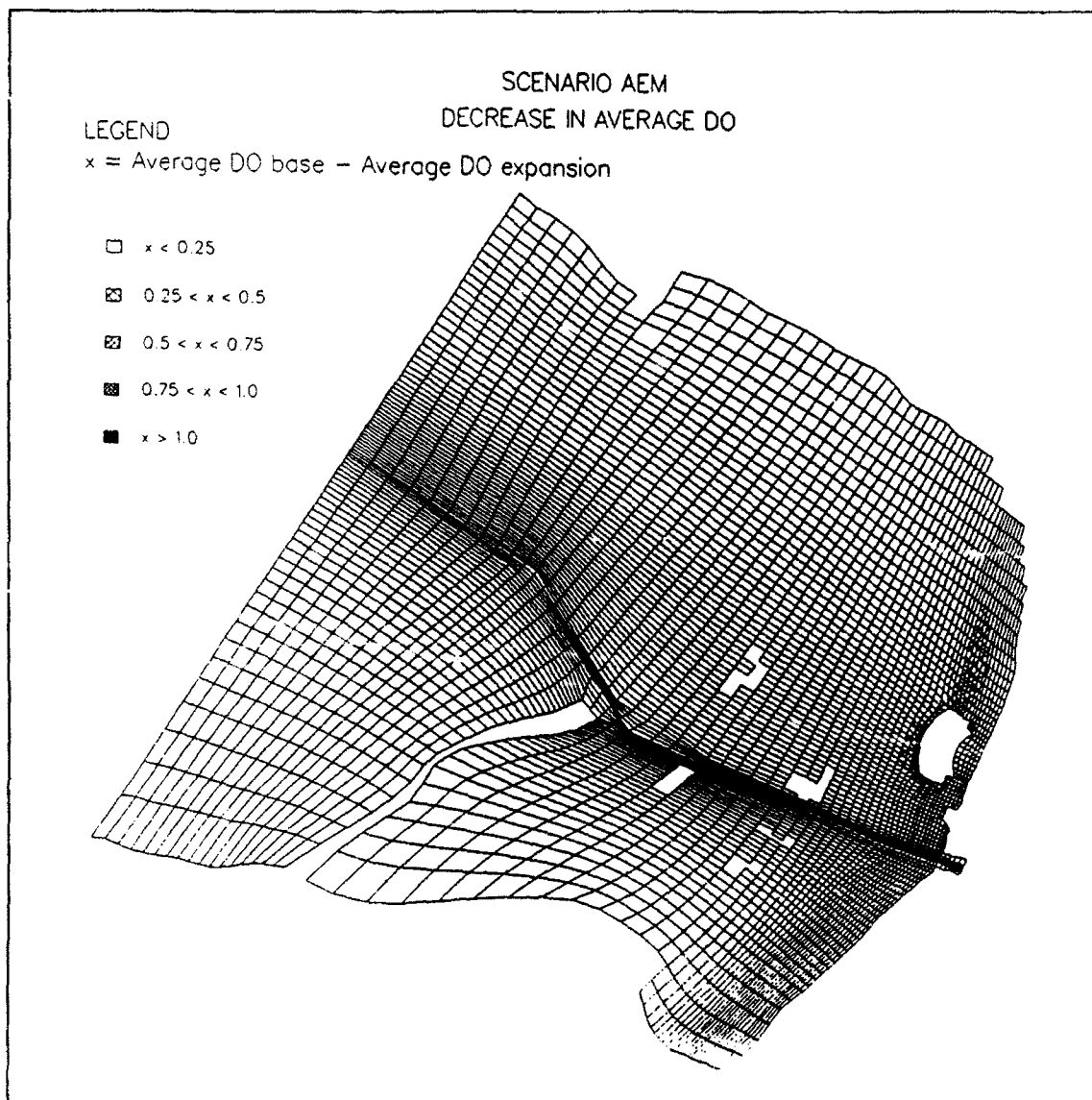


Figure D27. Decrease in average DO concentrations, Scenario AEM

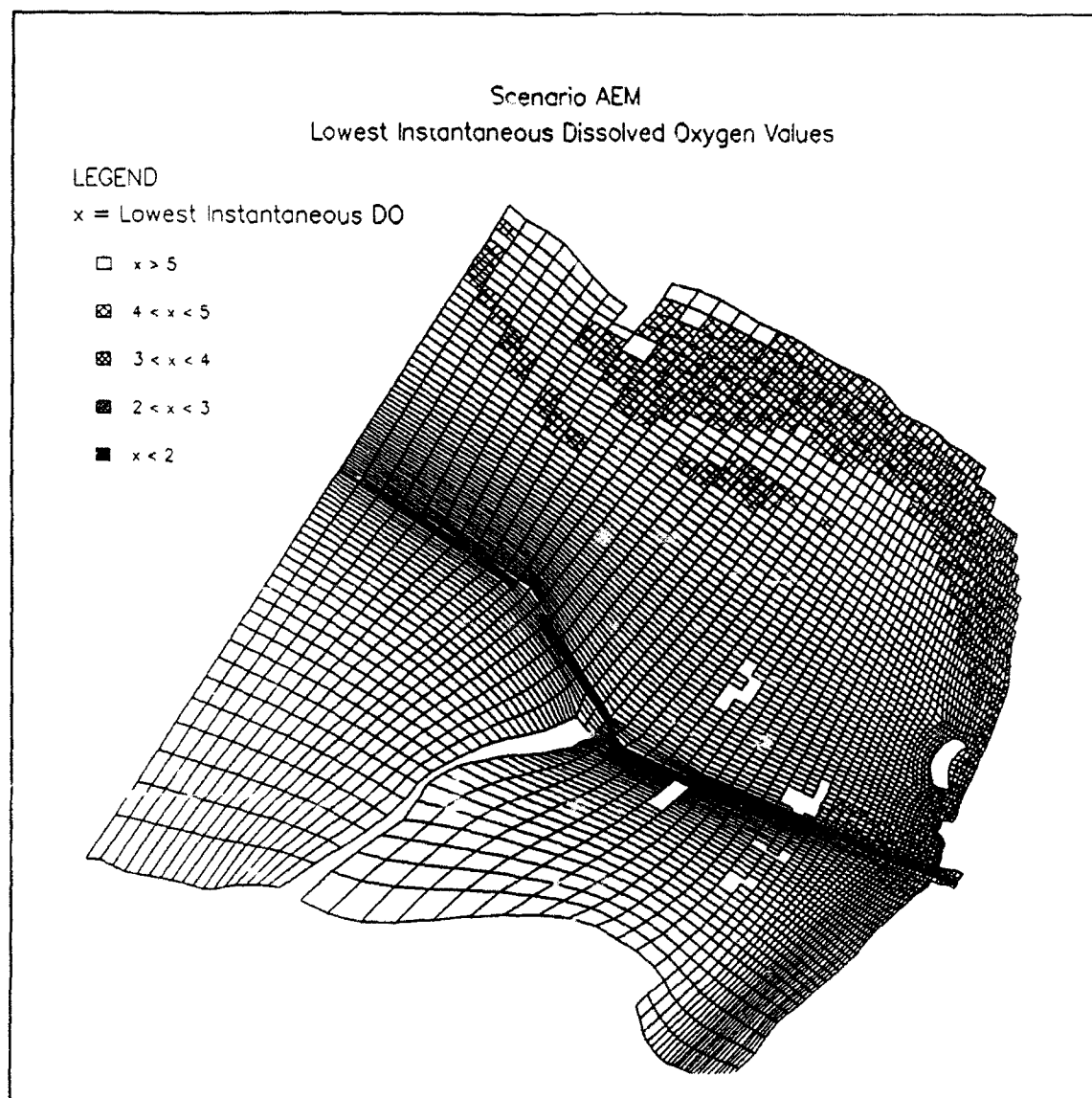


Figure D28. Lowest instantaneous DO, Scenario AEM (Continued)

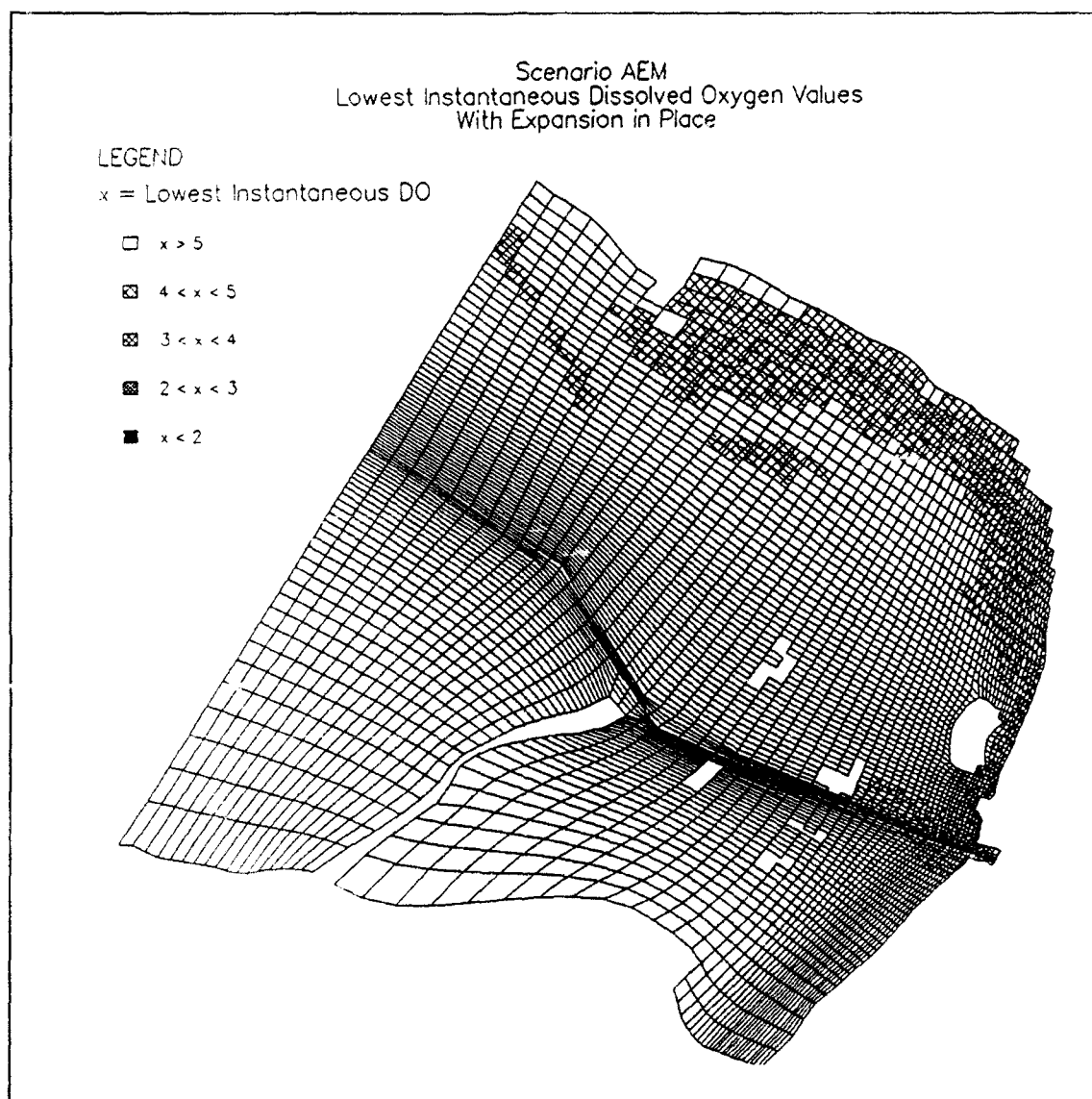


Figure D28. (Concluded)

SCENARIO MMM

**(Minimum Seiche, Minimum River Flows,
Minimum Lake Level)**

Figures D29 - D36

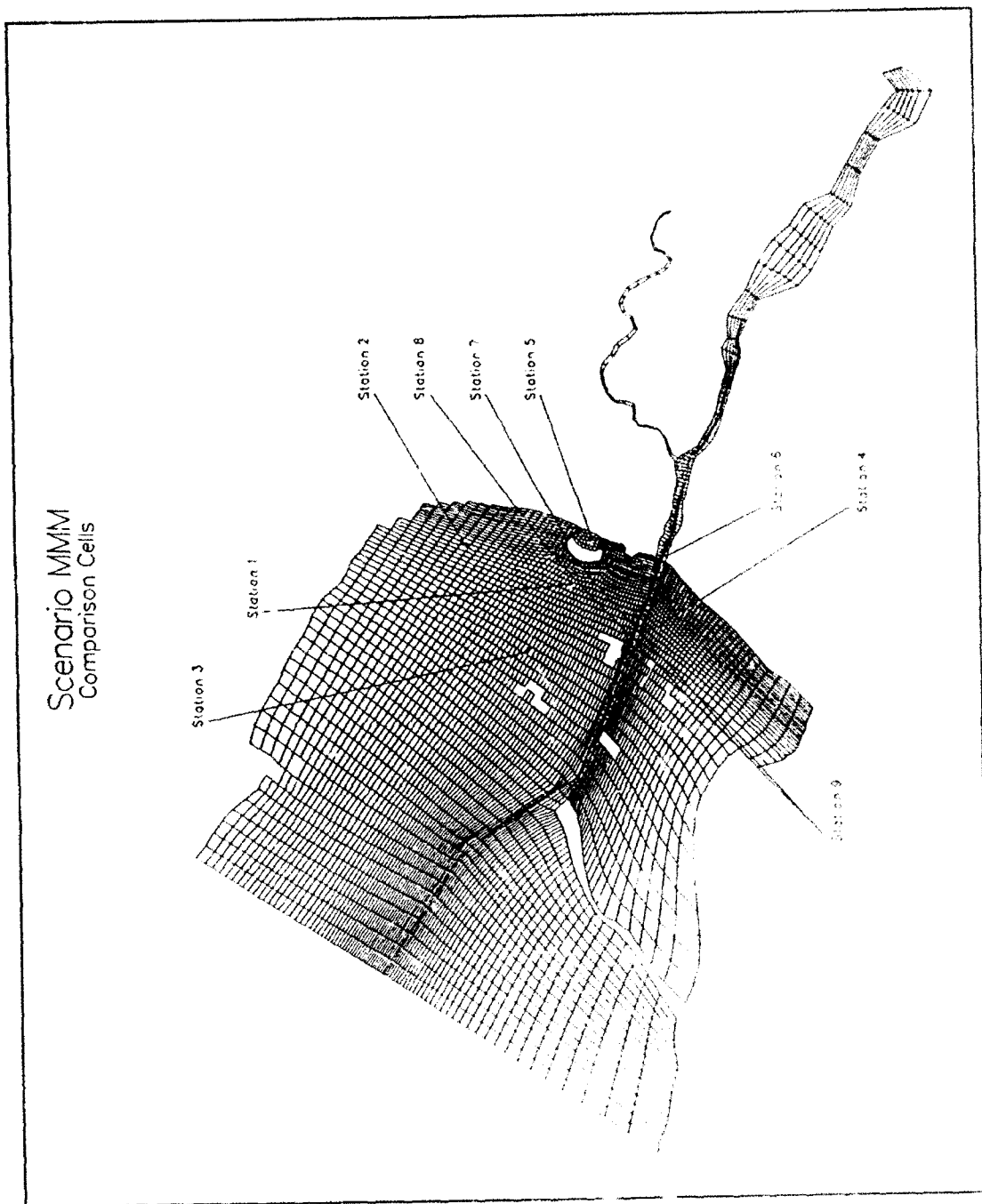


Figure D29. Pre- and post-expansion comparison stations, Scenario MMM

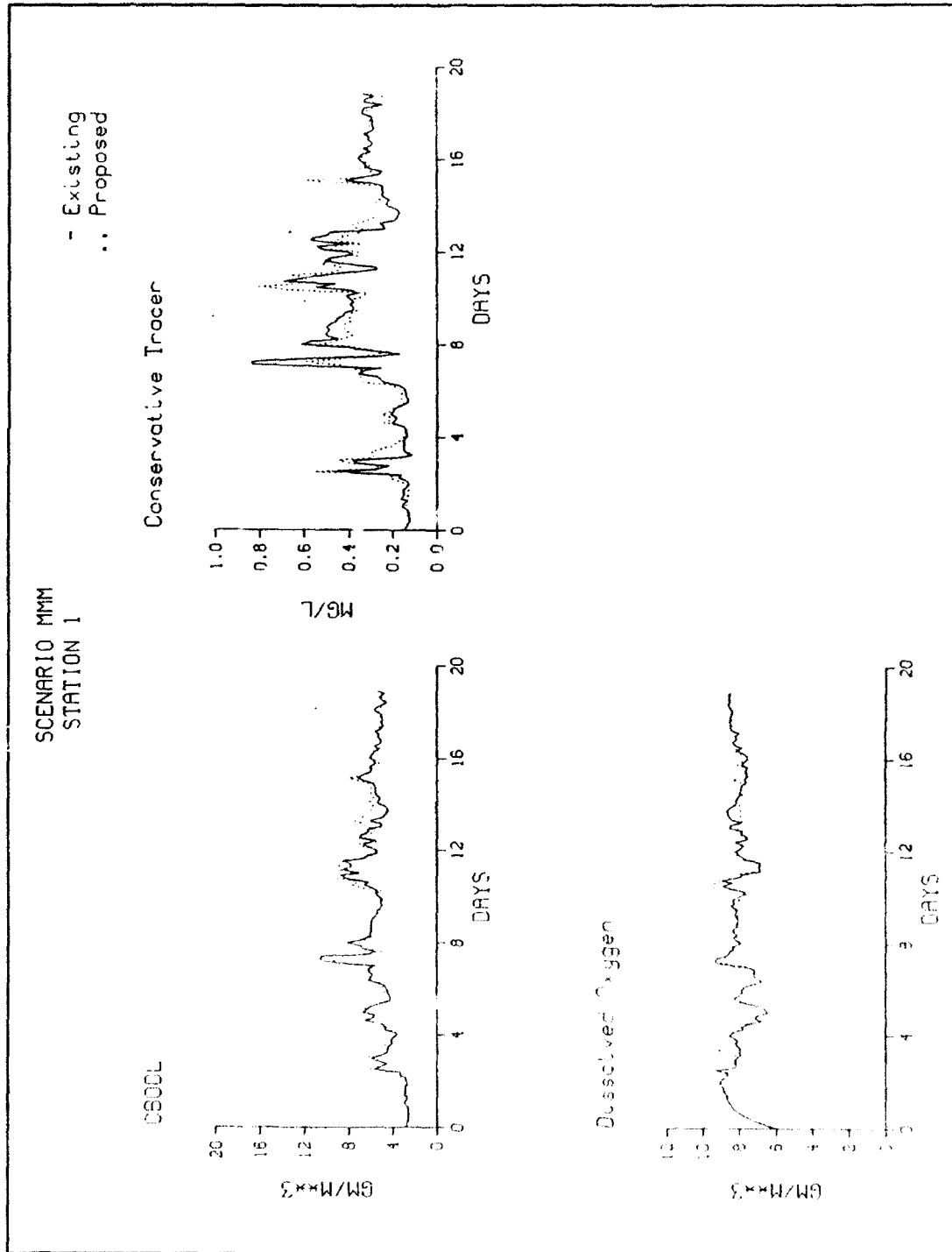


Figure D30. Time series for comparison stations, Scenario MMM (Sheet 1 of 9)

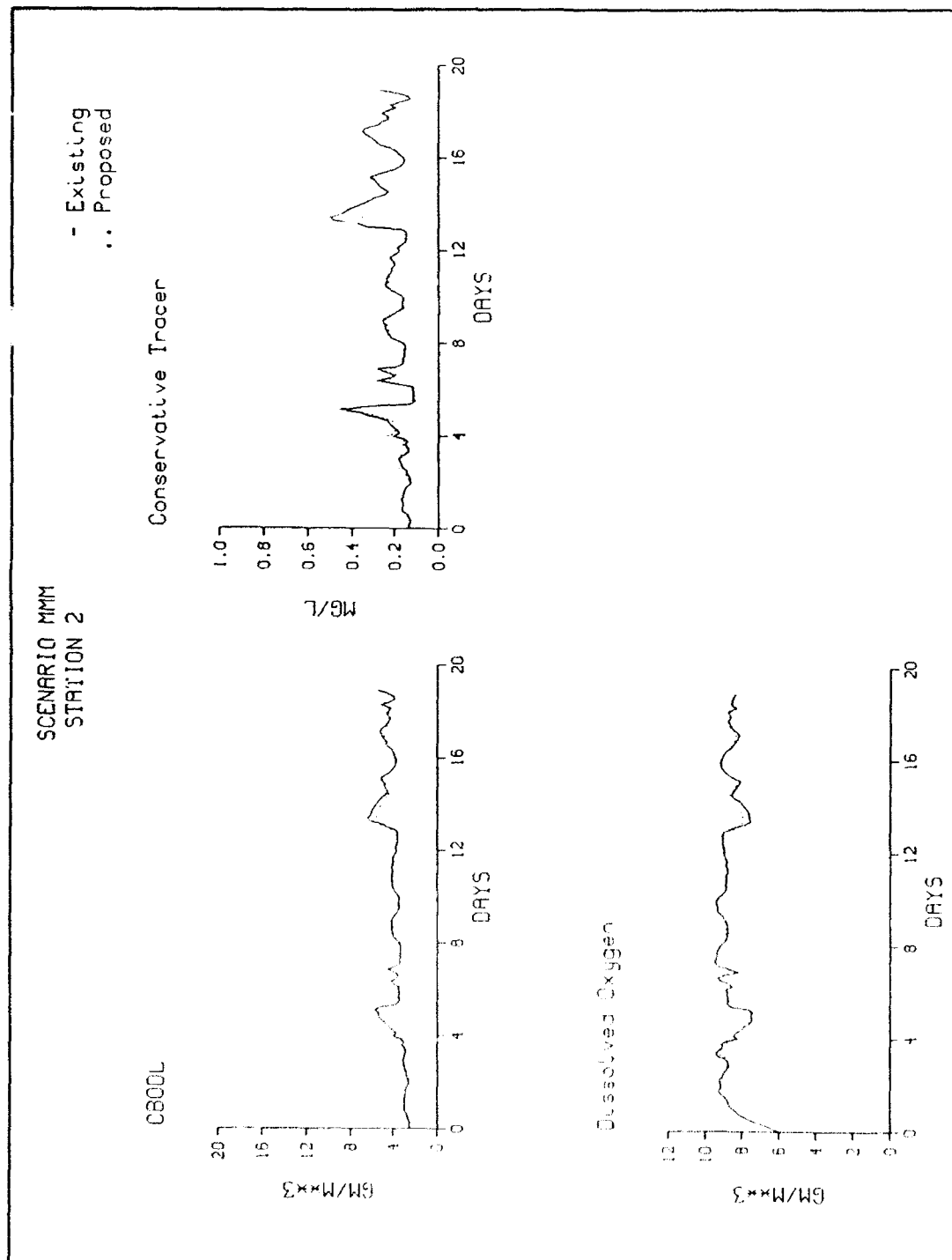


Figure D30. (Sheet 2 of 9)

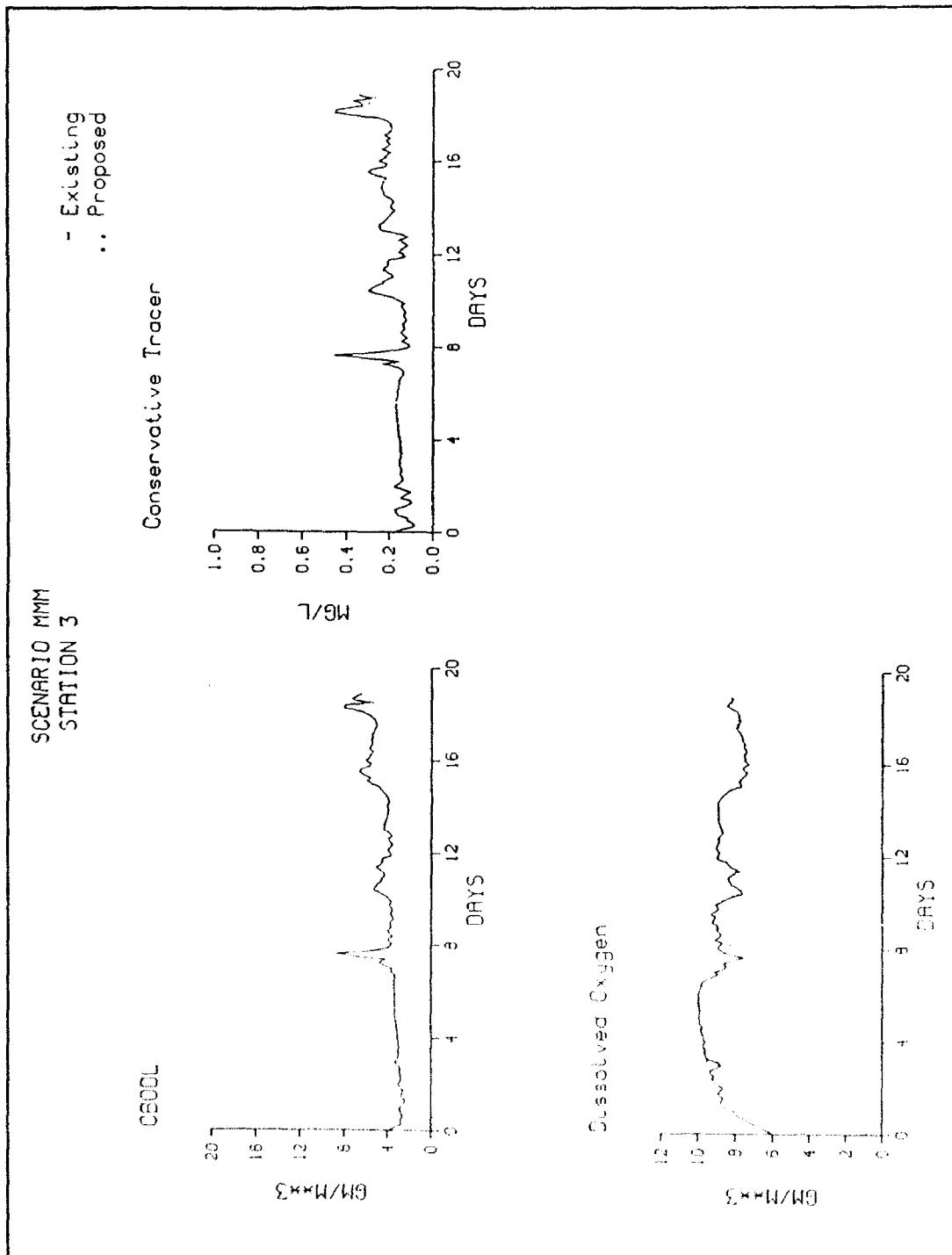


Figure D30. (Sheet 3 of 9)

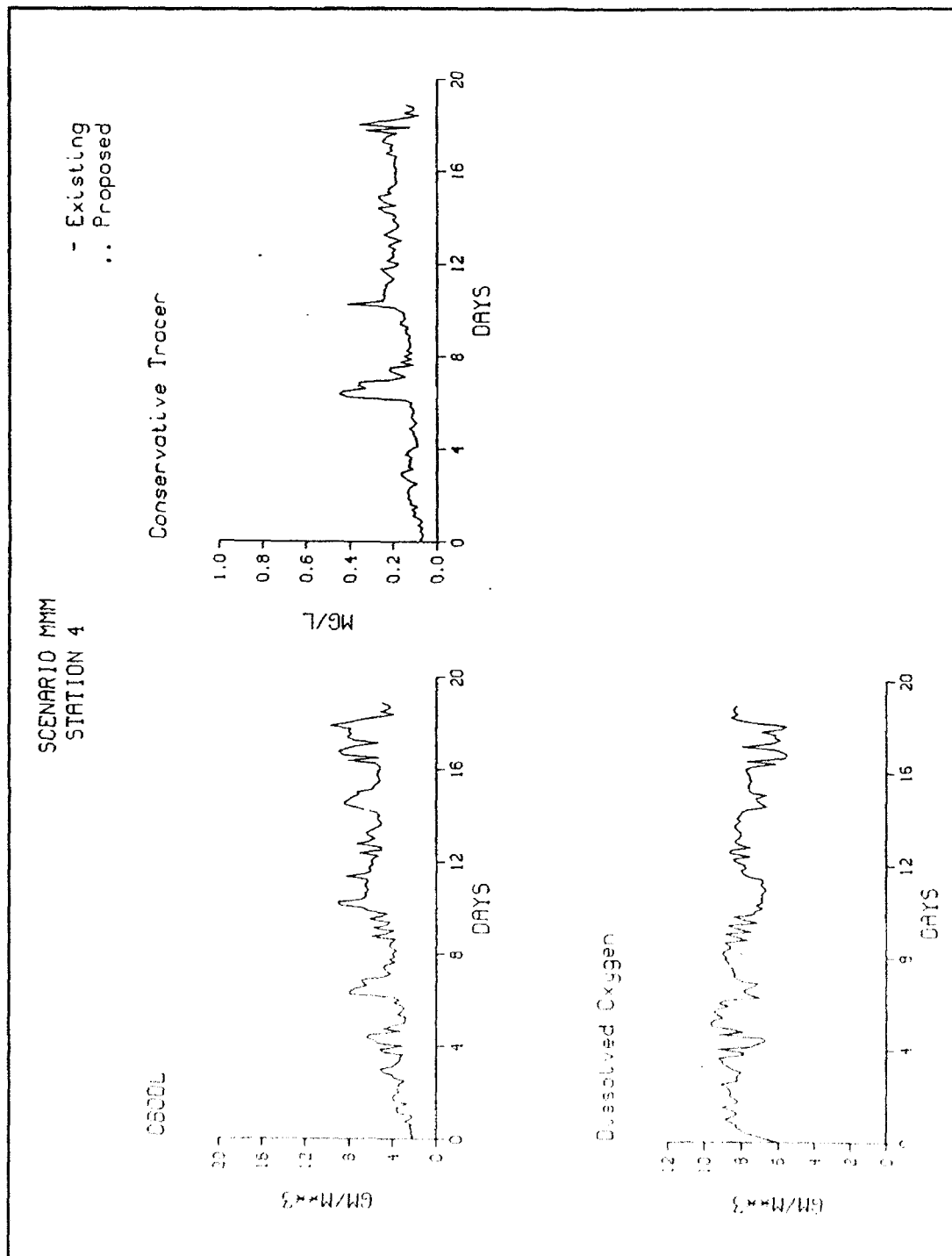


Figure D30. (Sheet 4 of 9)

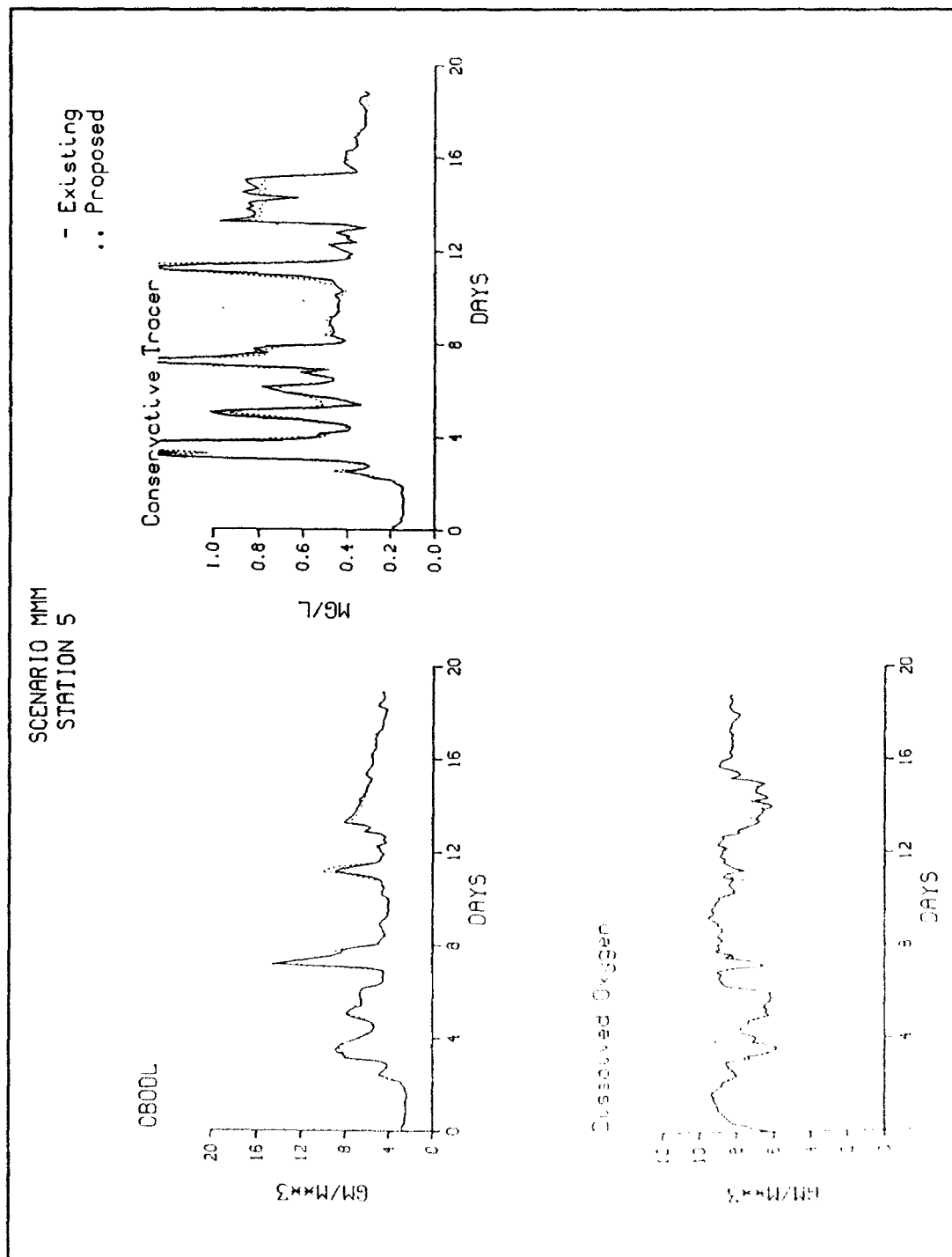


Figure D30. (Sheet 5 of 9)

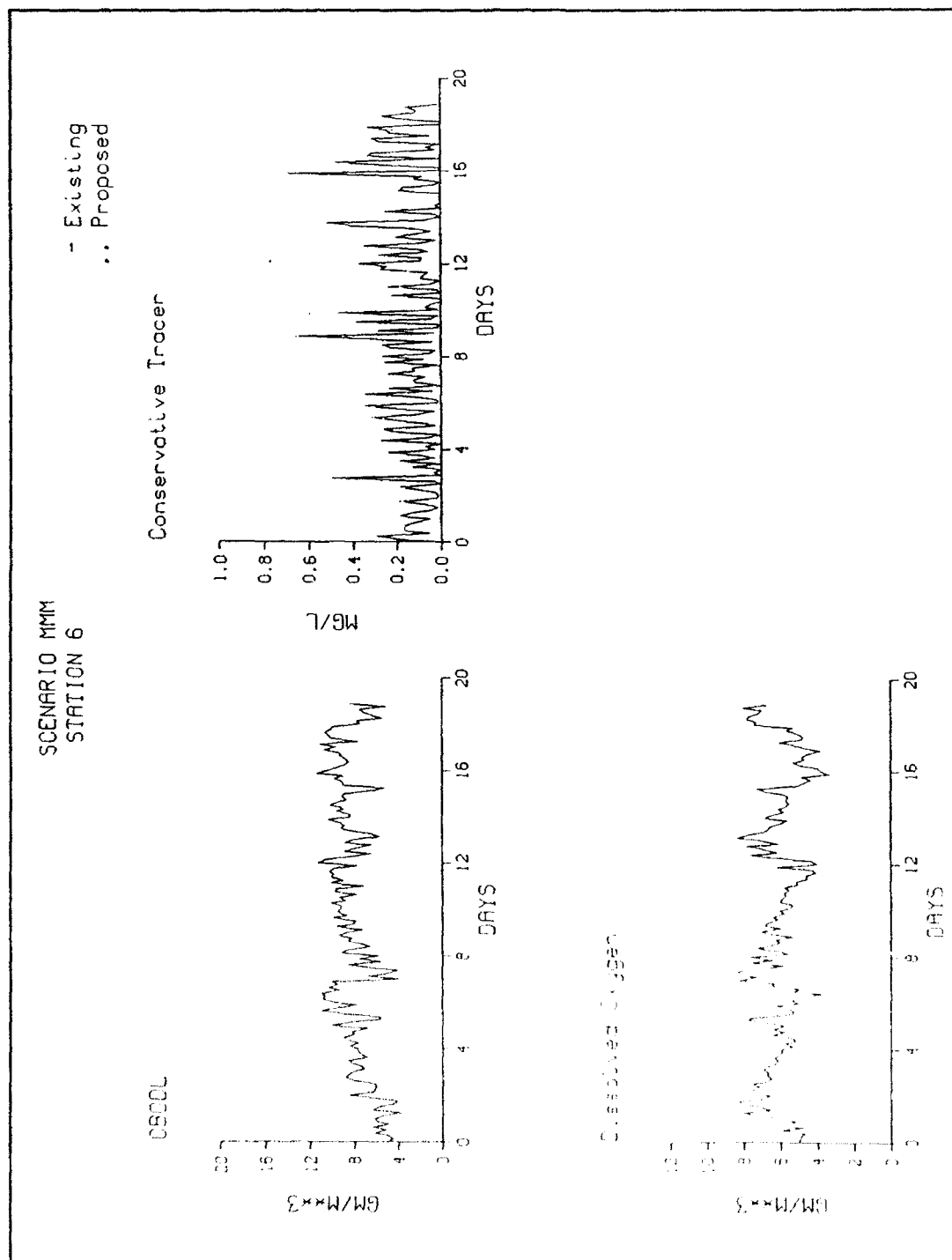


Figure D30. (Sheet 6 of 9)

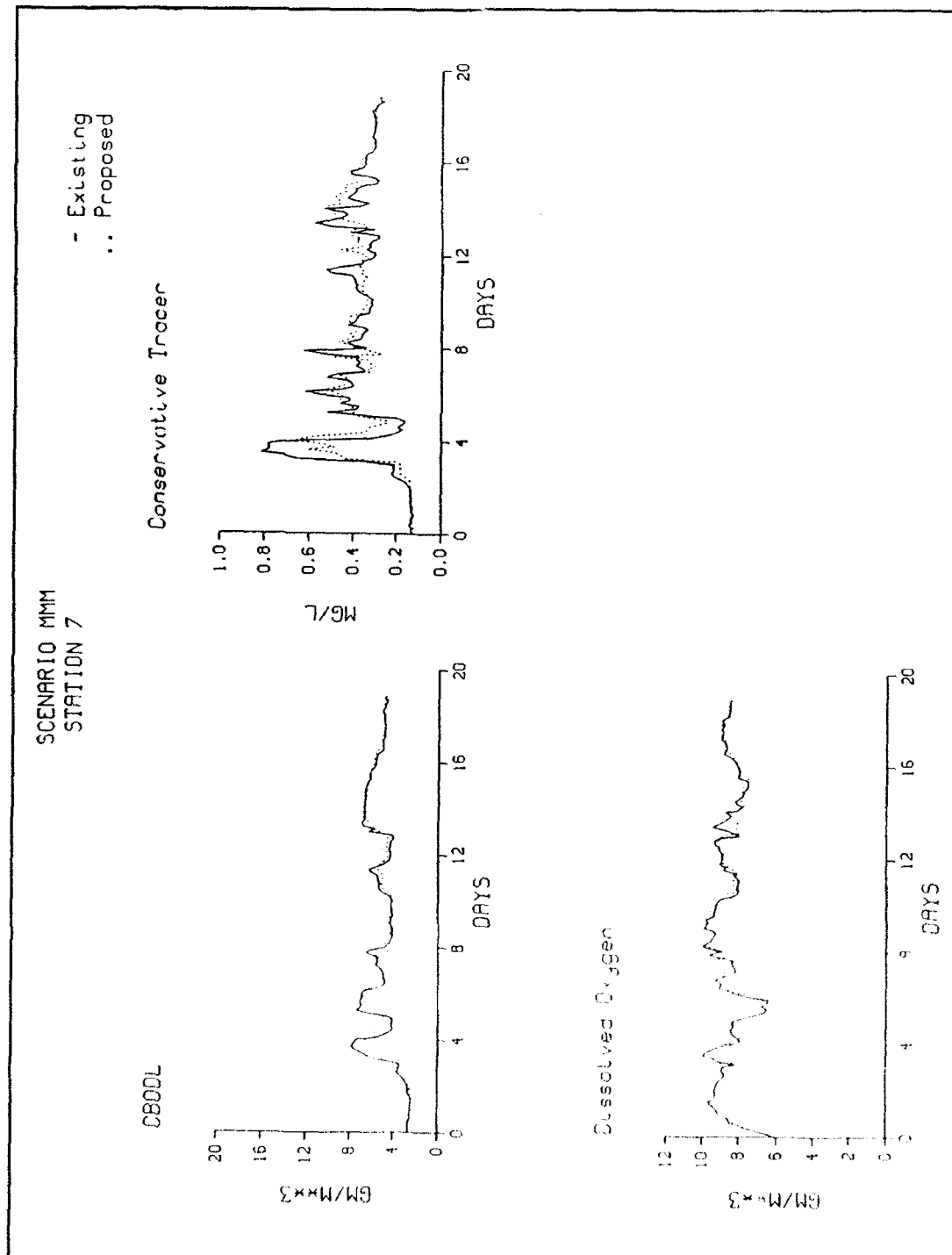


Figure D30. (Sheet 7 of 9)

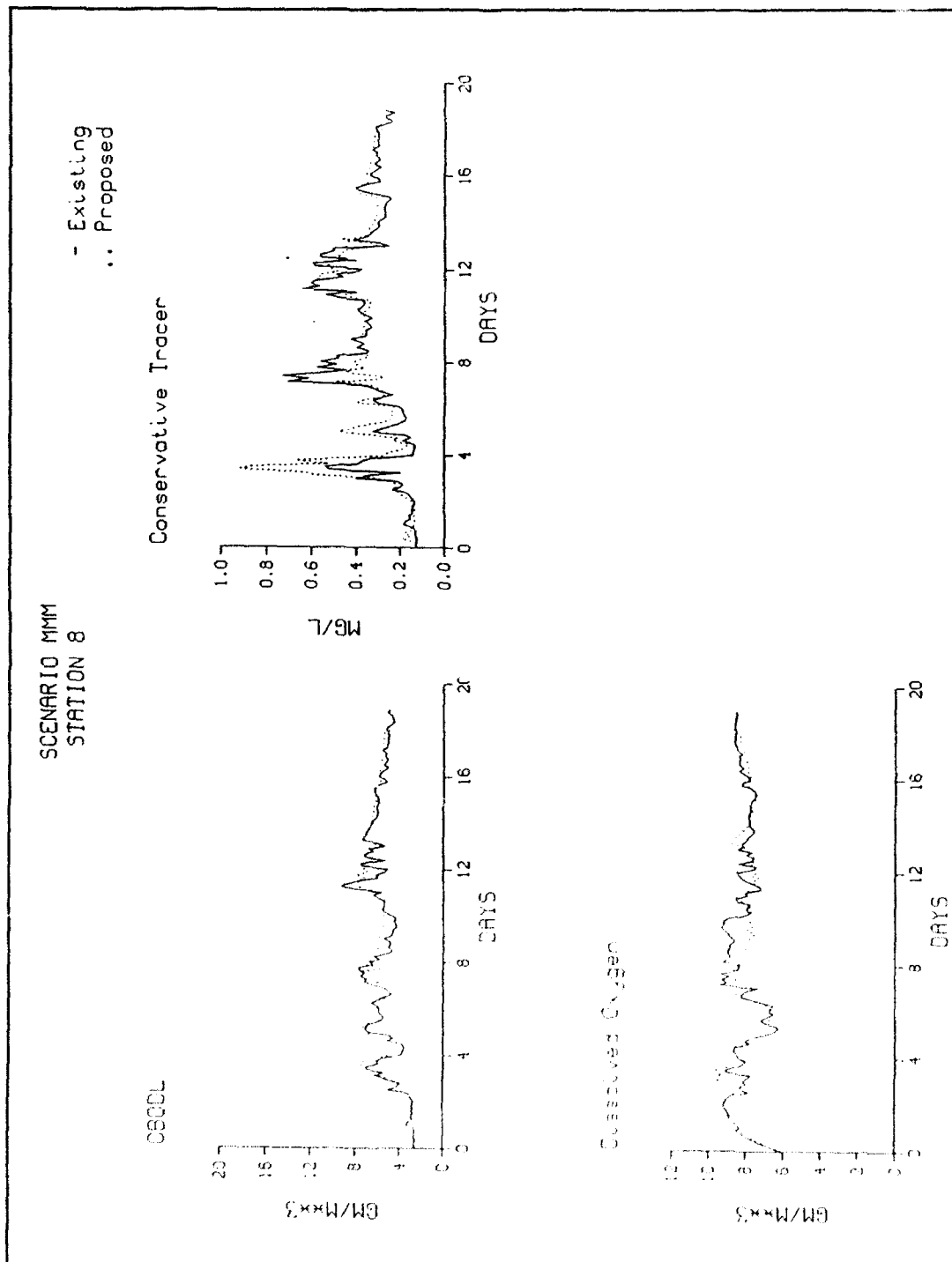


Figure D30. (Sheet 8 of 9)

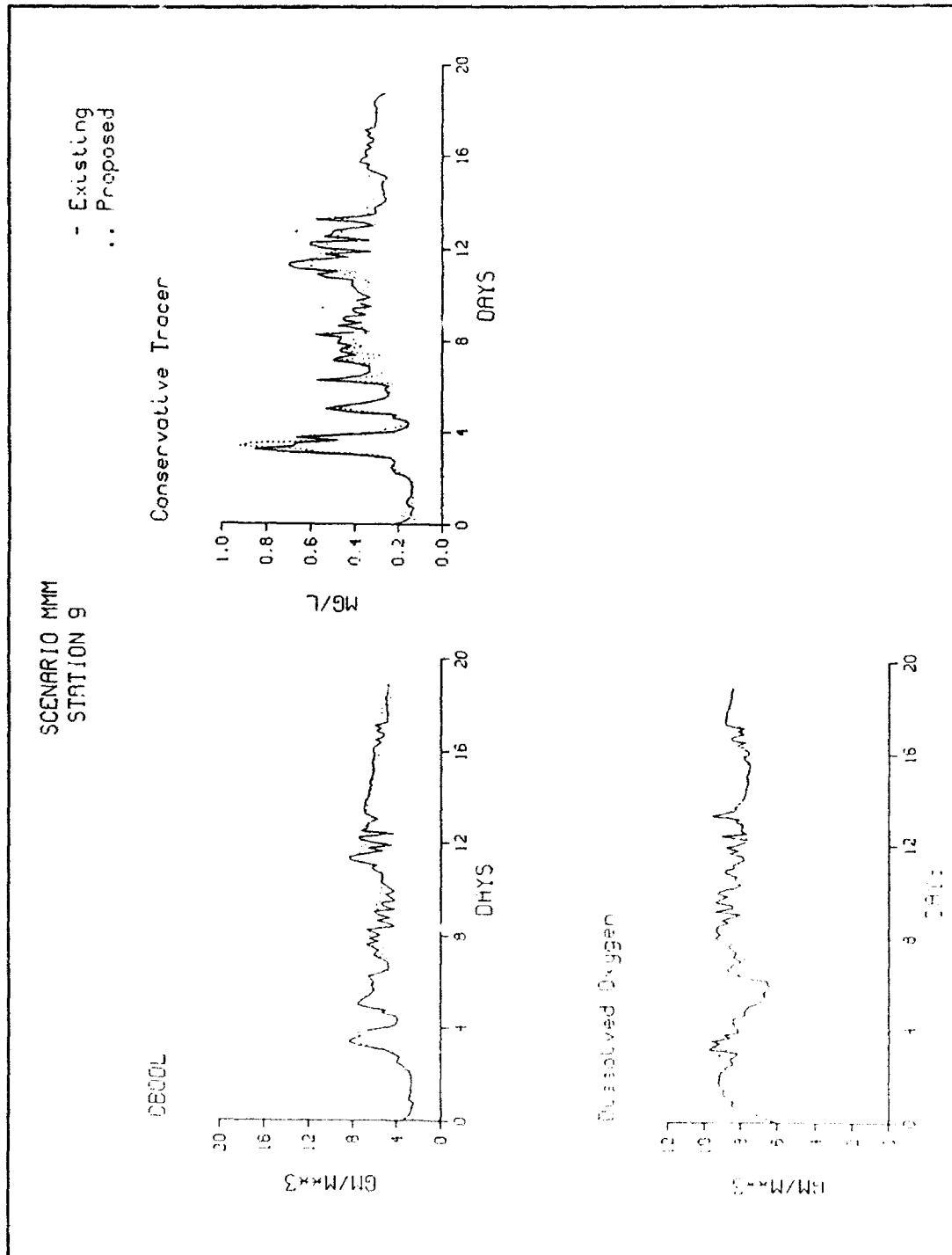


Figure D30. (Sheet 9 of 9)

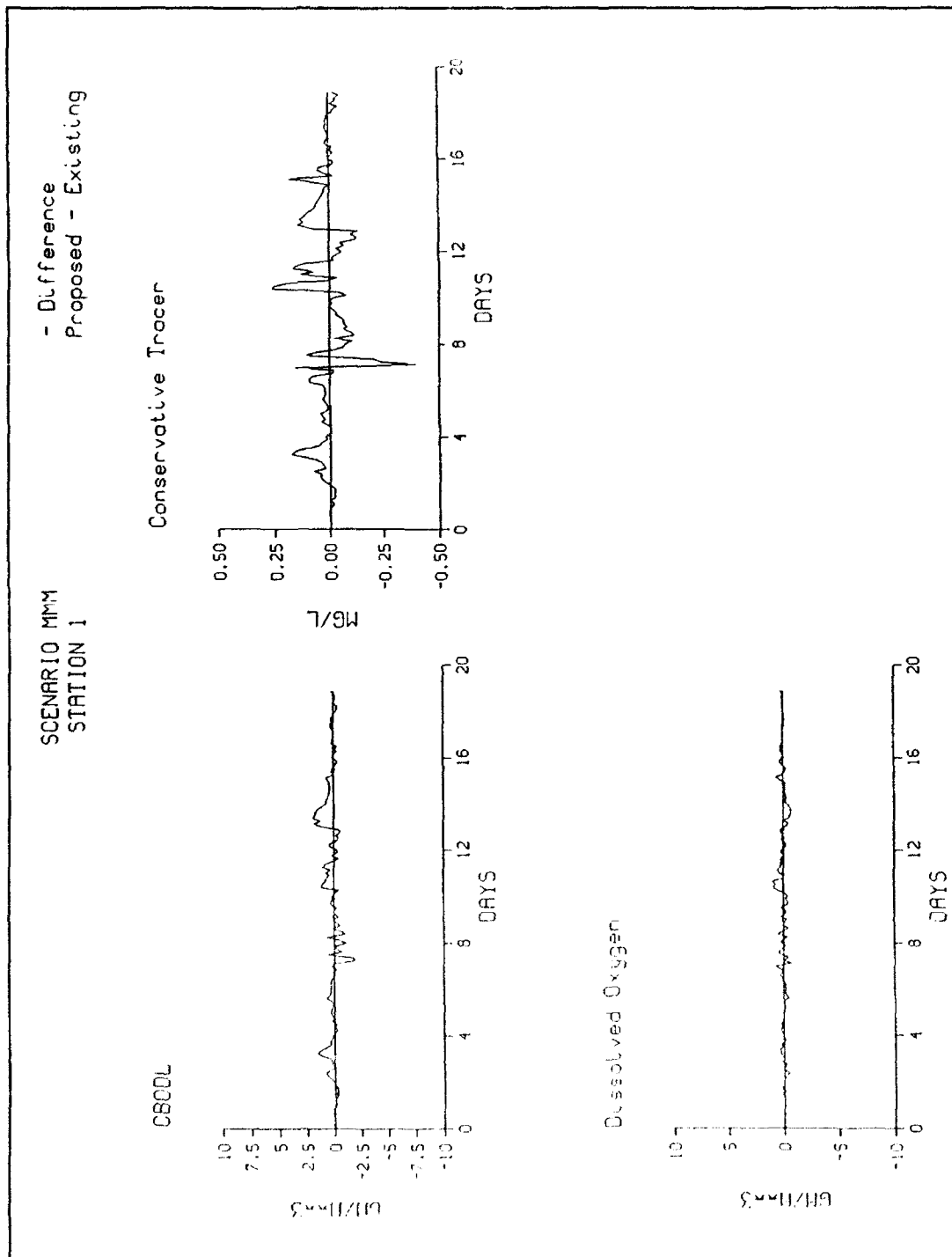


Figure D31. Time series differences for comparison stations, Scenario MMM (Sheet 1 of 8)

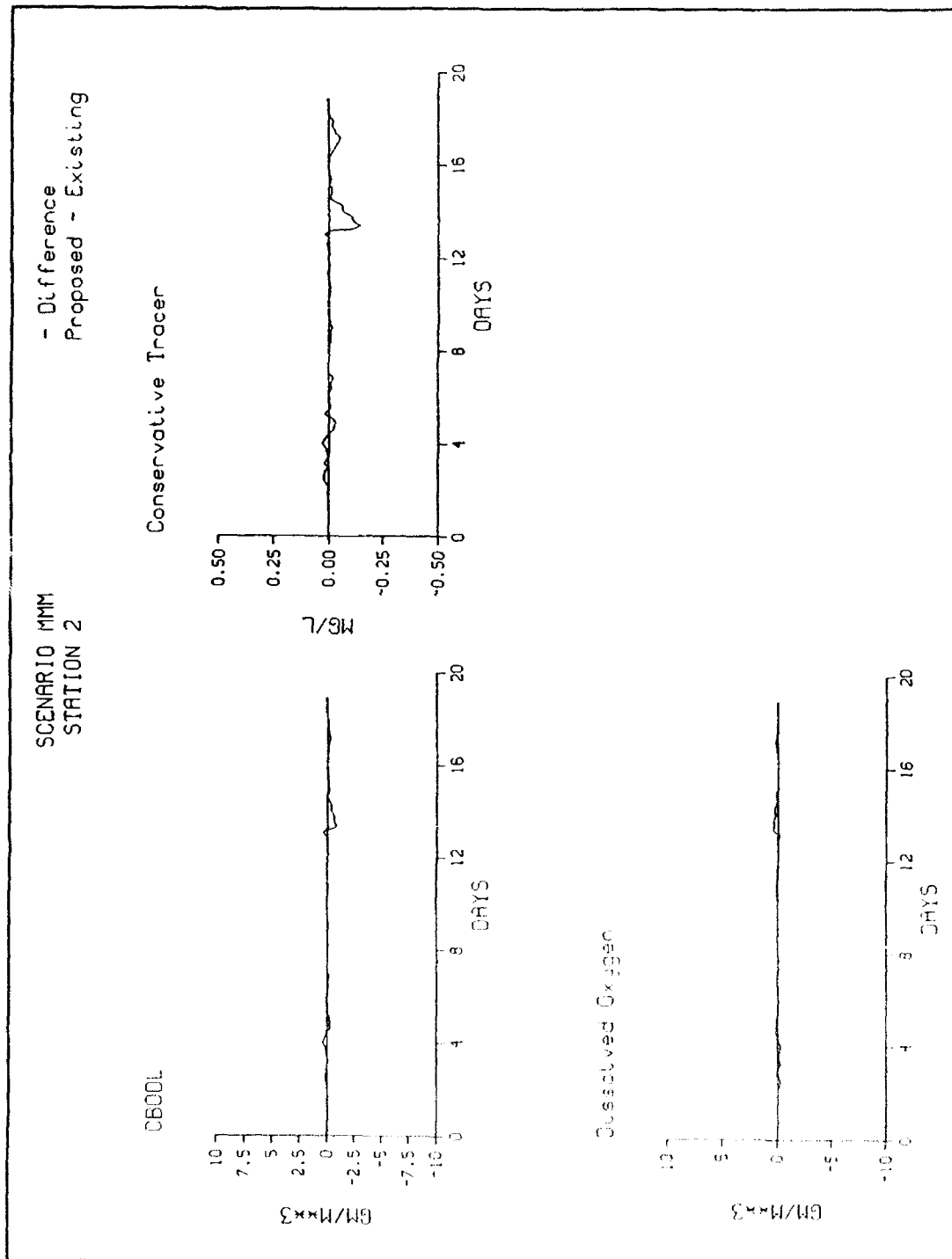


Figure D31. (Sheet 2 of 8)

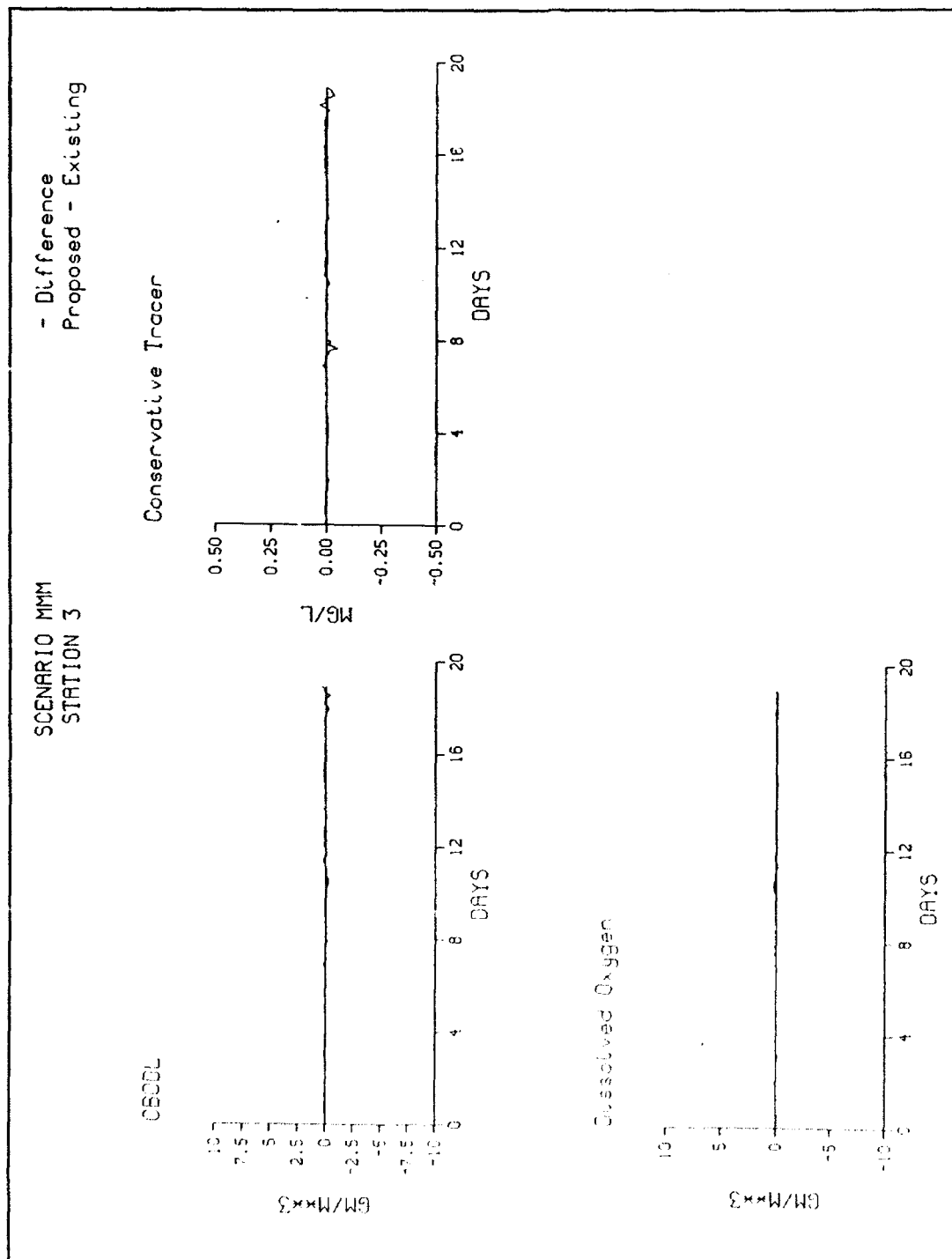


Figure D31. (Sheet 3 of 8)

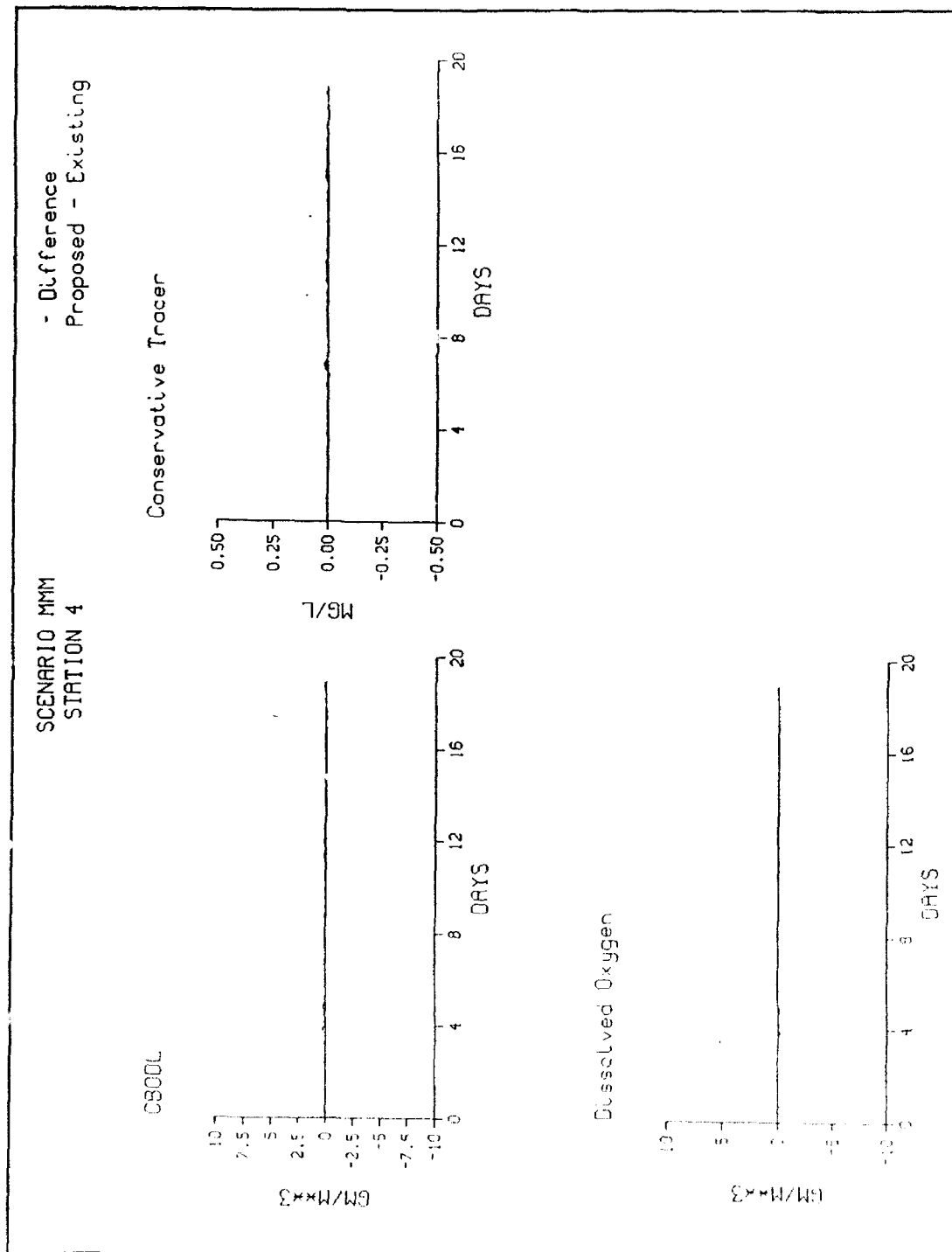


Figure D31. (Sheet 4 of 8)

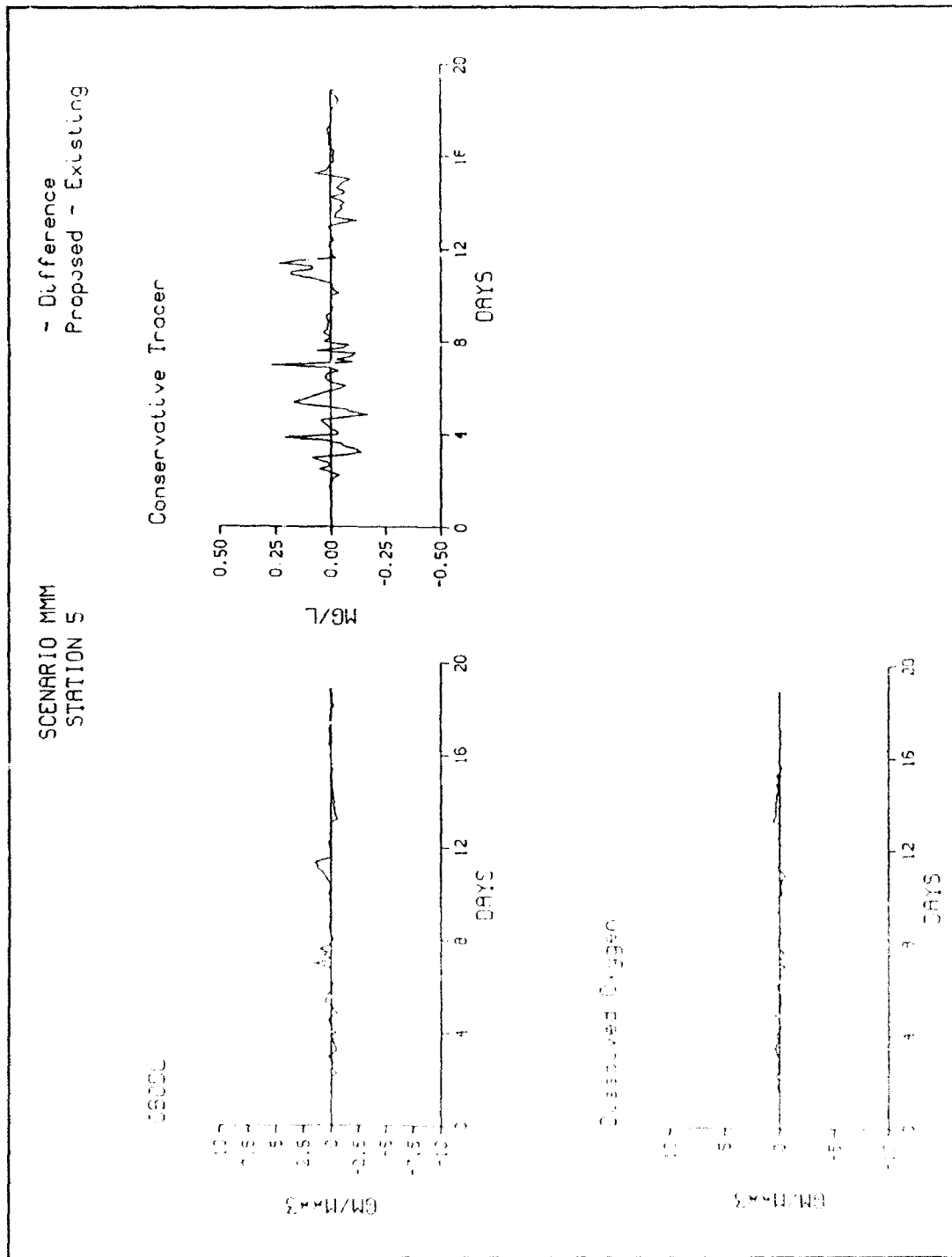


Figure D31. (Sheet 5 of 8)

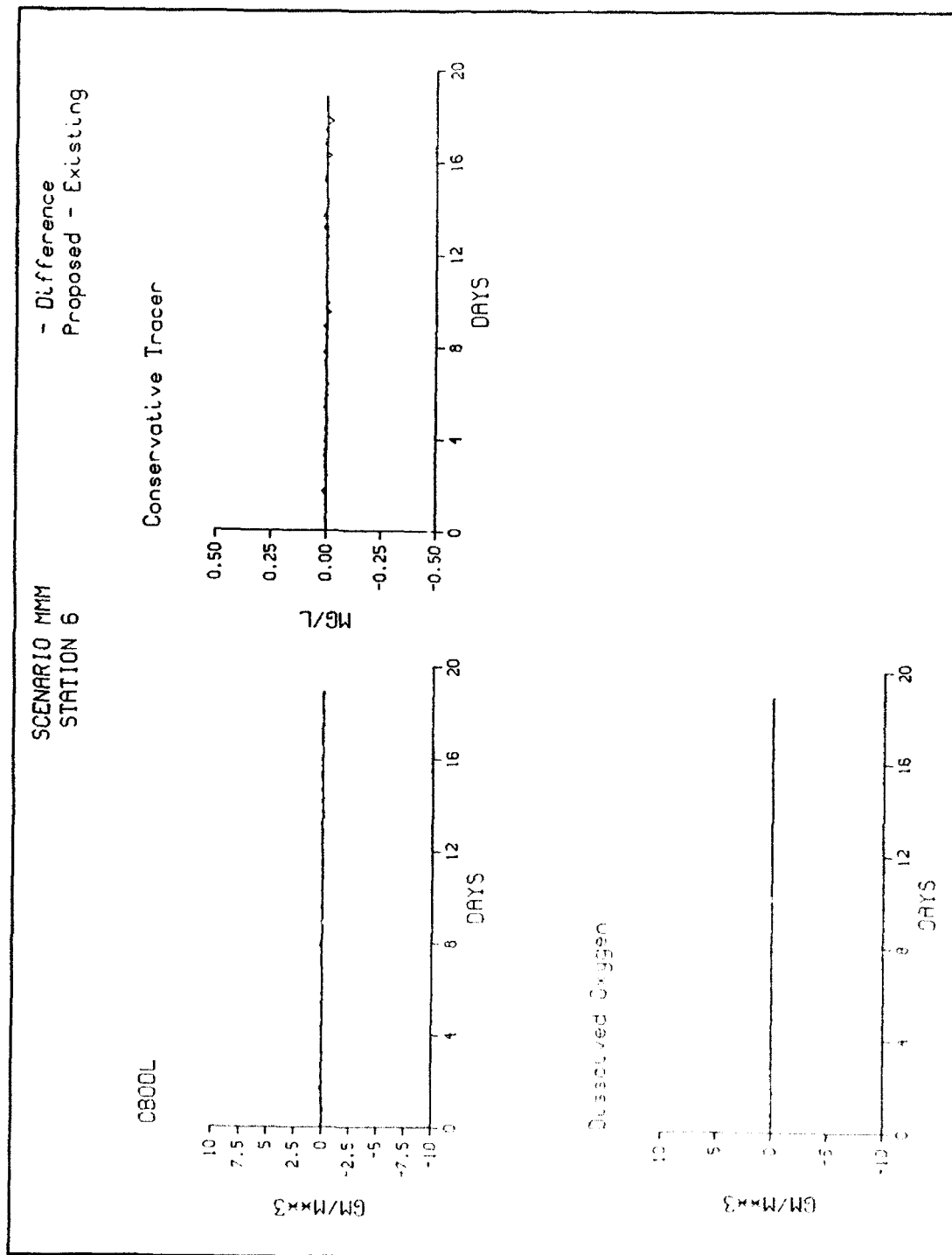


Figure D31. (Sheet 6 of 8)

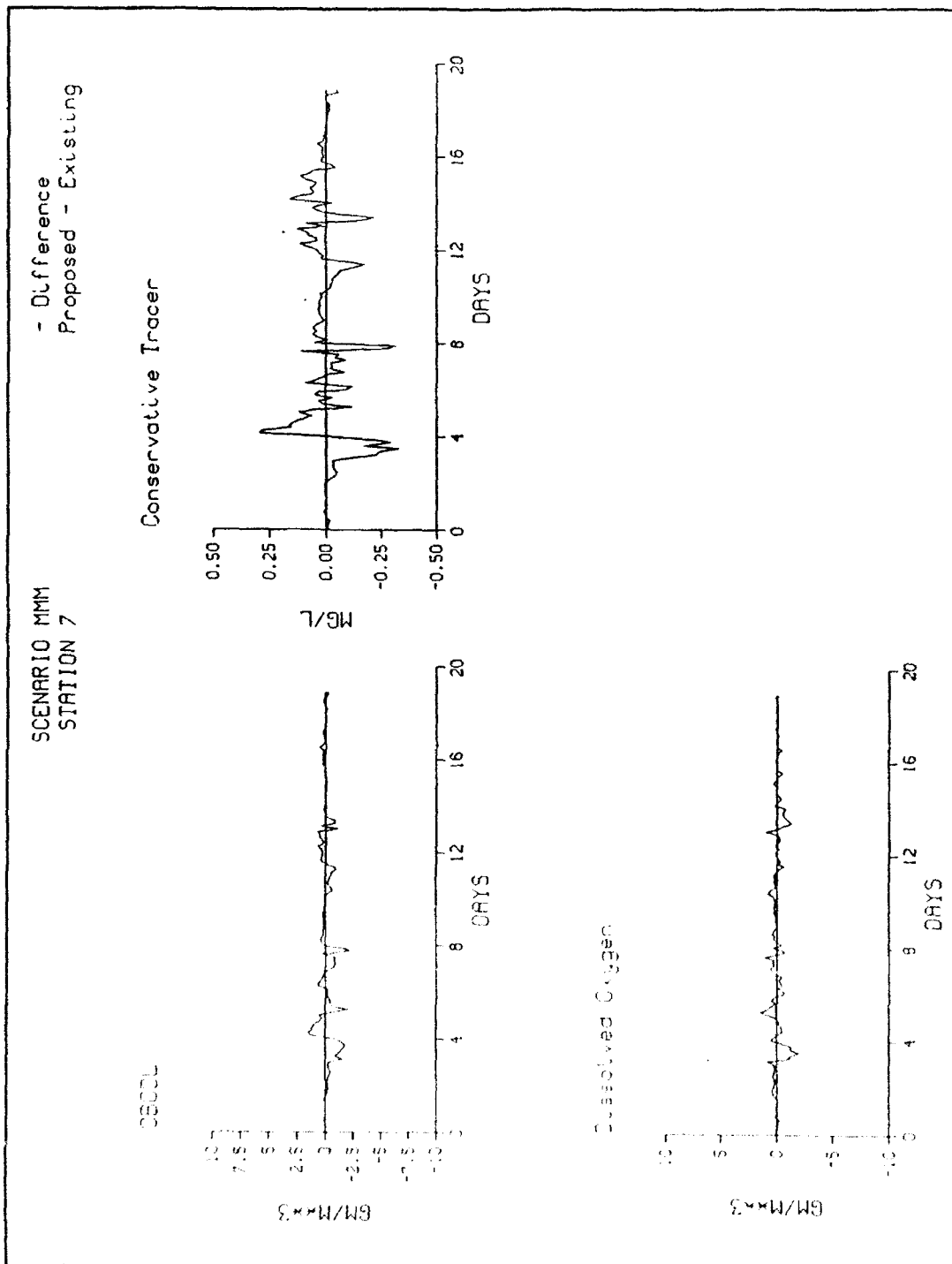


Figure D31. (Sheet 7 of 8)

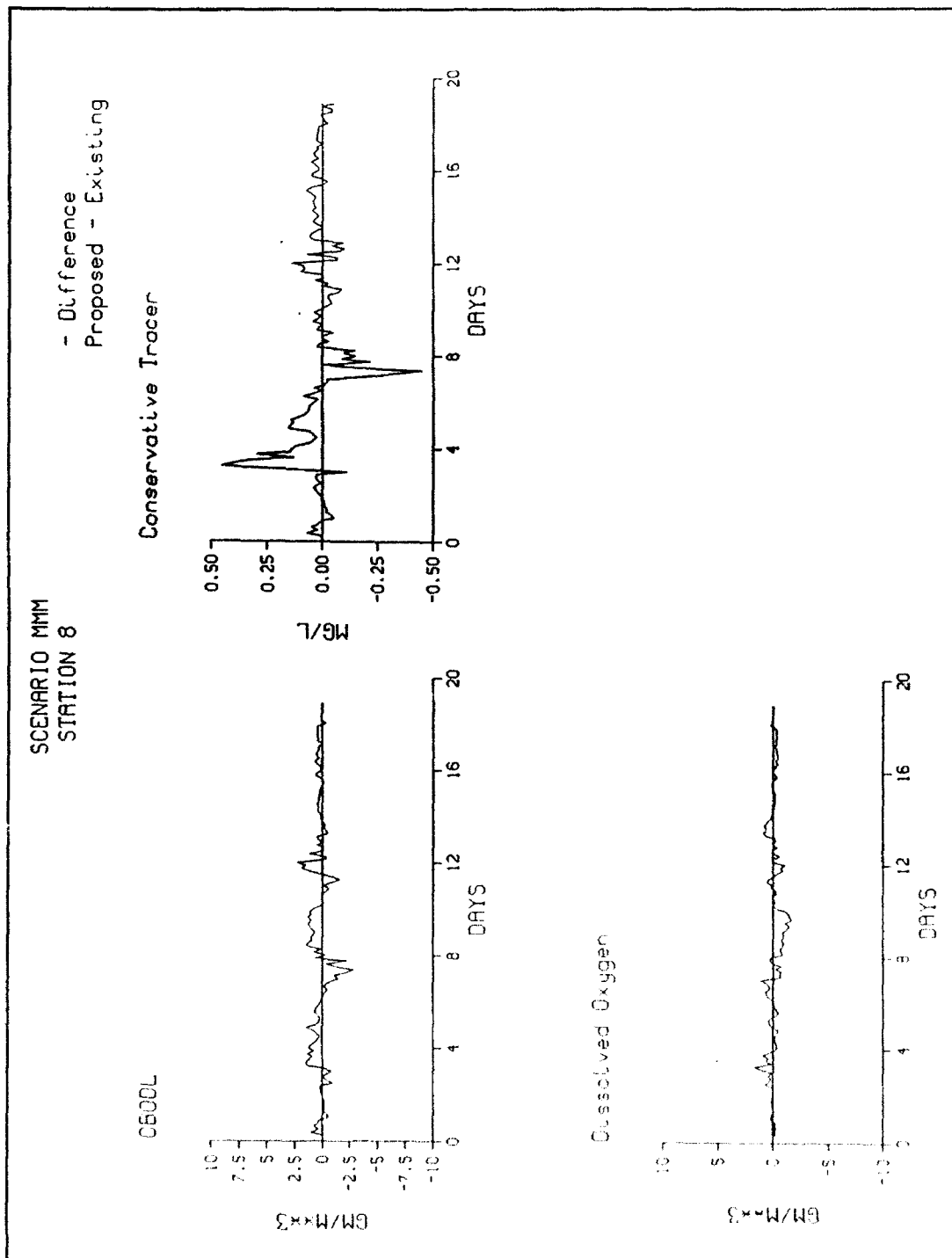


Figure D31. (Sheet 8 of 8)

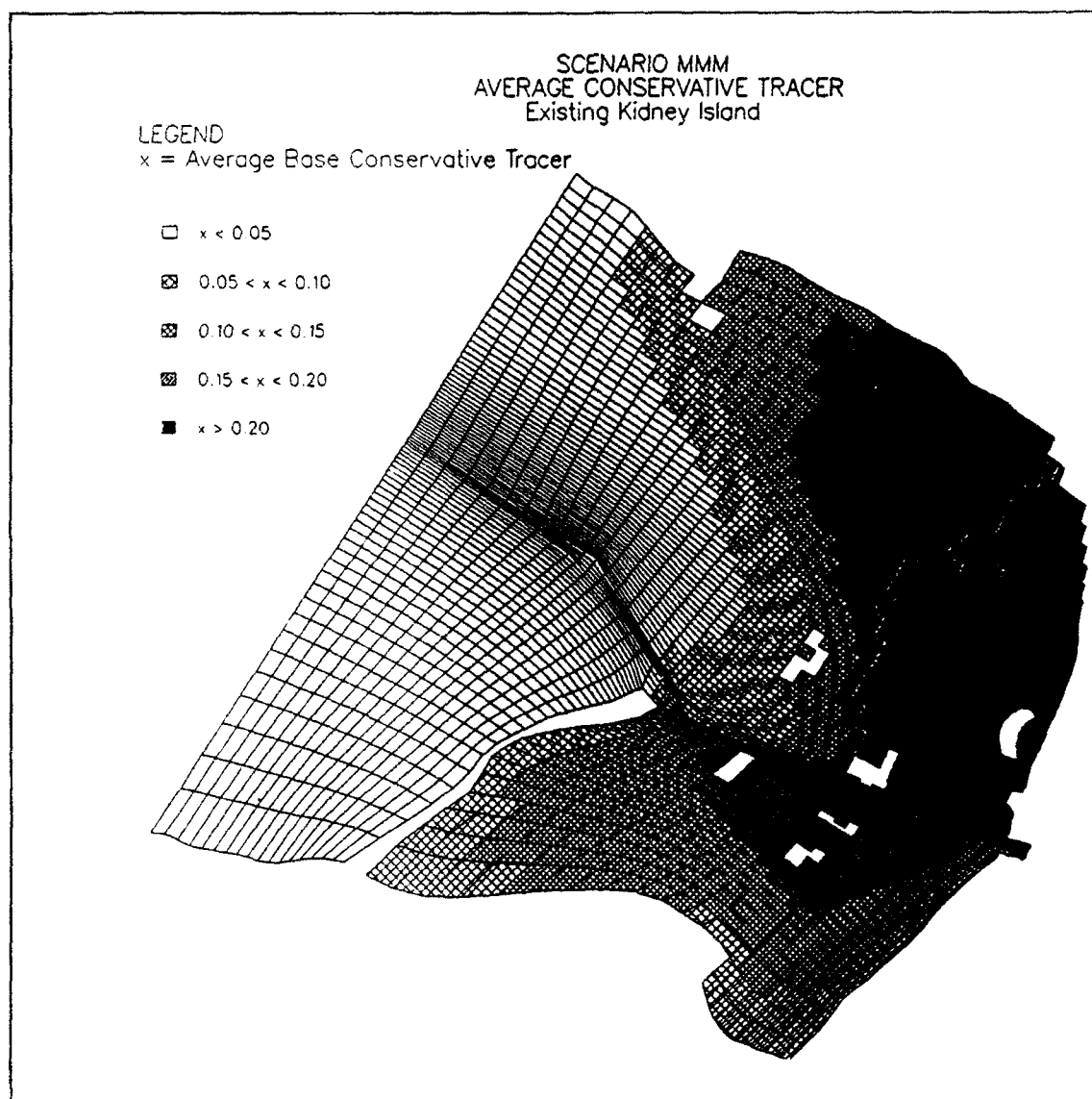


Figure D32. Average conservative tracer concentrations, Scenario MMM (Continued)

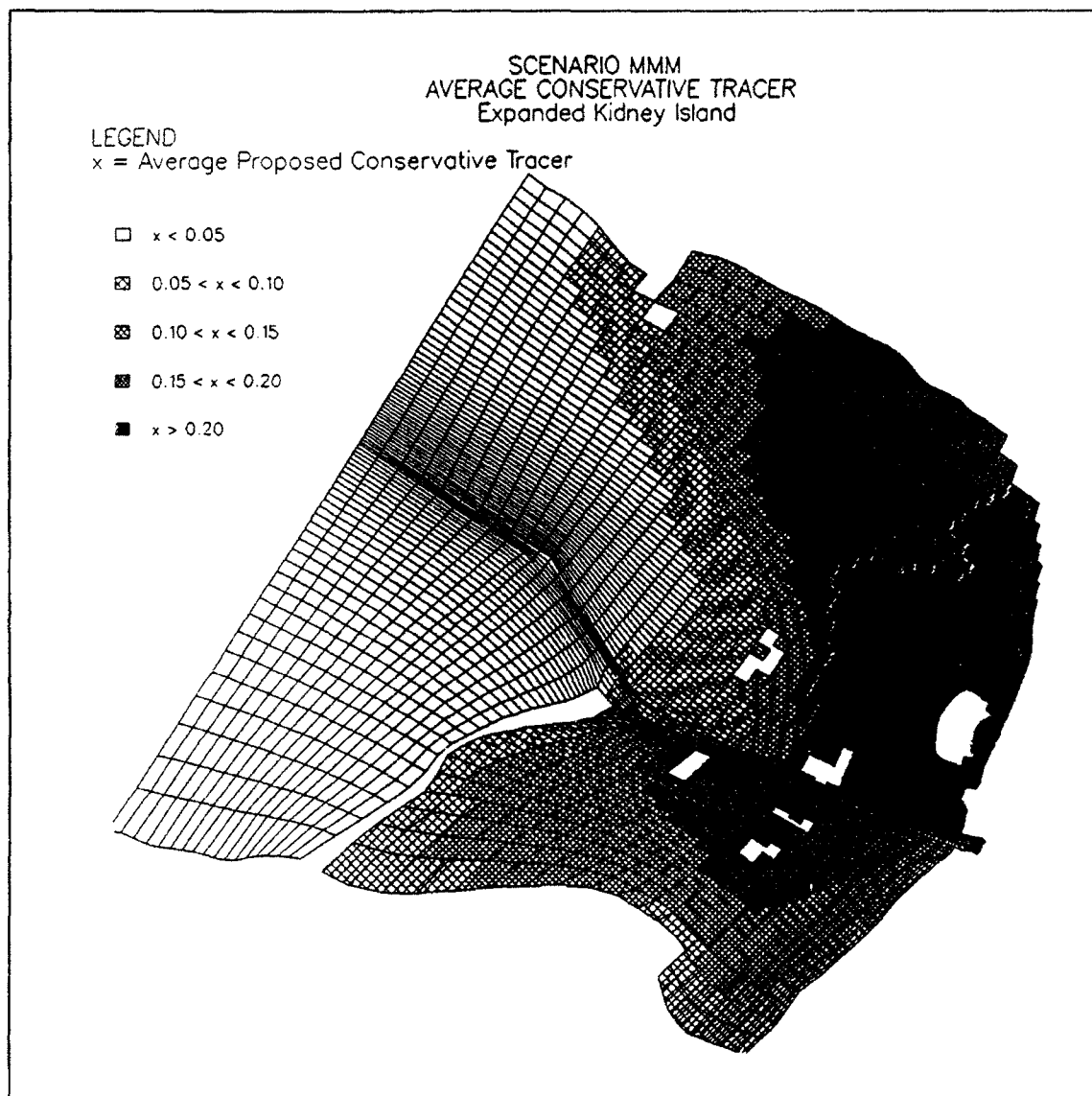


Figure D32. (Concluded)

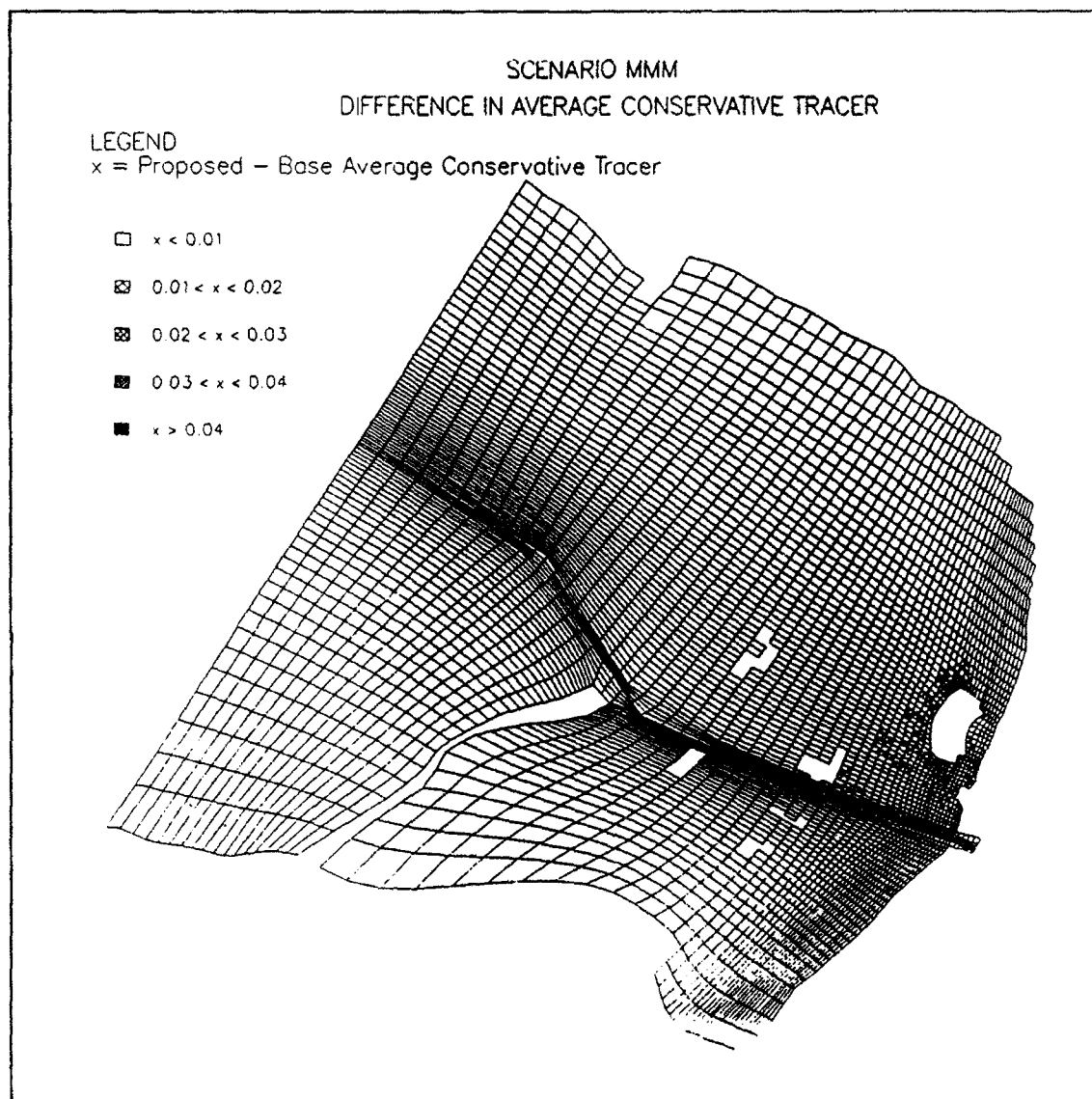


Figure D33. Difference in average conservative tracer, Scenario MMM

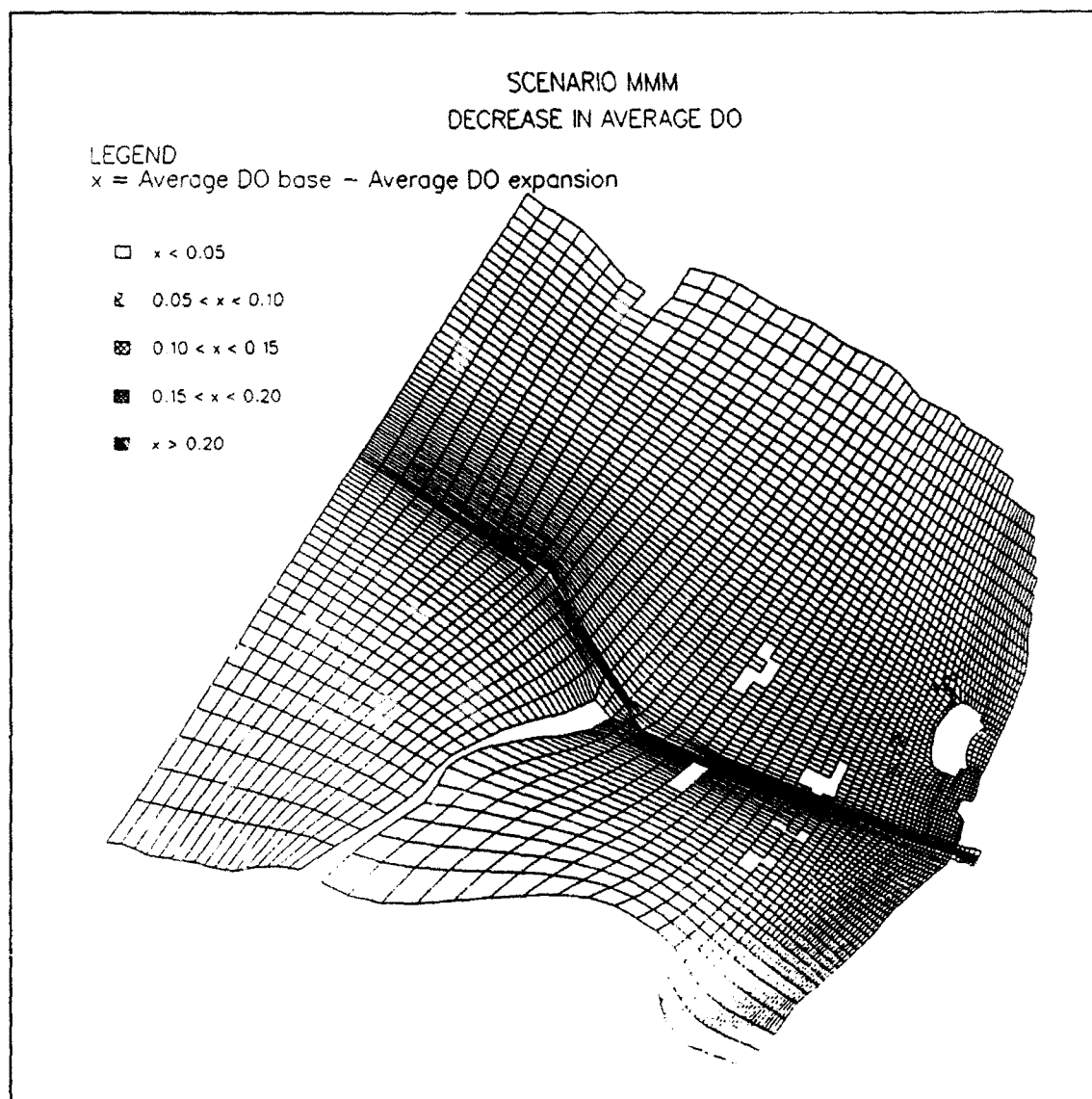


Figure D34. Decrease in average DO concentrations, Scenario MMM

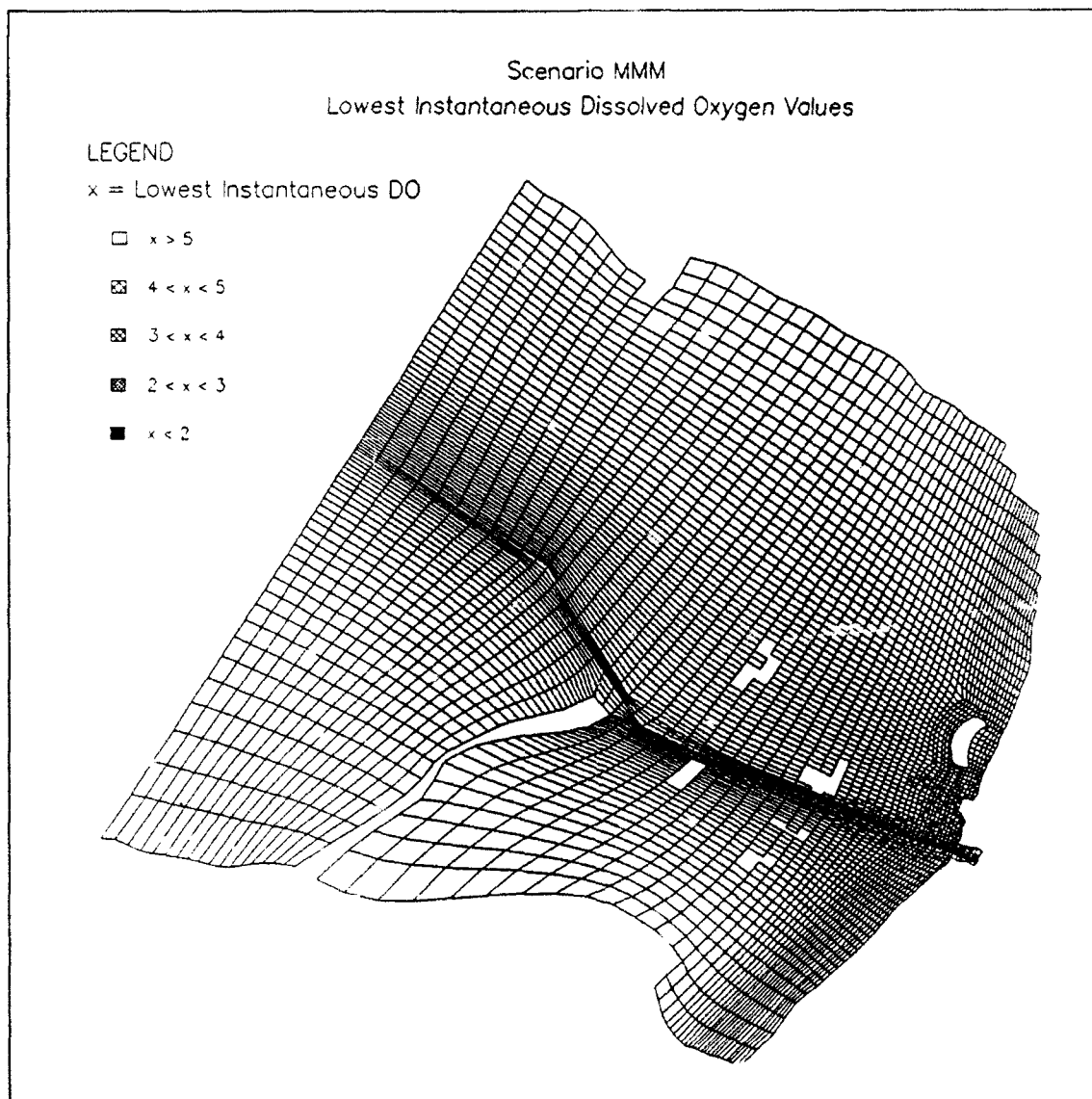


Figure D35. Lowest instantaneous DO, Scenario MMM (Continued)

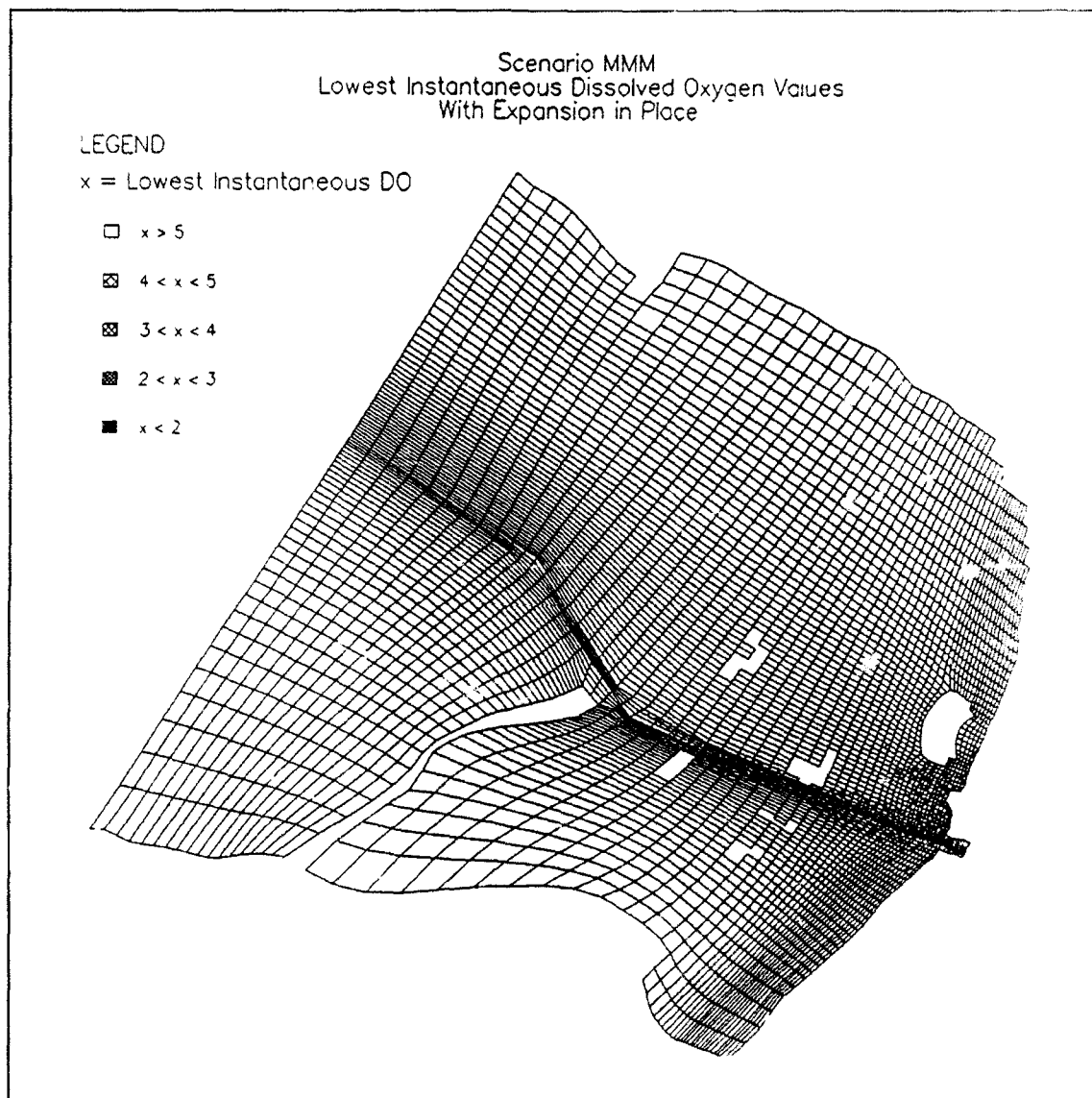


Figure D35. (Concluded)

Appendix E

DO Measurements During August 1992

Dissolved oxygen (DO) measurements were made in lower Green Bay in the vicinity of Kidney Island on five days during a two-week period of August 1992. Five stations were located on a transect stretching from the north shore through the center of Kidney Island to the open water beyond (Figure E1). Two sampling stations were located in the channel between the north shore and Kidney Island, while the other three were located on the bay side of Kidney Island. DO measurements were made 1 ft below the surface and 1 ft above the bottom at all stations. Measurements were made at 6:00 a.m., 12:00 noon, and 6:00 p.m. Depths of the five stations ranged from 5 to 8.5 ft.

Results indicated that wide fluctuations in DO occurred in both the surface and bottom waters at all sampling stations (Figures E2 and E3 and Table E1). The 6:00 a.m. measurements at all stations indicated that the DO was relatively uniform throughout the water column. DO measured 1 ft below the surface increased from the 6:00 a.m. sampling at all stations on all days and reached supersaturation levels at least once at all stations. The maximum DO recorded was 19.1 mg/L at Station D. At the same time that the DO at the surface was supersaturated, DO measured 1 ft above the bottom was generally less than one half the surface value. The supersaturated DO concentrations observed near the surface are attributed to algal photosynthesis. Possible reasons DO measurements near the bottom are lower than those at the surface could be poor mixing of bottom water with surface water and high SODs. Only at the station with the shallowest depth, Station E, was the DO near the bottom close to the DO near the surface at the time supersaturated values were observed.

The maximum DO concentrations measured 1 ft below the surface were observed during a period when the winds were low (≈ 1.5 mph), Table E2. When the winds were higher, such as on August 25, the differences between the surface and bottom DO were much smaller. The large fluctuations of these DO measurements reinforce the idea that lower Green Bay is a complex, hyper-eutrophic system.

The average of the DO measurements 1 ft below the surface at all stations is relatively high due to the supersaturated DO concentrations resulting from

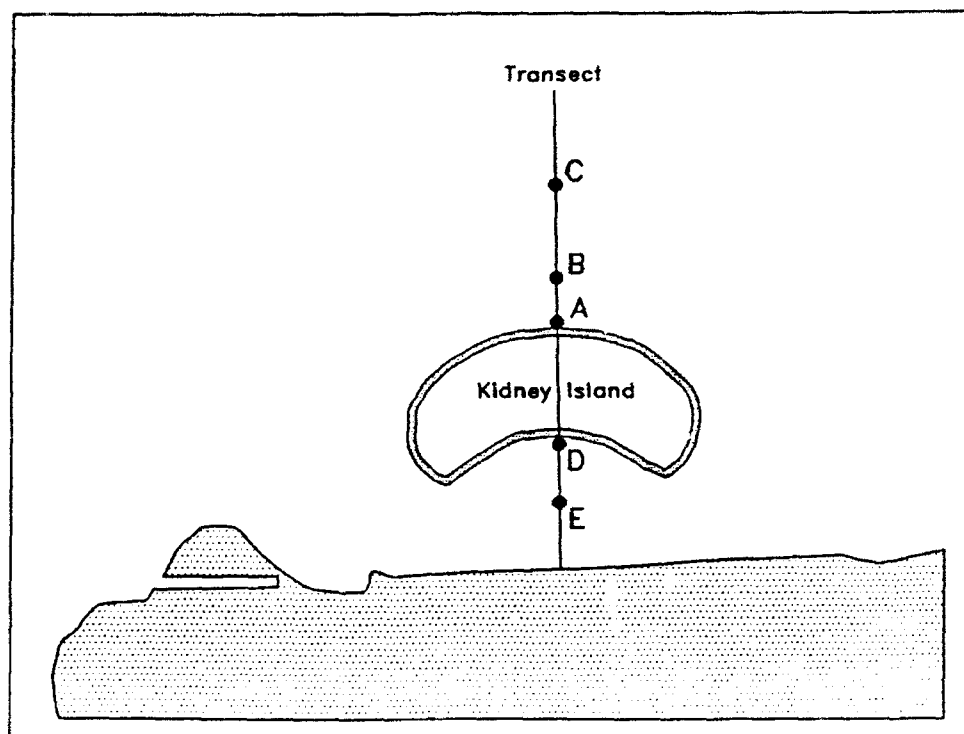


Figure E1. Location of DO monitoring stations, August 1992

algal photosynthesis. The minimum average DO 1 ft below the surface was 9.39 mg/L at Station A, which is just off the north boundary of Kidney Island. The average DO increased with distance away from this boundary (Figure E2). The average DO 1 ft below the surface at Stations D and E in the channel between the shore of Green Bay and Kidney Island was higher than the DO at the station located on the north side of Kidney Island.

The average of the DO measurements made 1 ft above the bottom indicated that the average DO along the bottom also increased with distance away from the boundary of Kidney Island. The lowest average of the DO measurements made 1 ft above the bottom was 7.51 mg/L at Station A (near the north boundary). The lower DO concentrations near the boundary of Kidney Island relative to the other stations supports the theory that DO is lower near the island boundary and increases away from the boundary. However, a statistical test of the means indicated that none of the DO means are significantly different. The greatest difference in means was for bottom measurements at Stations D and E, where the mean values of 7.79 and 8.65, respectively, are not significantly different ($P=0.22$).

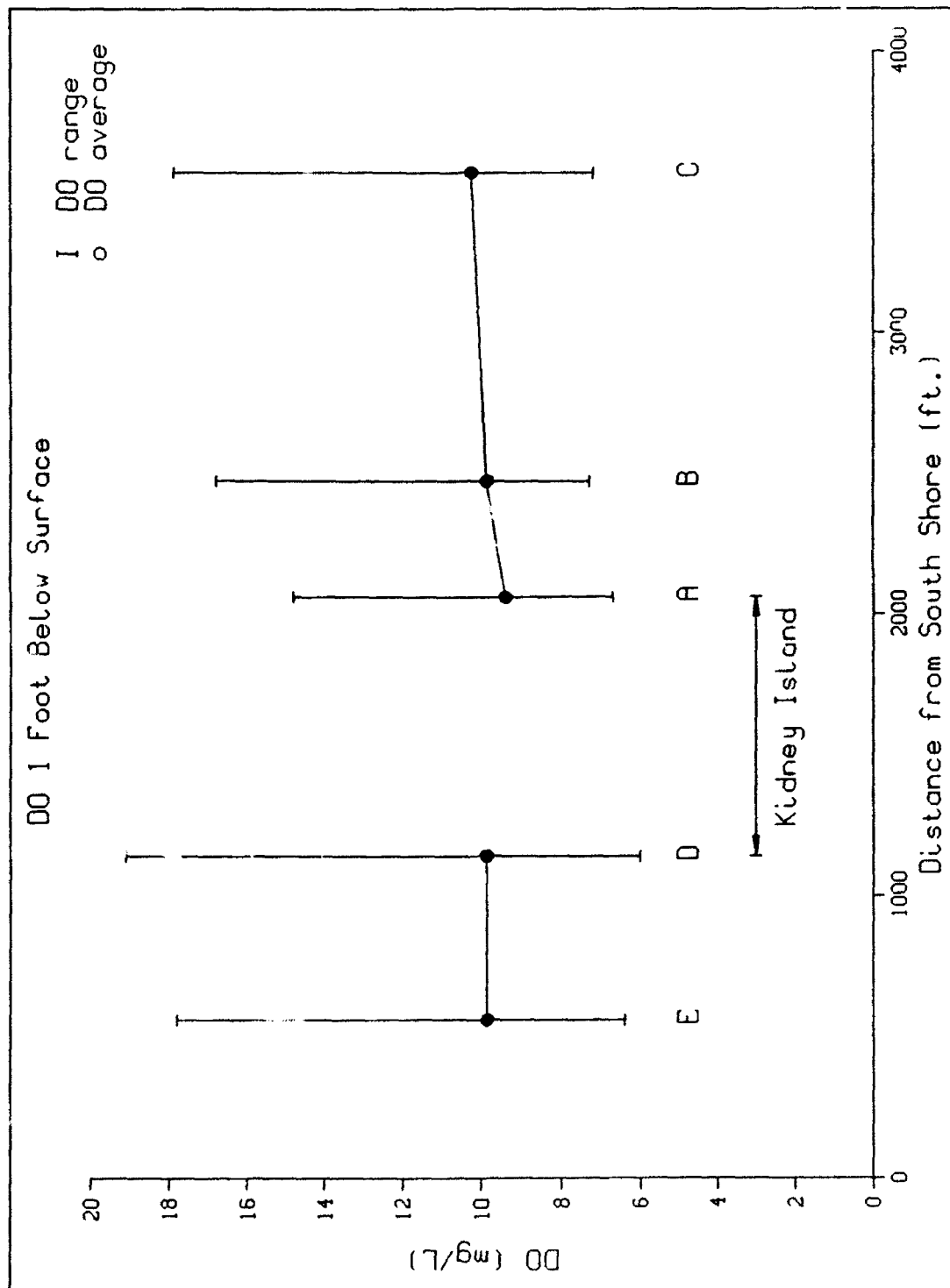


Figure E2. Average DO concentrations and variations 1 ft below the surface

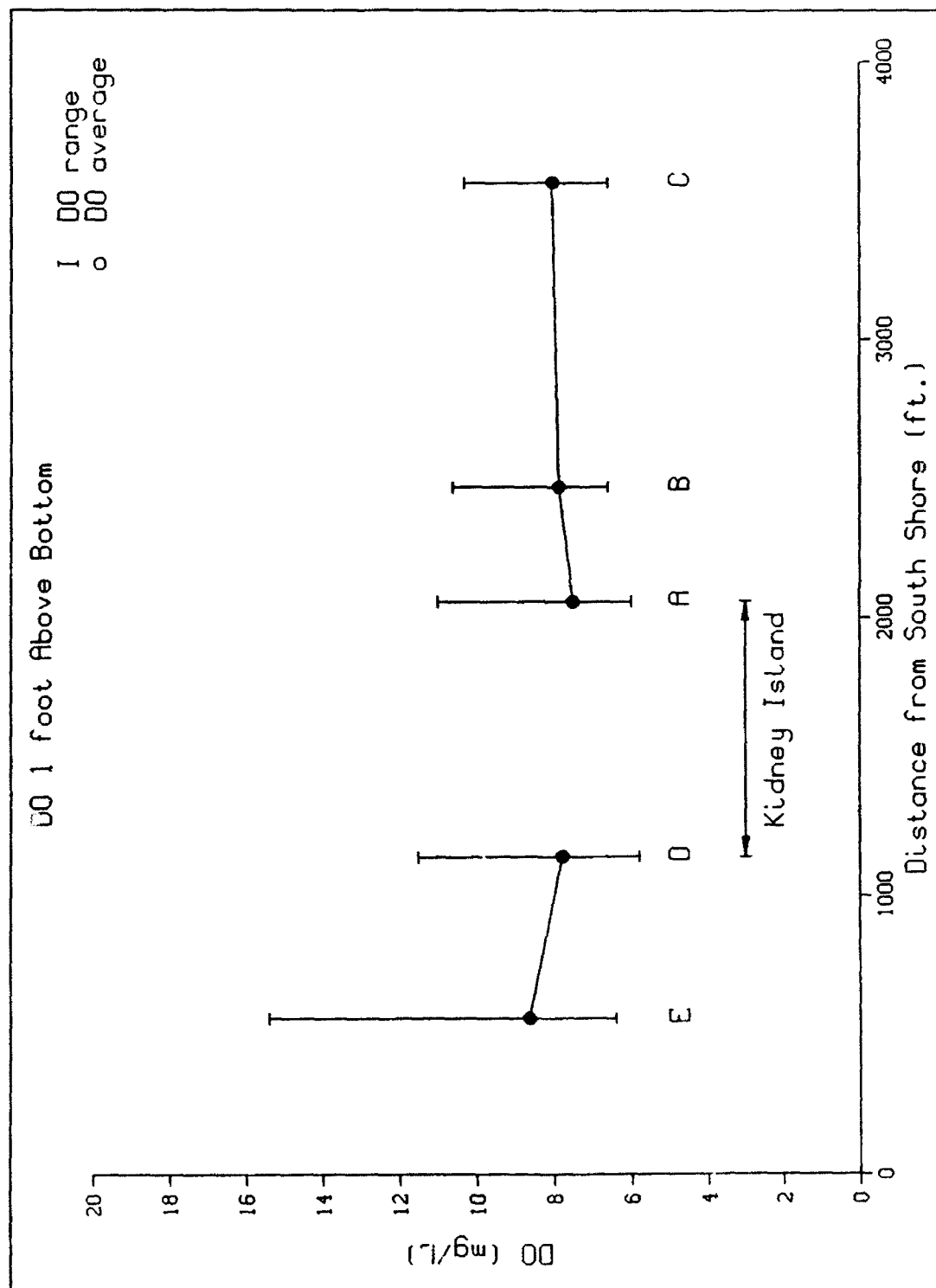


Figure E3. Average DO concentrations and variations 1 ft above the bottom

Table E1
DO (mg/L) Collected in Vicinity of Kidney Island

Date	Time	Station A		Station B		Station C		Station D		Station E	
		Upper	Lower	Upper	Lower	Upper	Lower	Upper	Lower	Upper	Lower
8-18	6:00	7.6	7.5	8.7	8.7	9.5	9.5	7.7	7.7	8.1	8.1
	12:00	10.3	9.5	10.2	8.9	10.1	9.1	9.0	8.8	9.4	8.7
	18:00	11.1	11.0	11.4	10.6	11.3	10.3	12.1	11.5	11.6	10.3
8-19	6:00	6.7	6.3	8.0	8.2	8.1	8.0	7.4	7.0	8.1	7.9
	12:00	14.8	6.3	13.6	7.4	14.7	7.7	12.2	6.4	11.5	9.0
	18:00	11.7	7.3	16.8	7.6	17.9	7.3	19.1	9.9	17.9	15.4
8-20	6:30	7.8	7.4	8.3	7.7	8.9	8.8	8.4	8.1	7.8	7.7
	12:00	12.0	6.7	11.4	6.6	13.6	7.0	12.0	6.6	11.5	10.1
	18:00	12.8	6.2	11.0	6.7	10.8	6.6	15.0	7.3	15.4	7.1
8-25	6:00	6.9	6.0	7.5	7.5	8.2	8.1	6.6	6.5	6.7	6.7
	12:00	7.3	7.1	8.0	6.9	8.8	7.5	8.4	8.1	8.1	8.0
	18:00	8.8	6.6	9.2	8.0	9.3	8.3	7.9	7.4	8.9	8.0
8-26	6:00	7.3	7.2	7.3	7.2	7.2	7.0	6.0	5.8	6.4	6.4
	12:00	7.4	7.3	7.6	7.5	7.3	7.2	7.0	6.7	7.5	7.4
	18:00	8.4	8.3	8.7	8.6	8.0	8.0	9.1	9.0	9.0	8.9

Table E2 Wind Speeds Recorded at Bay Beach, Green Bay			
Date	Time	Hourly Wind Speed (mph)	Daily Average Wind Speed (mph)
8-18	6:00	3.8	2.9
	12:00	1.5	
	18:00	1.5	
8-19	6:00	1.5	2.4
	12:00	1.5	
	18:00	1.5	
8-20	6:00	4.1	4.4
	12:00	1.5	
	18:00	5.9	
8-25	6:00	5.8	6.1
	12:00	9.1	
	18:00	1.5	
8-26	6:00	6.8	3.4
	12:00	1.5	
	18:00	1.5	

REPORT DOCUMENTATION PAGE			Form Approved OMB No. 0704-0188	
Public reporting burden for this collection of information is estimated to average 1 hour per response, including the time for reviewing instructions, searching existing data sources, gathering and maintaining the data needed, and completing and reviewing the collection of information. Send comments regarding this burden estimate or any other aspect of this collection of information, including suggestions for reducing this burden, to Washington Headquarters Services, Directorate for Information Operations and Reports, 1215 Jefferson Davis Highway, Suite 1204, Arlington, VA 22202-4302, and to the Office of Management and Budget, Paperwork Reduction Project (0704-0188), Washington, DC 20503.				
1. AGENCY USE ONLY (Leave blank)		2. REPORT DATE September 1993		3. REPORT TYPE AND DATES COVERED Final report
4. TITLE AND SUBTITLE Hydrodynamic and Water Quality Modeling of Lower Green Bay, Wisconsin; Volume I: Main Text and Appendixes A-E			5. FUNDING NUMBERS	
6. AUTHOR(S) David J. Mark, Norman W. Scheffner, H. Lee Butler Barry W. Bunch, Mark S. Dortch				
7. PERFORMING ORGANIZATION NAME(S) AND ADDRESS(ES) USAE Waterways Experiment Station, Coastal Engineering Research Center and Environmental Laboratory, 3909 Halls Ferry Road, Vicksburg, MS 39180-6199			8. PERFORMING ORGANIZATION REPORT NUMBER Technical Report CERC-93-16	
9. SPONSORING/MONITORING AGENCY NAME(S) AND ADDRESS(ES) U.S. Army Engineer District, Detroit MI 48231-1027			10. SPONSORING/MONITORING AGENCY REPORT NUMBER	
11. SUPPLEMENTARY NOTES Available from National Technical Information Service, 5285 Port Royal Road, Springfield, VA 22161				
12a. DISTRIBUTION/AVAILABILITY STATEMENT Approved for public release; distribution is unlimited.			12b. DISTRIBUTION CODE	
13. ABSTRACT (Maximum 200 words) A confined disposal facility (CDF) for dredged material presently exists in lower Green Bay, Wisconsin. A planned expansion of the CDF was studied to assess its impact on current patterns and subsequent redistribution of dissolved oxygen in the immediate vicinity of the proposed expansion. The redistribution is, in part, dependent on the magnitude and direction of currents generated by storm-induced seiches occurring in Lake Michigan and within the bay itself. Two-dimensional, vertically averaged hydrodynamic and water quality models were applied to make this assessment by investigating the spatial and temporal variations in dissolved oxygen concentrations for existing and proposed configurations. Field data collected over three summers were used for calibrating and validating the hydrodynamic model. The water quality model was calibrated with field data collected over one summer. Results and conclusions of the modeling effort are summarized in this report.				
14. SUBJECT TERMS Circulation Dissolved oxygen Great Lakes Green Bay Seiche Water quality			15. NUMBER OF PAGES 371	
			16. PRICE CODE	
17. SECURITY CLASSIFICATION OF REPORT UNCLASSIFIED	18. SECURITY CLASSIFICATION OF THIS PAGE UNCLASSIFIED	19. SECURITY CLASSIFICATION OF ABSTRACT	20. LIMITATION OF ABSTRACT	